Repair of Fatigue Cracks in Steel Members Using Adhesively Bonded Carbon Fiber Reinforced Polymers (CFRP)

by

Syed Salman Mobeen

A thesis submitted in partial fulfillment of the requirements for the degree of

Doctor of Philosophy

In

Structural Engineering

Department of Civil and Environmental Engineering
University of Alberta

Abstract

Bonding fiber reinforced polymer (FRP) composites is emerging as an alternative to the fatigue crack repair techniques because of its several advantages over the conventional fatigue crack repair methods and materials. Its major advantages include its higher stiffness and strength, choice of directional stiffness or strength, high strength-to-weight ratio and ease of application. Most of the previous research work on the use of FRP in repair of fatigue cracks exists mostly in the repair of aluminum, its alloys, and concrete/masonry members but the use of FRP in repair of steel members and its related research work is limited.

In current research work an attempt has been made to study in-depth the use of FRP in repair of fatigue cracks in steel members. More emphasis was put on the impact of bonded patch delamination on the stress intensity factor (SIF), which is a governing parameter for prediction of fatigue crack growth. It was so because most of the available research works on the repair of fatigue crack in steel structures using bonded FRP or CFRP patches showed the governing failure mode of such repairs as the progressive delamination of the FRP patch from the steel plate. Therefore, initial part of current research work focused on studying the impact of different patch parameters on initiation of the FRP patch delamination. It followed by the study of the impact of patch delamination on SIF at crack tip of the repaired plate. Properties of the interface adhesive layer were found to be affecting the interface stress distribution and its failure under high shear stress around the crack was found to be enhancing the SIF at the crack tip of repaired plate. Adhesive shear stiffness (G_A/t_A) was found to be the governing parameter in controlling the interface shear stress distribution near the crack, instead of adhesive thickness (t_A) or modulus (E_A) alone, within identical ETR repairs. ETR is the relative axial stiffness of bonded patch to the steel plate. It was also found, from the results of a numerical study of impact of patch delamination, that a stiffer CFRP patch could become less effective than a less stiff patch, if it delaminates more because of weaker adhesive.

An experimental phase was also carried out to study the fatigue behavior of CFRP repaired edge-cracked steel plates under constant amplitude fatigue cycles. Its results showed that all the specimens were failed in the progressive patch delamination mode, but, the delamination

itself found to be initiated from either the patch-end or from the near-crack locations. Specimens failed by the governing patch-end delamination achieved short and unexpected fatigue life while the specimens failed by the near-crack delamination achieved higher fatigue life. A methodology was developed to predict fatigue life of the edge-cracked steel plates, repaired with double sided bonded CFRP patches, incorporating the impact of patch delamination. It mainly included the use of linear elastic fracture mechanics (LEFM) to predict the fatigue life of cracked steel plates, but modified for the presence of bonded CFRP patch by including the numerically developed geometric factors ($f_{a/b}$) in the governing LEFM equations. The geometric factors were developed using finite element analysis of the cracked steel plate with bonded CFRP patches, incorporating the impact of patch delamination, through modelling of the adhesive shear failure. The developed methodology predicted well fatigue life of the tested specimens, failed by the near-crack patch delamination. Fatigue life of specimens failed in the governing patch-end delamination failure mode could not be predicted with the developed methodology, because of less sensitivity of the SIF or geometric factors on patch-end delamination.

After validating the developed methodology from the experimental results, an extensive parametric study was carried out to develop the geometric factors ($f_{a/b}$), which could be used to predict the fatigue life of cracked steel plates, repaired with double sided bonded CFRP patches, having different patch properties. These geometric factors were developed for the two more common cases of edge crack and central crack steel plates, and these were also incorporating the impact of patch delamination around the crack. The developed geometric factors were based upon the patch ETR, adhesive shear stiffness (G_A/t_A) and the shear strength of adhesive (τ).

Acknowledgement

I would like to thank my supervisor Dr. J. J. Roger Cheng for his intense support and advice, provided throughout the research program. He used to be a good supervisor as well as the one providing moral support at difficult stages of the research.

I would also like to acknowledge the technical support and assistance provided by the technologists Greg Miller and Cameron West of the I. F. Morrison Structural Laboratory at the University of Alberta in conducting the experimental phase of the current research.

Table of Contents

5. Experimental study of fatigue life evaluation of repaired steel plate with varying patch properties

6. Numerical evaluation of fatigue life of the tested specimens

7. Parametric study and the development of geometric factors

List of Tables

List of Figures

List of Symbols and Notations

a	=	Crack length
a_i	=	Initial crack length
a_f	=	final crack length
b	=	Plate width
C	=	material constant use in Paris equation
CFRP	=	Carbon fiber reinforced polymers
COD	=	Crack opening displacement
da/dN	=	crack growth rate with number of fatigue cycles N
da_i	=	local crack growth increment at an arbitrary point i
E	=	Modulus of elasticity
E_{frp}	=	elastic modulus of CFRP / FRP composite
E_a	=	elastic modulus of adhesive
E_s	=	elastic modulus of steel plate
ETR	=	Bonded patch axial stiffness or its effective thickness ratio ($E_{frp}\ t_{frp}$ / $E_s\ t_s$)
FEA	=	Finite element analysis
FEM	=	Finite element model
FRC	=	Fiber reinforced composites
FRP	=	Fiber reinforced polymers
$f_{(a/b)}$	=	Geometric correction factor
G	=	Shear modulus
G_A	=	Shear modulus of adhesive
HM	=	Higher modulus

J	=	J-integral
K_I	=	stress intensive factor for mode I (Crack Opening Mode)
K_{Imax}	=	Value of K_I corresponding to the maximum stress σ_{max}
ΔK	=	stress intensity factor range
ΔK_{eff}	=	Effective stress intensity factor range
L	=	No. of CFRP layers on each face of steel plate
LM	=	Lower modulus
m	=	material constant use in Paris equation
N	=	Number of fatigue cycle
n	=	Number of layer of CFRP sheet
R	=	Stress ratio (σ_{min} / σ_{max})
SIF	=	stress intensity factor (MPa$\sqrt{m}$)
t_{frp}	=	thickness of CFRP / FRP composite
t_A	=	Thickness of adhesive layer
t_s	=	thickness of cracked steel plate
u_A	=	displacements of adhesive along longitudinal direction
u_{frp}	=	displacements of FRP along longitudinal direction
u_s	=	displacement of steel plate along longitudinal direction
v_A	=	displacements of adhesive along the width of plate
v_{frp}	=	displacements of FRP along the width of plate
v_s	=	displacement of steel plate along the width of plate
w_A	=	displacements of adhesive along the thickness plate
w_{frp}	=	displacements of FRP along the thickness plate
w_s	=	displacement of steel plate along the thickness plate

W	=	Strain energy density
T	=	Traction vector
β	=	geometry correction factor
ϵ	=	axial strain
$\acute{\Gamma}$	=	arbitrary contour surrounding the crack tip
τ	=	shear strain
ν	=	Poisson's ratio
σ	=	axial stress / applied far field axial stress
σ_o	=	Crack opening stress
$\Delta\sigma$	=	Applied stress range
σ_{max}	=	maximum applied stress
σ_{min}	=	minimum applied stress
σ_{xx}	=	normal stress field at crack tip along x direction
σ_{yy}	=	normal stress field at crack tip along y direction
τ	=	shear strength of adhesive

1. Introduction

1.1 Back ground

Fatigue strength or fatigue life is important for structural elements subjected to repeated loads, like an aircraft under excessive and repeated wind pressure, a ship under repeated wave loading, or a bridge girder under repeated traffic loads, etc. The repeated loading, even with lesser applied stress than needed to cause static yielding or failure, can originate fatigue cracks from regions of high stress concentration, like the geometric offsets, surface flaws, macroscopic, and microscopic defects, etc. Once fatigue crack forms, it can grow into bigger crack, under the applied repeated loading, and its presence in a structural framing system can reduce the system stiffness and its overall load carrying capacity. Additionally, it can also affect the serviceability conditions of the system. If proper repair or retrofit is not applied in the early stages to the crack then there would be a great risk of crack growth. The crack size could grow and reach the critical crack size because fatigue crack growth varies exponentially with the applied load cycles in most metals, which can then trigger sudden fracture or collapse of the cracked structural element or the whole structure.

Examples of some historic fatigue failures includes failure of Comet aircrafts (1949 to 1952), due to origination of crack from their square window corners and reaching the critical size in a very short time, resulted in complete separation of some parts of the aircrafts (Meguid 1989). Figure 1.1 (Meguid 1989) shows the failure occurred during a full scale test of the pressure cabin of aircraft, under a simulated loading. Similarly, Figure 1.2 shows failure of one of the several Liberty ships, used in the World War II (Parker, 1957). The failure was caused by repeated loading of water waves, which initiated and propagated fatigue cracks, rapidly from bottom to top of the ship body, and resulted in complete separation of the ship in two parts.

Most of the time it is not feasible and sometimes even not possible to replace immediately the cracked parts of important engineering structures, like the portions of aircraft's wings, or of the bridge girders/piers, or a small part of industrial machines or automobiles, etc. Reasons

includes longer replacement time periods, affecting the efficiency of overall industrial or mechanical system, or the replacement being financially unfeasible because of localized nature of the problem, etc. Therefore, the need of an efficient and engineered repair always exists, which not only can fulfill the feasibility requirements but also suits the usual financial budget cycles of the operating and maintaining agencies.

Figure 1.3 schematically shows the impact of fatigue crack repair on a typical fatigue crack growth behavior. Figure 1.3 shows that if no repair applied to the cracked element then it would fail earlier, following the curve OBA. But if a reasonable repair applied to the crack at point B then its fatigue life may be increased, following the curve OBC. If a more efficient repair applied to the crack, which could result in a long lasting strong constraint to the crack opening, then the fatigue life may be increased following the curve OBD. It has also been found in some previous research works that the crack could completely be arrested. The crack growth not observed in some repairs applied at the wings of aircraft, even after 25 years, with a very large number of fatigue load cycles (Baker 1987). Fatigue repair would be more effective if applied to a smaller crack size than to the crack that has already grown larger or reaching the critical size. The critical crack size is usually accompanied with a faster crack growth rate and there is higher probability of the crack growth becoming unstable, causing complete failure of the object or element.

1.2 Traditional fatigue crack repair techniques in steel structures

Traditional fatigue crack repair techniques for steel structures involve cutting holes to remove crack tip (or blunting the crack tip), welding or bolting of cover plates over the crack region, overloading of cracked element to introduce a bigger compressive zone ahead of the crack tip, and shot peening, etc. These techniques or the methods are effective to some extent but still have many side effects and limitations. Cutting of holes can reduce net section capacity. New cracks may originate from the edges of the cut hole itself, and most importantly, the removal or cutting of actual crack tip is practically very difficult because of its very small size. Similarly, welding of cover plates over the cracks can introduce heat affected zone and residual stresses near the welded region (Bayraktar 2004), which might act as source of new

fatigue cracks (Alam 2005). Bolted cover plates over the crack region found to be better than the welded cover plates but still suffered with stress concentration, caused by the bolt bearing at the edges of bolt hole. Overloading of structure, although introduces compressive zone ahead of crack tip and found affective in reducing the crack growth rate, but during overloading the risk of structure instability increases. The crack itself can grow during overloading, which might affect the overall repair efficiency. One of the recent fatigue repair techniques involves ultrasonic peening, through which compressive stresses are induced in the metal ahead of the crack tip. it is mostly limited to some experimental studies, showing its effectiveness in relieving residual tensile stresses within the heat affected zones around the welds (Leitner et al. 2012), which would also increase the fatigue strength of the detail.

1.3 Crack bridging using bonded Fiber Reinforced Polymers (FRP)

Crack bridging, using bonded Fiber Reinforced Polymers (FRP) or Fiber Reinforced Composites (FRC), is emerging as an efficient repair technique to improve the residual strength and the remaining fatigue life of cracked metallic structural elements, compared to the other traditional techniques discussed before. It has been used successfully since last three to four decades in rehabilitation and strengthening of cracked and weakened structural elements made out of metals and concrete by improving their stiffness, ultimate strength and the remaining fatigue life. Aircraft industry is the most beneficial as well as pioneered in the successful use of FRC in repair of cracked and corroded parts of aircrafts (Baker, 1987). It involves bonding of high strength and stiff fibers over the crack, using prescribed bonding adhesives and epoxies.

Crack bridging using bonded FRP patch basically introduced two effective mechanisms in the repair system that jointly results in improved or enhanced residual strength or the fatigue life of cracked steel element. One of the mechanisms introduced by the bonded patch is the sharing of stress from the steel plate, while the other mechanism is the restriction to crack opening by the fibers bridging over the crack. The two effective mechanisms introduced by a bonded patch, applied to a cracked element, are illustrated schematically in Figure 1.4. Sharing of stress by the patch reduces stresses in the cracked plate, which is one of the factors

increasing the fracture strength and the fatigue life of a patched plate. The impact of sharing action depends upon the ratio of axial stiffness of the patch to the axial stiffness of cracked plate in perfect bond conditions (Duong and Wang, 2007). This relative axial stiffness is being referred to as 'Effective Thickness Ratio' or 'ETR' in several other researches (Kennedy 1998, Lam and Cheng 2008), as well as in this thesis. The ETR or the relative axial stiffness of the bonded FRP patch can be calculated using Equation 1.1.

$$ETR = \frac{E_{FRP}\, t_{FRP}}{E_S\, t_S} \qquad \text{Eq. 1.1}$$

where 'E' and 't' are modulus of elasticity and thickness and the subscripts 'FRP' and 'S' stand for the CFRP and steel respectively.

Restriction to crack opening by the fibers bridging over the crack is more effective patch action than the stress sharing (Marissen 1984, Lin et al. 1991). Restriction to the crack opening also depends upon the patch ETR but its effectiveness can be reduced by the patch delamination around the crack, at patch-plate interface (Marissen 1984, Lin at al. 1995, Denny and Mall 1997). Due to high shear stresses in the adhesive, at crack location, adhesive failure is expected there (Papanikos et al. 2006, Lin et al. 1991, Ahmad Al-Shawaf 2011), which results into patch delamination around the crack. Traditional way of increasing the patch ETR is to increase the number of fiber layers, which require more adhesive in between the FRP layers. With technology advancement ultra-high modulus carbon fibers have recently been produced, with elastic modulus greater than the modulus of elasticity of steel. Therefore, these can be effectively used to reduce the crack growth rate in cracked steel plates. But their susceptibility to patch delamination is needed to be investigated. It has been reported in some research works that their fatigue repair efficiency was found to be much below the efficiency of normal modulus FRP repairs because of rapid patch delamination (Jones et al. 2003).

There are several advantages of using bonded FRP in repair, over the other traditional methods. The most appealing, is the lesser stress concentration introduced in the base metal by the repair, which is an effective factor in fatigue loading. It is mainly because of fairly large bonding area of the repair which provides smooth transition of stresses from cracked plate to the repair patch and vice versa. Its other advantages include its high strength to weight ratio,

high stiffness to weight ratio, ease in handling and application, ease in application to any shape or geometry, and good fatigue and corrosion resistance.

Use of FRP in strengthening and repair of steel structures is not much common and is still flourishing in research phases (Bassetti 2000, Colombi et al. 2003, Dawood, Rizkalla and Sumner 2007, Holden 2012, Tavakkolizadeh and Saadatmanesh 2003, Taljsten et al. 2009) but still there are some recent practical examples of successful application of FRP on steel bridge girders (Shield et al. 2004, Mertz et al. 2002). Due to higher modulus of elasticity and strength of steel and FRP, compared to adhesives, the role of bond or adhesives becomes more important, as these resemble a weak link in the repair system of steel with FRP (Xia et al. 2005). Quality and properties of bond or adhesive, in a FRP strengthened steel structural element, becomes more important when the system is under fatigue loading because of the nature of fatigue crack initiation from existing imperfections, flaws or the regions of stress concentration.

Effectiveness of bonded FRP patch relies on its perfect bond with the base metal. Therefore, base surface preparation and FRP bonding methodology, are equally important in achieving good bond between FRP and base metal, which, in turn affect the fatigue life of repair. Factors and parameters, which can introduce the bond failure, other than surface preparation or environmental effects, can equally affect the fatigue life of bonded FRP repairs. Studies of such factors are the main focus of the current research work and those factors include the properties of adhesives, FRP and the applied stresses.

1.4 Problem statements

Most research works involving double sided bonded FRP in fatigue repair of metals consider ‘effective thickness ratio’ (ETR) or the relative axial stiffness of repair patch as the governing parameter of repair (Lam et al. 2008, Schubbe and Mall 1999, Madani et al. 2008, Liu et al. 2009). ETR is the product of modulus of elasticity (E_{FRP}) and thickness (t_{FRP}) of the FRP patch. However, several experimental and analytical research works involving two different E_{FRP} repair patches, with close or identical ETR values, resulted in quite different fatigue life.

Experimental work by Jones et al. (2003), on the fatigue behavior of double sided patched steel plates, used three types of CFRP with different E_{FRP} (38 GPa, 65 GPa, and 165 GPa). The results showed that the repair having highest ETR had the least efficiency with negligible improvement in the fatigue life of the repair. In some tests the difference in repair efficiency was ranging between 8% and 85%, although the ETR difference of approximately 100 % between the repairs. For the highest ETR specimens (that resulted in negligible fatigue life enhancement), authors reported faster patch delamination rate, as the reason of their early failure. Some of the results of experimental work by Lui et al. (2009) showed that the difference in fatigue life enhancement of the steel plates, repaired with high and low modulus CFRP, was not even proportional to the ratio of their ETR; higher ETR repairs shown to be only 70% better than the lower ETR repair, although the difference in the ETR was close to 200 %. Numerical work by Lam and Cheng (2008) on repair of cracked steel pipes using two different moduli CFRP also showed a 20 % to 24 % difference in stress intensity factor (SIF) within the repairs having identical ETR patches, but having different E_{FRP} and adhesive. Similarly, some research works reported big difference in static-tensile and fatigue strengths of identical ETR patched specimens, with varying adhesive properties (Harris and Fay 1991, Xia et al. 2005, Wu et al. 2012). In the same context some research works also showed numerically that the variation of different patch parameters affect the stress concentration factors (SCF) at the patch end as well as the shear stress distributions in the adhesive layer, while keeping the overall patch stiffness (or ETR) unchanged (Kennedy and Cheng 1998, Mokhtari et al. 2012, Benrahou et al. 2010). Those parameters included modulus of elasticity and thickness of FRP (E_{FRP} and t_{FRP}), modulus of elasticity and thickness of adhesive (E_A and t_A).

Therefore, keeping in view the above discrepancies in getting different fatigue life, SIF and SCF of bonded FRP repairs with close or identical ETR patches, it is important to explore and rationalize the reasons for these differences by studying the role of different patch parameters, including, E_{FRP}, t_{FRP}, E_A and t_A, in affecting the SIF (K_I) at the crack tip of crack in the plate being repaired.

Governing failure mode in majority of previous research works, involving fatigue behavior of cracked steel plates or double lap joints with adhesively bonded FRP, was shown to be the

progressive delamination of the repair patch (Jones et al. 2003, Schubbe and Mall 1999, Lin et al. 1991, Papanikos et al. 2006, Colombi et al. 2003, Bassetti 2000, Haris and Fay 1991, Alawi and Saleh 1992, Taljsten et al. 2009, Ahmad Al-Shawaf 2011). The fatigue life of repairs was found to be affected by the rate of FRP patch delamination (Naboulsi and Mall 1998, Schubbe and Mall 1999b), but, research work highlighting the factors affecting the initiation of patch delamination is limited (Papanikos et al. 2006, Ahmad Al-Shawaf 2011). Although some researchers have studied, numerically and analytically, the impact of patch delamination on several crack growth parameters like the Energy release rate or the SIF (Lin et al. 1991, Baker 1999, Schubbe and Mall 1999b, Naboulsi and Mall 1997, Colombi et al. 2003, Papanikos et al. 2006, Madani et al. 2008), but they used the dis-bond or the delamination geometry as observed in their experiments or reported in other research works. Even in some research work the delamination was propagated arbitrarily in the study. Therefore, it is needed to study, explore and rationalize the factors affecting initiation and propagation of the patch delamination, which can also lead to the exploration of reasons behind the discrepancies in fatigue life of identically stiffened repaired specimens.

Lam and Cheng (2008) numerically developed geometric factors $f_{(a/b)}$ to evaluate fatigue life of cracked steel plates repaired with bonded FRP patches using Paris Erdogan relation (1963). They considered ETR as the main patch parameter and used one adhesive property to develop the geometric factors and their work also did not consider the effect of patch delamination on the developed geometric factors. Their developed geometric factors could predict close fatigue life of repair if the adhesive properties of repair are close to the one selected in their study, and most importantly, the adhesive shear strength is high enough to minimize the patch delamination.

Therefore, it is needed to relate the geometric factor $f_{(a/b)}$ to different patch parameters, effecting the SIF at the crack tip, and additionally, to the patch delamination, which was shown to be affecting the SIF in previous research works.

1.5 Objective and scope

Objective of current research work is defined after analyzing the discrepancies in results of several experimental and numerical works, involving fatigue and tensile behavior of bonded FRP specimens, as mentioned in the problem statements. The objective is oriented towards investigation of impact of different patch parameters on initiation and propagation of delamination in the bonded FRP patch, applied to the cracked steel plates, and further to incorporate the impact of patch delamination in fatigue life evaluation of cracked steel plates with bonded FRP patch, using tools of linear elastic fracture mechanics (LEFM).

In order to achieve the objective of current research work, the following milestones are discretely defined:

a) To investigate numerically the impact of properties of repair patch components on the shear stress distribution within the adhesive layer at steel interface. The study will be conducted using finite element analysis (FEA) of cracked steel plate repaired with double sided bonded CFRP patches under uniaxial tensile stresses.

b) To investigate numerically the impact of properties of bonded patch components on the stresses intensity factor (K_I) at the crack tip in cracked steel plate, repaired with double sided bonded CFRP laminates, under uniaxial tensile stress (same numerical model will be used as mentioned in 'a' above).

c) To introduce CFRP patch delamination numerically (in the FEA of 'a' and 'b' above) through the adhesive failure under high shear stresses at critical bond locations and to study the impact of the patch delamination on the SIF (K_I) at the crack tip.

d) To study experimentally fatigue behavior of edge-cracked steel plates repaired with double-sided bonded CFRP patches with varying patch ETR, E_{FRP} and adhesive properties, under constant amplitude fatigue load cycles.

e) To evaluate fatigue life of the specimens, tested in 'd', by numerically developing their geometric factors '$f_{a/b}$' and using them in Paris equation (Paris and Erdogan 1963). The geometric factors for each specimen will be developed using the SIF (K_I) obtained from its relevant FEA, with consideration of the CFRP patch delamination.

f) After validating working of the numerically developed geometric factors from 'e' with consideration of patch delamination (through predicting the fatigue life of tested specimens from 'd'), a parametric study will be performed to evaluate '$f_{a/b}$' of edge

cracked and central cracked steel plates, repaired with double sided bonded CFRP patches with varying ETR, E_{FRP} and adhesive properties.

The scope of current research work is limited to the through thickness cracks in steel plates with double sided bonded CFRP patches under applied tension-tension constant amplitude fatigue loading and the crack propagation study is limited to the mode I (or the crack opening mode) fracture.

1.6 Organization of thesis

A review of previous research works, involving the use of FRP in enhancement of strength and fatigue life of cracked metallic structural elements, is presented in chapter 2. Conclusions of the detailed literature review also highlighted the research gap in previous works as well as the scope of current research work.

A detail numerical study of the impact of bonded FRP patch parameters on the magnitude and distribution of adhesive stresses, developed at patch-plate interface, is presented in chapter 3. The study additionally included the impact of same patch parameters on the SIF (K_I) at the crack tip of edge cracked steel plate being repaired with the bonded FRP patch.

Scope of the numerical study, presented in chapter 3, was then extended to include the impact adhesive failure, at patch-plate interface, under high shear stresses. The results of impact of adhesive failure or the patch delamination, on SIF (K_I) at the crack tip of steel plate being repaired, are presented in chapter 4. The studied parameters included patch ETR, modulus of elasticity and thickness of FRP and adhesive. Impact of patch delamination location, on the SIF (K_I) at the crack tip as well as the impact of layering FRP patch, was also studied and presented in chapter 4.

After studying and highlighting the impact of various patch parameters on the adhesive stresses as well as on the SIF (K_I) at the crack tip in the plate being repaired, a detailed experimental phase was planned. The experimental phase mainly involved fatigue tests of

edge cracked steel plates, repaired with bonded carbon fiber reinforced polymers (CFRP), but with varying patch parameters, like ETR, E_{FRP} and adhesive properties, so as to verify the impact of these parameters on the fatigue life of the tested specimens. Results of experimental phase are presented in chapter 5.

Chapter 6 is oriented towards development of predictive tool to evaluate the fatigue life of the tested edge cracked steel plates with bonded CFRP patches. The predictive tool mainly involved development of non-dimensionlized geometric factors $f_{(a/b)}$ for each tested specimen, using the augmentation of FEA results and application of LEFM. The non-dimensionlized geometric factors $f_{(a/b)}$ were evaluated using the SIF (K_I) at crack tip of each specimen, obtained from the FEA of the bonded repaired cracked steel plates, incorporating the impact of patch delamination.

After validating working of the developed methodology for evaluating fatigue life of cracked steel plates repaired with bonded FRP patches and incorporating the impact of patch delamination, chapter 7 presents a parametric study of evaluation of geometric factors '$f_{(a/b)}$' for varying patch parameters and adhesive strengths. It includes the cases of edge cracked and central cracked steel plates repaired with CFRP patches, with different patch ETR, E_{FRP} and adhesive properties. These geometric factors can be used to evaluate fatigue life of cracked steel plates repaired with bonded FRP patches, with varying patch ETR and adhesive properties as well as incorporating the impact of patch delamination.

Finally, summary, conclusions and recommendations from this study are covered in chapter 8.

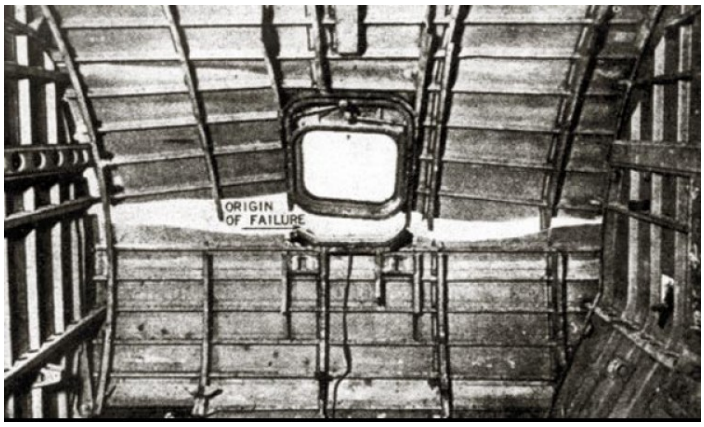

Figure 1.1 Failure of pressure cabin of Comet aircraft under full scale test (Meguid 1989)

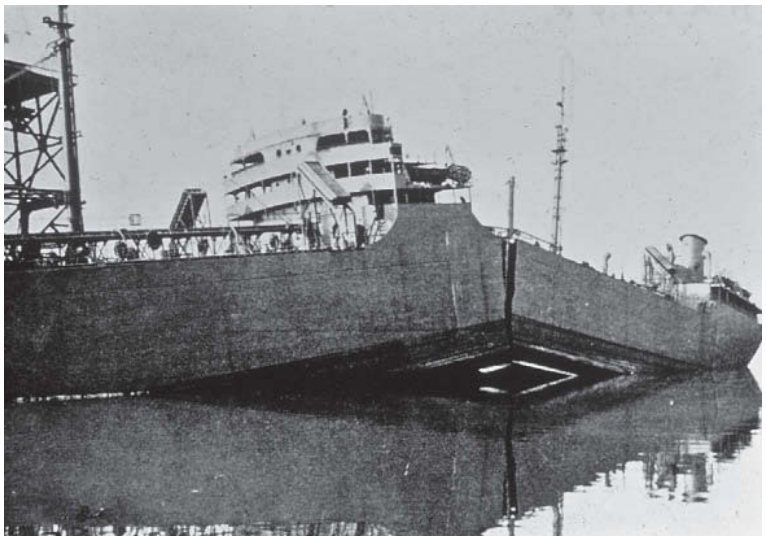

Figure 1.2 Fatigue failure of Liberty ship (Parker 1957)

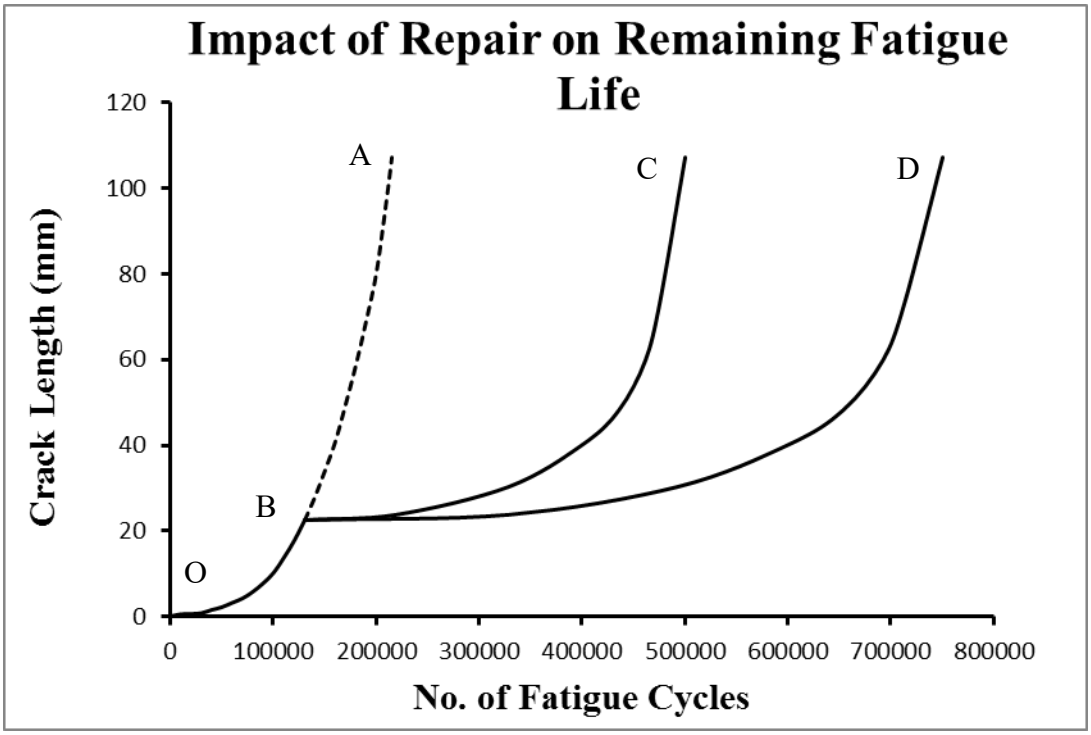

Figure 1.3 Impact of fatigue crack repair on the remaining fatigue life

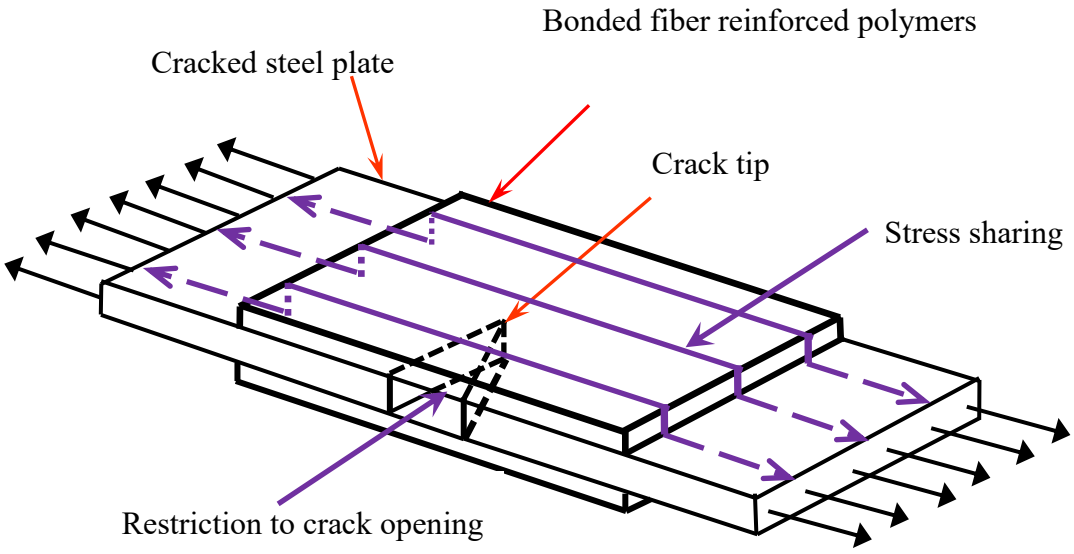

Figure 1.4 Two effective mechanisms develop in a bonded FRP patch over a crack

2. Literature Review

2.1 Introduction

Use of bonded fibre reinforced composite (FRC) or fiber reinforced polymers (FRP) patches, to enhance the ultimate strength, fracture strength or the fatigue life of metal and concrete structures (cracked and un-cracked), has been practiced in different areas of engineering application in last three to four decades. Vast applications of bonded fibre composites on metal structures have been carried out in mechanical engineering, more specifically in aircraft industry, for strengthening cracked and corroded parts of aging aircrafts. Tremendous amount of research, with practical application of the externally bonded FRP, on reinforced concrete members have also been carried out and found successful in enhancing flexural and shear strengths of reinforced concrete beams and girders as well as the confined compressive strength of concrete columns. In current thesis application of FRP on concrete members will not be discussed rather a brief overview of the researches involving FRP application on metals will be presented as these are more related to the scope of current research work.

2.2 Fibre reinforced composites (or FRP) in repair of metal structures

Baker (1984) provided an enormous contribution of experimental and numerical work on repair of cracked parts of Australian aircrafts using externally bonded boron fiber reinforced composites resulting in enhanced fatigue and ultimate strengths of the repairs. He showed successful performance of several repairs carried out and monitored for long time after being applied. The research included successful repair of 100 mm long cracks in Hercules helicopter wing assembly using BFRP (Boron FRP), the cracks were originated from the rivet holes of the wing's plank connection and might have been caused by stress corrosion. It also showed successful performance of repairs applied to wings of Mirage aircraft, landing wheel of Macchi aircraft and to the fuselage of Orion aircraft after being monitored for several years showing no sign of further crack growth.

Baker (1984) also summarized several other successful major repairs carried out to the aircrafts serving in Australian air force using BFRP, including cracks repair in the wings of Mirage II aircrafts in 1975 and crack repair in console truss of F-111 aircraft in 1980, etc. and still shown to be no sign of crack growth or complete crack arrest. These studies provided a great level of confidence in the reliable use of bonded FRC in repair of cracked metallic parts of critical structures.

Baker (1993) performed experimental research in repair of cracked Aluminum alloy plates with boron fiber patches having modulus of elasticity of 200 GPa. The main intension was to compare the impact of using two different types of adhesives at ambient and elevated temperatures on their fatigue behavior. He used two initial crack lengths: 5 mm and 25 mm, two types of adhesives: acrylic based adhesive and epoxy-nitrile film adhesive and used seven layers of the boron fiber composite (each layer was 0.13 mm thick), which made the patch stiffness ratio (ETR) of 0.8. The epoxy-nitrile film adhesive required curing at 120^{o} C and the tests were carried out under constant amplitude fatigue loading, at both ambient and elevated temperature reaching 100^{o} C.

Their test results showed that the specimens with acrylic based adhesive didn't suffer with any delamination at ambient temperature and showed no crack growth for about 15 times the total number of cycles the unrepaired specimen took before complete failure and then it further took approximately same number of cycles with a slower crack growth rate till failure, so the total fatigue life enhancement achieved in these specimens was approximately 30 times that of the unrepaired specimen. The nitrile epoxy specimens suffered with delamination and achieved lesser fatigue life compared to the acrylic adhesive specimens but still the fatigue life enhancement achieved was ranging from 10 to 20 times of the unrepaired specimen. The experimental observations also showed that the increase in crack growth rate due to delamination was qualitatively related to the size of delamination in the specimens. The results of fatigue tests at elevated temperature were surprisingly different than the ambient temperature ones, the specimens with nitrile epoxy showed better results at elevated temperature with somewhat decreased delaminated regions than the specimens with acrylic based adhesive, it appears from their test results that the acrylic adhesive specimen took one fourth of the number of average cycles achieved by the nitrile epoxy specimens and it was

also approximately one seventh of its own specimen achieved at ambient temperature. One possible and important reason deduced by the author for that result was related to the shear stiffness of the nitrile epoxy adhesive which was supposed to be much higher at ambient temperature thus resulted in induced higher shear stresses and that might had resulted in more delamination in those specimens. The increased temperature might have resulted in softening of shear stiffness resulting in lesser shear attracted and thus suffered with lesser delamination.

Work by Jones et al. (1979) is among the oldest numerical work to predict SIF of a cracked plate with a repair patch applied over the crack. They modelled the repaired plate using stiffness matrix they developed using a three layer approach with interlinking the displacements of patch to plate through the adhesive layer at their interfaces. Their resulting SIF well correlated with the SIF analytically evaluated for the unpatched plate and also found to be reduced due to the application of patch. Their results showed a 40% reduction of SIF due to increase in patch thickness by 6 times. They also showed that the increase of patch thickness also resulted in increase of the adhesive shear stress but their model assumed constant shear stress through the adhesive layer.

Rose (1982) studied analytically the crack extension force in terms of energy release rate G in a plate with semi-infinite crack at one edge and proposed a numerical model to predict the impact of FRC patch on the crack extension force in terms of G. He showed that the crack extension force G will have finite asymptotic value as the crack grows from semi-infinite to large size provided that the repaired structure can still carry the load. He also deduced the lower bound asymptotic value of the crack extension force G for short cracks and compared the results with numerical evaluation and found close correlation.

Madani et al. (2008) investigated analytically the impact of patch and adhesive layer thickness on the SIF at the crack tip and on the COD (crack opening displacement) of centrally crack aluminum plate (2024-T3) with bonded graphite repair patches. They modelled the adhesive as shear springs and solved numerically the analytical integral equations of displacements (developed previously by Ratwani et al. 2006) relating the adhesive shears and the body forces using the collocation technique. The main formulation of displacement equations was based upon the displacement continuity requirement, i.e. the relative displacement between the plate and patch should be equal to the shear deformation in adhesive springs. They considered the

patched plate as interaction system of a cracked plate with crack surface loading augmented with body forces transferred from the patch through the shear springs and the patch itself having the body forces different from the plate. The body forces in patch and plate are both related to the adhesive shear stress which was also assumed to be constant over the adhesive thickness. The system of displacement integral equation due to crack surface loading and body forces were initially formed and then solved numerically for the shear stress from the relation of displacement to shear stress.

SIF was then evaluated using superposition of that cause by the crack surface loading and the body forces in the cracked plate. Similar approach was also made to evaluate the COD, part of which was assumed to be contributed by the applied loads and part from the interaction of load transferred between plate and the patch. Although it was mentioned that the adhesive shear stresses had also been evaluated as part of the research output but it was not shown explicitly in the research output. Impact of patch delamination on SIF and COD was also investigated by introducing an elliptical dis-bond region surrounding the crack. The dis-bond elliptical shape was actually adopted from the outcome of another experimental research work by Ratwani (1977 and 1979). Two patch thicknesses were investigated; 1.78 mm (equivalent to 14 plies); 1.52 mm (equivalent to 12 plies). Adhesive properties were taken as for FM 73 epoxy, with elastic modulus of 0.482 GPa but its thickness was assumed to be ranging between 0.1 mm to 0.25 mm.

The results of analysis showed that the SIF of singly sided repair was much higher than that of double sided repair, which was because of the out-of-plane bending of single sided repairs that caused increased tensile stresses in the plate and reduced the tensile stresses in the patch. Impact of adhesive layer thickness was also obvious from the analysis results; thicker adhesive resulted in higher SIF and COD compared to the thinner adhesive layer both in single and double sided repairs, which was expected to be caused by increasing shear deformation in the adhesive layer with increase in the adhesive thickness. The impact of patch thickness on SIF and COD was obtained by comparing results of 14 plies patch and 12 plies patch, which showed that both SIF and COD were reduced by using a thicker patch (or 14 plies) and it was equally valid in single sided and double sided repairs.

The range of adhesive thickness chosen in the work by Madani et al. (2008) was from 0.1 mm to 0.25 mm which captured well a range of thinner and less viscous epoxies but still the study needs to be extended to more thicker adhesives as the available adhesive thickness for bonding some prefabricated types FRP plates exceeds 2 mm.

Schubbe and Mall (1999a) conducted experiments on the fatigue life enhancement of centrally cracked aluminum plates 508 mm long and 153 mm wide with two different thicknesses: 3.175 mm and 6.35 mm, repaired with boron fiber composite patches on one side. The central crack of 12.5 mm was initially developed by electric discharge method (EDM) and then the specimens were fatigue loaded till the crack length reached 25.4 mm, after which the boron fiber patches were applied and cured through the prescribed procedure and the specimens were retested again under the defined fatigue loading till complete failure of specimen. The ETR or the patch relative stiffness ratio was varied from 1 to 1.3 by increasing the number of boron fiber layers and the tests were conducted under constant stress range of 120 MPa with stress ratio of 0.1 and frequency of 10 Hz. Crack growth was monitored using travelling tele-microscope on the unpatched face while eddy current technique was used on the patched face to monitor the crack length. They also monitored patch delamination during testing using Infra-red (IR) thermography and additionally took ultra-sonic images (C-scan) periodically during the test by stopping it for a short time.

The test results showed that the bonded boron fiber patches enhanced the fatigue life of all the repaired plates by approximately 4 to 8 times, with higher enhancement of 8 times was achieved in thinner plates while overall lower enhancement was achieved in thicker plates. The impact of ETR was not much highlighted in the test results, especially in thinner plates which showed no enhancement in fatigue life for higher ETR specimens while thicker plates showed a small benefit of higher ETR and achieved 45% higher fatigue life than the specimens with lower ETR. Unequal crack growth observed in the tests between the patched and unpatched faces because of repairs being single sided and having out-of-plane bending as a result of that. This behaviour has already observed in many other tests and numerical works. They also monitored the delamination of the bonded patch during the tests which showed that

generally in all tests the delamination started after the crack length exceeded 80 mm and then spread in approximate elliptical shape with greater rate.

Schubbe and Mall (1999b) also investigated numerically the behaviour of their tested specimens that has already been discussed above in Schubbe and Mall (1999a). They used three-layer modelling technique to model aluminium plate, adhesive layer and the boron patch separately using two-dimensional four-nodes Mindlin plate elements and provided displacement compatibility constraints at the interface nodes of two adjacent layers. They also induced the delamination of boron patch observed during the tests in their numerical model by relaxing the compatibility constraints assigned at those locations where delamination occurred. The resulting crack opening displacement (COD) from their numerical model correlated well with their experimental observations up to the crack length of 80 mm after which the experimental values were shown to be much greater than the numerical prediction, which was believed to be because of patch delamination. When they induced patch delamination in their numerical model by relaxing the displacement compatibility constraint within the experimentally observed delaminated regions their numerical results moved closer to the experimental observations.

They also evaluated SIF for both patched and unpatched faces from the numerical model and predicted the respective crack growth rate for both faces and compared these with their experimentally observed rates which showed that the crack growth rate for the patched face was much under predicted by the numerical model while it well correlated for the unpatched face till 80 mm crack length, after which the numerical prediction deviated little bit from the experimental one. Additionally when they compared the crack growth rate for the case of induced patch delamination of unpatched face it was shown to be further deviated above the experimentally observed rate. They concluded the reason being the highly nonlinear crack front shape in the experiments which cannot be well captured using 2D linear Mindlin plate elements so they adjusted the crack length using the crack front shape and lag observed at the cracked faces of the tested specimens and called it effective crack length and using that effective crack length in their numerical model the crack growth rate matched well with the experimentally observed rate.

Naboulsi and Mall (1997) investigated numerically the impact of de-bond size and location on the crack growth rate in centrally cracked aluminum panels repaired with adhesively bonded single sided boron fiber composite patches. They also compared the numerical findings with another previous experimental work by Denney and Mall (1997) as part of their numerical model validation. They used three layered finite element procedure with 2D Mindlin plate elements having transverse shear deformation capability. SIF was computed using strain energy release rate and using that SIF together with ASTM E64-1991 the crack growth rate was predicted using Paris power law assuming material parameters to be of the unpatched panels.

Results of the numerical study showed that the de-bond size and location greatly effect and increased the SIF and the respective crack growth rate when the de-bond lied close to the crack. The largest increase in SIF was found for the case of full patch-width de-bond with the crack at its center (with the de-bond area equivalent to 20% of the total bonded area). Next critical de-bond location was found to be the crack tip region that increased the SIF or the crack growth rate. The de-bond located at the patch end was found to have lowest impact on the SIF compared to the fully bonded patch SIF while the de-bond at any intermediate location was found to have the impact on SIF in between the two extreme cases of least impact when de-bond at the patch end and most impact when the de-bond near crack tip.

They have also studied the crack growth rate with increasing crack length and found that it could be well represented by a linear variation for all the de-bond locations, although the slope of linear variation was different for different de-bond locations. That finding was contrary to the finding of Denney and Mall (1997) of constant crack growth rate within the bonded patch. Most critical slope was found for the full patch-width de-bond of 20% of the total bonded area (with crack lying at the de-bond center) and the least slope was found for the completely bonded case although there was very little difference found in the slope of end de-bond crack growth rate and the completely bonded patch. The crack growth rate was found different for the two faces of cracked plate because of difference in SIF variation on the two faces which was expected for the single sided repair. They also studied the transition of linear crack growth rate to non-linear because of the fact that the bare metal crack growth trend with respect to crack length is always nonlinear or most likely exponential. They found that a quite

bigger de-bond region (approximately 90% of total de-bond area) at the most critical location would give a non-linear crack growth rate.

Lin et al. (1991) studied the fatigue performance of carbon fiber-reinforced aluminum laminates (CRALL) which is basically carbon fiber layer sandwich between 1 mm thick 2024-T3 aluminum layers. The elastic modulus of CRALL was tested to be ranging from 77 GPa to 91 GPa for 2 and 6 carbon fiber layers respectively at 0^{o} C. Carbon fiber itself had the elastic modulus of 230 GPa. The fatigue specimens were prepared by machining the single edge notched (SEN) specimens 200 mm long x 30 mm wide from the CRALL sheets such that the 200 mm side was exactly aligned with the carbon fiber rolling direction. An initial notch of 2 mm was provided with a diamond saw and the fatigue tests were conducted under constant amplitude stress ratio 'R' of 0.1 and frequency of 10 Hz.

The results concluded that CRALL specimens showed superior performance in fatigue resistance and decreased the fatigue crack growth rate by an order of two compared to plain aluminum specimens. One very important finding was attributed to the role of fiber bridging in the wake of crack. The fiber bridging effect was evaluated during the experiments by simply saw cutting the carbon fibers from the wake of crack when the crack was already propagated 3.7 mm in the aluminum sheet (total crack length including initial notch was 5.7 mm) and then continuing the fatigue test. The result of removal of the bridging fibers over the crack on the crack growth is amazingly found to be an order of one, it is also shown in the Figure 2.1, which is taken from the results of the this research work.

Chester et al. (1999) studied repair effectiveness using boron epoxy patches applied to a lower wing skin of RAAF F-111 aircraft, after it developed a crack of approximately 48 mm. As this repair was supposed to be applied to a primary (or critical) structural element of the aircraft and the crack size was also reported to be reaching critical length so the repair itself required some special certifications for which the researchers also performed separate pre-tests to determine some specific adhesive properties like the fatigue behavior and for which they had also used and proposed special test procedure for evaluation of static shear and peel strengths as well as fatigue behavior of adhesive. The pre-tests for fatigue behavior using a modified double lap test showed that shear strain range is a better parameter for fatigue loading than the shear strain energy release rate. The big scale tests consisted of two types of specimens; one

type simulated the wing boxed structure itself and had size of 900 mm x 430 mm x 65 mm and; the other type simulated the lower skin itself and consisted of 20 panels with size 300 mm x 190 mm x 4mm. The repair patch composed of 14 plies of boron composite was applied with lay-up sequence of $(0_2, \pm 45, 0_3)_s$. which represents the layer set-up as 2 plies at 0^o, 1 ply at + 45^o, 1 ply at -45 ^{o} and then again 3 plies at 0 ^{o} and then the whole sequence was repeated as symmetric about the middle 0 ^{o} ply. Such ply lay-up sequence is common in loads creating in-plane shear as well as torsional stresses. The load spectrum applied to the repair was basically achieved from the multi-channel recorder actually connected to the RAAF F-111 aircraft thus applied actual loads expected to come on the wing box assembly.

The static test results of the 300 mm long panels showed that the unrepaired and cracked panel failed below the required design limit load but the boron fiber repaired specimen achieved the residual strength exceeding the original design ultimate load by a factor of 1.7. Similarly, the fatigue test results of 900 mm long boxed specimens showed excellent performance of the repaired specimens, the unrepaired specimen experienced rapid growth of the initial 48 mm crack and reached complete failure in just 15.8 flight hours while the repaired specimens survived for more than 200 hours.

Papanikos et al. (2006) studied numerically the impact of bonded FRP patch properties on initiation and progression of the patch delamination, which was considered to be based upon strength failure in adhesive and FRP layers as well as in the plate-adhesive and adhesive-FRP interfaces. The main criteria considered for delamination initiation or progression were the exceedance of shear and peel stresses above the material strengths at two critical and highly stressed locations within the patch, i.e. the crack surrounding region and the patch end region. The numerical model used for parametric study consisted of a centrally cracked metal plate with a finite size double sided bonded FRP patch and the varying parameters included thickness of adhesive and FRP layers or the axial stiffness of the bonded patch as well as the patch width.

The initial or delamination ignition investigation showed that the increase in adhesive layer thickness resulted in reduced shear stresses near crack and reduced peel stress for thinner base metal but for thicker base metal increase in adhesive thickness showed to be increasing the peel stress at patch end. Although the range of adhesive used in the study was from 0.05 mm

to 0.3 mm, which still did not include much thicker adhesives commonly used nowadays, i.e. 1 mm to 2 mm thick. Similarly the study considered only two thicknesses for metal plate, 1 mm and 2 mm, which also did not cover a wide range of thicknesses, especially those commonly used in civil / construction industry (mostly exceeding 7 mm).

The impact of increasing FRP patch thickness found to be more beneficial around the crack region as it reduced the shear stress in adhesive layer but at the same time it appeared to be detrimental at the patch end because of increasing peel stress there. Patch width also found to have beneficial effect both on the shear stress and peel stress, respectively near crack and the patch end locations because of taking off more stress from the base plate thus relieving it more. They have also studied the impact of the patch properties on the SIF at the crack tip in base metal and found that it varied in a reverse order compared to the beneficial or detrimental impact of patch parameters on the stresses or the stress to strength ratios. Increase in adhesive thickness already showed to decrease adhesive shear stress near the crack but when studying the SIF it was found to be increased, which was because of increase in the adhesive shear deformation near crack that allowed more crack opening or the increase in SIF.

Similarly, the impact of increase in FRP patch thickness was found to be increasing the patch-end peel stress but then it was also found to be reducing the SIF at crack tip, which was because of relief in the plate stresses as a result of increase in FRP thickness (or axial stiffness of the FRP patch). The study also concluded that patch-end delamination created a catastrophic failure situation because of huge increase in delamination growth rate started from patch-end and moves inwards towards the crack while the near-crack delamination did not create a catastrophic failure situation rather it showed a stable delamination growth situation. The impact of delamination growth on SIF showed that the near-crack delamination resulted in slower increase of SIF (with increase in the de-bond area) but the patch-end delamination resulted in larger increase in SIF with the increase in path-end de-bond area which ended up in catastrophic failure situation. Tapering of patch-end resulted in beneficial reduction of stress concentration there thus reducing the chances of peel strength failure there.

2.3 Fiber reinforced composites (or FRP) in repair of steel structures

Bocciarelli et al. (2009) investigated the stiffness degradation of the FRP strengthened steel plates resulting from delamination of the bonded FRP patch under applied fatigue loading. They used the stiffness degradation as an index of delamination for predicting further delamination and global failure. Their specimens were solid and un-cracked steel plates 100 mm x 50 mm x 6 mm thick, bonded with FRP patches on their both sides. The FRP used was one layer of Sika Carbodur, which was basically carbon fiber reinforced polymer (CFRP), with modulus of elasticity of 200 GPa and bonded to the unconditioned steel plates using the adhesive Sikadur 30. The fatigue tests were performed at frequency of 14 Hz. with stress ratio of 0.4 and the stress ranges used were 83, 100, 120 and 160 MPa.

The test observations showed that the patch delamination started from the patch ends because there was no crack in the steel plate and neither the specimens were double lap joints. The delamination further progressed inside the bond length at adhesive-steel interface, which was believed to be the weakest location in the bonded system. The test results showed that a 2% reduction in the stiffness corresponded to the onset of delamination while a 5% stiffness reduction corresponded to the onset of rapid delamination and the delamination reached mid bond-length when the stiffness dropped by 15%. They also predicted maximum peel and shear stresses in adhesive layer at the patch end using the elastic model developed by Stratford and Cardei (2006) and calculated maximum principal stress which was found to be close to the adhesive tensile strength at the maximum applied load of 80 kN. Finally S-N curves of the repaired specimens were developed and it was found that the S-N curves of the bonded CFRP cover plates were better than the category of welded cover plates being used in the respective Euro code.

A comparative study of the effectiveness of crack repairs using high modulus CFRP patches in fatigue life enhancement of cracked steel plates was conducted by Lui, Al-Mahaidi and Zhao (2009). Two different moduli CFRP were used in the study that was supplied by MBrace strengthening system with the fiber elastic modulus of 640 GPa and 240 GPa. The cracked steel specimens were conforming to the ASTM E-647 with dimensions 500 mm x 90 mm x 10 mm thick and had a central hole of 5 mm diameter with 1 mm machined notch on each side of

the hole. They studied both single sided and double-sided repairs with different CFRP patch configurations including full width and partial width covering patches, with and without central hole covering. The test specimens were repaired with three and five CFRP layers with an additional layer of glass fibre (elastic modulus 16 GPa) at the steel interface in all the test specimens. The tests were performed under tension-tension fatigue cycles with stress ratio of 0.1 and maximum applied tensile stress of 150 MPa until complete failure of the specimens.

The test results showed that the repairs provided with high modulus CFRP were very effective compared to those provided with lower modulus CFRP in both single sided and double-sided repairs, although the effect was more highlighted in double sided repairs. Failure mode of all specimens repaired with high modulus CFRP was fibre breakage and of all those repaired with lower modulus CFRP was the patch delamination. The study of crack front from the cracked faces showed that in single sided repairs the crack length was quite more at the un-patched face than at the patched face which was assumed to be because of non-uniform stress distribution in the thickness of plates caused by the eccentricity in the repaired system. The patch to steel stiffness ratio (ETR) of five layers high modulus CFRP and five layers low modulus CFRP is worked out from the information provided in the paper and is approximately 0.36 and 0.21 respectively for high and low modulus patches, which shows that the high modulus patches were approximately 1.7 times stiffer than the lower modulus CFRP patch.

The fatigue life enhancement results of double sided repairs showed that the high modulus patch enhanced the fatigue life of cracked specimen by 6.6 times while the lower modulus patch enhanced the fatigue life by 2.7 times. The comparative effectiveness of the two shows that high modulus patch was 2.44 times more effective than the low modulus patch, although it was only 1.7 times stiffer than the lower modulus one but if the effectiveness of five layers of both types of CFRP is compared then the high modulus CFRP specimen appears to be 2.9 times more effective than the low modulus CFRP and it was also 2.88 times more stiffer than the lower modulus specimen.

Colombi et al. (2003) studied numerically the impact of different patch parameters (including adhesive thickness, CFRP elastic modulus, etc.) on the strain energy release rate G corresponding to progressive delamination of the bonded CFRP patch around the crack. They initially studied experimentally fatigue behaviour of cracked steel plates repaired with bonded

CFRP patches and found the governing failure mode being the progressive delamination of the CFRP patch occurred at steel-adhesive interface. The patch delamination was monitored in the experiments using Speckle Interferometry technique, which was based upon the evaluation of relative displacement field on the patch surface due to the passage of crack front through it by the help of the change in the fringe spacing.

The experimental observations together with the help of finite element model behavior concluded that the delaminated region surrounded the crack tip closely represented by an ellipse. The numerical model was then used to predict the delamination strain energy release rate along the delaminating crack front in adhesive corresponding to the delamination shape and size actually observed during the experiments. The developed 2-D finite element model was based upon three-layer technique and used Mindlin plate assumption in which the strain distribution in plate, adhesive and FRP layers was considered to be linear. The developed model was then used to study the impact of different patch parameters on the energy release rate due to crack extension through progressive patch delamination.

The results of numerical study showed that an increase of modulus of elasticity of patch 'E' by four times reduced the delaminating strain energy release rate by 12% which appeared not a big advantage. Comparing the maximum value of G released due to delamination progression with the expected G value released from the crack extension in steel plate for a crack length of 50 mm it was found that the G corresponding to the delamination extension was very small compared to the G corresponding to the crack extension in steel plate. Authors believed it to be because of high stiffness of steel plate compared to the CFRP patch that had resulted in lesser stress shared by the patch and thus lesser amount of G released due to less stressed CFRP patch.

The numerical study also showed that increase in the thickness of adhesive by 9 times (from 0.15 mm to 1.2 mm) the crack delaminating energy release rate was decreased by 75 % which was thought to be because of reduction in the relative displacement at the steel interface but on the other hand it might increase the SIF at the crack tip in steel plate due to increased crack opening through adhesive shear deformation. On the other hand a decrease in adhesive thickness was shown to increase in delaminating energy release rate G and thus it can cause larger adhesive delamination, so, it appeared to be a trade-off as thicker adhesive might not

delaminate more but can increase the SIF at the crack in steel plate but the thinner adhesive might be delaminated more but because of lesser shear deformation in it the corresponding SIF might not be much effected. The introduction of pre-tension in the FRP patch showed significant reduction in delaminating energy release rate especially at higher level of pre-tension. It was shown that an increase in the pre-tension in the CFRP patch from 0 to 1000 MPa, before its application, resulted in 87% reduction in the delaminating energy release rate and additionally it was expected to cause crack closure effect by reducing the applied stress ratio.

Dawood, Rizkalla and Sumner (2007) carried out full scale test on steel-concrete composite beams strengthened with high modulus CFRP to study their behaviour under static and fatigue loading. They also studied possible delamination of the CFRP strip from the flanges of steel beams in four point bending tests as well as in tensile tests of double lap splice joints. The CFRP used was pitched-based carbon fibres with elastic modulus of 460 GPa and was pultruded into 100 mm wide plates. The fibre volume fraction used was 70%. The test specimen consisted of CFRP double lap splice joints as well as steel beams W 200 X 19 steel beam 3.05 m long with a composite concrete top slab 525 mm wide and 65 mm thick and bonded with CFRP strips at the bottom flange. The double lap splice specimens were provided with variable FRP-end details to study their possible impact on the patch delamination, those included the normal square end, reverse tapered and reverse tapered plus rounding in plan.

Test results showed that all double lap specimens failed by the sudden delamination of the CFRP plate. The specimens provided with reverse tapered edge at both ends of CFRP strip achieved maximum axial joint capacity, which was about double to that of specimen with normal square end CFRP (i.e. without any tapering), which showed the importance of tapering at the patch end. The beam specimens were tested in 4 point loading condition under fatigue loading with frequency 3 Hz. The minimum P and maximum P applied were respectively 30% and 60% of the yield loads of the unrepaired and repaired beams. The two strengthened beams with high modulus CFRP differed in the adhesive application and thicknesses with one beam the CFRP was bonded without controlling the adhesive thickness while in the second beam the adhesive thickness was controlled using glass beads. All the beams were tested to 3 million cycles together with monitoring of their stiffness and the mean deflection. It was

found that the un-strengthened beam suffered with a 30% increase in the mean deflection while the two strengthened beams showed very close behaviour and both suffered only 10% increase in the mean deflection without any noticeable CFRP delamination.

Tavakkolizadeh and Saadatmanesh (2003) tested cracked steel beams repaired with bonded CFRP under fatigue loads and performed reliability based design approach to analyze the results of the retrofitted beams using the AASHTO design S-N curves. Total 13 steel beam S127 x 4.5, including 7 control specimens with 1.22 m span were tested under the stress ranges from 69 MPa to 379 MPa in four point bending condition. The bottom flanges were pre-cracked with an initial saw cut 12.7 mm long on both sides of flanges and then repaired with CFRP strips 400 mm long x 76 mm wide x 1.27 mm thick, with elastic modulus of 144 GPa applied on each side of bottom flange.

Reliability based analysis of the results showed that the unrepaired specimens were having little less steeper slope than the AASHTO category C and D while the repaired specimens were shown improvement in the category and were lying between categories B to C. It shows the improvement in category D to C of such detail due to application of CFRP repair patches. The fatigue life enhancements of the repaired beams ranged from 3.4 to 2.6 for the stress ranges 345 MPa to 207 Mpa. The stiffness of the repaired beams was started decreasing at the crack length of 22.5 mm while the stiffness reduction in unrepaired beams was started at crack length of 14.5 mm.

Haris and Fay (1991) studied the behavior of two commonly used adhesives in automotive body shell construction: M-51 and XW-1012, under static and fatigue loads using single lap joint specimens. They studied the impact of adhesive thickness used as a bond line between two mild steel plates, each 100 mm x 40 mm x 0.9 mm thick, to form single lap joint specimens with a lap length of 15 mm. The main test parameters were the adhesive thickness and the temperature range. The three adhesive thicknesses used were 0.2 mm, 0.9 mm and 2 mm while the three test temperatures used were -30^{o}C, +20^{o}C and +90^{o}C to accomplish the temperature range which also included the glass transition temperatures, T_g, of the adhesives. The results of static tension test showed that the tensile strength of joints increased by 4 to 6 times with the decrease in test temperature irrespective of the adhesive type or adhesive thickness and the thickest adhesive (2 mm) specimens achieved approximately 25% to 50%

lesser loads than the joints with thinnest adhesive layer (0.2 mm) for both adhesive types at all temperature ranges. This reduction in static strengths at higher temperatures was basically because of the test temperatures reaching or exceeding the T_g although the M-51 adhesive specimens showed 25% to 500% lesser strength than the XW-1012 with the largest difference observed at the test temperature of 20^o C.

Results of fatigue tests were similar to those of the static tests, high temperature tests achieved lesser fatigue life while at any particular temperature thicker adhesive achieved lesser fatigue life compared to thinner adhesive specimens. Their test used single lap joints in which secondary stresses due to system eccentricity may affect the comparison while applying it on the double-sided repairs and very high temperature range (reaching the glass transition temperature) may not resemble the service temperature range for civil structures. Also, the bond length used in the tests was only 15 mm, which is quite less than the minimum required to develop strain compatibility region, as predicted by Hart Smith (1973), Kennedy and Cheng (1998) and Lam and Cheng (2008).

Alawi and Saleh (1992) studied experimentally the impact of bonded FRP patching on fatigue crack growth rate in steel using compact tension specimens. Parameters included patch eccentricity (single sided vs double sided patching), patch thickness (ETR) and the bonded width of patch (partial vs complete). The test results showed that the crack growth rate in single sided repairs always greater than the double-sided repairs for all the cases of either partial plate width or full plate width covering bonded patches. The crack growth rate was least improved by the partial plate width patches, covering only partial plate width (equal to the initial crack length, although covering full plate length in longitudinal direction) while the most effective patch configuration was found to be the double sided patch covering full plate width. The effectiveness of double sided patches, fully covering the plate width, was further enhanced by increasing the patch thickness (ETR) on both faces, which was found to be the best scenario in reducing the crack growth rate and increasing the fatigue life of the specimen (within the range of the testing constraints).

Karbhari and Shully (1995) studied the durability aspect of the bond of different types of FRP laminates with the steel including different types of carbon and glass fibers. They used the modified wedge test to measure the crack extension with time under six possible environment

conditions; ambient; sea water at 25ºC; hot water at 65ºC; freezing (at -18ºC); water at room temperature (25ºC); and freeze thaw cycles in water between -18ºC and 25ºC. Hot water effect was found to be most severe while freezing temperature results were found least affecting the crack growth rate, which was explored to be because of loss of bond, micro cracking and increased plasticization (irreversible damages) occurred in the epoxy and resin at higher temperatures.

Freeze and thaw cycles resulted in more damage than the freezing only because of interphasial deterioration occurred in the former situation. E-glass type fiber laminate also suffered with larger crack extension during freeze thaw and salt water environments but the S-glass type fiber laminates showed overall least crack extension in nearly all types of environments except the freezing environment (but still it was not the worst in that environment) and suffered with least deterioration. The authors recommended using a hybrid fiber laminate for best results, with the S-glass layer at steel interface and remaining layers to be of carbon fibers, to achieve better strength and stiffness together with higher bond durability.

Benraho et al. (2010) studied analytically the impact of adhesive mechanical properties on the distribution of inter-facial shear and peel stresses in the adhesive layer of a FRP bonded beam under bending. The developed analytical model was based upon stress equilibrium and deformation compatibility conditions at steel-adhesive or adhesive-FRP interfaces assuming linear elastic material behavior. The developed analytical model also considered shear deformation within adherent's thickness and considered a more realistic parabolic shear stress distribution along the depth of beam cross-section in contrast to linear shear stress distribution but the shear stress variation across the adhesive thickness was assumed constant because of its smaller thickness.

The analytical model was then validated by comparing its prediction with the results of a previous experimental program and it showed that the prediction of the developed model was quite close to the experimental results. A parametric study was also carried out to study the impact of variation of adhesive mechanical properties on inter-laminar stresses and its results showed that an increase in modulus of elasticity of adhesive resulted in noticeable increase in the interfacial patch-end shear and peel stresses but the impact of varying adhesive Poisson's ratio showed minimal impact on the patch-end stresses. The work didn't consider a singular

stress situation at the patch end and validated its model predictions with a concrete beam test results bonded with a steel plate with steel anchors at the plate end.

Lenwari et al. (2006) studied numerically and experimentally the impact of CFRP and adhesive layers properties on the static and fatigue de-bonding strength of partial length CFRP plates bonded to bottom flange of steel beams. They treated the patch end as a bi-material wedge with singular stress field and calculated a critical stress intensity factor using a previously developed analytical procedure. Their developed procedure evaluated a critical SIF at the patch end using reciprocal work contour integration whose locus lied at the steel-adhesive interface right at the point where the bonded patch end. They also developed finite element model of their tested beams to work out the part of their contour integral lying outside the singular stress filed region. Their experimental program included both static and fatigue tests of steel beams with bonded partial length CFRP strips at their bottom flanges under four point loading. The adhesive layer properties were constant with thickness of 1mm while the bonded lengths of CFRP strips were varied from 500 mm to 1200 mm.

The static-load test results showed that longer CFRP bond lengths resulted in CFRP rupture and higher failure loads compared to the shorter CFRP specimens, in which CFRP delamination was the dominant failure mode. The fatigue test results analysis showed that the fatigue life cycles for de-bond initiation better correlated to the critical SIF than the nominal stress range. Their numerical results showed that the evaluated critical SIF was not affected by the CFRP bonded length, which was in contrast to their experimental result, so, it was concluded that it could not be used to predict the delamination static strength of the CFRP bonded beams. The results of parametric study showed that the critical SIF increased with increase in CFRP plate thickness, CFRP modulus and the adhesive modulus but the adhesive thickness had a negligible impact on it.

Similarly, the study of variation in SIF with spew fillet angle showed that the SIF value could not represent the severity of the patch end susceptibility to delamination so it was recommended to be helpful in predicting failure for a particular angle of spew fillet. Although their beam flange was uncracked and the locus of SIF was the point lying at the intersection of adhesive-steel interface and the patch-end but still their work highlighted the impact of FRP and adhesive properties on the stresses at the patch end location. Their work concluded that

increase in the FRP patch thickness and modulus increases the shear and peel stresses at the patch end while increase in adhesive modulus also resulted in increase in the patch-end stresses but adhesive layer thickness has a minimal impact on the patch-end stresses.

Mokhtari et al. (2012) studied numerically the impact of variation in bonded composite layer properties on shear and peel stress developed at composite-adhesive interface and within the inner layers of composite itself, in a double lap joint using finite element analysis. They developed a three dimensional finite element model of the double lap joint consisted of three main layers; two composite layers and one adhesive layer, using solid elements. The main layers of any composite-type were also having 16 sublayers but without any adhesive between those sublayers.

The varying parameters included the composite type (or the type of fiber used with various elastic modulus), the composite layer thickness, the fiber orientation in different layers of composite. The study included properties of four most commonly used fiber composites; boron-epoxy (elastic modulus = 193 GPa); T300/934 graphite-epoxy (elastic modulus = 127 GPa); carbon-epoxy (elastic modulus = 109 GPa); aramid-epoxy (elastic modulus = 76 GPa). Six types of plies stacking sequence were used with all four composite-types, which were formed by changing the ply orientation of 12 (out of 16) composite sublayers. In all six laminate types the bottom most two sublayers (at interface) were assigned 0^o fiber orientation while the top most two layers (at free edge) were assigned 90^o fiber orientation. The rest of 12 sublayers, in between the extreme top and bottom of 90^o and 0^o (2 each), were assigned 75^o, 60^o, 45^o and 15^o fiber orientations (in a set of 2 each, respectively from top to bottom). The applied far-field tensile stress was 40 MPa and the adhesive properties were kept constant throughout the study with elastic modulus of 2.7 GPa and thickness of 0.2 mm.

The results showed that von-Mises and peel stresses at the composite-adhesive interface were higher for the stiffer composite types (maximum in boron composite) and with the fiber orientation of 0^o (along the applied tension direction) and were also decreasing in the order of decreasing composite stiffness (boron-graphite-carbon-aramid) and increasing fiber orientation from horizontal (0^o, 15^o, 30^o, 45^o, 60^o and 75^o). The shear stress found to have an opposite trend, i.e. it was maximum in the lowest modulus composite or the least stiff one (aramid composite) with fiber orientation of 30^o and then it decreased with the order of

increasing composite stiffness (boron-graphite-carbon-aramid). They have also studied the impact of providing hybrid composite laminate or a stiffness modified laminate developed by replacing 2 top and 2 bottom sublayers of aramid laminate by carbon plies while the rest of 12 layers were still aramid composite.

The results of stiffness modified laminate showed that the peel and von Mises stress at adhesive interface were increased for each fiber orientation, compared to that of plain aramid composite (but still lesser than that of pure carbon composite), which was because of increased composite stiffness at interface due to the replaced aramid sublayers by carbon. The shear stress little bit increased compared to the aramid alone (but still lesser than that of pure carbon composite) for all fiber orientation, which might be due to increased interface stiffness but for 30^o fiber orientation (in which the shear stress was higher for all fiber orientations) the shear stress of the stiffness modified hybrid composite was very much close to that of only aramid composite.

Further the researchers also studied the impact of increased thickness of 12 inner plies of the carbon composite by 60% while keeping the thickness of extreme top and bottom plies constant. The results showed that the von Mises stress was again in the hierarchy of the stiffness (for 0^o fiber orientation); the maximum was in the patch with modified or increased inner layer's thicknesses more than the plain original carbon patch itself because of increased overall thickness and the content of carbon fibers. The results of peel stress showed that it was decreased in the thickness modified patch compared to the original carbon but still higher than the original aramid (for 0^o fiber orientation) while the results of shear stress showed that it was also decreased from the original aramid laminate but was higher than the original carbon laminate (for 0^o fiber orientation).

Finally the researchers also combined the two modifications (the stiffness and thickness modifications) in a single patch of aramid composite, i.e. the top and bottom most set of two layers in aramid composite laminate were replaced by carbon layers and at the same time the 12 inner layers of aramid were thickened by 60%. The results showed that the peel and shear stresses were close to the original aramid laminate but the von Mises stress was little bit below the original carbon laminate (for 0^o fiber orientation). They concluded that very stiff composites like boron or carbon induces high peel and von Mises stresses at adhesive

interface while a less stiffer composite like aramid induced high shear stress at the interface and these high stresses could lead to laminate delamination. By hybridizing the interfacial plies of the less stiffer composite (like aramid) with plies of very stiff composite (like carbon) and also increasing the thickness of inner plies of the less stiffer composite could reduce the interface shear stress quite below that was caused by the less stiffer composite alone but at the same time the peel and von Mises stress would increase little bit but those would still be lower than that caused by the stiffer composite itself. Additionally, the strength of hybrid composite would also be higher than the less stiff composite alone.

Xia et al. (2005) studied experimentally the bond behavior of CFRP-steel interface with varying adhesive type and thickness using pull-out type tests of CFRP bonded to steel plate and proposed a bond-slip model to predict the bonded joint capacity based upon the properties of adhesive and FRP patch. The test setup was arranged in such a way that the single CFRP layer bonded to the top of steel box system was pulled from its unbounded out-projected end while holding the steel box system from translation or rotation. Three types of adhesives were used, having elastic modulus of 4 GPa, 5.4 GPa and 10.8 GPa with tensile strengths of 22.5 MPa, 13.9 MPa and 20.5MPa, respectively, while four adhesive thicknesses; 1 mm, 2 mm, 4 mm and 6 mm were used for each type of adhesive. The CFRP plate was 1.2mm thick, 50mm wide with an elastic modulus of 165 GPa and it was bonded to steel box assembly using 350mm bond length with a free out-projecting end went to the horizontal grips for pulling.

Governing failure mode observed was delamination of the CFRP plate and it was categorized based upon the location of de-bonding plane, i.e. whether it occurred within the adhesive layer or in the CFRP matrix. The main impact of increasing adhesive thickness was observed in ductility of the specimens together with shifting of the delamination plane from within-adhesive layer towards the CFRP matrix. The thinner adhesive specimens failed in ductile failure mode while the thicker adhesive specimens failed in sudden CFRP plate delamination. It is obvious from their results of the two adhesive types used (out of total three) that the increase in adhesive thickness increased the joint failure load while in the tests with first adhesive type, which also had the greatest tensile strength within the three adhesive types, the thickest adhesive specimen failure load was 88% of the specimen with thinnest adhesive layer. So, irrespective of the specimen ductility the failure load with increasing adhesive thickness

does not drop down for a particular adhesive type (except for one adhesive type mentioned above).

The authors also developed the bond-slip relation of different specimens using the strain gauge data mounted on the surface of CFRP plate at 25 mm interval and found that it was quite consistent for different locations of a particular specimen. They proposed a bi-linear bond-slip model for a FRP to steel bond based upon properties and thickness of adhesive but also found that the interfacial fracture energy (the area under bond-slip diagram) dependent upon the ultimate strain of adhesive in addition to its shear strength. The bond-slip model was basically relation of shear stress in the bond and its slips (displacement) at any location in the bond length and the shear stress developed in bond was calculated from the strains gauge data recorded during experiments. The shear strength of FRP-steel bond (not of the adhesive) which was also the peak point of the proposed bond-slip model was observed to be approximately 80% of the tensile strength of the adhesive used. The slope of the ascending branch of the developed bond-slip model was proposed to be equal to the shear stiffness (G/t) of the adhesive used, although it was observed little higher than it in the tests. Their proposed joint capacities with the experimentally obtained found to be quite consistent.

Taljsten et al. (2009) investigated experimentally fatigue life enhancement of cracked steel plates repaired with double sided bonded CFRP patches. The test specimens were actually cut from girders of an old dismantled truss bridge which was initially constructed in 1896 in Sweden and the intension of research was to study the effectiveness of repairing old steel bridges with real aged surface conditions and mechanical properties. Two types of CFRP used with elastic moduli of 155 and 260 GPa and these were bonded using two different adhesives. Adhesive used to bond 155 GPa CFRP was approximately 60% more stiffer and stronger than that used to bond 260 GPa CFRP and additionally pre-stressed CFRP laminate were also used in some of the specimens. All specimens were 670 mm long and 205 mm wide with a central 10mm diameter hole and two symmetrical starter notches 5 mm long extending diametrically out of the cut hole on its two sides. CFRP patches 400 mm long and 50 mm wide were applied just clear off the starter notch on each side of hole and to both faces of plate so there were two CFRP patches applied on each face of the plate. Tension-tension fatigue loading with nominal maximum stress of 106 MPa and stress ratio of 0.086 was applied with frequency of 13.5 Hz.

Test results showed that the fatigue life of repaired plates was enhanced by 2.45 times to 3.74 times of the unrepaired specimen, for non-pre-stressed specimens, and 8 times to 34 times for pre-stressed specimens and there was also one specimen with high modulus CFRP pre-stressed patch whose test was stopped after the load cycles reached 34 times the fatigue life of unrepaired specimen. Although the test results showed successful application of CFRP patch resulting in noticeable enhancement of fatigue life but comparing the fatigue life enhancement of lower modulus CFRP specimen with that of higher modulus CFRP specimen (for non-pre-stressed case) it can also be noted that the difference in fatigue life enhancement within the two is just 16% while their elastic moduli were differed by 70% approximately, i.e. the fatigue life enhancement is not even proportional to the CFRP relative stiffness ratio.

One possible reason behind such difference can be attributed towards the difference in adhesive properties within the two specimens. The specimen repaired with high modulus CFRP (70% stiffer than the low modulus) was actually applied with adhesive having lower shear modulus and lower shear strength, so, possibility of adhesive shear failure was very high that might have resulted in CFRP delamination around the crack thus increased SIF and not much increased fatigue life.

Ahmed Al-Shawaf (2011) studied behavior and failure modes of steel-CFRP double lap joints and investigated the impact of varying FRP patch parameters on the behavior and failure modes of the double lap joints. The study was conducted over a big temperature range, from -40^{o} C to +60^{o} C, included numerical simulation of double lap joints using 2-D finite element models as well as their experimental verifications. The finite element model included three separate layers of adhesive and CFRP bonded to steel plate using boundary constraints to resemble more common practical situations. Steel plate was 150 mm long and 50 mm wide and the bond length used for patch was 100 mm on each side of central gap such that the total length of a double lapped specimen was 300 mm. Two different types of CFRP with elastic moduli of 240 GPa and 640 GPa and three different types of adhesives with different properties at different temperatures were used, which included Araldite, MBrace Saturant and Sikadur 30 adhesives.

From coupon tests of all adhesives at all temperatures within the range from -40^{o} C to 60^{o} C Sikadur 30 was shown to have greater elastic modulus at ambient temperature of 20^{o} C than

the other two adhesives while MBrace Saturant was shown to have the least elastic modulus at that temperature but the order of ductility at ultimate stage was exactly in reverse order of the elastic moduli. Regarding adhesive tensile strengths at 20ºC Araldite was found to have 50% higher tensile strength than the other two adhesives while MBrace Saturant and Sikadur 30 were shown to have close tensile strengths. The lapped specimens were tested in displacement control mode at rate of 2 mm / min. until failure.

Ambient temperature test results for normal modulus CFRP showed that Araldite specimens achieved highest joint strength which was 105% and 60% higher than the MBrace and Sikadur specimens respectively, while the test results for -40º C for the same CFRP showed even much higher strength of Araldite specimens than the rest of adhesive's specimens. The comparison of ambient as well as below freezing temperature tests results showed dominating impact of adhesive strength on the overall joint strength, although the elastic moduli of Araldite and MBrace adhesives were approximately one fourth and one fifth of the Sikadur adhesive, respectively.

Results of high modulus CFRP specimens showed similar trend but the difference between the strengths of Araldite and the rest of adhesives reduced significantly because of unusual drop in the strength of Araldite specimens themselves compared to the normal modulus CFRP specimens. Although there was 15% to 30% increase in the strengths of MBrace and Sikadur specimens in the case of high modulus CFRP but the Araldite specimens suffered with 15% to 32% strength loss but still greater than the MBrace and Sikadur adhesive specimens.

Wu et al. (2012) studied the behavior of double lap joints with bonded ultra high modulus CFRP (UHM CFRP) patches applied to the steel plates under tensile loading and further verified their experimental results theoretically and numerically. They studied the impact of using two different adhesives with varying bond lengths in the double lap joints on the overall joint strength. The steel plates were 300 mm long x 50 mm wide x 20 mm thick such that the total joint length was 600 mm while UHMC used was in the form of prefabricated 1.43 mm thick plate with elastic modulus of 460 GPa. The two adhesives used were Araldite and the Sikadur 30 with elastic tensile moduli of 1.9 GPa and 9.3 GPa respectively and with tensile strengths of 29 MPa and 24 MPa respectively. They used only one layer of UHM CFRP and

constant adhesive thickness of 0.4 mm while the bond lengths was varied from 50 mm to 250 mm for each type of adhesive.

The experimental results showed that the Araldite specimens achieved 80% higher joint strength compared to the Sikadur 30 specimens with maximum bond length but their effective bond length (after which joint capacity doesn't increase) was found to be 110 mm (on average) which was approximately 30% bigger than that of Sikadur 30 specimens. The failure mode of Sikadur specimens was cohesive failure in adhesive layer at nearly all bond lengths while the failure mode in Araldite specimens was transitioned from the CFRP delamination to the CFRP rupture when varying the bond length from smaller to longer. Their experimental results highlighted the impact of using ideal properties of adhesive in achieving the maximum possible joint strength corresponding to the CFRP rupture, since Araldite adhesive was expected to be 5 times more flexible than the Sikadur 30 which might have relieved most stress concentration at critical load transfer locations and on the other hand it had higher tensile / shear strength than Sikadur 30 which further have helped the specimen in achieving optimum joint capacity.

It is also important to note that the axial stiffness (ETR) of UHM CFRP used in all the specimens was constant or identical but the joint strengths were differed only because of getting the optimum failure mode in the Araldite specimen, which also showed that the success in optimizing the bonded joint strength relies not only on the laminate or FRP properties but most importantly on the deformation capability and strength of adhesive as well. Further in the research they have also developed the bond-slip relation of the specimens with UHM CFRP and compared these with previously developed models in other researches, for normal modulus CFRP laminate and low modulus CFRP sheets, but because of the CFRP rupture failure mode with the Araldite specimens and cohesive failure mode with Sikadur spemens the bond-slip model was developed only for the Sikadur specimen which showed greater fracture energy achieved in the UHM CFRP bond-slip model.

Kennedy and Cheng (1998) studied minimum lap length requirements in the double lap steel joints as well as in cracked steel plates, repaired with single sided CFRP patches. They performed both experimental and numerical work involving double lap steel joints and center-cracked steel plates repaired with single sided CFRP patches, with varying bond lengths and

patch stiffness. They studied stress variation along the bond length and proposed minimum lap length requirements of the bonded patch so as to develop the strain compatibility region within the bond length, which was shown to be depending upon the relative patch stiffness (or ETR) but it was valid only up to the maximum ETR of 0.25.

The results of experimental and numerical work on double lap joints showed that stiffer patches developed lesser shear stress in adhesive at the gap and the same effect could also be produced by a longer lap length of a particular stiffness patch, which was because of the reduction of stress concentration in steel plate at the gap by increase in the lap length. They also investigated numerically the impact of bonded patch properties on the stress concentration factor in the steel plate and showed that the shear flow in adhesive layer is a function of FRP patch ETR as well as of the rate of change of axial strain in the FRP patch.

They also showed that the stress concentration in steel plate at the gap (which also enhances shear stress in the adhesive) is more affected by changing the elastic modulus of a patch rather than its thickness. The conclusion was then translated in their numerical study by using hybrid patches, with a lesser modulus FRP layer replaced some higher modulus FRP layers right at the interface such that the overall ETR remained constant, which showed 11% reduction in stress concentration in steel plate compared to the original complete higher modulus patch. They also proposed minimum bond length requirement in cracked steel plates repaired with single sided CFRP patches which was again valid for a maximum relative patch stiffness (or ETR) of 0.25 and was shown to be requiring larger bond length for a particular ETR patch compared to the double lap case.

They further studied minimum lap required to attain strain compatibility for different crack lengths in the plate, which was based upon the criterion of restoration of stress flow after flowing around the crack. The results showed that the minimum lap requirement for that criterion came out to be greater than the previous other criteria. Their numerical and experimental work showed that the single sided repaired patches reduced strain on the patched face of specimens, compared to unpatched plate, but at the same time developed larger strains on the unpatched face of specimen, even larger than the unpatched plates, because of the bending introduced by the eccentricity in the single sided repairs which increased the strains on the unpatched side. They also concluded that the width of patch has no noticeable effect on

the strain distributions and the most governing parameter in controlling the strain distributions was the patch stiffness ratio (ETR). They have also studied the impact of lap length, patch relative stiffness (ETR) and the patch-end tapering on the stress concentration in steel at the patch end and at plate end (or the crack) locations. They found that the stiffer patches reduced stress concentration near the crack but these increased the stress concentration at the patch end while the less stiff patches can affect in an opposite way.

Finally, they studied the impact of patch-end tapering in reducing the stress concentration and found that a reasonably longer taper step (3 to 6 mm in their study) could effectively redistribute the stresses and could attain strain compatibility. It could also considerably reduce the stress concentration at patch-end. But, too short taper steps (1.5 mm in their study) were found not much beneficial in reducing the stress concentration due to their inability in attaining strain compatibility within the shorter step.

Lam and Cheng (2008) carried out extensive numerical research work in studying the role of bonded repair patches in enhancing the fatigue life of cracked steel plates. They also studied numerically and experimentally bond behavior in double lap steel joints using bonded CFRP patches and extended the ETR range used by Kennedy and Cheng (1998), greater than 0.25. They further refined the study of minimum lap length requirements using nonlinear elastic-plastic behavior of adhesive in double lap joints and proposed relation to predict minimum bond length which depends upon ETR as well as upon the adhesive elastic-plastic shear modulus, thickness and shear strength.

Their experimental results showed that increasing the bond length greater than the minimum lap length required for developing strain compatibility region could not much increase the joint capacity but could introduce ductility before its failure. They also carried out extensive numerical work in studying the strain distributions and the corresponding stress intensity factors (SIF) in single sided and double sided bonded repairs with varying patch stiffness ratios (ETR) and the crack lengths. They concluded that in double sided repairs ETR was found to be the most affecting parameter in reducing the SIF at the crack tip but in single sided repairs the increase in ETR although reduced the SIF at the patched face but increased it on the unpatched face (even more than the unrepaired specimen), which implied that the crack growth would also be different on the two faces of a single sided repaired steel plate. Using

this non-linear distribution of SIF through the plate thickness in a single sided repaired plate they performed numerical study with inclined crack front through the plate thickness and showed that the crack growth in single sided repairs will be slower on the patched face than the unpatched face, which would cause the crack front to be inclined along plate thickness.

They also compared the variation of stress intensity factor along the plate thickness using the Mindlin plate assumption with that predicted by using 3-D solid elements in their finite element study and found that the three-layer Mindlin plate model is slightly un-conservative in predicting the SIF on the unpatched face of the single sided repaired plates, compared to the 3-D solid elements model. They also developed geometric factors f(a/b) to be used in calculation of the stress intensity factor for semi-infinite edged cracked and central cracked plates with varying crack lengths and varying repair patch ETR.

Using the developed geometric factors f(a/b), they successfully predicted fatigue life of a single sided repaired plate with boron fiber composite, tested in other previous research work. They also evaluated fatigue life of cracked steel pipes by using the SIF obtained from the developed 3-D elements model for various ETR and crack lengths and found that the fatigue life enhancement was about 21 times compared to the unpatched pipe. In that particular study they also compared results of using two different types of CFRP; one with higher elastic modulus (Plate type) and; the other with lower elastic modulus (Sheet type). This was done just to incorporate the use of lower modulus sheet type CFRP on pipes because of its curved surface. They have also mentioned a surprizing 25% difference in the SIF values obtained from the finite element results between the two types of CFRP, although the overall patch stiffness ratio (ETR) was kept constant. This result showed that there might be impact of other patch parameters existed, apart from the ETR alone, like the modulus of elasticity of the FRP or the properties of adhesive etc., which have additional impact on the SIF. The researchers also put their recommendations to further explore the impact of other patch parameters which might be the impacting the SIF of identically stiff repair patches.

Holden (2012) studied the effectiveness of CFRP sheets in improving the fatigue life of coped steel beams with a pre-crack of 10 mm at the cope location. The researcher performed five full-scale tests on 4,267 mm long W410 X 54 steel beams with their flanges cut to form the cope at the support resembling a common beam to column or beam to girder connection

detail. The applied load range used was expected to create a nominal 80 MPa stress range at the cope location with stress ratio of 0.2 and the frequency of 4 Hz. The main test parameters were the repair patch orientation, the patch stiffness ratio (ETR) and the repair eccentricity. Three repair patch orientations were used at the cope; longitudinal patch (parallel to the beam length); angular patch (at an inclination of 45^{o} from horizontal) and; orthogonal patch (mixer of horizontal, vertical and angular) while the impact of repair eccentricity was incorporated by using single-sided and double-sided repairs.

The overall experimental results showed that the single sided repairs were less effective in enhancing the fatigue life of the beams because of induction of out-of-plane bending by the repair eccentricity of the system which caused more stress and thus reduced fatigue life. Within single sided repairs the angular repair found to be much effective because of being close to the perpendicular to the crack. The fatigue life enhancements obtained in single sided repairs were 1.16, 1.24 and 1.30, respectively for the longitudinal, orthogonal and the angular repairs, compared to the unrepaired beam. Impact of ETR was not much pronounced in the tests because of being applied only in single sided repairs in which the secondary bending effects ruined the positive impact of ETR, for example the fatigue life enhancement obtained in (single sided) angular repair using 3 CFRP layers was 1.3 while for the same repair configuration but using 6 layers CFRP the fatigue life enhancement was 1.34, which means only 3% more effective than the 3 layers.

Maximum patch effectiveness was achieved in double sided angular repair with 3 CFRP layers on each side (corresponded to the ETR of 0.264), which showed the fatigue life enhancement of 2.85 times compared to the unrepaired beam. It was the only test conducted using double sided repair so the impact of ETR in double sided repairs could not be compared but a comparison of impact of repair eccentricity (i.e. impact of single sided and double sided repair) can be seen by comparing its effectiveness with the beam with single-sided 6 CFRP angular patches that already shown to be 1.34 times more effective than the un-patched beam. The comparison showed that the double sided application of same ETR patch enhanced the effectiveness from 1.34 in single sided case to 2.85, or, about 112%. An analytical model was also developed based upon the principles of LEFM to predict the fatigue lives of the repair details applied at the cracked cope location using Paris-Erdogan relation with additionally

developed geometric factors corresponding to the crack location, stress gradient and the patch effect. The additional geometric factor for the patch effect was adopted from the work by Lam and Cheng (2008) and the fatigue life was calculated for a crack growth of 30 mm from an initial size of 10 mm. The numerical model predicted close number of fatigue cycles for the only one double sided repair, in which case the test to predict ratio was 1.05, but for the rest of all single sided repairs the test to predicted ratio was close to 0.6, even it showed not much difference between the cases of 6 single side angular layers and the 3 single sided angular layers.

2.4 Summary

There exists an extensive amount of research work on the repair of cracked structural elements made up of aluminum, nickel and its alloys using bonded FRC patches, which shows high efficiency of the FRC through their successful application and working in enhancing strength, stiffness and fatigue life of cracked, corroded and weakened parts of important structures made up of aluminum, nickel and their alloys (like aircrafts). The successful application of FRC in repair of aircrafts skins as well as its continuous monitoring for more than twenty years (Baker 1991) provides a good level of confidence in using FRC in repair of structures made up of aluminum and its alloys. Similarly, the use of FRP (or FRC) in strengthening and repair of concrete or reinforced concrete structures is also common and found successful as well as durable, but there is comparatively less work being done in the repair of steel structures using bonded FRC (or FRP) patches, highlighting the factors affecting the efficiency of the bonded patch.

Most of the previous work, involving fatigue behavior as well as the tensile behavior of the steel with bonded FRP repair, showed patch delamination as the governing failure mode of the repair, but there is less work available highlighting the parameters and factors affecting the delamination itself. There is also little work available, studying the impact of patch delamination on crack growth predicting parameters in repaired cracked steel members, like the energy release rate or SIF, although the patch delamination has already been shown to be the governing failure mode in bonded steel structures. Therefore, aim of current research work

is intended towards adding some more work to the research, involving FRP in repair of steel structures, with emphasis on exploration of impact of different patch parameters on adhesive stresses that may initiate patch de-lamination at the patch-steel interface. The aim also includes the study of impact of patch delamination on the crack growth predicting parameter SIF (K_I), and its use in developing fatigue life predictive procedure for cracked steel plates, repaired with FRP patches, considering the impact of patch delamination.

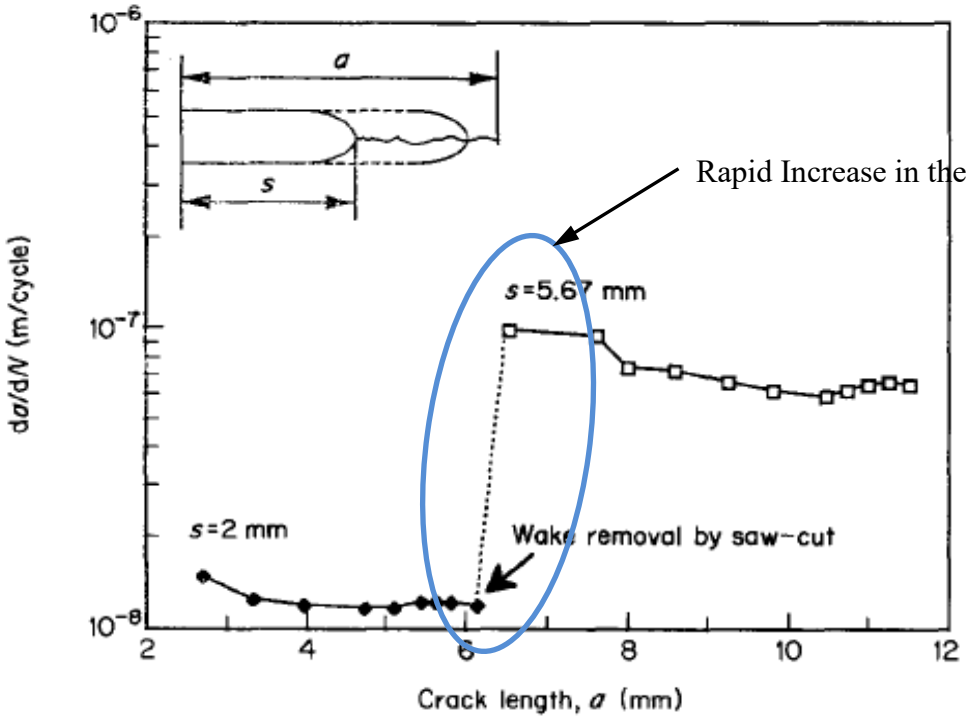

Figure 2.1 Increase in the crack growth rate after cutting crack bridging fibers, Source : Lin et al. (1991)

3. Impact of Properties of Bonded FRP Patch on Interface Stresses and SIF at the Crack Tip

3.1 Introduction and background

Failure mode in most of the experiments, involving bonded FRP patch on cracked or un-cracked steel plates under tensile or fatigue loading, is found to be patch delamination from the patch-metal interface (Lin et al. 1991, Alawi and Saleh 1992, Schubbe and Mall 1999a, Colombi et al. 2003a, Lenwari et al. 2006, Papanikos et al. 2007, Taljsten et al. 2009, Bocciarelli et al. 2009, Liu et al. 2009, Kennedy and Cheng 1998, Ahmed Al-Shawaf 2011, Holden 2012, Mobeen et al. 2012, Mobeen and Cheng 2015), although most of the time the delamination occurs after significant enhancement in tensile capacity or in the remaining fatigue life of the un-bonded plate. But, research work highlighting the factors affecting the initiation of patch delamination are limited (Papanikos et al. 2006, Ahmad Al-Shawaf 2011). Although some researchers studied the impact of patch delamination on several crack growth parameters like the energy release rate or the SIF (Lin et al. 1991, Baker 1999, Schubbe and Mall 1999b, Naboulsi and Mall 1997, Colombi et al. 2003, Papanikos et al. 2006, Madani et al. 2008), but they used the delamination geometry either observed during their experiments or reported in other research works. Even in some works the delamination was propagated arbitrarily in the numerical analysis (Colombi et al. 2002, Lin et al. 1995, Denney and Mall 1997). Some previous and recent works also showed that the adhesive stresses and its distribution is varied by varying properties of FRP or adhesive layers at the interface, without changing the overall ETR (Kennedy and Cheng 1998, Mobeen and Cheng 2014, Mokhtari et al. 2012, Benraho et al. 2010).

Patch delamination usually starts due to localized adhesive or bond failure at patch-steel interface where the localized adhesive or bond stresses (shear or peel stresses) exceeds their respective strengths. These localized failures usually lie within the high stressed regions of bond where the strain incompatibility also exists between the bonded patch and the base metal. Strain incompatibility region exists near discontinuity of either base metal or the bonded FRP patch and these regions also act as stress transfer region for the bonded patch or

the base metal plate. The incompatibility of axial strain between the base metal and the FRP patch results in shear deformation in the adhesive layer between the two, and the maximum value of that shear stress lies at the patch end (Hart Smith 1987, Duong and Wang 2007, Kennedy and Cheng 1998). That is why the FRP patch delamination initiates from these locations. Higher adhesive stresses play an important role in triggering the patch delamination near the crack and the at the patch-end, resulting in increased stress intensity factor (SIF) and crack growth rate (Lin et al. 1991, Papanikos et al. 2007). In bonded repair tests under fatigue loading, the extent of delaminated region observed to grow inside the bonded region through further failure of the bond or adhesive (Papanikos 2007, Colombi et al. 2003a, Bocciarelli et al. 2009) and the rate of delamination depends upon the applied stress range and the strength of adhesive or bond in resisting the delamination growth.

Therefore, in order to study the impact of bonded FRP patch delamination on the crack growth rate in a cracked and bonded-FRP element it is important to explore the factors and parameters leading towards the patch delamination, or more precisely, the patch parameters affecting the magnitude and distribution of localized stresses in adhesive at critical locations. It is obvious from the mechanical properties of the elements of a bonded repair system, involving steel and FRP, that the weakest element in the repair system is adhesive (Xia et al. 2005), compared to steel or FRP. Therefore, a big demand on adhesive properties deemed essential in order to ensure efficient performance of the FRP patch. But, keeping in view the range of strengths of adhesives and epoxies locally available, it becomes much important to explore the parameters and patch properties that would lead to a lesser stress demand on the adhesives.

Previous analytical and numerical works predicting the magnitude and distribution of stresses in adhesive layer (Duong and Wang 2007, Hart Smith 1987) have mentioned that these do not consider the stress concentration at the stress transfer locations, which is found in other numerical works (Kennedy and Cheng 1998). Therefore, in the current chapter, a numerical study of the cracked steel plates double-sided bonded with fiber reinforced polymers (FRP) is carried out with varying patch parameters. The aim is to study and highlight the impact of varying different patch parameters on distribution and magnitude of the adhesive stresses, which might lead to the patch delamination if exceeded the respective strength of adhesive or bond, at patch-steel interface.

3.2 Review of previous work on impact of patch properties on interface adhesive stresses

Work done by Kennedy and Cheng (1998), in investigating analytically the impact of bonded patch properties on the stress concentration factor in the steel plate, showed that the shear flow in adhesive layer is a function of FRP patch ETR as well as of the rate of change of axial strain in the FRP patch. They performed experimental and numerical verifications using their analytically developed relationship between the FRP strain and the adhesive shear flow but due to practical limitations adhesive strains were acquired indirectly from the experimentally determined FRP surface strain. Similarly, most of their numerical work consisted of elastic analyses of two-dimensional finite element models of FRP patch bonded to the steel plate, without adhesive layer in the patch, and they computed shear flow in the adhesive layer in a similar way as they treated the experimental results. Just in one model they included the adhesive layer at the steel-FRP interface, which showed a 33 % reduction in the maximum shear strain at the top of steel plate, compared to the rest of their work (without considering the adhesive layer). They also showed numerically that keeping the overall patch stiffness constant and reducing the stiffness of only one FRP layer at steel-FRP interface, the stress concentration factor in steel can be reduced by 11 %.

Haris and Fay (1991) studied the impact of temperature range (including the glass transition temperature) on static and fatigue strengths of single lap joints with a range of adhesive layer thickness for the two commonly used adhesives in automotive body shells construction. Their results showed that the tensile strength of joints with thicker adhesive were 50 % to 25 % lesser than the joints with thinner adhesives layers for both adhesive types, while the thinner adhesive also showed better fatigue performance than the thicker ones. Their test used single lap joints in which secondary stresses due to system eccentricity may govern, compared to the double-sided repairs. Similarly, very high temperature range (reaching the glass transition temperature) may not resemble the service temperature range for civil structures. Also, the bond length used in the tests was only 15 mm, which is quite less than the minimum required to develop strain compatibility region, as predicted by Hart Smith (1973), Kennedy and Cheng (1998) and Lam and Cheng (2008).

Benraho et al. (2010) studied analytically the impact of adhesive Poisson's ratio and modulus of elasticity on the interfacial shear and normal stresses developed at the edge of a FRP plate, bonded to the bottom flange of a steel beam. Their study showed that an increase in the modulus of elasticity of adhesive results in noticeable increase in the interfacial patch-end shear and peel stresses. But, variation in adhesive Poisson's ratio has minimal impact on the patch-end stresses.

Lenwari et al. (2006) studied numerically and experimentally the impact of properties of CFRP patch and interface adhesive layer on the static and fatigue de-bonding strength of steel beams, with bonded partial length CFRP plates on their bottom flanges. They calculated a critical stress intensity factor at the end of bonded CFRP plate using analytically developed procedure. Their developed procedure was based upon a critical SIF at the patch end, evaluated using reciprocal work contour integral, whose locus lied at the steel-adhesive interface right at the point where the bonded patch end. Although their beam flange was uncrack and the locus for the calculation of SIF was not any crack tip in the steel beam flange, but still, their work shows the impact of FRP and adhesive properties on the stresses at the patch-end location. Their work concluded that increase in the FRP patch thickness and modulus increases the shear and peel stresses at the patch end. Their results also showed that increase in adhesive modulus resulted in increase in the patch-end stresses but adhesive layer thickness has a minimal impact on the patch-end stresses.

Mokhtari et al. (2012) studied numerically the impact of fiber modulus and orientation on adhesive shear, peel and von Mises stresses in a double lap joint using finite element analysis (FEA). They showed that the stiffest fiber type with 0^{o} fiber orientation generated maximum adhesive stresses while the 75^{o} fiber orientation generated least adhesive stresses. They also showed that the adhesive stresses can be varied by using a hybrid laminate but in their work the axial stiffness of laminates, with different fiber types, might not be same because of different elastic modulus of each fiber type.

Xia et al. (2005) studied experimentally the bond behavior of CFRP-steel interface with varying adhesive type and thickness using pull-out tests of CFRP bonded to steel plate. They proposed a bond-slip model to predict the bonded joint capacity based upon the properties of adhesive and FRP patch. The researchers categorized the modes of failure observed during the

experiments, based upon the location of de-bonding plane, i.e. whether it lied within the adhesive layer or in the CFRP matrix. It is obvious from their results of the two adhesive types used (out of total three), that the increase in adhesive thickness increased the joint failure load. The tests with first adhesive type, which also had the greatest tensile strength within the three adhesive types, the thickest adhesive specimen failure load was 88% of the thinnest adhesive specimen. The thinnest adhesive layer was 1 mm thick while the thickest adhesive layer was 6 mm thick in their tests. Therefore, irrespective of the specimen ductility, the failure load with increasing adhesive thickness does not drop down for a particular adhesive type (except for one adhesive type mentioned above), although the de-bonding plane was shifted to the CFRP matrix from the adhesive layer.

Madani et al. (2008) investigated analytically the impact of adhesive layer thickness on the SIF at the crack tip and the COD of centrally crack aluminum panels with bonded graphite repair patch. They modelled the adhesive as shear springs and solved the analytical integral equations of displacements (developed previously by Ratwani et al. 2006) for the adhesive shears and the body forces numerically, using the collocation technique. Although it has been mentioned in the paper that the adhesive shear stresses were also evaluated, but it only showed the results of adhesive layer thickness on SIF and COD. The research concluded that adhesive layer thickness affects the SIF and COD; the thicker the adhesive more will be the SIF and COD. But the range of adhesive thickness chosen was from 0.1 mm to 0.25 mm which captured well a range of thinner and less viscous epoxies but still the study needs to be extended to more thick adhesives because the currently available adhesive thicknesses even exceeds 2 mm for some prefabricated types FRP plates.

Ahmed Al-Shawaf (2011) studied numerically the behavior and failure modes of steel-CFRP double lap joints and investigated the impact of varying FRP patch parameters on the behavior and failure modes of the double lap joints. Two different types of CFRP, with elastic moduli of 240 GPa and 640 GPa and three different types of adhesives, with different properties at different temperatures, were used. They also performed experimental verifications of some of their specimens. The experiment results showed that for identical CFRP patch the specimen with higher adhesive strength achieved maximum tensile strength, although the elastic

modulus of the adhesive used in it was very low. The resultys also highlighted the importance of adhesive strength over the elastic modulus.

Papanikos et al. (2006) studied numerically the impact of bonded FRP patch properties on initiation and progression of the patch delamination due to the strength failure in adhesive and FRP layers, as well as at the plate-adhesive and adhesive-FRP interfaces. Initial investigations showed that the increase in adhesive layer thickness resulted in reduced shear stresses near the crack as well as reduced peel stress at patch-end for thinner base metal (1mm), but for thicker base metal (2 mm) the peel stress increased at the patch end. The increase in FRP patch thickness resulted in reduced adhesive shear stress around the crack region but it increased the peel stress at patch-end. They have also studied the impact of the patch properties on the SIF at the crack tip in base metal and found that the SIF increased by increasing adhesive thickness but reduced by increase in FRP patch thickness, although the peel stress at patch-end also increased by the increase in the patch thickness.

3.3 Description and scope of work to be carried out in current chapter

Conclusively, there is a limited research work available, relating the impact of properties of both the patch and adhesive on the shear and peel stresses develop at the adhesive-steel interface. Further relating these to the SIF at the crack tip of cracked steel plate being repaired, using bonded double sided FRP patch, is also rare. Therefore, it is needed to study and highlight the factors affecting initiation and propagation of the patch delamination, including the patch parameters. This study can also lead to the exploration of reasons behind the discrepancies in fatigue life of identically stiffened repaired specimens, as mentioned in several research works. Therefore, main intention of this chapter wass to study the impact of variation in properties of different parameters of bonded FRP patch (like the thickness and modulus of elasticity of adhesive and FRP) on the interface stresses as well as on the SIF at the crack tip in the steel plate.

The study mainly focused on the magnitude and distribution of stresses developed in the adhesive layer at steel-adhesive interface because the patch delamination is expected to be

caused by failure of adhesive at the locations where the respective shear and bond strengths exceeded. The scope of current study was limited to edge cracked steel plate repaired with double-sided bonded fiber reinforced polymers (FRP) patch under far field tensile stresses and it was carried out numerically using finite element analysis code ABAQUS (Hibbitt et al. 2010).

As already showed in several research works that the number of FRP layers or the overall FRP axial stiffness (ETR) has great impact on increasing the fatigue life of FRP repaired steel structural elements (Lam and Cheng 2008, Liu et al. 2009a 2009b, Jones et al. 2003, Zhao and Zheng 2007). Some numerical works also showed that the increase in ETR or FRP layers reduces the SIF at the crack tip in steel members, being repaired by the bonded FRP patches (Colimbi et al., 2003 and Rose et al. 2012). Therefore, it can be concluded from the abovementioned researches that ETR of the bonded FRP patch has great impact on the SIF of the cracked steel members and it would also affect their fatigue life. The aim of current chapter was to study the impact of other patch parameters, apart from ETR, on the interface stresses and on the SIF at the crack tip in cracked steel plate, so that the discrepancies in the previous research works of getting different fatigue life or SIF of identical or close ETR repairs could be explored. In order to eliminate the impact of ETR in current study the ETR was kept constant throughout in this chapter by maintaining the product of E_{FRP} and t_{FRP} constant in all of the finite element models in current chapter. It is also important to mention here that the same finite element model have also been used in the study of the impact of patch delamination on SIF at the crack tip of crack in steel plate, but, it will be discussed in detail in chapter 4. In chapter 3 the discussion was limited to the impact of patch properties on the SIF at the crack tip of crack in steel plate, without consideration of any patch delamination.

3.4 Stress Intensity Factor (SIF)

Objective of the current research work shows that the SIF or K_I is the most important parameter of the current study. Therefore, its back ground description deemed necessary in the thesis, which is provided in this section. Further discussion related to its evaluation in the current finite element model is also discussed in conjunction.

Irvin (1957) showed that the elastic stress field distribution around the crack tip, or similar singularity dominated regions, is invariant when subjected to one of the three given modes of deformation. The three modes of crack deformations are Modes I, II and III, or namely, the opening, shearing and tearing modes, respectively, as schematically shown in Figure 3.1. He showed that the three planer stress components in the vicinity of a crack for a 2-D case, corresponding to the opening mode or the Mode I, are given by Equations 3.1, 3.2 and 3.3. These stress components are also schematically shown in Figure 3.2, where r is the radial distance of the element (on which stress components are being computed) from the crack tip and θ is the angle between the x-axis and the element radial vector, measured counter clockwise direction (these are also shown in Figure 3.2).

$$\sigma_{xx} = \frac{K_I}{\sqrt{2\pi r}} \cos\frac{\theta}{2}\left(1 - \sin\frac{\theta}{2}\sin\frac{3\theta}{2}\right) \tag{3.1}$$

$$\sigma_{yy} = \frac{K_I}{\sqrt{2\pi r}} \cos\frac{\theta}{2}\left(1 + \sin\frac{\theta}{2}\sin\frac{3\theta}{2}\right) \tag{3.2}$$

$$\tau_{xy} = \frac{K_I}{\sqrt{2\pi r}} \sin\frac{\theta}{2}\cos\frac{\theta}{2}\cos\frac{3\theta}{2} \tag{3.3}$$

In Equations 3.1, 3.2 and 3.3 it is obvious that the magnitude of elastic stress field can be determined by a single parameter K_I, which is defined as the stress intensity factor (SIF) for Mode I (the crack opening mode). Equations 3.1, 3.2 and 3.3 also show that the applied stress, crack size and shape, or the structural configurations, associated with any structural component subjected to this type of crack deformation mode, can affect the magnitude or

value of the K_I (SIF), but the stress field distribution around the crack tip remain unaltered. Stress intensity factor can be determined from the dimensional analysis of the equations 3.1, 3.2 and 3.3 and is given in a general form through Equation 3.4,

$$K_I = \beta\sigma\sqrt{\pi a} \tag{3.4}$$

where 'σ' is the applied nominal stress, 'a' is the crack length and 'β' is the geometrical parameter that depends upon the crack and specimen geometry etc. For an infinitely long and wide plate, with a sharp through thickness crack of length 2a at its center, this factor β converges to unity. For all other cases of plate and crack geometry, the parameter β is treated as a geometric correction factor. It relates the situation of any crack geometry in any structural component, subjected to the same deformation mode, to that of a sharp through thickness crack lying in the center of an infinitely long and wide plate with the crack length 2a. Equations 3.1 through 3.4 shows that SIF relates the local stress field around a sharp crack, in any structural member, to the far-field (or global) stress applied to that member away from the crack.

It is also important to mention here that the impact of a bonded FRP patch over a cracked plate on the SIF has also been treated in most of previous researches through evaluation of the geometric correction factor β, which affects the SIF and thus the crack growth rate in a bonded plate compared to the unrepaired plate. Therefore evaluation of the geometric factor β is one of the main underlying tasks of the current research work, through which the impact of bonded FRP patch on the SIF for different crack locations, has been worked out and shown in the later part of this thesis. It is also important to mention that the geometric correction factor has been represented and notated in the current thesis by $f_{a/b}$ instead of β.

It has also been shown in a linear elastic material condition that SIF is related to the energy release rate 'G' through Equation 3.5 below (Irvin 1968, Barsom 1987, Broek 1986). In equation 3.5 the 'G' can simply be defined as the change in potential energy in a body per unit crack extension area, for a unit width of material.

$$K_I = \sqrt{GE} \tag{3.5}$$

It has also been shown for linear elastic material that the energy release rate G is equal to the J-integral or the contour integral (Broek 1986), so the Equation 3.5 can also be written in terms of J-integral for linear elastic condition, as shown in Equation 3.6 below,

$$K_I = \sqrt{JE} \tag{3.6}$$

where J is the J-integral, as defined by Rice (1968), and in its simplest form it is shown in Equation 3.7 below. J-integral is basically energy conservation criterion, which requires work done by the external force must be converted into internal strain energy. The first term in Equation 3.7 shows the strain energy and the second term shows the work done by forces. Therefore, J-integral is path independent by virtue of energy conservation and is zero for a close loop. Rice (1968) applied it around a crack region and formulated it for any loop or patch Γ around crack tip as shown in Figure 3.3.

$$J = \int_{\Gamma} (W dy - T \frac{\delta u}{\delta x} ds) \tag{3.7}$$

where Γ is an arbitrary contour surrounding the crack tip as shown in Figure 3.3, 'W' is strain energy density, 'y' is the displacement in perpendicular-to-crack direction, 'T' is the traction vector, 'u' is the displacement vector and, 'ds' is the differential distance along the contour.

For linear elastic condition and known material modulus of elasticity E, K_I around a crack tip can be determined by evaluating J-integral using Equation 3.7 and submitting it into Equation 3.6. ABAQUS software has the capability of evaluating J-integral around a defined crack tip by applying Equation 3.7 internally to the analysis output of the available nodes around the crack tip. Further knowing the material modulus of elasticity E, K_I can be evaluated by ABAQUS and it is available as an analysis output parameter.

ABAQUS evaluates SIF (K_I) around every node which is part of the crack tip because in a three dimensional problem the crack tip becomes a crack front through the thickness of material, having several nodes formed by the meshing provided in the thickness of any model. Therefore, if there are n numbers of nodes lying on a crack front along the thickness of a cracked plate then ABAQUS evaluates J-integral and the corresponding SIF around the crack front at each n^{th} node. In this way SIF distribution through the thickness of material can be

obtained, which provides a mean to study SIF variation within the material thickness. Additionally, ABAQUS could also evaluate the J-integral and the corresponding K_I at more than one loop around a single node by selecting different coplanar loops around the same node with increasing loop size, just like drawing increasing radii circles around a single point. In current study three values of K_I , corresponding to three different loops, were considered at each node of the crack front to arrive at a stable K_I value.

3.5 Finite element analysis

A three-dimensional finite element model, comprised of cracked steel plate with bonded layers of FRP and adhesive, was developed and analyzed using finite element code ABAQUS Standard (Hibbitt et al. 2010). Figure 3.4 schematically shows the selected edge cracked steel plate with bonded FRP patch, under axial tensile loading. The crack opening is exaggerated in Figure 3.4 and the layers of bonded patch are just representative, as there may be more than one FRP layer in the models being studied. Plate size was selected to be 300 mm long x 50 mm wide x 7.5 mm thick. Plate length was sufficient to provide 75 mm to 100 mm bond length of FRP patch on each side of crack, which was more than the minimum required to develop strain compatibility region within the bond length, as mentioned in the previous research works (Lam and Cheng 2008, Kennedy and Cheng 1998). Existence of strain compatibility within the bond length was also confirmed later on in the FEA by checking the presence of elastic trough (minimal shear stress region) in the adhesive shear stress distribution and it has also been discussed in detail in later part of this chapter. Applied far field stress was selected to be 100 MPa, which was close to one third of the yield strength of steel and was reasonable to study stresses in adhesive and FRP layers.

Crack length was selected to be 15 mm in the current study in all bonded FRP finite element models, except in the validation phase, in which the crack length was varied from 10 mm to 40 mm in the FEA of un-patched steel plate, which is discussed in detail in section 3.5.1. Crack length of 15 mm, which was equivalent to the ratio of crack length to plate width of 0.3, was selected keeping in view the ease in crack detection during inspection of civil infra structures, which was not too small neither too big. The thickness of plate was chosen to be

representative of a typical web plate of a steel beam or girder in civil structures, in which fatigue cracks are more expected due to the stress concentration in typical connection details.

Several previous researchers studied the behavior of bonded plate with FRP patching using different numerical techniques including FEA. Most of these researches performed two-dimensional analysis and modelled the adhesive layer with shear springs at the interface of FRP patch and the base plate (Madani et al. 2008, Sun et al.1996). Later on some researchers used more realistic approach by modelling the adhesive layer with continuum shell elements (or Mindlin plate elements) and found it more realistic than the shear springs (Naboulsi and Mall 1996, Schubbe and Mall 1999a, Colombi et al. 2003). This approach is well renowned as the three-layer technique and is based upon linear variation of displacement field through the element thickness, with identical displacement boundary constraints at the interface nodes of adjacent layers. Lam et al. (2008) compared the behavior of a three-layered model that uses Mindlin plate assumption with a modified three-layered model using 3-D solid elements in the metal plate. They found that the SIF distribution was non-linear through the plate thickness in the modified 3-D model, in contrast to the linear variation assumption in the model that uses Mindlin plate elements. They found that in a single sided repaired cracked plate, the SIF was slightly conservative on the patched face of the plate but it was un-conservative on the unpatched face, if using the Mindlin plate elements.

Keeping in view the research outcome of Lam et al. (2008), 3-D solid elements (brick elements) were selected in the current research work to model the steel plate and the patch layers. Since the scope of current research was limited to the double-sided repairs, in which bending is expected to be minimal, therefore, the selection of Solid elements suited more in this case because of the unavailability of rotational degrees of freedom in these elements. Other advantages of using Solid elements were the availability of the all stress components at its six faces and the ease in assignment of different boundary conditions at different faces of the same element. This advantage of Solid elements was found to be extremely useful in defining the boundary constraints at the interfaces of FRP and adhesive layers, in which the two opposite faces of same element were needed to be assigned different displacement constraints. It was also helpful in relaxing the displacement constraints in some portions of the first FRP layer, after localized failure in the adjacent adhesive layer. It is described and

demonstrated in detail in chapter 4 of the thesis, in which patch delamination was introduced through failure of the interface adhesive layer.

Keeping in view the SIF to be extracted from the analysis, a very fine mesh deemed necessary around the crack tip. Therefore, two distinct regions were defined in the model of steel plate; a near crack region; and a farther region. Near crack region was fine meshed and was intended to evaluate SIF, so, its size was not required to be much bigger. It was selected to be 20 mm along the plate longitudinal direction, with the crack at its center, while its width was selected to be full width of the steel plate. Since farther region was acted as the medium through which the applied stress was transferred from the plate edges to the near crack region, therefore, a varying mesh seeding was assigned to it. Finer mesh was assigned near the crack region and at the loading face, while coarser mesh was assigned in region lying between the crack region and the loading face. The finite element model with the near crack and farther region is schematically shown in Figure 3.5.

Due to the presence of crack in plate, elements surrounding the crack tip were expected to be capable of capturing singular properties of strain or the stress field. Barsom (1976) showed that singularity of strain and stress at the crack tip could be achieved in 8 nodes iso-parametric elements or in 20 nodes 3-D iso-parametric elements by displacing mid nodes of the element's sides connecting the crack tip to the quarter point of the sides. ABAQUS has the option of introducing the crack tip singularity by displacing the mid nodes of element's sides to their quarter length as well as collapsing the corner nodes of the side near crack tip to a single node linking the crack tip. These elements are named as collapsed nodes elements in ABAQUS and are schematically shown in Figure 3.6. In the current plate model, the crack tip singularity was introduced by using the collapsed nodes elements.

Crack was defined by a through thickness crack front (or the crack tip in 3D) at the desired crack length (15 mm here), as shown in Figure 3.7. The crack extension direction was defined perpendicular to the applied load direction, using a space vector option in that direction. Taking the advantage of available planes of symmetry in the model, one quarter of the complete model was generated and used in the analysis. Figure 3.8 shows the two planes of symmetry; one lying at the half plate length and the other at the half plate thickness. To model actual layup of the bonded patch, layers of adhesive and FRP were assigned in the same

sequence as followed in wet layup process. Each layer of adhesive and FRP was assumed to have perfect bond at its interface with the adjacent layers, which was accomplished by introducing the displacement constraint between the two adjacent surfaces, at all the interfaces of patch. The displacement constraint only restricted the surface nodes of the two adjacent surfaces to have identical displacement, but, within the thickness of any layer of adhesive or FRP, the displacement or strain could be varied independently.

Therefore, at steel-adhesive, adhesive-FRP and FRP-adhesive interfaces the displacement constraint could be mathematically expressed by Equations 3.8, 3.9 and 3.10 below, respectively for the displacements in three orthogonal directions; u, v and w. The subscripts s, a and frp stands for steel, adhesive and FRP, respectively.

$$u_a = u_s \qquad v_a = v_s \qquad w_a = w_s \tag{3.8}$$

$$u_{frp} = u_a \qquad v_{frp} = v_a \qquad w_{frp} = w_a \tag{3.9}$$

$$u_a = u_{frp} \qquad v_a = v_{frp} \qquad w_a = w_{frp} \tag{3.10}$$

Displacement constraints, as defined by the Equations 3.8, 3.9 and 3.10, were introduced in the FEA using the option of master-slave tie boundary constraint. It was assigned in such a way that at any interface the lower (inner) surface was assigned as master surface and the upper (outer) surface as the slave. The lower and upper surfaces were designated by keeping in view the physical layup process, in which, the lower layer was assumed to be applied first (or already existed before the upper layer) and the upper surface is that surface of the upper layer which was facing the lower layer. The assignment of master-slave tie surface constraints between the layers of a three layered FRP patch is schematically shown in Figure 3.9.

In this way each adhesive or internal CFRP layer was assigned slave boundary constraint on its one face and master boundary constraint on its other face and this was one of the main advantages of using Solid / Brick elements as mentioned before. In general, the displacement constraint applied through master-slave tie boundary constraint at all interfaces can generally be represented by Equation 3.11 below.

$u_{slave} = u_{master}$ $v_{slave} = v_{master}$ $w_{slave} = w_{master}$ (3.11)

3.5.1 Finite element analysis of plain steel plate and its validation

In order to validate working of the developed finite element model, initially an unpatched or plain steel plate, with the edge crack, was analyzed using ABAQUS. One quarter of the complete model of plain steel plate (as shown in the Figure 3.8) was developed using the planes of symmetry as already discussed in section 3.2. Overall dimensions of the one-quarter plate became 150 mm x 50 mm x 3.75 mm thick and the same is shown in Figures 3.7 and 3.8. Collapsed nodes elements C3D20R were assigned in the near crack region and the crack was defined using the procedure of section 3.2. Crack length in the validation phase was varied from 10 mm to 40 mm, with interval of 10 mm, by developing successive models for each crack length. It was carried out to obtain SIF (K_I) for increasing crack length and to compare the SIF variation with the standard case of edge cracked plate, already developed in other research works.

The crack length was only varied in the validation phase of FEA, while in rest of the study in this chapter the crack length was constant and provided to be 15 mm, as already discussed in section 3.5. Modulus of elasticity of steel (E_s) was provided to be 200 GPa and linear elastic analysis was performed under a far field tensile stress of 100 MPa, applied at the outer face of the one quarter model. Figure 3.10 shows the resulting deformed geometry of the plain steel plate, with visible near crack and farther regions and with crack being opened-up. Mesh refinement was carried out within the crack region by monitoring the variation in SIF values at the crack tip, with increasing mesh density. It was found that meshing in the thickness of crack region had little impact on the SIF (K_I) values and the convergence was achieved by increasing the number of elements from 4 to 20, which brought the difference in the successive values of SIF (K_I) from 3 % to 1 %. Therefore, 20 elements were used in the thickness of the crack region (or 10 elements in the quarter model). Similarly, mesh refinement in the plane of the steel plate achieved with element size of 0.5 mm x 0.5 mm, which brought the difference in K_I values to less than 0.6 %.

Therefore, in further FEA, presented in the current chapter as well as in rest of chapters, the element size near crack-tip was always provided lesser than the maximum size achieved in the refinement process. Mesh refinement was also carried out in the farther region, especially on its edges adjacent to the crack region but it was found that it has no impact on the SIF (K_I) values at the crack tip. Farther region was provided with a double biased mesh, which turned finer near the crack region and at the loading face, as shown in Figures 3.5, 3.7, and 3.8, to optimize the file size and the analysis run time.

SIF (K_I) values obtained from the results of FEA were for the full crack front through the plate thickness. The SIF values were extracted from the results of FEA of the five crack lengths (5 mm, 10 mm, 15 mm and 20 mm) and these are shown in Figure 3.11. It can be noted from the figure that the SIF was varying across the plate thickness in all the crack lengths. It can also be noted that the crack lengths mentioned in Figure 3.11 were non-dimensionlized by dividing these with the plate width of 50 mm. It is also reflected in Figure 3.11 that the values of SIF (K_I) were little higher near the plate center and comparatively lower near the outer free surface. It was mainly because of relatively plain strain condition in the center of plate and plain stress condition near the outer free surface. The difference in SIF (K_I) values between the plate center and the exterior surface was approximately around 10 % for all crack length, which was very much similar to that reported in the previous research work by Lam and Cheng (2008).

In order to validate working of current FEM of plain steel plate, the SIF (K_I) obtained from FEA (already shown in Figure 3.11) were then needed to be compared with SIF (K_I) values available in previous literature for the standard case of edge cracked plate. Tada et al. (2000) provided a fourth order polynomial function for geometric correction factor β to predict SIF (K_I) of an edge cracked semi-infinite plate under applied far-field tensile stress, which is again reproduced here in Equation 3.12.

$$\beta = 1.12 - 0.231\left(\frac{a}{b}\right) + 10.55\left(\frac{a}{b}\right)^2 - 21.72\left(\frac{a}{b}\right)^3 + 30.39\left(\frac{a}{b}\right)^4 \qquad (3.12)$$

The SIF (K_I) obtained from current FEA (as shown in Figure 3.11) were then re-plotted with respect to the non-dimensionalized crack length (a/b), as shown in Figure 3.12 to compare with those provided by using β from Tada (2000). The same figure also shows the SIF

variation calculated using Equation 3.4 with β evaluated from Equation 3.12. It is obvious from Figure 3.12 that the SIF variation obtained from the FEA were very close to the predicted using Equations 3.4 and 3.12. The validation provided a good level of confidence on working of the developed FEM. It can also be noted from Figure 3.12 that the SIF values using Equation 3.4 and Equation 3.12 were lying closer to the SIF values obtained from the FEA for the nodes located near the outer free surface of plate, compared to the SIF values of nodes located near the plate center. It was because of limitation of Equation 3.4 to the plane stress condition, which was more likely to exist in the exterior portion of the plate compared to its interior region.

3.5.2 FEA of cracked steel plate with bonded FRP patch

After gaining confidence over working of the developed plain steel model through its validation carried out in section 3.5.1, the next step was to develop the model of bonded FRP patch and to further study the impact of bonded patch parameters on SIF variation at the crack tip in the steel plate and their impact on the interface adhesive stresses, which were the main tasks of the current research phase. Finite element models developed in this study were basically consisted of the cracked steel plate (same as the one used previously in the validation phase) with added bonded FRP and adhesive layers. Most of the developed FEM in the current phase have one FRP layer bonded to the steel plate with one interfacial adhesive layer but later on in the end of the current chapter FEM with more than one FRP layers were also analyzed to study the impact of FRP layering on the selected studied parameters.

It is also important to mention here that throughout in current chapter the crack length was selected to be 15 mm and the ETR of FRP patch was kept constant. These parameters were kept constant in order to eliminate their impact on the results and to study mainly the impact of other patch parameters within identically ETR patched specimens. The variable patch parameters included the elastic modulus and thickness of adhesive and the FRP, i.e. E_A, E_{FRP}, t_A and t_{FRP}. Impact of the varying parameters was studied on the SIF (K_I) at the crack tip of the crack in steel plate and on the interface adhesive stresses (shear and peel). These parameters were selected to be studied because SIF (K_I) value is an indicator of vulnerability to the crack growth and the magnitude of stresses in interface adhesive layer is an indicator of

vulnerability to the patch de-lamination. It is also important to mention here that the adhesive properties t_A and E_A were varied independently in this study but the FRP properties t_{FRP} and E_{FRP} couldn't be varied independently in order to maintain the ETR constant, therefore, these were varied in such a way that the ETR remained constant. Keeping in view the variable parameters to be studied, the finite element models (FEMs) were divided into three groups such that each group contained one variable parameter to be studied. Tables 3.1a, 3.1b, and 3.1c show details of the developed FEMs to study the impact of main variables. FEMs in Table 3.1a have adhesive thickness t_A as the variable parameter, the FEMs in Table 3.1b have adhesive elastic modulus E_A as the variable parameter and the FEMs in Table 3.1c have FRP thickness t_{FRP} and elastic modulus E_{FRP} as the variable parameters. FRP and adhesive properties used in this study were selected from a range of commonly and commercially available carbon fiber reinforced polymers (CFRP) with their compatible adhesives. However, in some cases the properties were selected to achieve upper or lower bound of ranges. In general the adhesive thickness t_A used was ranging from 0.1 mm to 4 mm, adhesive elastic modulus E_A ranged from 1.25 GPa to 20 GPa, FRP thickness t_{FRP} ranged from 1mm to 5mm and FRP elastic modulus E_{FRP} ranged from 40 GPa to 200 GPa.

Nomenclature of the FEMs was adopted such that the initial portion of name of any model represented the variable parameter (in short form) followed by the value of that variable in the FEM. As an example, in Table 3.1a the variable parameter was t_A so all of its models started with "Adh-T-" and then followed by the value of the adhesive thickness in mm. Therefore, Adh-T-0.5 represented a model with t_A as the variable parameter and it was having adhesive thickness of 0.5 mm. In Table 3.1c, apparently there are two variable parameters; t_{FRP} and E_{FRP}, but these two were actually not independent to each other to keep the ETR constant. The model's names in Table 3.1c contained both CFRP parameters in their names. It is also reasonable to mention here that in Tables 3.1a and 3.1b the adhesive properties were varied but the FRP properties were kept constant. These were adopted for a plate-type thicker FRP and that is why the adhesive thickness in these tables includes quite thicker adhesives, which are mostly recommended for the pre-fabricated FRP plates. To incorporate properties of thinner adhesive or epoxies, which are also practically common, the FEMs in Table 3.1c were assigned properties of thinner adhesives. For the same reason the range of FRP properties in this table also includes properties of some sheet-type FRP, which requires thinner adhesives.

Adhesive and FRP layers were modeled and applied to the cracked steel plate by assigning displacement constraints at interfaces between steel-adhesive and adhesive-FRP, following the procedure of section 3.5 and a typical one layered FEM is shown in Figure 3.13. Material properties of steel plate were assigned corresponding to those of mild steel, with modulus of elasticity of 200 GPa and Poisson's ratio of 0.3, respectively. Linear elastic analysis was performed under the far field applied stress of 100 MPa and the results of FEA are presented and discussed in detail in the subsequent sections.

3.5.3 Results of finite element analysis

As already described in section 3.5.2 that the impact of adhesive and FRP properties will be studied on two parameters; interface adhesive stresses; SIF (K_I) at the crack tip in steel plate. But before going into details of FEA results, the assumption of FRP patch length fulfilled the minimum effective bond length criterion, was needed to be validated, as required in section 3.5. Effective bond length is the minimum bond length that can form strain compatibility region between the steel plate and the FRP patch. The existence of effective bond length could be indicated by the existence of region of negligible or zero shear stress in the adhesive layer, within the strain compatibility region. Therefore, the existence of strain compatibility between the steel plate and FRP patch was validated in all the FEMs by studying their adhesive shear stress distribution. Due to the crack being on one edge of plate, more critical stress distribution was expected on the crack side within the plate width, and therefore, it was chosen to study the shear stress distribution in the bond length in all FEM.

Figure 3.14 shows deformed shape of a typical FRP bonded model and it also shows the location of the section chosen for studying adhesive shear stresses. Interface adhesive shear stress distribution in all the specimens, along the bond length, was extracted and is shown in Figures 3.15, 3.16 and 3.17, respectively for specimens of Tables 3.1a, Table 3.1b and Table 3.1c. These figures show that irrespective of the main variable parameter in these figures, the adhesive shear stress in mid-bond region was very small, indicating the existence of strain compatibility between the steel plate and FRP patches. The shear stress was then increased near the crack and the patch-end locations, indicating the existence of non-compatibility of

strain between the plate and FRP patch. The existence of enough strain compatibility region within the bond lengths also indicated that the selected bond length in current study was sufficient to be qualified for the effective bond length. Figures 3.15, 3.16 and 3.17 also show that the peak adhesive shear stress near the crack and the shear stress distribution in all the specimens differed noticeably, although, ETR in all the specimens was provided to be 0.264. It also indicated that the chances of adhesive shear failure within all these specimens would not be same for a given adhesive shear strength.

Comparing the shear stress distribution for specimens of Table 3.1a in Figure 3.15, it can be concluded that for a given FRP properties and adhesive modulus, increase in adhesive thickness decreases the magnitude of peak shear stress in non-strain-compatibility regions, although the peak shear stress decays much rapidly in thinner adhesives. The peak shear stress value becomes more important when it is comparable to the shear strength of adhesive or bond because localized patch delamination could be initiated through the shear failure of adhesive or bond at interface. Figure 3.16 also shows that for a given FRP and adhesive thickness increase in modulus of elasticity of adhesive also resulted in increase in the peak adhesive shear stress, in the same way as it varied with decreasing adhesive thickness in Figure 3.15. The two conclusions from Figures 3.15 and 3.16 could be combined in a single one; increase in either the elastic modulus of adhesive or decrease in its thickness results in increase in the peak adhesive shear stress near the crack. Therefore, patch de-lamination can be triggered at those locations if the developed shear stress exceeds adhesive shear strength or the bond shear strength at the steel-adhesive interface. Figure 3.17 shows the adhesive shear stress distribution in specimens of Table 3.1c. This figure shows that the distribution as well as magnitude of peak shear stress was approximately identical in all specimens. It indicated that adhesive shear stress would not be affected by changing the elastic modulus or thickness of FRP while keeping the patch ETR (or its axial stiffness) constant.

3.5.3.1 Individual impacts of adhesive thickness and modulus on peak shear stress

The peak value of adhesive shear stress, right at the crack location in all the models of Table 3.1a and 3.1b, was extracted and is respectively shown in Figures 3.18 and 3.19. Both figures show that the variation in maximum adhesive shear stress with respect to the variation in

adhesive modulus E_A or thickness t_A was not linear. Figure 3.18 shows that the peak adhesive shear stress increased by 210 % by decreasing the adhesive thickness by 40 times, but it was not a linear variation and the major increase in adhesive shear stress occurred for adhesive thickness less than 1 mm. If adhesives thickness lesser than 1 mm are taken out of the comparison then it can be shown that the increase in adhesive stress became 68 % due to decrease in adhesive thickness by four times only (from 4 mm to 1 mm). Similarly, Figure 3.19 shows that the peak adhesive shear stress increased by 4.5 times due to increase in adhesive modulus of elasticity by 16 times (from 1.25 GPa to 20 GPa). This variation in adhesive shear stress although wasn't linear but it appeared to be of lesser order than the variation obtained in Figure 3.18, for varying adhesive thickness. Therefore, use of thinner adhesive or adhesive with higher E_A introduces higher shear stress around the crack and can cause patch delamination if the adhesive shear strength is not sufficient to overcome the developed shear stress. It can also to be noted that the current comparison shown in Figure 3.19 corresponds to one adhesive thickness of 2 mm, therefore, the order of variation may vary for different adhesive thicknesses.

3.5.3.2 Individual impacts of adhesive thickness and modulus on peak peel stress

It has already shown in previous literature (Duong and Wang 2007) that the peel stress is maximum at the end of bonded patch and it generates mainly due to the minor eccentricity between the line of action of forces in the plate and the patch. The peel stress concentrates more at the patch end due to the strain incompatibility between the patch and steel plate as well as due to no patch left after it to resist the peeling action, which results in minor rotation of free end of the bonded-patch, thus resulting in an outward peel-off stress. Figure 3.14 is again drawn in Figure 3.20 with the highlighted patch-end showing small patch-end rotation due to the action of peel stress. Peel stress in all current models was found approximately constant along the patch width due to uniaxial nature of the applied stress. Its peak value at the patch-end location was extracted for the specimens of Table 3.1a and 3.1b and is respectively shown in Figures 3.21 and 3.22. It is obvious from Figure 3.21 that adhesive thickness is shown to have minimal impact on the peel stress. For an increase in adhesive thickness by 8 times the adhesive peel stress decreased by only 17 %. It was an important finding because it

is contrary to a common understanding in most of the previous experimental research works that thicker adhesives results in higher peel stress. In contrast to adhesive thickness the impact of adhesive elastic modulus was found more prominent in enhancing the peel stress, as shown by Figure 3.22, from which it can be evaluated that 15 times increase in adhesive modulus results in 500 % increase in the peel stress.

3.5.3.3 Individual impacts of adhesive thickness and modulus on SIF at crack tip of steel plate

Impact of adhesive properties on the SIF (K_I) at the crack tip of crack in the steel plate being repaired was studied in a similar way the peak shear and peel stresses were studied. SIF (K_I) distribution was extracted from the analysis results for the specimen of Table 3.1a and 3.1b, in a similar way as it was extracted for the plain un-patched steel plate (as discussed in section 3.5.1), but here the through thickness SIF variation was not considered to be much important for each model because the SIF distribution within plate thickness in each model was expected to follow similar pattern. Therefore, the numerical value of SIF was considered more important for a comparative study within the models. The SIF (K_I) at the centroid of steel plate was then selected for the comparative study and the numerical value of SIF at steel centroid was extracted for all the specimens of Table 3.1a and 3.1b, which is shown in Figures 3.23 and 3.24, respectively. It can be noted in these figures that the SIF (K_I) also affected by the adhesive properties, which was not much highlighted in previous researches.

Figure 3.23 shows that increase in adhesive modulus of elasticity resulted in exponential decrease in the K_I at the crack tip. For 15 times increase in the adhesive modulus E_A the K_I at the steel centroid was decreased by 46 %. Similarly, Figure 3.24 shows the impact of adhesive thickness on the SIF (K_I) and it shows that increase in adhesive thickness resulted in increased K_I at the crack tip. But the variation of SIF was not linear and its rate of increase was much higher for adhesive thickness less than 1 mm. For the overall range of adhesive thickness, it was evaluated that an increase in adhesive thickness by 40 times resulted in the increase in K_I magnitude by 60 %. If the adhesive thickness less than 1 mm were taken out of the comparison then it could be shown that the increase in K_I would be only 15 % for a 300 % increase in adhesive thickness greater than 1 mm. One of the expected reasons of getting impact of adhesive thickness on the K_I was because of the contribution of adhesive shear

deformation to the crack opening displacement (COD), which is related to the K_I. But the adhesive shear deformation itself depends upon adhesive thickness, therefore, thicker adhesive allows more crack opening, through more shear deformation, which can result in increased K_I. This impact of adhesive thickness on K_I is similar to the impact of adhesive thickness on peak adhesive shear stress (section 3.5.3.1) but the trend is reverse, therefore, the two impacts of adhesive thickness found from the Figures 3.18 and 3.24 can be jointly described as the increase in adhesive thickness decreases the peak adhesive shear stress at the crack location but at the same time it also increases K_I at the crack tip due to more adhesive shear deformation.

3.5.3.4 Combined impact of adhesive thickness and modulus on interface stresses and SIF

After analyzing individual impacts of adhesive thickness t_A and adhesive elastic modulus E_A on the stresses in interface adhesive layer and on the SIF (K_I) at the crack tip, it was needed to study the combined impact of the two parameters. It could be helpful in practical situations in which two different adhesives are to be compared, having different thickness and elastic modulus. Sections 3.5.3.1, 3.5.3.2 and 3.5.3.3 and Figures 3.18, 3.19, 3.21, 3.22, 3.23 and 3.24 show that the individual impact of adhesive thickness t_A and modulus E_A were opposite on the adhesive stresses or on the SIF (K_I). Therefore, in order to obtain the joint impact of these two parameters their simple product, like $E_A \times t_A$ (the adhesive axial stiffness), didn't seem to work because of their opposite individual impacts. In order to have a combined parameter of these two parameters, it was needed to consider inverse of any one these in their product, therefore one possible combination would be $E_A \times 1/t_A$. But keeping in view the governing shear deformations in behavior of an adhesive, its shear modulus G_A suited better over its E_A in the product, which finally provided $G_A \times 1/t_A$ or simply G_A / t_A as the combined parameter of adhesive properties. It contained the impact of adhesive thickness (geometric property) as well as its shear modulus G_A (material property). Duong and Wang (2007) have developed equation for predicting maximum adhesive shear stress at the crack location for bonded patches, which is reproduced below as Equation 3.13. It is obvious from this equation

that it inhibits the parameter G_A/t_A, along with other parameters. The parameter G_A/t_A can also be treated as the shear stiffness of adhesive; higher its value more rigid the adhesive in shear.

$$\tau_{max} = \frac{G_A}{\beta_A t_A}\left[\frac{\sigma_o}{SE_s}\right] \tag{3.13}$$

where β_A was given by

$$\beta_A{}^2 = \frac{G_A}{t_A}\left[\frac{1}{E_p t_p} + \frac{1}{E_s t_s}\right] \tag{3.14}$$

Note that the subscripts s and p in Equations 3.13 and 3.14 denote steel plate and patch, respectively, while 'S' is the ETR and σ_o is the applied stress in these equations.

3.5.3.4.1 Variation of peak adhesive shear stress with adhesive G_A / t_A

After merging the two adhesive parameters by observing their individual impacts, as discussed in the previous section 3.5.3.4, variation of adhesive stresses was then analyzed with respect to this combined parameter 'G_A/t_A' or the adhesive shear stiffness. All models of Tables 3.1a and 3.1b were then rearranged with respect to their G_A/t_A and these are shown in Table 3.2, with only modification that their shear stiffness was non-dimensionalized with the shear stiffness of steel plate and is shown in the form of relative shear stiffness. The results of FEA of the models of Tables 3.1a and 3.1b, which have already been discussed in section 3.5.3.1 and presented in Figures 3.18 and 3.19, were rearranged with respect to their adhesive G_A/t_A, and are redrawn in Figure 3.25. It is reflected from Figure 3.25 that the two oppositely varying results of Figures 3.18 and 3.19 have now better synchronized with the parameter G_A/t_A. It is needed to mention that in Table 3.2 and Figure 3.25 some of the models of Table 3.1a were dropped out because of having their G_A/t_A values out of the comparison range. Figure 3.25 shows that the trend of variation of adhesive shear stress within models of Tables 3.1a and 3.1b becomes similar when compared with respect to the adhesive G_A/t_A. Figure 3.25 also shows that, for a given G_A/t_A value of two extremely different adhesives, there is small

difference in the corresponding shear stress. It can also be noted from Figure 3.25 that the impact of adhesive G_A was little higher than the adhesive G_A/t_A alone, but still not a huge difference. For example, the difference in peak adhesive shear stress in the two types of models of Table 3.2, corresponding to the adhesive relative G_A/t_A of 1.29 %, was about 14 %. The difference of only 14% appeared much smaller compared to the 300 % difference in their elastic moduli and thicknesses. It can now be summarized that adhesive thickness or adhesive elastic modulus might not be independent parameters, affecting the peak adhesive shear stress at the crack location, in bonded FRP patches and a better parameter would be G_A/t_A to study the impact of adhesive properties on peak adhesive shear stress. The parameter G_A/t_A contains effect of both the individual adhesive parameters of thickness and elastic modulus. Therefore, if in a bonded FRP repair patch the adhesive has a higher G_A/t_A, whether it is because of high G_A or a very small t_A, then the peak shear stress in the adhesive layer at the crack location will be higher.

3.5.3.4.2 Variation of SIF (K_I) with adhesive G_A/t_A

It has already been found and shown in section 3.5.3.3 that the SIF (K_I) at the crack tip of crack in steel plate varied inversely to the peak adhesive shear stress, irrespective of the adhesive thickness or its elastic modulus. Since it has also just been shown in section 3.5.3.4.1 that the adhesive shear stress varied well with the parameter G_A/t_A, irrespective of the adhesive thickness or its elastic modulus, therefore, it was expected that SIF variation at the crack tip could also vary with the same parameter, but with opposite variation trend. The SIF variation of the models of Tables 3.1a and 3.1b, which had already shown in Figures 3.23 and 3.24, were then studied again with respect to the adhesive G_A/t_A and the results are shown in Figure 3.26. The figure shows that the SIF (K_I) variation also synchronized and better varied with the adhesive parameter G_A/t_A than its variation with the adhesive thickness or adhesive modulus, individually. But, similar to the case of adhesive shear stress, the impact of adhesive modulus still appeared more than the G_A/t_A. Figure 3.26 shows that the difference in K_I values between the two specimens of Table 3.2, having identical adhesive G_A/t_A of 1.29 %, was 14 %, which was not huge compared to the 300 % difference in their thickness and elastic modulus. The SIF (K_I) at the crack tip in steel plate and the adhesive peak shear stress at the

crack location have now found to be varying well with the adhesive G_A/t_A, but with an inverse trends; when the adhesive peak shear increases the SIF at the crack tip decreases. In other words, if the adhesive shear stiffness G_A/t_A is higher, then shear stresses in adhesive, at the crack location, will be high, but with reduced SIF at the crack tip. Variations of the peak adhesive shear stress and SIF (K_I) with adhesive G_A/t_A can also be seen collectively in Figure 3.27. The figure shows a simpler conclusion of current study that increase in adhesive G_A/t_A increases the peak shear stress in adhesive but reduces the SIF at crack tip of the plate being repaired. Therefore, increased G_A/t_A appeared to be beneficial in reducing the crack growth by reducing the K_I, but on the other hand, it enhances the adhesive shear stresses. Therefore, it requires higher shear and bond strengths of adhesive to avoid interface failure in adhesive or bond, which might result in the patch delamination. It will be studied and discussed in detail in the chapter 4.

3.5.3.4.3 Variation of peak adhesive peel stress with adhesive G_A/t_A

After studying the variation of peak adhesive shear stress and the SIF at crack tip in steel plate with respect to the combined adhesive parameter G_A/t_A, as discussed in sections 3.5.3.4.1 and 3.5.3.4.2, similar study was carried out for the variation of adhesive peak peel stress. Variation of adhesive peak peel stress, which has been studied in section 3.4.2 with respect to adhesive thickness and adhesive modulus, was again studied with respect to the adhesive G_A/t_A for the models of Tables 3.1a and 3.1b and the results are shown in Figure 3.28. The figure shows that the peel stress did not vary well with adhesive G_A/t_A for the FEMs of Table 3.1a. It was mainly because the variation in G_A/t_A of the models of Table 3.1a was provided in FEA through the variation in adhesive thickness t_A, which has already shown to be less affecting the peel stress in Figure 3.21. Figure 3.28 also shows that the peel stress varied well with adhesive G_A/t_A for the models of Table 3.1b, in contrast to the models of Table 3.1a. It was because the variation in G_A/t_A, for the models of Table 3.1a, was provided in FEA through the variation in elastic modulus E_A (or the shear modulus G_A) of adhesive, which has already been found affecting the peels stress in Figure 3.22. It can also be evaluated from Figure 3.28 that the difference in adhesive peel stress, between the FEMs of Tables 3.1a and 3.1b with identical G_A/t_A of 1.29 %, was 90 %, which was a huge difference. The difference reduced to 37 % for G_A/t_A of 0.646 %, but still not as small when the variation in G_A/t_A was introduced

through the variation in adhesive thickness. Therefore, the peel stress varied well with adhesive G_A/t_A when the variation in G_A/t_A was provided through variation in the adhesive modulus rather than its thickness.

3.5.3.5 Impact of FRP properties on peak adhesive stresses and SIF (K_I)

After studying the impact of adhesive properties on interface stresses and the SIF (K_I) at the crack tip of crack in steel plate, the impact of the FRP properties was also studied in a similar way through the FEA of the specimens of Table 3.1c. The results are discussed separately for peak adhesive shear stresses, the SIF (K_I) at the crack tip and the peak peel stress, in the subsequent sections.

3.5.3.5.1 Variation of peak adhesive shear stress and SIF (K_I) with FRP properties

To study the impact of the FRP properties on the peak adhesive shear stress and SIF (K_I) at the crack tip of crack in steel plate (being bonded with the FRP patches), FEA results of the models of Table 3.1c were studied with respect to the peak adhesive shear stress and the SIF (K_I) parameters, and the results are shown in Figures 3.29 and 3.30. It is again important to mention that in the models of Table 3.1c both the FRP elastic modulus (E_{FRP}) and the FRP thickness (t_{FRP}) were varied in order to keep the ETR constant and these parameters could not be varied independently. Figure 3.29 shows the impact of varying FRP modulus of elasticity (E_{FRP}) on peak adhesive shear stress, keeping the adhesive properties constant. It is obvious from the figure that E_{FRP} variation has negligible impact on the peak adhesive shear stress at the crack location. After having negligible impact of E_{FRP} on the peak adhesive shear stress, it was also expected that the SIF at the crack tip would also be less affected by the variation in the E_{FRP}. Figure 3.30 shows the impact of E_{FRP} on the SIF (K_I) at the crack tip, from which it is found that the E_{FRP} variation has also negligible impact on the SIF (K_I) at the crack tip (as expected). Therefore, it can be concluded that for a given ETR of a FRP patch and given adhesive properties, the variation in FRP thickness or elastic modulus has negligible impact on the peak adhesive shear stress at the crack location as well as on the SIF at the crack tip.

3.5.3.5.2 Variation of peak adhesive peel stress with FRP properties

Finally, the impact of FRP properties on peel stress at patch-end location was studied and the results of peel stress at patch-ends were extracted from the FEA of the models of 3.1c. Figure 3.31 shows the variation of peak peel stress in the FEMs of Table 3.1c with the FRP modulus of elasticity (E_{FRP}) used in each model. It can be noted in the figure 3.31 that although the peel stress was varied with the E_{FRP} but, as already mentioned before, that in order to keep the ETR constant the thickness t_{FRP} was also varied in the current FEA. Therefore, both E_{FRP} and t_{FRP} were actually varied simultaneously in the FEMs of Table 3.1c. Figure 3.31 shows that both E_{FRP} and t_{FRP} affect the peak adhesive peel stress at the patch end. The peak peel stress was increased by 42 % due to a 400 % decrease in E_{FRP} (or a 400 % increase in the t_{FRP}). It has now better understood, through the current results, that a thicker FRP patch can develop high peel stress at the patch end if the patch thickness increases by increasing the FRP thickness, rather than the adhesive thickness. Although in practice, tapering or stepping of FRP patch at the patch-end, has been found to be successful in reducing the stress concentration in steel plate at the patch end and the same has also found equally helpful in reducing the peel stress at the patch end (Baker 1987).

3.5.4 FEA for studying impact of layering of the FRP patch and the properties of inner adhesive layers

It is important to note that the study and discussion up to this point considered the FRP patch consisting of one layer, which is contrary to most of the practical situations because the FRP patch usually consists of several layers in practical situations. In order to study the impact of layering of the FRP patch on the interface adhesive stresses and SIF at the crack tip in the bonded plate, some more finite element models were additionally developed, which are also included in Table 3.3. It is again to be noted that the ETR has been kept constant in these FEMs, which has been the basic assumption throughout in this chapter. The main intention behind selection of these models was to study and compare the peak interface adhesive shear stress and the SIF (K_I) at the crack tip with those obtained for the single layered FRP patch. Within the FEMs of Table 3.3 some models were also chosen to study the impact of properties of further inner adhesive layers. Nomenclature of the FEMs in Table 3.3 was also self-

describing; the first part of name showed the number of FRP layers; followed by the adhesive properties with modulus of elasticity as 'E' and thickness as 'T'. As an example, the specimen 3-L-AD-E5-T2 contained 3 FRP layers with adhesive elastic modulus of 5 GPa and thickness of 2 mm. First three models in Table 3.3 have the E_{FRP} of 165 GPa and these actually resembled the stiffer plate-type prefabricated CFRP, which is usually accompanied with a 2 mm to 3 mm thick adhesive. Similarly, the FEMs in Table 3.3, having 3 FRP layers and the E_{FRP} of 72 GPa, resembled the sheet-type CFRP, which usually accompanied with a 0.1 mm to 0.2 mm thinner epoxy resins. A typical FEM of the three layered FRP patch used in the study is shown in Figure 3.32. Specimen 3-L-AD-E5-T2 and 3-L-AD-E5-T0.66 of Table 3.3 were developed by dividing the thickness of FRP used in the one layered specimen 1-L-AD-E5-T2 into three equal thickness FRP layers. The main difference between these two specimens was the thickness of adhesive, which was provided in later specimen as one third of the former specimen. The specimen 3-L-AD-E5-T2 have 2 mm thick adhesive layers while the specimen 3-L-AD-E5-T0.66 have 0.66 mm thick adhesive layers, which were 1/3rd of the 2 mm, with the idea of dividing the thickness of adhesive used in one layered specimen 1-L-AD-E5-T2 into three equal thickness adhesive layers. The specimen 1-L-AD-E1.7-T0.1 was identical to the three layered lower model 3-L-AD-E1.7-T0.1 (with E_{FRP} of 65 GPa) but with all the three layers combined together to form one thick layer of FRP. The specimens 1-L-AD-E1.7-T0.2 and 3-L-AD-E1.7-T0.2 were basically selected to compare the impact of providing identical adhesive layer in the one layered (stiffer plate-type) CFRP patch and the three layered (sheet-type) lower modulus CFRP patches. But both of these were provided with the thinner epoxy having 0.2 mm thick adhesive layer, which is commonly used with the sheet-type lower modulus CFRP in practical situations. The last two FEMs of the Table 3.3 were the three layered FEMs, resembling lower modulus sheet-type CFRP patch, but with different adhesive thicknesses of the three inner adhesive layers. These models were developed to study the impact of different thickness of the first (or the interface) adhesive layer.

3.5.4.1 Results of FEA of the study of impact of FRP layering

It has already been shown in section 3.5.3.4 that the adhesive parameter G_A/t_A was found to be a better parameter to study the variation of adhesive peak shear stress or the SIF (K_I) at the

crack tip of the crack in bonded steel plate. Therefore, the FEA results of this section were also presented with respect to the same parameter, for keeping the consistency of results with the previous study.

Figure 3.33 shows the impact of providing the plate-type stiffer FRP in layers, on the peak adhesive shear stress at crack location, while keeping the adhesive layer identical in the three layers. It could be seen from the Figure 3.33 that the adhesive peak shear stress was not changed by providing the same FRP in three thinner layers. Figure 3.33 also shows the result of specimen 3-L-AD-E5-T0.66, in which the adhesive layer thickness was also reduced to 1/3rd. It shows that the peak adhesive shear stress in that specimen was increased by 43 % because of increase in adhesive G_A/t_A by 200 %. Similarly, Figure 3.34 shows the impact of same parameter on the SIF (K_I) at the crack tip in steel plate and it shows that the SIF didn't change noticeably when providing the FRP in three layers, while keeping the same adhesive properties. It was also expected from the output of the adhesive shear in Figure 3.33. But in further reducing the adhesive thickness by 1/3rd in specimen 3-L-AD-E5-T0.66, the SIF (K_I) was found to be reduced by 10% in Figure 3.34. This comparison showed that the layering of FRP patch doesn't affect the adhesive peak shear neither the SIF, until and unless the adhesive G_A/t_A remained constant, the impact of which has already been discussed before in previous section. Figure 3.35 and 3.36 shows the comparison of the peak adhesive shear stress and SIF in the lower E_{FRP} FRP patch and it shows the same trend as obtained for higher modulus plate-type FRP in Figures 3.33 and 3.34, although, the absolute G_A/t_A values were higher in this case because of very thin adhesives, but the relative comparison bears the same conclusions obtained from Figures 3.33 and 3.34.

In Figures 3.37 and 3.38 the peak adhesive shear stress and the corresponding SIF (K_I) were respectively compared within the three models; a single layered higher E_{FRP} FRP with thicker adhesive or with lower G_A/t_A; similar model as the first one but with thinner adhesive or higher G_A/t_A, and; a three layered lower E_{FRP} FRP patch with thinner and higher G_A/t_A adhesive (similar to the second specimen). Figures 3.37 and 3.38 showed that when the three-layered lower modulus FRP patch and one-layered higher modulus FRP patches were provided with identical adhesives or epoxies then the peak adhesive shear stress and the SIF at crack tip became very close in the two, with less than 3 % difference. Other interesting observation that can be seen from Figures 3.37 and 3.38 was that if only the adhesive of one

layered high modulus FRP (with lower adhesive G_A/t_A) was interchanged with the thinner adhesive having three times higher G_A/t_A, then the peak adhesive shear was increased by 18 % and the corresponding SIF reduced by 11 %.

In Figures 3.39 and 3.40 the peak adhesive shear stress and the corresponding SIF (K_I) were compared within three models; a three-layered lower E_{FRP} FRP patch with all adhesive layers 0.1 mm thick; model similar to the first one but with first adhesive layer 0.1 mm thick and the remaining two adhesive layers were 0.2 mm thick, and; model similar to the first and second one but the first adhesive layer was 0.2 mm and the remaining two adhesive layers were 0.1 mm thick. The arrangement of adhesive layers was opposite in the second and third models. Figures 3.39 and 3.40 shows that the peak adhesive shear stress and the SIF at the crack tip in the first and second models (which were having identical first adhesive layer), were very close and approximately identical. But the peak adhesive shear and the SIF in the third model (having the thickness of first adhesive layer double than the previous two models), showed a drop in the peak adhesive shear of 25 %, with a corresponding increase in SIF of 9 %. The comparison highlighted the differences with respect to the variation in adhesive G_A/t_A and again verified that the G_A/t_A is a better parameter to compare the adhesive shear stress and SIF (K_I) at the crack tip in the bonded plate within different patch parameters.

Similar comparative study was also conducted for the adhesive peel stress at the patch-end location for all the models used in the above study for the peak adhesive shear stress and the SIF at the crack tip. The results of maximum peel stress with respect to the adhesive G_A/t_A are shown in Figures 3.41, 3.42, 3.43 and 3.44, respectively for the same FEMs groups selected in Figures 3.33, 3.35, 3.37 and 3.39. Figures 3.41, 3.42, 3.43 and 3.44 show that the adhesive maximum peel stress at the patch-end location was not varied well with the adhesive shear stiffness G_A/t_A in most of the cases because of its dependency on other parameters more than the adhesive G_A/t_A. It has already been shown in sections 3.5.3.4.3 and 3.5.3.5.2 that the peel stress is less sensitive to adhesive thickness and varies proportionally with FRP thickness and adhesive modulus of elasticity. In Figure 3.41 all the models have identical adhesive modulus with higher modulus FRP and the peel stress is almost same in the first two models although the total patch thickness in the second model was more than double of that in the first model. It was because the increase in patch thickness was mainly contributed by the adhesive and not by the FRP and it has already been shown to have less impact on peel stress. Similarly, Figure

3.41 also shows that the peel stress was increased by 12 % in the third model in which the adhesive G_A/t_A was increased by 200 %, compared to the first and second models. It was caused by a 200 % reduction in the adhesive thickness, which was still not a huge increase, compared to the increase in adhesive shear stress for the same increase in adhesive G_A/t_A. Figure 3.42 shows the peel stress in the three models, having identical adhesive modulus and with lower modulus FRP. The figure shows that the peel stress was almost identical in the first two models, showing no impact of providing FRP in layers. But the peel stress was shown to be increased in the third model by 65 % due to a 200 % increase in the adhesive G_A/t_A, which was more than expected on the basis of the findings of sections 3.5.3.2 and 3.5.3.4.3. The unexpected increase in the peel stress might be because of an extraordinary thin adhesive layer which was not considered in sections 3.5.3.2 and 3.5.3.4.3. In Figure 3.43, the first and second models have identical FRP properties but different adhesive properties. The first model has higher adhesive modulus but with lower adhesive G_A/t_A while the second model has higher adhesive G_A/t_A but with lower adhesive modulus. The peel stress found to be 56 % higher in first model because of governing impact of higher adhesive modulus, as it has already been found less sensitive to the adhesive G_A/t_A. In the same figure, adhesive properties were identical within the second and third models but the peel stress is shown to be 29 % higher in the third model. It was because of decreased FRP modulus and a simultaneous increase in the FRP thickness, as it has already been shown in section 3.5.3.5.2 that the peel stress varies inversely to the FRP modulus and proportionally to the FRP thickness.

3.6 Summary and conclusions

In this chapter, a numerical study has been carried out, using finite element analysis, to study the impact of different patch parameters (except ETR) on the shear and peel stresses in interface adhesive layer as well as on the stress intensity factor (SIF) at the crack tip of crack in the bonded steel plate. Role of ETR was already well known in enhancing the strength and fatigue life of bonded FRP repairs but the role of other patch parameters, like modulus of elasticity and thickness of FRP and adhesive, were still not much clear in affecting the interface stresses and the SIF and it was the main focus of study in this chapter.

The results of FEA showed that the impact of increasing adhesive thickness resulted in reducing the adhesive shear stress, but enhancing the SIF (K_I) on the other hand. Similarly, the impact of adhesive elastic modulus has found to be enhancing the adhesive shear stress, around the crack, but at the same time, reducing the SIF (K_I) at the crack tip. Adhesive shear stress at crack location and the SIF (K_I) at the crack tip have always found to be varied inversely to each other. After observing the opposite impacts of adhesive elastic modulus (E_A) and its thickness (t_A), a combined parameter G_A/t_A was studied that contained both the effects of adhesive modulus (E_A) and the thickness (t_A), in a product form, but having the inverse of thickness parameter in it. The combined parameter G_A/t_A can be treated as the adhesive shear stiffness and through this parameter, different adhesives having different thickness and elastic modulus, can be compared. It was found that the adhesive shear stress and the SIF (K_I) at the crack tip varied well with the parameter G_A/t_A but still the impact of adhesive modulus of elasticity found little bit higher when two adhesives with identical G_A/t_A were compared. Adhesive peel stress was found to be negligibly affected by adhesive thickness but found to be more affected by the modulus of elasticity of adhesive, therefore, the peel stress was found not varying well with the adhesive G_A/t_A if the variation in G_A/t_A was caused by the adhesive thickness, rather than its modulus of elasticity.

The impact of FRP thickness (t_{FRP}) and modulus (E_{FRP}) were also studied on the adhesive peak shear stress and the SIF (K_I) at the crack tip of crack in the steel plate. Within the models of identical ETR, the FRP thickness or modulus could not be varied independently; therefore, if one of these parameters increased the other was decreased in order to keep the ETR constant. It was found from the results of the FEA that the FRP modulus or its thickness have negligible impact on the adhesive shear stress at the crack location as well as on the SIF (K_I) at the crack tip. But it has a noticeable impact on the peak adhesive peel stress at the patch-end location. It was found that the peak peel stress at patch-end increased with the increase in FRP thickness (or a decrease in FRP modulus). The increase in peel stress in the interface adhesive layer at the patch-end location due to increase in the FRP thickness, in a way, validated the findings of most previous researches showing high peel stress in thicker FRP patches.

At the end, a separate FEA study was conducted to study the impact of FRP patch layering, on the SIF and adhesive stresses. It was also compared with the single layered FRP patch, because, in most practical situations the bonded FRP patch have more than one layer.

Additionally, the impact of properties of inner adhesive layers, on SIF and interface stresses, was also studied. The study basically compared the peak adhesive shear stress and the SIF (K_I) at the crack tip in steel plate, within different FEMs having one layer as well as more than one-layer FRP patch with varying adhesive properties, but with identical patch ETR. The study concluded that within identical ETR specimens, providing the FRP patch in layers does not affect the peak adhesive shear stress or the SIF (K_I) at the crack tip in steel plate, compared to the single layered FRP patch unless the G_A/t_A of first adhesive layer changes. The study also verified G_A/t_A to be a better parameter for comparing the peak adhesive shear stress and SIF (K_I) at the crack tip, within different FRP patches with identical ETR but with varying properties and number of FRP and adhesive layers. It was shown that in multi-layered FRP patches the G_A/t_A of first adhesive layer was governing in generating the peak adhesive shear stress and the SIF (K_I) at the crack tip. Variation of peak peel stress in multi-layered FRP patches also confirmed that the peel stress is less sensitive to the adhesive thickness or the adhesive G_A/t_A and is more sensitive to the adhesive modulus and the FRP thickness.

Table 3.1a Finite element models to study impact of adhesive thickness

FEM ID	E_{FRP} (GPa)	t_{FRP} (mm)	FRP Layers (Each face)	ETR	t_A (mm)	E_A (GPa)
Adh-T-0.2	165	1.2	1	0.264	0.2	5
Adh-T-0.5	165	1.2	1	0.264	0.5	5
Adh-T-1	165	1.2	1	0.264	1	5
Adh-T-2	165	1.2	1	0.264	2	5
Adh-T-3	165	1.2	1	0.264	3	5
Adh-T-4	165	1.2	1	0.264	4	5

Table 3.1b Finite element models to study impact of adhesive modulus

FEM ID	E_{FRP} (GPa)	t_{FRP} (mm)	FRP Layers (Each face)	ETR	t_A (mm)	E_A (GPa)
Adh-E-1.25	165	1.2	1	0.264	2	1.25
Adh-E-2.5	165	1.2	1	0.264	2	2.5
Adh-E-5	165	1.2	1	0.264	2	5
Adh-E-7.5	165	1.2	1	0.264	2	7.5
Adh-E-10	165	1.2	1	0.264	2	10
Adh-E-20	165	1.2	1	0.264	2	20

Table 3.1c Finite element models to study the impact of FRP properties

FEM ID	E_{FRP} (GPa)	t_{FRP} (mm)	FRP Layers (Each Face)	ETR	t_A (mm)	E_A (GPa)
FRP-E-198-T-1	198	1	1	0.264	0.1	1.724
FRP-E-99-T-2	99	2	1	0.264	0.1	1.724
FRP-E-72-T-2.75	72.1	2.75	1	0.264	0.1	1.724
FRP-E-66-T-3	66	3	1	0.264	0.1	1.724
FRP-E-49-T-4	49.5	4	1	0.264	0.1	1.724
FRP-E-39-T-5	39.6	5	1	0.264	0.1	1.724

Table 3.2 Rearrangement of models of Tables 3.1a and 3.1b w.r.t adhesive G_A/t_A

FEM ID	G_A (GPa)	t_A (mm)	$\frac{G_A/t_A}{G_S/t_S}$	FEM ID	G_A (GPa)	t_A (mm)	$\frac{G_A/t_A}{G_S/t_S}$
Table – 3.1a Specimens				**Table – 3.1b Specimens**			
Adh-T-0.5	1.867	0.5	1.292	Adh-E-1.25	0.466	2	0.081
Adh-T-1	1.867	1	0.646	Adh-E-2.5	0.933	2	0.161
Adh-T-2	1.867	2	0.323	Adh-E-5	1.867	2	0.323
Adh-T-3	1.867	3	0.215	Adh-E-7.5	2.799	2	0.484
Adh-T-4	1.867	4	0.107	Adh-E-10	3.731	2	0.646
				Adh-E-20	7.463	2	1.292

Table 3.3 Finite element models to study the impact of FRP layering on SIF

Model ID	E_{FRP} (GPa)	t_{FRP} (mm)	FRP Layers	ETR	E_A (GPa)	t_A (mm)
1-L-AD-E5-T2	165	1.2	1	0.264	5	2
3-L-AD-E5-T2	165	0.4	3	0.264	5	2
3-L-AD-E5-T0.66	165	0.4	3	0.264	5	0.67
3-L-AD-E1.7-T0.1	72	0.92	3	0.264	1.72	0.1
1-L-AD-E1.7-T0.1	72	2.75	1	0.264	1.72	0.1
3-L-AD-E1.7-T0.033	72	0.92	3	0.264	1.72	0.033
1-L-AD-E1.7-T0.2	165	1.2	1	0.264	1.72	0.2
3-L-AD-E1.7-T0.2	72	0.92	3	0.264	1.72	0.2
3-L-AD-E1.7-T0.1-0.2-0.2	72	0.92	3	0.264	1.72	0.1-0.2-0.2
3-L-AD-E1.7-T0.2-0.1-0.1	72	0.92	3	0.264	1.72	0.2-0.1-0.1

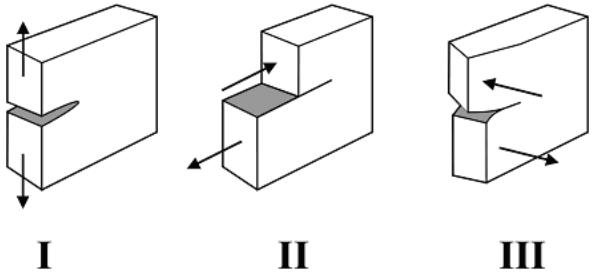

Figure 3.1 Three modes of crack propagation; Crack Opening; Crack Shearing; Crack Tearing (Broek 1986)

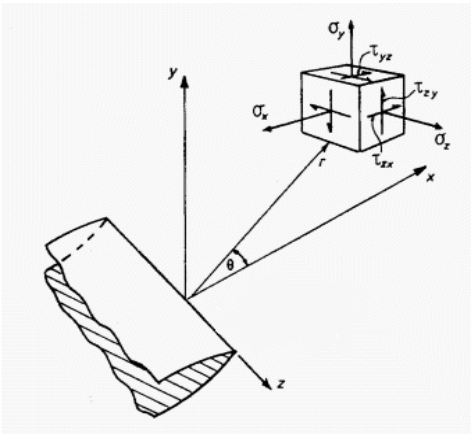

Figure 3.2 Stress components around the crack tip (Barsom 1999)

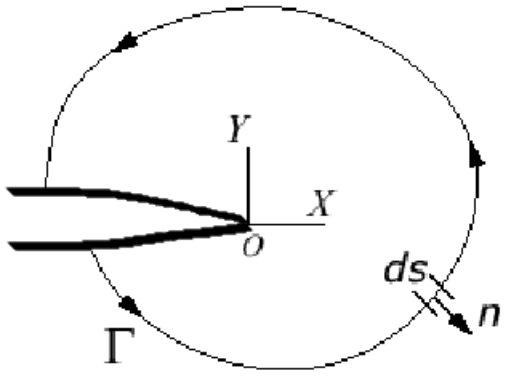

Figure 3.3 Arbitrary contour Ґ around crack

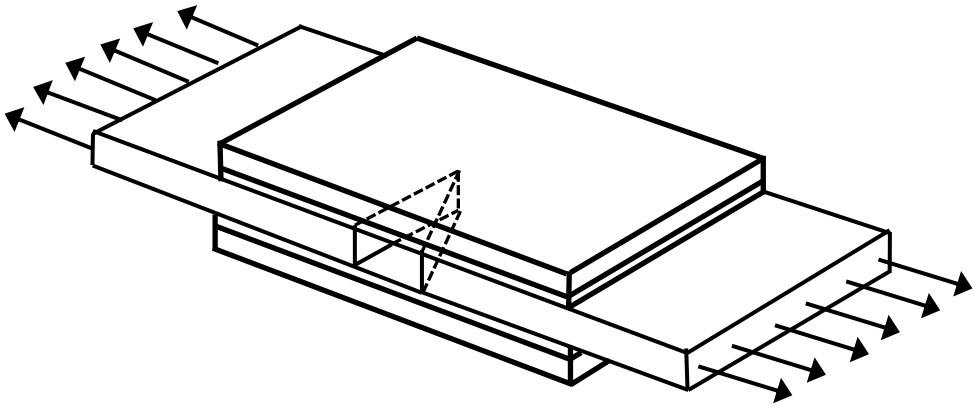

Figure 3.4 Schematic edge-cracked steel plate with bonded FRP repair patch

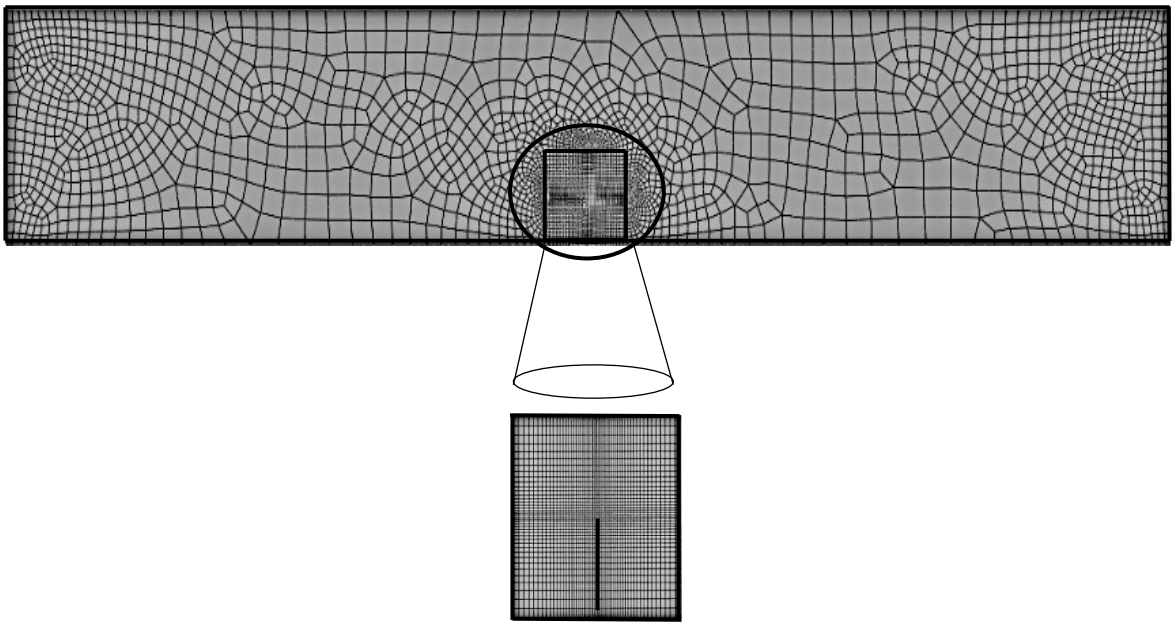

Figure 3.5 Finite element model of edge cracked steel plate with dense meshing in near-crack region

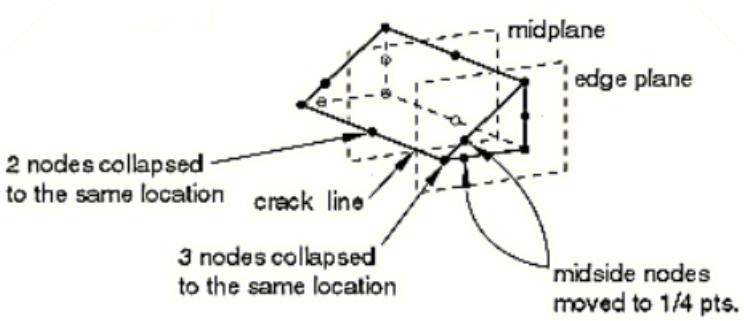

Figure 3.6 Collapsed nodes element in ABAQUS (Source: ABAQUS user manual)

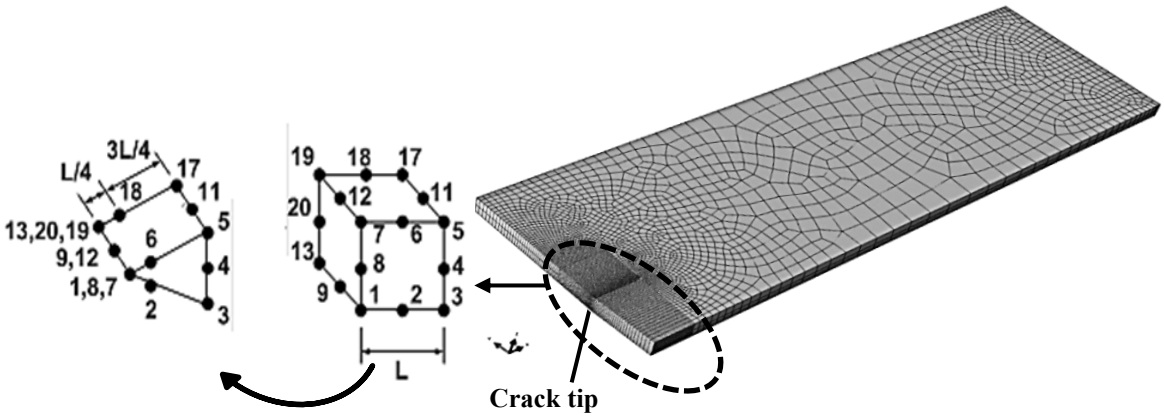

Figure 3.7 Collapsed nodes elements at the crack tip (or crack front) in steel plate model

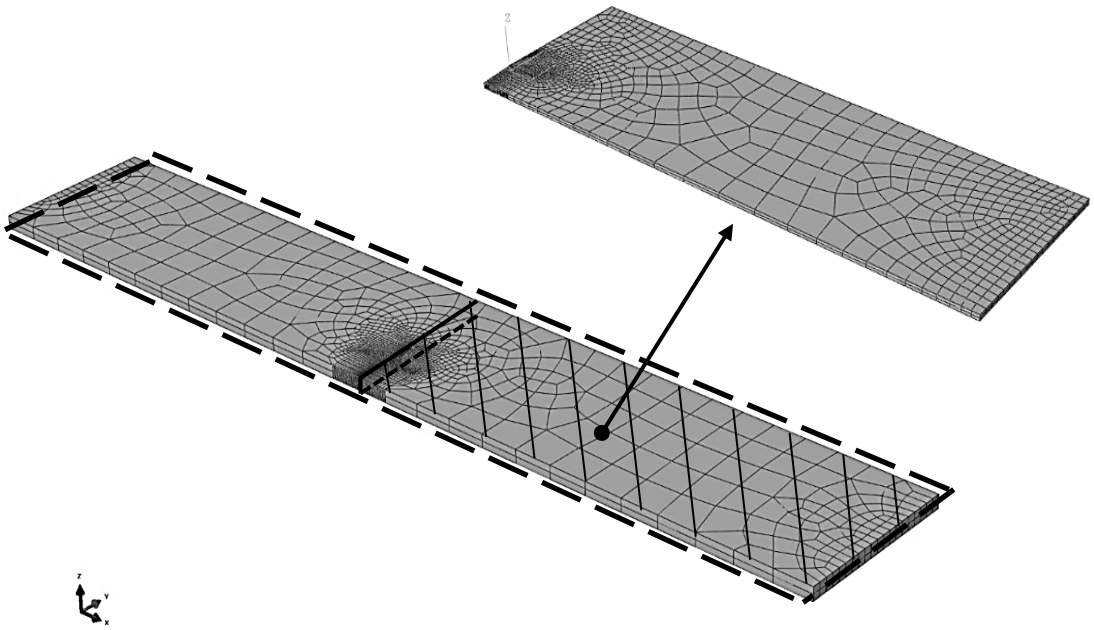

Figure 3.8 Reduced FEM developed using planes of symmetry in actual plate

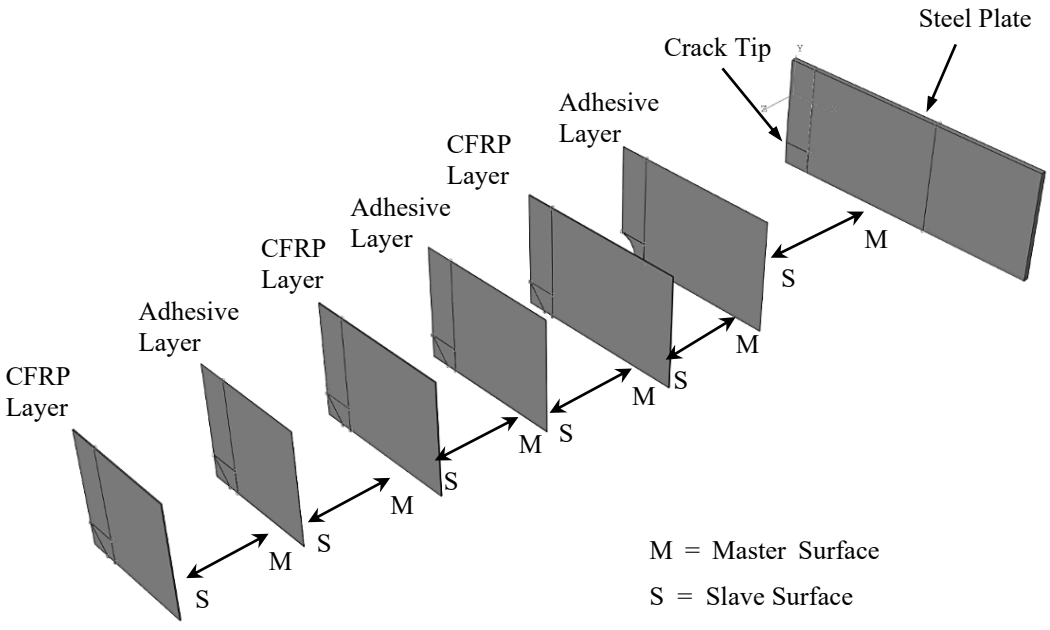

Figure 3.9 Displacement constraint assigned at all interfaces

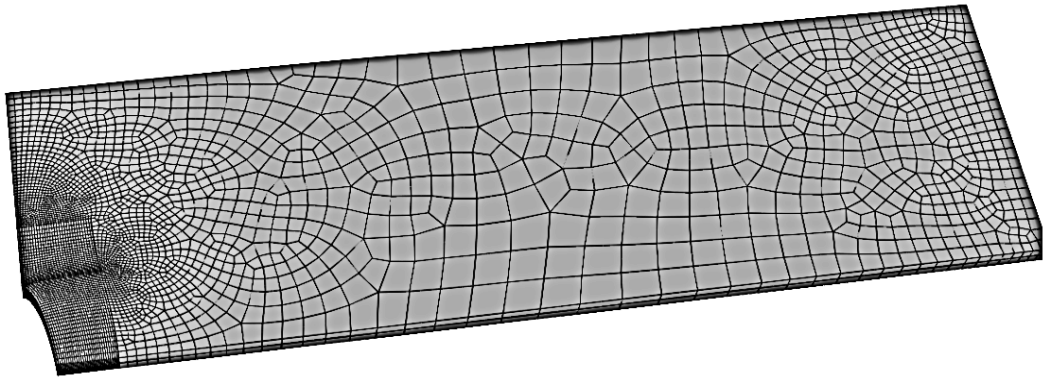

Figure 3.10 Deformed geometry of plane steel plate model

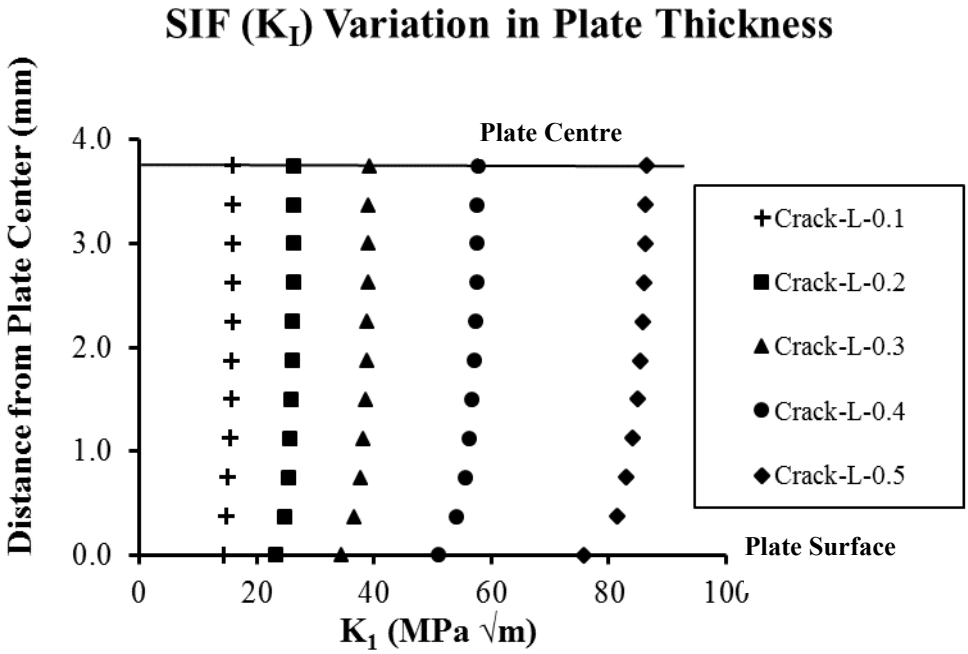

Figure 3.11 Distribution of stress intensity factor through plate thickness for different crack lengths

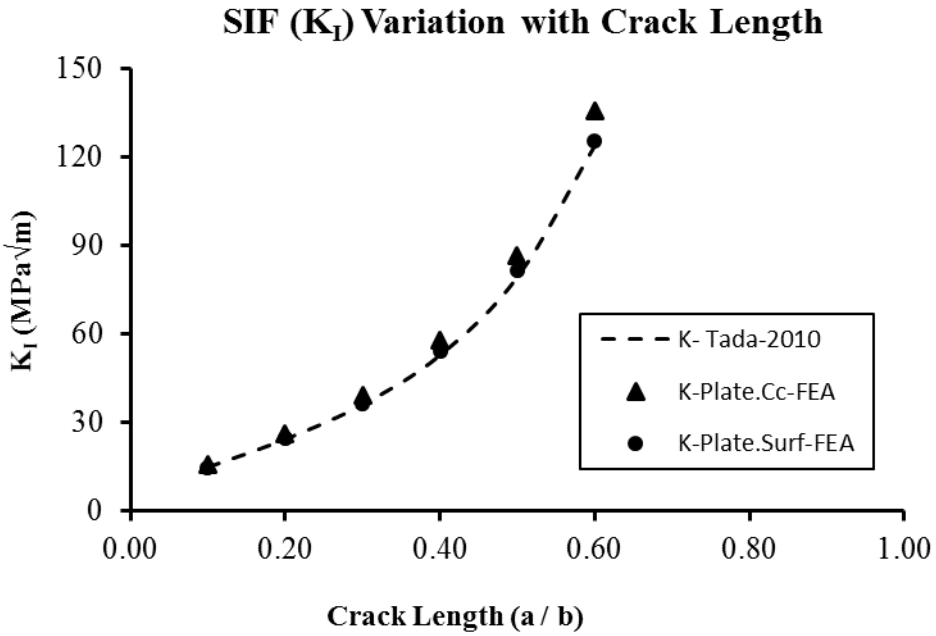

Figure 3.12 Comparison of SIF obtained from FEA and Eq. 3.12 (Tada et al. 2010)

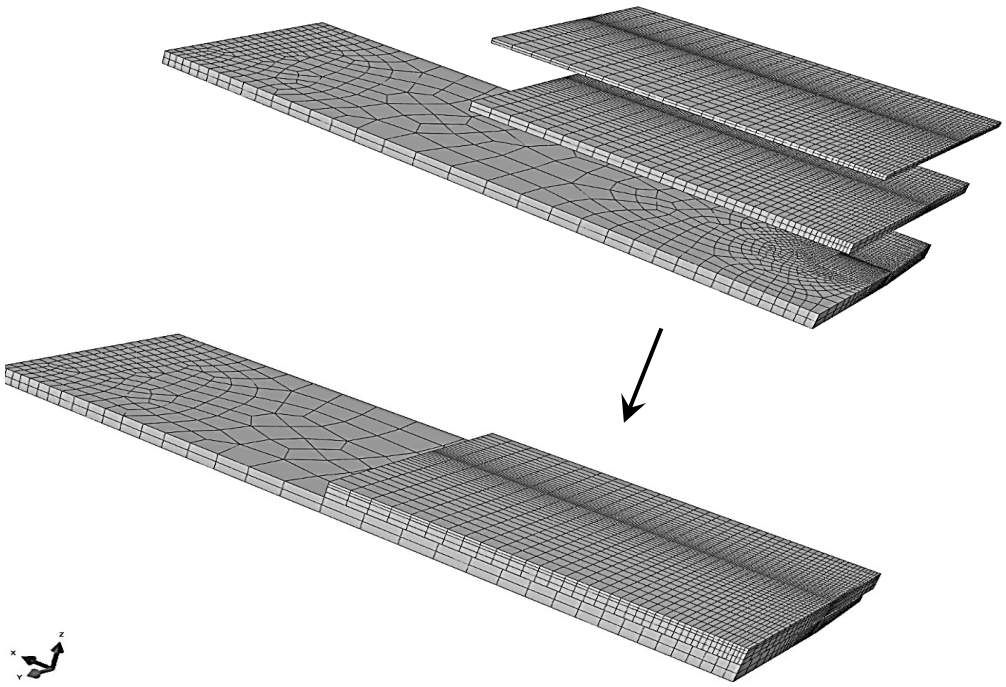

Figure 3.13 Typical one-layered FRP model showing layers of adhesive and FRP

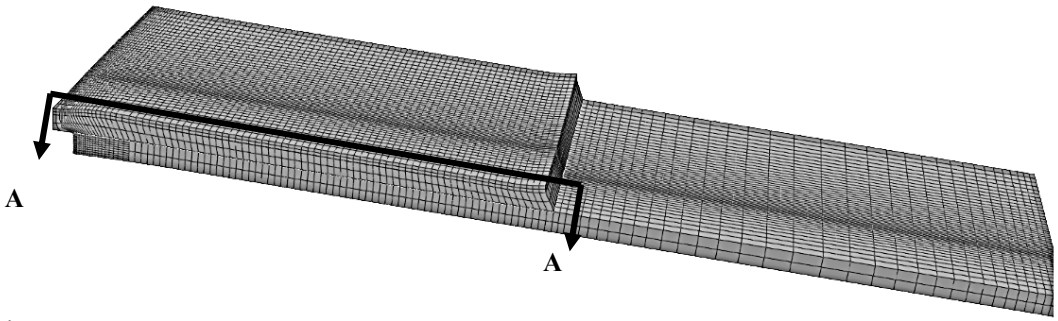

Figure 3.14 Section used for studying the adhesive shear stress distribution in FEA

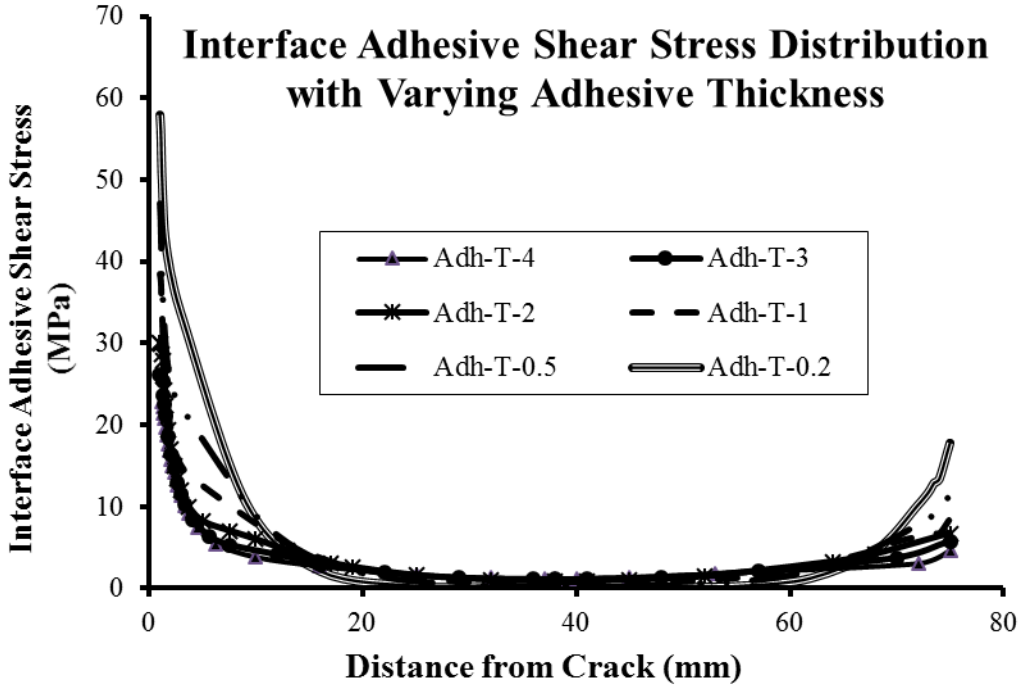

Figure 3.15 Adhesive shear stress distributions with varying adhesive thickness

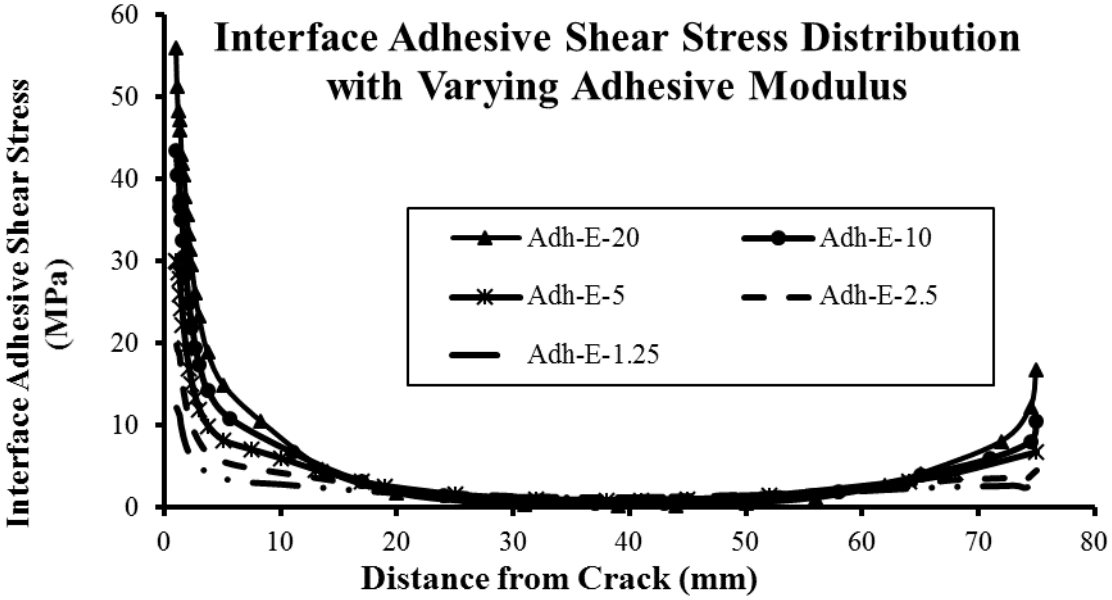

Figure 3.16 Adhesive shear stress distributions with varying adhesive modulus of elasticity

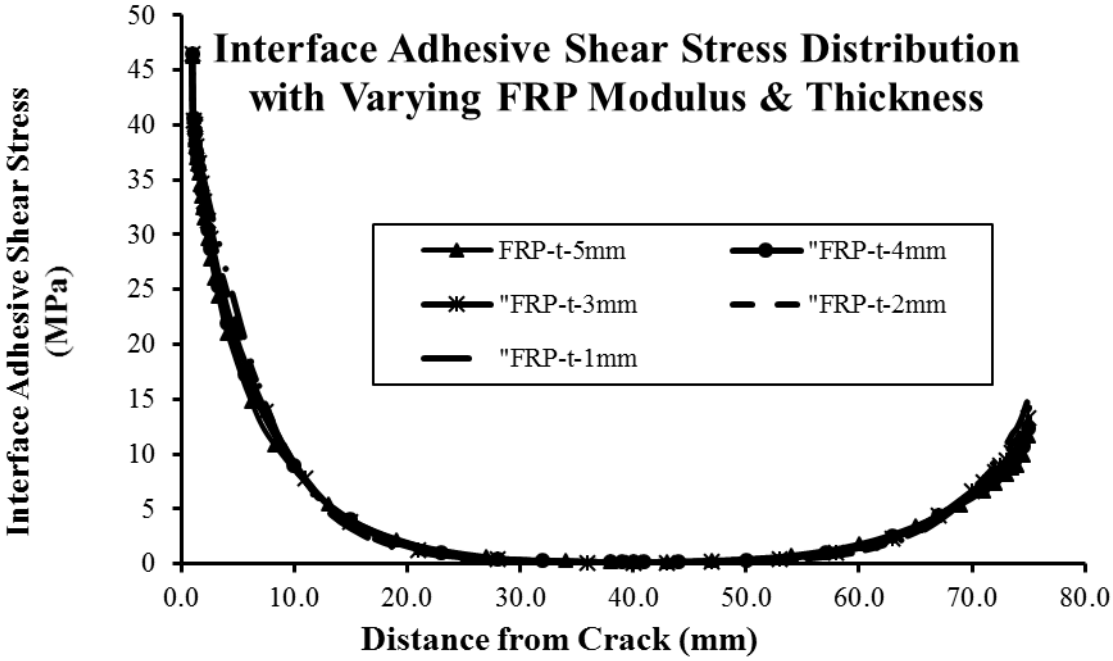

Figure 3.17 Adhesive shear stress distributions with varying FRP thickness and modulus

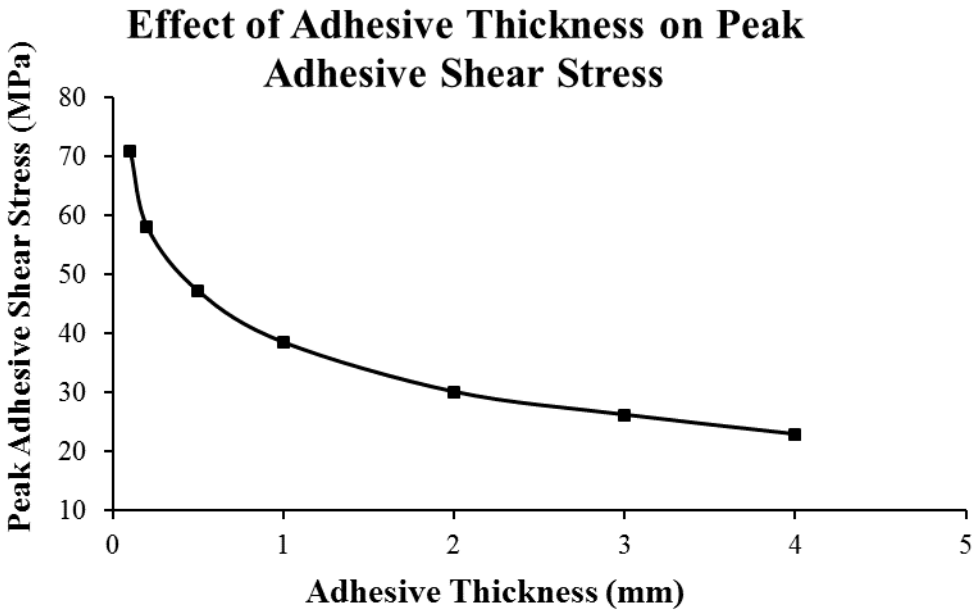

Figure 3.18 Variation of peak adhesive shear stress at crack with varying adhesive thickness

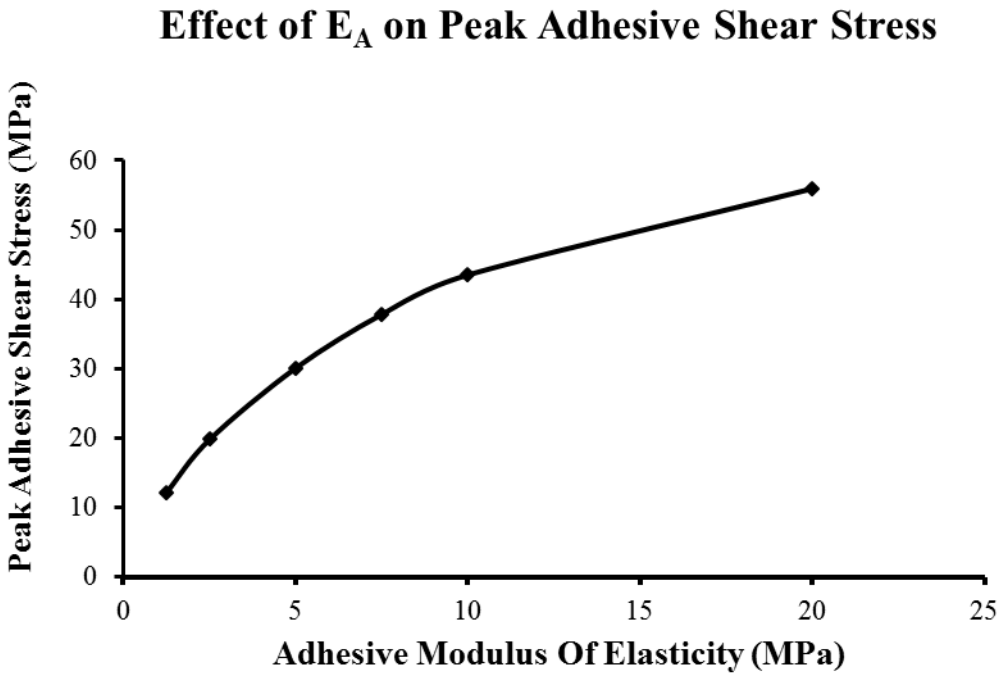

Figure 3.19 Variation of peak adhesive shear stress at crack for varying adhesive modulus of elasticity

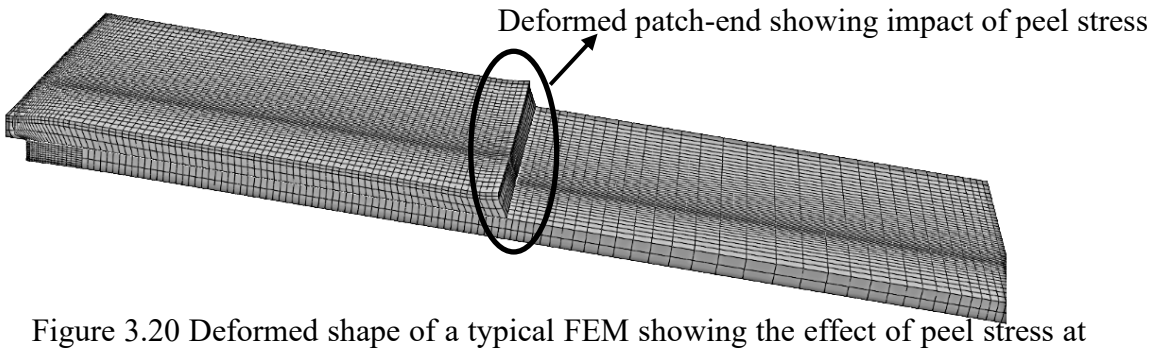

Figure 3.20 Deformed shape of a typical FEM showing the effect of peel stress at patch-end

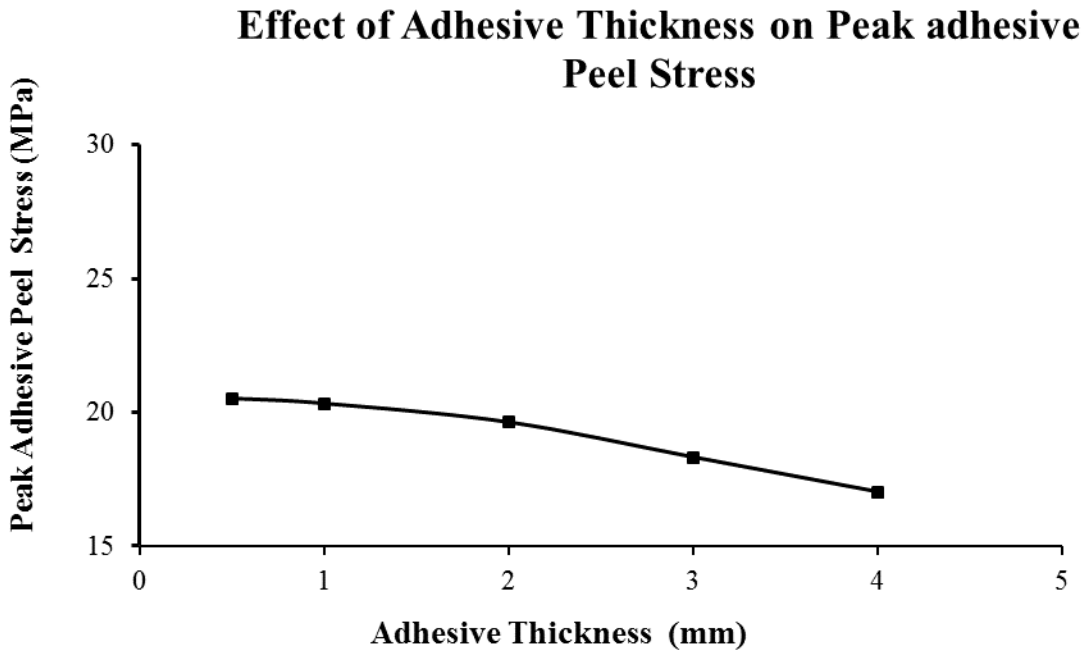

Figure 3.21 Variation of peak adhesive peel stress at patch-end with adhesive thickness

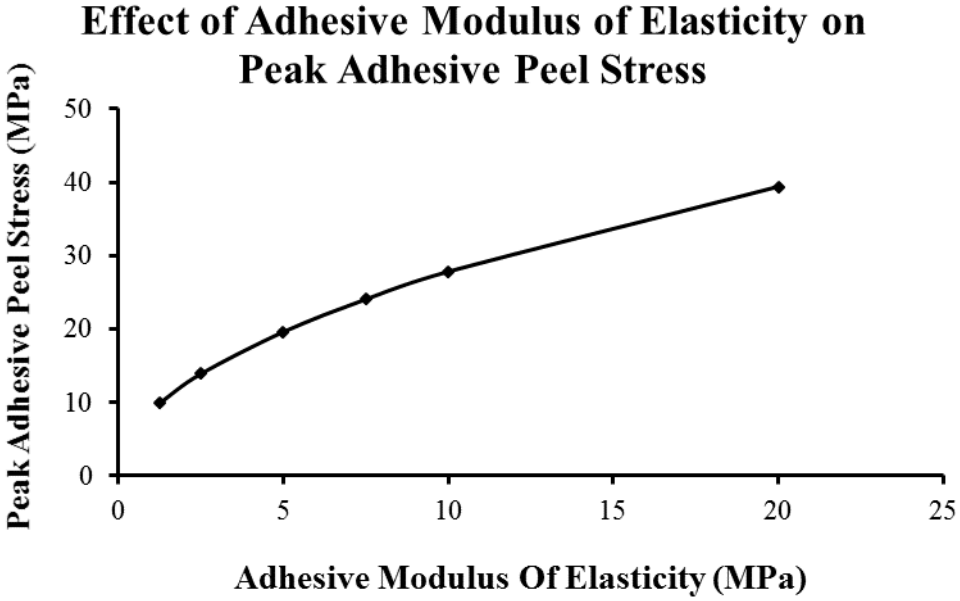

Figure 3.22 Variation of peak adhesive peel stress at patch-end with adhesive modulus of elasticity

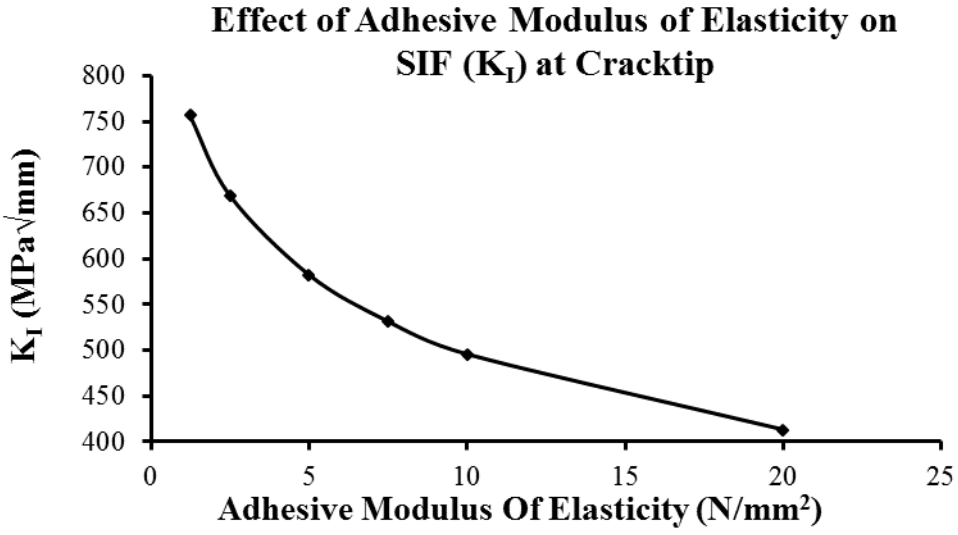

Figure 3.23 Variation of SIF at crack tip with varying adhesive modulus of elasticity

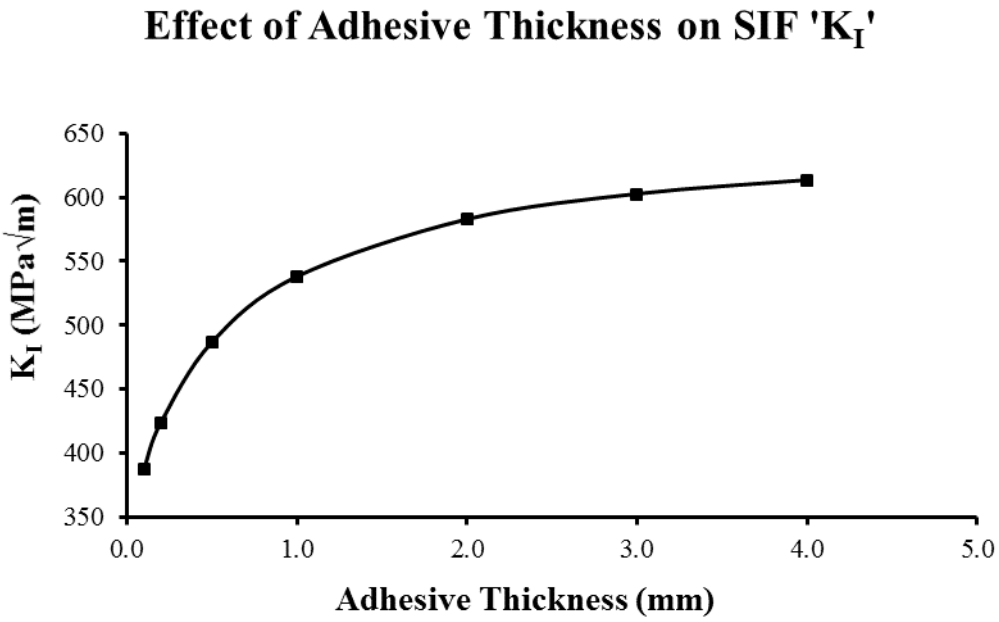

Figure 3.24 Variation of SIF at crack tip with adhesive thickness

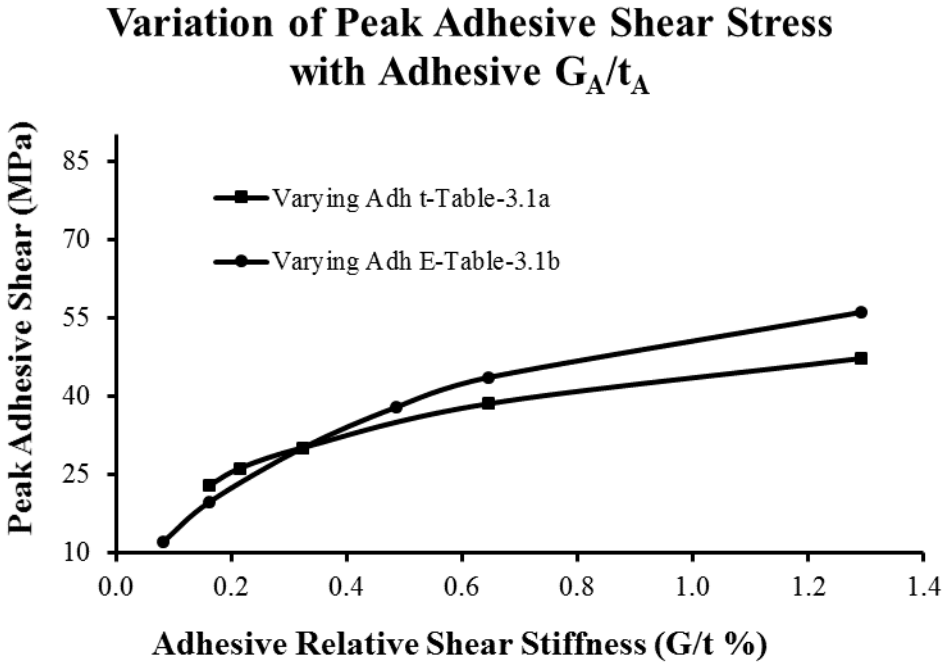

Figure 3.25 Variation of peak adhesive shear stress with adhesive shear stiffness G_A/t_A

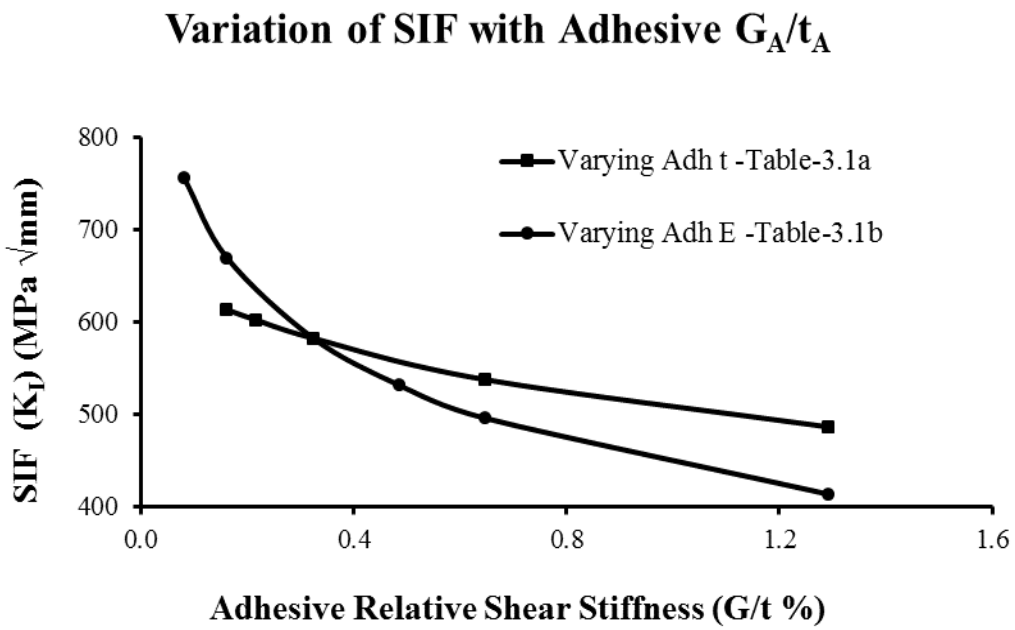

Figure 3.26 Variation of SIF at crack tip with adhesive shear stiffness G_A/t_A

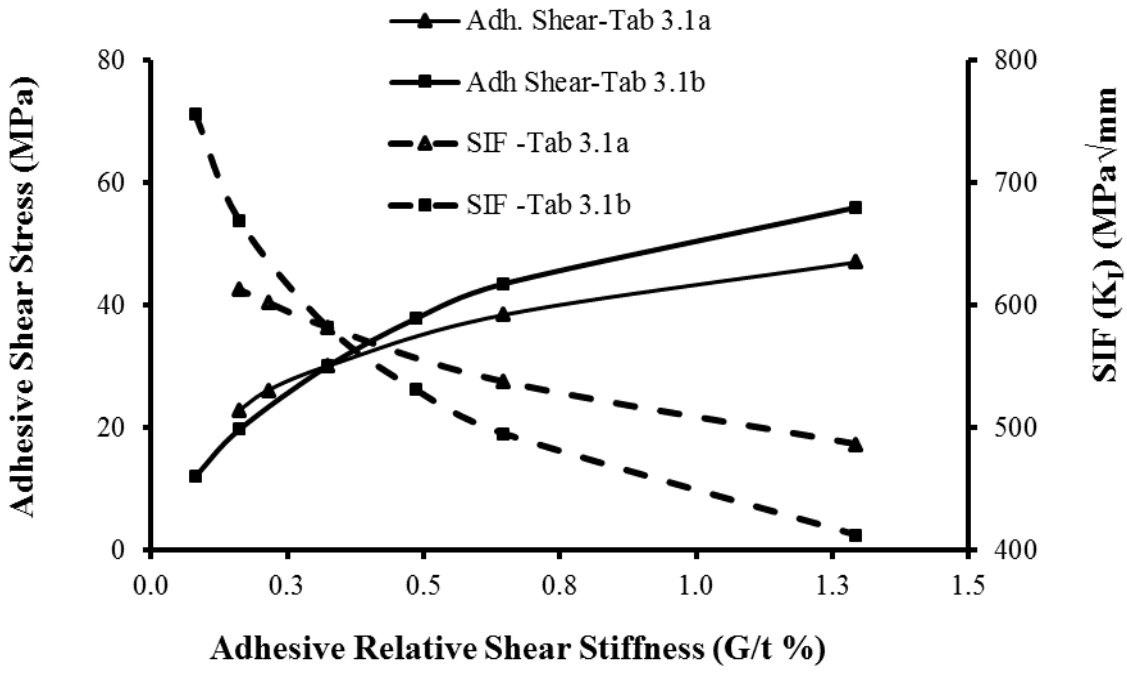

Figure 3.27 Variation of adhesive peak shear stress & SIF at crack tip with adhesive G_A / t_A

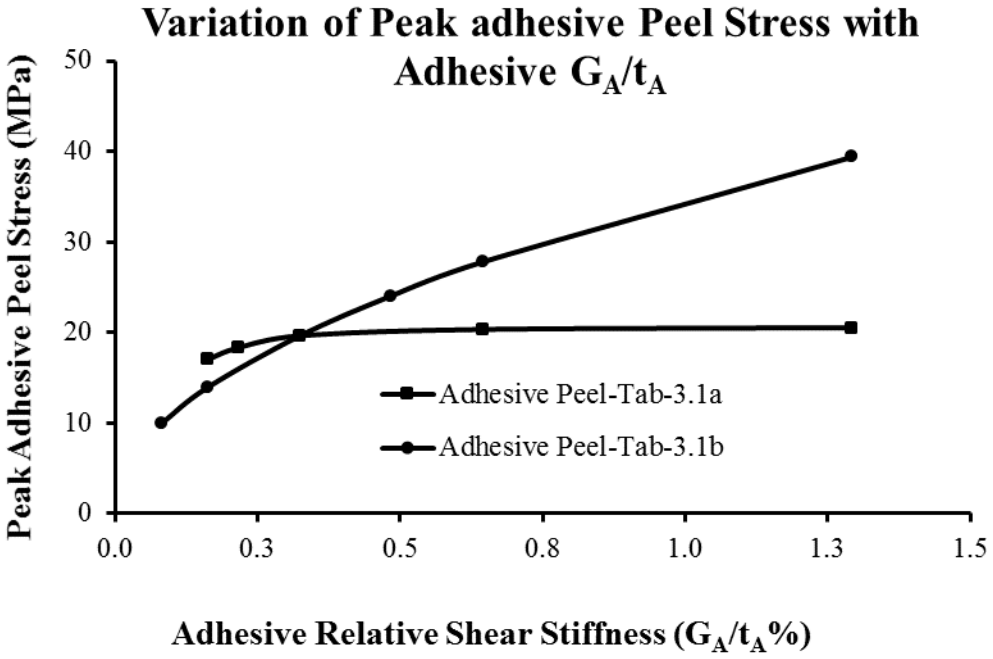

Figure 3.28 Variation of adhesive peak peel stress with adhesive shear stiffness G_A / t_A

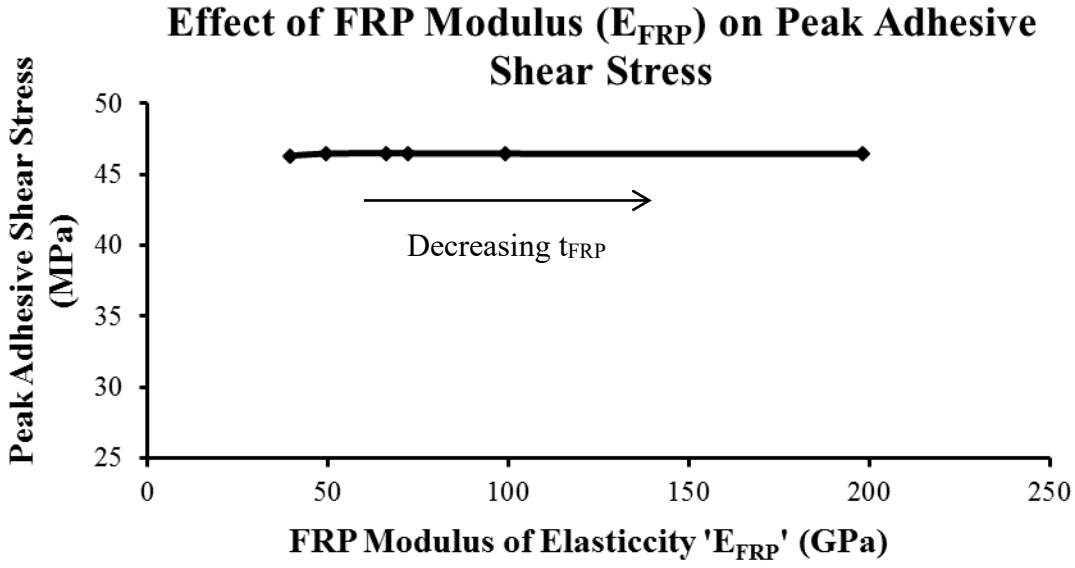

Figure 3.29 Variation of peak adhesive shear stress with FRP modulus of elasticity

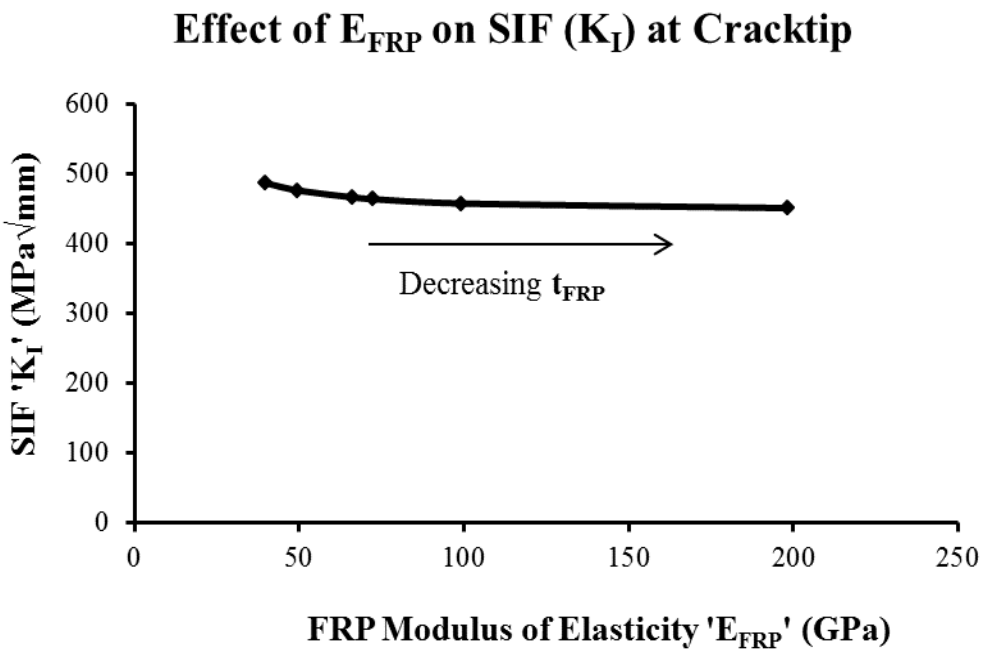

Figure 3.30 Variation of SIF at crack tip with FRP modulus of elasticity

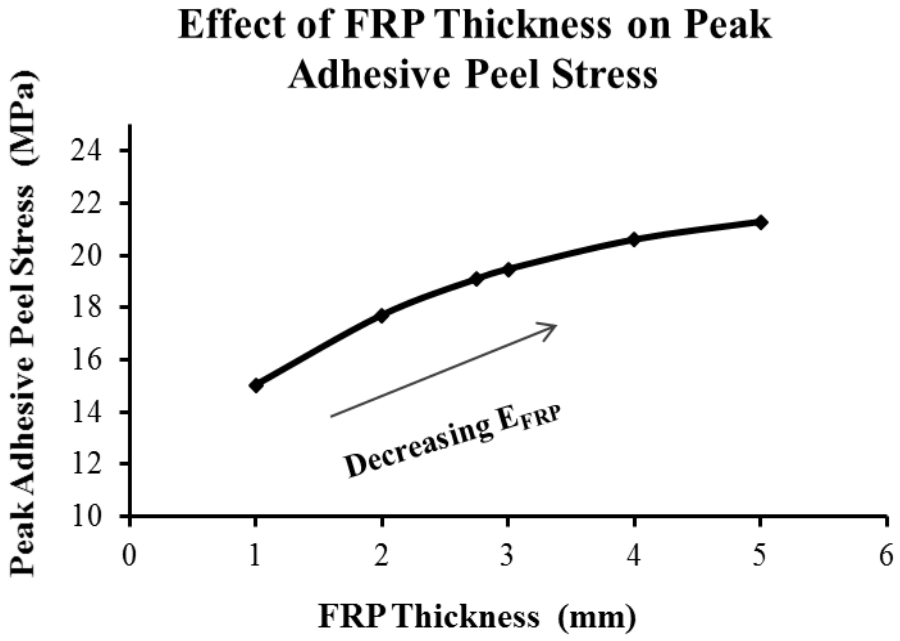

Figure 3.31 Variation of peak adhesive peel stress at patch-end with FRP thickness

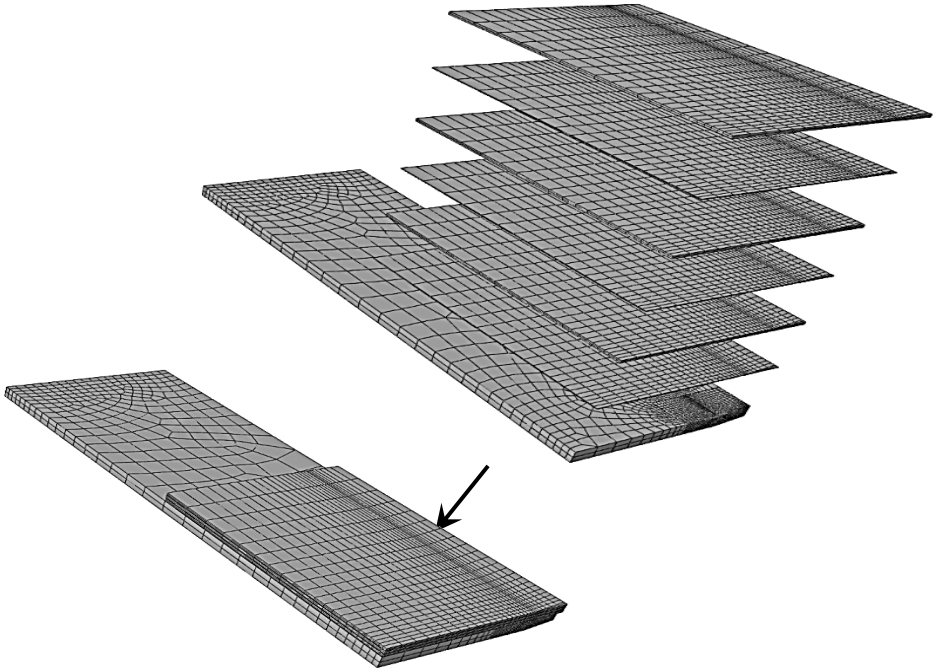

Figure 3.32 Typical three-layered CFRP model showing layers of adhesive and CFRP

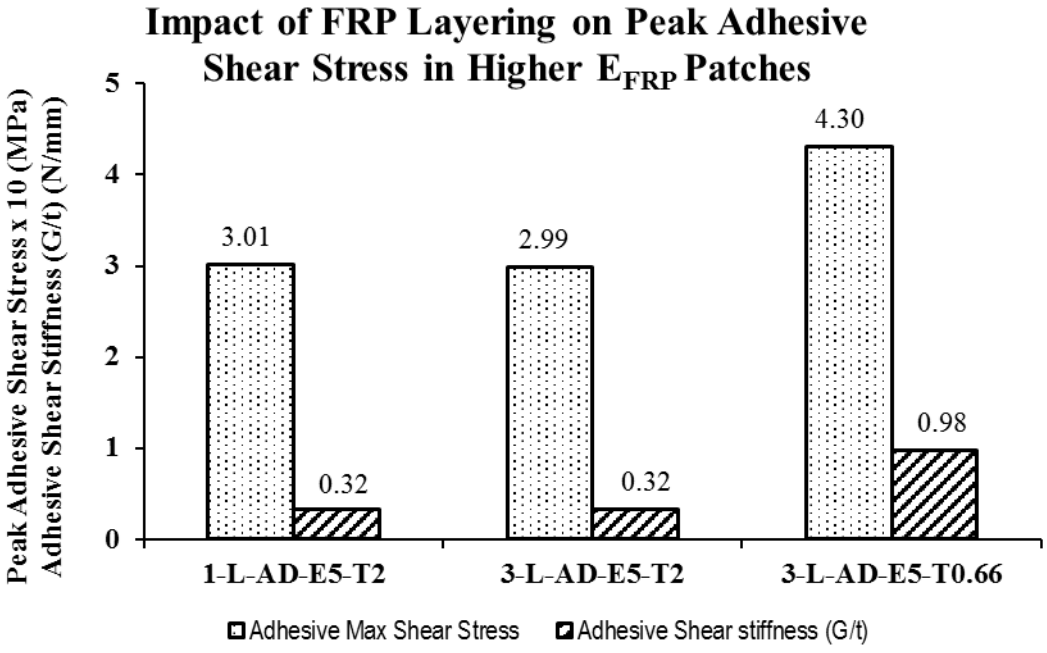

Figure 3.33 Impact of FRP layering on peak adhesive shear stress in higher modulus FRP patches

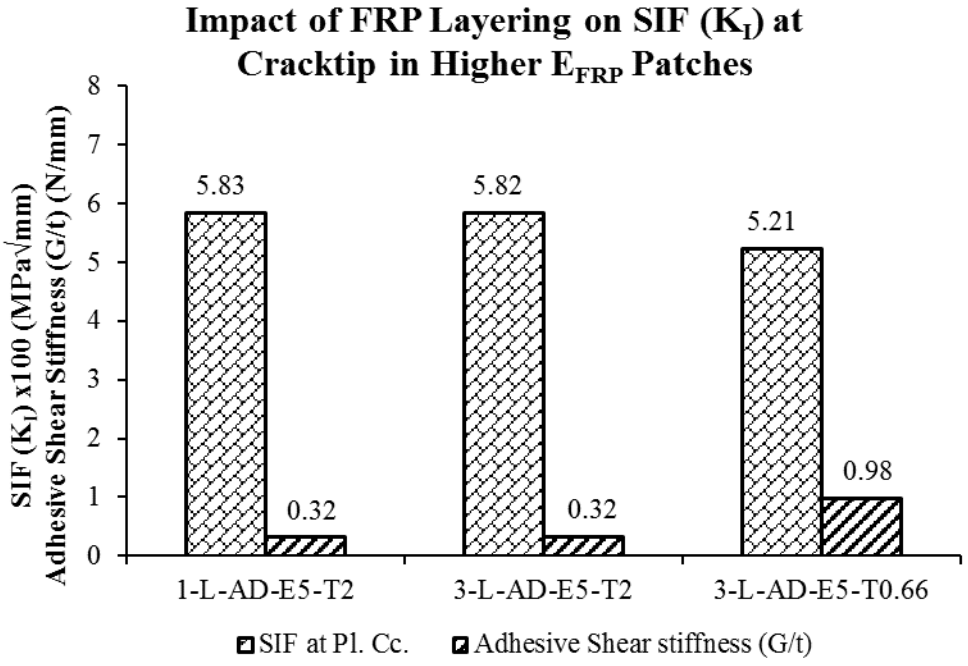

Figure 3.34 Impact of FRP layering on SIF in higher modulus FRP patches

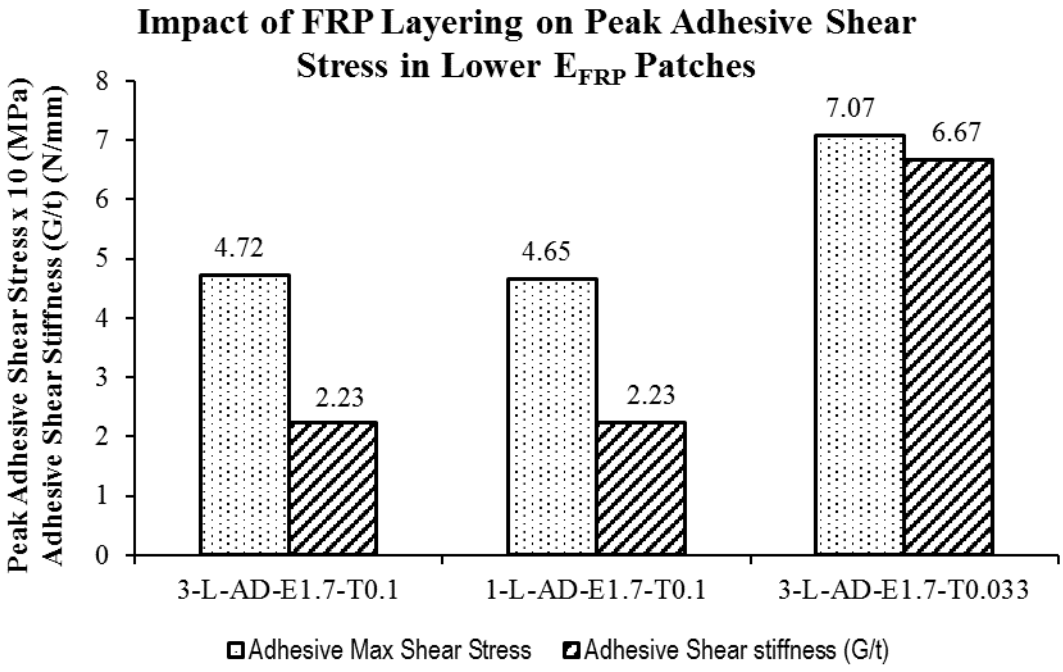

Figure 3.35 Impact of FRP layering on peak adhesive shear stress in lower modulus FRP patches

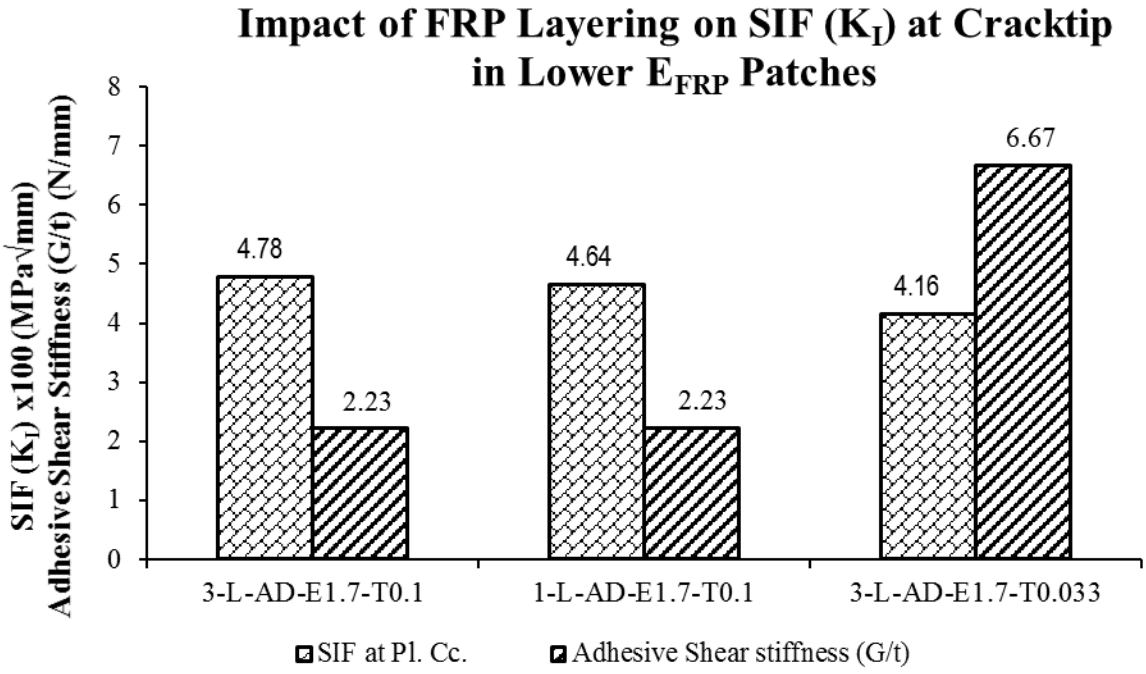

Figure 3.36 Impact of FRP layering on SIF in lower modulus FRP patches

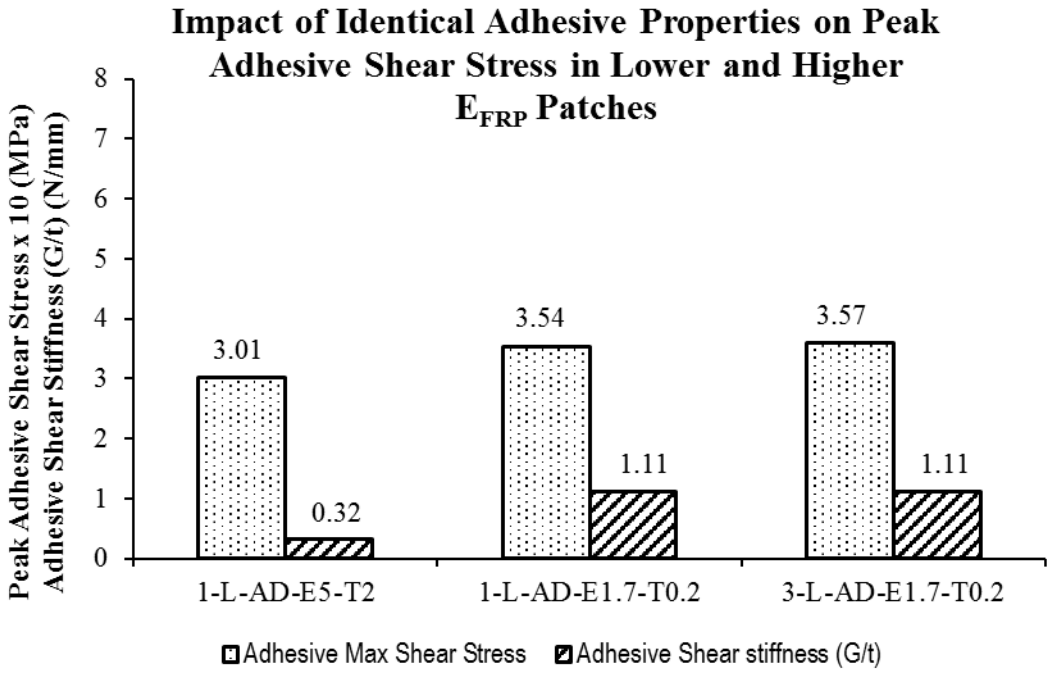

Figure 3.37 Impact of providing identical adhesive on peak adhesive shear stress in higher and lower modulus FRP patches

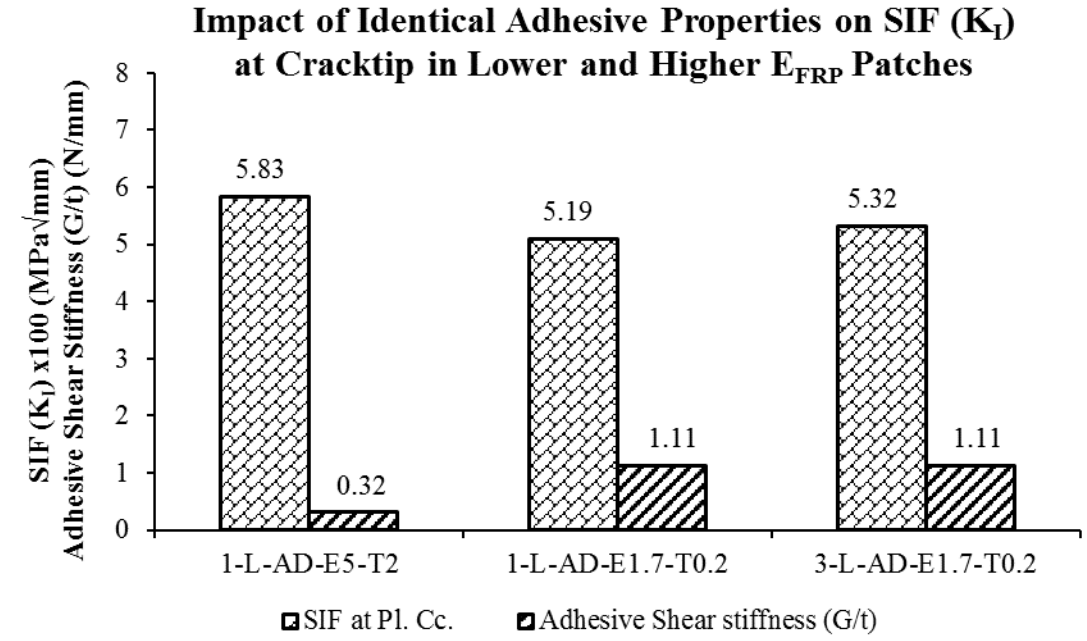

Figure 3.38 Impact of providing identical interface adhesive layer on SIF in higher and lower modulus FRP patches

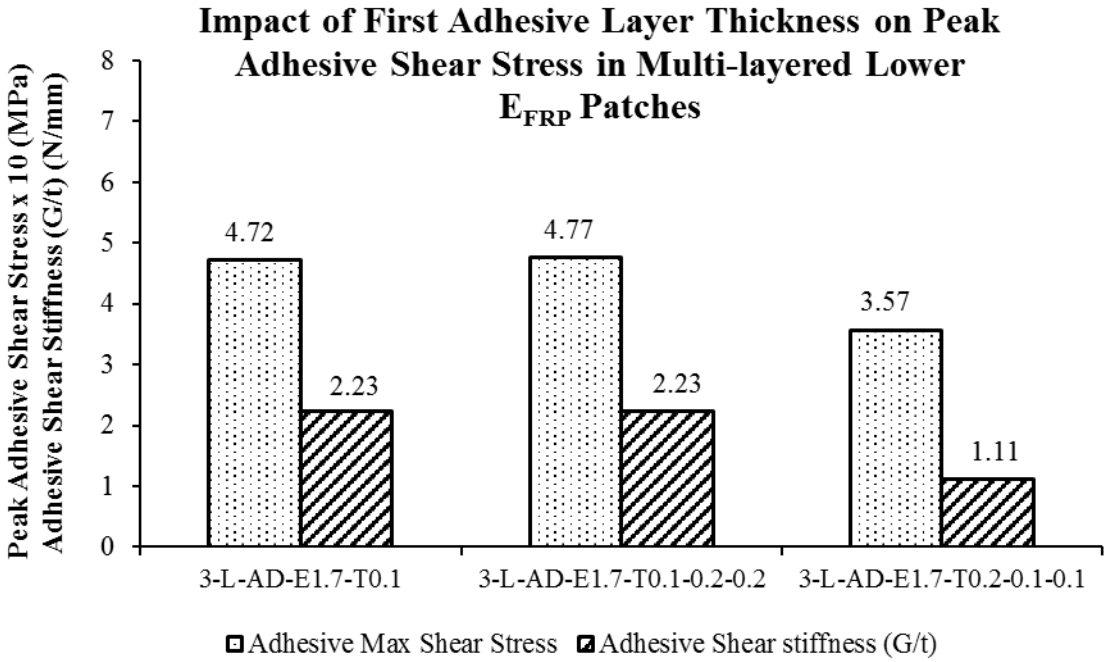

Figure 3.39 Impact of first adhesive layer properties on peak adhesive shear stress in lower modulus multi-layered FRP patches

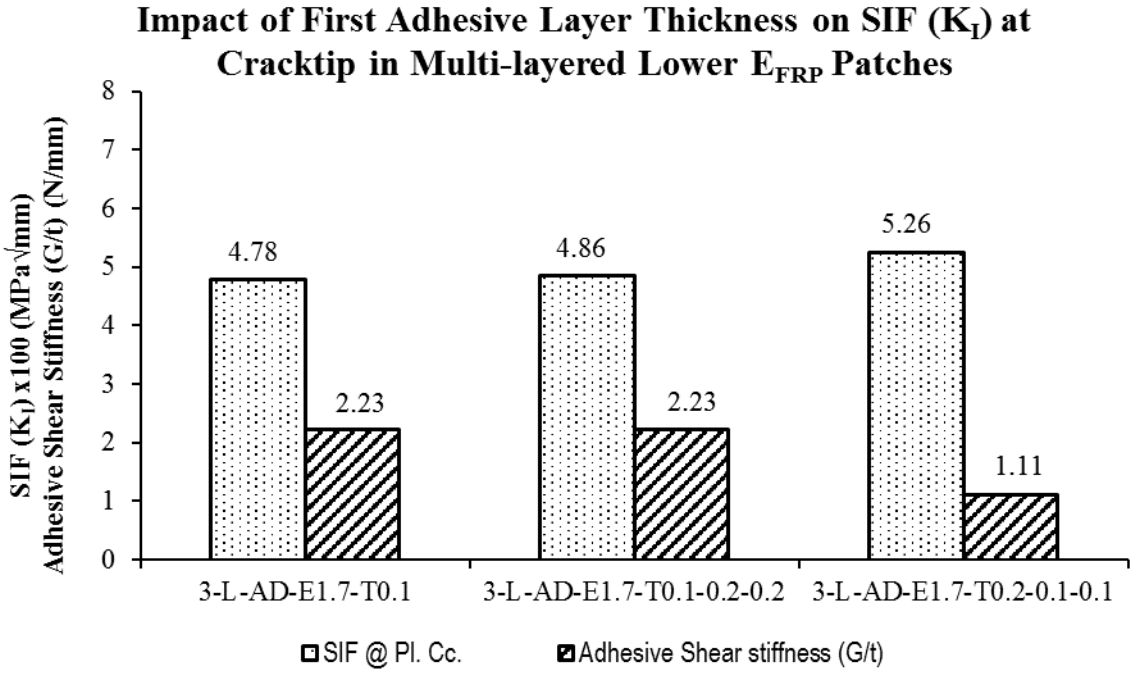

Figure 3.40 Impact of first adhesive layer properties on SIF at the crack tip in lower modulus multi-layered FRP patches

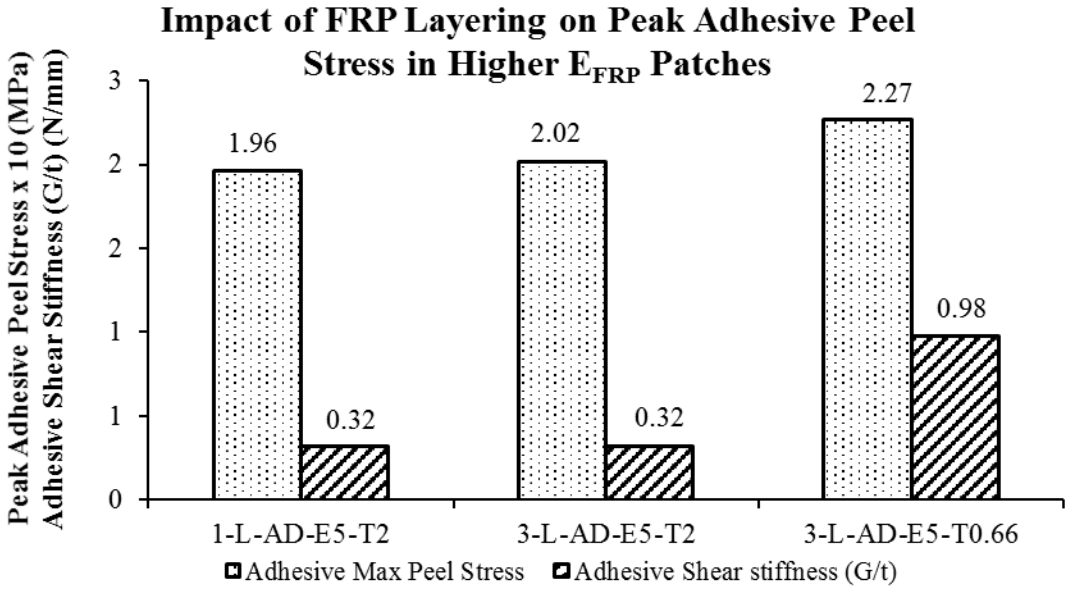

Figure 3.41 Impact of FRP layering on peak adhesive peel stress in higher modulus FRP patches

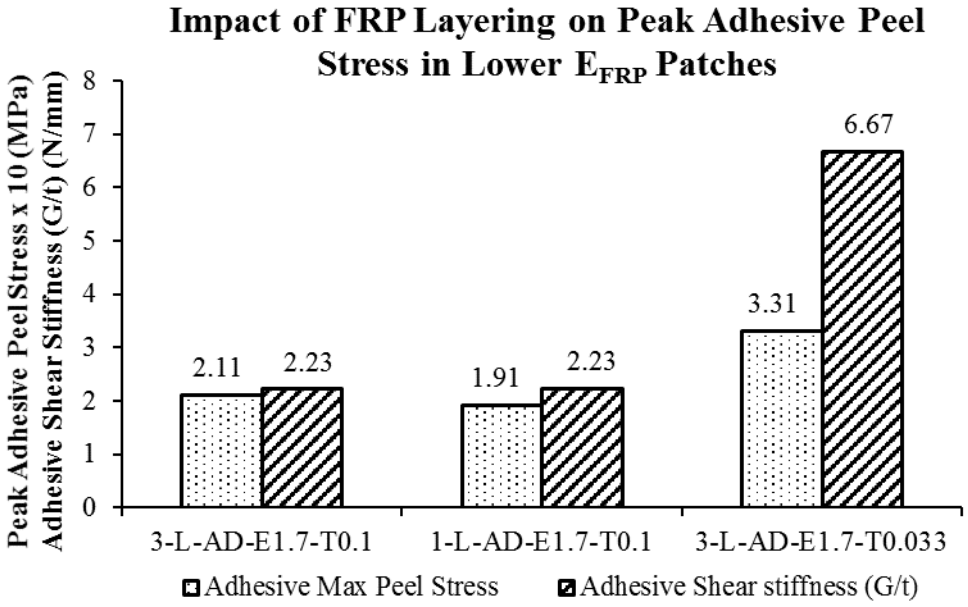

Figure 3.42 Impact of FRP layering on peak adhesive peel stress in lower modulus FRP patches

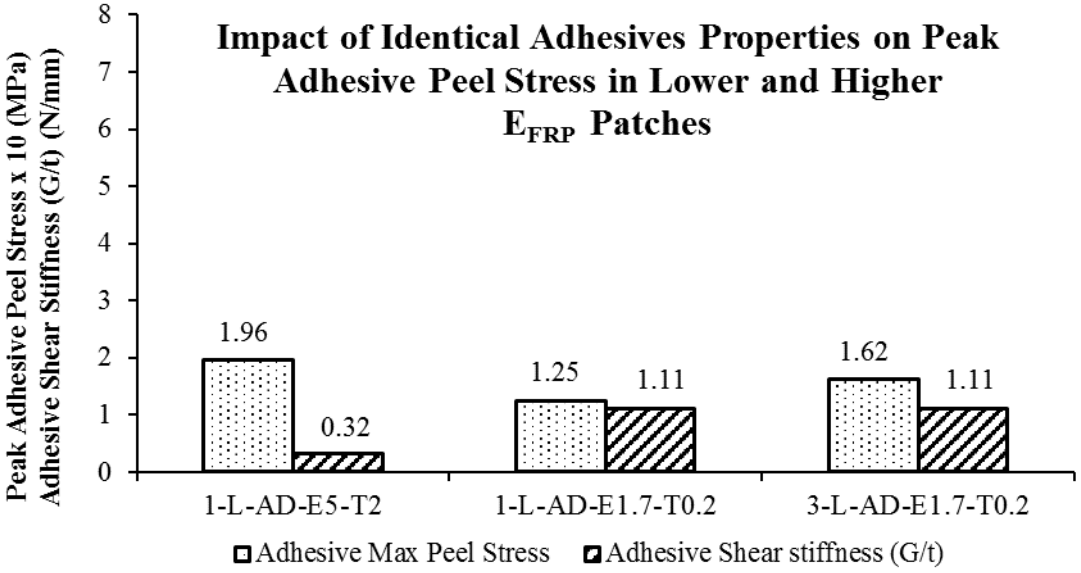

Figure 3.43 Impact of providing identical interface adhesive layer on peak peel stress in higher and lower modulus FRP patches

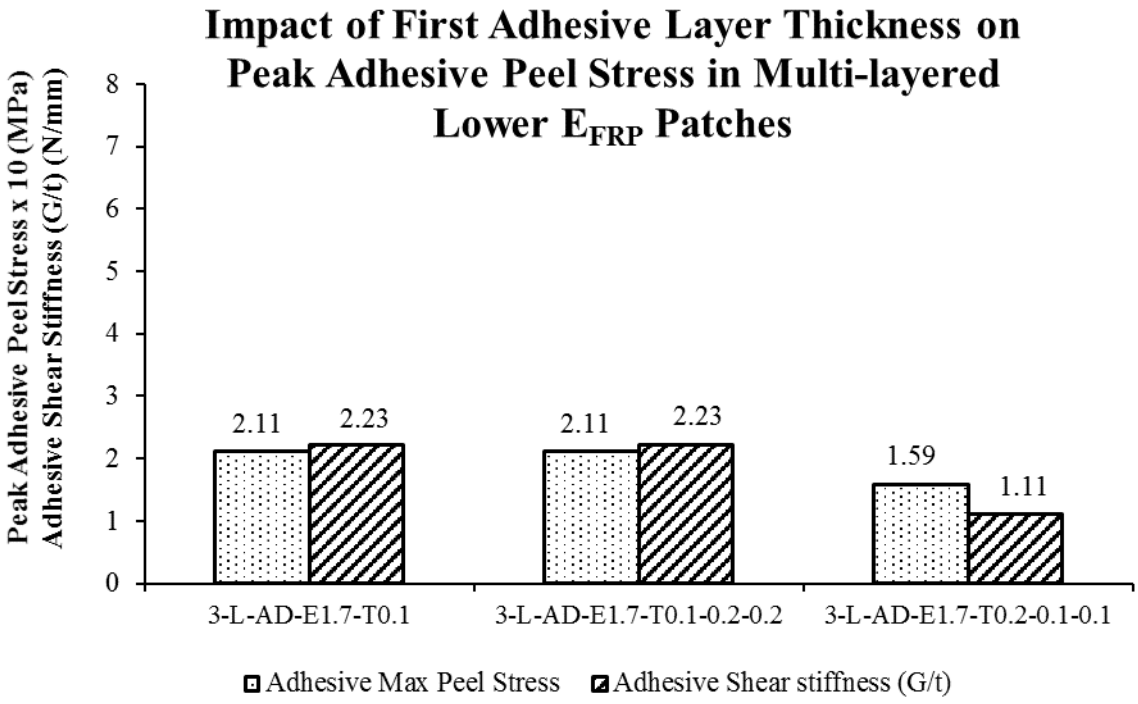

Figure 3.44 Impact of first adhesive layer properties on peak adhesive peel stress in lower modulus multi-layered FRP patches

4. Impact of Patch Delamination on Stress Intensity Factor

4.1 Introduction and background

As discussed in chapter 3 that the failure mode observed in most of the experiments, involving bonded FRP patch on metal plates (cracked or un-cracked) under fatigue (or tensile loading), is the delamination of the bonded patch from the patch-metal interface (Lin et al. 1991, Alawi and Saleh 1992, Schubbe and Mall 1999a, Colombi et al. 2003a, Lenwari et al. 2006, Papanikos et al. 2007, Taljsten et al. 2009, Bocciarelli et al. 2009, Liu et al. 2009, Kennedy and Cheng 1998, Ahmed Al-Shawaf 2011, Holden 2012, Mobeen et al. 2012, Mobeen et al. 2015). But limited research work available on the factors affecting initiation of the patch delamination (Papanikos et al. 2006, Ahmad Al-Shawaf 2011, Benraho et al. 2010, Mokhtari et al. 2012). There is also limited research work available on the impact of patch delamination on crack growth parameters, like the energy release rate or the SIF (Lin et al. 1991, Baker 1999, Schubbe and Mall 1999b, Naboulsi and Mall 1997, Colombi et al. 2003, Papanikos et al. 2006, Madani et al. 2008). Most of these researches used the shape of delaminated region either observed in experiments or the delamination was propagated arbitrarily (Colombi et al. 2002). Papanikos et al. (2006) introduced patch delamination in the numerical analysis of cracked plates with bonded CFRP patch through strength failure of the interface adhesive layer but his work was on the repair of aluminum plate with patch ETR values greater than one.

Lam and Cheng (2008) numerically developed the geometric correction factors for the edge crack and central cracked steel plates bonded with CFRP patches to predict their remaining fatigue life using Paris Erdogan equation (Paris 1960). However, they didn't consider the impact of the patch delamination on the developed geometric correction factors. Thus, their approach would well predict the fatigue life of bonded steel repairs having very strong adhesive such that patch delamination do not occur. But these geometric factors may not be conservative to predict the fatigue life of repair having weaker adhesive and that undergoes the patch delamination. It has already been shown in several researches that the patch delamination increases the SIF or the energy release rate at the crack tip of the repaired plate

(Lin et al. 1991, Baker 1999, Schubbe and Mall 1999b, Naboulsi and Mall 1997, Colombi et al. 2003, Papanikos et al. 2006, Madani et al. 2008), which would result in increased crack growth rate and thus reduced fatigue life of the repair would be expected. Therefore, patch delamination has to be considered in any fatigue life predictive tool or model.

Conclusively, there is limited research work available that has studied the impact of bonded patch delamination on the SIF in cracked steel plates. Within the available research works, the patch delamination has rarely been provided on the basis of adhesive tensile or shear strength. Therefore, the main intention of this chapter is to initially study and evaluate the failure of adhesive or bond under high shear stresses at the steel interface in CFRP bonded cracked steel plate, which could cause patch delamination of the bonded FRP patch. Later on, the impact of patch delamination is studied on SIF at the crack tip of crack in steel plate being repaired.

4.2 Methodology of introducing patch delamination in FEA

To accomplish the tasks of current chapter, finite element analysis of cracked steel plates with bonded repair patches of CFRP, was carried out similar to chapter 3. Even similar FEM has been used here but with additional introduction of patch delamination in the analysis. The patch delamination was introduced in FEA through modeling the failure of bond or adhesive layer under high shear stresses at the patch-steel interface. An over view of the methodology is shown in a Figure 4.1 in a flow chart form, while details of the procedure involved in each step has been discussed later in this chapter. As showed in the results of the FEA in chapter 3 the adhesive stresses were higher near the crack and at the patch-end locations due to the incompatibility of strains between the steel plate and FRP patch and the properties of adhesive and FRP affect the distribution and magnitude of the interface stresses.

Therefore, to incorporate the impact of FRP and adhesive properties on the adhesive stresses, as well as on the patch delamination, three different ETR patches with two different adhesive properties were selected. Increasing ETR was selected to incorporate the impact of patch stiffness while different adhesive properties were selected to incorporate their impact on the magnitude and distribution of shear stress develops at the steel interface, leading towards the

patch delamination. As found from the results of FEA in section 3.5.3.5 that the adhesive shear stress distribution at the adhesive-steel interface and the SIF (K_I) at the crack tip of crack in steel plate were not much affected by the variation in FRP thickness (t_{FRP}) or its elastic modulus (E_{FRP}) until and unless the patch ETR changes, therefore, for a given patch ETR the properties of FRP were not needed to be varied. But in current study two different properties of FRP were used for a given patch ETR just to incorporate the properties of the two most commonly available CFRP types and their compatible adhesives, recommended by the suppliers. Therefore, in the current chapter FEA of cracked steel plates with bonded CFRP patches has carried out using three patch ETR groups and within each ETR group two different types of adhesive and CFRP were used keeping in view their compatibility and local availability.

The FEA was carried out through out in this chapter, under an applied far-field stress (σ_o) of 100 MPa. The interface adhesive shear stresses were then studied from the results of FEA for at critical locations. If the resulting shear stresses were found to be exceeding the adhesive shear or the bond strength then the failed portion of adhesive layer was removed from the finite element model (FEM), which also caused the delamination of the CFRP patch within those failed locations. Therefore, in way, the delamination of the CFRP patch was introduced in the FEA through removal of the failed adhesive region of the adhesive layer. Due to the nature of elastic analysis, selected for the current FEA, the failure process was not expected to be completed in one analysis step. Therefore, to allow for the stress redistribution after removal of the failed portions of adhesive, re-analysis was again performed. The interface adhesive shear stresses were again studied and the process of removal of failed adhesive region was again carried out. This process of successive re-analysis after every adhesive removal step was carried out repeatedly until the area of the failed adhesive region in any adhesive removal step was found to be less than 1% of the initial bonded area of the CFRP patch. It was then assumed to be the converged stage in adhesive failure process. This type of failure analysis has also been performed by Papanikos et al. (2006).

After achieving the convergence in FEA for the adhesive removal process, the SIF (K_I) was then obtained from the results of converged FEA and it was also expected to be incorporating the impact of patch delamination. It is important to mention again that throughout in this

thesis the SIF has been considered for the mode I of crack growth (or the crack opening mode) and mostly it has been notated by SIF or the K_I in current thesis. Keeping in view ETR as one of the parameters to be studied here, three increasing ETR values were selected, 0.264, 0.52, and, 0.792 (from herein, they are referred as ETR 0.264, ETR 0.52 and ETR 0.8, respectively). The higher ETR patches were developed in the FEA by doubling and triplicating the layers of CFRP patch of ETR 0.264 models, respectively. Therefore, each FEM of a given crack length was analyzed for three ETR patches and for two different adhesive and CFRP properties. For each finite element model the progressive adhesive failure process was performed until the convergence achieved.

4.3 Material properties

The current study would include two types of adhesives along with their compatible CFRP types, with main intension to study the impact of varying adhesive properties on the interface stresses and SIF at the crack tip of crack in steel plate being repaired. The properties of adhesives and CFRP were selected from range of commonly and commercially available adhesives and CFRP. Therefore, two different CFRP properties along with their compatible types of adhesives were selected for current study. One CFRP type resembled a commercially available lower E_{FRP} sheet-type CFRP which usually requires an impregnating resin for its application, so, its modulus of elasticity (E_{FRP}) was chosen to be 65 GPa. The second type of CFRP was selected to be having a relatively higher E_{FRP} and it resembled a typical locally available plate-type prefabricated CFRP which usually requires an adhesive to bond it, so, its modulus of elasticity (E_{FRP}) was selected to be 165 GPa. The two selected E_{FRP} could be found within the range of lower to medium E_{FRP} CFRP available commercially.

Similarly, two different adhesive properties (E_A and t_A) were also selected that suited for the two types of CFRP. Nominal material properties of the two types of CFRP and their adhesives are shown in Table 4.1, which were taken from the supplier's data sheets (Sika Canada Inc. 2007). Thickness of the adhesive recommended for higher E_{FRP} CFRP was ranging from 2 mm to 3 mm and it was selected to be 2.5 mm while the thickness of epoxy resin for lower E_{FRP} CFRP was not provided specifically in the supplier's information and as it was assumed

to be included within the properties of cured CFRP. Therefore, its thickness was assumed to be 0.2 mm, after considering its less viscous and more flow able nature, compared to the thicker adhesive selected for the higher E_{FRP} CFRP. The thickness and modulus of the lower E_{FRP} CFRP were then adjusted for the removal of the adhesive layer thickness in such a way that its total axial stiffness remained same as provided by the supplier, for a cured ply. Similarly, the shear strength of epoxy for lower E_{FRP} CFRP (or its bond strength) was also not mentioned in the supplier's data and it was just assumed to be half of the shear strength of the adhesive of the higher E_{FRP} CFRP. In this way the current study would include two different adhesive shear strengths. It is important to mention here that the intension of current FEA was to study the impact of patch delamination on the SIF at the crack tip of crack in steel plate, and the delamination itself could be caused by adhesive shear failure or the bond failure (in shear) at the steel interface.

4.4 FEA of primary models of all ETR groups

The three-dimensional finite element model of edge cracked steel plate was developed following the procedure already described in detail is section 3.5, with varying number of bonded CFRP and adhesive layers, depending upon the patch ETR. The FEM of one quarter of the actual specimen was consisting of 150 mm long x 50 mm wide and 3.75 mm thick steel plate and the bonded CFRP patch, having adhesive and CFRP layers, applied through the displacement constraints at their interface surfaces, as already described in detail in section 3.5. The increasing crack length was modelled by developing separate finite element models of four successive crack lengths; 10 mm, 15 mm, 20 mm and 25 mm. These crack lengths were also equivalent to the non-dimensionlized crack lengths (a/b) of 0.2, 0.3, 0.4 and 0.5 respectively, with the plate width 'b' of 50mm. Three increasing ETR values were selected; 0.264; 0.52 and; 0.8, in which the higher ETR patches were developed by doubling and triplicating the layers of CFRP patch of ETR 0.264 models. Therefore, each FEM of a given crack length was analyzed for three ETR patches and for two different adhesive properties. For each FEM the progressive adhesive failure process was carried out until the convergence achieved as mentioned earlier in section 4.2.

Details of the parameters and finite element models, included in the current study, are shown in Table 4.2. The table shows that the increase in ETR was achieved by increasing the CFRP layers but for each ETR group there were two types of patches; one with lower adhesive shear strength along with lower E_{FRP} CFRP type; the other with higher adhesive shear strength along with higher E_{FRP} CFRP type. For each specimen of Table 4.2 four crack lengths were analyzed; 10 mm, 15 mm, 20 mm, and, 25 mm. Nomenclature of the specimen shown in Table 4.2 is self-describing, for example the specimen 3L-Lo-Str had 3 layers of the lower E_{FRP} CFRP, on each face of the steel plate, and it was having lower shear strength of adhesive. Therefore 24 basic finite element models were analyzed for the given crack lengths, CFRP and adhesive properties.

All FEM of Table 4.2 were analyzed using linear elastic material properties, as specified in Table 4.1, and the resulting shear stress distribution in the adhesive layer at steel interface was studied for evaluation of the overstressed region in shear. These regions were then removed from their finite element models for further re-analysis, as per section 4.2. The process of introducing adhesive failure is discussed in detail in the coming sections of thesis. Figure 4.8 shows deformed geometry of a FEM of ETR 0.264, with crack length of 15mm (or a/b of 0.3) and having the higher and lower E_{FRP} CFRP. Similar behavior was obtained in all the specimens of this ETR group but all of them are not shown here. Discussion regarding the failed interface adhesive regions and introduction of patch delamination (through removal of the failed adhesive regions) in each specimen is provided separately for each ETR category in the following sub sections. These are then discussed jointly in the end to draw conclusions.

4.4.1 Results of FEA of primary models of ETR 0.264 group

Adhesive shear stress distribution at steel interface along the bond length at the crack face, for all primary finite element models of ETR category 0.264, is shown in Figure 4.9. The figure shows that the peak shear stress near the crack was higher in the models having lower modulus (E_{FRP}) CFRP patch than the models with higher (E_{FRP}) CFRP patch. But it had also shown in section 3.5.3 that the shear stress distribution for identical ETR patches greatly depends upon the adhesive shear stiffness G_A/t_A and it will be higher for the patch with higher

value of adhesive G_A/t_A. Therefore, the G_A/t_A of the two types of adhesive were evaluated and it was found that the shear stiffness G_A/t_A of the adhesive used in the lower E_{FRP} patch was 4 times higher than the G_A/t_A of the adhesive used in the higher E_{FRP} patches. Therefore, large difference in the G_A/t_A of the two types of adhesives could be held responsible for getting higher shear stresses in the lower E_{FRP} CFRP models.

Figure 4.9 also shows that the shear stress varied with the crack length, irrespective of the CFRP type or the E_{FRP}, and it was higher for bigger crack lengths. The maximum or the peak value of the adhesive shear stress at crack location, being important from the delamination point of view, was also extracted for each model and is shown in Figure 4.10. This figure shows that for each crack length the peak shear stress was approximately 17 % to 33 % higher in the models with lower E_{FRP} CFRP (the one having higher adhesive G_A/t_A) and the shear stress was increasing with the crack length in each type of the CFRP patch. Therefore, more delamination was expected in the patches with higher adhesive G_A/t_A, but, it also depends upon the shear strength of the bond or the adhesive itself.

The longitudinal or axial stress in the FRP patches at their bottom surface, along the crack edge, was also extracted for each model of ETR 0.264 group and is shown in Figure 4.11. This figure shows that the peak value of longitudinal stress in the CFRP at the crack location was higher in the CFRP patch with lower E_{FRP} (the one having higher adhesive G_A/t_A). But the rate of stress dropped in these patches was also higher compared to the higher E_{FRP} patches (those having lower adhesive G_A/t_A).

4.4.1.1 Introduction of patch delamination in FEA of specimens of ETR 0.264

Shear stress distribution in the adhesive interface layer of each model of ETR 0.264 group, as shown in Figure 4.9, was studied near the crack and the overstressed regions of adhesive layer in shear were identified, which were needed to be removed from their primary finite element models. Figure 4.12 shows the shear stress distribution in interface adhesive layer of the primary finite element model of non-dimensionlized crack length 0.2 of the patch with ETR of 0.264, and having lower shear strength adhesive. The process of removal of failed adhesive

region and successive re-analysis was then carried out with this specimen until convergence achieved in the adhesive failure process as mentioned in section 4.2.

Figure 4.13 shows boundary of the failed adhesive region, obtained after successive adhesive removal process during successive re-analysis cycles of the lower adhesive strength model of crack length 0.2, and it also highlights the boundary of the failed adhesive region obtained after the convergence in the adhesive removal process. Figure 4.14 shows the FEM of this specimen with the reduced geometry of the interface adhesive layer, obtained after the failure convergence. Similar process of patch delamination, through removal of the failed adhesive regions around the crack, was carried out in FEA of the remaining crack length models of lower adhesive shear strength of ETR 0.264 and these are discussed successively in later sub sections.

Figures 4.15, 4.16 and 4.17 show respectively the adhesive shear stress distribution, failed adhesive regions and the reduced geometry of interface adhesive layer, obtained after failure convergence in the FEA of the non-dimensionalized crack length of 0.3. These figures show larger delamination, compared to the crack length of 0.2, because of increased adhesive shear stresses. Similarly, Figures 4.18 through 4.23 show the adhesive shear stress distributions, the corresponding failed adhesive regions in successive analysis steps and the reduced geometry of the interface adhesive layers obtained after failure convergence in the FEA of non-dimensionlized crack lengths of 0.4 and 0.5. These figures show that the patch delaminated region or the adhesive failure increased with the increase in crack length because of the corresponding increase in the interface adhesive shear stresses near the crack.

Similar procedure was repeated for the remaining specimens of ETR 0.264 of higher adhesive shear strength. The resulting adhesive shear stresses, failed adhesive regions and reduced adhesive geometries are successively shown in Figures 4.24 through 4.35, for the four non-dimensionlized crack lengths of 0.2, 0.3, 0.4 and 0.5. The Figures 4.12 through 4.35 show that most of the patches with higher adhesive shear strength delaminated less, compared to the lower adhesive shear strength specimens, and these required no or less re-analysis cycles. Number of re-analyses cycles to achieve convergence in patch delamination process, in the FEA of lower adhesive shear strength, was dependent upon the crack length; larger crack

length required more re-analysis cycles while smaller crack length required less number of the re-analysis cycles.

Main reasons of getting more adhesive failure in FEM of lower adhesive shear strength (or lower E_{FRP} CFRP patches) were the values of parameters G_A/t_A and the adhesive (or bond) shear strength. The parameter G_A/t_A was much higher in the lower adhesive shear strength specimens, therefore, using the conclusions of chapter 3 higher adhesive shear stresses were expected to develop at the adhesive-plate interface around the crack. On the other hand the adhesive shear strength in these patches was selected lower in the current study. Therefore, large portions of adhesive regions were expected to be failed in shear in these patches. The situation was reversed in the specimens with higher E_{FRP} CFRP patches because the adhesive G_A/t_A was lower and the adhesive shear strength was higher in these specimens, which jointly resulted in lesser adhesive failure regions or less patch delamination in these specimens.

Comparison of the delaminated area or the failed adhesive region (as % of original bonded area) achieved at the converged delamination stage of analysis in the two types of CFRP models is also shown in Figure 4.36. This figure showed that the delaminated region increased with crack length irrespective of the adhesive or CFRP type but for any particular crack length the delaminated region was much larger in the models with lower adhesive shear strength or lower E_{FRP} CFRP patch because of the higher adhesive G_A/t_A and lower adhesive shear strength. The difference in delaminated area between the lower and higher E_{FRP} CFRP patches (from Figure 4.36) was ranging between 8 to 13 times, with 8 times difference found in the model with smallest crack length while 13 times difference was found in the model with largest crack length.

4.4.1.2 Impact of patch delamination on SIF (K_I) and crack opening displacement (COD) in models of ETR 0.264 group

The SIF (K_I) and COD of all the finite element models included in ETR-0.264 group of Table 4.1 were extracted and analyzed, similar to the section 3.5.3.3, with increasing adhesive failure. Figure 4.37 shows the variation of SIF (K_I) in all the models of lower adhesive shear strength or the lower E_{FRP} patch, with increasing delamination area, for the four non-dimensionlized crack lengths of 0.2, 0.3, 0.4 and 0.5. The SIF shown in Figure 4.37 was considered at the centroid of the steel plate. Figure 4.37 shows that the CFRP patch delamination near the crack enhanced the SIF at the crack tip in all crack lengths. The SIF enhancement, due to the CFRP patch delamination, was more in bigger crack length than in the smaller crack length, because of more patch delamination or more adhesive failure in these. The SIF in the lower adhesive shear strength models, after the patch delamination, were evaluated from Figure 4.37. These were found to be enhanced by 14 %, 36 %, 64 % and 100 %, compared to the un-delaminated case, respectively for the four crack lengths. It can also be noted from Figure 4.37 that the SIF values are also quite less than the fracture toughness (K_{IC}) of steel, which is approximately 55 MPa.$m^{1/2}$. These results are also shown in Figure 4.38. Crack opening displacement (COD) was also extracted from the analysis results of each basic and delaminated model of ETR-0.264 group and is shown in Figure 4.39 for the lower adhesive shear strength models, with increasing delamination area. Figure 4.39 shows that the COD enhanced by 36 % to 206 % due to patch delamination in the lower adhesive shear strength models. The 36 % enhancement was found in the model with smallest crack length of 0.2 while 206 % enhancement was found in the model with largest non-dimensionalized crack length of 0.5.

Similarly, the SIF (K_I) and the COD for the specimens of ETR 0.264, having higher adhesive strength (or higher E_{FRP} CFRP), were also obtained from their FEA results. These are respectively shown in Figures 4.40 and 4.41, before and after the patch delamination. Impact of CFRP patch delamination in these specimens was not much highlighted because of very small patch delamination, as can be seen from Figure 4.36. The reasons of lesser delamination in these have already been mentioned in sections 4.4.1 and 4.4.1.1 as the lower adhesive shear stiffness G_A/t_A and higher adhesive shear strength. Lower shear stiffness G_A/t_A of adhesive released shear stress concentration near the crack in the first step and reduced the magnitude

of peak shear stress. Higher shear strength of adhesive then yielded lesser area of failed adhesive to be removed from the FEM. Therefore, the combined effect of these adhesive properties resulted in lesser delamination as well as lesser enhancement in the SIF (K_I) or COD.

Figures 4.40 and 4.41 also show that the impact of delamination on the SIF and COD was increased with the crack length because of increasing delamination area. The values of SIF (K_I), before and after patch delamination, for the higher adhesive strength models of ETR 0.264 are summarized in Figure 4.40. The figure shows that the SIF (K_I) was enhanced by 2 %, 12 %, 18 % and 23 %, after the delamination, respectively in the four crack lengths models. Comparing the SIF enhancement from Figures 4.38 and 4.40, respectively for the lower and higher adhesive shear strengths, it can be concluded that the SIF enhancement in lower E_{FRP} models was higher than the enhancement in higher E_{FRP} models by 3 to 7 times. But it has already been discussed and shown in section 3.5.3.4 and 3.5.3.5 that the main reason for having the noticeable difference in the results of two types of CFRP patches was not the CFRP modulus of elasticity (E_{FRP}) but it was mainly the difference in adhesive properties. The root cause of the difference in delamination of the two types of patches was the difference in their adhesive shear stiffness G_A/t_A and shear strengths.

Comparison of Figures 4.38 and 4.40 also show that, before the introduction of patch delamination in the finite element models, the SIF (K_I) was higher in the models of higher adhesive shear strength by 7 % to 14 %. It was because of 12 % to 28 % higher COD in these models. Main reason for more COD was the higher shear flexibility of the adhesive layer in these models at the steel-patch interface. This comparison also highlighted the importance of the adhesive shear strength. The adhesive shear strength was lower in the CFRP patches with lower E_{FRP} CFRP, and it resulted in more delamination area, thus increasing the SIF and the COD. If the adhesive shear strength in the lower E_{FRP} CFRP patches was not selected lower than in higher E_{FRP} CFRP patches then the results might be reversed of that achieved here.

A combined representation of the SIF (K_I) variation in lower and higher adhesive shear strength patches (or in lower and higher E_{FRP} CFRP patches) was preferred more useful and therefore it is shown in Figure 4.42. The Figure 4.42 contains all the previous results of Figures 4.37, 4.38 and 4.40, and additionally, it shows the SIF (K_I) of an edge cracked plain

steel plate. The SIF of plain steel plate was evaluated from the FEA of the plain steel plate, as well as from Tada et al. (2000), as already been discussed in section 3.5.1. The equations of SIF, as obtained from Tada et al. (2000) and already shown as Equations 3.4 and 3.12, are reproduced here for quick reference. The SIF (K_I) shown in Figure 4.42 was evaluated from the Equations 3.4 and 3.12.

$$K_I = \beta\sigma\sqrt{\pi a} \tag{3.4}$$

$$\beta = 1.12 - 0.231\left(\frac{a}{b}\right) + 10.55\left(\frac{a}{b}\right)^2 - 21.72\left(\frac{a}{b}\right)^3 + 30.39\left(\frac{a}{b}\right)^4 \tag{3.12}$$

It is obvious from the Figure 4.42 that the SIF of plain steel plate was significantly reduced by both types of patches without consideration of patch delamination. After the patches suffered with delamination, their efficiency was reduced and SIF (K_I) increased again. In the specimens of lower adhesive shear strength, the initial reduction in SIF, before introduction of patch delamination, was ranging from 37 % to 75 %, for varying crack lengths. But after introduction of patch delamination the SIF reduction was reduced to 29 % to 51 %, compared to the SIF of plain steel plate. It can also be noted in Figure 4.42 that even after the patch delamination the values of K_I didn't reach the fracture toughness (K_{IC}) of steel (55 MPa.$m^{1/2}$)

The delamination and its impact was found lesser in specimens with higher adhesive shear strength (or higher E_{FRP}), compared to the lower adhesive shear strength (or lower E_{FRP}) specimens. Before introduction of patch delamination in FEA of higher adhesive shear strength specimens, the SIF reduction was ranging from 33 % and 72 % for different crack lengths, compared to that of plain steel plate. But after introduction of patch delamination, the SIF (K_I) reduction was reduced to 31 % to 66 %. In general, specimen with higher adhesive strength (or higher E_{FRP}) suffered with lesser patch delamination, and therefore, the impact of delamination on SIF (K_I) was also less in these specimens.

4.4.2 Results of FEA of the primary models of ETR 0.53 group

Finite element analysis of specimens of ETR 0.53 group was also performed similar to the specimens of ETR 0.21 and the SIF were obtained before and after the introduction of patch delamination. Figure 4.43 shows the deformed geometry of two specimens of this group, having the higher and lower adhesive shear stiffness G_A/t_A, and having the crack length of 15 mm (a/b 0.3). Adhesive shear stress distribution, at steel interface, obtained from the results of primary finite element models of ETR 0.53, is shown in Figure 4.44. Peak values of adhesive shear stresses at the crack location were extracted from their distributions and are presented in Figure 4.45 for all the models. Similarly, the corresponding longitudinal stress at the bottom of CFRP patch at patch-adhesive interface is also shown in Figure 4.46 for all the specimens of ETR 0.53.

Figure 4.44 shows that the interface adhesive shear stress distribution in the specimens of ETR 0.53 was similar to the specimens of ETR 0.264 but the magnitude of stresses were lower in ETR 0.53 specimens. Comparing the absolute values of peak adhesive shear stress or the CFRP longitudinal stress, shown in Figures 4.45 and 4.46 with the specimens of ETR 0.264, it is can be seen that these are reduced by 20 % and 27 % in ETR 0.53 specimens, respectively in the lower and higher E_{FRP} CFRP patches. The reduction in magnitude of peak stresses was because of higher patch ETR in current patches. Figure 4.45 shows that the difference in magnitudes of the shear stresses within the two types of the CFRP specimens of ETR 0.53 was ranging from 10 % to 30 %, similar to that found in the models of ETR 0.264. Although the absolute values of the stresses in the FEM of ETR 0.53 were lower than that of ETR 0.264 but the comparison of shear stress or other parameters within the specimens of two different adhesive properties in any ETR group was similar. The possible reasons for the difference in the magnitude and distribution of adhesive shear stresses within the two types of CFRP patches were already discussed in detail in section 4.4.1, which concluded the main reason to be the difference in adhesive G_A/t_A in the two types of CFFRP patches rather than the modulus of elasticity of the CFRP.

4.4.2.1 Introduction of patch delamination in models of ETR 0.53 group

After analyzing the results of finite element analysis of specimens with patch ETR of 0.53, the resulting shear stress around the crack in the adhesive interface layer of each model was studied. The process of introduction of progressive patch delamination was carried out through repetitive removal of the failed adhesive region, similar to that carried out in the models of ETR 0.264. The adhesive shear stress distribution, along with the failed adhesive regions, and the resulting reduced interface-adhesive geometry in the respective FEMs of ETR 0.53, are shown in Figures 4.47 through 4.67, for the four non-dimensionlized crack lengths of 0.2, 0.3, 0.4 and 0.5. It can be noted that these figures do not show the failed adhesive region for the FEM of the higher adhesive strength with crack length 0.2, because of having no adhesive failure found in its primary FEM. Comparing the failed adhesive regions in the specimens of ETR 0.264 and 0.53, it was apparent that the relative difference in the failed regions between the two adhesive shear strength models was similar, although the area of the failed regions were reduced in the ETR 0.53 models. Specimens with lower adhesive shear strength (or with lower E_{FRP}) delaminated more than the specimens of higher shear adhesive shear strength (or higher E_{FRP}). For any particular adhesive shear strength (or E_{FRP} type), the delamination increased with the crack length, similar to that found in the models of ETR 0.264.

Possible reasons of these differences have already been discussed in detail in section 4.4.1.1, highlighting the adhesive shear stiffness G_A/t_A and shear strength as the main reasons of getting variation in delaminated regions within the two types of CFRP patches. The failed adhesive regions or the patch delaminated areas, obtained after the failure converged in the two types of CFRP patch models of ETR 0.53, are shown in Figure 4.68. The figure shows that the delaminated region increased with the crack length, irrespective of the adhesive strength or the CFRP type. But for any particular crack length, the delaminated region was much larger in the models with lower adhesive shear strength, similar to that obtained in specimens of ETR 0.264. The failed adhesive regions were found higher in specimens of lower adhesive shear strength. The difference in failed adhesive regions was similar to that obtained in the specimens of ETR 0.264. The possible reasons were already discussed in detail in section 4.4.1.1. Maximum difference in the failed regions between the models of

higher and lower adhesive shear strengths, was found in the non-dimensionlized crack length of 0.5 (or 25 mm), similar to that obtained in the FEMs of ETR 0.264.

4.4.2.2 Impact of patch delamination on SIF (K_I) and crack opening displacement (COD) in models of ETR 0.53 group

The SIF (K_I) at the crack tip of crack in steel plate and the COD of all the specimens, included in ETR 0.53 group of Table 4.1, were obtained from their FEA, before and during the intermediate successive patch delamination cycles. These were then studied with the adhesive failure in each delamination cycle. Figure 4.69 shows the variation of SIF (K_I) in the lower adhesive strength models of ETR 0.53 group, with increasing adhesive failure in the four non-dimensionalized crack lengths of 0.2, 0.3, 0.4 and 0.5. Figure 4.69 shows that the CFRP patch delamination near the crack enhanced the SIF at the crack tip in all the crack lengths. The trend of SIF (K_I) enhancement with patch delamination in the models of ETR 0.53 was similar to the trend of the SIF enhancement in the FEMs of the ETR 0.264. The absolute values of SIF (K_I) were reduced in specimens of ETR 0.53 by 25 % to 30 % due to higher patch ETR, which primarily reduced the stresses in the steel plate. The SIF enhancement due to the CFRP patch delamination was found more in the FEMs with larger crack length because of more patch delamination, and it was also similar to the results of the ETR 0.264 specimens.

The SIF (K_I) enhancement in FEM of ETR 0.53 group, having lower adhesive shear strength (or lower E_{FRP}), was found to be 13 %, 28 %, 54 % and 77 %, after introduction of the patch delamination, respectively in the four crack lengths, and the same is also shown in Figure 4.70. Impact of patch delamination on COD was also studied from the results of FEA of each basic and delaminated models of ETR-0.53 group and it is shown in Figure 4.71 for the lower adhesive shear strength models (or lower E_{FRP} models). Figure 4.71 shows similar trends of the COD enhancement after the patch delamination as obtained for the ETR 0.264 models except that the magnitude of COD was lesser in the FEMs of ETR 0.53 group by 25 % to 35 %. The impact of patch delamination on COD in the FEMs of ETR 0.53 was similar to the FEMs of ETR 0.264. COD enhancement after patch delamination was found to be ranging from 33 % to 155 % in the lower adhesive shear strength (or lower E_{FRP}) models. The 33 % enhancement was found in the FEM with smallest non-dimensionalized crack length of 0.2 (or

10 mm) while the 155 % enhancement was found in the FEM with largest non-dimensionalized crack length of 0.5 (or 25 mm).

The impact of CFRP patch delamination in the specimens of higher adhesive shear strength (or higher E_{FRP} CFRP) was not much prominent because of less delamination in these, as shown in Figure 4.68. Lesser patch delamination in these specimens of ETR 0.53 group was similar to that found in the higher adhesive shear strength specimens of ETR 0.264. But the magnitude of delamination in the FEMs of ETR 0.53 was further reduced by 20 % to 30 % than the ETR 0.264 specimens. Possible reasons of getting lesser delamination in these have already been discussed in detail in section 4.4.1.2. In summary it was because of the lower adhesive shear stiffness G_A/t_A and higher adhesive shear strength in these specimens. The values of SIF (K_I), before and after delamination, in the higher adhesive shear strength models of ETR 0.53 are summarized in Figure 4.72. This figure shows that the SIF (K_I) was enhanced by 0 %, 11 %, 14 % and 17 %, respectively in the four crack length models. No enhancement was found in the non-dimensionlized crack length of 0.2 because of no delamination or adhesive failure found in this crack length. The 17 % enhancement was found in the largest non-dimensionlized crack length of 0.5 (or 25 mm). Lesser delamination impact on SIF in the models of ETR 0.53, was because of more stress sharing by the patch thus leaving lesser stress in the steel plate.

Comparing SIF after the patch delamination, from Figures 4.70 and 4.72, respectively for the lower and higher adhesive shear strength models of ETR 0.53, it can be concluded that after the patch delamination the SIF was increased three to five times more in lower adhesive shear strength models, compared to the higher adhesive shear strength models. Similar conclusions have already been obtained for the two types of specimens in the ETR 0.264 group in section 4.4.1.1. Reasons of getting this significant difference in the two types of the CFRP patches have already been discussed in detail in section 4.4.1.1. But in summary it was mainly because of adhesive shear stiffness G_A/t_A and shear strength, resulted in lesser adhesive failure in the FEM of higher adhesive shear strength, causing lesser increase in the COD and the corresponding SIF (K_I).

It is again important to see from the comparison of Figures 4.70 and 4.72 that before the introduction of patch delamination, the SIF (K_I) was higher in the models of higher adhesive

shear strength patches by 9 % to 15 %, for different crack lengths. But after the patch delamination it reversed. Its reasons have already been discussed in detail in section 4.4.1.1, highlighting that it was because of more shear flexibility or lower adhesive G_A/t_A in models of higher E_{FRP} CFRP or higher adhesive shear strength, which allowed more crack opening before any patch delamination. Impact of patch delamination on the COD, in higher adhesive shear strength (or higher E_{FRP}) patches of ETR 0.53, was also studied from their FEA results, and these are shown in Figure 4.73, before and after the patch delamination. Figure 4.73 shows similar trends of variation of COD as that of the SIF variation obtained in these models.

A combined representation of the SIF (K_I) variation in lower and higher adhesive shear strength patches was preferred more useful. Therefore, it is shown in Figure 4.74. Note that the Figure 4.74 contains all the results of Figures 4.69, 4.70 and 4.72. Additionally, Figure 4.74 shows the SIF (K_I) of an edge cracked plain steel plate, evaluated through the FEA results of plain steel plate as well as that provided by Tada et al. (2000). Figure 4.74 shows that the SIF of plain steel plate was significantly reduced by both types of CFRP, without consideration of patch delamination, but after the patches suffered with delamination, their efficiency were reduced and SIF increased again. In the specimens of lower adhesive shear strength the initial reduction in SIF (compared to the plain steel plate) without introduction of patch delamination, was ranging from 50 % to 82 %, for varying crack lengths. But it reduced to the range of 43 % to 67 %, after the patch delamination introduced in FEA.

In the specimens of higher adhesive shear strength, the delamination was lesser and the impact of delamination was also lesser. Before consideration of patch delamination, the SIF was reduced by 45 % and 78 % (compared to the plain steel plate), in the models with higher adhesive shear strength, respectively for the non-dimensionlized crack lengths of 0.2 and 0.5 (10 mm and 25 mm). But after the patch delamination, the SIF reduction was found to be 45 % and 75 %, respectively, for the same two crack lengths. It can also be seen that the higher E_{FRP} (or higher adhesive shear strength) specimens suffered with lesser patch delamination. The delamination itself further reduced in smaller crack length models, like the FEM of non-dimensionalized crack length of 0.2 (10 mm), which showed no delamination and therefore its SIF remained unchanged.

4.4.3 Results of FEA of the primary models of ETR 0.8 group

Finite element analysis of specimens of ETR 0.8 was performed similar to the specimens of ETR 0.21 and 0.53 and SIF (K_I) was studied before and after the introduction of patch delamination in FEA. Figure 4.75 shows the deformed geometry of the two specimens of ETR 0.8, having the higher and lower adhesive shear stiffness G_A/t_A, and with crack length of 15 mm (or a/b 0.3). Adhesive shear stress distribution at steel interface, obtained from the results of all primary finite element models of ETR 0.8, is shown in Figure 4.76. The figure shows similar distribution within the two types of CFRP patches, as obtained in the FEMs of ETR 0.264 and 0.53. Peak adhesive shear stress near the crack was extracted from Figure 4.76 and is shown separately in Figure 4.77, from which it was evaluated that the difference in magnitudes of the shear stresses within the two types of the patches was ranging from 15 % to 30 %, similar to that found in the models of ETR 0.53 and 0.264. Although the absolute values of the stresses in the models of ETR 0.8 were lower than the models of ETR 0.264 or ETR 0.53, but their comparison within the two types of CFRP patch in any ETR group, showed similar trends. Longitudinal normal stress at the bottom of the CFRP patch at the patch-adhesive interface is also shown in Figure 4.78. The peak adhesive shear stress or the CFRP normal stress, in the specimens of ETR 0.8, is reduced by 15 % to 23 %, compared to the specimens of ETR 0.53 group, due to higher patch ETR. Possible reasons for the difference in the magnitude and distribution of adhesive shear stresses, within the two types of CFRP patches, were already discussed in detail in sections 3.5.3 and 4.4.1. It was found that the difference in adhesive shear stiffness G_A/t_A in the two types of patches could be the main reason of the variation in adhesive shear stresses within identical ETR specimens, rather than the difference in the modulus of elasticity E_{FRP} of the CFRP.

4.4.3.1 Introduction of patch delamination in models of ETR 0.8 group

After analyzing the results of primary finite element analysis of ETR 0.8 specimens, the resulting shear stress around the crack in the interface adhesive layer was studied in each model. The process of introduction of progressive patch delamination was also carried out through repetitive removal of the failed adhesive region, similar to that carried out in the

models of ETR 0.264 and 0.53. Interface adhesive shear stress distribution, along with the failed adhesive regions, and the resulting reduced interface-adhesive geometry in the FEMs of ETR 0.8, are shown in Figures 4.79 through 4.99, for the FEM of four non-dimensionalized crack lengths of 0.2, 0.3, 0.4 and 0.5. These figures do not show the failed adhesive regions of higher adhesive shear strength patch with crack length 0.2. It was because of no adhesive failure in its primary FEM. Comparing the failed adhesive regions of ETR 0.8 specimens with ETR 0.53 and ETR 0.21 specimens, it was found that the difference in the failed adhesive regions within the two types of the CFRP patches, having different adhesive shear strengths, was similar in the models of ETR 0.264, 0.53 and 0.8. Although the magnitude of the delaminated areas were further reduced in the ETR 0.8 specimens. Specimens with lower adhesive shear strength (or lower E_{FRP}) delaminated more than the higher adhesive shear strength (or higher E_{FRP}) specimens. But for any particular adhesive strength (or the E_{FRP} type), the delamination increased with the crack length, similar to that obtained in the specimens of ETR 0.264 and 0.53. The possible reasons of these variations have been discussed in detail in sections 3.5.3, 4.4.1.1 and 4.4.2.1. These sections highlighted the adhesive shear stiffness G_A/t_A and shear strength, as the main reasons of getting different delaminated regions in the two types of CFRP patches with identical ETR.

The failed adhesive regions, obtained at the converged delamination stage, in the two types of CFRP patch models of ETR 0.8, are shown in Figure 4.100. The figure shows that the delaminated region increased with the crack length, irrespective of the CFRP type. But for any particular crack length the delaminated region was much larger in the models with lower adhesive shear strength (or lower E_{FRP} CFRP) patches, similar to the delamination in models of ETR 0.264 and 0.53. Comparison of the failed adhesive regions from Figure 4.100, within the models of the two different adhesive shear strengths, provides similar conclusions already obtained in the ETR 0.264 and 0.53 groups. The delamination in specimens with lower adhesive shear strength (or lower E_{FRP} CFRP) was larger than the delamination in the specimens with higher adhesive shear strength (or higher E_{FRP} CFRP), by similar percentages as that obtained for the ETR of 0.264 and 0.53. The possible reasons were already discussed in detail in sections 3.5.3, 4.4.1.1 and 4.4.2.1. Maximum difference in the patch delaminated regions or the failed adhesive regions, within the specimens of lower and higher adhesive

shear strengths of ETR 0.8 group, was found in the non-dimensionlized crack length of 0.5 (or 25 mm), similar to that obtained in the FEMs of ETR 0.264 and 0.53.

4.4.3.2 Impact of patch delamination on SIF (K_I) and crack opening displacement (COD) in models of ETR 0.8 group

The SIF (K_I) at the crack tip of crack in steel plate and the COD of all the specimens of ETR 0.8 group were obtained from the results of FEA, before and during the intermediate patch delamination cycles. These were then studied with the adhesive failure in each delamination cycle. Figure 4.101 shows the variation of SIF (K_I) in the lower adhesive strength models (or the lower E_{FRP} patches) of ETR 0.8 group, for the four non-dimensionlized crack lengths of 0.2, 0.3, 0.4 and 0.5. Figure 4.101 shows that the CFRP patch delamination near the crack, enhanced the SIF (K_I) at the crack tip in all the crack lengths. The trend of SIF enhancement with patch delamination in the models of ETR 0.8 was similar to the trend of the SIF enhancement in the FEMs of the ETR 0.264 and 0.53. But the magnitude of SIF were reduced in ETR 0.8 by 15 % to 20 %, compared to the models of ETR 0.53, due to reduction in plate stresses by the higher patch ETR. The SIF enhancement due to the CFRP patch delamination was found more in bigger crack lengths because of more patch delamination in these. It was similar to the results of the ETR 0.264 and 0.53 FEMs, shown in sections 4.4.1.2.and 4.4.2.2. The SIF (K_I) in the specimens of ETR 0.8, with lower adhesive strength, was found to be enhanced by 8 %, 22 %, 41 % and 67 %, after introduction of patch delamination in the four crack lengths. The same is also summarized in Figure 4.102.

Impact of patch delamination on COD was also studied from the results of FEA of the un-delaminated and delaminated models of ETR 0.8 group. Figure 4.103 shows the COD variation of the specimens of lower adhesive shear strength of ETR 0.8 group. Figure 4.103 shows similar trends of the COD enhancement, after the patch delamination, as already obtained in the ETR 0.264 and 0.53 specimens. But the magnitude of the COD was further reduced in the FEMs of ETR 0.8 group by 13 % to 17 %, compared to the specimens of ETR 0.53, due to similar reasons provided for the SIF above. The impact of patch delamination on COD in the FEMs of ETR 0.8 was similar to the FEMs of ETR 0.264 and 0.53. The COD enhancement after patch delamination was found to be ranging from 24 % to 151 % in the

models of lower E_{FRP}. The 24 % enhancement was found in the smallest non-dimensionalized crack length of 0.2 while 151 % enhancement was found in the non-dimensionlized crack length of 0.5.

The impact of patch delamination on FEMs with higher adhesive shear strength (or higher E_{FRP} CFRP) was not much highlighted because of very small patch delamination in these models, as shown in Figure 4.100. Lesser patch delamination in specimens of higher adhesive shear strength was similar to that obtained in the specimens of ETR 0.264 and 0.53. But the magnitude of delamination in the ETR 0.8 specimens was further reduced by 8 % to 13 % compared to the specimens of ETR 0.53. The possible reasons have already been discussed in detail in sections 3.5.3, 4.4.1.2 and 4.4.2.2, but in summary it was because of the lower adhesive shear stiffness G_A/t_A and higher adhesive shear strength used in these specimens.

The SIF (K_I) values, in the specimens of higher adhesive shear strength (or higher E_{FRP} CFRP) of ETR 0.8, before and after delamination, were obtained from results of FEA and these are also summarized in Figure 4.104. It shows that the SIF (K_I) was enhanced by 0 %, 3 %, 12 % and 14 %, respectively in the FEM of their four crack lengths. No SIF enhancement found in the non-dimensionlized crack length of 0.2 (or 10 mm) because of no adhesive failure in it. The 14 % enhancement was found in the largest non-dimensionlized crack length of 0.5. The delamination impact found lesser in the models of ETR 0.8, compared to the models of ETR 0.53 or 0.264, because of more stress sharing by the patch, thus leaving lesser stress in the steel plate. Comparing the SIF (K_I) enhancement from Figures 4.102 and 4.104, respectively for the lower and higher adhesive shear strength of ETR 0.8, it can be concluded that the SIF enhancement after the patch delamination in lower E_{FRP} models was higher than the SIF enhancement in higher E_{FRP} models. It was also similar to the conclusions already obtained in the ETR of 0.264 and 0.53. Reasons of that large variation in SIF, in the two types of the CFRP patches, have already been discussed in detail in sections 3.5.3, 4.4.1.1 and 4.4.2.2.

It is important to note from comparison of Figures 4.102 and 4.104 that before the introduction of patch delamination in the FEA, the SIF was higher in the specimens with higher E_{FRP} CFRP by 8 % to 18 %. But after the patch delamination it was reversed. The reasons have already been discussed in detail in section 4.4.1.1, highlighting that it was because of lower adhesive G_A/t_A in the models of higher E_{FRP} patches, which had allowed

more crack opening, before the patch delamination. Impact of the patch delamination on the COD, in higher E_{FRP} patches of ETR 0.8, was also studied from results of their FEA, which is also shown in Figure 4.105. This figure shows similar trends of COD variation as obtained for the SIF in these models.

Combined representation of the SIF (K_I) variation in lower and higher E_{FRP} patches (with lower and higher adhesive shear strength) was preferred more useful, and therefore, it is also shown in Figure 4.106. This figure contains all the results of Figures 4.101, 4.102 and 4.104 and additionally it also contains the SIF (K_I) of plain steel plate, evaluated from the results of FEA of plain steel plate as well as using the equation 3.12 (Tada et al. 2000). Figure 4.106 shows that the SIF of plain steel plate was significantly reduced by both types of CFRP patches, before the patch delamination. But after the patches suffered with delamination, their efficiency was dropped and the SIF increased again. In the specimens of lower adhesive shear strength, the initial reduction in SIF (compared to the plain steel plate) was ranging from 57 % to 84 %, without introduction of patch delamination. But after the introduction of patch delamination in FEA, it reduced to 52 % to 73 %, for different crack lengths.

The delamination and its impact were found lesser in specimens of higher adhesive shear strength (or higher E_{FRP} patches) than the lower adhesive shear strength specimens (or lower E_{FRP} patches). Before introduction of patch delamination in FEA of higher adhesive shear strength specimens, the SIF reduction was ranging from 53 % and 82 %, compared to the SIF of plain steel plate. But after the introduction of patch delamination, the SIF (K_I) reduction was reduced to 53 % to 78 %. Higher adhesive strength specimens (or higher E_{FRP} patches) suffered with lesser patch delamination, and therefore, its impact on SIF was also lesser. It can be seen from SIF results that no adhesive failure or the patch delamination was found in the FEM of crack length of 0.2 (10 mm), and therefore, its SIF was remained unchanged after delamination.

4.5 Impact of delamination location on SIF – Near crack delamination versus Patch-end delamination

The impact of patch delamination on SIF (K_I) has been studied in this chapter in detail but in all the previous cases the delamination was actually provided around the crack. There might still be possibility of getting delamination in other parts of the patch. The shear stress distribution of adhesive layer at steel interface, as shown in Figures 3.14, 3.15 and 3.16, also indicates that the adhesive shear stress is also high at the patch end, in addition to the near-crack location. At the patch-end, the shear stress although not greater than the near-crack region, but still it could be comparable to the shear strength of adhesive, which might also results in the patch delamination there.

Therefore, in order to study the impact of delamination location on SIF (K_I) at the crack tip of crack in the plate, a further discretization of the delamination location was made for the two possible locations caused by the adhesive shear failure; the near-crack and the patch-end locations. To accomplish the task, same delaminated area was introduced at the two selected critical locations, in the two separate but identical finite element models, which are also schematically shown in Figures 4.107 and 4.108. A three-layered specimen, with patch ETR of 0.264 and non-dimensionlized crack length of 0.3, was selected for this study. The SIF (K_I) variation for this FEM (the case of Figure 4.107), caused by adhesive failure around crack, has already been provided in section 4.4.1.2 and shown in Figure 4.37. The delamination, obtained in the first cycle of FEA of Figure 4.37, was then provided at the patch-end of same specimen, along the full patch width, as shown in Figure 4.108. The SIF (K_I) for the patch-end de-laminated model was then compared with the SIF (K_I) of the un-delaminated model, as well as with the SIF of the case when the same delaminated area was provided around the crack.

The resulting comparison is shown in Figure 4.109, which shows that the SIF (K_I) of the patch-end delaminated case was identical to the un-delaminated case. The SIF (K_I), for the case of the delamination around the crack, was much higher than the SIF (K_I) of both the cases of patch-end delamination as well as the un-delaminated plate. The reason might be because of the patch-end being far away from the crack and the delamination there could not affect the stress distribution around the crack because of a large bonded region in between the

patch-end and the crack. Therefore, for the same reasons, the patch-end delamination could also not affect the patch restriction to the crack opening, and thus the SIF (K_I) at the crack tip.

Another possible case of patch-end delamination was also studied, in which the total patch-end delamination was provided at the patch-end but within a region in-line with the crack, instead of providing it along the full patch width. Figure 4.110 schematically shows this patch-end delaminated region. The resulting SIF (K_I) at the crack tip was then compared with that obtained for the previous cases, as well as with the SIF of un-delaminated model, and the results are shown in Figure 4.111. It is obvious from the Figure 4.111 that the SIF (K_I) of the latest patch-end delaminated model was similar to both the full width patch-end delaminated model and the un-delaminated model. Therefore, after comparing the SIF results of the two end-delamination models with the un-delaminated model, and the one with delamination near the crack, it can be concluded that the patch-end delamination has a negligible impact on the SIF (K_I) at the crack tip, because SIF (K_I) of the end-delaminated models were found to be very close to the completely un-delaminated model. The near-crack delamination found to be significantly affecting the SIF at the crack tip, which has been shown throughout in this chapter. Therefore, from now on, further study on the impact of patch delamination on SIF (K_I) would only be considering the delamination around the crack. Another important conclusion that can be drawn from this end delamination study was that the end delamination could also be caused by the peel stresses. It has been shown in section 3.5.3.2 that peel stress also develops and acts at the patch-end, therefore, if any delamination caused by the peel stress were to be modeled in FEA, then, it would also have no or minimal impact on the SIF at the crack tip.

4.6 Variation of SIF (K_I) with adhesive shear stiffness (G_A/t_A)

In chapter 3, it was shown in section 3.5.3.4 that the variation of adhesive maximum shear stress near the crack and the SIF (K_I) at the crack tip can be better studied with the shear stiffness of the interface adhesive layer (G_A/t_A), instead of the adhesive thickness t_A or the adhesive modulus of elasticity E_A, independently. Variation of SIF (K_I) at the crack tip had shown to be varying with adhesive shear stiffness G_A/t_A in Figure 3.26 for the two sets of FRP

patches; one had the varying adhesive thickness t_A and the other had varying adhesive modulus of elasticity E_A. It was concluded there that the resulting SIF (K_I) in the specimens of both sets varied well with the adhesive shear stiffness G_A/t_A. But for any two specimens of these groups, having identical G_A/t_A, the SIF (K_I) of specimens with lesser E_A or G_A were slightly higher than the specimens of higher E_A or G_A. It has also been shown in chapter 4 that the patch delamination also affects the SIF (K_I), which was not considered in chapter 3. Therefore, in order to observe the impact of patch delamination on the SIF (K_I) variation (with adhesive G_A/t_A), patch delamination was introduced in all the models of the two groups included in Figure 3.26, using the higher adhesive strength provided in Table 4.2. Only one cycle of adhesive removal was performed and the results are shown in Figure 4.112. This figure also includes the contents of Figure 3.26. It can be seen from Figure 4.112 that the difference in SIF (K_I) variation in the two models, which existed before the patch delamination, has now been reduced to minimal after introduction of the patch delamination. This comparison further supported the use of adhesive shear stiffness G_A/t_A as a better parameter in studying adhesive impact, rather than its thickness t_A or elastic modulus E_A independently. But keeping in view that the adhesive shear strength was assumed identical in the two different types of adhesives, it could be expected that that the results might be different for different adhesive shear strengths. The impact of adhesive shear strength will be explored more in the parametric study carried out in the chapter 8 of the thesis.

4.7 Summary and conclusions

This chapter presented an extension in the numerical study of double sided bonded edge cracked plate, presented in chapter 3, by introducing patch delamination in their FEA. The impact of patch delamination was further studied on the SIF (K_I) at crack tip of the crack in steel plate being repaired. Double sided bonded CFRP patches were selected, with two different adhesive and CFRP properties. Three patch ETR values of 0.264, 0.53 and 0.8 were selected, and for each ETR group four crack length models were developed, with non-dimensionlized crack lengths (a/b) of 0.2, 0.3, 0.4 and 0.5. Within each ETR group two types of CFRP patches were selected, with different CFRP type and adhesive. The CFRP patches

were having different adhesive shear strengths and shear stiffness (G_A/t_A) but have identical ETR. The two CFRP types were selected from the range of commercially available CFRP, which were found more compatible with the two selected adhesives. The two selected CFRP types were having higher and lower modulus of elasticity (E_{FRP}) because of having different fiber volumetric content.

Initial FEA of all the finite element models in each ETR group was carried out similar to chapter 3. After studying the shear stress distribution in the interface adhesive layer from the results of initial FEA, patch delamination was introduced in the analysis. The patch delamination was modelled in FEA of each specimen, through introduction of shear failure of the adhesive layer at the patch-plate interface. The adhesive failure was introduced by progressive removal of the failed adhesive region (in shear), around the crack and re-analyzing it until convergence achieved in the adhesive failure and removal process.

The impact of patch delamination, on SIF (K_I) at the crack tip and on the COD, was then finally studied, before and after the introduction of the patch delamination, for each specimen of the three ETR groups. These results were further studied on the basis of the adhesive shear stiffness (G_A/t_A) and shear strengths within identical ETR specimens. It was found that the K_I enhanced after the patch delamination in each FEM, caused by the adhesive failure. The K_I enhancement due to patch delamination was found different in the two identical ETR specimens of any ETR group because of having different shear stiffness (G_A/t_A) and shear strengths of adhesives. Before introduction of the patch delamination in identical ETR specimens, the SIF (K_I) was higher in the specimen with lower adhesive G_A/t_A. But after the introduction of patch delamination, the SIF (K_I) was found to be dependent upon the shear strength of adhesive; higher the shear strength lesser was the delamination and lesser increase in the SIF (K_I). Within the ETR 0.264 group, the increase in SIF (K_I) in the FEM of lower adhesive shear strength, was found to be 14 % to 100 %. The 14 % increase in SIF (K_I) was found in the FEM of smallest crack length (10 mm), while 100 % increase in SIF (K_I) was found in the FEM of largest crack length (25 mm). The SIF (K_I) enhancement in the FEM of higher adhesive shear strength was found to be ranging from 2 % to 22 %, which was quite less compared to that achieved in the FEM of lower adhesive shear strength. It was because of lesser adhesive failed region or lesser patch delamination in these specimens.

The impact of patch delamination on SIF (K_I) was also studied in the ETR groups of 0.53 and 0.8, but due to the higher patch ETR the SIF (K_I) enhancement was found lesser in these ETR groups. The impact of patch delamination was also found to be decreasing with increasing patch ETR. The SIF (K_I) enhancement in the specimens of lower adhesive shear strength, after patch delamination, in the ETR 0.53 group, was found to be ranging between 13 % and 77 %. The 13 % found in the smallest crack length while 77 % found in the largest crack length. Similarly, the SIF (K_I) enhancement in the FEMs of higher adhesive shear strength, after the patch delamination, was found to be ranging between 0 % and 17 %, which was quite less compared to the lower adhesive shear strength specimens and it was because of high shear strength. No enhancement (0 %) was found in smallest crack length of 10 mm, while 14 % enhancement was found in the largest crack length of 25 mm. No SIF (K_I) enhancement obtained in the crack length of 10 mm because of no patch delamination or adhesive failure found in its FEM.

The impact of patch delamination on SIF (K_I) was also found in the specimens of ETR 0.8 but the SIF (K_I) enhancement (after patch delamination) was further reduced, compared to the previous two ETR groups. In FEM of the lower adhesive shear strength the SIF (K_I) enhancement was found to be ranging between 8 % and 67 %, after the patch delamination. The 8 % found in the lowest crack length and 67 % in the largest crack length FEM. Similarly, in the FEM of the higher adhesive shear strength, the SIF (K_I) enhancement was found to be ranging between 0 % and 14 %, after the introduction of the patch delamination. No SIF (K_I) enhancement (0 %) was obtained in smallest crack length of 10 mm, while the 14 % SIF enhancement was obtained in the largest crack length of 25 mm. No SIF (K_I) enhancement obtained in the crack length of 10 mm because of no patch delamination or adhesive failure found in its FEM.

Therefore, for identical ETR specimens, adhesive shear strength was found to be more impacting the SIF (K_I) at the crack tip of the bonded steel plate, than the adhesive shear stiffness (G_A/t_A), with consideration of patch delamination or the adhesive failure around the crack.

Table 4.1 Material Properties

Material	Modulus of elasticity 'E' (GPa)	Thickness 't' (mm)	Shear Strength (MPa)
Steel	200	7.5	230
Lower Modulus CFRP	81	0.816	-
Higher Modulus CFRP	165	1.2	-
Epoxy for lower Modulus CFRP	1.724	0.2	7.5
Adhesive for higher Modulus CFRP	5	2.4	15

Table 4.2 Details of finite element models

Specimen's ID	ETR	FRP Layers Each Face	Crack length (mm)	Description
3L-Lo-Str	0.264	3	10,15,20,25	Lower adhesive shear Strength
1L-Hi-Str	0.264	1	10,15,20,25	Higher adhesive shear Strength
6L-Lo-Str	0.53	6	10,15,20,25	Lower adhesive shear Strength
2L- Hi-Str	0.53	2	10,15,20,25	Higher adhesive shear Strength
9L- Lo-Str	0.8	9	10,15,20,25	Lower adhesive shear Strength
3L- Hi-Str	0.8	3	10,15,20,25	Higher adhesive shear Strength

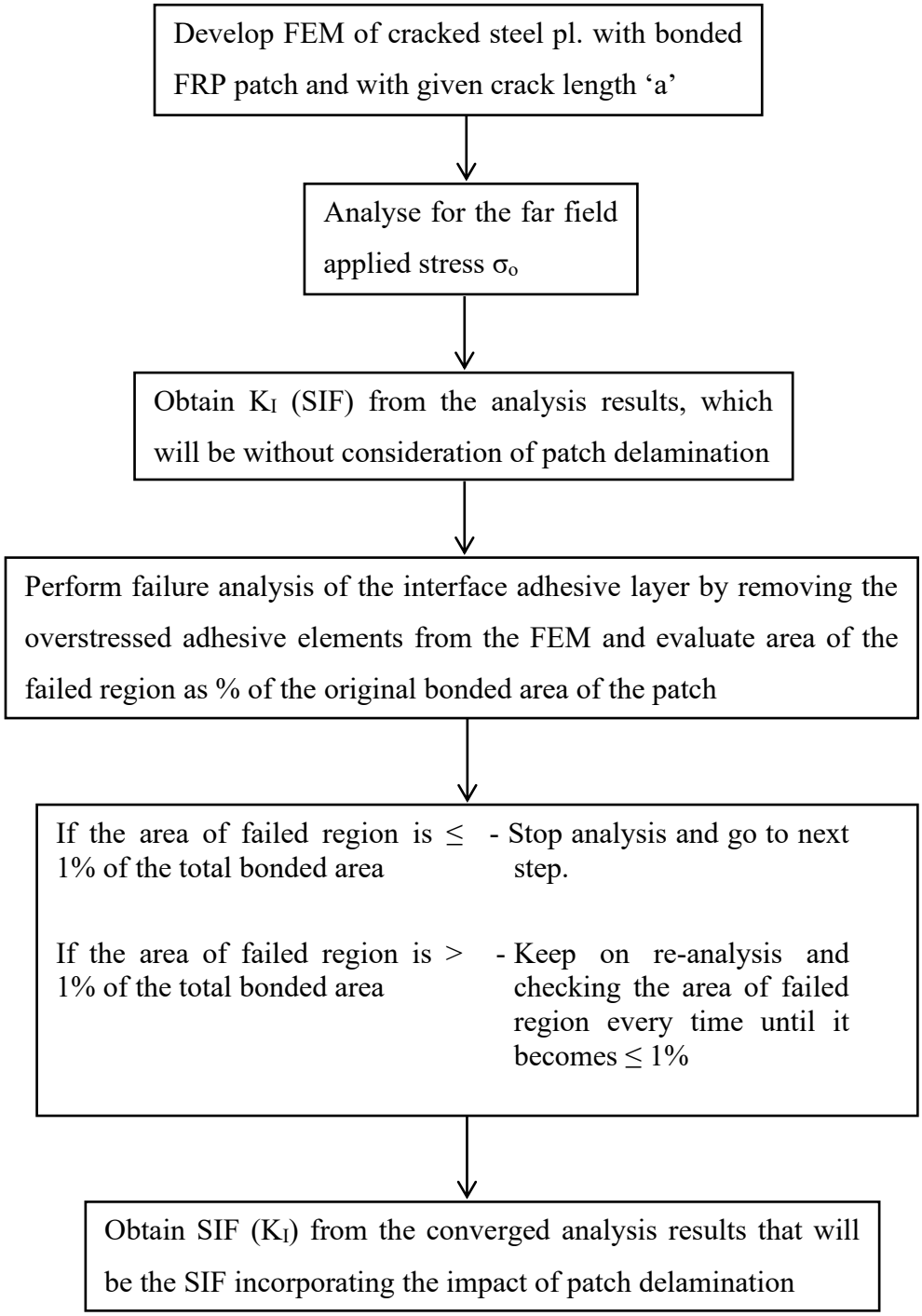

Figure 4.1. Methodology of obtaining impact of patch delamination on SIF

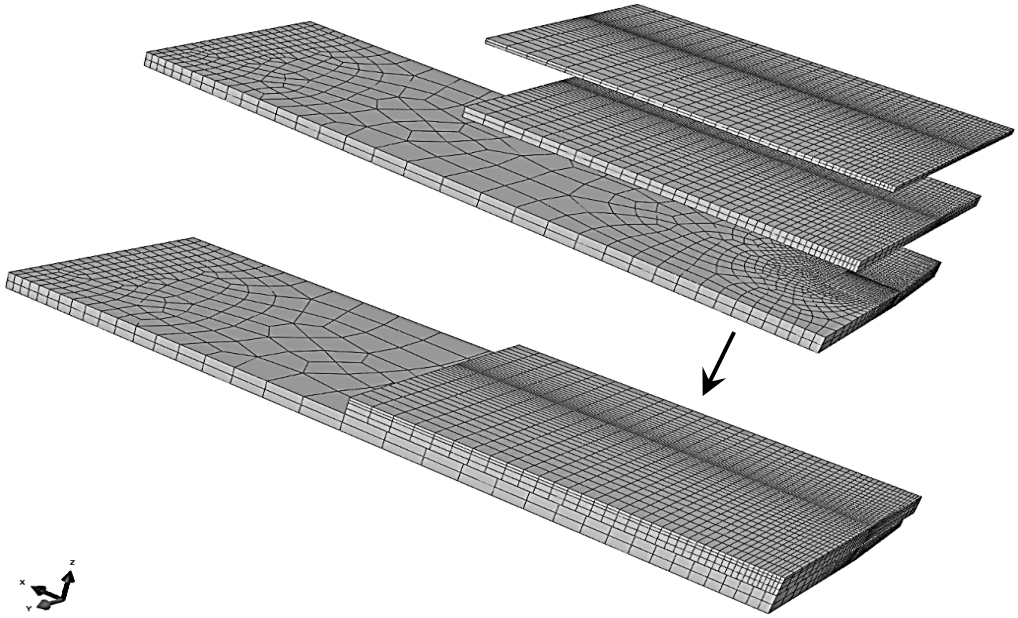

Figure 4.2 Typical 1-layered FEM with higher E_{FRP}, lower adhesive G/t and with ETR 0.264

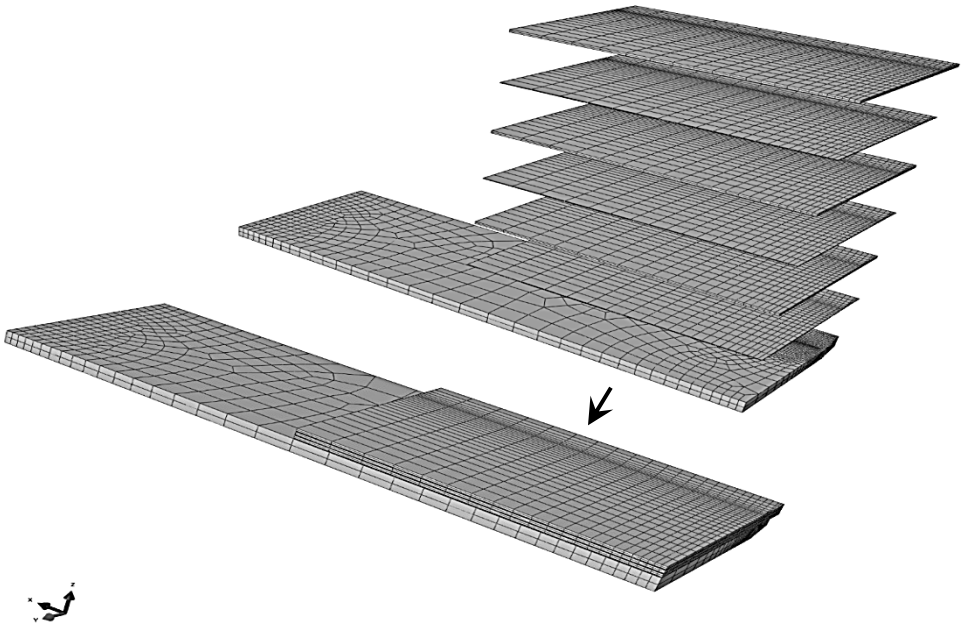

Figure 4.3 Typical 3-layered FEM with lower E_{FRP}, higher adhesive G/t and with ETR 0.264

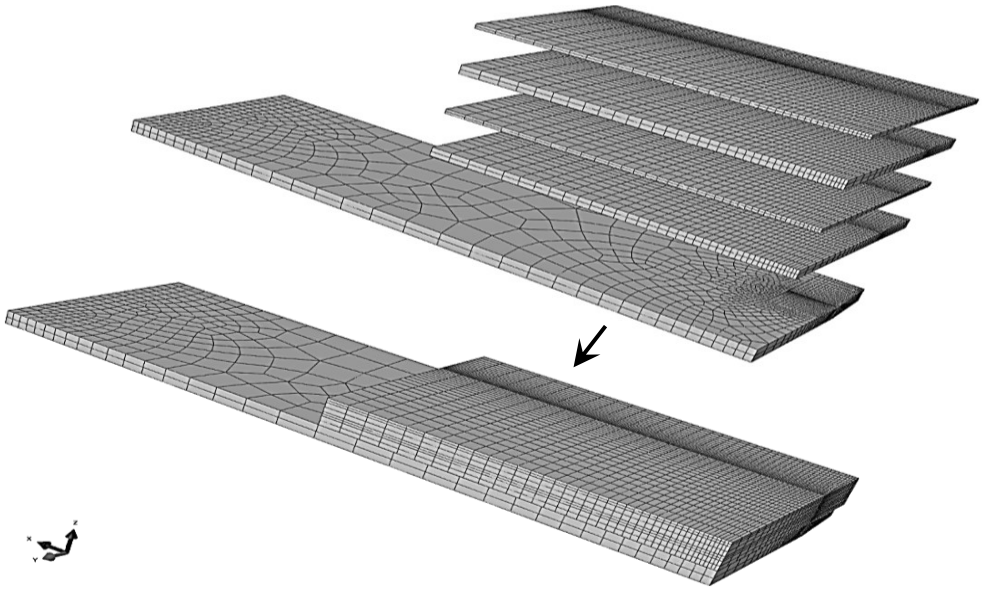

Figure 4.4 Typical 2-layered FEM with higher E_{FRP}, lower adhesive G/t and with ETR of 0.53

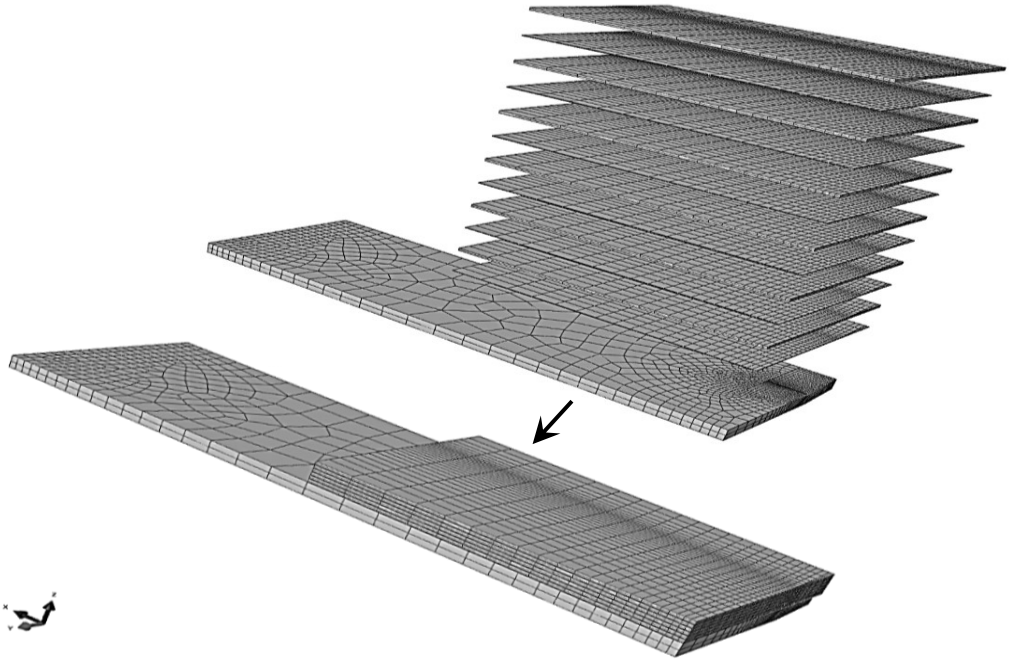

Figure 4.5 Typical 6-layered FEM with lower E_{FRP}, higher adhesive G/t and with ETR of 0.53

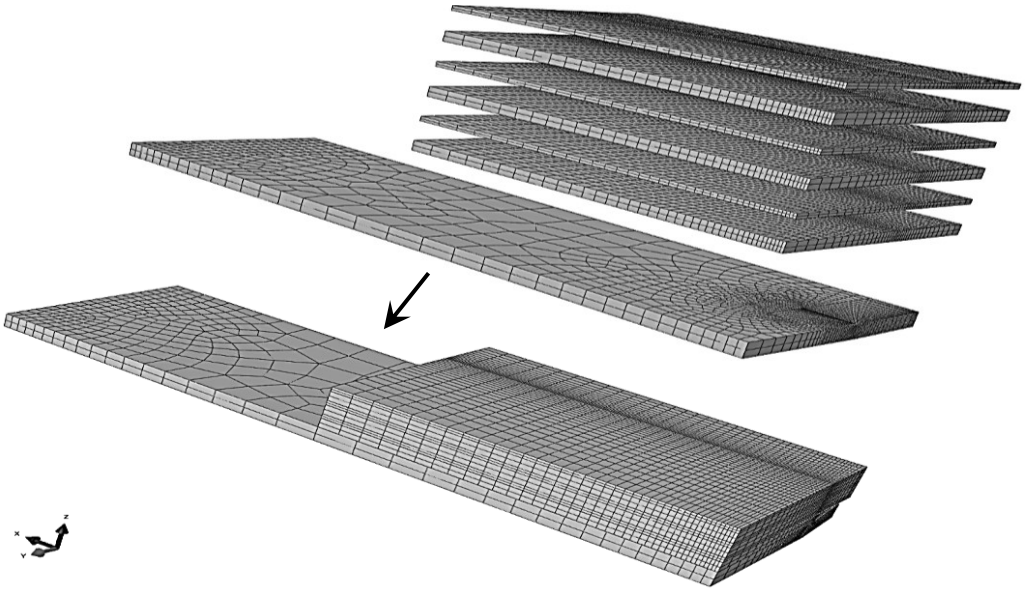

Figure 4.6 Typical 3-layered FEM with higher E_{FRP}, lower adhesive G/t and with ETR of 0.8

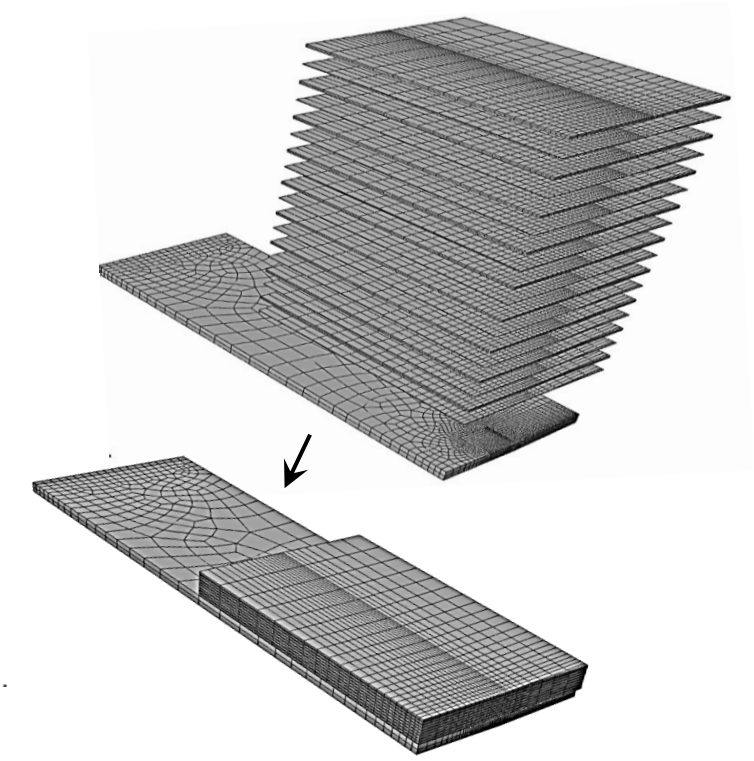

Figure 4.7 Typical 9-layered FEM with lower E_{FRP}, higher adhesive G/t and with ETR of 0.8

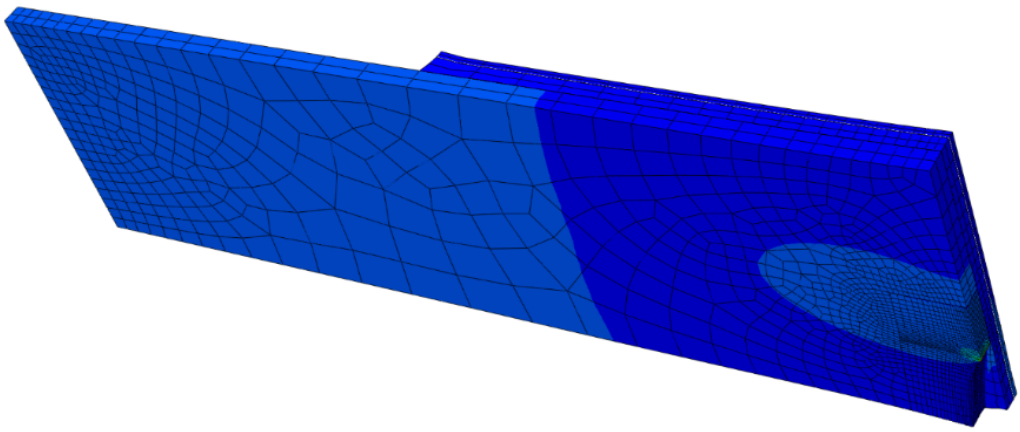

(a)

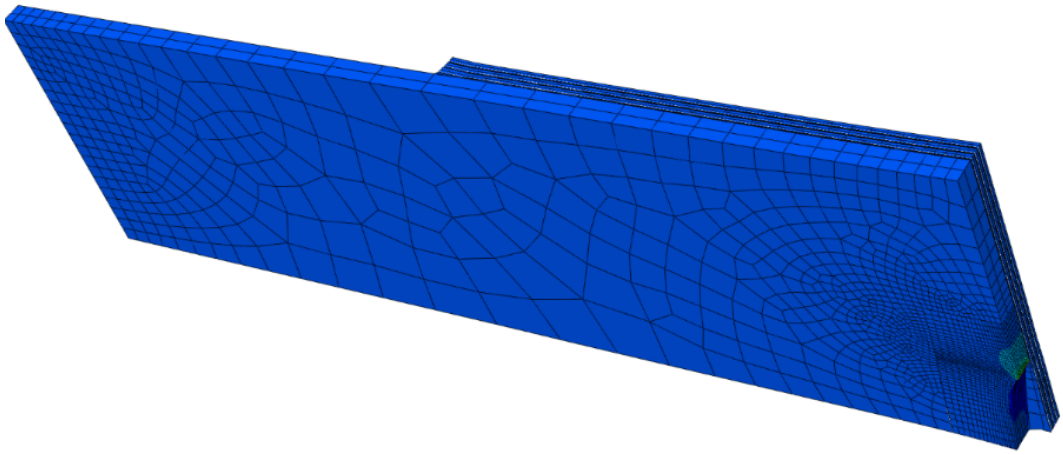

(b)

Figure 4.8. Deformed geometry of finite element models of ETR 0.264 with crack length 15mm.
(a) Higher E_{FRP} CFRP patch (with lower adhesive G/t & higher adhesive shear strength)
(b) Lower E_{FRP} CFRP patch (with higher adhesive G/t & lower adhesive shear strength)

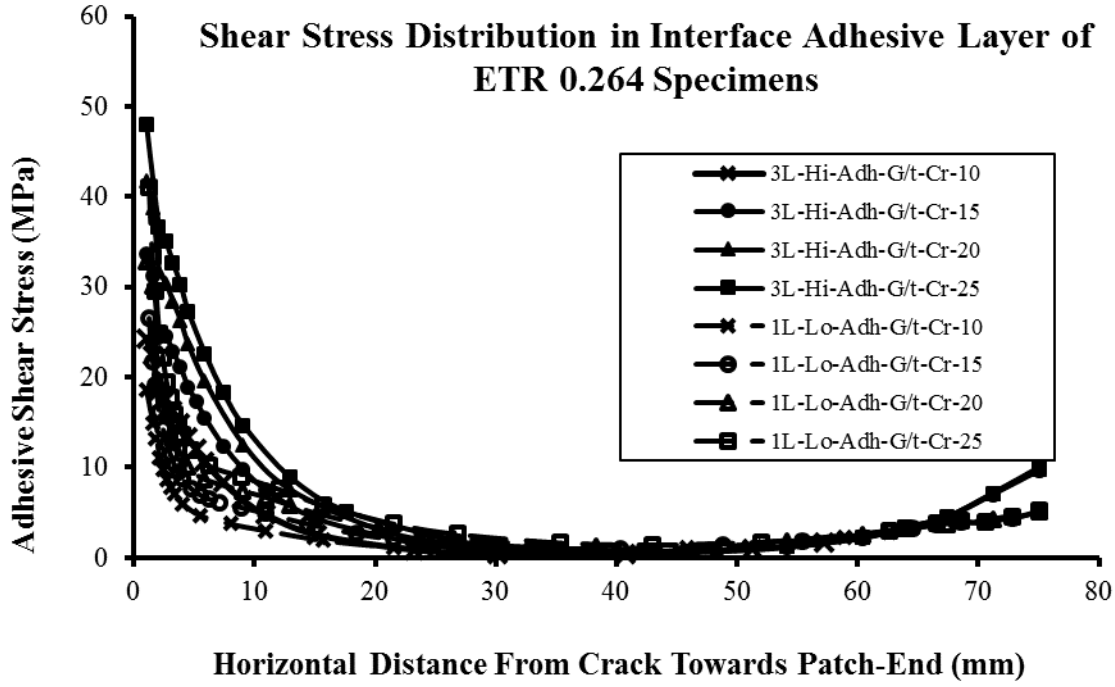

Figure 4.9 Shear Stress distribution in interface adhesive layer of ETR 0.264 models

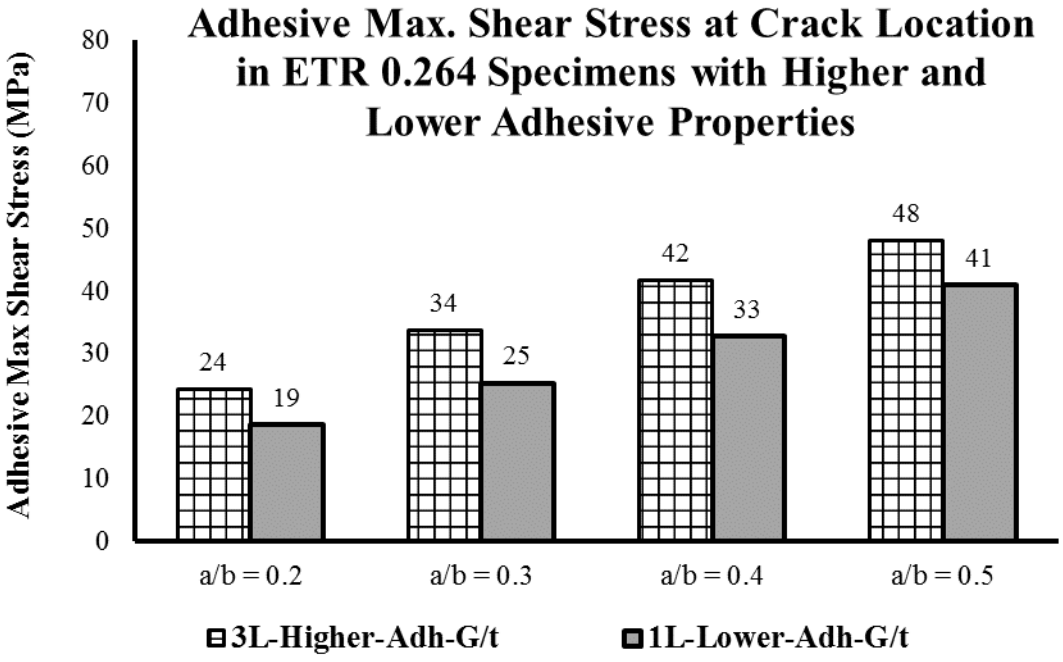

Figure 4.10 Peak adhesive shear stress at crack location in ETR 0.264 models

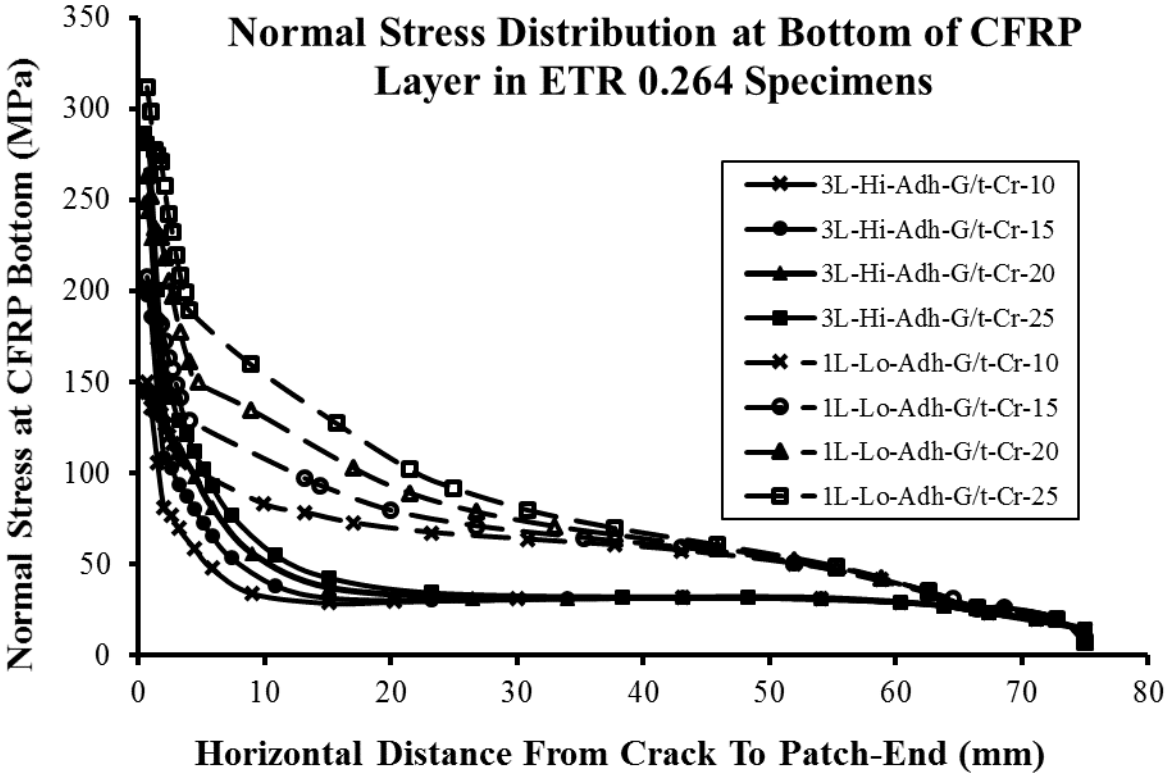

Figure 4.11 Normal stress distribution at bottom of CFRP patch in ETR 0.264 specimens

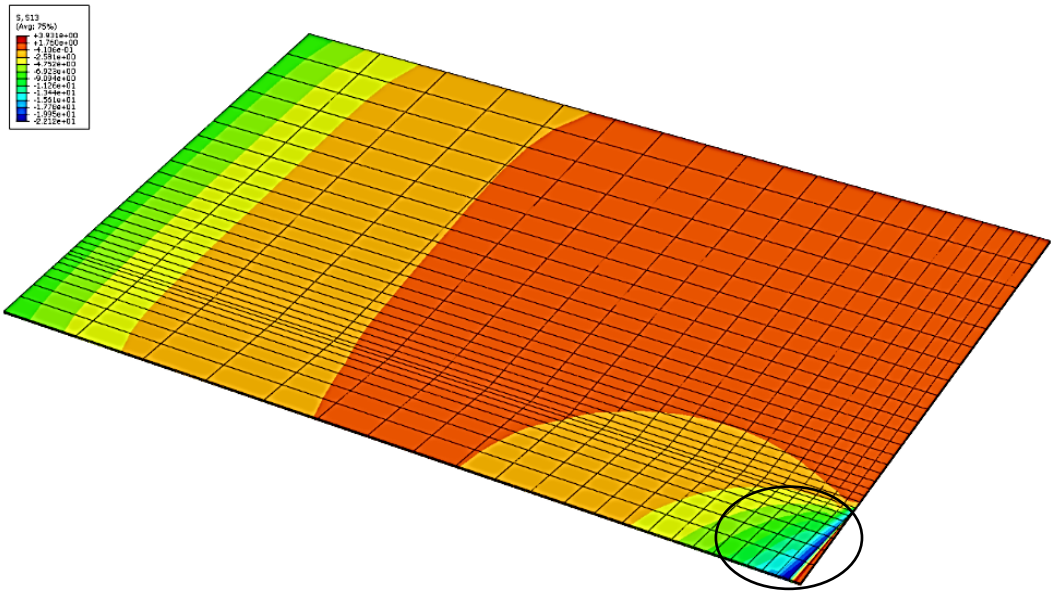

Figure 4.12 Shear stress distribution in adhesive layer in lower E_{FRP} & lower adhesive strength FEM with crack 10mm & ETR-0.264

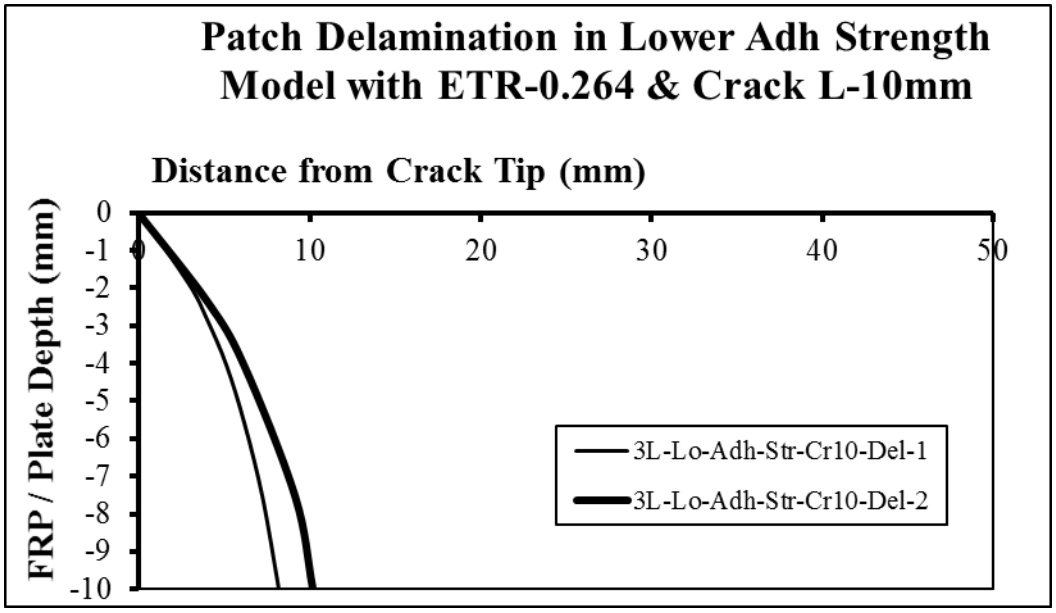

Figure 4.13 Failed adhesive region in lower E_{FRP} and lower adhesive strength FEM with crack 10mm & ETR-0.264

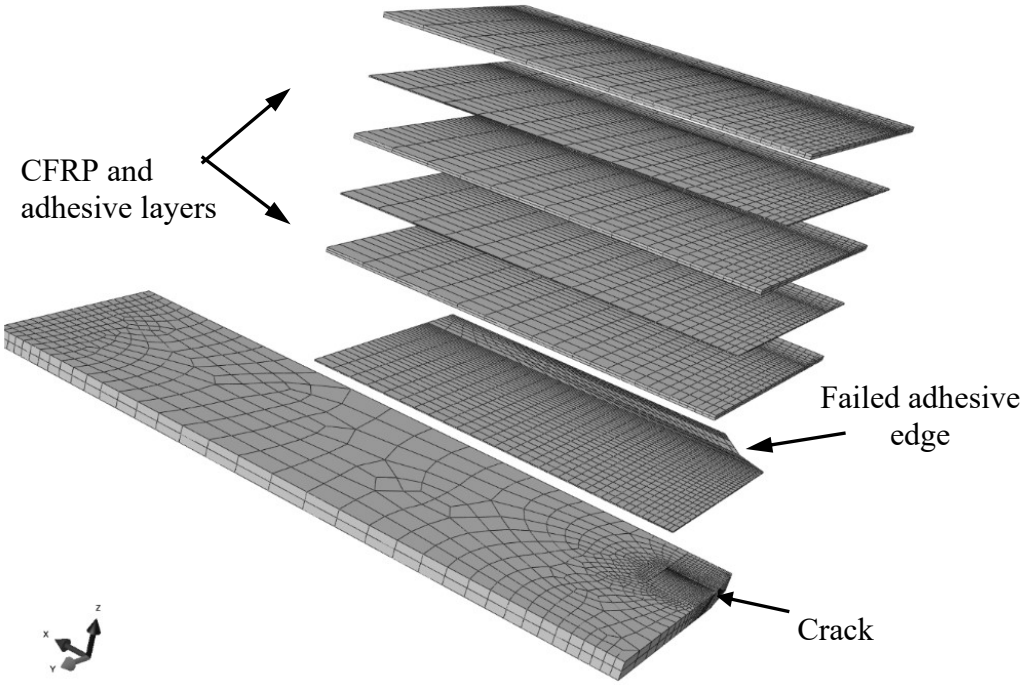

Figure 4.14 Failure incorporated adhesive layer in lower adhesive strength FEM with crack 10mm & ETR-0.264

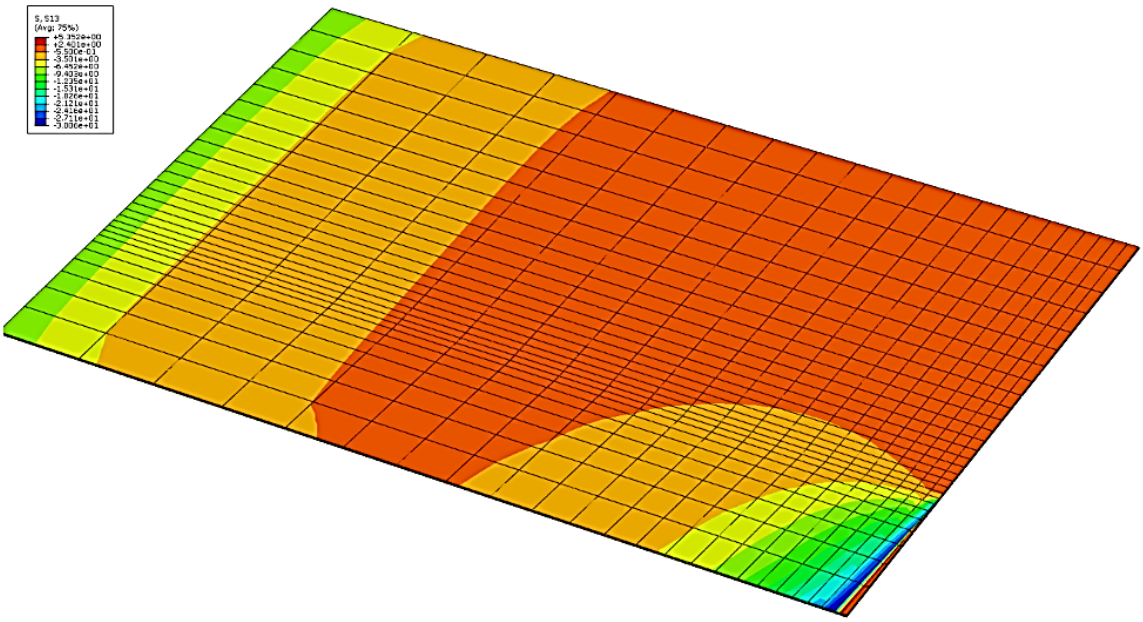

Figure 4.15 Shear stress distribution in adhesive layer in lower adhesive strength FEM with crack 15mm & ETR-0.264

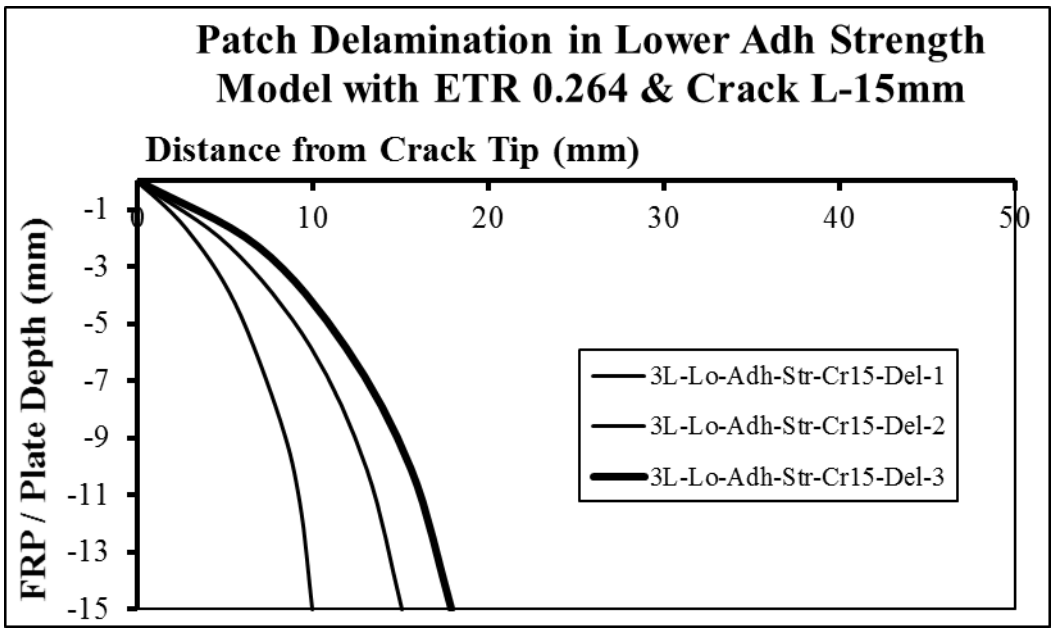

Figure 4.16 Failed adhesive region in lower adhesive strength FEM with crack 15mm & ETR-0.264

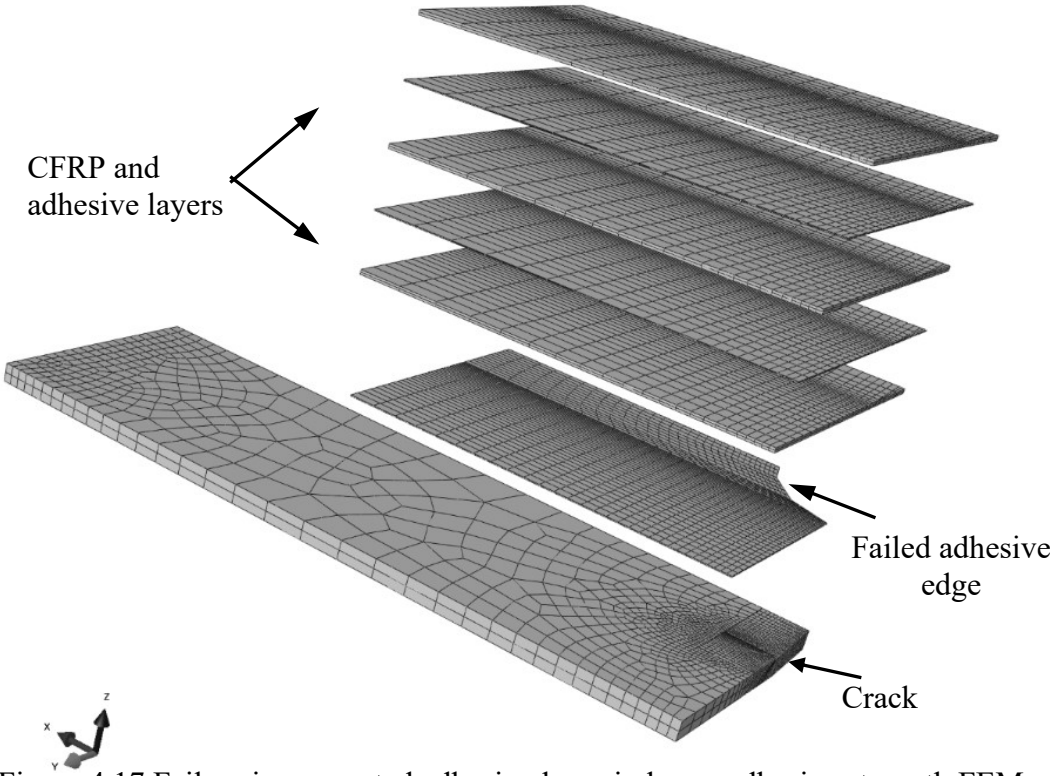

Figure 4.17 Failure incorporated adhesive layer in lower adhesive strength FEM with crack 15mm & ETR-0.264

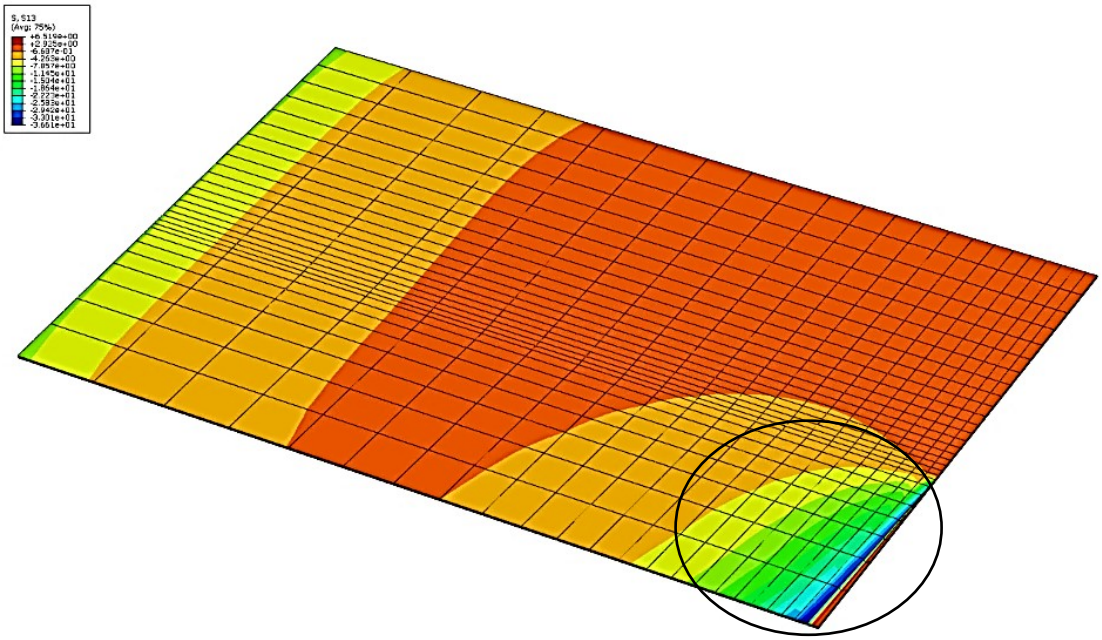

Figure 4.18 Shear stress distribution in adhesive layer in lower adhesive strength FEM with crack 20mm & ETR-0.264

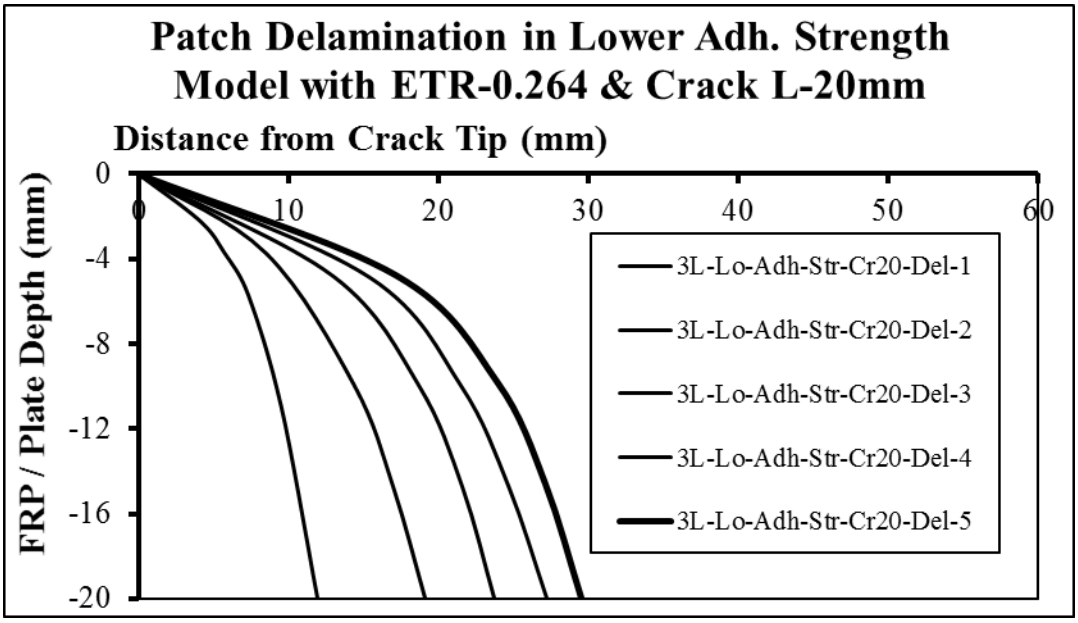

Figure 4.19 Failed adhesive region in lower adhesive strength FEM with crack 20mm & ETR-0.264

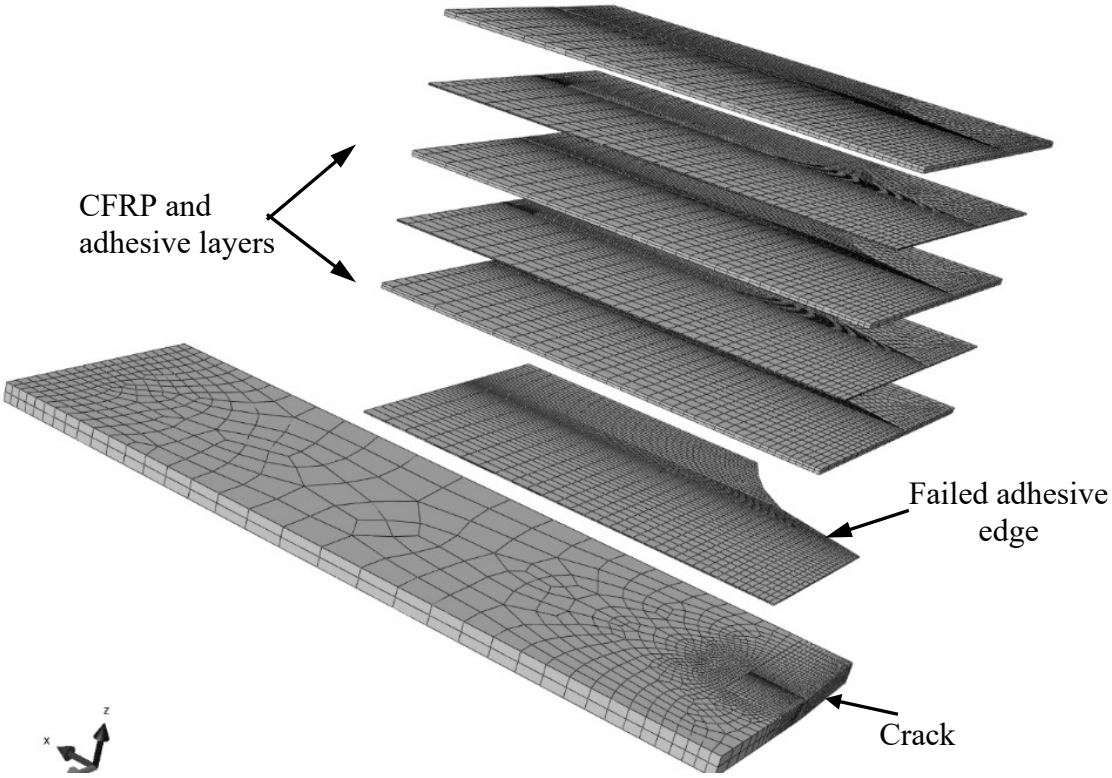

Figure 4.20 Failure incorporated adhesive layer in lower adhesive strength FEM with crack 20mm & ETR-0.264

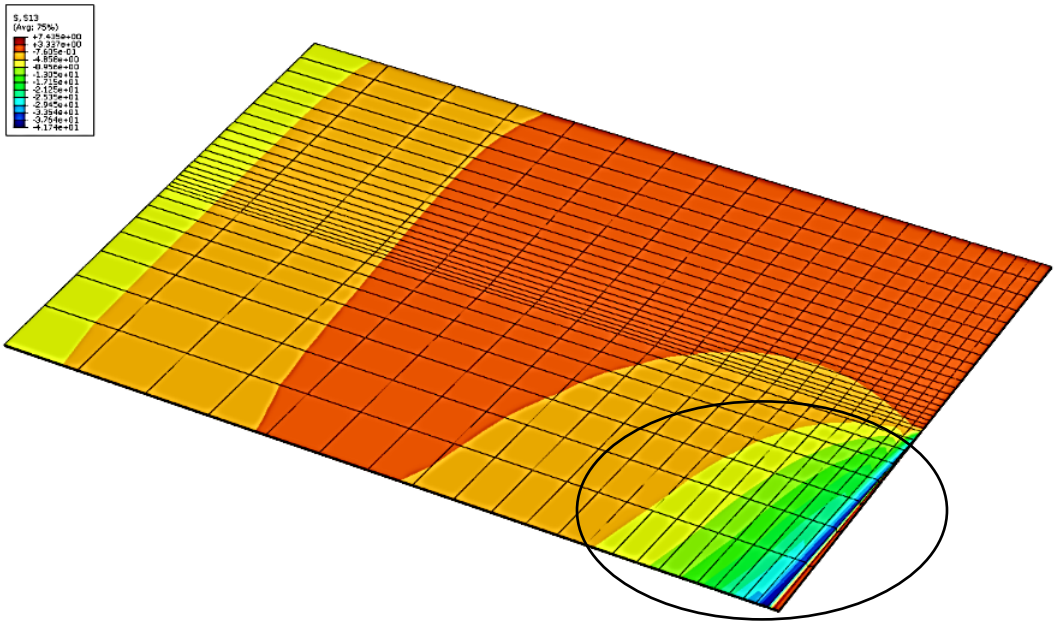

Figure 4.21 Shear stress distribution in adhesive layer in lower adhesive strength FEM with crack 25mm & ETR-0.264

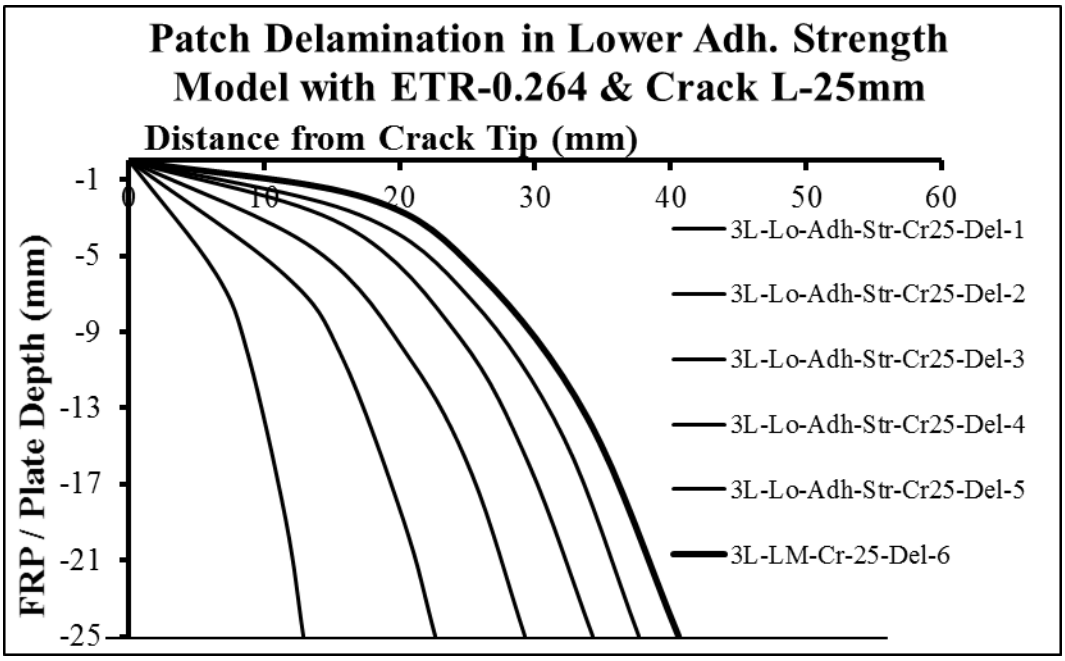

Figure 4.22 Failed adhesive region in lower adhesive strength FEM with crack 25mm & ETR-0.264

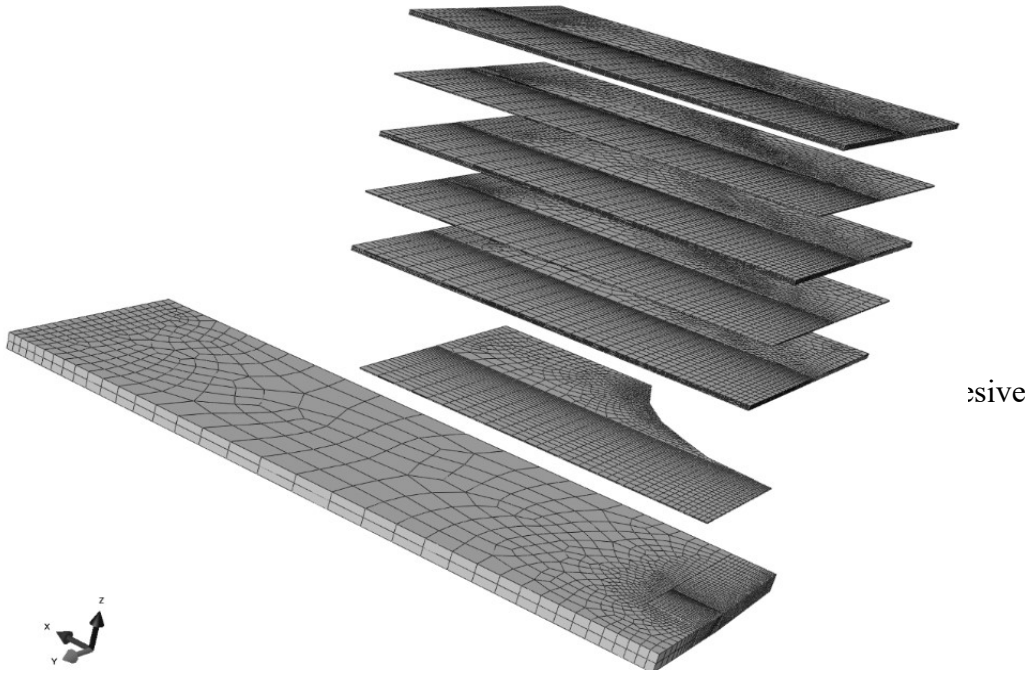

Figure 4.23 Failure incorporated adhesive layer in lower adhesive strength FEM with crack 25mm & ETR-0.264

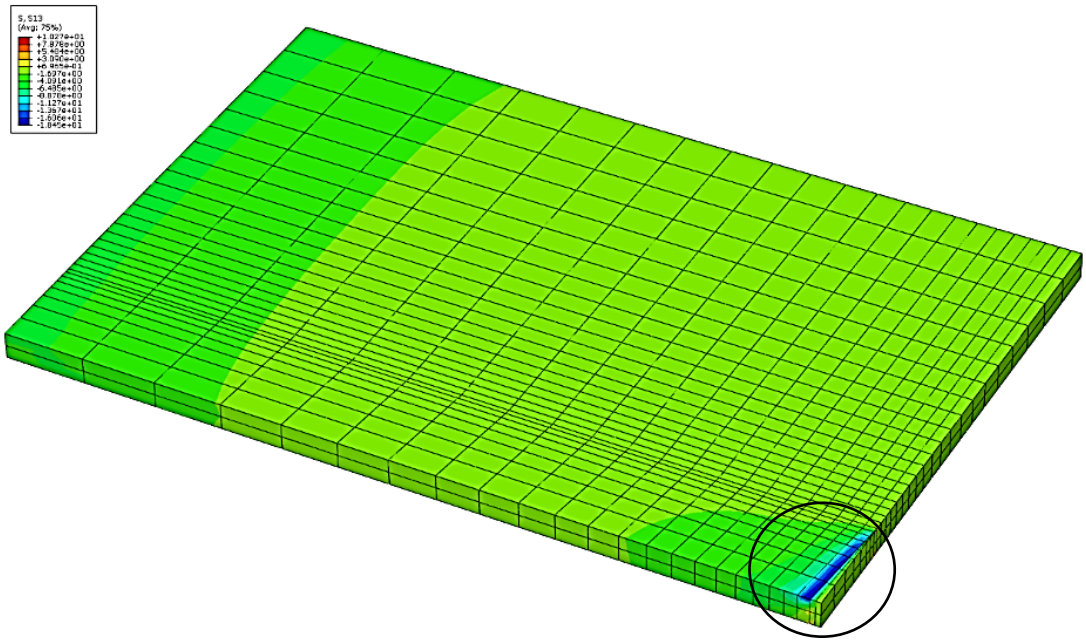

Figure 4.24 Shear stress distribution in adhesive layer in higher adhesive strength FEM with crack 10mm & ETR-0.264

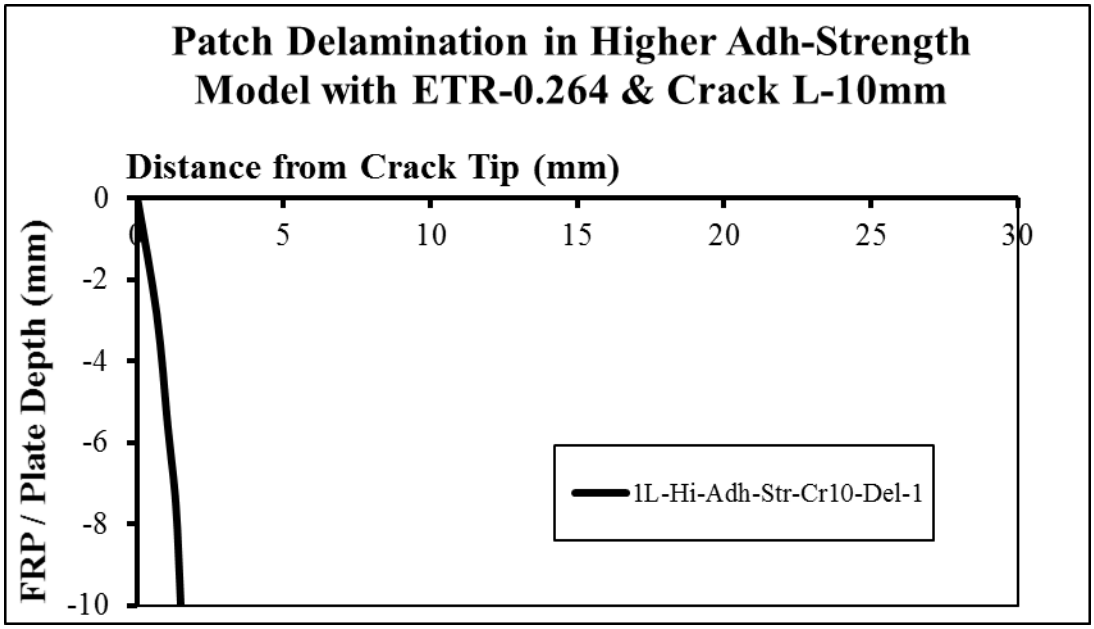

Figure 4.25 Failed adhesive region in higher adhesive strength FEM with crack 10mm & ETR-0.264

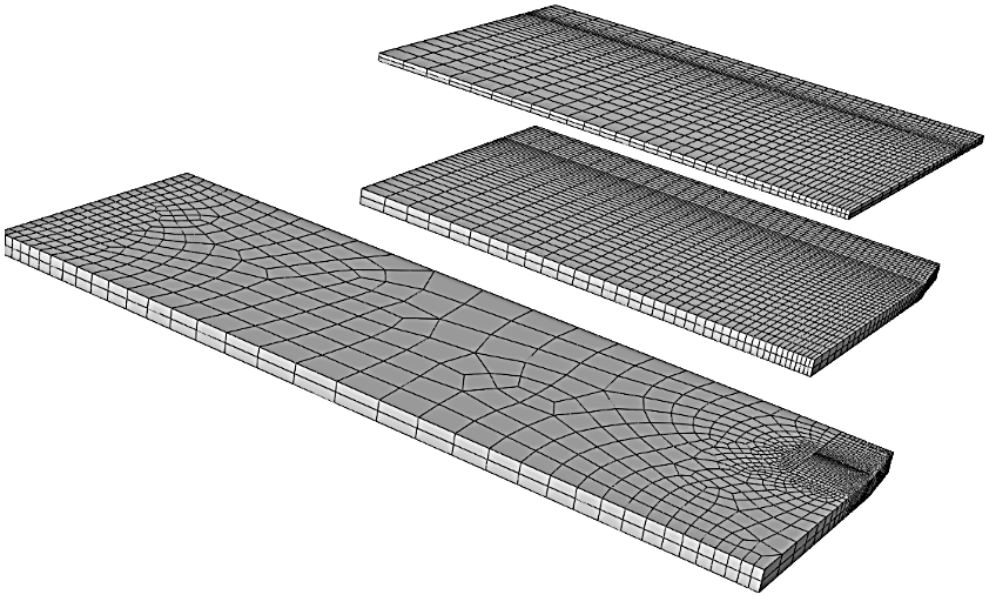

dhesive
ge

Figure 4.26 Failure incorporated adhesive layer in higher adhesive strength FEM with crack 10mm & ETR-0.264

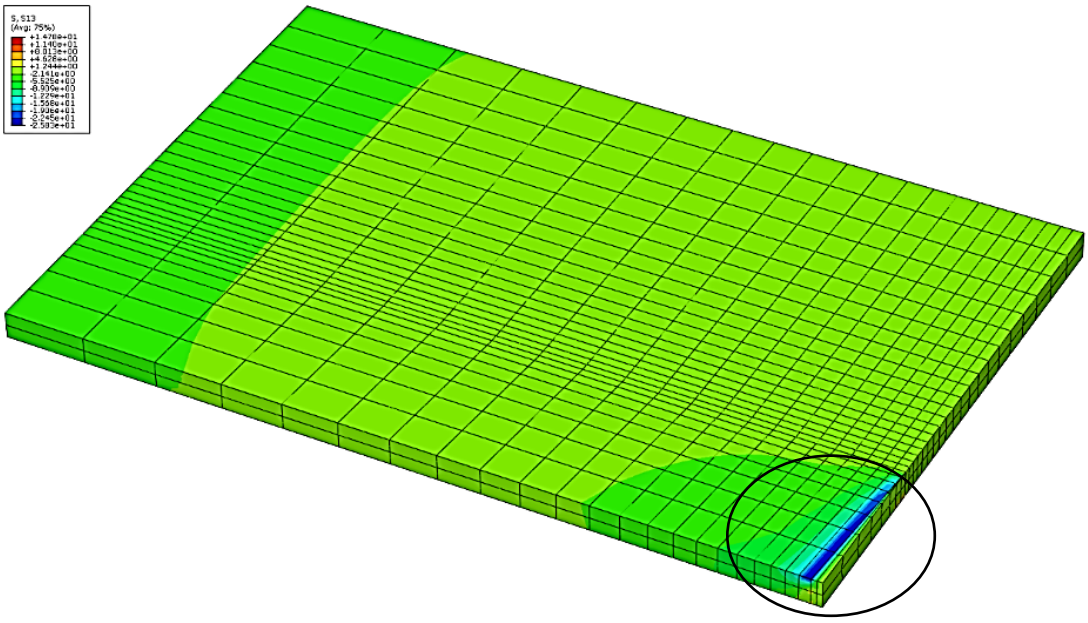

Figure 4.27 Shear stress distribution in adhesive layer in higher adhesive strength FEM with crack 15mm & ETR-0.264

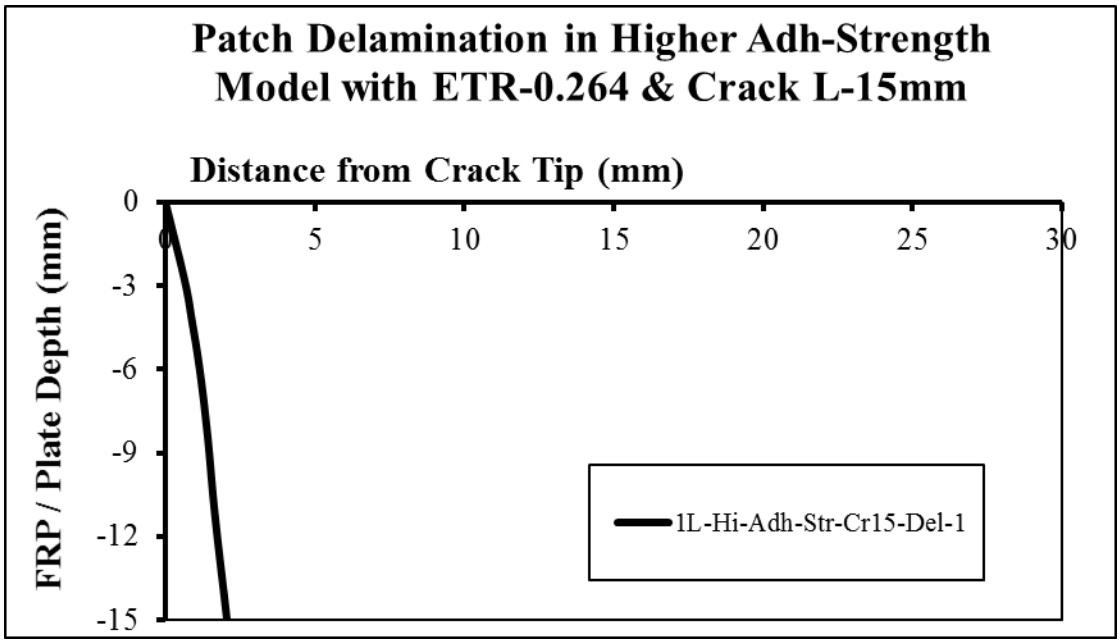

Figure 4.28 Failed adhesive region in higher adhesive strength FEM with crack 15mm & ETR-0.264

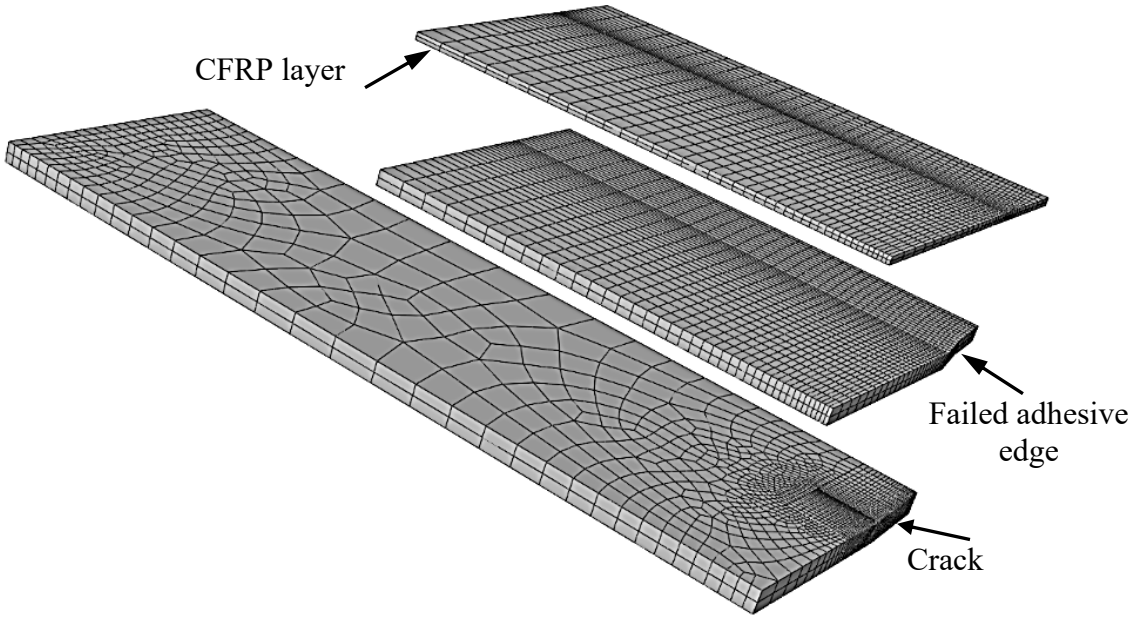

Figure 4.29 Failure incorporated adhesive layer in higher adhesive strength FEM with crack 15mm & ETR-0.264

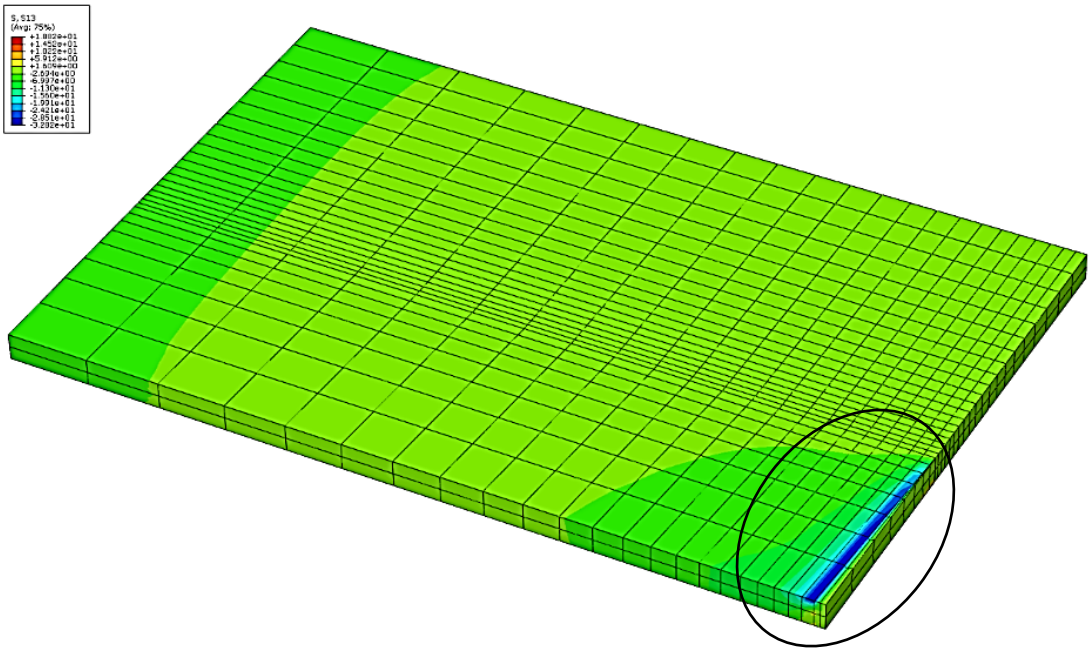

Figure 4.30 Shear stress distribution in adhesive layer in higher adhesive strength FEM with crack 20mm & ETR-0.264

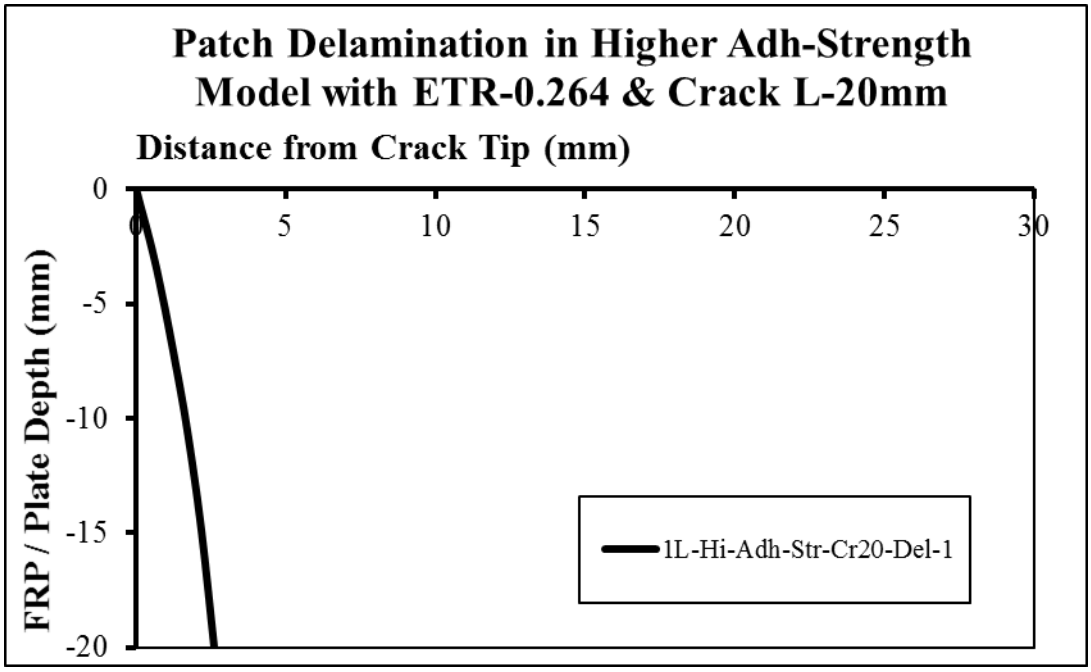

Figure 4.31 Failed adhesive region in higher adhesive strength FEM with crack 20mm & ETR-0.264

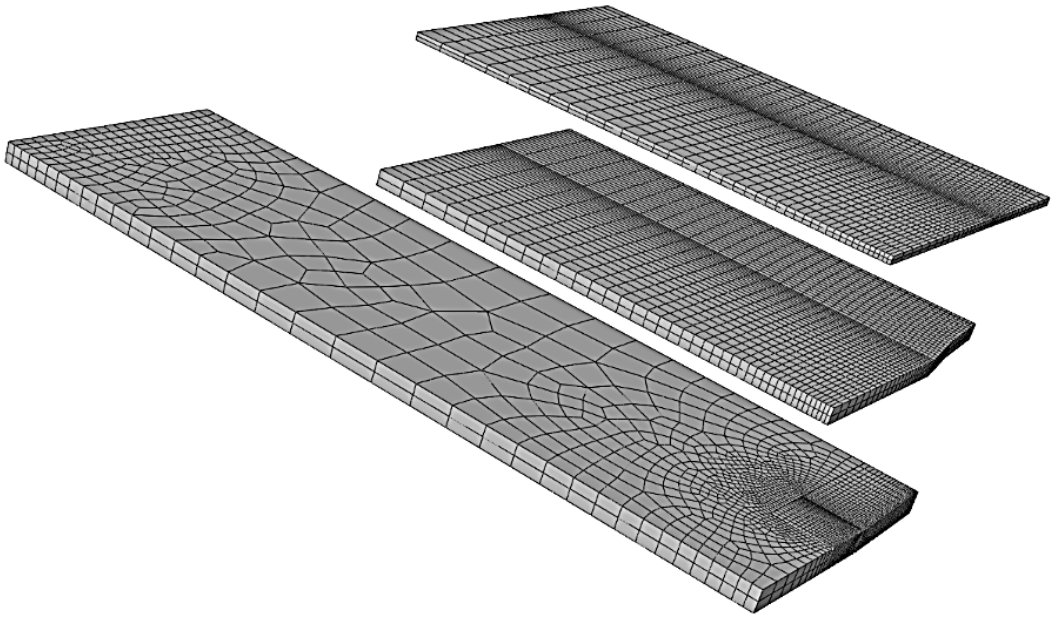

esive

Figure 4.32 Failure incorporated adhesive layer in higher adhesive strength FEM with crack 20mm & ETR-0.264

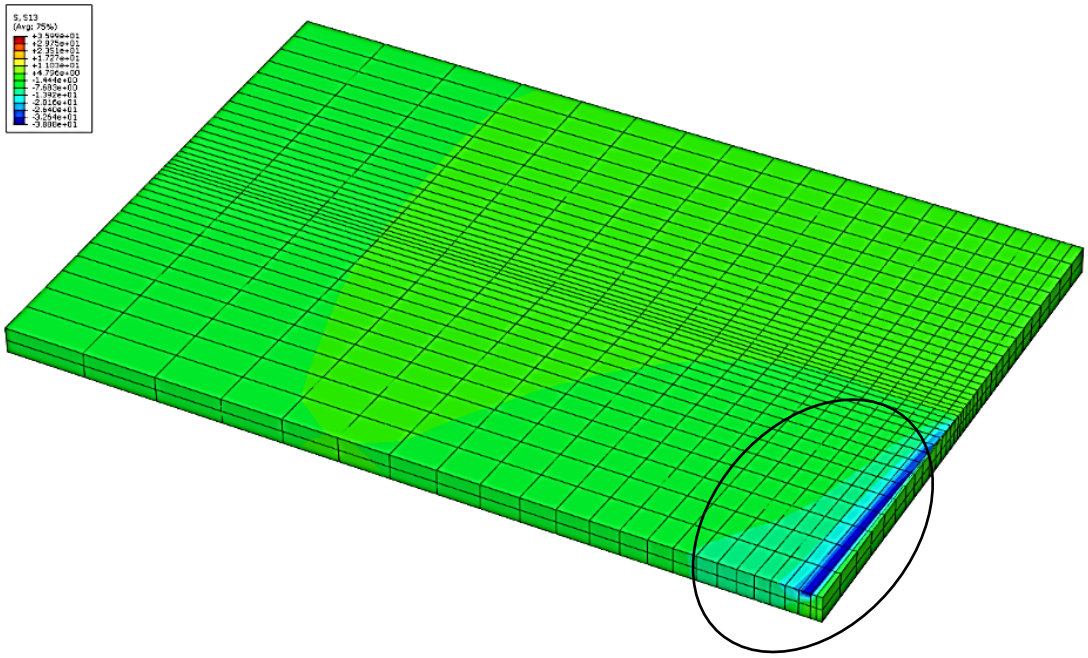

Figure 4.33 Shear stress distribution in adhesive layer in higher adhesive strength FEM with crack 25mm & ETR-0.264

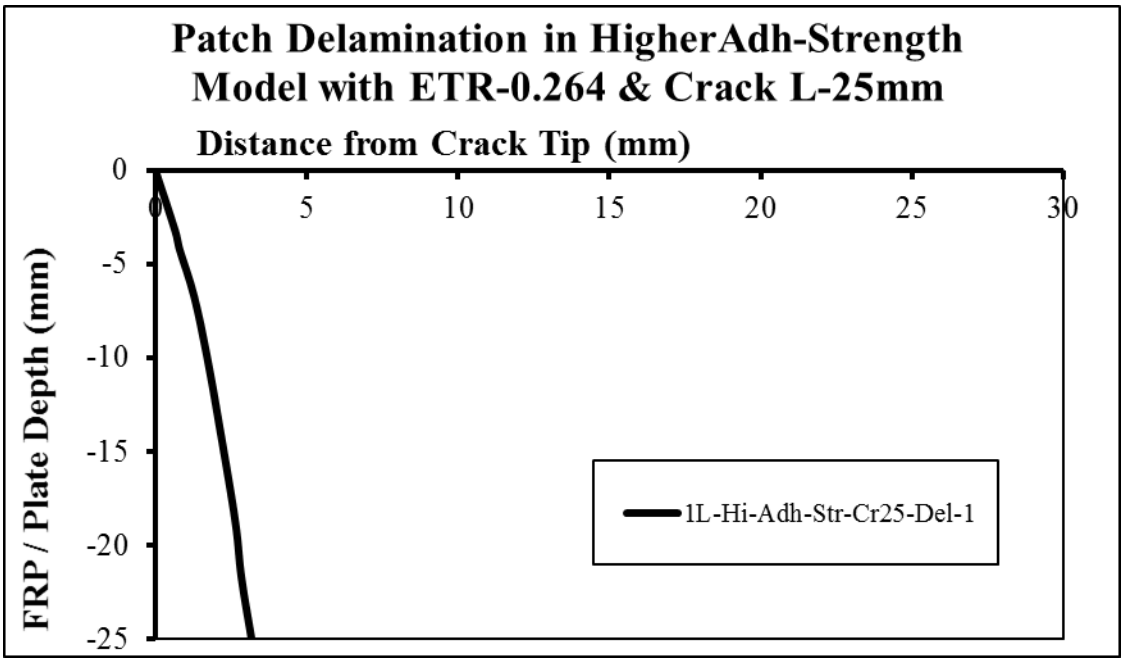

Figure 4.34 Failed adhesive region in higher adhesive strength FEM with crack 25mm & ETR-0.264

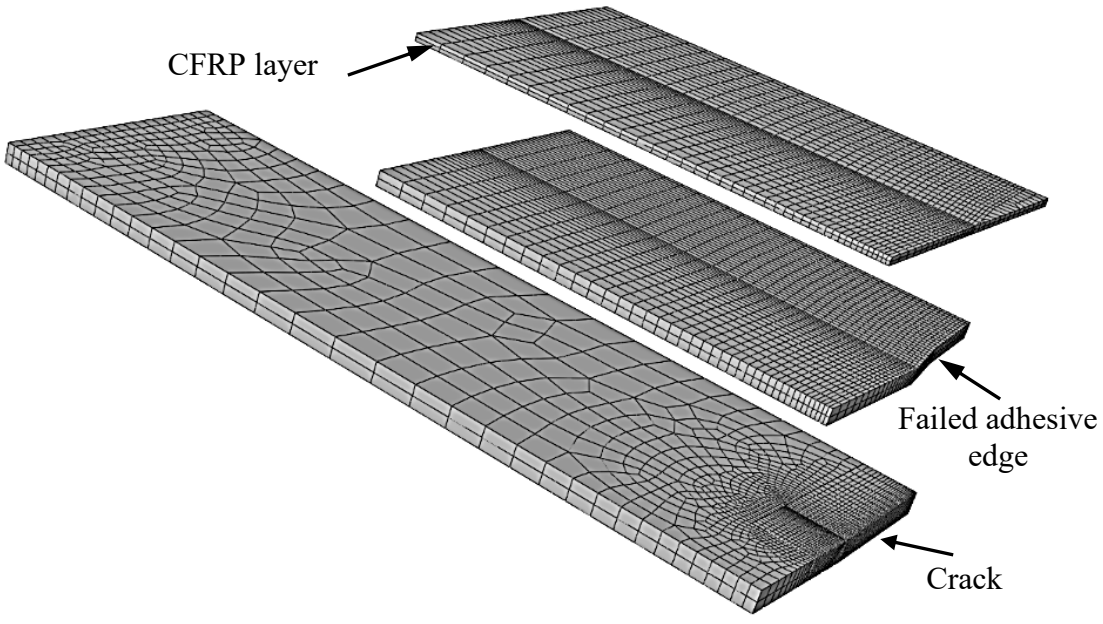

Figure 4.35 Failure incorporated adhesive layer in higher adhesive strength FEM with crack 25mm & ETR-0.264

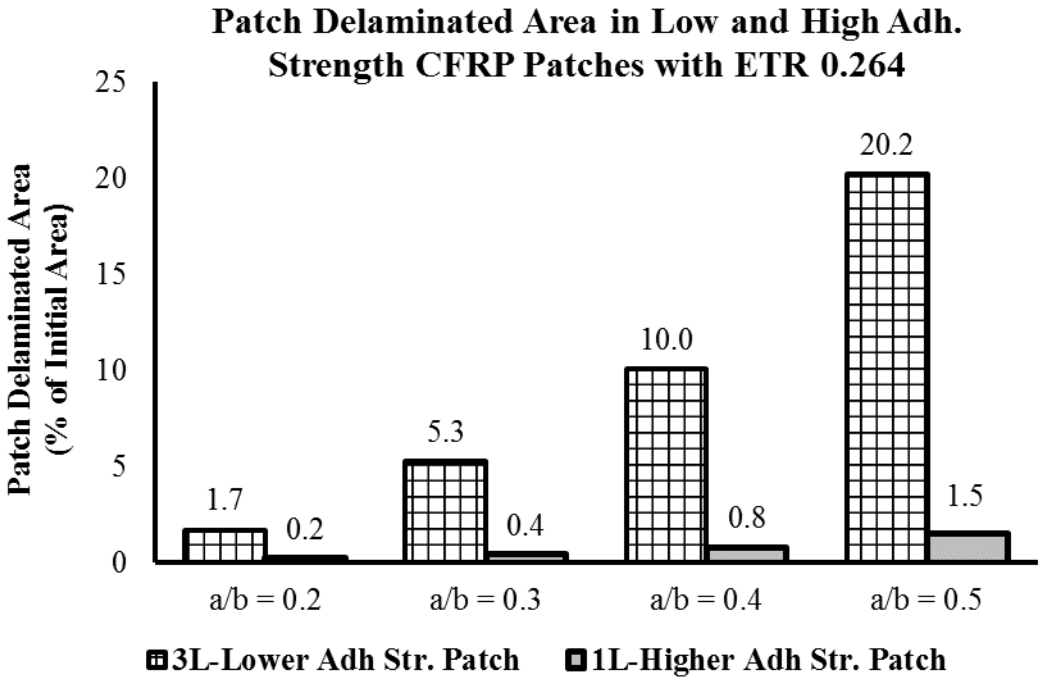

Figure 4.36 Delaminated regions in higher and lower adhesive strength models with ETR-0.264

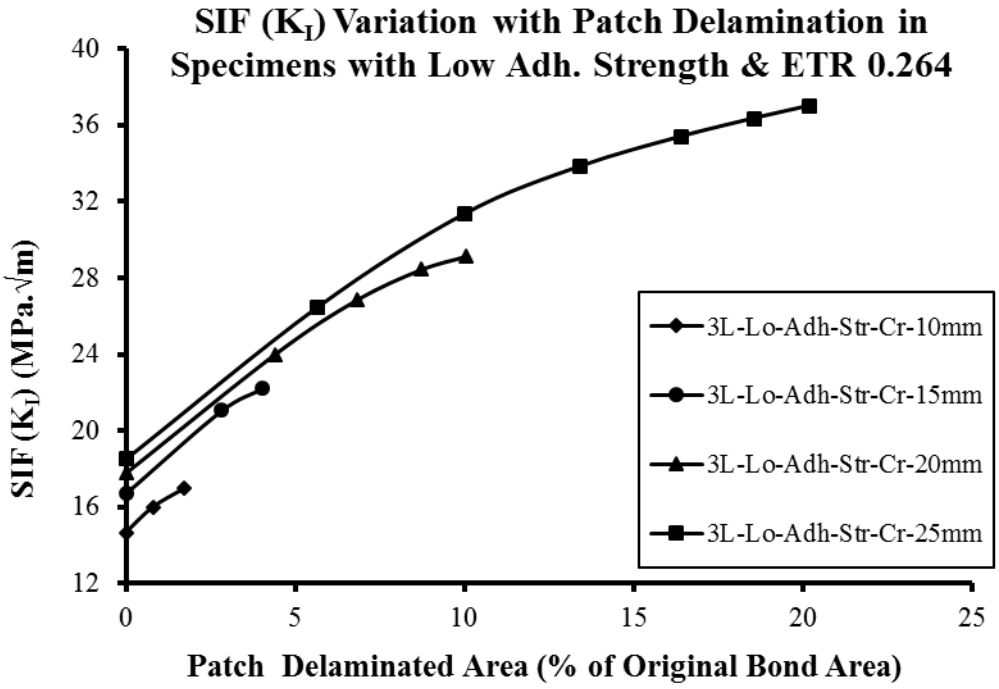

Figure 4.37 SIF (K_I) variations in lower adhesive strength models with ETR-0.264

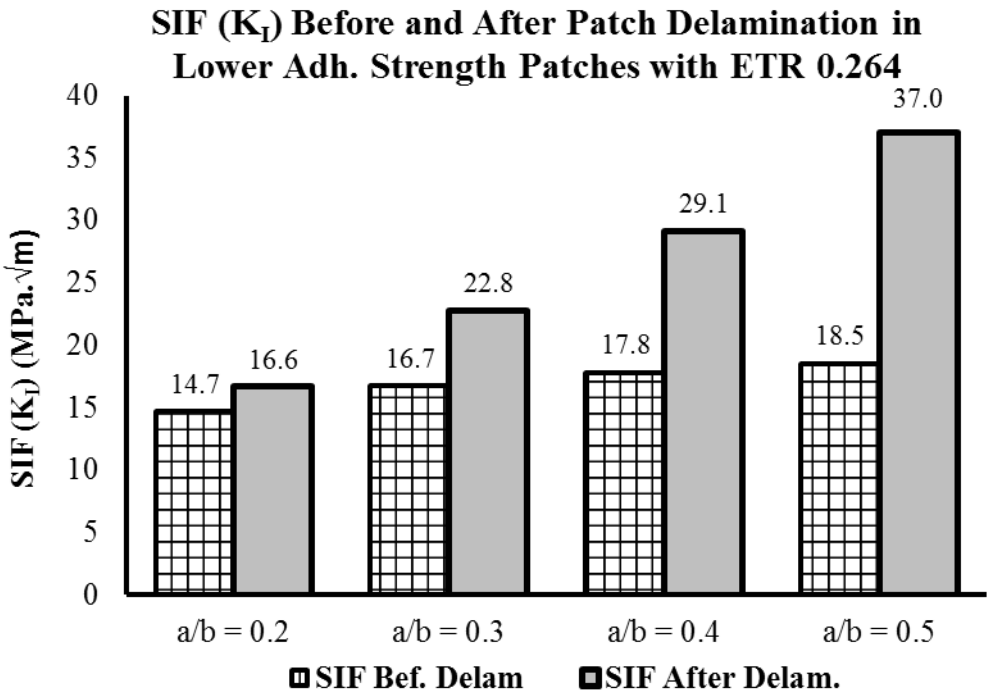

Figure 4.38 Delamination impact on SIF in lower adhesive strength models with ETR-0.264

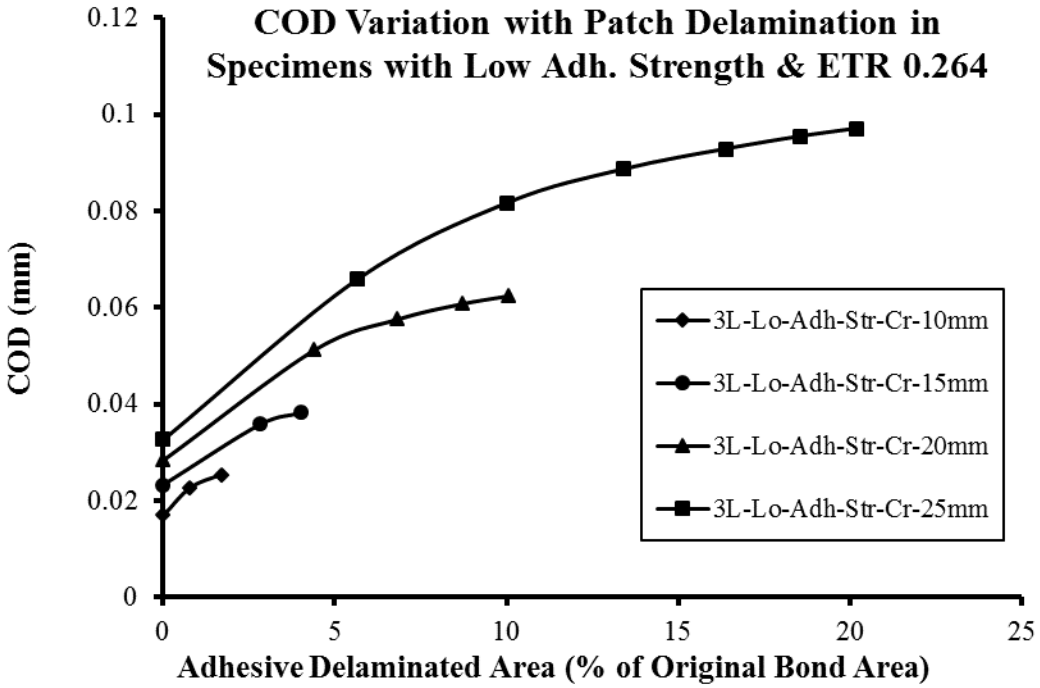

Figure 4.39 COD variation in lower adhesive strength models with ETR-0.264

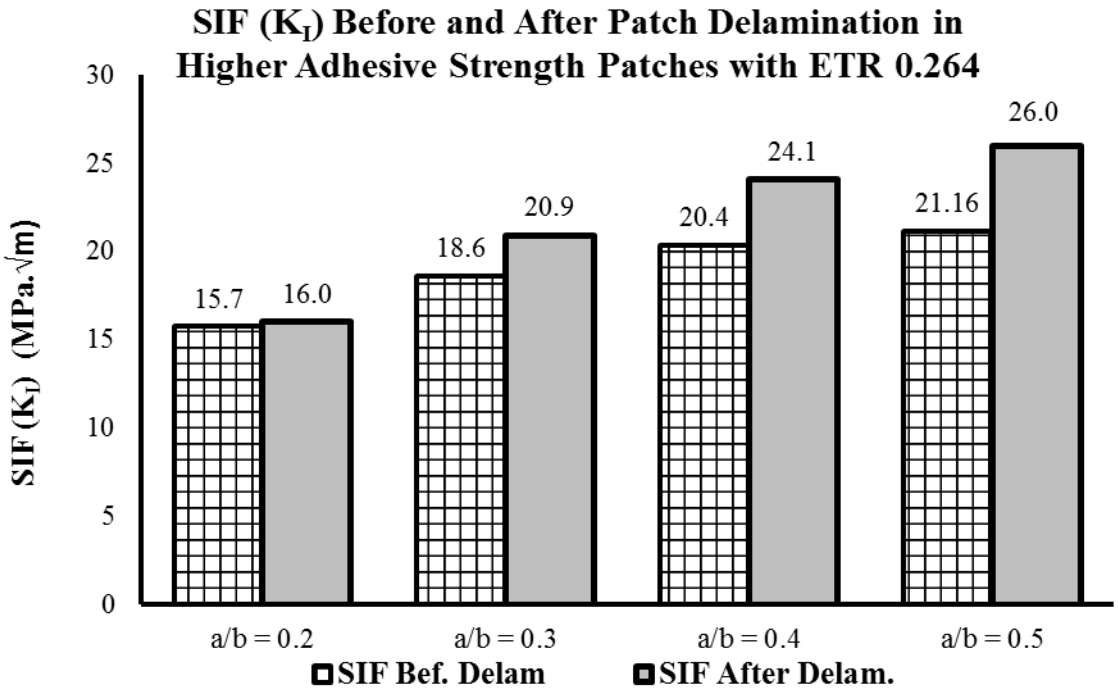

Figure 4.40 Delamination impact on SIF in higher adhesive strength models with ETR-0.264

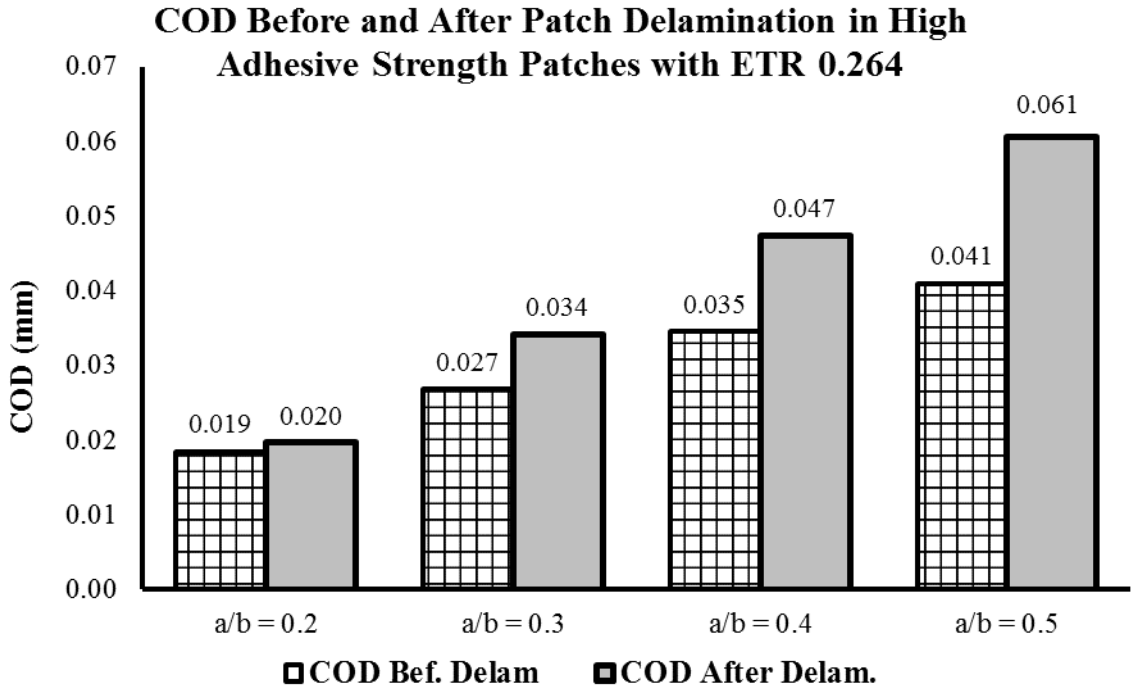

Figure 4.41 Delamination impact on COD in higher adhesive strength models with ETR-0.264

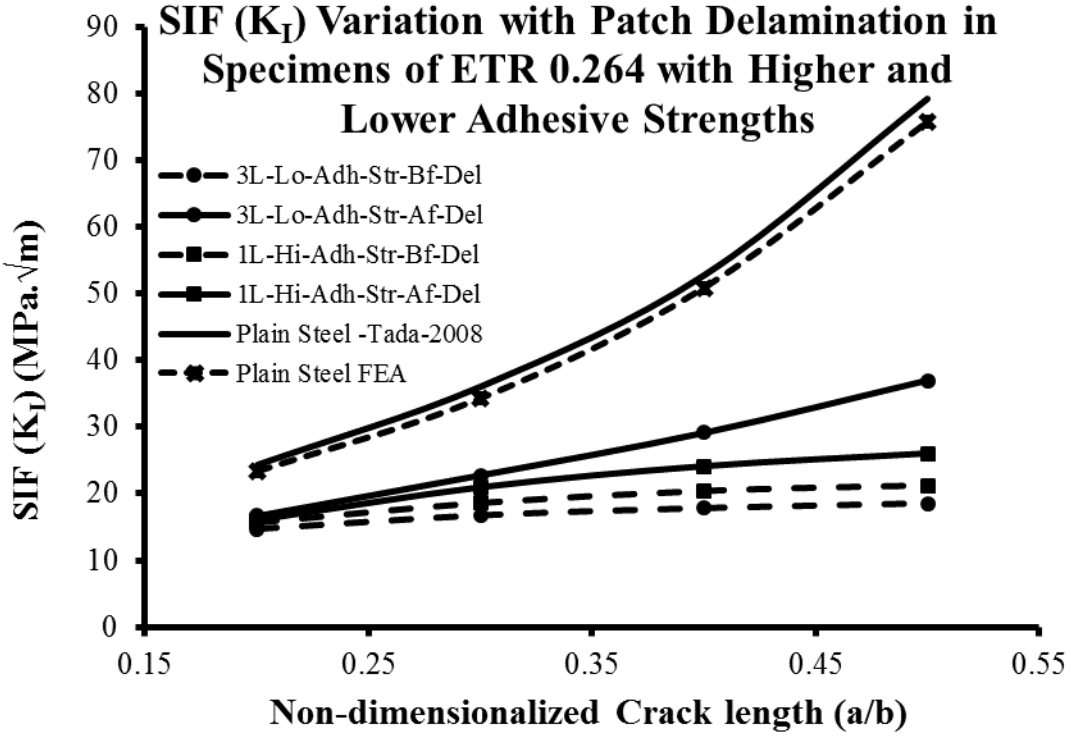

Figure 4.42 Delamination impact on SIF in higher & lower adhesive strength patches with ETR-0.264

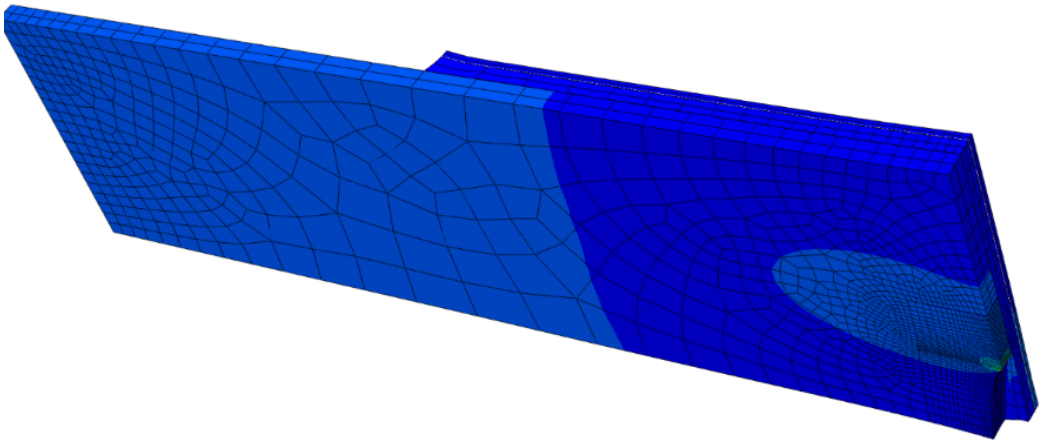

(a)

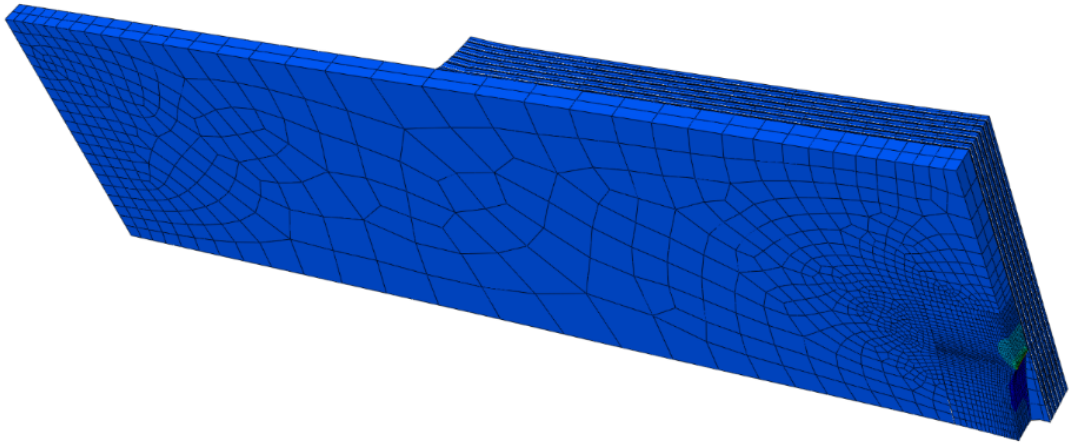

(b)

Figure 4.43 Deformed geometry of finite element models of ETR 0.53 with crack length 15mm and having (a) Higher E_{FRP} CFRP patch (with lower adhesive G/t & higher adhesive strength (b) Lower E_{FRP} CFRP patch (with higher adhesive G/t & lower adhesive strength)

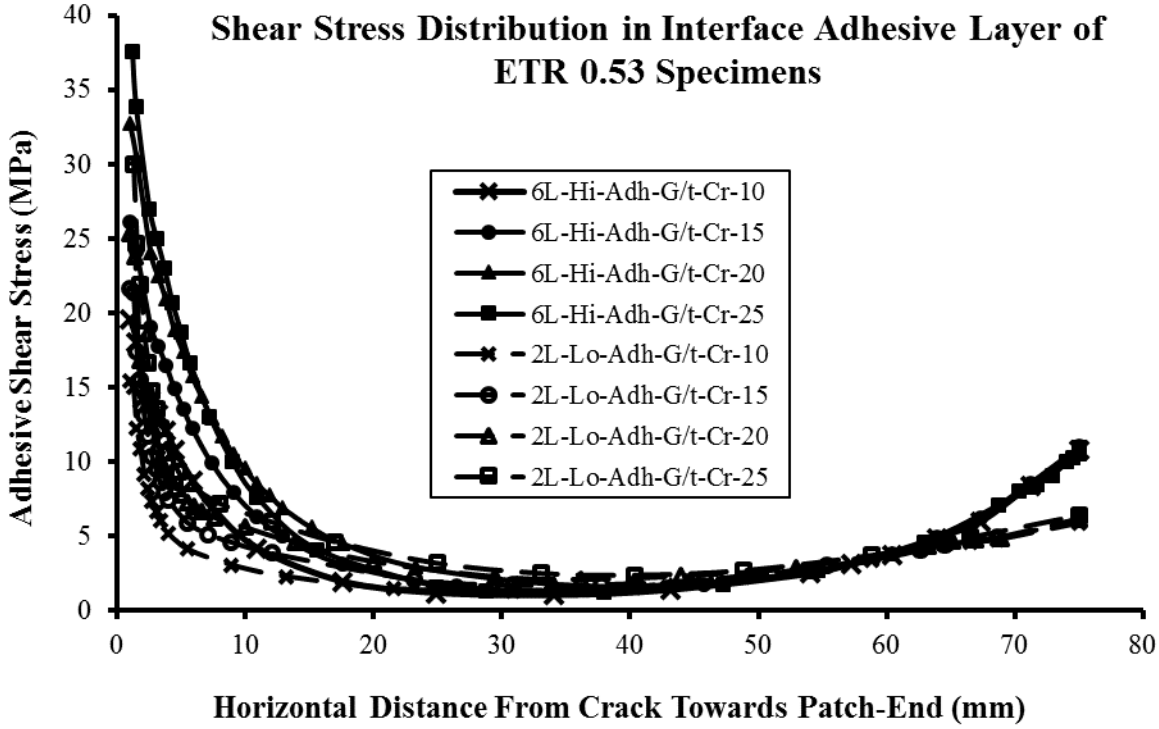

Figure 4.44 Shear Stress distribution in interface adhesive layer of ETR 0.53

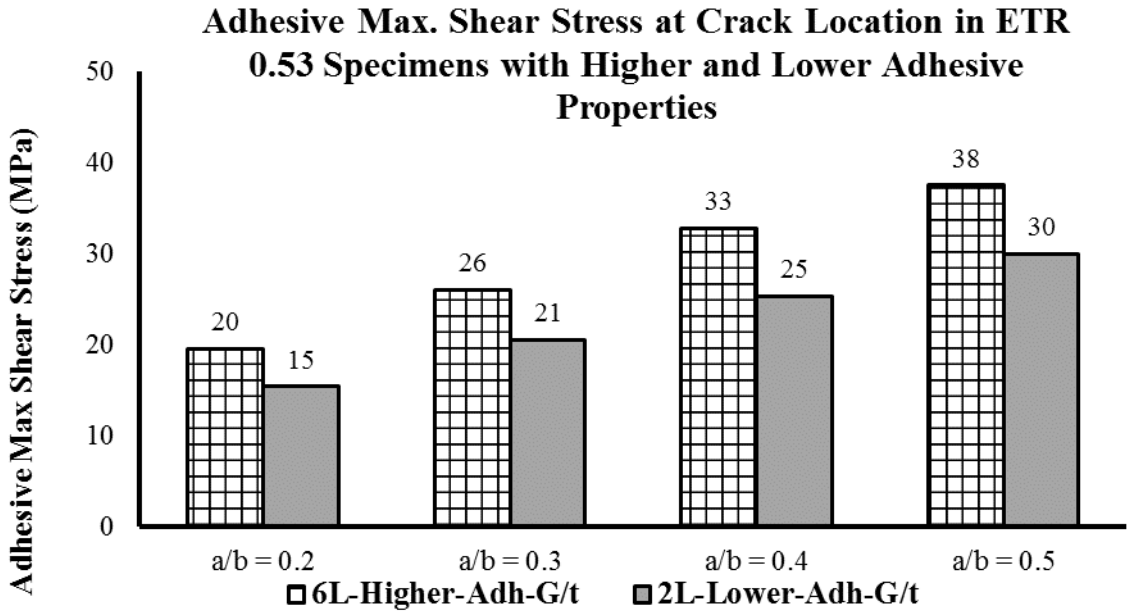

Figure 4.45 Peak adhesive shear stress at crack location in ETR 0.53 models

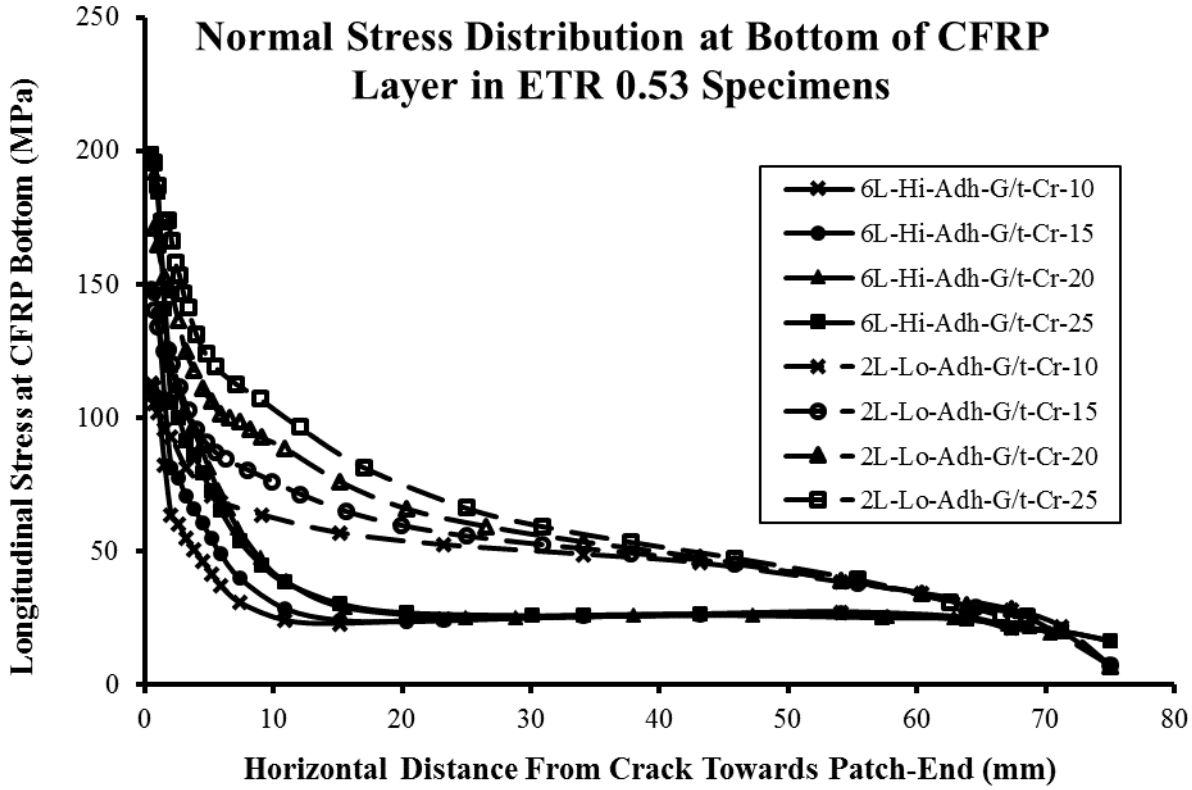

Figure 4.46 Normal stress distribution at CFRP patch bottom in ETR 0.53 models

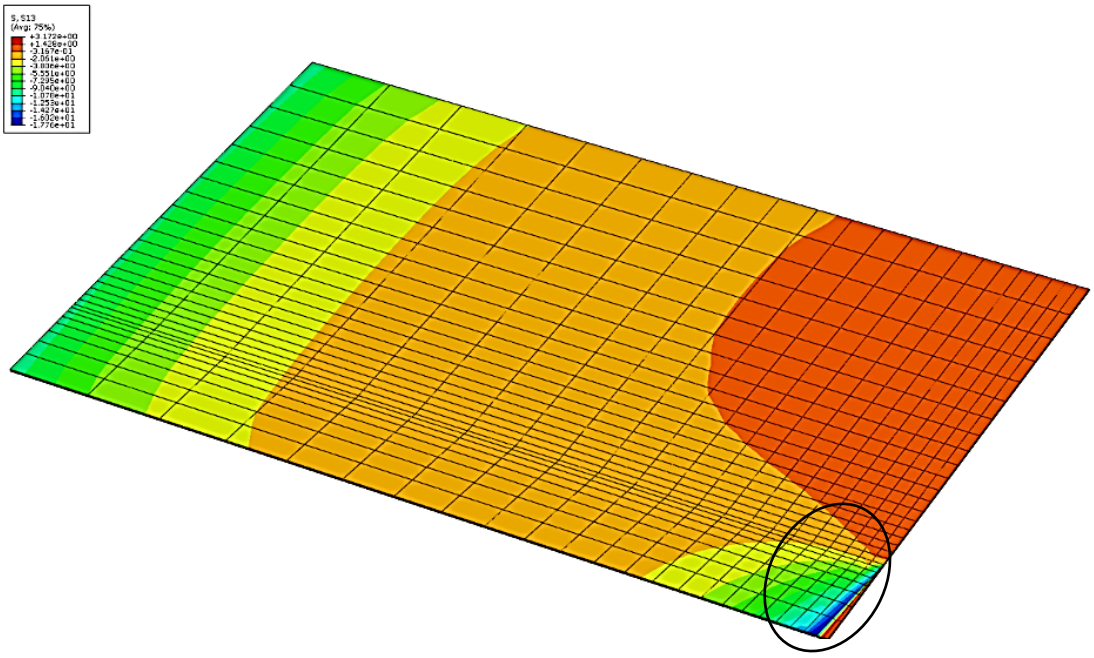

Figure 4.47 Shear stress distribution in adhesive layer of lower adhesive strength FEM with crack 10mm & ETR-0.53

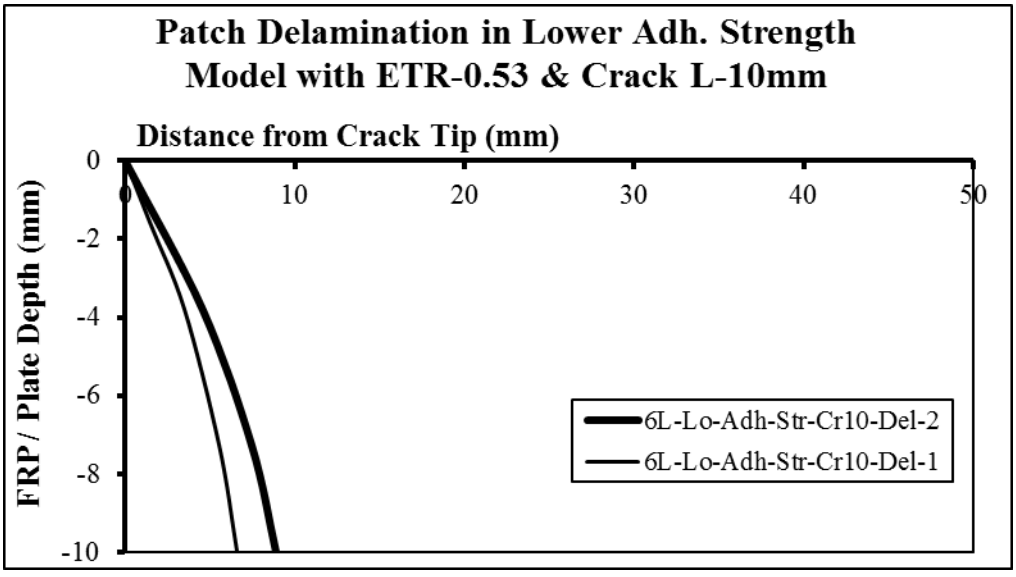

Figure 4.48 Failed adhesive region in lower adhesive strength FEM with crack 10mm & ETR-0.53

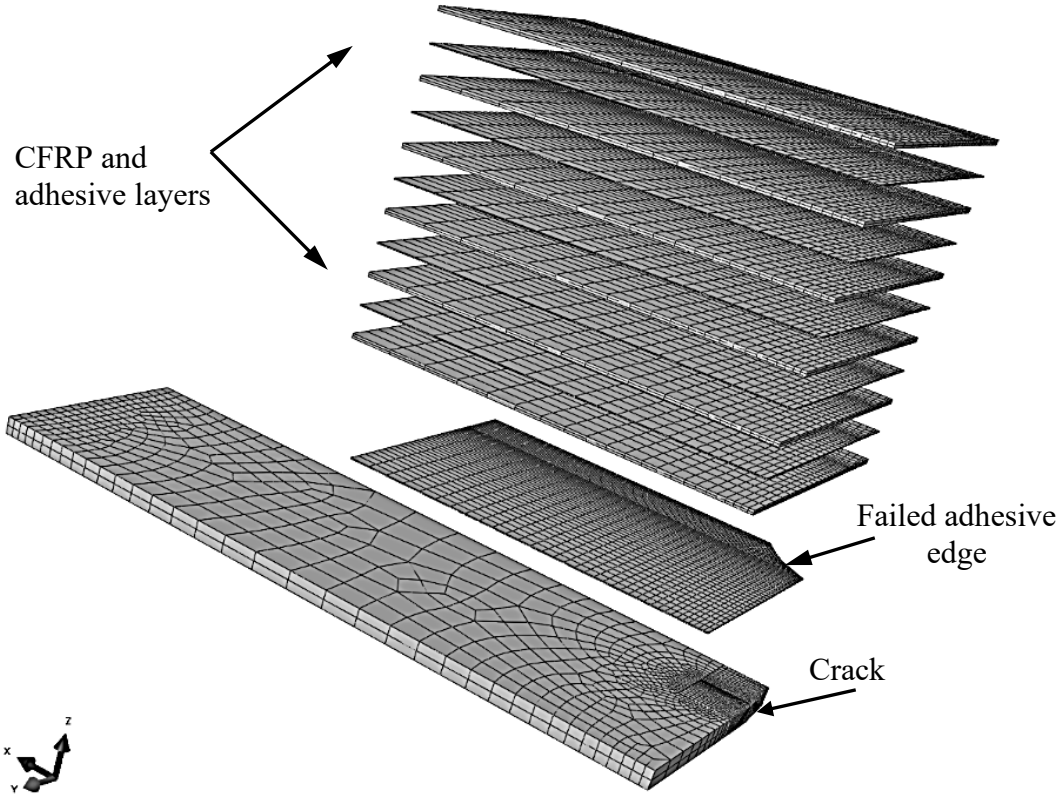

Figure 4.49 Failure incorporated adhesive layer in lower adhesive strength FEM with crack 10mm & ETR-0.53

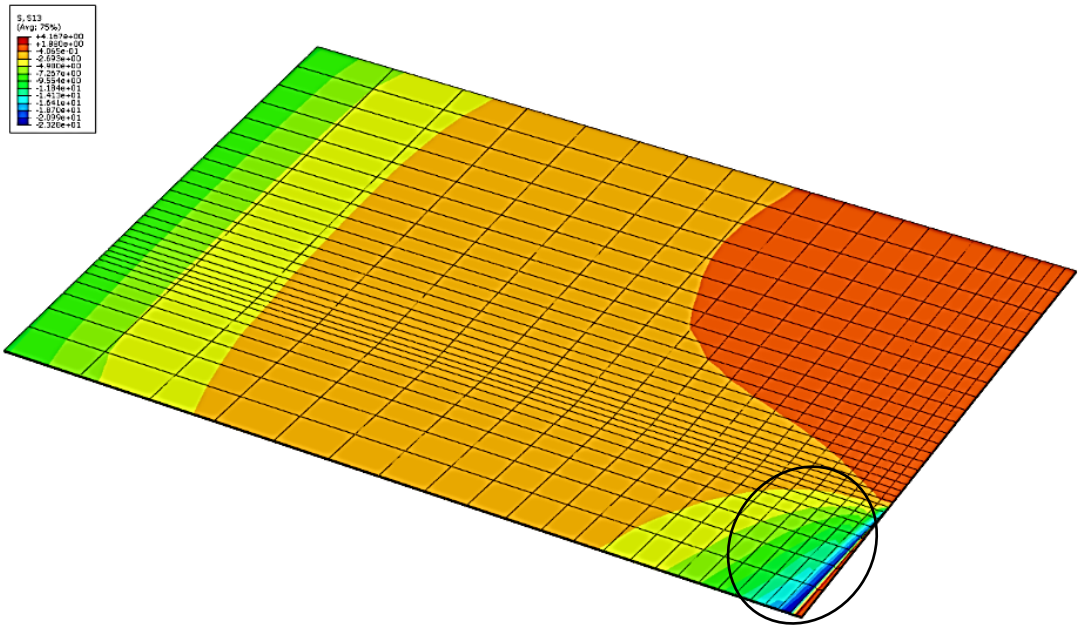

Figure 4.50 Shear stress distribution in adhesive layer of lower adhesive strength FEM with crack 15mm & ETR-0.53

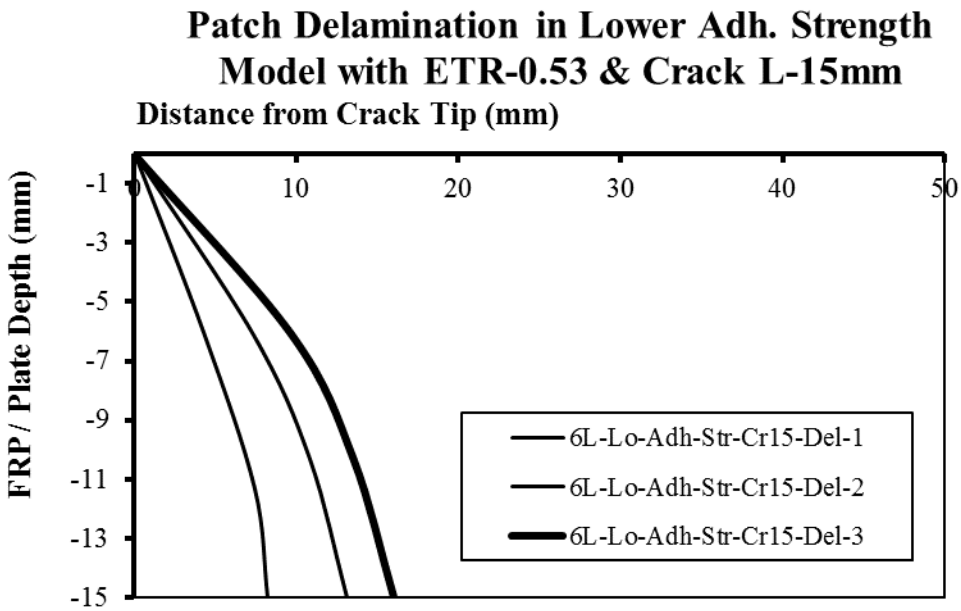

Figure 4.51 Failed adhesive region in lower adhesive strength FEM with crack 15mm & ETR-0.53

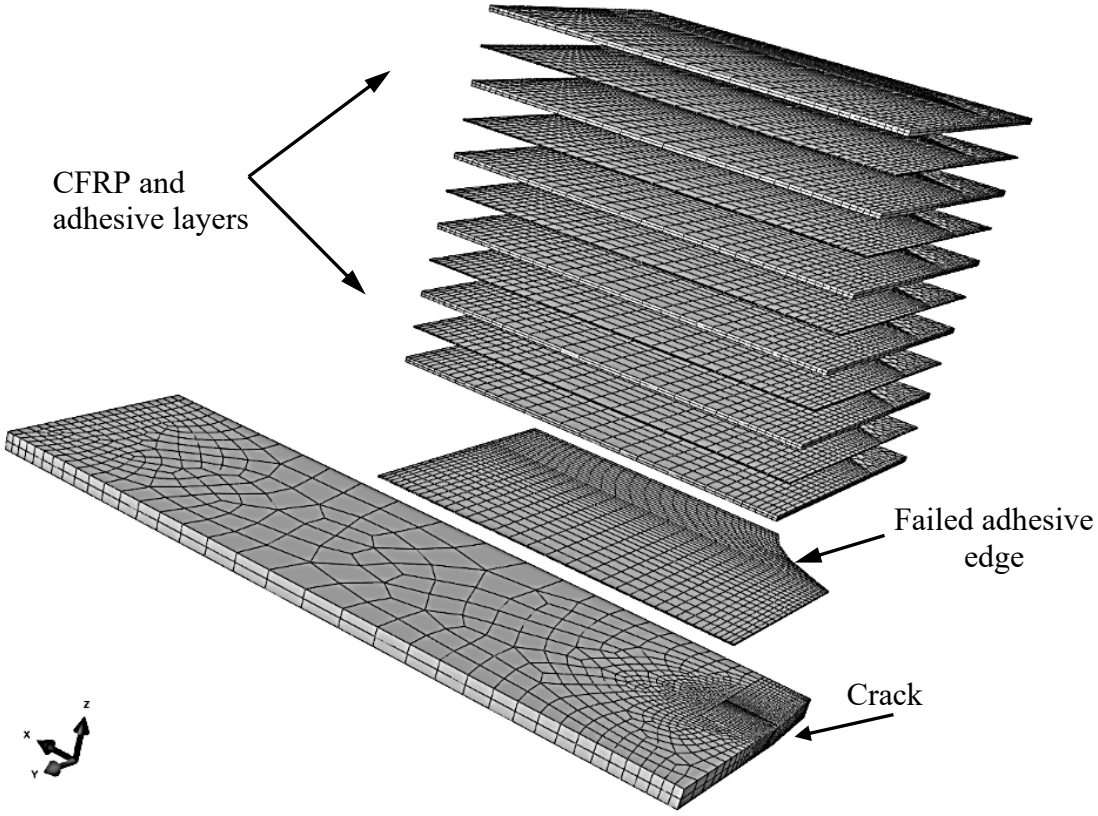

Figure 4.52 Failure incorporated adhesive layer in lower adhesive strength FEM with crack 15mm & ETR-0.53

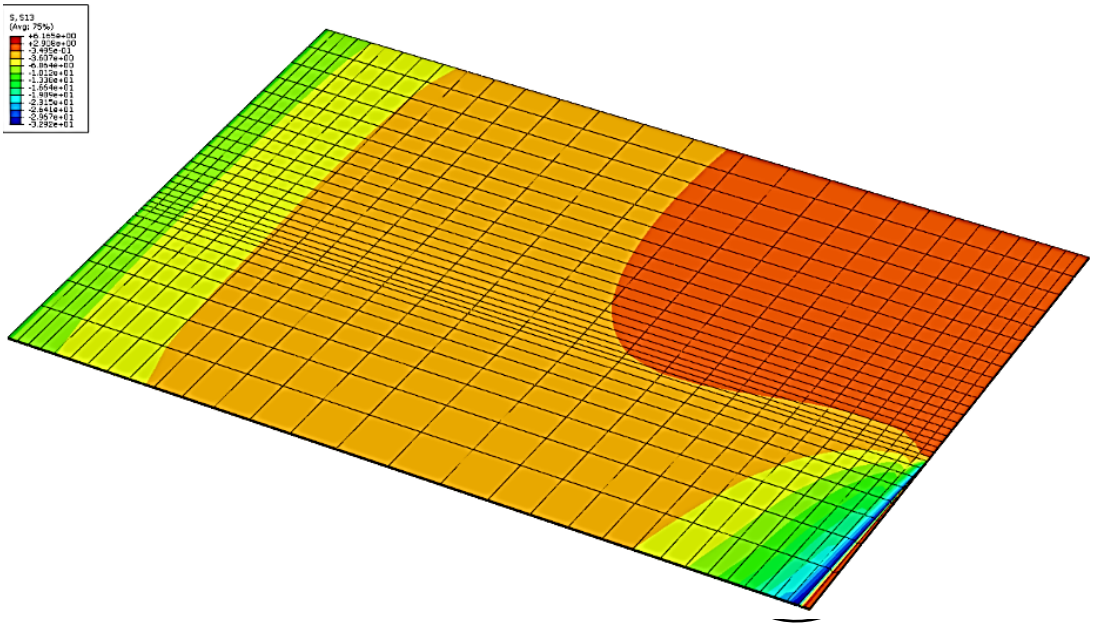

Figure 4.53 Shear stress distribution in adhesive layer of lower adhesive strength FEM with crack 20mm & ETR-0.53

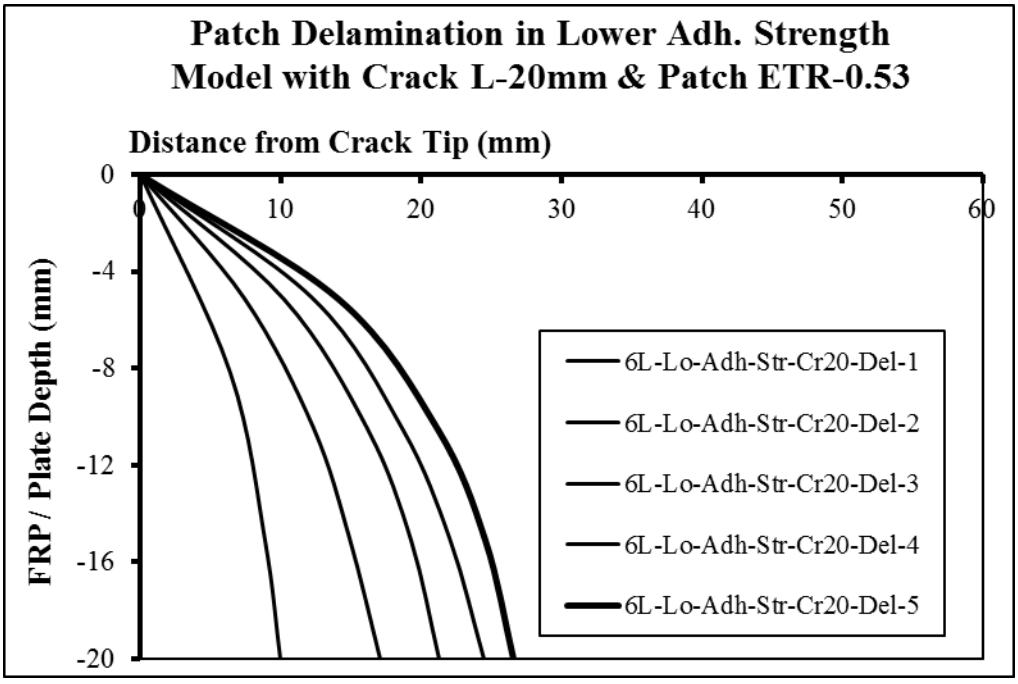

Figure 4.54 Failed adhesive region in lower adhesive strength FEM with crack 20mm & ETR-0.53

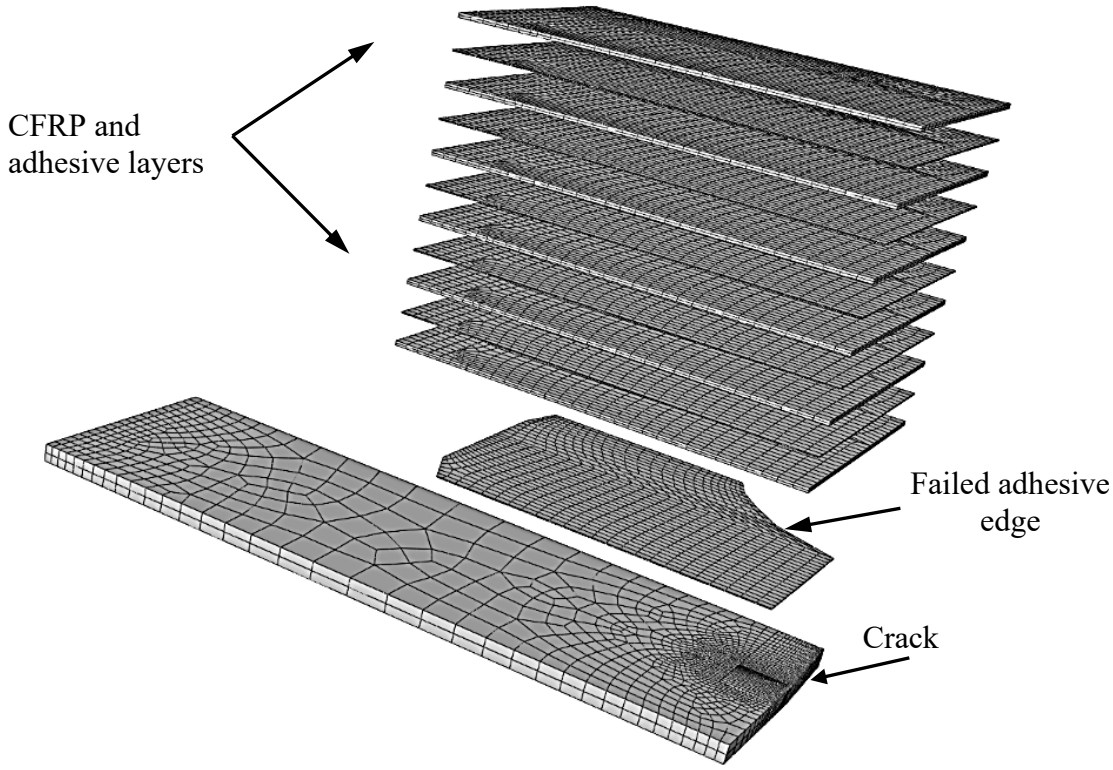

Figure 4.55 Failure incorporated adhesive layer in lower adhesive strength FEM with crack 20mm & ETR-0.53

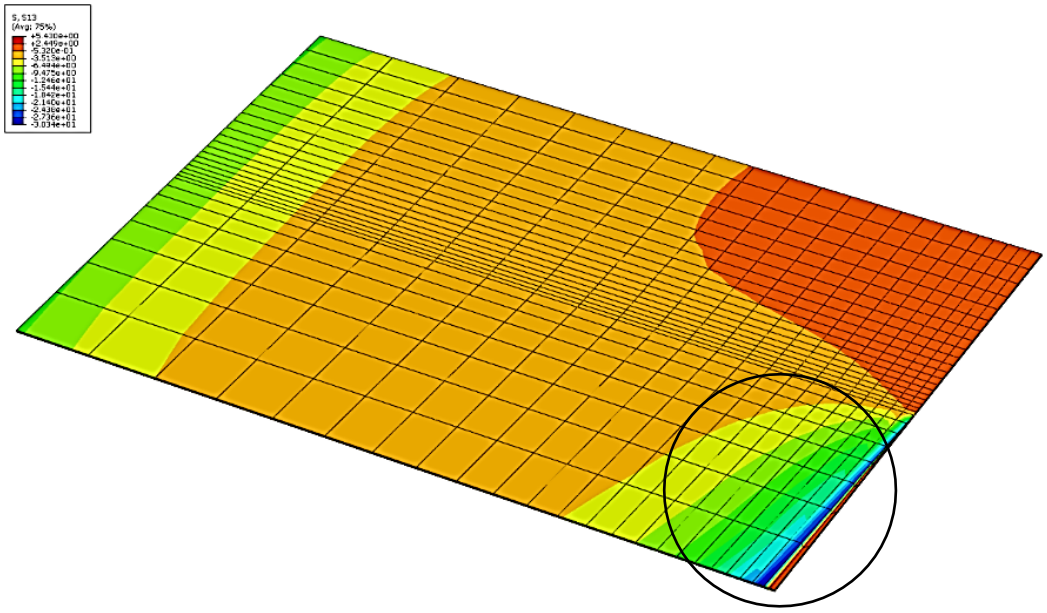

Figure 4.56 Shear stress distribution in adhesive layer of lower adhesive strength FEM with crack 25mm & ETR-0.53

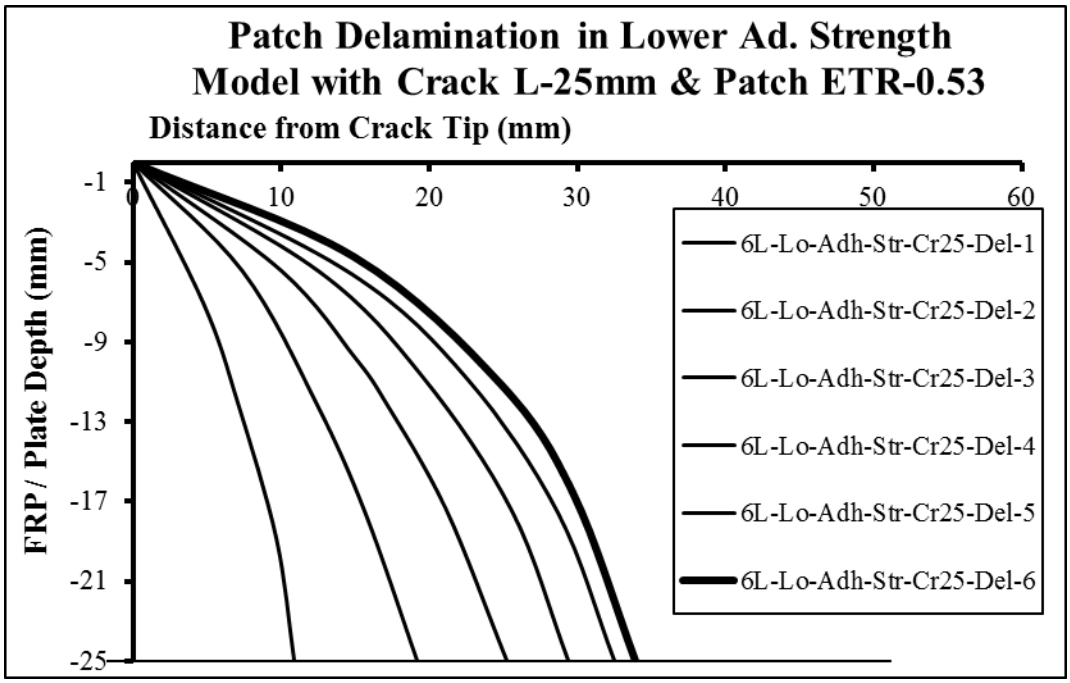

Figure 4.57 Failed adhesive region in lower adhesive strength FEM with crack 25mm & ETR-0.53

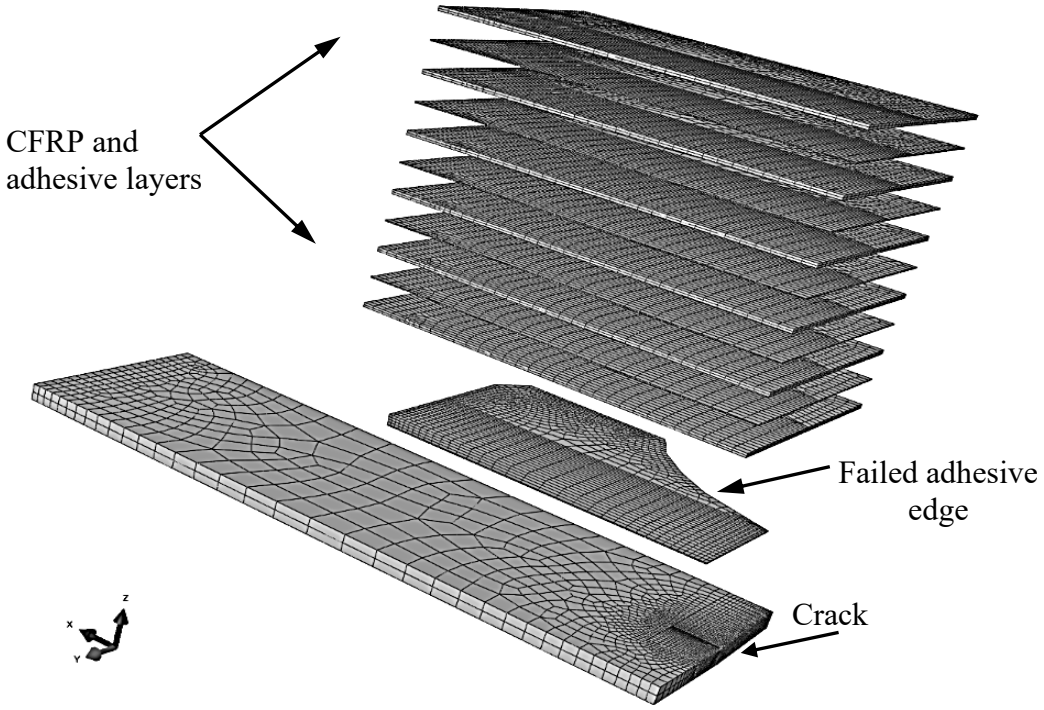

Figure 4.58 Failure incorporated adhesive layer in lower adhesive strength FEM with crack 25mm & ETR-0.53

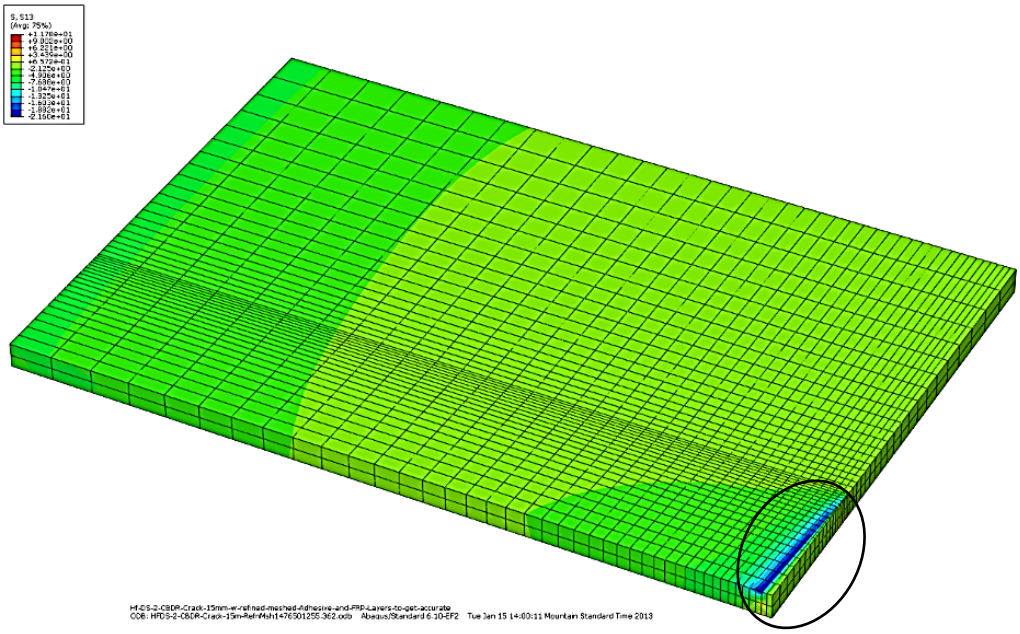

Figure 4.59 Shear stress distribution in adhesive layer of higher adhesive strength FEM with crack 15mm & ETR-0.53

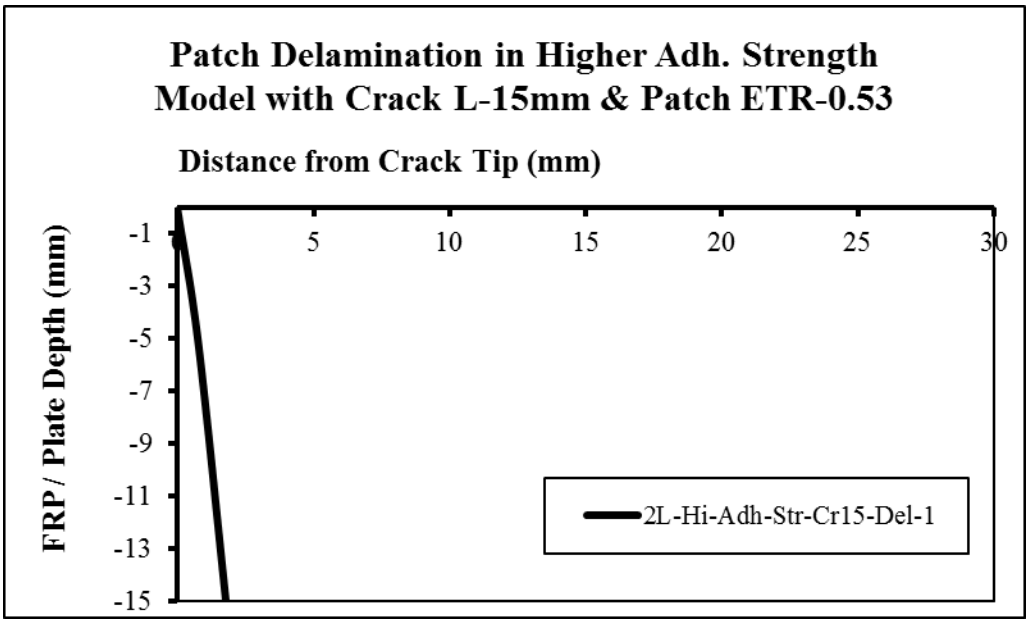

Figure 4.60 Failed adhesive region in higher adhesive strength FEM with crack 15mm & ETR-0.53

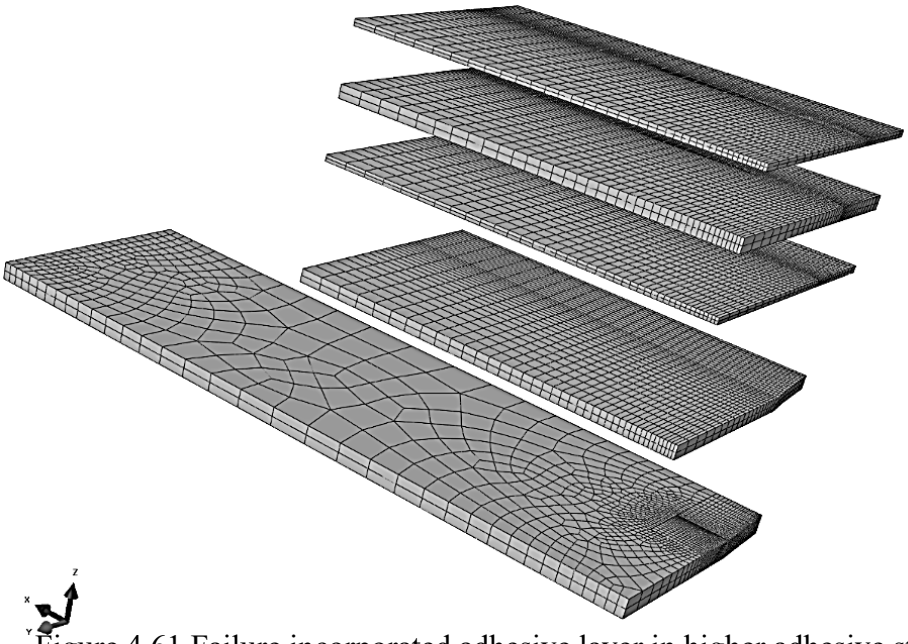

ed adhesive
edge

Figure 4.61 Failure incorporated adhesive layer in higher adhesive strength FEM with crack 15mm & ETR-0.53

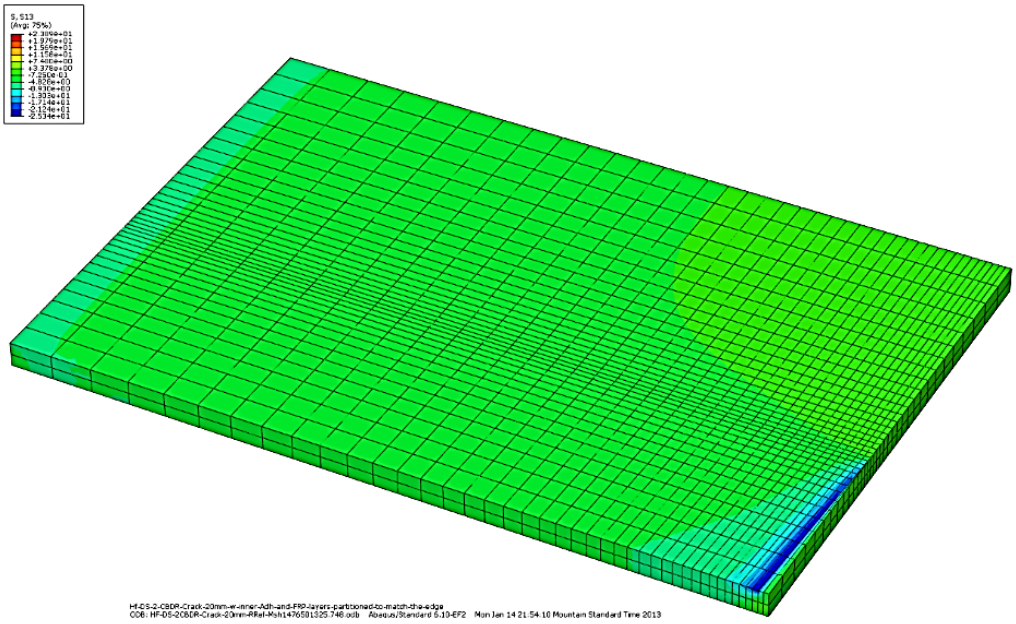

Figure 4.62 Shear stress distribution in adhesive layer of higher adhesive strength FEM with crack 20mm & ETR-0.53

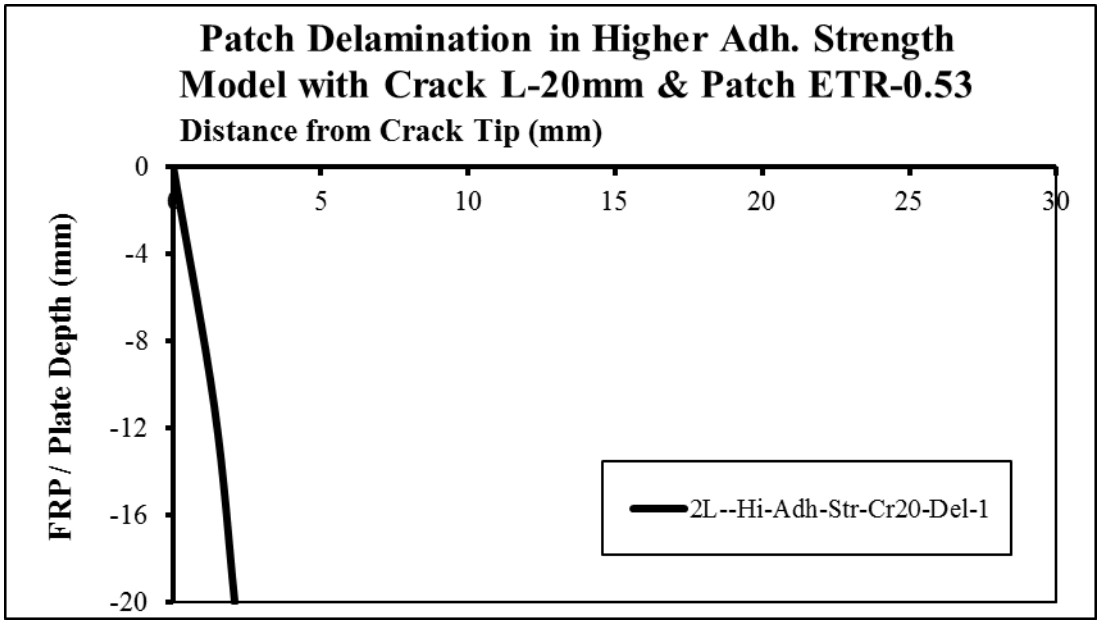

Figure 4.63 Failed adhesive region in higher adhesive strength FEM with crack 20mm & ETR-0.53

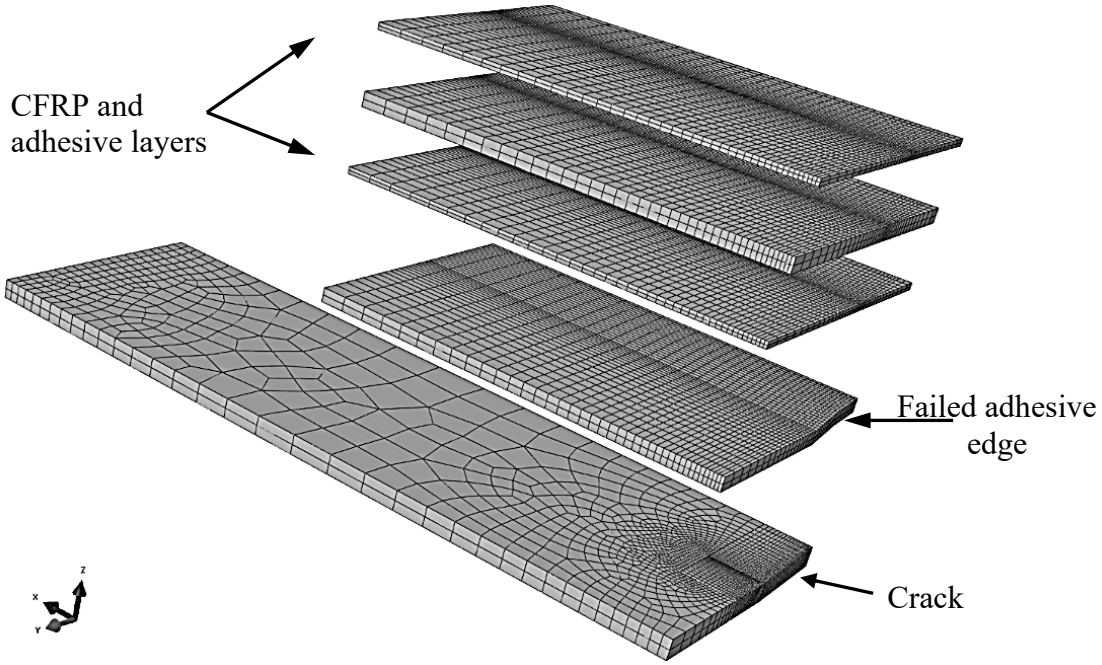

Figure 4.64 Failure incorporated adhesive layer in higher adhesive strength FEM with crack 20mm & ETR-0.53

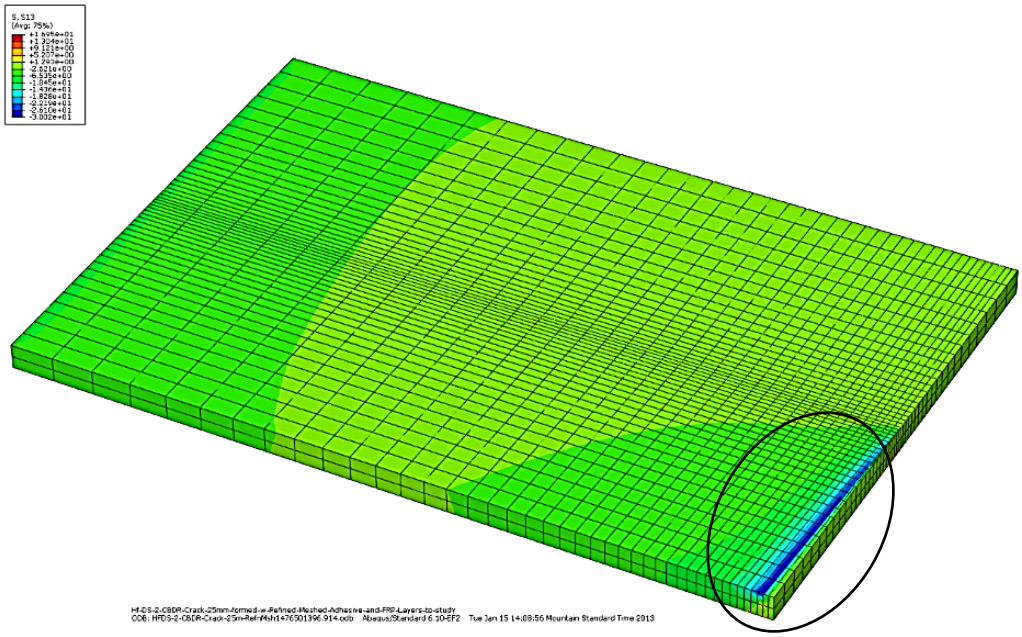

Figure 4.65 Shear stress distribution in adhesive layer of higher adhesive strength FEM with crack 25mm & ETR-0.53

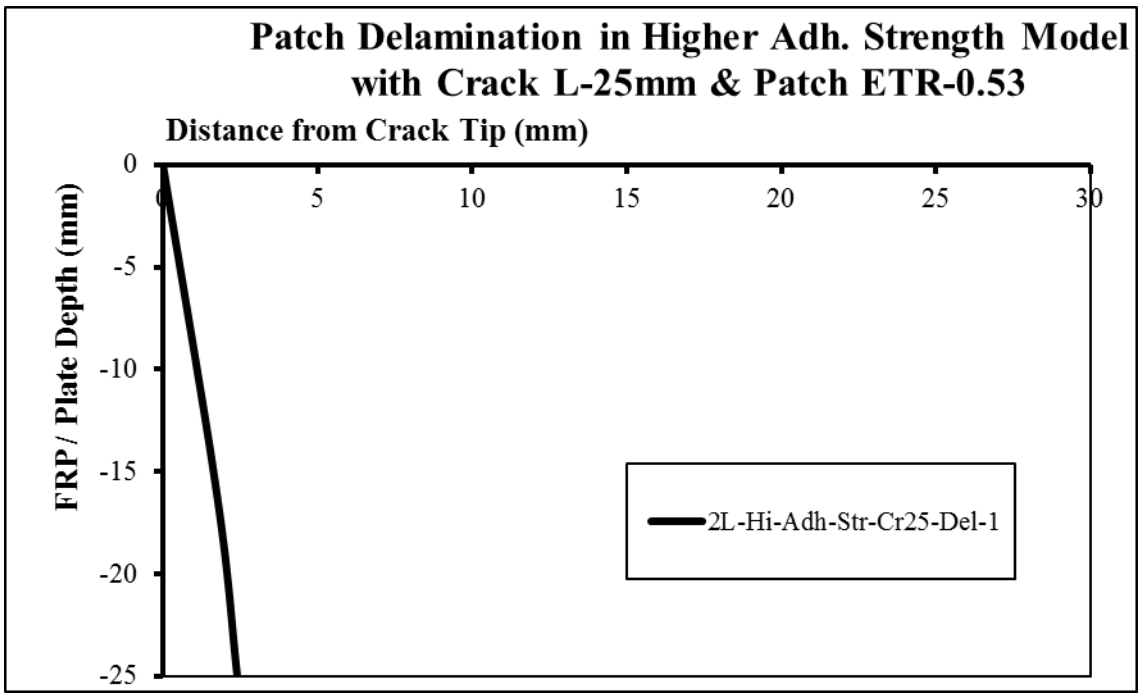

Figure 4.66 Failed adhesive region in higher adhesive strength FEM with crack 25mm & ETR-0.53

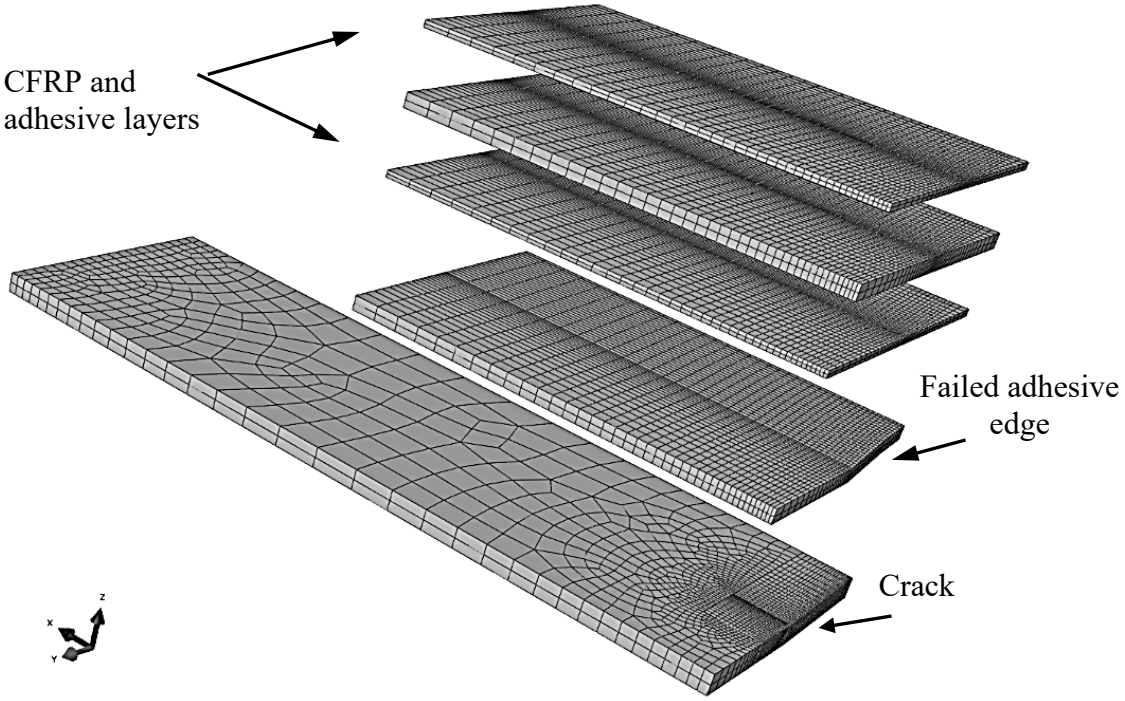

Figure 4.67 Failure incorporated adhesive layer in higher adhesive strength FEM with crack 25mm & ETR-0.53

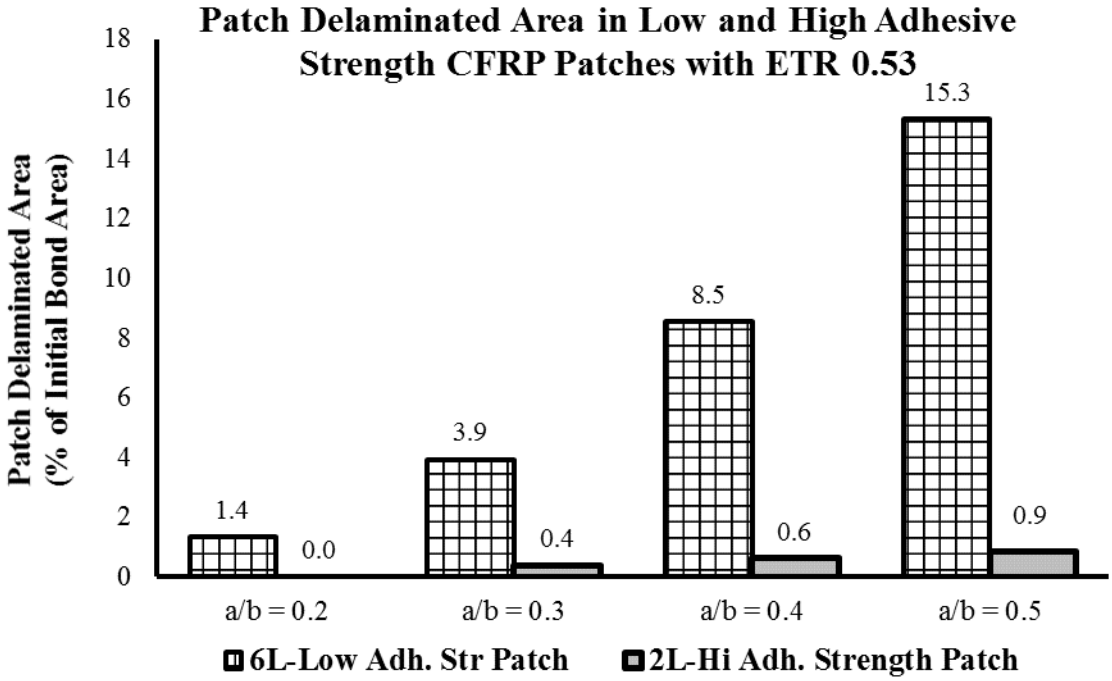

Figure 4.68 Delaminated regions in higher and lower adhesive strength models with ETR of 0.53

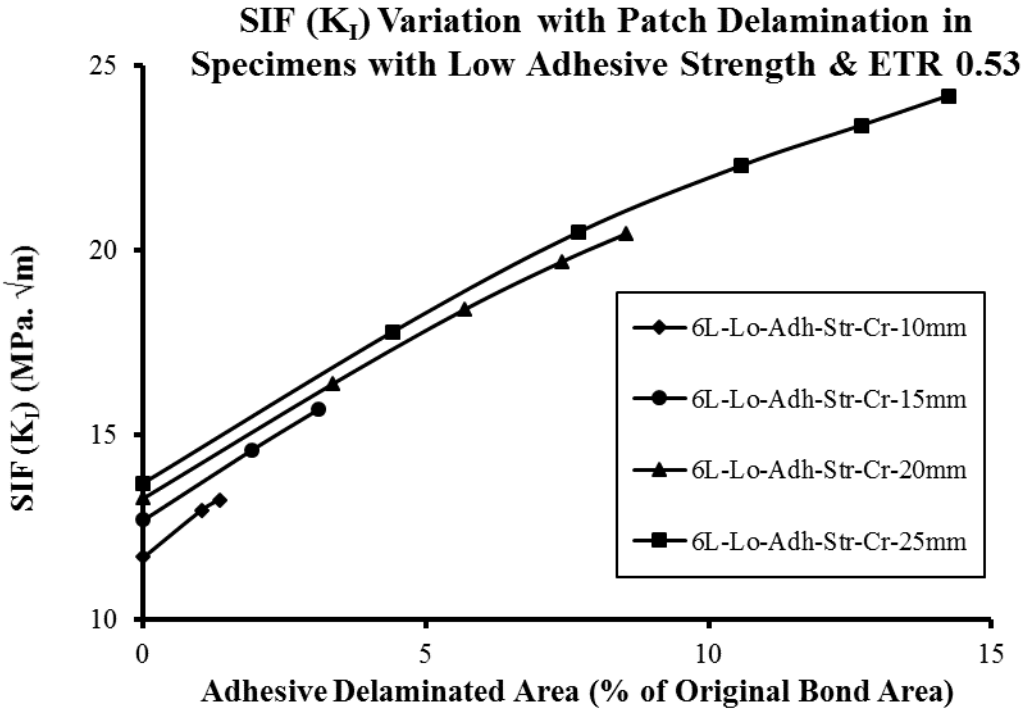

Figure 4.69 SIF variations with patch delamination in lower adhesive strength models with ETR of 0.53

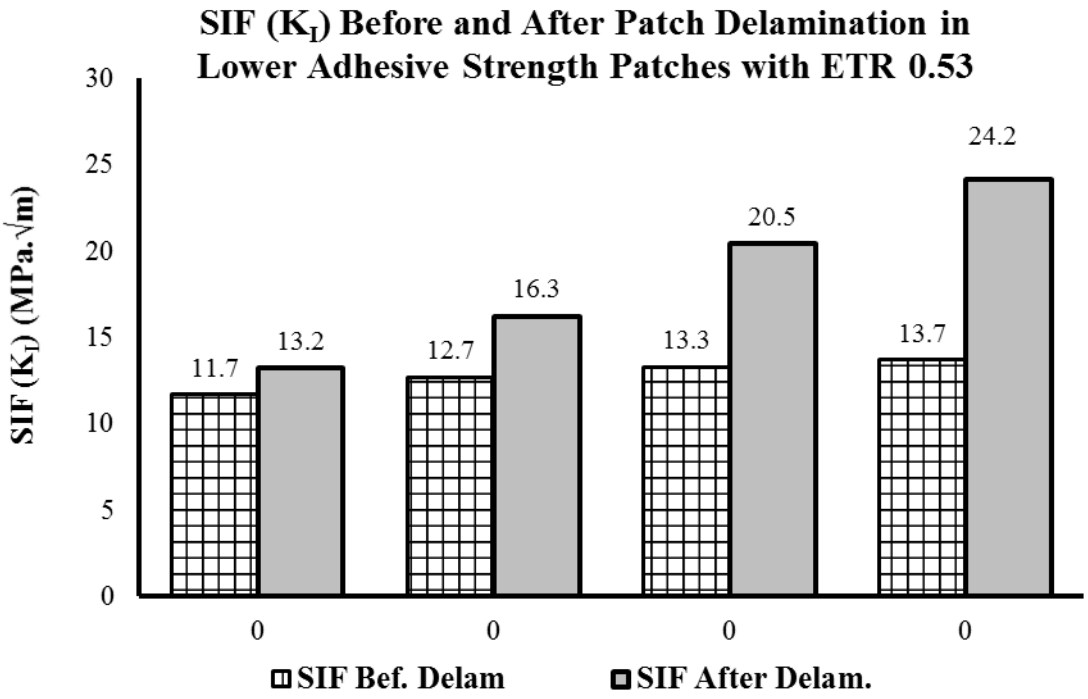

Figure 4.70 Delamination impact on SIF in lower adhesive strength models with ETR of 0.53

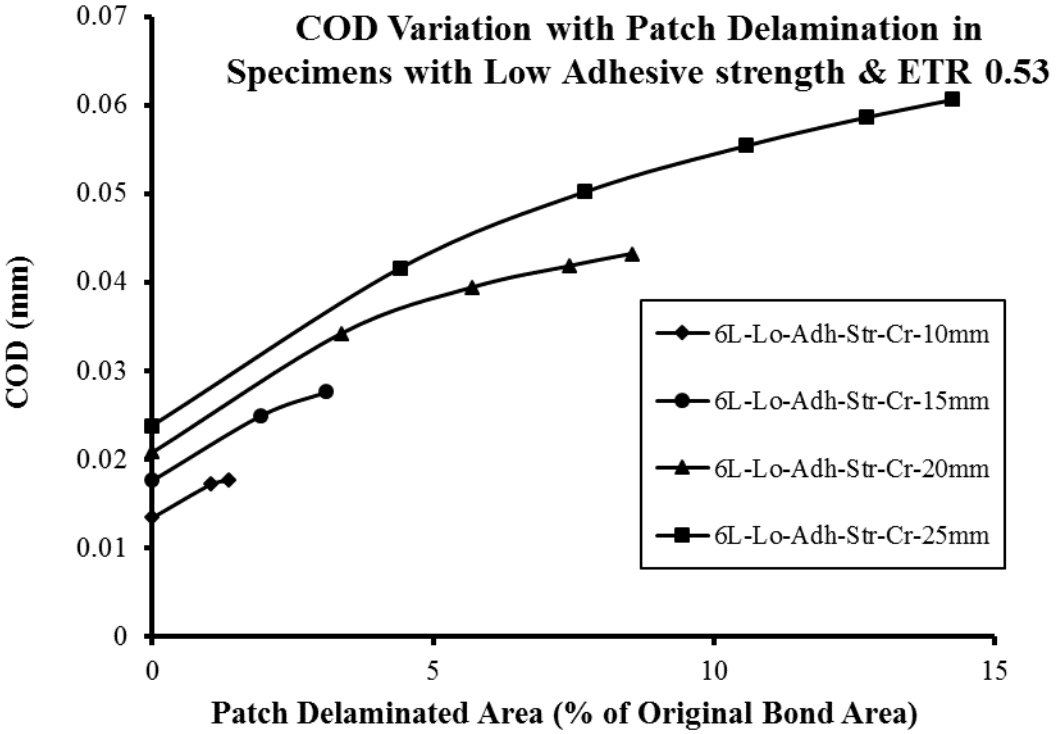

Figure 4.71 Delamination impact on COD in lower adhesive strength models with ETR of 0.53

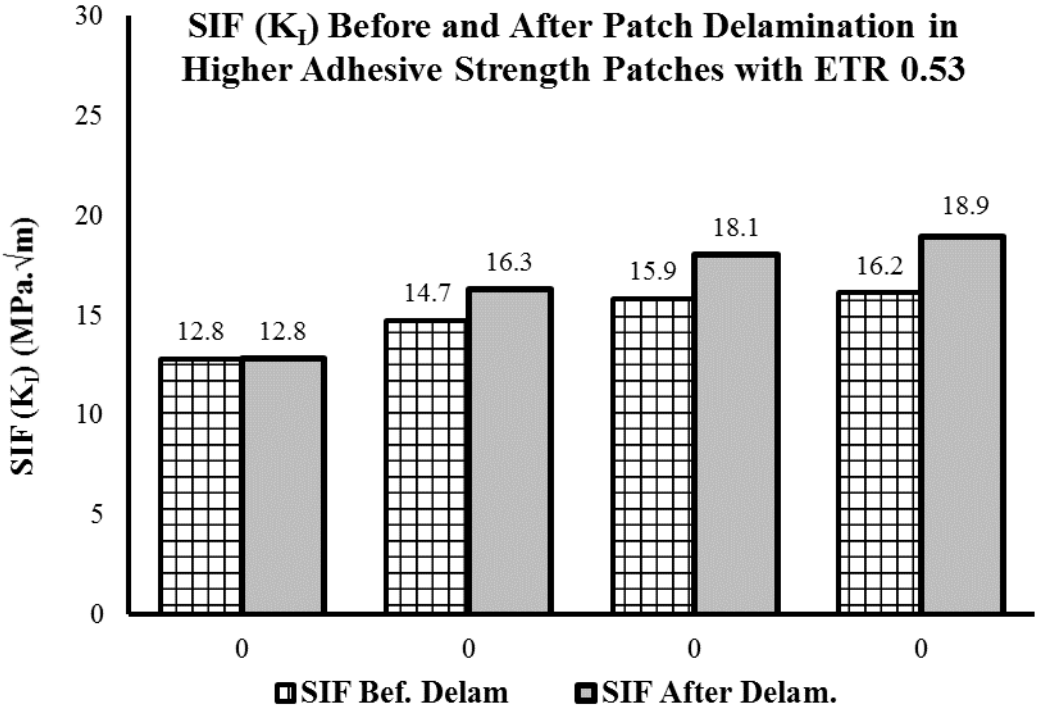

Figure 4.72 Delamination impact on SIF in higher adhesive strength models with ETR 0.53

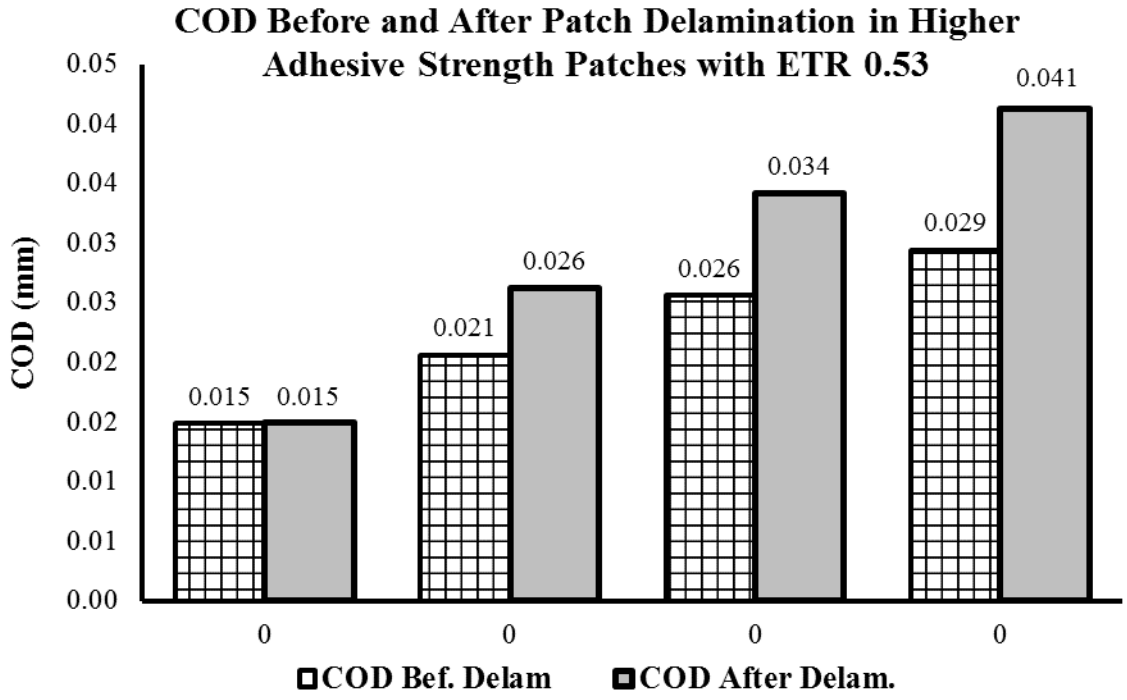

Figure 4.73 Delamination impact on COD in higher adhesive strength models with ETR 0.53

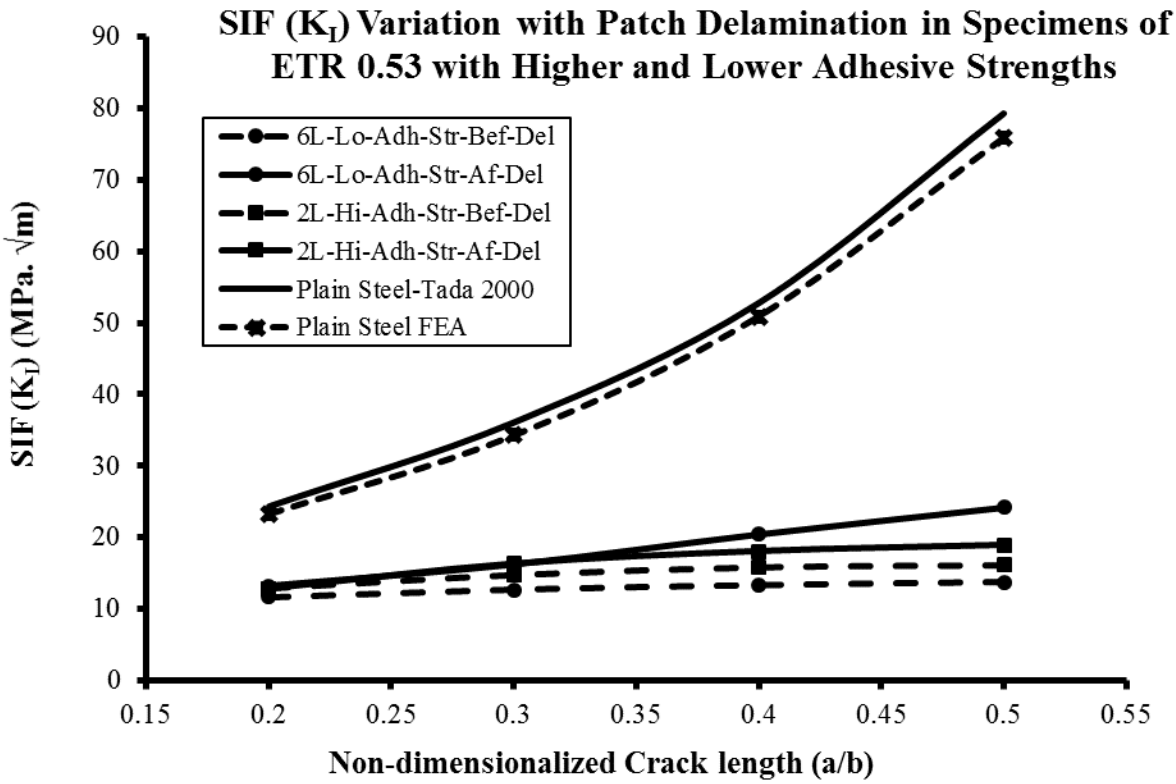

Figure 4.74. Delamination impact on SIF (K_I) in higher & lower adhesive strength models with ETR-0.53

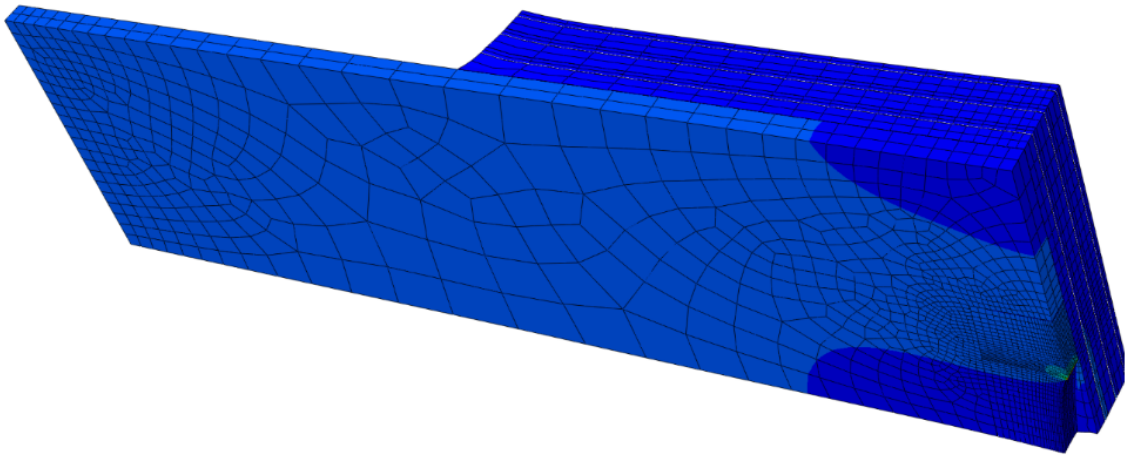

(a)

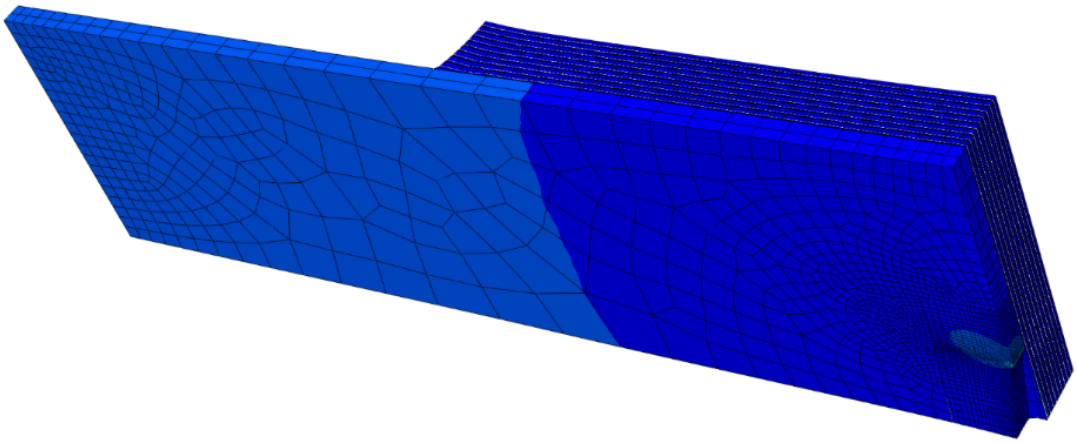

(b)

Figure 4.75 Deformed geometry of finite element models of ETR 0.8 with crack length 15mm and having (a) Higher E_{FRP} CFRP patch (with lower adhesive G/t & higher adhesive strength) (b) Lower E_{FRP} CFRP patch (with higher adhesive G/t & lower adhesive strength)

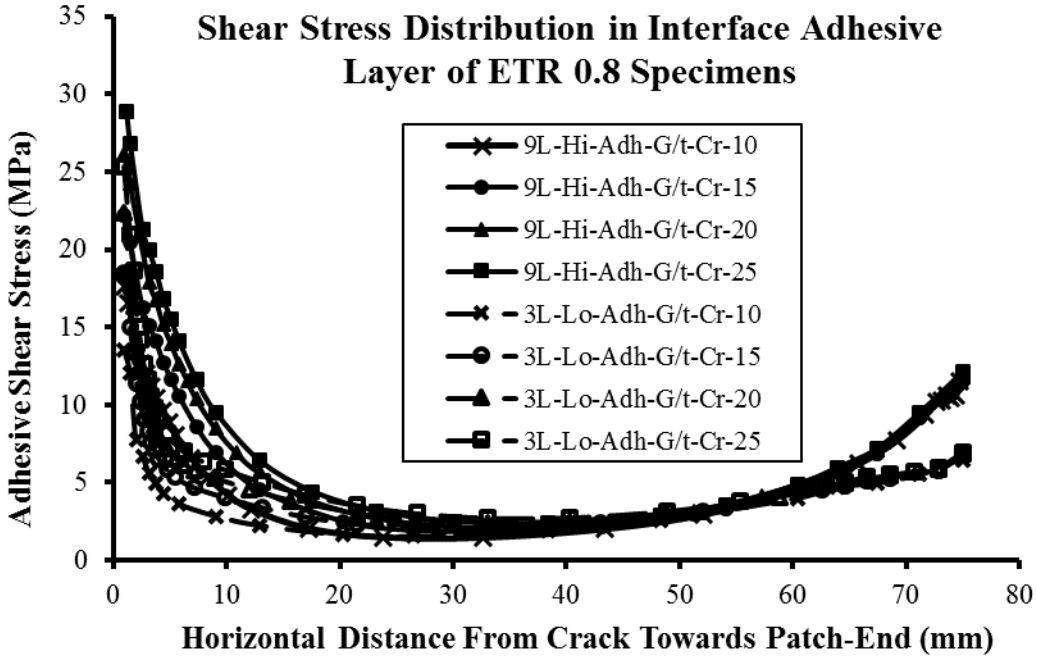

Figure 4.76 Interface adhesive shear stress distributions in specimens of ETR 0.8

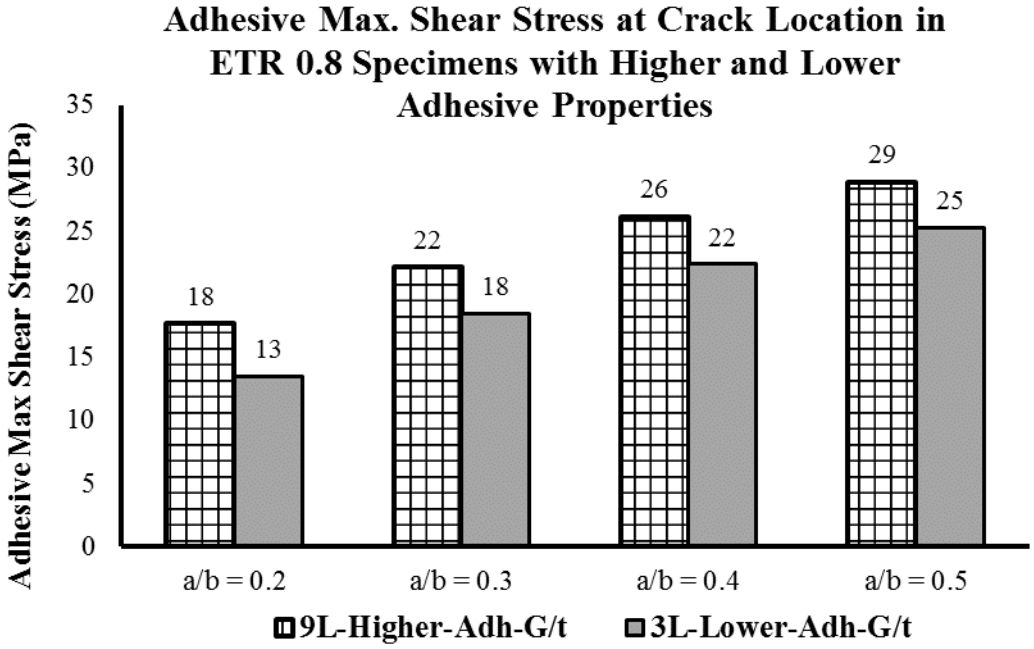

Figure 4.77 Peak adhesive shear stress at crack location in ETR 0.8 models

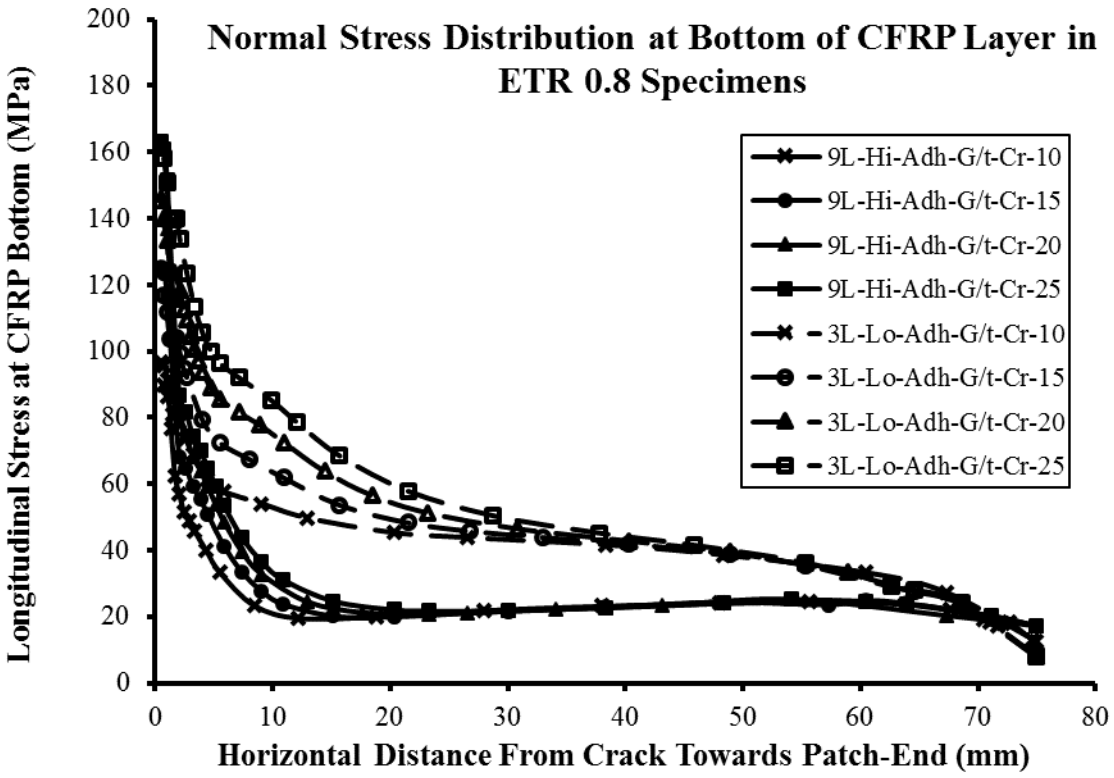

Figure 4.78 Normal stress distribution at bottom of CFRP patch in ETR 0.8 models

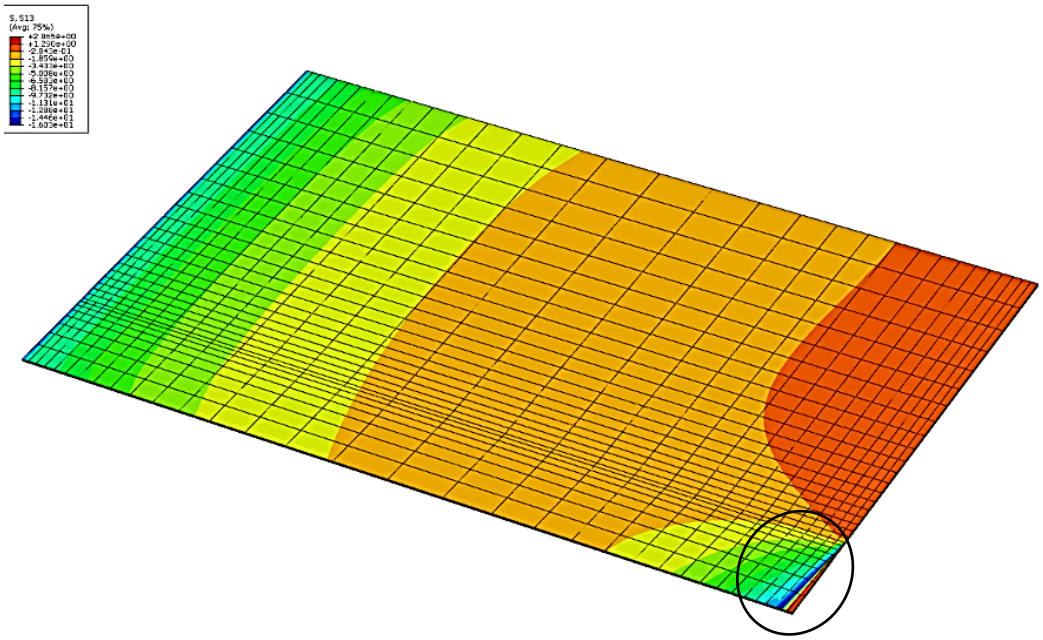

Figure 4.79 Shear stress distribution in adhesive layer in lower adhesive strength FEM with crack length 10mm & ETR-0.8

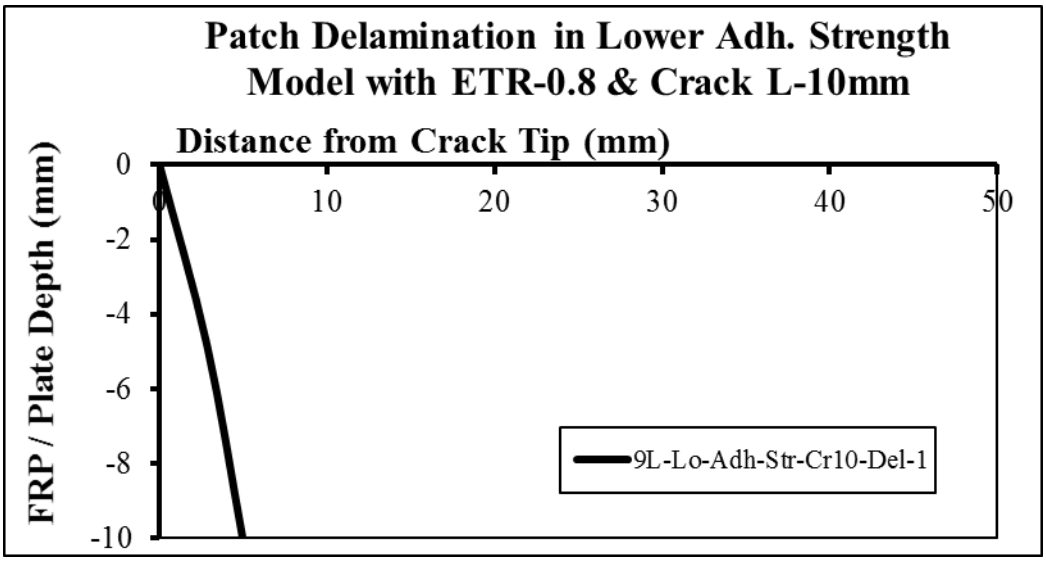

Figure 4.80 Failed adhesive region in lower adhesive strength FEM with crack length 10mm & ETR-0.8

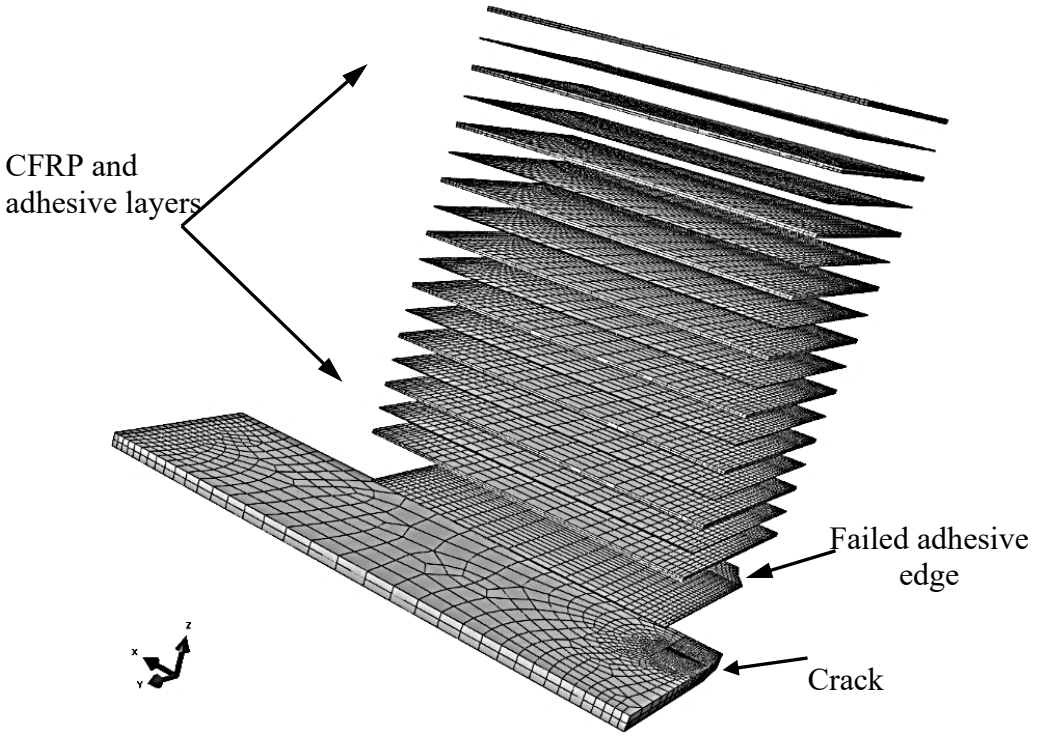

Figure 4.81 Failure incorporated adhesive layer in lower adhesive strength FEM with crack length 10mm & ETR-0.8

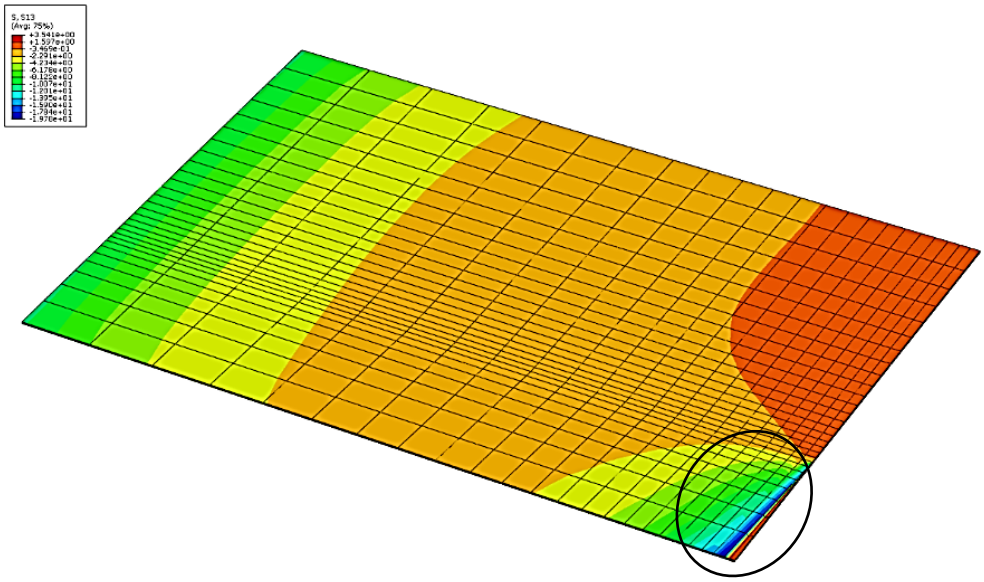

Figure 4.82 Shear stress distribution in interface adhesive layer in lower adhesive strength FEM with crack length 15mm & ETR-0.8

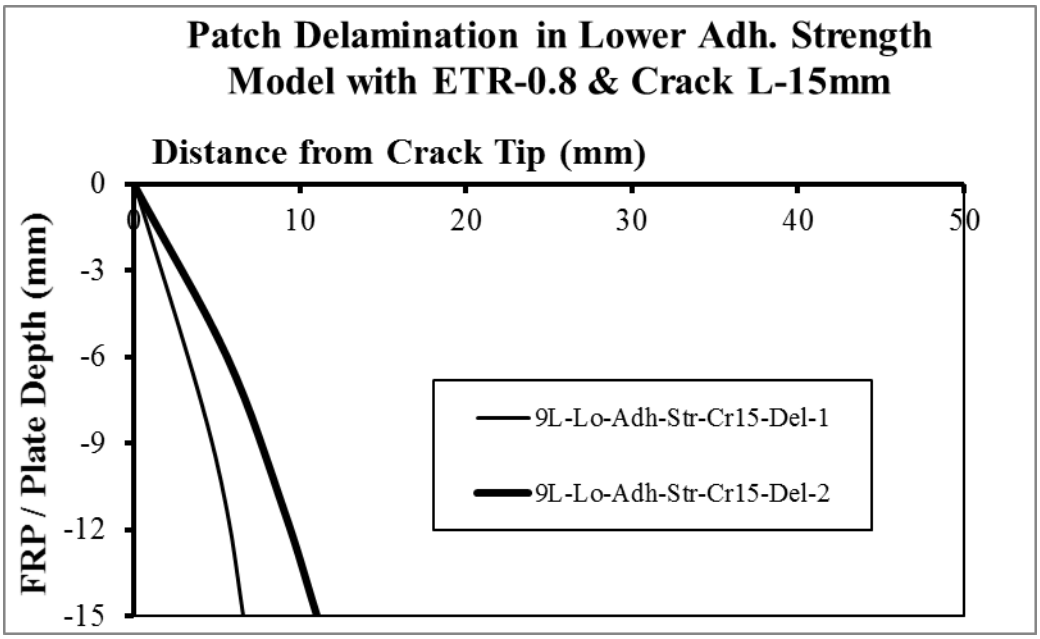

Figure 4.83 Failed adhesive region in lower adhesive strength FEM with crack length 15mm & ETR-0.8

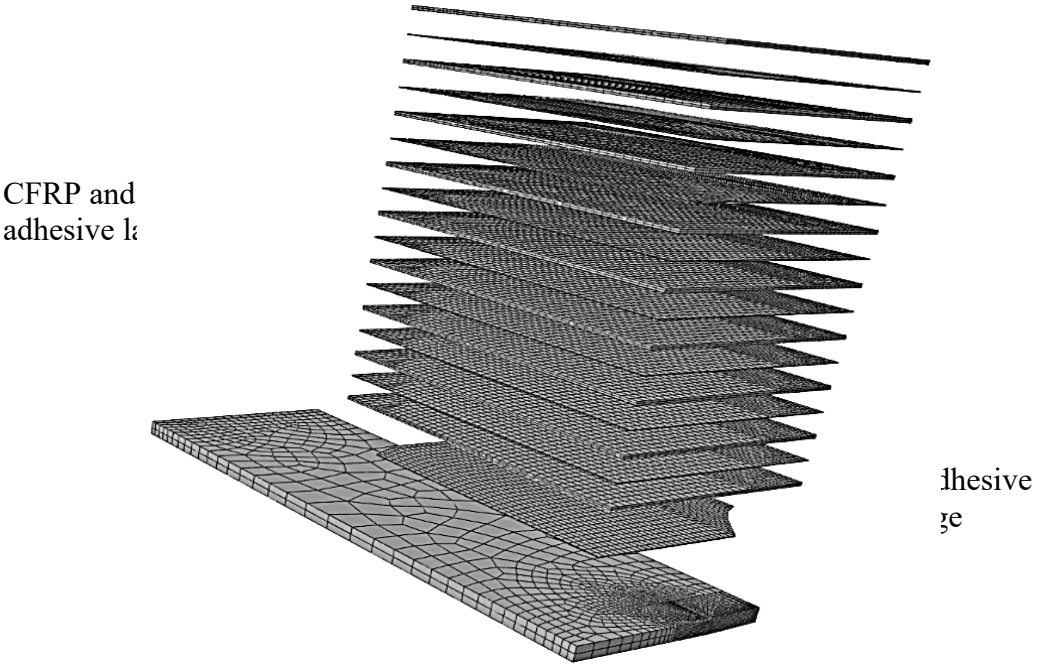

Figure 4.84 Failure incorporated adhesive layer in lower adhesive strength FEM with crack length 15mm & ETR-0.8

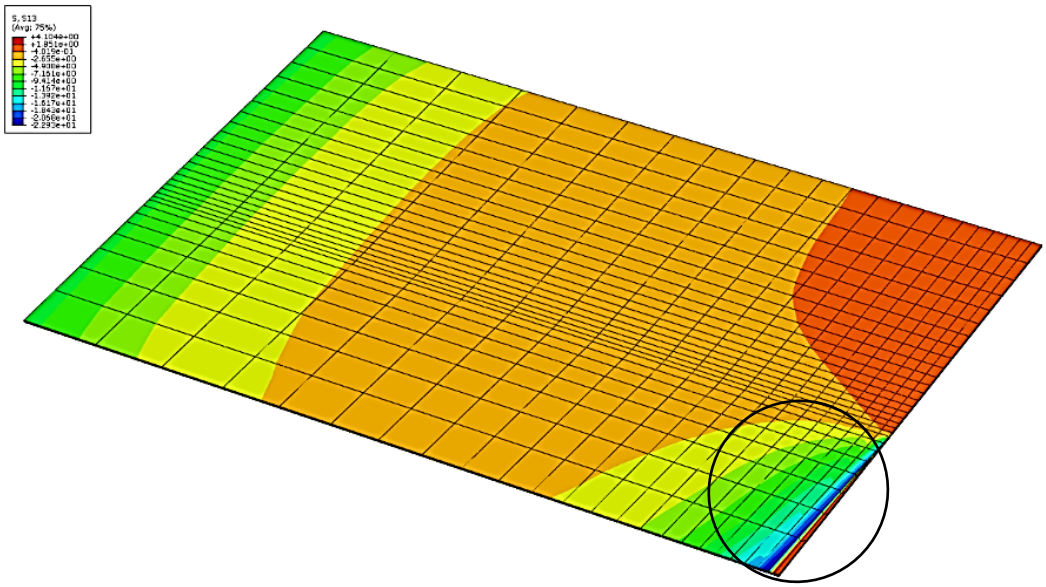

Figure 4.85 Shear stress distribution in interface adhesive layer in lower adhesive strength FEM with crack length 20mm & ETR-0.8

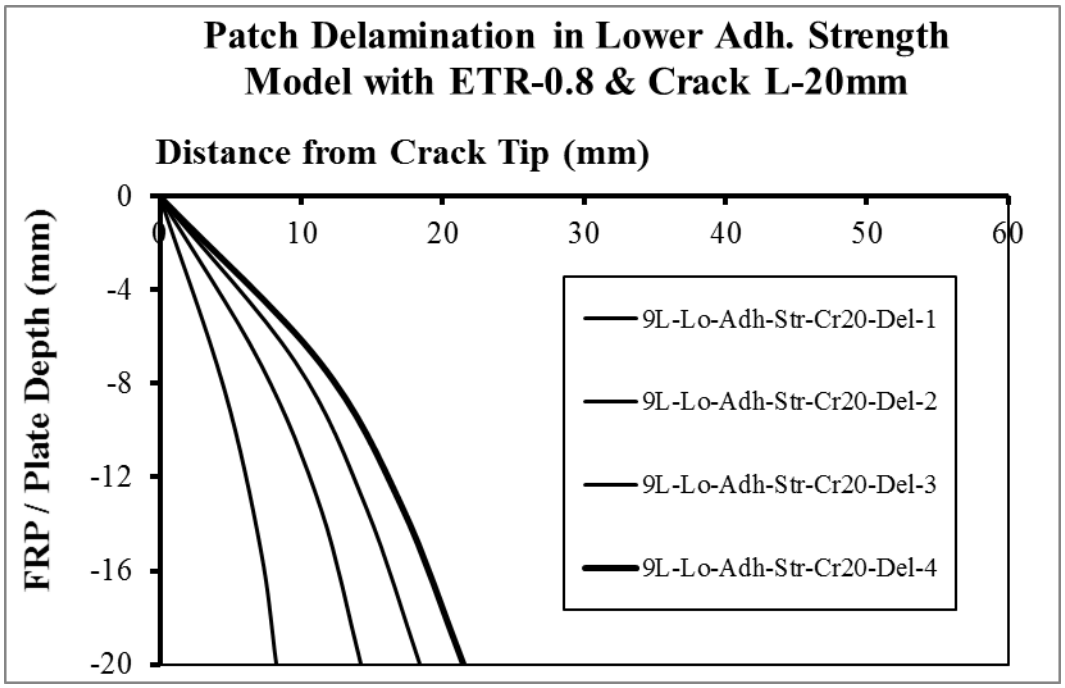

Figure 4.86 Failed adhesive region in lower adhesive strength FEM with crack length 20mm & ETR-0.8

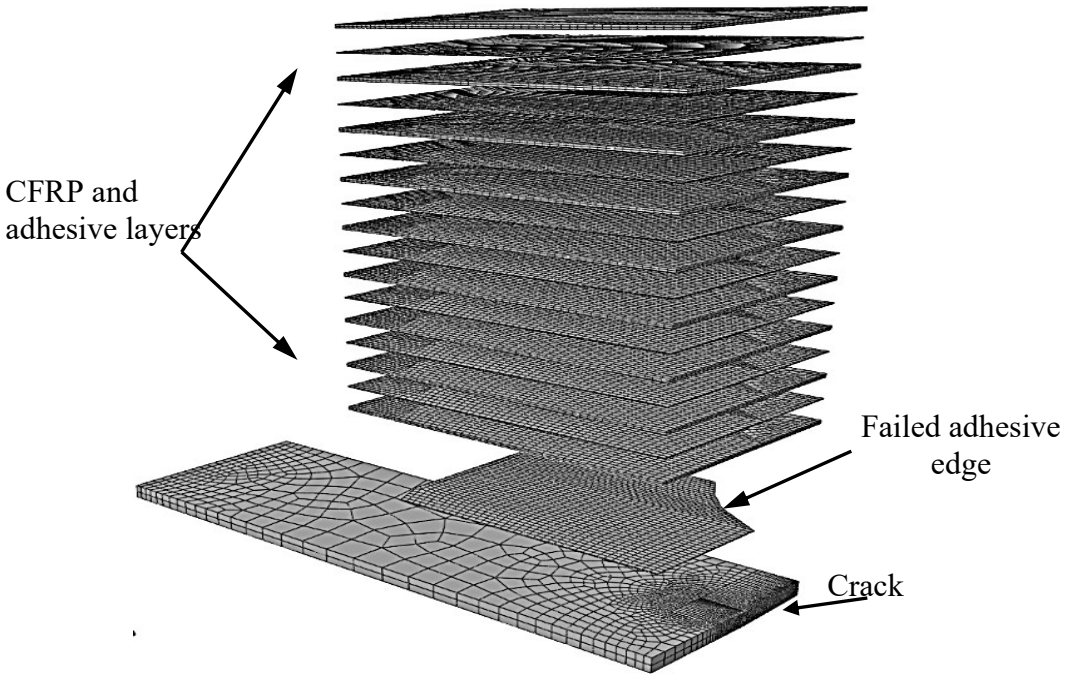

Figure 4.87 Failure incorporated adhesive layer in lower adhesive strength FEM with crack length 20mm & ETR-0.8

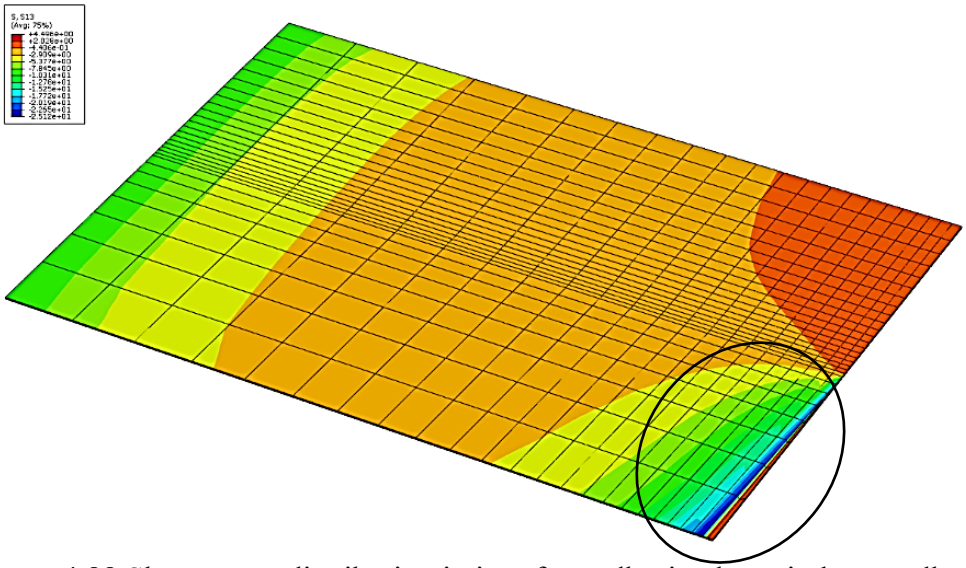

Figure 4.88 Shear stress distribution in interface adhesive layer in lower adhesive strength FEM with crack length 25mm & ETR-0.8

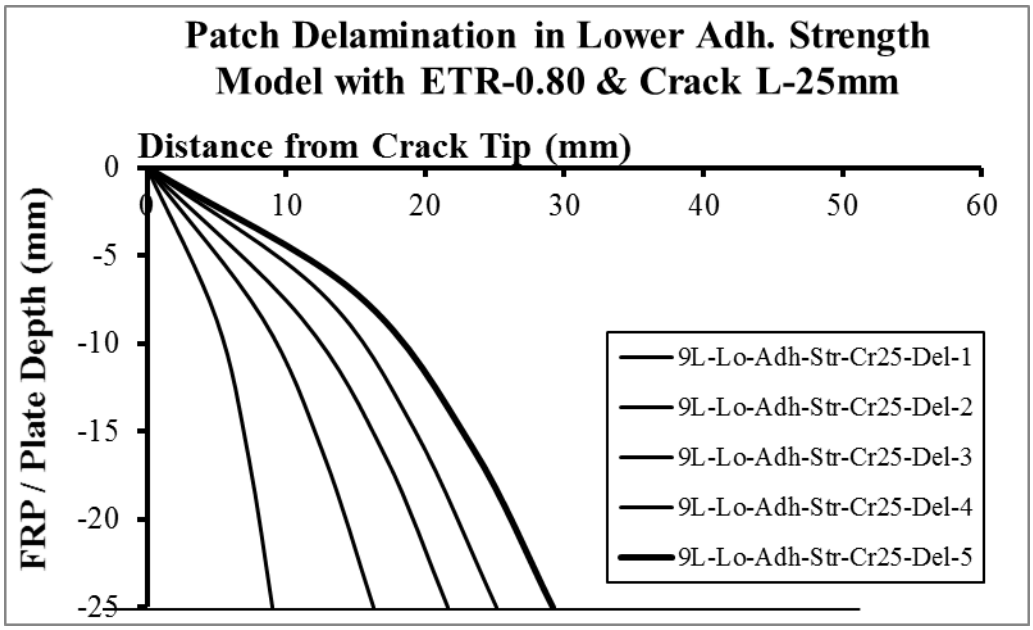

Figure 4.89 Failed adhesive region in lower adhesive strength FEM with crack length 25mm & ETR-0.8

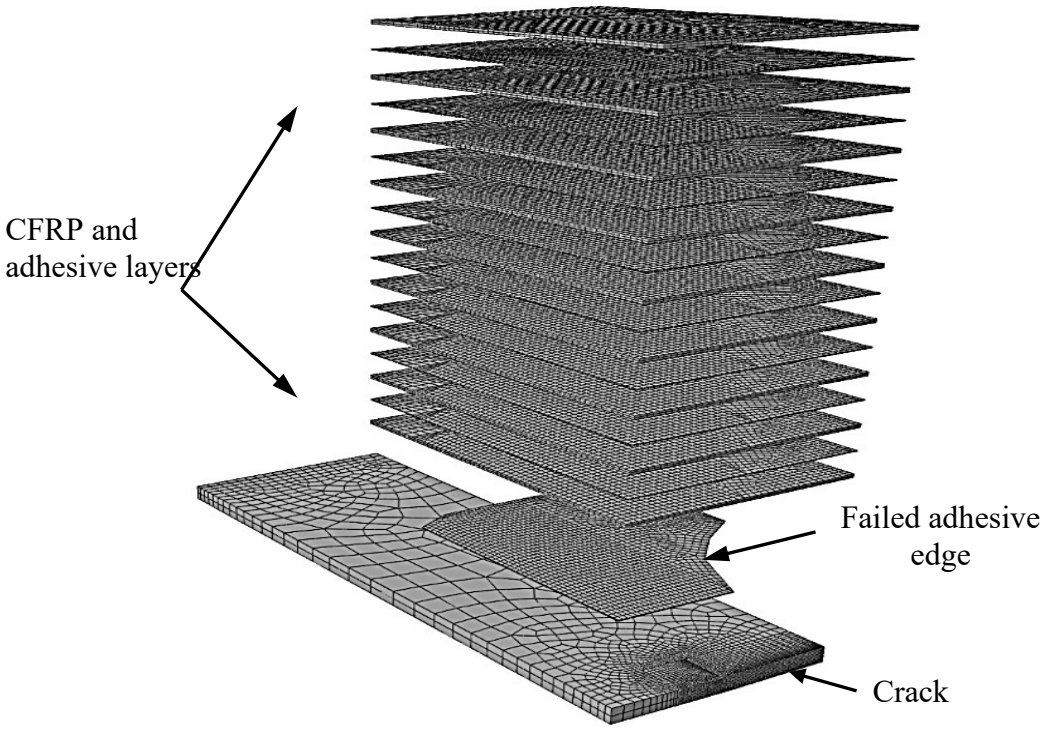

Figure 4.90 Failure incorporated adhesive layer in lower adhesive strength FEM with crack length 25mm & ETR-0.8

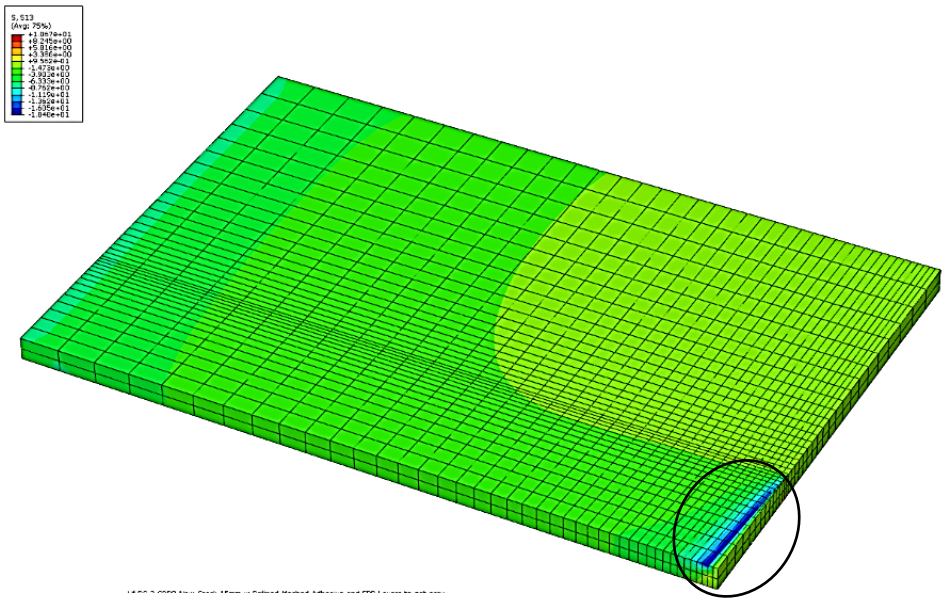

Figure 4.91 Shear stress distribution in interface adhesive layer in higher adhesive strength FEM with crack length 15mm & ETR-0.8

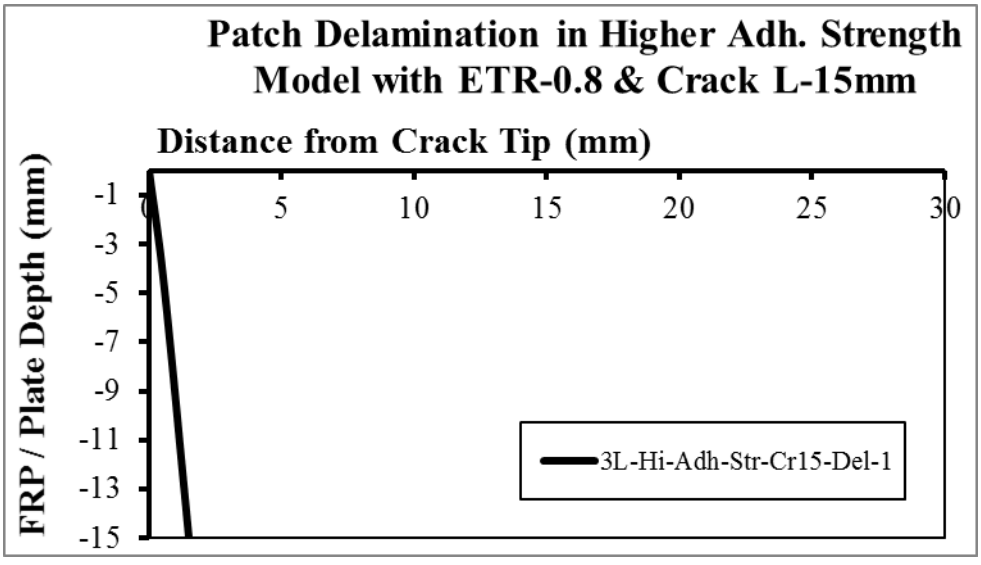

Figure 4.92 Failed adhesive region in higher adhesive strength FEM with crack length 15mm & ETR-0.8

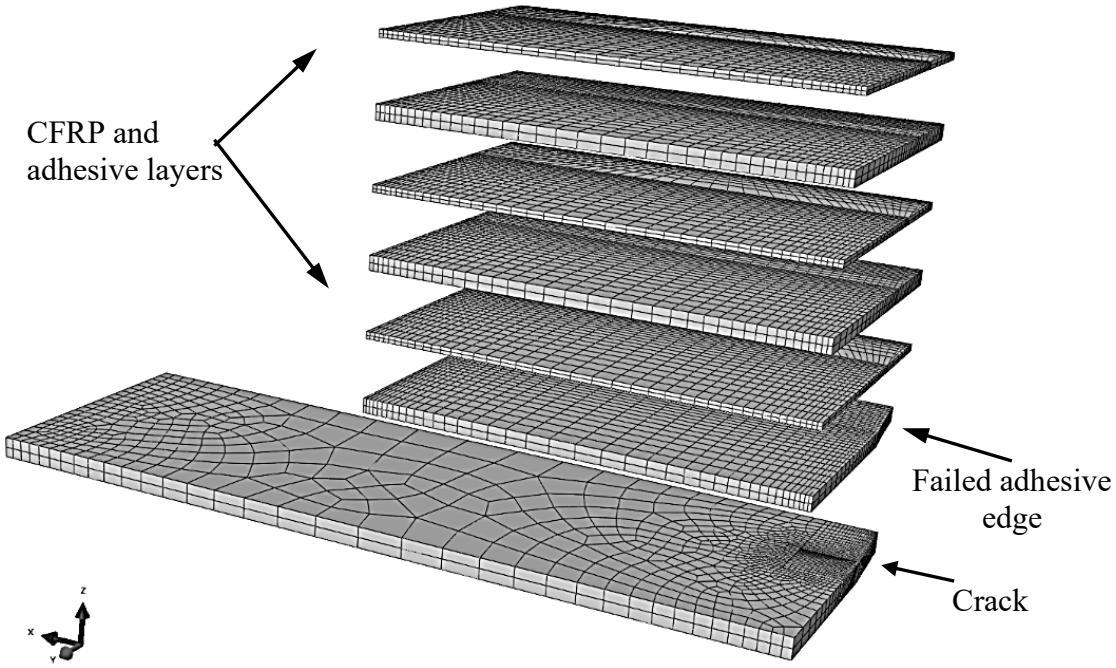

Figure 4.93 Failure incorporated adhesive layer in higher adhesive strength FEM with crack length 15mm & ETR-0.8

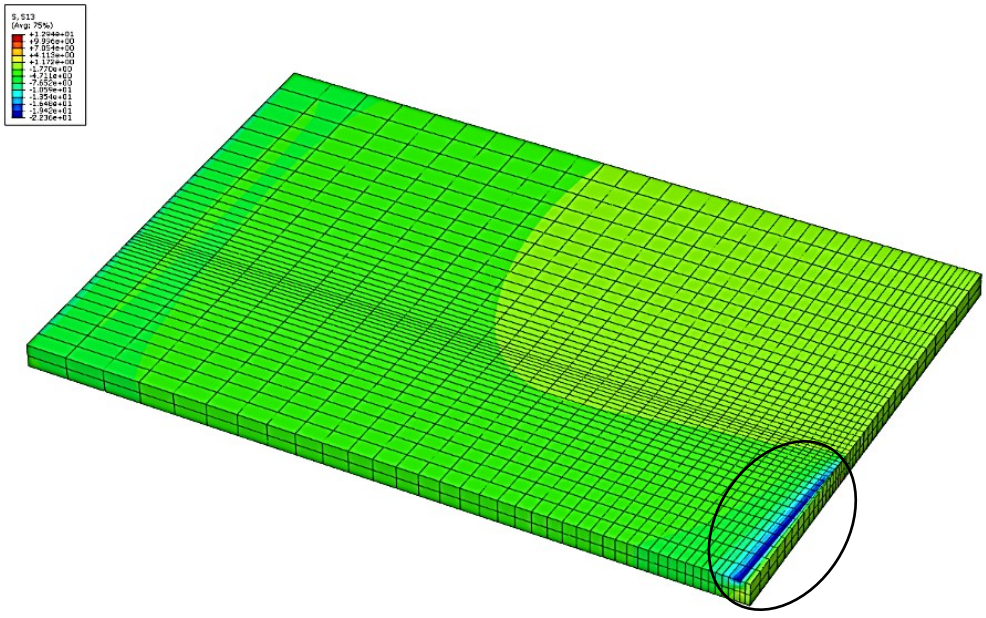

Figure 4.94 Shear stress distribution in interface adhesive layer in higher adhesive strength FEM with crack length 20mm & ETR-0.8

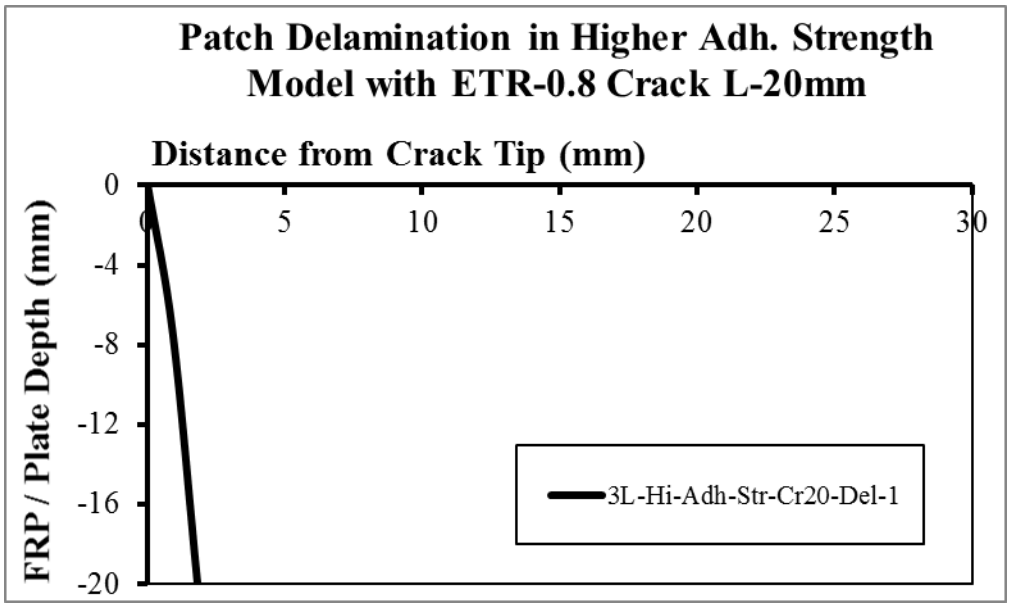

Figure 4.95 Failed adhesive region in higher adhesive strength FEM with crack length 20mm & ETR-0.8

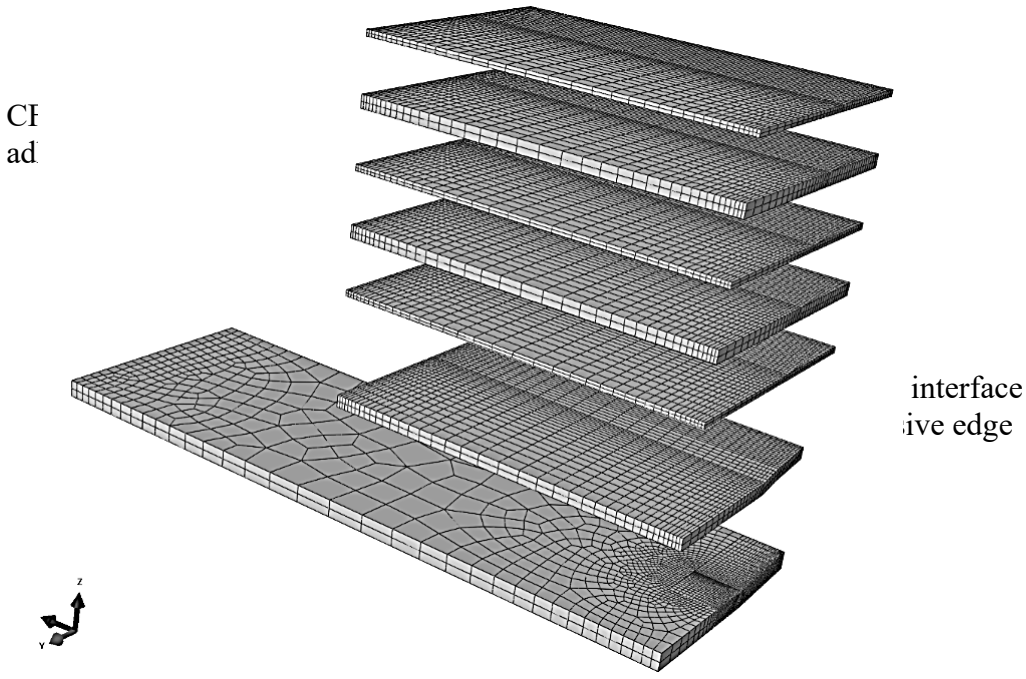

Figure 4.96 Failure incorporated adhesive layer in higher adhesive strength FEM with crack length 20mm & ETR-0.8

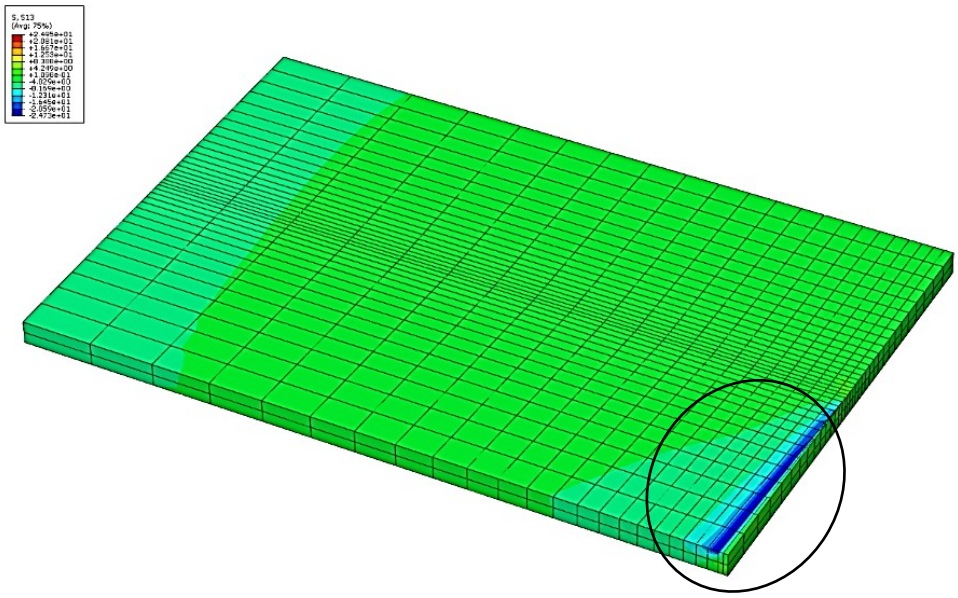

Figure 4.97 Shear stress distribution in interface adhesive layer in higher adhesive strength FEM with crack length 25mm & ETR-0.8

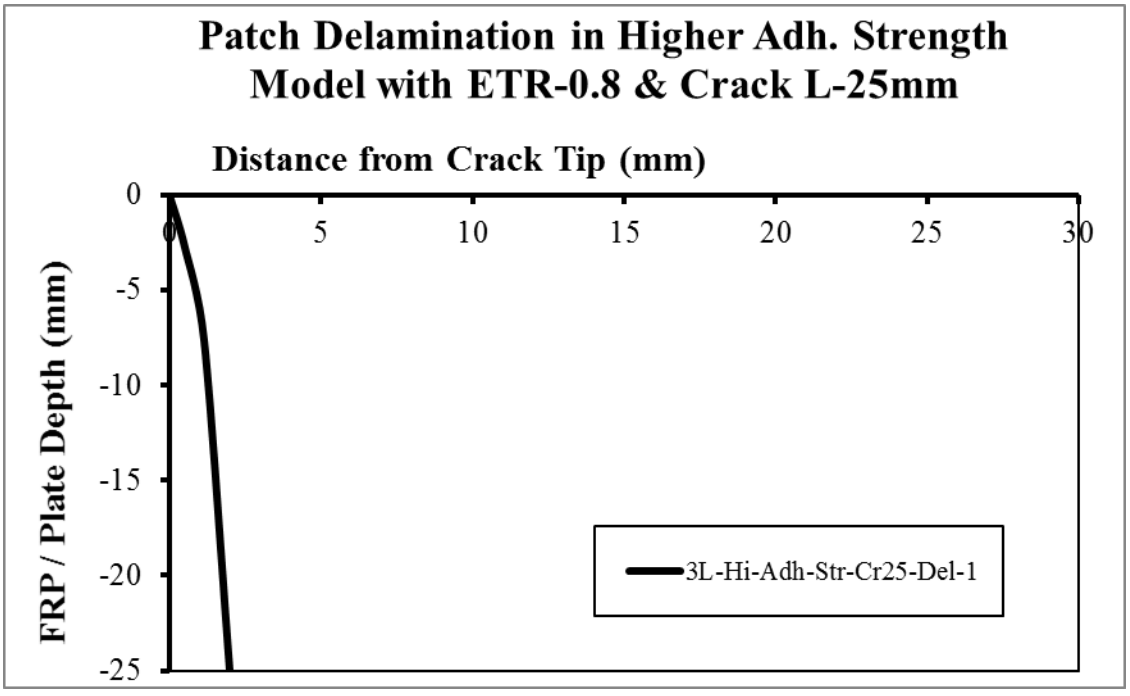

Figure 4.98 Failed adhesive region in higher adhesive strength FEM with crack length 25mm & ETR-0.8

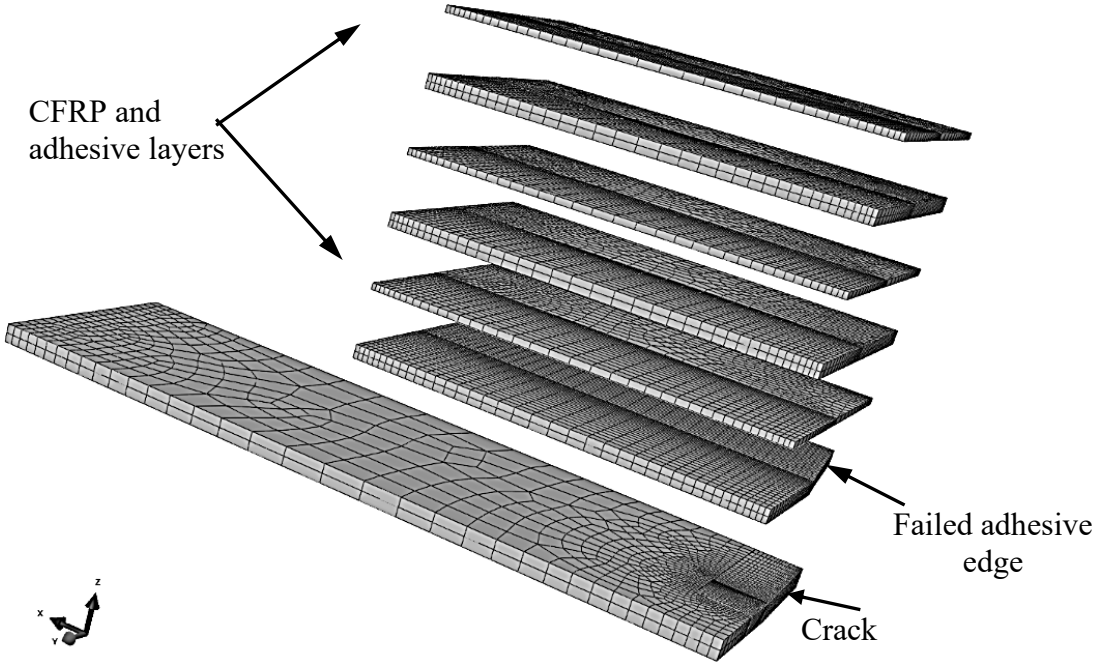

Figure 4.99 Failure incorporated adhesive layer in higher adhesive strength FEM with crack 25mm & ETR-0.8

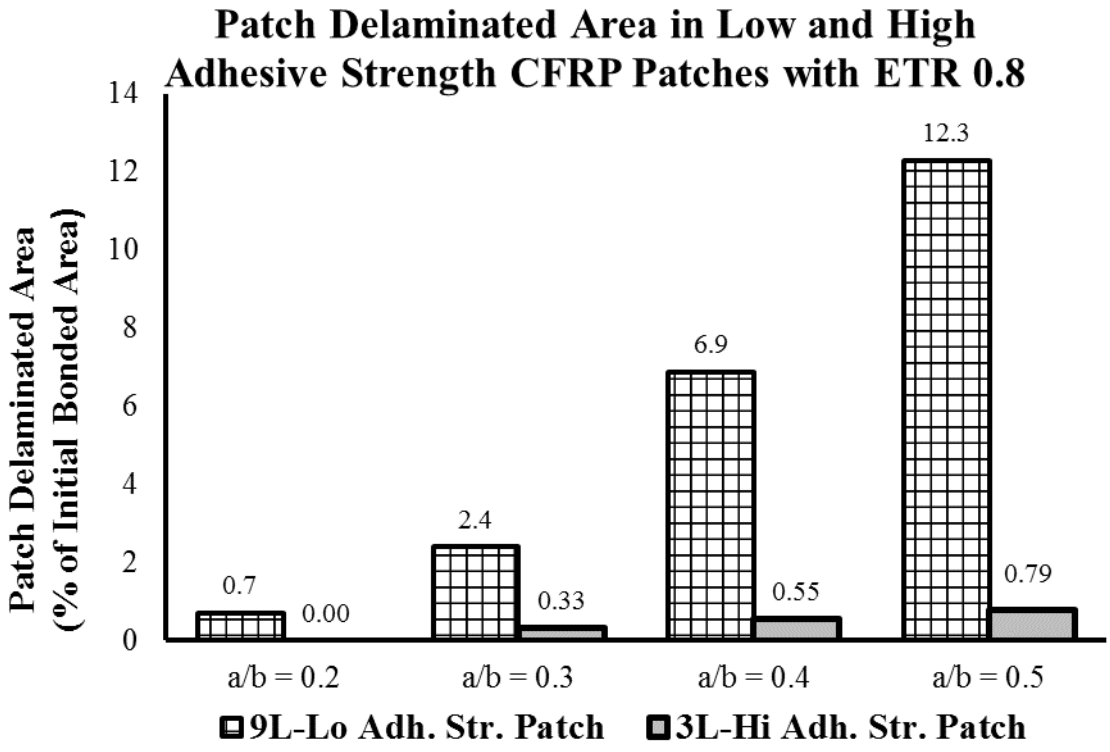

Figure 4.100 Delaminated areas in models of ETR-0.8 with higher and lower adhesive and CFRP properties

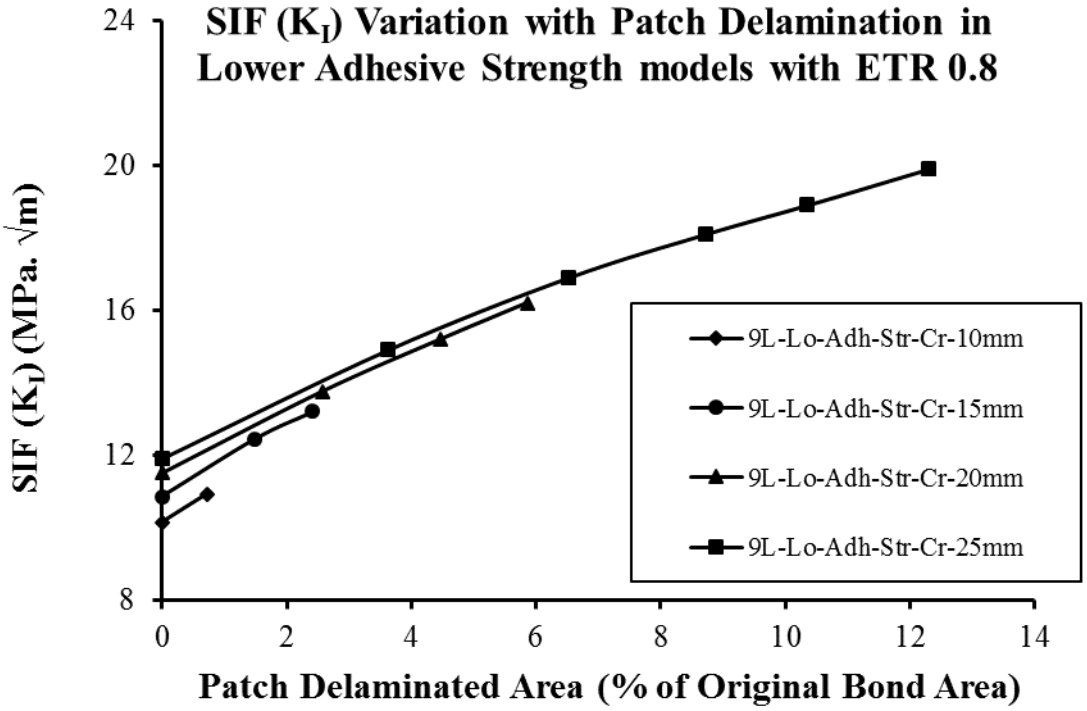

Figure 4.101 SIF (K_I) variations with patch delamination in lower adhesive strength models of ETR-0.8

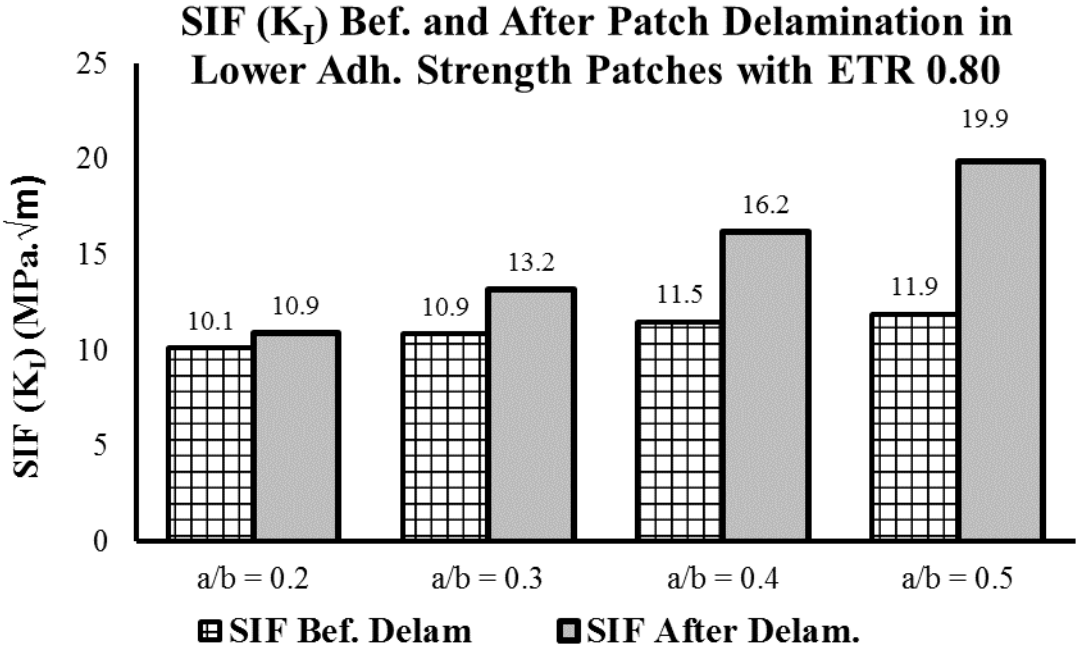

Figure 4.102 Delamination impact on SIF (K_I) in lower adhesive strength models of ETR-0.8

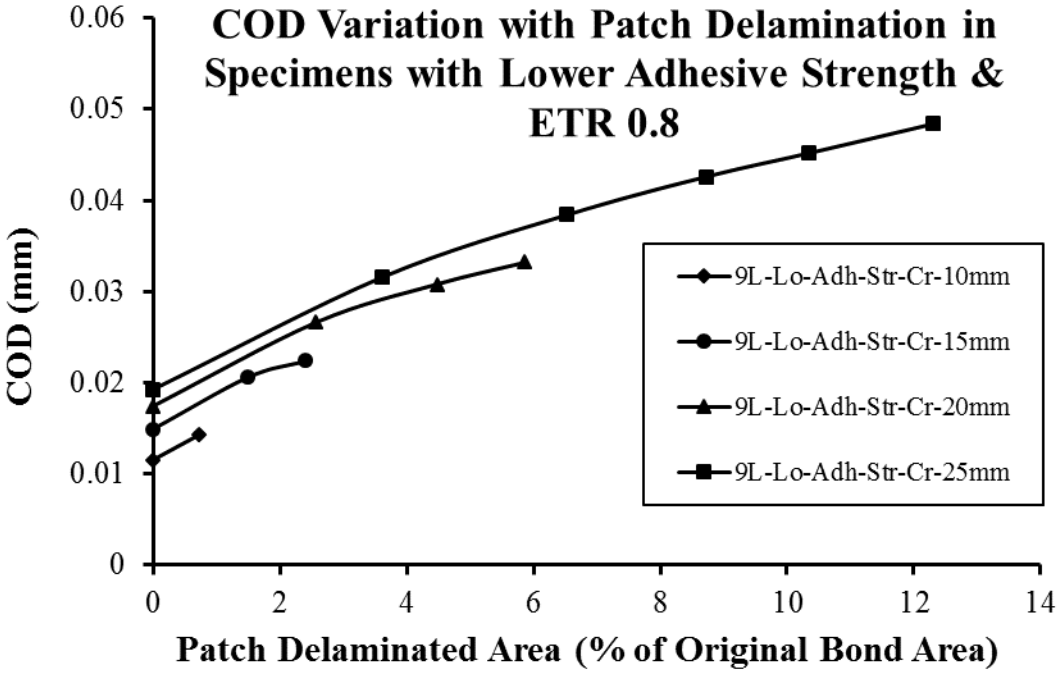

Figure 4.103 COD variation with patch delamination in lower adhesive strength models of ETR-0.8

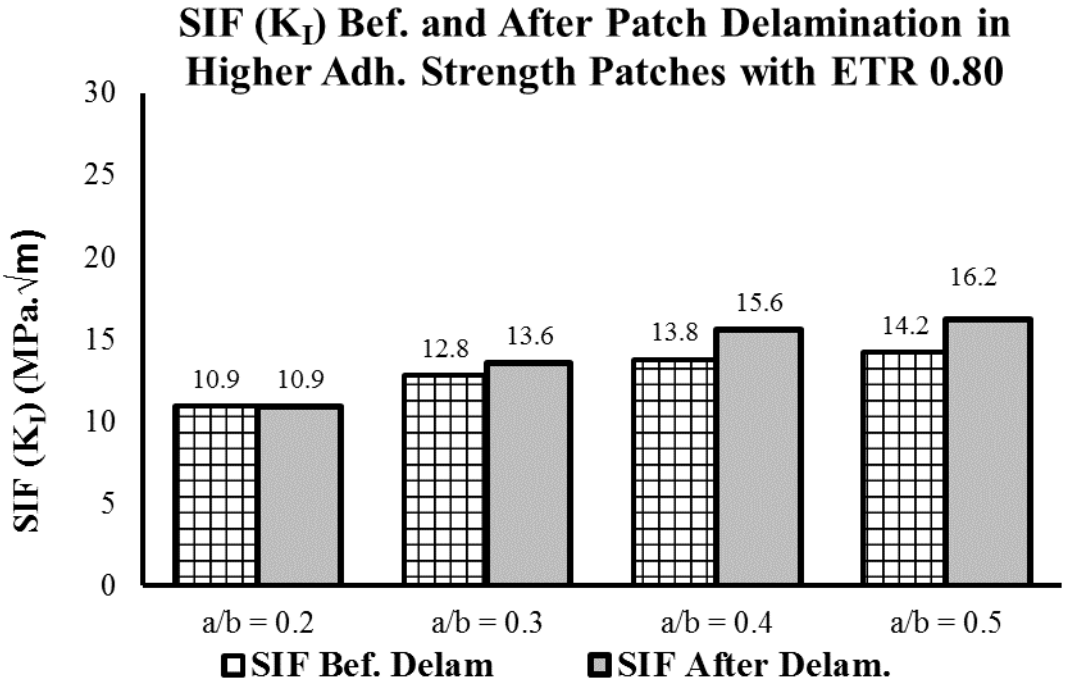

Figure 4.104 Delamination impact on SIF (K_I) in higher adhesive strength models of ETR-0.8

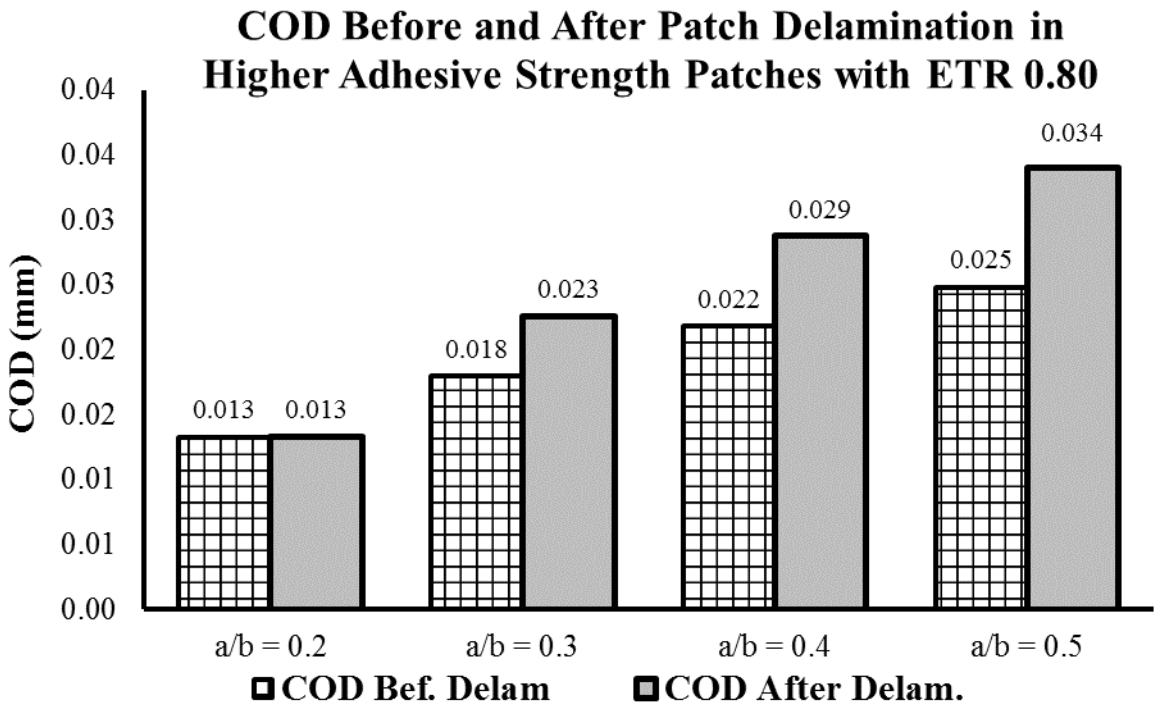

Figure 4.105 Delamination impact on COD in higher adhesive strength models of ETR-0.8

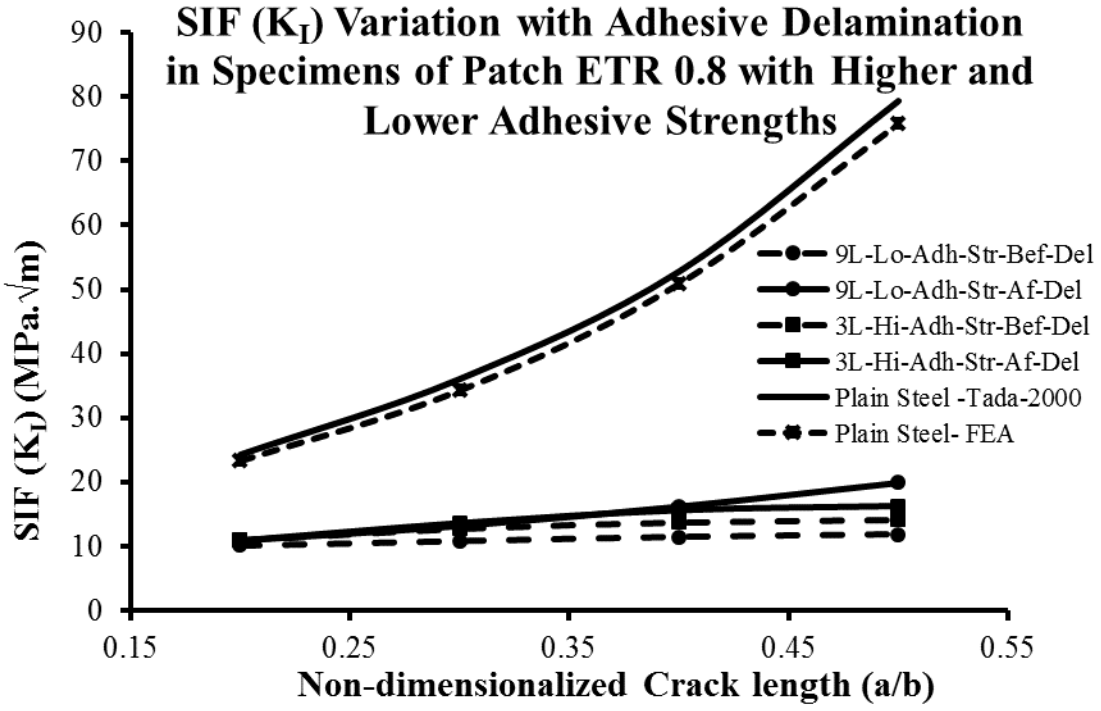

Figure 4.106 Delamination impact on SIF (K_I) in models of ETR 0.8 with higher & lower adhesive strengths

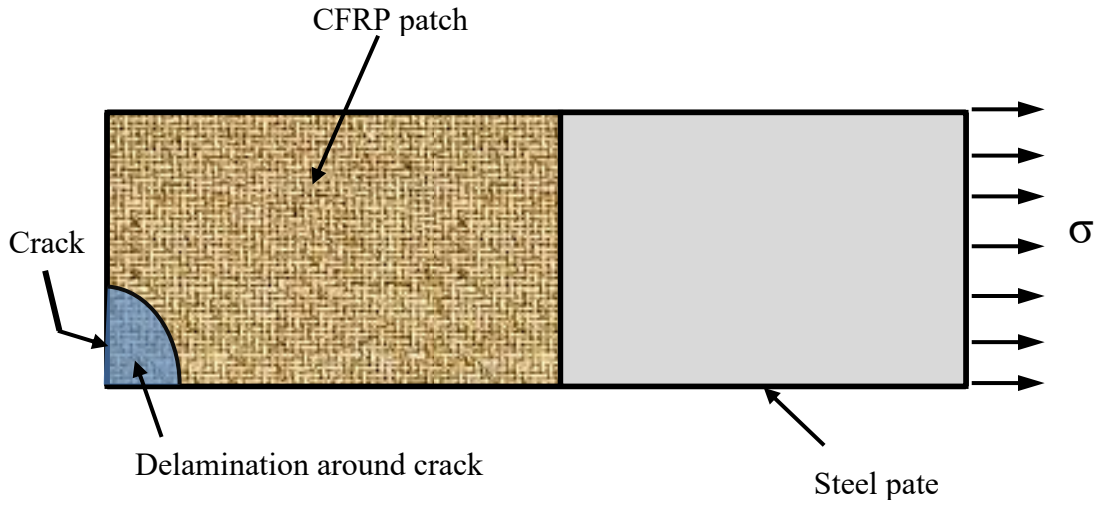

Figure 4.107 Delamination location study – Model with delamination around crack

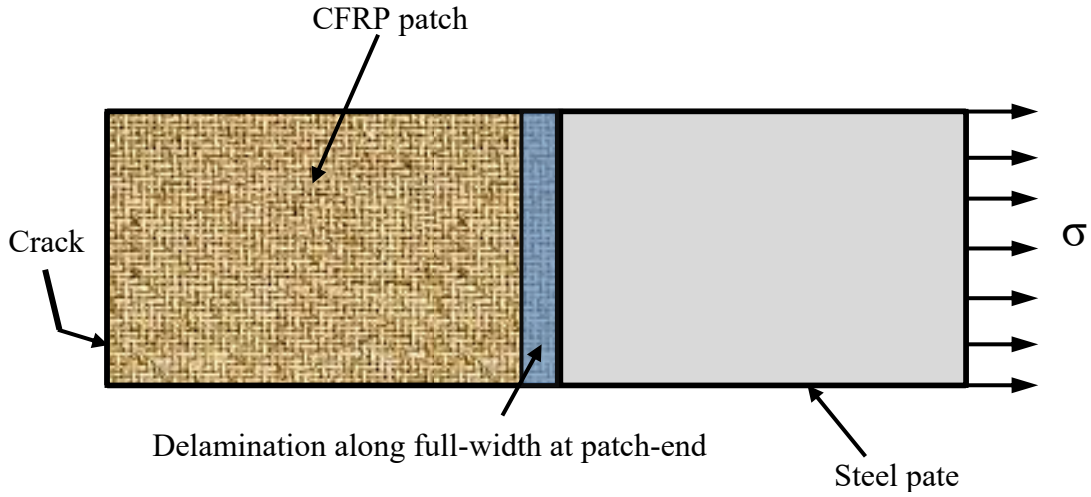

Figure 4.108 Delamination location study – Model with delamination along whole patch width

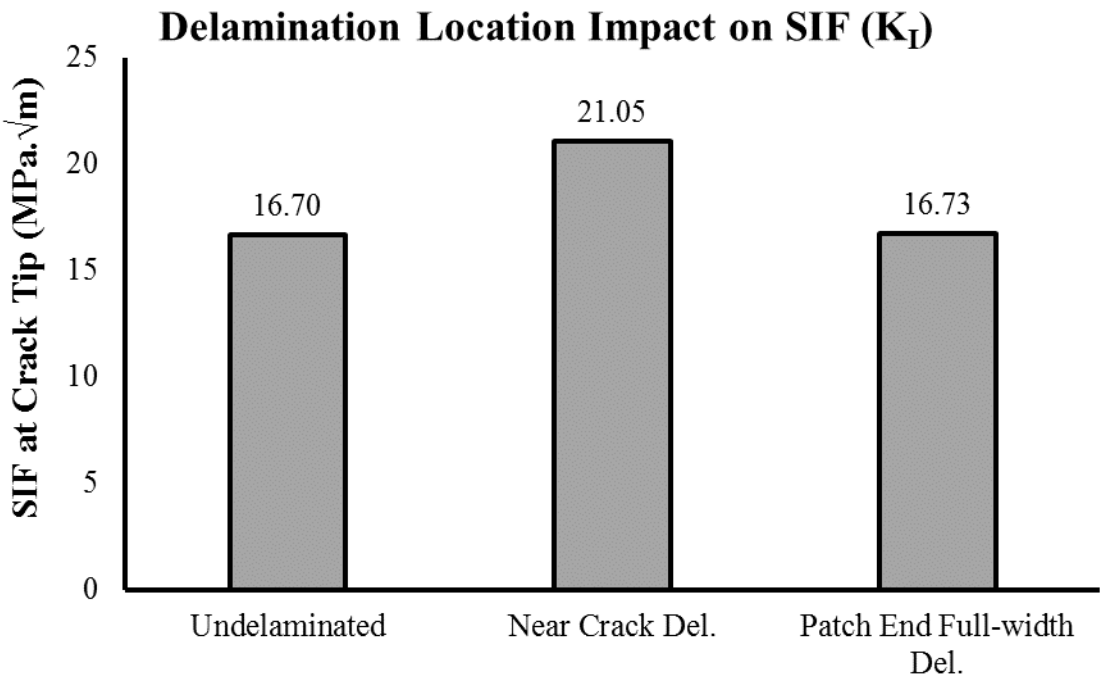

Figure 4.109 Impact of delamination location on SIF (K_I) at crack tip

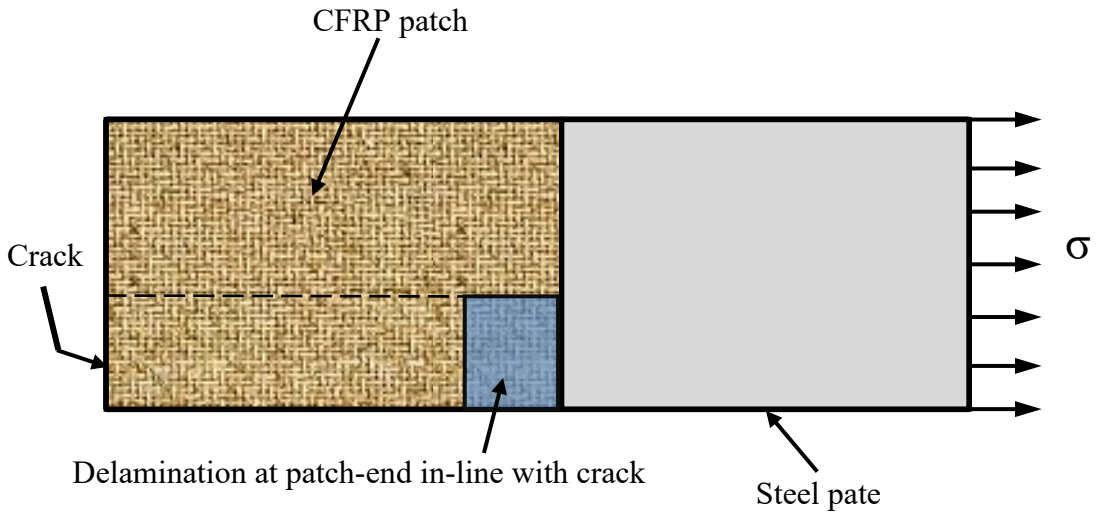

Figure 4.110 Delamination location study – End delamination at patch-end but in-line with crack

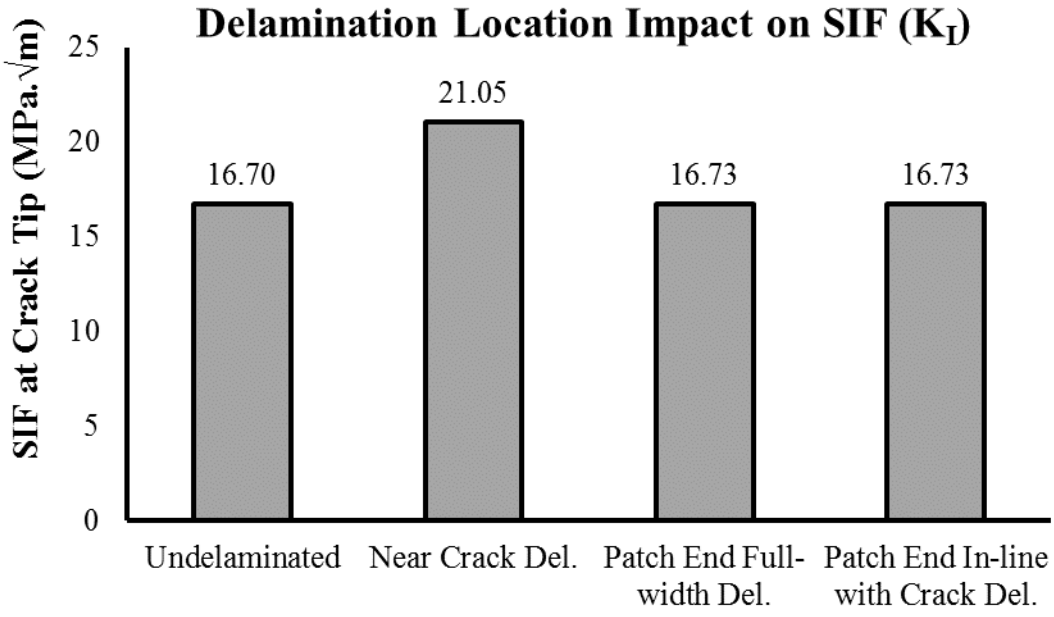

Figure 4.111 Impact of delamination location on SIF (K_I)

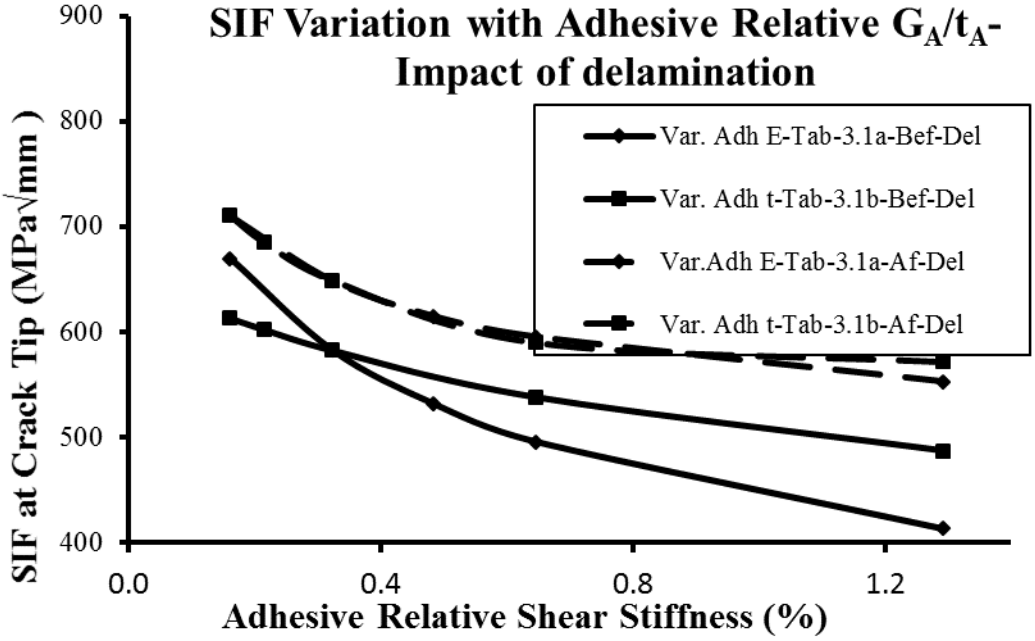

Figure 4.112 Delamination impact on SIF variation with adhesive shear stiffness (G_A/t_A)

5. Fatigue behavior of cracked steel plates with bonded CFRP patches - Experimental study

5.1 The experimental program

Keeping in view the objectives of current research work as well as results of the numerical study carried out in chapters 3 and 4, an experimental program was designed to study the impact of governing parameters of current research work on the fatigue behavior of cracked steel plates. The experimental work mainly included fatigue tests of edge cracked steel plates repaired with double-sided bonded patches of carbon fiber reinforced polymers (CFRP). Main parameters of the test included effective thickness ratio (ETR), moduli of elasticity of the CFRP (E_{FRP}) and adhesive (E_A), hybrid CFRP patches, adhesive thickness (t_A) and adhesive shear strength (τ). ETR has been defined in section 1.3 as the ratio of axial stiffness of bonded CFRP patch to the axial stiffness of steel plate but for a quick reference it is again shown in the Equation 5.1,

$$ETR = \frac{E_{FRP}\, t_{FRP}}{E_S\, t_S} \qquad \text{Eq. 5.1}$$

where 'E' and 't' are modulus of elasticity and thickness and the subscripts 'FRP' and 'S' stood for FRP/CFRP and steel respectively.

Total 14 specimens were included in the experimental program as shown in Table 5.1, including two control specimens. The specimens were primarily divided into three groups, corresponded to three ETR values of 0.21, 0.42 and 0.63. Within each ETR group the specimen were differentiated by the CFRP and adhesive properties. It was so provided to study the impact of other patch parameters, in addition to the ETR, on the fatigue behavior of the cracked steel plates repaired with identical ETR patches. It included the comparison of fatigue behavior of repairs with identical ETR but with varying modulus of elasticity of CFRP, to incorporate properties of two commonly and commercially available CFRP types. Similarly, it also included specimens with identical ETR as well as the CFRP modulus but having different adhesive properties (thickness, modulus and the shear strength).

Two different types of commercially available CFRP used in the current experimental work, having different elastic moduli, and their details are provided in section 5.2. In the first group of specimens with ETR of 0.21 the specimens 1CBDR-Sk30 and 1CBDR-Hf-Sk30 were having one layer of identical CFRP type on each face but the adhesive thickness was half in the later specimen. The specimen 1CBDR-Sk300 was identical to 1CBDR-Sk-30 but having different adhesive. It was selected to study and compare the impact of varying adhesive properties in the higher modulus CFRP repairs, although the adhesive used in 1CBDR-Sk300 was not recommended by the supplier. Similarly, the specimens 3SKWRP-Sk-300 and 3SKWRP-Sk-330 were having three layers of identical CFRP type but were having different adhesives and these were also selected to study the impact of different adhesive properties in the lower modulus CFRP patches.

Higher ETR groups of 0.42 and 0.63 were developed by doubling and tripling the CFRP layers of the specimens of ETR 0.21. Additionally, one hybrid CFRP patch was also included in each higher ETR group to study the impact of hybridizing higher and lower modulus CFRP on the fatigue life, compared to the plain CFRP patches. In each hybrid CFRP patch the first layer was provided of higher modulus CFRP (Sika Carbodur) while the rest of upper layers were of the lower modulus CFRP (SikaWrap Hex), with the main intension of keeping higher modulus layer closer to the steel plate. The other reason for this sequence was also the practical limitation of pasting a fabric kind of CFRP over a flat finished stiff CFRP plate compared to pasting the stiff CFRP plate over rough finished fabric type CFRP. Adhesive properties were not much varied in the two higher ETR groups, although the adhesives for two basic types of CFRP used were already different but specific repair patches, with identical CFRP and with different adhesives, were not included in the higher ETR groups.

5.2 Materials

Table 5.2 shows the nominal mechanical properties of steel, CFRP and adhesive used in the experimental work. Steel type used was 44W CSA G40.21 which had the nominal yield and ultimate strengths of 363 MPa and 491 MPa. respectively. Two types of CFRP used in the experimental work were having different modulus of elasticity (E_{FRP}) as can be seen in Table 5.2 and these were supplied by the Sika Canada Inc. The CFRP with lower E_{FRP} was

SikaWrap Hex 103C and it had nominal modulus of elasticity and tensile strength of 65 GPa and 850 MPa, respectively. The second type of CFRP was the Sika Carbodur Type-S which had the nominal E_{FRP} and tensile strength of 165 GPa and 2400 MPa, respectively. Mechanical properties of these two types of CFRP were also evaluated using ASTM standard D 3039. Modulus of elasticity and tensile strengths of Sika Carbodur were evaluated to be 170.12 GPa and 1715 MPa, respectively. For SikaWrap Hex 103C these were evaluated to be 69.5 GPa and 685 MPa, respectively. SikaWrap Hex 103C resembled a thick woven fabric sheet, as shown in Figure 5.1, and it had the fiber volumetric content close to 50%. Sika Carbodur had fiber content close to 70% and resembled a thin stiff plate, as shown in Figure 5.1. All adhesives or epoxy resins were two-components and were mostly specified by the supplier for each CFRP type. But in some specimens these were selected to study the impact of variation of the adhesive properties. Adhesive Sikadur 300 had elastic tensile modulus of 1724 MPa and tensile strength of 55 MPa and it was the recommended adhesive and impregnating resin for the SikaWrap Hex 103C. Similarly adhesive Sikadur 330 was also one of the recommended adhesive for the SikaWrap Hex 103C, with tensile strength of 30 MPa. Its tensile modulus of elasticity was not provided in the supplier's information so it was taken from CCLAB report (2005) and is shown in Table 5.2. Adhesive Sikadur 30 was a thick cementitious-mortar type adhesive, having tensile modulus and tensile strength of 4500 MPa and 25 MPa, respectively and it was the recommended adhesive for the CFRP Sika Carbodur.

It is important to mention here that the ETR of one layer of higher E_{FRP} Sika Carbodur was approximately equal to the ETR of three layer of lower E_{FRP} CFRP SikaWrap Hex. In other words applying one layer of Sika Carbodur was approximately equivalent to applying three layer of SikaWrap Hex, in terms of the repair axial stiffness (ETR).

5.3 Specimen details, instrumentations, test setup and test procedure

5.3.1 Specimen's details

Geometry of the test specimen was conforming to the ASTM E647 standard for tension-tension fatigue testing. Specimen length was selected to be greater than the minimum required by the ASTM E647 and additionally satisfying the minimum effective bond length criteria

mentioned in previous researches (Kennedy and Cheng 1998, Lam and Cheng 2008). The minimum effective bond length criterion provided by Lam and Cheng (2008) was also conforming to the lap length required to develop maximum joint capacity of double lap bonded joints as predicted by Hart Smith (1973). The length of specimen was selected to be 500 mm, which was more than the minimum required by the ASTM E647 and it could also accommodate the bond lengths more than the minimum effective bond length. Specimen's width was selected to be 100 mm in order to match exactly the supplied width of Sika Carbodur strip. It was also satisfying the ratio of half-length to the width of 1.85, as required by the ASTM E647. Thickness of specimen was selected to be 9.5 mm (3/8 inch) because of its local availability as well as it was within 1/20 to 1/4 of the width, as required by the ASTM E647. Details of a typical test specimen, with and without the bonded CFRP patch, are shown in Figure 5.2. A starter notch 5 mm long, conforming to the notch requirements of ASTM E647, was also provided at the mid-length of one of the longer side of the specimen. The notch was cut using the electrical discharge method (EDM) and is also shown in Figure 5.2.

5.3.2 Instrumentations and test setup

Strain gauges were used to monitor the strains in the CFRP patch and an extensometer was used to monitor the COD of the edge crack, these are schematically shown in Figure 5.3. Extensometer with 10 mm gauge length was used to monitor the COD due to unavailability of proper COD clip gauge. Locations of strain gauges were selected mainly to monitor the initiation and propagation of patch delamination, in addition to getting the indication of the crack propagation (at some locations) through straining of the CFRP patch. A series of strain gauges were installed at the center of specimen over the CFRP patch, along the expected crack propagation direction, with practically possible closed intervals. These strain gauges were installed on both faces of the specimens and these are shown in Figure 5.3 as the crack-region strain gauges. These strain gauges were used mainly to get the indication of initiation and propagation of the patch delamination as well as the straining of CFRP due to the movement of crack tip beneath the patch. It is also important to mention here that the increase in crack length with number of fatigue load cycles was measured throughout in the tests using the beach mark load-cycles and the data from crack-region strain gauges was mainly helpful in getting indication of increase in crack opening or of the propagation of patch delamination.

The names of these strain gauges were 5 mm, 25 mm, 50 mm and 75 mm and these were directly showing their distance from the plate edge containing the crack. The gauge 5 mm was installed at approximately 5 mm from the cracked edge of the plate and the gauge 25 mm was installed at 25 mm from the same plate edge and so on. Strain gauges were also installed at the ends of the bonded CFRP patch to monitor initiation of patch-end delamination. Additionally, strain gauges were installed at the mid bond length to capture the propagation of patch delamination, either from the crack region towards the patch-end or from the patch-end towards the crack region. It is important to mention here that a constantly decreasing strain reading from a strain gauge mounted at the CFRP patch was expected to indicate the progression of delamination of the CFRP patch beneath it. One strain gauge was also installed at the 9.5 mm edge of steel plate, opposite to the edge containing the crack, and it is mentioned as edge strain gauge in Figure 5.3. The strain gauges at both faces of the specimens were identical but in some specimens lesser number of strain gauges used at one face within the crack region, compared to the other face, but the mid-region and the end-region strain gauges were identical on both the faces.

The test setup is shown in Figure 5.4 which shows the test specimen gripped vertically in servo-hydraulic MTS-1000 machine, whose capacity was close to 1000 kN and it was capable of applying repeated loading with frequency of 25 Hz., although the frequency used in the tests was 4 Hz. A data acquisition system was also externally attached with the MTS-1000 to record the data from strain gauges and extensometer.

5.3.3 Test procedure

The test procedure was basically consisted of three major phases, pre-crack phase, CFRP bonding & curing phase, and, repaired specimen testing phase. In the pre-crack phase the specimens were provided with a 5 mm long starter notch using electric discharge method (EDM). These specimens were then fatigue loaded to originate a sharp 5 mm long fatigue crack from the starter notch so that the total notch plus fatigue crack became 10mm, as shown in Figure 5.2. After achieving total crack length of 10 mm the specimens were removed from the test frame for pasting of the CFRP patch. The crack length of 10 mm was then treated as the initial crack length for all the repaired specimens. A view of one of the repaired specimen

in the MTS grips with all the instrumentations on it is shown in Figure 5.4. Fatigue loading applied in the pre-crack phase as well as in the repaired phase had the stress range $\Delta\sigma$ of 180 MPa and stress ratio (R) of 0.1, as schematically shown in Figure 5.5. In repaired phase additional beach-mark load cycles were inserted within the large fatigue load cycles to achieve the track of crack tip movement from the inspection of the failed steel surface after the test.

Before CFRP bonding, all specimens were sand blasted to remove the mill scale and cleaned thoroughly with acetone. CFRP was cut into desired lengths and sizes using scissors and saw, depending upon the type of CFRP, and was applied following the supplier's instructions. CFRP with lower E_{FRP} (Sikawrap Hex 103C) was cut to the desired sizes using sharp scissors and cleaned with acetone before applying to the steel plate. To minimize the risk of patch-end delamination by the peel stress the CFRP layers were cut in decreasing sizes to form tapering at the patch end, as shown in Figure 5.6. The taper step required for the 1.1 mm nominal thickness of one layer of the lower Sikawrap Hex 103C was calculated to be at least 12.5 mm, to maintain the taper angle less than 5^o as recommended by Baker (1988). But in the thickest patch having total 18 layers of the lower E_{FRP} CFRP (9 on each face of the plate) the taper angle was compromised for the upper 6 layers to avoid these layers becoming too short and the angle was provided to be 7.8^o instead of 5^o. However, it was maintained to be 5^o in the initial 3 layers close to the steel interface.

The lower E_{FRP} patch was applied to the sand blasted and cleaned steel plate surface using wet-on-wet procedure. Each CFRP layer was applied to the steel plate or to the previous CFRP layers after soaking it into the adhesive, with continuous application of hand rollers to remove any air bubble inside the adhesive or CFRP patch. Different steps involved in the CFRP laying procedure are shown in Figure 5.7, including the adhesive-resin mixing, CFRP soaking and application of hand rollers during the CFRP application. The shiny surface of steel plate appeared in Figure 5.7 was because of the sand blasting. After application of all the CFRP layers to one face of the steel plate these were left undisturbed for at least 24 to 48 hours and then the process was repeated for the other face of the plate. After completion of the CFRP bonding process on both faces of the specimens these were left for curing for a minimum of 15 days, although the average minimum curing time noted in the current experimental work was approximately four weeks.

The CFRP Sika Carbodur didn't require impregnation as it was already prefabricated and cured and it was just needed to be bonded to the steel plate. These were also cut to the desired size, with due consideration of the tapering requirements, using sharp saw because of being harder and stiffer. In addition to providing the tapering steps at the patch-end, the Carbodur sheets were additionally ground at their ends to form inclined tapered edge within their own thickness, as shown in Figure 5.8. Higher E_{FRP} plates were then bonded to the cracked steel plate using their recommended adhesive Sikadur 30. A hopper was fabricated to achieve the specified adhesive thickness of 2.5 mm by the supplier (Sika Carbodur Manual 2012).

The CFRP plates were first cut to the required size using sharp saw and were ground at their ends to make the taper-ends. These were then cleaned with acetone to remove any loose carbon fibers and dust. Two-part adhesive Sikadur 30 was prepared following the supplier's instructions and applied at the pre-cracked, sand blasted and cleaned steel plate. The fabricated hopper was then slide over the adhesive mortar to make its thickness uniform and close to the required, while the excess adhesive was removed through sliding of the hopper. CFRP plate was then pressed over the adhesive layer with small hand pressure and then tapped with the rubber hammer to remove any air bubble. Finally, a hard hand-roller was rolled over the CFRP surface with sufficient hand pressure to further press it until the adhesive popped out from all around the CFRP edge.

After bonding the CFRP plate to one face of specimen, it was left undisturbed for at least 24 hours to set under small pressing pressure of light steel washers and nuts. After 24 hours, the specimen was overturned and the same process of bonding CFRP plate was repeated on the other face of specimen. After completion of bonding process, the specimens were left for curing for at least 3 weeks before start of any instrumentation or test. Figure 5.9 shows the prepared specimens of both types of CFRP.

After completion of the bonding and curing phases, strain gauges and extensometer were installed at their desired locations, as shown in Figure 5.3. The instrumented specimens were again loaded under fatigue loading, with $\Delta\sigma$ of 180 MPa and stress ratio of 0.1. Fatigue loading continued until the COD readings started to increase, indicating start of propagation of the crack. After which the beach-mark load cycles were inserted in the loading procedure along with the large fatigue load cycles. The beach-mark load cycles were having half the

stress range ($\Delta\sigma$) of the full load cycles but having the same σ_{max}, as shown in Figure 5.10. The number of beach-mark cycles was varied from 5000 to 1000 and the total number of beach-mark sets within a single test was varied from 4 to 12. The number of beach-mark cycles used in each test was dependent upon the condition of the specimen. If the specimen was near the failure, as indicated by faster rate of increase in the COD readings, then the lower number of beach-mark cycles (i.e. 1000) was provided. But if the COD readings started to increase with a slower rate than the larger number of beach-mark cycles (i.e. 5000) were provided. Similarly, the number of beach-marks per specimen was also varied depending upon the condition and failure rate of specimen, but a minimum of five beach marks were initially planned per specimen. Some specimens achieved longer fatigue life with a stable and slower rate of increase in the COD readings and thus these specimens were able to be provided with 10 to 12 beach marks, while those specimens in which the rate of increase in COD was very fast then the number of beach marks were limited to 4.

Two control specimens, without any CFRP patch, were included in the testing program, which were tested under same fatigue loading as that of the repaired specimens, as shown in Figure 5.10. The control specimens were having the initial 5 mm EDM notch, and the fatigue loading was applied to generate and propagate the fatigue crack until their complete failure. The fatigue behavior of control specimen was normalized to 10 mm crack length, or, in other words, its fatigue life was considered after the crack length became 10 mm. In order to evaluate CFRP repair efficiency the fatigue life of each CFRP bonded specimen was compared to the normalized fatigue life of the control specimens, since all the repaired specimens were having the starter crack length of 10 mm before the repair patch was applied to them.

5.4 Test results

Test results are presented for all the tested specimens under the broad categories of three ETR groups. The results mainly included fatigue behavior, the a-N curve (crack length versus the number of fatigue cycles) and the COD variation. The a-N curve for each specimen was developed from the knowledge of the beach-marks location on the failed steel surface and their correlation with the fatigue cycles. The beach marks were studied on the failed steel

surface through a magnifying glass. COD data was deducted from the data output of the extensometer by further multiplying it with its gauge length. Additionally, strain outputs from the strain gauges are also provided to get an idea about the initiation and propagation of patch delamination, which would be indicated by declining strain readings. CFRP strain out-puts were not only helpful in indicating the instantaneous CFRP patch delamination but also in tracking the delamination propagation direction when the strain output of the whole face of specimen was studied with respect to increasing fatigue load cycles.

5.4.1 Test results of ETR 0.21 group

All specimens of the current testing program were failed by the progressive patch delamination from the steel-patch interface without any failure in the CFRP or upper adhesive layers. After studying the location of beach marks from the failed steel surface and correlating these with the beach mark cycle's set count, the a-N curves were developed for each specimen. Crack length versus the number of fatigue load cycles (a-N curves) of all specimens of ETR 0.21 group is shown in Figure 5.11 along with the results of control specimen. Since the fatigue life of the two control specimens (normalized for 10 mm starter crack) were differ by 15%, so, the results of Control-2 specimen have been used here in all further comparative study as it achieved higher fatigue life than the Control-1 specimen.

Figure 5.12 shows the failed surfaces of the specimens of ETR 0.21 group, highlighting the beach marks on failed steel surface, resulting from the beach mark cycles. Fatigue life of all specimens of the ETR 0.21 group is also summarized in Table 5.3, along with their repair efficiencies. The repair effectiveness was the ratio of fatigue life of any repaired specimen to the fatigue life of control specimen, normalized for the 10 mm crack length. The contents of Table 5.3 are further elaborated in bar-chart form in Figures 5.13 and 5.14, respectively, for the fatigue life and the corresponding repair effectiveness of each specimen. Figures 5.11, 5.13, 5.14 and Table 5.3 show that the specimen 3SKWRP-Sk330 achieved the maximum fatigue life of 229,260, which was approximately 14 times higher than the fatigue life of the control specimen. Figures 5.11, 5.13 and 5.14 further show that the specimen 3SKWRP-Sk300 achieved 188,375 fatigue cycles, which was 12 times higher than the fatigue life of the control specimen. It is important to note that both the specimens were provided with identical

ETR and CFRP modulus but different adhesive properties yielded the difference in their fatigue life or repair effectiveness by 18%. Similarly, the repair effectiveness of specimens 1CBDR-Sk-30 and 1CBDR-Hf-Sk-30 were found to be 9 and 11 respectively, which approximately differ by 18%. These two specimens were having identical ETR and CFRP modulus but with the adhesive thickness in later specimen was provided to be 50% of the former. Shortest fatigue life of 47,873 was achieved in specimen 1CBDR-Sk-300, which made its repair effectiveness 3. It was because of improper bonding of CFRP with the steel plate and it is discussed in detail in the individual results of the specimen in subsequent sections.

A visible conclusion can also be drawn from Figures 5.11, 5.13 and 5.14 that the specimens having the lower E_{FRP} CFRP type (i.e. SikaWrap Hex 103C) achieved more fatigue life and showed better fatigue performance than the specimens with the higher E_{FRP} CFRP type (i.e. Sika Carbodur). The main reason of their better performance might not solely be the E_{FRP} of the CFRP but it might also be related to the different failure modes as well as different adhesive properties. It will also be discussed in later part of the current chapter.

COD variation in the tested specimens of ETR 0.21 was evaluated from their extensometer data by further multiplying it with the gauge length and it is also shown in Figures 5.15 and 5.16. These two figures are similar but having a little difference. Figure 5.15 represents the COD variation from the start of test till near-failure situation, the instant when the extensometer was removed from the specimen to avoid its damage. Figure 5.16 shows the COD variation from the start of test till the instant just before the rapid increase in the COD was started. Comparison of Figures 5.11, and 5.15 shows similar trend of variation of crack length and COD.

Impact of progressive patch delamination around the crack on COD was further analyzed in detail at three different stages of the fatigue life of each specimen. These three stages included the start of fatigue life, the middle of fatigue life and near the end of fatigue life. The early stage corresponded to the 10% of fatigue life, the middle stage corresponded to 50% of fatigue life and the final stage corresponded to the 95% of the fatigue life. These stages were selected in order to compare the COD of different specimens at different stages, which might also be related to the patch delamination initiation and its rate of progression around the crack. Figure 5.17 shows the effectiveness of each repair in reducing the COD of plain steel plate by

comparing it to the COD of control specimen at the three selected stages of the fatigue life. The reduction in COD at the three stages might also be reflecting the rate of patch delamination, as it was expected that the patch delamination increases the rate of crack growth and the COD.

After having an overview of the fatigue life, crack length versus fatigue load cycles and the COD variation, the data output from the CFRP strain gauges are presented in detail in the next section to have more detailed information about the initiation and propagation of the patch delamination in the specimens of ETR 0.21. It is important to mention that the strain output corresponding to the peak stress within each fatigue cycle is shown in the detailed strain output for each strain gauge, because the adhesive failure or the patch delamination was expected at the maximum stress within a complete stress cycle.

5.4.1.1 Specimen 1CBDR-Sk-300

1CBDR-Sk-300 was found to be the least effective repair in the current test group. It increased the fatigue life of the repaired specimen by 3 times compared to the unpatched specimen and achieved only 47,873 fatigue cycles. The main reason was found to be improper bond of the higher modulus CFRP with the steel, which resulted in very early delamination of half of one face of the repair patch.

Figure 5.18 shows the strain output of the four strain gauges installed at the four patch-ends, and 5.19 shows the strain output of the four strain gauges installed at the four mid-bond-length locations, on both faces of the specimen. Figure 5.18 shows that the delamination started quite early from the upper end of the front face of patch, i.e. within 5000 fatigue cycles, which is indicated by the high rate of strain dropped in these gauges, which quickly reached to zero. Figure 5.19 shows that the delamination, already started from the front-face upper end, reached the mid-bond-length in very small number of fatigue cycles. At about 7500 fatigue cycles; the front face upper portion had already been delaminated by more than 50%. A loud delaminating sound was also heard at that stage in the test and a large portion of the upper half of front face was found to largely delaminated. Figure 5.18 further shows that the back face

patch-end strain gauges were then started showing delamination at about 25000 fatigue cycles, which meant that all the four ends of the CFRP patch had delaminated by that time. Figure 5.19 shows that the mid-bond-length strains at the back face were mostly delaminated at about 45000 cycles or close to the final failure.

Figures 5.20 and 5.21 show the strain output of the near-crack regions, respectively at the front and back faces. Figure 5.20 shows that the front face strain gauge at 5 mm from the plate edge started to delaminate at about 4000 fatigue load cycles while the remaining front-face strain gauges were also started delaminated soon after it. By 10000 fatigue cycles all these strain gauges had shown delamination signs, and thus it is believed that the upper half of the front face patch was largely delaminated by 10000 fatigue cycles. It was expected that after the large delamination in the upper half of front patch there would have been lesser constraint to the crack growth, which then resulted in faster crack growth rate as reflected in the a-N curve of this specimen in Figure 5.11. Figure 5.21 shows that the back face strain gauges were working till the end of the test with constant strain, showing less sign of delamination. But near the end of test these showed a rapid increase in their strain readings indicating the final stage of the test. At that stage the front face had already been delaminated and the back face was just left with a small bonded central portion, as the mid-region gauges were also delaminated at approximately 40000 fatigue cycles.

The bonded central portion which contained the back-face crack-region gauges was finally delaminated with a large sound, indicated by the rapid increase and then sudden decrease in the strains of these gauges in Figure 5.21. It is also important to note from the Figure 5.11 and the Figures 5.18 through 5.21 that the specimen took approximately 5000 more fatigue cycles after the bonded CFRP patch was delaminated by huge amount from the two half portions of its two faces. Figure 5.22 shows the strain output from the strain gauge installed on the edge of steel plate just opposite to the notched face and it was the only strain gauge which was installed on the steel plate. Figure 5.22 shows that the strain in steel plate was little bit increased in the early stages of the test because of the delamination of the CFRP patch in its surrounding, resulted in transfer of stress from patch to the plate. After that, the strain approximately remained constant throughout the test before the failure stage. Near the failure stage, with excessive patch delamination, the strain dropped at this edge of steel plate,

probably because of the in-plane bending of the specimen, introducing compressive stress on this side. Just in the last few hundreds cycles the strain reversed back to tensile because the failure happened in tension and resulted in complete failure of the specimen in two pieces.

After complete failure of the specimen into two pieces, close examination of the delaminated surface of CFRP showed the impression of numerous air bubbles on it showing the lack of proper bond between steel plate and the CFRP patch. It is important to mention that the adhesive Sikadur 300 used in this repair was actually not the recommended adhesive for the CFRP Carbodur and the only reason of making this repair was to study the impact of using different adhesives with higher E_{FRP} CFRP. However, due to lack of bonding between the patch and steel plate, it is believed that the results of this specimen could not be compared with the results of other specimens. The main reason of improper bonding between the Carbodur and steel plate was expected to be the existence of numerous air bubbles in the bond. These bubbles could not be removed during the specimen preparation because of the higher stiffness of the CFRP plate and lower viscosity of the adhesive which resulted in flow-out of the adhesives from all sides during rolling, thus leaving air bubbles inside. Figure 5.23 showed the delaminated surface of CFRP and the broken specimen after the test with clear marks of small and large air bubbles on it.

5.4.1.2 Specimen 1CBDR-Sk-30

The specimen ICBDR-Sk-30 was fabricated with higher E_{FRP} CFRP (Carbodur) and its recommended adhesive Sikadur 30. The nominal adhesive thickness for this adhesive was recommended to be 2.5 mm to 3 mm in the supplier's data sheets, which is quite thick compared to the other adhesives used in this testing program. Figures 5.24 and 5.25 show the strain outputs of the strain gauges mounted at the patch-ends and the mid-bond-lengths, respectively. It is obvious from Figure 5.24 that early patch delamination was started from the lower end of front face patch and the upper end of back face patch, followed by the delamination from the rest of the other two patch-ends. Figure 5.25 shows that the delamination that had started from the two opposite ends of the two opposite faces of repair patch, reached nearly the mid-bond-length of the same two faces at about 80000 fatigue cycles. The delamination at the mid-bond-lengths of other two sides of the patches reached at

120000 and 165000 fatigue cycles, respectively. It showed that only the upper portion of the front face patch, which took 165000 fatigue cycles, remained bonded till the end of test.

Figures 5.26 and 5.27 show the strain output of the near-crack region strain gauges, respectively at the front and back faces of specimen. These two figures show that the front face delaminated earlier and suffered with more delamination than the back face. The earlier initiated delamination of front face near-crack region was expected to be caused by the delamination already progressing from the lower end of front face. That delamination had already crossed the mid-bond-length at about 80000 fatigue cycles and it was then most expected to affect the near-crack region. It can also be concluded from these figures that the crack growth at any instant could not be accurately judged from these strain outputs because of several reasons, including the gauge length of the strain gauges and the surrounding delamination. The gauge length of strain gauges was 5 mm and it was much larger than the crack opening beneath it. Therefore, it could be possible that the instant when the crack tip passed beneath any gauge the strain in it not changed by a huge amount because of the large portions of the strain gauges remained bonded to the steel plate. Similarly, there might also be an additional but opposite impact of the patch delamination in the surrounding of gauge, caused by the advancing delamination from the patch-ends. Therefore, it might be possible that the strain in a gauge was actually increasing due to the crack opening but at the same time the surrounding delamination have reduced it.

Figure 5.28 shows the strain output from the strain gauge installed on the 9.5 mm edge of steel plate, opposite to the starter notch. Figure 5.28 shows that the strain mostly remained constant throughout the test and it started to drop after approximately 140,000 fatigue load cycles. It can also be noted from Figures 5.26 and 5.27 that at the same cycle count the strain in the near-crack region strain gauges started to drop by a faster rate, showing that the patch-end delamination might have reached close to the near-crack region. It is also interesting to note from Figure 5.15 that the COD had also started increasing at a faster rate around same cycle count due to the excessive patch delamination. These strain conditions showed that the crack must also have started propagating with faster rate at this stage, which then resulted in the in-plane bending of plate. The in-plane bending of plate released the tensile stress from the face at which the edge strain gauge was mounted, which is also indicated from the drop in its strain

readings in Figure 5.28. The strain in edge strain gauge eventually dropped into compression close to the failure of specimen. But it then again reversed back into tension during the last failure cycles because the failure occurred in the tensile part of the cycle.

Lesser fatigue cycles appeared in the strain dropping region of the edge strain gauge shows that the surrounding patch was remained bonded in most of the fatigue life. But then around 140,000 fatigue cycles the surrounding patch region started to delaminate at a faster rate, and within a small number of fatigue cycles it delaminated completely from one face. The specimen's un-cracked portion (ligament) then became extremely thin and it finally broke in tension into two pieces. This repair achieved 171,992 fatigue cycles till complete failure and it was successful in enhancing the fatigue life of the repair by approximately 11 times, compared to the unpatched specimen, as already shown in Figures 5.11 through 5.14.

Figure 5.29 shows the delaminated surfaces of CFRP and steel after the test, which shows a very thin layer of adhesive remained on the delaminated steel surface. Bare steel surface is also visible within some localized regions in Figure 5.29. It shows that the delamination mostly occurred at the adhesive-steel interface, involving adhesive layer. Figure 5.29 also confirms that a pure bond failure was not occurred, which would otherwise be reflected by a bare steel surface all over.

5.4.1.3 Specimen 1CBDR-Sk-30/2

This specimen was identical to the specimen 1CBDR-Sk-30 except that the adhesive thickness was provided half of the adhesive thickness provided in 1CBDR-Sk-30. The recommended thickness of adhesive Sikadur 30 was ranging from 2.5 mm to 3 mm, therefore, the desired adhesive thickness in current specimen was 1.25 mm to 1.5 mm, and it was achieved by decreasing the height of the spatula developed for the specimen 1CBDR-Sk-30. The as built thickness of adhesive layer, as calculated from the difference of thickness between the finished specimen and the Carbodur plate, was noted to be 1.7 mm. It was approximately 13% higher than the planned nominal thickness of the adhesive layer in this specimen.

Figures 5.30 and 5.31 respectively show the strain output of the strain gauges installed at the patch-ends and the mid-bond-lengths locations of the CFRP patch. Figure 5.30 shows that the

patch delamination was started early from the lower end of front face and upper end of back face. Figure 5.31 shows that the initiated delamination didn't progress into the mid-bond regions of any face till the end of test, as indicated by a constant strain level in these strain gauges. It was initially supposed to be beneficial for enhancement of fatigue life of the repair but surprisingly this repair achieved lesser fatigue life then the 1CBDR-Sk-30, in which the patch-end delamination had even reached the mid-bond-length.

Figures 5.32 and 5.33 respectively show the strain output of strain gauges at the near-crack regions of front and back faces, which show initially constant strains in these gauges. The strain then started increasing at the two faces. One more observation from these figures was the increase in strains with respect to the distance of strain gauge from the crack edge, i.e. strain in the gauge at 5 mm from the crack edge started rising first, followed by the rise in strain of gauges at 25 mm, 50 mm and 75 mm from the crack edge. The rise in strain in the CFRP was expectedly due to combined effect of crack opening and the localized patch delamination right beneath the strain gauge. Extremely localized patch delamination, right beneath the strain gauge, could result in the transfer of stress from steel plate to the CFRP patch, thus, increasing the CFRP strain. Similarly, increase in the crack opening could also results in more straining in the CFRP right above it. It is important to note that this delamination was different than the patch-end delamination in which case the delaminated patch-end just became stress free after being delaminated completely.

It can be interpreted from Figures 5.32 and 5.33 that the increase in the crack length can be reflected by the increasing strains in the gauges on the patch right above the crack if the surrounding region does not delaminate. The delamination situation in the surrounding of near-crack region can be obtained from the strains in the mid-bond-length strain gauges and Figure 5.31 shows no sign of delamination in the mid-bond-length strain gauges. Therefore, it confirms that the strain in the near-crack region was increased because of the localized near-crack patch delamination, followed by the propagation of crack in steel. Increased crack length then increased the COD, which further increased the strains in the patch. Fast rate of crack opening was already shown Figures 5.15 through 5.17. Therefore, because of more near-crack delamination and rapidly increasing COD, faster crack propagation resulted in this specimen, and finally the failure occurred in it with breaking of the specimen in two pieces.

Due to faster crack propagation rate the fatigue life of this specimen was lesser than the specimen 1CBDR-Sk-30. Figure 5.34 shows strain output from the strain gauge installed on the 9.5 mm edge of steel plate, opposite to the face having starter notch. It shows a big region of decreasing strain before failure because of faster crack growth in this specimen, which resulted in bending of the specimen, thus reducing the tensile strains in the extreme edge of the specimen.

This specimen achieved total 150,336 cycles before failure, as already shown in Figures 5.11, 5.13 and 5.14. This repair patch increased the fatigue life of unpatched specimen by approximately 9 times. Fatigue life enhancement of this specimen was better within the ETR 0.21 group. But comparing the results of this specimen and 1CBDR-Sk-30 also showed that thinner adhesive may not always be helpful in enhancing the fatigue life of a repair. The results are also somewhat opposite to the common understanding in some previous research works. Figure 5.35 shows the failed specimen and the delaminated surfaces of CFRP and steel. These surfaces show similar patches of very tiny holes in the adhesive surface as that found in the specimen 1CBDR-Sk-30. Figure 5.35 also shows some thicker adhesive portions remained stuck with the steel surface, with some marks of the CFRP matrix on these, because no fiber was found in these marks on the adhesive surface.

5.4.1.4 Specimen 1CBDR-Sk-330

This specimen was fabricated using higher E_{FRP} Carbodur plate, bonded using the adhesive Sikadur 330. The adhesive was not recommended for this type of CFRP but it was used in this specimen to study the impact of variation in adhesive properties on the fatigue life of repair. Unfortunately, the specimen couldn't reach the complete failure because of an accidental increase in the applied load, caused by some problems in the operating software. The accident happened when the first beach mark cycle was being provided. The applied load accidently reached a huge value of 337 kN instead of the maximum cycle load of 190 kN. The huge load actually applied a stress of 355 MPa, instead of the desired 200 MPa, and it resulted in a large delamination of the CFRP patch at one face of the specimen. The specimen was then unloaded and removed from the test frame because of any unknown crack growth, which might have occurred in the specimen during the large accidental load.

It is important to note that this specimen achieved approximately 147,530 fatigue cycles before the accidental increase in the load, but, that number of fatigue cycles was approximately equal to the total fatigue life of the specimen 1CBDR-Sk-30/2. In other words this specimen could have achieved higher fatigue life than the other specimens of higher E_{FRP} CFRP if the accidental increase in load not happened. This repair enhanced the fatigue life of the cracked specimen by 9 times even after being suffered with a pre-mature accidental failure, which indicates that if the accidental failure not happened then this specimen could have shown more higher efficiency.

Figures 5.36 and 5.37 show the strain outputs of the strain gauges installed at the patch-end and the mid-bond-length, respectively. Figure 5.36 indicates that the patch delamination was started from the lower end of the front face and upper end of the back face of the patch. Figure 5.37 shows signs of start of the delamination in some of the mid-bond-length gauges but not in all. Figures 5.38 and 5.39 show the strain output of the strain gauges mounted at the near-crack regions, respectively on the front and back faces of specimen. These show very small signs of patch delamination because of having nearly constant strains. Figures 5.38 and 5.39 also show that the strain in the strain gauge at 5 mm from the edge was higher throughout than the rest of the gauges, which might be because of the localized grinding of the FRP surface while setting the extensometer near this gauge. Similarly, Figure 5.40 shows the strain output from the strain gauge installed at the 9.5 mm face of steel plate, opposite to the starter notch. The figure shows that the strain in steel plate was remained constant till the accidental end of the test. It also reflects that there must have been negligible surrounding patch delamination to this strain gauge, up to the instant of accidental load increase. Figure 5.41 shows the unbroken specimen 1CBDR-Sk-330 removed from the test frame.

5.4.1.5 Specimen 3SikaWrap-Sk-300

This specimen was provided with the lower E_{FRP} CFRP, the SikaWrap Hex 103C, and it was provided with three layers of the CFRP sheet on each face. The adhesive used in it was Sikadur 300, which was the recommended epoxy for it by the supplier. This adhesive also served as an impregnating medium in addition to bonding. The supplier's information showed that this adhesive has the tensile strength and tensile modulus of elasticity of 50 MPa and

1724 MPa., respectively. The specimen showed quite stable behavior throughout the test, without any sign of delamination at the patch ends or at the mid-bond-lengths, as indicated from the strain output in Figures 5.42 and 5.43, respectively for the patch-ends and mid-bond-lengths locations. Strain output of the near-crack region strain gauges are shown in Figures 5.44 and 5.45, respectively for the front and back faces of the specimen. These figures show that the crack had propagated by the localized patch delamination within the near-crack region, similar to the specimen 1CBDR-Hf-Sk-30. The strain in these gauges rose one after the other, caused by localized patch delamination beneath these gauges, similar to the specimen 1CBDR-Hf-Sk-30. Figure 5.46 shows the strain output from the strain gauge installed at the 9.5 mm face of steel plate, opposite to the starter notch. It shows that the strain remained approximately constant there until 60% of the fatigue life, indicating a good bond between steel plate and CFRP patch. The strain then started decreasing with slow rate after 70% of the fatigue life, and then with a faster rate after 87% of the fatigue life. After the crack became bigger due to more delamination in the near-crack region, in-plane bending started in the specimen. Figure 5.46 shows that the strain in the 9.5 mm edge strain gauge then dropped into compression due to excessive bending of the specimen and it then reversed back into tension rapidly in the final stages of the test because the failure occurred in tensile part of the fatigue load cycle.

This specimen achieved 188,375 total fatigue cycles till complete failure of the specimen as already shown in Figures 5.11 and 5.13, which was more than achieved by the specimens of higher E_{FRP} Sika Carbodur. Figure 5.14 shows that this CFRP patch increased the fatigue life of plain specimen by 12 times, which was 33% more than achieved by the specimens 1CBDR-Sk-330 or 1CBDR-Hf-Sk-30 and 10% more than that achieved by 1CBDR-Sk-30. Figure 5.47 shows the delaminated surfaces of CFRP and steel plate after completion of the test. It is obvious from Figure 5.47 that the delaminated steel surface shows no marks of the adhesive on it and appears as the bare steel surface prior to the application of the CFRP patch. The CFRP surface shows a very thin layer of adhesive still remained on it after the delamination. The surface conditions of steel and CFRP, after the delamination, show that the delamination mainly occurred at the adhesive-steel interface rather than the adhesive-CFRP interface but after a good enhancement in the fatigue life of the repair.

5.4.1.6 Specimen 3SikaWrap-Sk-330

This specimen was the second in the ETR 0.21 group which was provided with three layers of the lower E_{FRP} CFRP sheets on its each face, similar to the 3-SikaWrap-Sk-300. The adhesive used in this specimen was Sikadur 330, which although is a recommended impregnating resin for this type of CFRP but it is mostly recommended as a primer and for overhead or vertical applications of the CFRP sheets. It was included in the experimental phase to study the impact of different adhesives on the fatigue life of repair, while keeping identical CFRP type. Supplier's information showed its tensile strength to be 30 MPa, which is 40% less than that of adhesive Sikadur 300. The tensile modulus of elasticity E_A of this adhesive was not provided in its technical information but tests by Julia de Castro (2005) showed that this adhesive has the tensile modulus of 4.5 GPa.

This specimen showed good fatigue behavior but suffered with patch-end delamination at the front face and later on at the back face as indicated by the strain output of patch-end strain gauges in Figure 5.48. Similarly, the strain out-put data of mid-bond-length gauges, as provided in Figure 5.49, shows that the delamination did not start in most of these strain gauges till the end of test. Only the strain gauge at front patch shows the propagation of the patch-end delamination into the mid-bond-length location. Figures 5.50 and 5.51 show the strain data of the crack region strain gauges, respectively for the front and back faces and these shows similar strain output as found in the specimen 3-SikaWrap-Sk-300. From these figures, it could be judged that the patch-end delamination didn't reach the near-crack region. The crack propagation in this specimen was expected to occur through localized small delamination around the crack, resulting in increased COD. The increase in COD as well as in the crack length further resulted in increased strains in the near-crack region strain gauges. The sequence of increase of strains in the near-crack region strain gauges in Figures 5.50 and 5.51 was similar to the specimen 3-SikaWrap-Sk-300. It indicates the progressive propagation of the crack tip beneath these strain gauges.

Figure 5.52 shows the strain in the 9.5 mm wide steel face, opposite to the starter notch. Figure 5.52 shows that the strain was approximately remained constant for the 65% of fatigue life of the specimen. It indicates a good bond between steel plate and CFRP patch in the

surrounding of this gauge, which mainly included the near-crack region. The strain was then started decreasing with a slow rate after 78% of the fatigue life, showing some impact of the patch delamination in its surrounding. The strain was then started decreasing with a faster rate after 90% of the fatigue life, showing the impact of bending of the specimen due to much increase in the crack size. The strain then dropped to compression near the end of test but it reversed back to tension quickly just before the specimen broke into two pieces.

This specimen achieved 229,260 fatigue cycles till complete failure of the specimen, which was the maximum in the ETR 0.21 group. It was approximately 20% higher than the fatigue life of 3-SikaWrap-Sk-300. Figure 5.53 shows the specimen after failure with visible delaminated CFRP and steel surfaces. Figure 5.53 shows that the delamination mostly occurred at the adhesive-steel interface, because most of the steel surface does not show remains of the adhesive. However, some localized regions of steel surface show the remains of quite thick adhesive layer on these. Most of these thicker patches of adhesive are shown to be surrounding the starter notch in Figure 5.53 and extended to half the plate width. These patches also show some fibers remained sticking on their surface, which provides some good reasons of having higher fatigue life of this specimen. Figure 5.53 also shows better bonding of this adhesive to steel compared to the other adhesives used in previous specimens.

5.4.1.7 Impact of adhesive type on the fatigue behavior of specimens of ETR 0.21

Impact of adhesive properties on the fatigue behavior of repaired specimens was studied by comparing the results of the specimens having identical CFRP type but with different adhesive properties. For the higher E_{FRP} CFRP type, it could be studied by comparing the results of specimens 1-CBDR-Sk-300, 1-CBDR-Sk-30 and 1-CBDR-Sk-330. These specimens had identical CFRP type and the number of its layers but differed only by the type of adhesive. Unfortunately the results of the specimen 1-CBDR-Sk-300 could not be compared with other specimens because of its premature bond failure as discussed in section 5.4.1.1. Results of the remaining two specimens could be compared but up to point where the specimen 1-CBDR-Sk-330 was failed by the accidental load increase. The accidental failure happened when the specimen 1-CBDR-Sk-330 had completed 147,530 fatigue load cycles and at that point its

COD was 0.0424 mm. At the same number of fatigue load cycles the specimen 1-CBDR-Sk-30 had the COD 0.05219 mm. Therefore, the COD of specimen with adhesive Sikadur 330 was 20% lesser than the COD of the specimen with adhesive Sikadur 30.

The tensile strength, shear strength and modulus of elasticity of Sikadur 30 are reported to be 24.8 MPa, 15 MPa 4.5 GPa, respectively, in the supplier's data sheet. The tensile strength of the adhesive Sikadur 330 is reported to be 30 MPa but its shear strength and modulus of elasticity are not mentioned in its supplier's data sheet. Tensile properties of Sikadur 330 have been evaluated by Julia de Castro (2005) and published in the technical report of École Polytechnique Fédérale De Lausanne, which shows the tensile strength and tensile modulus of elasticity of Sikadur 330 as 38 MPa and 4.55 GPa, respectively. In summary, the adhesive Sikadur 330 was expected to be stronger than the adhesive Sikadur 30 and its thickness was also noted to be just 10% to 15% of the Sikadur 30. Therefore, the G/t ratio of Sikadur 330 must be at least 5 times higher than the adhesive Sikadur 30. With reference to the findings of sections 3.5.3.4 and 4.6, the SIF (K_I) in the Sikadur 330 specimen must be lesser than the Sikadur 30 specimen and that is why the specimen 1-CBDR-Sk-330 showed lesser COD. It is also obvious from the behavior of 1-CBDR-Sk-330 that it could have achieved higher fatigue life than the specimen 1-CBDR-Sk-30, but because of the accidental load increase, its test was stopped at the fatigue life of 147, 530 cycles.

Similar comparison can be drawn between the specimens of the lower E_{FRP} CFRP specimens 3-SikaWrap-Sk-300 and 3-SikaWrap-Sk-330 because both of these specimens were having identical CFRP type and were differed only by the adhesive properties. The specimen 3-SikaWrap-Sk-300 was having adhesive Sikadur 300 and achieved 188,375 fatigue cycles, while the specimen 3-SikaWrap-Sk-330 was provided with adhesive Sikadur 330 and achieved 229,260 fatigue cycles. Therefore, the specimen 3-SikaWrap-Sk-330 achieved approximately 20% more fatigue cycles than the specimen 3-SikaWrap-Sk-300. Tensile strength of adhesive Sikadur 300 was much higher than the Sikadur 330 but the tensile modulus of Sikadur 330 has been reported to be more than 3 times that of Sikadur 300 (Technical Data Sheet for Sikadur 300 and Sikadur 330 by Sika, 2013, Julia de Castro, 2005). The thickness of Sikadur 300 was noted to be 0.1 mm to 0.2 mm in the tests (from the knowledge of the thicknesses of finished specimen and the raw SikaWrap) while the thickness

of Sikadur 330 was ranging between 0.10 mm to 0.25 mm. Therefore, the G/t ratio of adhesive Sikadur 330 must be greater than twice of the Sikadur 300. Therefore, on the basis of the G/t ratios and the outcome of chapters 3 and 4, it was expected that the SIF (K_I) at the crack tip in the specimen with Sikadur 330, before any adhesive failure, must be quite lower than the specimen with Sikadur 300. After the adhesive failure (or the patch delamination) the SIF must have increased, but being quite low before the delamination, it might still be less than that in the specimen with Sikadur 300.

The evidence of this reasoning can be obtained by comparing the COD of these two repairs from Figure 5.17. Figure 5.17 shows that in the start of test, the COD of these repairs was quite similar, but after half the fatigue life the COD of 3-SikaWrap-Sk-300 specimen became 6% higher than that of 3-SikaWrap-Sk-330. Finally, near the end of test the COD of 3-SikaWrap-Sk-300 became 22% greater than the COD of 3-SikaWrap-Sk-330. The behavior of any adhesive used in the current testing program (or of their bond with steel), under fatigue loading, are not known or provided in supplier's information. But on the basis of current test results and the conclusions of chapters 3 and 4, it appears that adhesive Sikadur 330 performed better with both the types of the CFRP in the ETR 0.21 group.

5.4.1.8 Impact of adhesive thickness on the fatigue behavior of specimens of ETR 0.21

Impact of adhesive layer thickness on the fatigue behavior of the repaired specimens could be studied by comparing the results of specimen 1CBDR-SK30 and 1CBDR-SK30/2. These specimens were provided with higher E_{FRP} CFRP (Sika Carbodur) and the adhesive Sikadur 30, but these were having a difference of 40% in their adhesive layer thickness. The difference was actually planned to be 50% but due to the fabrication limitations it ended up being 60%. The as-built thickness of adhesive layer was calculated by the difference in thickness of the finished specimen and the thickness of the plain CFRP Carbodur plate. The thickness of adhesive layer in specimen 1CBDR-SK30 was found to be 2.7 mm while in specimen 1CBDR-SK30/2 it was approximately 1.7 mm. Therefore, the difference was not exactly 50% but it was approximately 60% due to the limitation of the specimen preparation methodology. Fatigue life of specimen 1CBDR-SK30 was approximately 15% higher than the specimen

1CBDR-SK30/2, as shown in Figure 5.13. The COD of specimen 1CBDR-SK30/2 was also approximately 10% higher than the 1CBDR-SK30 at all stages of fatigue life, as shown in Figure 5.17. Using the outcome of chapters 3 and 4 the difference in COD and fatigue life can be explained. The adhesive thickness in specimen 1CBDR-SK30/2 was 60% of the adhesive in 1CBDR-SK30. Therefore, adhesive G/t ratio should be approximately double in specimen 1CBDR-SK30/2 and higher shear stresses were expected in its adhesive layer, but the adhesive strength was identical in the two specimens. Therefore, the near-crack adhesive failure was expected more in the specimen 1CBDR-SK30/2, which has caused higher COD in the specimen 1CBDR-SK30/2.

Comparing the strains output of the two specimens from Figures 5.24 to 5.27 and 5.30 to 5.33, it is obvious that the strains jumped up to 3000με in the near-crack strain gauges of specimen 1CBDR-SK30/2, while it was just 900με in the specimen 1CBDR-SK30. Although the mid-bond-length strain gauges of specimen 1CBDR-SK30/2 showed no delamination sign, compared to the specimen 1CBDR-SK30. Therefore, it can be concluded that the higher adhesive G/t ratio in specimen 1CBDR-SK30/2 must have resulted in higher near-crack stresses and more adhesive failure. Because of more adhesive failure in the near-crack region of specimen 1CBDR-SK30/2, the COD was higher in it throughout the test. Due to higher COD in specimen 1CBDR-SK30/2 the crack growth rate must have been higher in it, thus resulted in lesser fatigue life. This comparison also shows that thinner adhesive layer might not always be beneficial, without considering the adhesive G/t and shear strengths.

5.4.1.9 Impact of CFRP properties on the fatigue behavior of specimens of ETR 0.21

Impact of CFRP properties on fatigue life and fatigue behavior of repaired specimens was studied by comparing the results of specimen with identical adhesive but with different CFRP types. Behavior of specimens 3-SKWRP-Sk-300 and 1CBDR-Sk-300 could be compared to study the impact of CFRP type but unfortunately the results of the specimen 1-CBDR-Sk-300 could not be compared with other specimens because of its premature bond failure as discussed in section 5.4.1.1. The other set of specimens that can be compared were the

specimen 3-SKWRP-Sk-330 and 1CBDR-Sk-330, which were having identical adhesive but different CFRP types.

Again, in this case comparison of the results was possible up to the point where the specimen 1CBDR-SK330 suffered with an accidental increase in the load. Figures 5.15 through 5.17 show that the COD of 1CBDR-SK330 was 0.0370mm when the accidental increase in the load occurred and at that stage it had taken 147,530 fatigue load cycles. COD of the specimen 3SKWRP-Sk330 at the same number of fatigue load cycles was found to be 0.047 from Figure 5.15, which is approximately 25% more than that of 1CBDR-SK330 specimen. The reason of this difference in the two might be because of more adhesive content in 3SKWRP-Sk330 as well as presence of delaminated regions at its near-crack and patch-ends. The average thickness of adhesive layer in 3SKWRP-Sk330, as noted in the tests (from the knowledge of thicknesses of finished specimen and raw SikaWrap sheet), was found to be approximately 0.15 mm while the adhesive layer thickness in the specimen 1-CBDR-Sk-330 was in the range of 0.2 mm to 0.4 mm. Therefore, higher adhesive G/t ratio was expected in the specimen 3SKWRP-Sk330 which might have caused near-crack adhesive failure and thus resulted in comparatively larger COD.

5.4.2 Test results of ETR 0.42 group

All specimens of ETR 0.42 group were also failed in the progressive patch delamination failure mode, similar to the specimens of the ETR 0.21. In this failure mode the CFRP patch was delaminated slowly from the steel plate interface without any failure in the CFRP or adhesive upper layers. The detail experimental observations and the result of ETR 0.21 specimens have already shown that the patch delamination in the tested specimens occurred either from the patch-end or from the near-crack region. But still more negative impact of the patch-end delamination was not much highlighted in the specimens of ETR 0.21 compared to that found in the specimens of ETR 0.42. It will be discussed in detail for each specimen after the presentation of overall test results and general discussion of the specimens of ETR 0.42.

Combined crack length versus the number of fatigue load cycles (a-N curves) for the specimens of ETR 0.42 group are shown in Figure 5.54, along with the results of control specimen. The crack length used to develop a-N curves in Figure 5.54 was obtained from the study of the beach marks location on the failed steel surfaces and correlating these with the beach mark cycle's counts provided during the test. Figure 5.55 shows the failed surfaces of the specimens of ETR 0.42 group, highlighting the beach marks on the failed steel surface, resulted from the beach mark cycles. Fatigue life of all specimens of the ETR 0.42 group was extracted from the Figure 5.54 and is summarized in Table 5.4, along with their repair efficiencies. The repair efficiency has been defined as the ratio of fatigue life of any repaired specimen to the fatigue life of the control specimen, normalized at the 10 mm crack length. Fatigue life and repair efficiency of each specimen is also represented in Figures 5.56 and 5.57, respectively.

Table 5.4 or Figures 5.56 and 5.57 show that the maximum fatigue life and the maximum repair efficiency of 450,559 and 28, respectively, was achieved by the specimen 6SKWRP-Sk300. Similarly, the lowest fatigue life of 56500 was surprisingly achieved by specimen 2CBDR-Sk-30, which was totally unexpected. The unexpected and very short fatigue life of the specimen 2CBDR-Sk-30 was not because of any inappropriate bond issues, but it was because of the dominated and rapid proceeding patch-end delamination failure mode. It will be discussed in detail in the subsequent individual specimen's sections. It is important to note that the patch-end delamination was also originated in the specimens of ETR 0.21, but it didn't dominate till the failure of specimens. The details of failure mode of each specimen will also be discussed in detail in the individual results of each specimen.

This ETR group also contained one hybrid patch specimen 1-CBDR-3-SkKWRP. It was provided with the first layer of higher E_{FRP} CFRP (Carbodur) and then 3 layers of lower E_{FRP} CFRP (SikaWrap Hex), on each face. Figures 5.54, 5.56 and 5.57 showed that even the hybrid specimen did not achieve better fatigue life. Although its fatigue life was more than the specimen 2-CBDR-Sk-30, but still it was 3 times lesser than the SikaWrap specimens. It is found in these figures that the fatigue life of hybrid specimen 1-CBDR-3-SkKWRP was lesser than all the specimens of ETR 0.21 (excluding the prematurely failed specimen 1-CBDR-Sk-

300). It will also be discussed in detail in the individual results of each specimen in the subsequent section.

It can also be noted from Figures 5.54, 5.56 and 5.57 that the results of two specimens of 6-SKWRP-Sk-300 are presented in these figures. It was not initially planned to have two specimens of this repair patch but because of some unintentional mishandling and improper gripping issues with the first specimen, the test was repeated. Figure 5.54 shows that the specimens of lower E_{FRP} CFRP achieved more fatigue life and better fatigue performance than the specimens of higher E_{FRP} CFRP. This result was similar to the results obtained in the ETR 0.21 group. Although the main reason of better performance of lower E_{FRP} CFRP specimens might not solely be the E_{FRP} of the CFRP. It might also be related to the adhesive properties, which will also be discussed in later part of the current section.

COD variation in the specimens of ETR 0.42 was evaluated from their extensometer data by multiplying it with its gauge length and it is shown in Figures 5.58 and 5.59. Figures 5.58 and 5.59 are similar but with a small difference. Figure 5.58 shows the COD variation from the start of test till near-failure situation, which was the instant when the extensometer was removed from the specimen to avoid its damage. Figure 5.59 shows the COD variation from the start of test till the instant just before start of rapid rate of increase in the COD. Figure 5.54 and 5.58 show similar trend of the variation of crack length and COD with the fatigue load cycles.

Impact of progressive patch delamination around the crack on COD was further analyzed in detail at three different stages of the fatigue life of each specimen. These three stages included the start of fatigue life, the middle of fatigue life and near the end of fatigue life. The early stage corresponded to the 10% of fatigue life, the middle stage corresponded to 50% of fatigue life and the final stage corresponded to the 95% of the fatigue life. These stages were selected in order to compare the COD of different specimens at different stages, which might also be related to the patch delamination initiation and its progression rate around the crack. Figure 5.60 shows the effectiveness of each repair in reducing the COD by comparing it to the COD of control specimen at the three selected stages of the fatigue life. The reduction in COD at the three stages might also be reflecting the rate of patch delamination, because it was expected that the patch delamination increases the rate of crack growth and the COD.

After having an overview of the test results in the form of fatigue life, a-N curves and the COD variation, the data output from the strain gauges are presented in detail in the next section to have a more detailed picture about the initiation and propagation of the patch delamination in the specimens of ETR 0.42 group. It is important to mention that the strain output corresponding to the peak stress within each fatigue cycle is shown in the detailed strain output for each strain gauge, because the adhesive failure or the patch delamination was expected at the maximum stress within a complete stress cycle.

5.4.2.1 Specimen 2-CBDR-Sk-30

This specimen suffered with early patch-end delamination from the upper end of patch at the front face and lower end of patch at the back face. Figure 5.61 shows the strain data of the strain gauges at the four patch-ends and it shows the sign of patch-end delamination at the two patch-ends through the declining strain output. Figure 5.61 shows that the early patch-end delamination started at about 3000 fatigue cycles from the upper end of front patch. It was also noticed by a glitch-type sound during the test. Two patch-ends are shown to be largely delaminated at about 8000 fatigue cycles in Figure 5.61, while the other two were also delaminated but still showed intact till 44,000 load cycles, but with a very low strain.

Figure 5.62 shows the strain data from the mid-bond-length strain gauges and it indicates that the delamination that had started from the upper patch-end of front face had quickly reached the mid-bond-length in just 1000 to 2000 more cycles. The delamination at the back face also reached the mid-bond-length at both of its upper and lower regions by 12,000 fatigue cycles, as found in Figure 5.62. Only the lower portion of front face showed more intact evidence from its strain output than its upper portion or the back face, and it remained intact till the end of test.

Figures 5.63 and 5.64 shows the strain data of the near-crack strain gauges, respectively of the front and back faces. It is again found in these figures that, at both the faces, early initiated patch-end delamination had reached the near crack region quickly after crossing the mid-

bond-lengths. Big portions of the lower half of back face and upper half of front face were delaminated, as visually noted and observed during the test.

It is important to note that the near-crack strain gauges were installed on each specimen in such a way that their half portions were laid on each side of the horizontal center line of specimens or the hypothetical line of crack propagation. Therefore, whenever a big region of any one half of the patch was delaminated at any face then the strain in the strain gauges at that face was dropped to a very low value. It can be noted in Figure 5.63 that strain in most of the back face strain gauges dropped significantly at about 15000 load cycles, showing that large delamination had occurred at the lower back region of patch. Similarly, Figure 5.64 shows that the front face behaved better than the back face but suffered with large delamination around its central portion at 15000 load cycles. The strains in these strain gauges were lowered but not dropped to zero at that instant. These were then dropped consecutively at 30,000, 40,000 and 46,000 load cycles.

The specimen finally failed after taking 56,500 total fatigue cycles, which are still 20% more than the specimen 1-CBDR-Sk300 took, which was failed due to improper bonding with steel plate. Comparing the fatigue life of this specimen with the fatigue life of 1-CBDR-Sk30 and 1-CBDR-Hf-Sk30 it is surprising to see that its fatigue life was only 32% and 37% of the fatigue life of these two specimens. Those two specimens were having half the ETR and only one layer of the CFRP (Carbodur) compared to this specimen.

Figure 5.65 shows the strain output of the strain gauge installed on the 9.5 mm wide steel face, which was just opposite to the starter notch. It shows the strain little bit increased in the early stages of the test due to the large delamination of the CFRP patch from the two half faces, causing the stress transfer from the patch to steel. After significant patch delamination, crack in the steel propagated with a faster rate because of less constraint from the patch. Due to the crack became sufficiently large, bending started in the specimen, as shown by the decreasing strain in Figure 5.65. Further increase in the crack length caused more bending of the specimen and the strain in the edge strain gauge suddenly dropped into compression. The strain then reversed back to tension in the final stages of test because the failure occurred in the tensile part of the fatigue cycle and the specimen broke into two pieces.

Figure 5.66 shows the delaminated faces of the CFRP and steel surfaces after the test. It shows that most of the regions of delaminated steel at one face have remains of an extremely thin adhesive layer, with some small regions showing the bare steel plate. The other delaminated steel face shows more proportion of bare steel surface along with the remains of extremely thin adhesive layer.

Figure 5.66 shows that the delaminated CFRP surfaces were having a thick portion of adhesive layer, remained bonded to the CFRP, showing no sign of failure at the adhesive-CFRP interface. The thick adhesive layer remained bonded to the CFRP surface shows clusters of numerous small voids in the adhesive, which might be because of the mortar-like nature of the adhesive, just like the fine-sand and cement mortar. The voids were smaller in size than found in specimen 1-CBDR-Sk-300 and these were also not through the adhesive thickness. Close inspection of the two delaminated faces of the specimen it can be concluded that the delamination mostly occurred at the steel-adhesive interface involving a very thin layer of adhesive in most of its region.

Comparing the failed surfaces of the specimens 1-CBDR-Sk-30 and 2-CBDR-Sk-30 from Figures 5.29 and 5.66 it is found that the CFRP failed surfaces in the two specimens contained similar type and content of small voids in the adhesive. It shows that the specimen 2-CBDR-Sk-30 was not failed by a premature or improper bond; otherwise, the specimen 1-CBDR-Sk-30 should also have failed early. The specimen 1-CBDR-Sk-30 achieved 200% more fatigue life than the specimen 2-CBDR-Sk-30. Most possible reason of getting smaller fatigue life of specimen 2-CBDR-Sk-30 was the faster growth of the patch-end delamination, at the steel-adhesive interface. It was initiated due to adhesive failure under combined peel and shear stresses at the patch-end. It then propagated with a faster rate, under combined action of peel and shear stresses and quickly reached the near-crack region, thus, made the repair patch ineffective.

The only difference between the specimens 1-CBDR-Sk-30 and 2-CBDR-Sk-30 was the number of CFRP layers or the CFRP thickness, which was double in the 2-CBDR-Sk-30 specimen. Therefore, using the conclusions of section 3.5.3.5 peel stresses must have been much higher at the patch-ends in the specimen 2-CBDR-Sk-30. Although the CFRP patch-ends were ground taper before their application to the steel plate but still it is expected that the

peel stress in the specimen 2-CBDR-Sk-30 was higher. It has already shown in section 4.4 that shear stress also acts at the patch-end, therefore, the patch-end delamination and its propagation was expected under combined action of high peel and shear stresses. Comparing the delaminated steel surfaces in specimens 1-CBDR-Sk-30 and 2-CBDR-Sk-30 from Figures 5.29 and 5.66, it is found that these were more or less similar. These show a very thin layer of adhesive remained on the steel surface but the bare steel surface appears more on one face of the specimen 2-CBDR-Sk-30.

5.4.2.2 Test results of specimen 1-CBDR-3SKWRP

This specimen also suffered with early delamination from its patch-ends at the back face. At 10,000 fatigue cycles both the upper and lower patch-ends, at the back face, were completely delaminated, as reflected in the patch-end strains output in Figure 5.67. Figure 5.67 also shows that the front face patch-ends were remained intact up to around 68,000 fatigue cycles. The already initiated delamination from the patch-ends at the back face quickly reached the mid-bond-length of the back face, as reflected in the mid-bond-length strain data shown in Figure 5.68. It can be seen from Figure 5.68 that the back face suffered with comparatively larger delamination than the front face. Around 35,000 fatigue cycles, the delamination in back face had reached approximately up to the mid bond lengths, at its both upper and lower portions.

Till that stage patch-end strain gauges of the front face were still showing less delamination impact. After reaching 35,000 fatigue cycles the lower patch-end of front face started delaminated, followed by the delamination in upper patch-end. The front face patch-end delamination proceeded comparatively slowly towards the mid bond length than the back face. Figure 5.68 shows that the delamination at the front face affected largely the mid-bond-length strain gauges after 100,000 fatigue cycles. Figures 5.69 and 5.70 show the strain output of the crack region strain gauges, respectively of the back and front faces, and it can be seen from these figures that the back-face crack-region strain gauges started delaminated earlier because of the fast proceeding patch-end delamination.

Visual test observations also noticed the early start of patch-end delamination at the back face. The progressing delamination was monitored from the side view of specimen through the relative motion of the patch and steel plate. Figure 5.69 shows continuous declining strains in all strain gauges of the near-crack region of the back face, showing growing impact of the proceeding pat-end delamination. Figure 5.70 shows no impact of the proceeding patch-end delamination in the near-crack strain gauges until about 80,000 fatigue cycles. The strain in the front face crack-region gauges then started declining after approximately 80,000 fatigue cycles, as can be seen in Figure 5.70. It shows that the growing patch-end delamination might have reached close to the near-crack region at the front face.

This specimen achieved total 137,417 fatigue cycles and at its failure the back face was completely delaminated and the specimen broke into two pieces by further delamination of the upper portion of front face from the steel plate. Figure 5.71 shows the strain in the 9.5 mm wide steel face, opposite to the starter notch. This figure shows that up to 100,000 fatigue cycles the plate strain approximately remained constant. After which, it little bit increased because of the large patch delamination at the back face, resulting in the transfer of patch stress to the steel plate. The strain then dropped down into compression because of in-plane bending of specimen caused by increased crack length. Finally, it reversed back to tension in the few last cycles, because the final failure occurred in the tensile part of fatigue cycle.

Figure 5.72 shows the failed specimen and the delaminated surfaces of the CFRP and steel plate. This figure shows similar surface conditions of steel and CFRP as found in the failed surfaces of specimens 1-CBDR-Sk-30 and 2-CBDR-Sk-30. Figure 5.72 also shows that the patch delamination mostly occurred at the steel-adhesive interface. The failed front face steel surface showed remains of a very thin adhesive layer while the back face showed more bare steel surface, even more than the specimen 2-CBDR-Sk-30. The delaminated CFRP surfaces show thick adhesive layer remained stuck on it and these also showed patterns of very small voids similar to the specimens 1-CBDR-Sk-30 and 2-CBDR-Sk-30.

Comparing the results of this specimen with those of 1-CBDR-Sk-30 and 2-CBDR-Sk-30 it is obvious that all of these failed by the governing patch-end delamination. However, the rate of growth of the patch-end delamination in this specimen was little bit faster than that of specimen 1-CBDR-Sk-30 but quite less than that of 2-CBDR-Sk-30. The main difference in

these specimens was in their patch thicknesses. 2-CBDR-Sk-30 was thickest among these while 1-CBDR-Sk-30 was thinnest, and 1-CBDR-3-SKWRP was in between the two. Their fatigue life was found to be in the reverse order of their patch thicknesses, or, the rate of patch-end delamination was in the order of their patch thicknesses. One common thing in all of these specimens was the interface adhesive layer and the first CFRP layer.

5.4.2.3 Specimen 6SKWRP-Sk-300-A

This specimen was having six layers of lower modulus CFRP on each face and it showed better fatigue performance than the specimens of higher E_{FRP} CFRP type of this ETR group. It suffered with some minor problems during its instrumentation and initial gripping in the test frame. It was therefore expected to have some initial weaknesses and that is why this test was further repeated. During instrumentation, the CFRP at the crack edge was accidentally hit by the grinder and it was expected to cause some localized damage. Similarly, just after start of the test it was realized that even the load became zero the CFRP showed strains, which was thought to be because of some initial gripping error. The specimen was released and re-gripped but it was expected that the specimen had taken some initial overstressed load cycles.

Figures 5.73 and 5.74 show the strain output of the four patch-end strain gauges and the four mid-bond-length strain gauges, respectively. It can be seen in these figures that most of the patch didn't suffer with either the patch-end or the mid-bond-length delamination throughout its fatigue life. Only the upper end of the back face showed some delamination, which had also affected its nearest mid-bond-length strain gauges close to the end of test, as reflected in Figures 5.73 and 5.74. Figures 5.75 and 5.76 show the strain outputs of the crack region strain gauges, respectively for the front and back faces. These two figures show that the crack had propagated through the near-crack localized delamination, resulted in increase in the COD and the further crack propagation.

The strain gauge installed at 5mm from the crack edge showed higher and more increasing strains, compared to the rest of gauges. It was expected to be because of the grinder slippage incident happened during instrumentation process, as already mentioned. Comparing the

crack-region strains of this specimen with that of 3-SKWRP-Sk-300 it is obvious that these are similar except the sequential rise in the strains in the specimen 3-SKWRP-Sk-300. It might be because of more CFRP layers used in the current specimen which brought the strain gauges away from the steel plate and involved many CFRP layers between the steel plate and these strain gauges. Additionally, because of some initial damage near the crack the delamination might be more in this specimen than the specimen 3-SKWRP-Sk-300, which little bit nullified the strain rising in it.

Figure 5.77 shows the strain in the 9.5 mm wide steel face, just opposite to the starter notch. Figure 5.77 shows that the strain approximately remained constant in initial portion of test and then it decreased with a slow rate. After 90% fatigue life the strain in 9.5 mm edge strain gauge then quickly dropped down into compression because of more crack growth and the in-plane plate bending. The strain then finally reversed back to tension in the last failure cycles because the final failure occurred in the tensile part of fatigue cycle. This specimen achieved total 4,23,156 fatigue cycles, which is equivalent to the repair effectiveness of 26. In other words, this repair increased the fatigue life of the cracked plate by 26 times compared to the plain unpatched steel plate.

Figure 5.78 shows the failed specimen and the delaminated surfaces of the CFRP and steel plate. It is obvious from the bare steel surface that the patch delamination had occurred at the steel-adhesive interface. It is more evident from the delaminated CFRP surface in Figure 5.78, showing the thin adhesive layer on the CFRP surface. It provides more evidence of the delamination being occurred at steel-adhesive interface.

5.4.2.4 Test results Specimen 6SKWRP-Sk-300-B

This specimen was a repeat of the specimen 6-SKWRP-Sk-300. It was carried out because of some initial problems with its first specimen, as already discussed, and which were expected to affect the fatigue life of the first specimen. The results of this repeat specimen showed little improvement in the results compared to the first test. Figures 5.79 and 5.80 respectively show strain output of the patch-end and patch mid-bond-length strain gauges. These figures show

that the strain at these locations remained constant up to 95% of the total fatigue life, indicating that the patch-ends didn't delaminate. But just after achieving 95% fatigue life, the back face suddenly delaminated from the patch-end, followed by the delamination of its mid-bond-length region. The front face strain gauges show a sudden drop in their strain output at the same instant but they regain straining and continued till the end of test. Figures 5.81 and 5.82 show the strain output of the near-crack region strain gauges, respectively for the front and back faces. These figures show that the crack had propagated through the localized near-crack patch delamination, which allowed the COD to increase and resulted in further crack propagation. Its trend was similar to the specimen 6-SKWRP-Sk-600-A.

The impact of the bigger patch delamination at the back face at 95% fatigue life also appears in Figures 5.81 and 5.82 with a sudden drop in strains of back face near-crack strain gauges. Near-crack strain gauges at the front face show an increase in the strains at that instant. Comparing the Figures 5.81 and 5.82 it could also be noticed that the near the end of test the back face delaminated first. At that instant strains in the front face gauges suddenly dropped but regained to a lower level. Within approximately two to three thousand more cycles, complete failure of the specimen occurred by the delamination of the upper portion of the front face from the steel plate.

Figure 5.83 shows the strain in the 9.5 mm wide steel face, just opposite to the starter notch. It is obvious from Figure 5.83 that the strain approximately remained constant in most of the test. The strain then increased a little bit after some delamination in its surrounding patch (within the near-crack location), causing transfer of stress from the patch to steel plate. The strain then dropped down to compression quickly near the failure stage because of more crack growth and plate in-plane bending. The strain then finally reversed back to tension in the last failure cycles, because the final failure occurred in the tensile part of fatigue cycle. This specimen achieved 4,50,559 fatigue cycles, which was 7% higher than the previous specimen-A. It shows that this repair had increased the fatigue life of the cracked plain steel plate by 28 times, which was the highest repair efficiency within the ETR 0.42 group.

Figure 5.84 shows the failed specimen and the delaminated surfaces of the CFRP and steel plate. It shows similar surface conditions at the steel and CFRP surfaces as found in the

specimen 6-SKWRP-Sk-600-A. The bare steel surface after delamination, as appeared in the Figure 5.84, showed that the delamination occurred at the adhesive-steel interface.

5.4.3 Test results of ETR 0.63 group

All specimens of ETR 0.63 group were also failed in the progressive patch delamination failure mode. In this failure mode, the CFRP patch progressively delaminated from the steel plate, without any failure in the CFRP or upper adhesive layers. Crack length versus the number of fatigue load cycles (a-N curves) for the specimens of ETR 0.63 group is shown in Figure 5.85, including results of the control specimen. Crack length used to develop a-N curves in Figure 5.54 was measured after studying the location of beach marks on the failed steel surface and correlating these with the beach mark cycle's counts provided during the test.

Figure 5.86 shows the failed surfaces of the specimens of ETR 0.63 group highlighting the beach marks on the failed steel surface formed as a result of the beach mark load cycles. The fatigue life of all specimens of the ETR 0.63 group was extracted from the Figure 5.85 and is summarized in Table 5.5 along with their repair efficiencies. The repair efficiency has been defined as the ratio of fatigue life of any repaired specimen to the fatigue life of the control specimen, normalized to the 10 mm crack length. Fatigue life and the corresponding repair efficiency of each specimen are also shown in Figures 5.87 and 5.88, respectively.

Table 5.5 and Figures 5.85, 5.87 and 5.88 show that the maximum fatigue life and the maximum repair efficiency of 1,154,118 and 71, respectively, were achieved by the specimen 9SKWRP-Sk300. The lowest repair efficiency of 4 was achieved in specimen 3CBDR-Sk-30, which was again an unexpected result. The unexpected short fatigue life of the specimen 3CBDR-Sk-30 was similar to the fatigue life of specimen 2CBDR-Sk-30 and was not because of any inappropriate bond issues. It was because of the dominated and rapidly proceeding patch-end delamination failure mode, which had also been found in the higher E_{FRP} specimens of ETR 0.21 and 0.42 groups.

It has been discussed in detail in section 5.4.2 that this failure mode was dominant throughout the test till complete failure of the higher E_{FRP} specimens of ETR 0.42 groups. But it was not

dominant till complete failure of the specimens of ETR 0.21 group with higher E_{FRP} because of the least patch thickness in the ETR 0.21 specimens.

There was one hybrid CFRP specimen in ETR 0.63 group, the 1-CBDR-6-SkKWRP. It was having the first layer of higher E_{FRP} Carbodur plate on each face, added with six more layers of lower E_{FRP} SikaWrap Hex over it. Figures 5.85, 5.87 and 5.88 showed that even the hybrid specimen did not achieve better fatigue life. Although its fatigue life was more than the specimen 3-CBDR-Sk-30, but still 10 times lesser than the specimen of lower E_{FRP} CFRP SikaWrap Hex. It can be noted that its fatigue life was even less than the fatigue life of the weakest specimen of the ETR 0.21 and 0.42 groups (excluding the prematurely failed specimen 1-CBDR-Sk-300).

Figures 5.85, 5.87 and 5.88 also show that there were two specimens of 9-SKWRP-Sk-300 included in this group, and the fatigue life of the first specimen is shown to be very short. It was because of some fabrication issues with the first specimen, which impacted its fatigue life. It will be discussed in detail in its respective section. Figure 5.85 shows that the specimens of lower E_{FRP} CFRP achieved more fatigue life and showed better fatigue performance than the specimens of higher E_{FRP} CFRP. This result was similar to the results obtained in the ETR 0.21 and 0.42 groups. Although the main reason of better performance of lower E_{FRP} CFRP specimens might not solely be the E_{FRP} of the CFRP. It might also be related to the adhesive properties, which will also be discussed in later part of the current section.

COD variation in the specimens of ETR 0.42 was evaluated from the extensometer data by multiplying it with its gauge length and it is also shown in Figures 5.89 and 5.90. Figures 5.89 and 5.90 are similar but with a small difference. Figure 5.89 shows the COD variation from the start of test till near-failure situation, which was the instant when the extensometer was removed from the specimen to avoid its damage. Figure 5.90 shows the COD variation from the start of test till the instant just before start of rapid rate of increase in the COD. Figure 5.85 and 5.89 show similar trend of the variation of crack length and COD with the fatigue load cycles. Impact of progressive patch delamination around the crack on COD was further analyzed in detail at three different stages of the fatigue life of each specimen. These three stages included the start of fatigue life, the middle of fatigue life and near the end of fatigue life. The early stage was considered to be the 10% of fatigue life, the middle stage was

considered to be 50% of fatigue life and the final stage was considered to be the 95% of the fatigue life. These stages were selected in order to compare the COD of different specimens at different stages. It might also be related to the patch delamination initiation and its progression rate around the crack. Figure 5.91 shows the effectiveness of each repair in reducing the COD by comparing it to the COD of control specimen at the three selected stages of the fatigue life. The reduction in COD at the three stages might also be reflecting the rate of patch delamination, as it was expected that the patch delamination increases the rate of crack growth and the COD.

After having an overview of the test results in the form of fatigue life, a-N curves and COD variation, the data output from the strain gauges are presented in detail in the next section to have more detailed information about the initiation and propagation of the patch delamination in the specimens of ETR 0.63group. It is important to mention that the strain output at the peak load, within each fatigue cycle, is shown in the detailed strain output of each strain gauge, because the adhesive failure or the patch delamination was expected under the peak stress within any complete load cycle.

5.4.3.1 Test results of Specimen 3-CBDR-Sk-30

This specimen showed some stable behavior during its starting 8,000 fatigue cycles, after which patch-end delamination started. Figure 5.92 shows strain data of the strain gauges installed at the four patch-ends of the CFRP patch. Figure 5.92 shows that the patch-end delamination was initiated from the upper-end of back face and the lower-end of front face. After just two to four thousand more fatigue cycles the other two patch ends were also started delaminating as can be seen in the Figure 5.92. The patch-end delaminations advanced quickly towards their closest mid-bond-lengths as can be seen in Figure 5.93, which shows the strain data of the four mid-bond-length locations. It can also be seen from Figures 5.92 and 5.93 that the upper portion of back face and lower portion of the front face suffered with large patch delamination at about 15,000 fatigue cycles. The remaining two half-portions of the patch showed comparatively lesser delamination impact but still large enough to bring their strains to some lower values. These two less delaminated portions showed lower strain values till the

end of test, as reflected in Figure 5.93. It shows that if large delamination already occurred in nearly half of the patch at any face then the strains in the remaining half of patch could not be increased by a large amount. One more conclusion can also be drawn on the basis of the strain in the remaining two intact faces that the back face suffered with more delamination than the front face because the strain in it was close to zero and approximately 25% of the strain in the intact portion of front face.

The impact of fast advancing patch-end delamination also appeared on the crack region strain gauges. Figures 5.94 and 5.95 show strains in the near-crack regions, respectively of the front and back faces and these figures show nearly constant strains in these gauges until the first drop occurred. These figures show that the strain suddenly dropped in these strain gauges, at approximately the same instant when the strains dropped in the mid-bond-length strain gauges, as shown in Figure 5.93. The complete study of delamination at a face shows that there might be a quite larger delamination occurred at about 15,000 fatigue cycles at the two faces of specimen, which not only affect the mid-bond-length strain gauges but also the crack-region strain gauges. It can be seen in Figures 5.94 and 5.95 that at the back face of specimen the CFRP patch was delaminated approximately up to its central region by 50,000 fatigue cycles. The front face showed little bit more intact and its near-crack region strain gauges showed strains up to the end of test.

Visual observations of test also showed that the two diagonally opposite half portions of the patch were delaminated nearly up to the crack region at the end of test. This specimen achieved total 61,257 fatigue load cycles which was very close to the fatigue life of specimen 2-CBDR-Sk-30. Therefore, results of these two specimens show that the fast advancing patch-end delamination had reduced their fatigue life to an approximately same level. Figure 5.96 shows the strain output of the strain gauge installed on the 9.5 mm wide edge of steel plate, opposite to the starter notch. It shows approximately constant strain throughout the test but with a very small rise in the strain at about 15,000 fatigue cycles. It was due to the large delamination occurred at the two opposite half-portions of the patch. After delamination of the nearly half portion of the back patch and a large portion of front patch the crack propagated with a very small resistance from the back-face patch. That is why the decreasing strain pattern in Figure 5.96 is similar to the plain steel without a patch. The strain in Figure 5.96

then reversed back to tension (like in all other specimens) because the failure happened in the tensile part of the fatigue cycle, and the specimen broke into two pieces.

Figure 5.97 shows the delaminated faces of the CFRP and steel surfaces after the test. Comparing the delaminated surfaces of this specimen with the 2-CBDR-Sk-30, it can be seen that these are approximately identical. The delaminated CFRP surface in Figure 5.97 shows clusters of small voids in the remained of the thick adhesive layer on it, which was similar to the specimens 1-CBDR-Sk-30 and 2-CBDR-Sk-30. Close inspection of the two delaminated faces of the specimen it can be concluded that the delamination mostly occurred at the steel-adhesive interface involving a very thin layer of adhesive in most of its region. The steel surface showed a very thin left over adhesive layer and it mostly appeared bare steel surface.

5.4.3.2 Test results of Specimen 1-CBDR-6SKWRP

This specimen also suffered with early patch-end delamination from its upper ends of back and front face patches. Although the delamination did not propagate as quickly as it did in the specimen 3-CBDR-Sk-30 but at around 8,000 fatigue cycles the upper portion of back face had mostly delaminated. Figure 5.98 shows the strain data of patch-ends strain gauges and the delamination of back face upper-end is indicated in this figure through the dropped strains in the respective strain gauges. At about 20,000 fatigue cycles the lower end of back face also showed large delamination signs in the Figure 5.98. The front face patch-ends found comparatively more intact and strain drop in their strain gauges after 20,000 total fatigue cycles. These two patch-ends of the front patch were then delaminated completely between 60,000 and 80,000 fatigue load cycles in Figure 5.98.

The fast advancing patch-end delamination of the upper portion of back face quickly affected its mid-bond-length at about 20,000 fatigue load cycles, as indicated from the strain output of the mid-bond-lengths strain gauges in Figure 5.99. The middle region of the upper portion of back face was expected to be largely delaminated at about 40,000 fatigue load cycles, as indicated by zero strains in the mid-bond-length strain gauges in Figure 5.99. At that instant strains in the front face strain gauges were also dropped by four to five times but continued

with a lower strain levels. It showed that at that stage there must be large delamination occurred at the back face and a comparatively lesser delamination at the front face. Figure 5.99 also shows that strain in the two strain gauges of front face at the two mid-bond-length locations was continued till complete failure of the specimen, indicating that these locations of the front face remained bonded till complete failure of specimen.

Figures 5.100 and 5.101 show the strain output of the crack region strain gauges, respectively of the front and back faces, and it is obvious from these figures that the back face crack region suffered more with the proceeding patch-end delamination. Strains in the near-crack strain gauges at back face started dropping with a faster rate after the advancing patch-end delamination reached closer to it. Figure 5.101 shows that finally strains in all the strain gauges of back face reached to zero at about 75,000 fatigue load cycles. It shows that the upper half of the back patch was largely delaminated at 75,000 fatigue cycles. Figure 5.100 also shows that the front face strain gauges also started delaminating at a faster rate after 50,000 fatigue cycles, due to the impact of the advancing patch-end delamination. Strain in mid-bond-length strain gauges of front face was already found to be dropped in Figure 5.99, but still not zero. Front face patch resisted and remained intact till complete failure of the specimen but at about 100,000 fatigue cycles strain in the near-crack gauges dropped to some very low values, as can be seen in the Figure 5.100.

The specimen achieved total 115,393 fatigue cycles. After early delamination of two halves of the patches at opposite faces, the crack was expected to be propagated fast till complete failure of the specimen. Figure 5.102 shows the strain in the 9.5 mm wide steel face, opposite to the starter notch. It can be seen in this figure that up to approximately 40,000 fatigue cycles plate strain was approximately constant. Plate strain then increased noticeably, most possibly because of large delamination of both halves of the front and back faces, which had affected the bond of patch surrounded to this strain gauge. After delamination in the surrounding patch the strain in this strain gauge was increased because of transfer of stress from patch to the plate. The strain in this gauge then dropped into compression because of more crack growth and corresponding in-plane plate bending. Finally, the strain reversed back to tension in the last failure cycles because final failure occurred in the tensile part of fatigue cycle.

Figure 5.103 shows the failed specimen and the delaminated surfaces of the CFRP and steel plate. Figure 5.103 shows clusters of small voids in the remained of the thick adhesive layer on the CFRP. These were similar to that found in specimens 1-CBDR-Sk-30, 2-CBDR-Sk-30 and 3-CBDR-Sk-30. Close inspection of the two delaminated faces of the specimen it can be concluded that the delamination mostly occurred at the steel-adhesive interface involving a very thin layer of adhesive in most of its region. Bare steel surface was less visible in this hybrid specimen, compared to the plain specimen 3-CBDR-Sk-30.

5.4.3.3 Test results of specimen 9SKWRP-Sk-300-A

As mentioned in section 5.4.3 that this specimen had suffered with some construction issues during its preparation and that is why it resulted in shorter fatigue life. During specimen preparation for the test, the flow-out hardened adhesive was needed to be cleaned off the specimen's ends to facilitate its properly gripping in MTS. Due to quite large amount of hardened adhesive at the ends of this specimen a metallic scrapper was used to scrap and clean the specimen's ends. Unfortunately, during the scrapping, the scrapper hit the patch ends at some locations. In other words, there arose a big possibility of having some unintentional localized bond failure at the patch-ends, even before the start of test. It was then seen just after the 100,000 fatigue load cycles from the start of test that the patch-end delamination was initiated from the upper portion of the back patch. The lower end of back face also showed the signs of delamination soon after the upper end.

The signs of patch end delamination can be seen from the strain output of the strain gauges at the patch end locations in the Figure 5.104. Early patch end delamination at the back face also reached its nearest mid-bond-lengths in just 25,000 to 50,000 more fatigue cycles, as can be seen in Figure 5.105. At about 181,490 total fatigue cycles the delamination at the back face had reached the two mid-bond-lengths. This early initiation and its fast rate of propagation were thought to be caused by the unintentional initial damage of bond at localized patch-ends locations caused by the scrapper. It might have created cracks in the bond at the patch-ends from where the delamination initiated and propagated. Figures 5.106 and 5.107 show the strain output of the crack-region strain gauges, respectively for the front and back faces. It

shows declining of strains at the same instant when the delamination had reached and crossed the mid-bond-lengths of the back face. This specimen achieved 181,490 fatigue cycles, which was less than that achieved by the specimen 6-SKWRP-Sk-300, which had 67% lesser ETR. The main reason was expected to be the patch-end delamination in this specimen, originated from initial bond failures at its patch-ends, caused by the accidental slippage of scrapper.

Figure 5.108 shows strain output of the 9.5 mm thick steel face, opposite to the starter notch. This figure shows that the plate strain was approximately constant till 135,000 cycles, after which it increased a little bit because of the patch delamination in its surrounding, resulting in stress transfer from patch to steel plate. When the crack became sufficiently large, the in-plane plate bending started, reducing the tensile stresses at this face. The strain then dropped into compression, but it finally reversed back into tension in final stages, because final failure occurred in the tensile part of fatigue cycle.

Due to construction issues with this specimen, which were also reflected in the specimen's behavior and the test result, it was decided to drop this specimen from the comparative study. The results of this specimen have highlighted the consequences of localized bond problem or the fabrication errors, specially, the location of bond weakness. If patch-end delamination initiates then the fatigue life will be short. Patch-end delamination found to be much rapidly propagating after it initiated, especially in the thicker patches, therefore, these has to be avoided to save the specimen's early failure. Figure 5.109 shows the failed specimen and its delaminated surfaces. Figure 5.109 shows shiny bare steel surface with very less adhesive, showing that the patch delamination mostly occurred at the adhesive-steel interface. The CFRP surface shows most of the adhesive remained stuck to its delaminated surface, which also supports the delamination location at adhesive-steel interface

.

5.4.3.4 Test results of specimen 9SKWRP-Sk-300-B

This specimen was a repeat test of the specimen 9-SKWRP-Sk-300. The test was repeated due to the premature failure of the first specimen, caused by specimen's preparation errors, which had resulted in its short fatigue life. The results of this specimen showed quite stable and

much improved behavior than the first specimen. Figures 5.110 and 5.111 respectively show the strain output of the patch-end and patch mid-bond-length strain gauges. It is obvious from these two figures that the strain at these locations did not dropped till approximately the end of test, showing no sign of delamination, rather a perfect bond situation at all patch ends.

Figures 5.112 and 5.113 respectively show the strain output of the near-crack region strain gauges, respectively for the back and front faces. These two figures show that the crack had proceeded through the near-crack localized patch-delamination. It resulted in the increase in COD, similar to the specimen 6-SKWRP-Sk-600-B. Figures 5.112 and 5.113 show that the strain in these strain gauges started increasing after approximately 600,000 fatigue cycles with a very slow rate and then with a higher rate close to complete failure of the specimen. Comparing the response of these strain gauges with the near crack strain gauges of the three layered specimens 3-SKWRP-Sk-300 or 3-SKWRP-Sk-330, it can be seen that these were quite similar, especially near the failure.

Figure 5.114 shows strain in the 9.5 mm wide steel plate face, opposite to the starter notch. This figure shows that the strain there approximately remained constant in most of the test span. The strain then slightly increased after half fatigue life of the specimen and it was also close to the instant when the delamination in its surrounding patch was started, which caused the transfer of stress from the patch to steel plate. The strain then dropped slowly due to the increased in-plane bending, and near the end of test it dropped into compression. It was because of the crack size become quite large. The strain then finally reversed back into tension in the final failure cycles, as can be seen in Figure 5.114, because the final failure occurred in the tensile part of fatigue cycle. This specimen achieved 1,154,118 fatigue cycles which was the highest in the current testing program and it was approximately 71 times more than the fatigue life of the control specimen.

The results also confirmed that the previous specimen's results were affected by the fabrication and handling issues at its patch-end. Figure 5.115 shows the failed specimen and delaminated surfaces of the CFRP and steel plate. It shows similar surface conditions as found in all previous specimens of CFRP SikaWrapHex with adhesive Sikadur-300. Shiny bare steel surface shows that the delamination occurred at the adhesive-steel interface.

5.4.4 Comparison of test results of three ETR group of lower E_{FRP} CFRP

After studying fatigue behavior and failure modes of the tested specimens it can be seen that impact of patch ETR could not be studied in the specimens of the higher E_{FRP} CFRP because of their unexpected very short fatigue life, caused by the patch-end delamination failure mode. But it could be studied through the results of specimens of lower E_{FRP} CFRP because of their better and stable fatigue behavior, with negligible impact of the patch-end delamination. Fatigue life and the respective patch effectiveness of the three specimens of lower E_{FRP} CFRP of three ETR groups are compared in Figures 5.116 and 5.117. It can be seen from these figures that the ETR 0.21 patch increased the fatigue life of control specimen by 12 times, while the specimens of ETR 0.42 and 0.63 respectively increased the fatigue life of control specimen by 28 and 71 times, respectively. The specimens of ETR 0.41 and 0.63 were also found to be 2.3 and 6 times more effective than the specimen of ETR 0.21, respectively. Therefore, the repair effectiveness increased with increasing ETR by more than the corresponding increase in ETR itself.

5.5 Summary and conclusion

In this chapter, experimental phase of current research work has been presented including the details of test parameters, specimen preparation, test procedure, failure modes and the test results. The selected test specimens were divided into three groups, representing the three patch ETR of 0.21, 0.42 and 0.43. The impact of other test parameters was then studied with reference to these three ETR groups. All the specimens were tested under constant amplitude tension-tension fatigue loading with the applied stress range of 180 MPa, the stress ratio of 0.1 and σ_{max} of 200 MPa. The three ETR values were selected on the basis of the available properties of the CFRP from local suppliers and the cracked steel plate used in the experiments. Two different types of CFRP used in each ETR group having different modulus of elasticity (E_{FRP}) and different physical properties. Lower modulus CFRP had the E_{FRP} of 65 GPa while the higher modulus CFRP was prefabricated and had the E_{FRP} of 165 GPa.

In each ETR group the specimens were fabricated using both types of CFRP. In the ETR 0.21 group the specimens were so designed that the impact of adhesive properties on the fatigue life of the repair could also be studied. In the two higher ETR groups of 0.41 and 0.63 the specimens were designed to study the impact of E_{FRP} with their respective adhesives. The testing program also included some hybrid specimens which were having the first layer of higher E_{FRP} CFRP and its specified adhesive, while the rest of the upper layers were of the lower E_{FRP} CFRP with their specified adhesive. The impact of ETR was studied by comparing the behavior and fatigue life of different specimens within the three ETR groups having identical CFRP type and adhesive. Effectiveness of all repaired specimens was evaluated by comparing the fatigue life of any repair with the fatigue life of control specimen, which was tested without CFRP patch.

Test results showed that the repair ETR has a great impact on enhancing the fatigue life of bonded CFRP repairs but it could also be affected by other patch parameters. Failure mode of all the specimens was observed to be the progressive patch delamination from plate interface with the fatigue load cycles, followed by increase in the crack length in steel specimen. The delamination of CFRP patch at the end of test was observed to be from any two half portions of the patch. Although the failure mode of all specimens was the progressive patch delamination, followed by the crack progression in steel plate, but, more precisely the delamination initiation and propagation was further observed to be in three different modes.

The first mode of delamination observed in the tests was started or originated from the end regions of the repair patch. It then propagated with a faster rate inside the bond length towards the crack region or the middle portion of the specimen. The delamination progression from the patch-ends was not occurred from all four ends of the repair patch. It mostly progressed faster from any two ends of the opposite faces of patch, and, when it reached the near-crack region the remaining two half portions also started to delaminate. The efficiency of repairs was found to be dropped significantly when the patch-end delamination reached the central regions of specimen. It caused the plate mostly freed from the patch effect and the crack in steel plate grew rapidly and resulted in complete failure of the specimen into two pieces. This type of patch delamination mode resulted in short and unexpected fatigue life of the repairs. It mostly occurred in thicker repairs, having higher E_{FRP} CFRP and with ETR values greater than 0.21.

The second mode of delamination was not governed by the patch-end delamination and the patch-ends remained intact till the end of test. In this mode very slow and stable crack growth was observed, mostly through small patch delamination in the near-crack regions, which allowed COD and the crack length to increase slowly with fatigue load cycles. When both the crack length and the near-crack patch delamination became sufficiently large, final failure occurred through a sudden delamination of the remaining bonded portion of the patch within small number of fatigue cycles. It was noted that almost 75% to 80% of the fatigue life of the specimens failed under this failure mode was having very stable and slow crack growth rate. Faster crack growth rate or faster COD increasing rate was observed only in the last 15% to 20% of the fatigue life. This mode of failure was found in the specimens having lower E_{FRP} CFRP in all ETR groups and these specimens also achieved higher fatigue life and maximum repair efficiency within each ETR group.

The third delamination mode was observed to be mix up of the previous two modes in which the patch delamination initiated from the patch-ends but propagated slowly inside the bond length. In most cases of this failure mode the patch-end delamination affected little bit the mid-bond-lengths but the rate of delamination propagation beyond the mid-bond-lengths was very slow. Another differentiating observation in this failure mode was that after the start of delamination at patch-end, the strains there did not reach zero after small number of fatigue cycles. In some cases, the delaminated patch-ends showed straining until the end of test, although with lesser strain magnitude. It was not found in the dominating patch-end failure mode, in which once the patch-end delamination started it quickly delaminated the patch-ends completely. In some cases of the mixed delamination failure mode, the patch-end delamination did not even reach or affected the mid-bond-length regions until the end of test. Crack growth in the mixed delamination failure mode occurred mostly through the near-crack patch delamination in the early stages of test. Later on, the proceeding patch-end delamination merged with the near crack delamination and caused the crack to propagate at a faster rate near the end of test. The third mode of delamination was observed mainly in the specimens of the ETR 0.21, which were provided with higher E_{FRP} CFRP. Hybrid-patch specimens of higher ETR groups also failed in the mixed delamination failure mode. Therefore, in general, the specimens provided with higher E_{FRP} CFRP type showed lesser patch efficiency in ETR 0.21 group, while in further higher ETR groups their efficiency was shown to be least.

Lesser fatigue life of the specimens of higher E_{FRP} CFRP, failed in the dominating patch-end delamination failure mode, was not because of the modulus of elasticity of CFRP but it was expected to be because of two weaker properties of the adhesive. The first weakness of adhesive appeared from its lesser resistance to the early initiation of patch-end delamination, under high peel and shear stresses. Rough or mortar like porous finish of the adhesive might also be facilitating the early initiation of the patch-end delamination. The second weakness of adhesive was appeared from its lesser resistance to the fast propagation of delamination from the patch-ends towards the central region of specimen, which mostly occurred at the adhesive-steel interface. This propagation was faster in thicker patches and slower or much slow in the thinner patches. Therefore, the failure of thicker patches in the dominating patch-end delamination mode showed that the adhesive was incapable of resisting the combined action of peel and shear stresses at the patch-ends, as well as in resisting faster delamination at adhesive-steel interface.

Failure mode of hybrid specimens was also lying in the third type of patch delamination mode, showing some benefit of hybridization but still their repair effectiveness were far below the repair effectiveness of the specimens failed in near-crack delamination failure mode. The delaminated surfaces of these specimens also confirmed that their failure was similar to the plain non-hybrid specimens of higher E_{FRP} CFRP, failed either by the governing patch-end or the mixed delamination failure modes. Therefore, it can be concluded that their fatigue life and failure mode was not improved because of having same adhesive at the interface, which had already resulted in reduced fatigue life in the plain (non-hybrid) specimens of higher E_{FRP} CFRP.

It is also important to note that the patch delamination occurred at the adhesive-steel interface in all the tested specimens, including the specimens of lower E_{FRP} CFRP, but because of strong adhesive properties the patch-end delamination could not be initiated in the specimens of lower E_{FRP} CFRP. It was also found in some thicker patches of the lower E_{FRP} CFRP that if any localized bond weakness existed at the patch ends, as a result of any mishandling or fabrication mistake, then the delamination growth occurred similar to the thicker specimens of higher E_{FRP} CFRP. Those results have highlighted the impact of any unintended mishandling

or minor fabrication mistake on the fatigue life of the repair. It showed the impact became detrimental if it initiated the patch-end delamination.

Impact of decreasing adhesive thickness to 60%, within the specimens of ETR 0.21, was found to be decreasing the fatigue life of repair by 11%. Lower E_{FRP} CFRP specimens achieved the repair effectiveness of 12, 28 and 71 respectively in the ETR 0.21, 0.42 and 0.63 groups. One specimen of the lower E_{FRP} CFRP in the ETR 0.21 group also achieved the repair efficiency of 14 but it was prepared with a different adhesive not used in the specimens of higher ETR groups. The impact of increasing ETR by two and three times was found to be enhancing the fatigue life of un-repaired specimen by approximately 2.3 and 6 times, respectively, compared to the enhancement provided by the specimen of lowest ETR group.

Table 5.1 Specimen details

Specimen details	CFRP type	CFRP layers each face	Adhesive	ETR	Notes
Plain Steel	—	—		—	Unrepaired specimen
1-CBDR-Sk30	Carbodur	1	Sikadur 30	0.21	
1-CBDR-Hf-Sk30	Carbodur	1	Sikadur 30	0.21	Half adhesive thickness than prescribed
1-CBDR-Sk300	Carbodur	1	Sikadur 300	0.21	Adhesive of SikaWrap used
1-CBDR-Sk330	Carbodur	1	Sikadur 330	0.21	
3-SKWP-Sk-300	Sikawrap Hex	3	Sikadur 300	0.21	
3-SKWP-Sk-330	Sikawrap Hex	3	Sikadur 330	0.21	
2-CBDR-Sk-30	Carbodur	2	Sikadur 30	0.42	
6-SKWP-Sk-300	Sikawrap Hex	6	Sikadur 300	0.42	
1-CBDR-3-SKWP	Carbodur + SikaWrap	1 + 3	Sikadur 30 + Sikadur 300	0.42	Hybrid patch
3-CBDR-Sk-30	Carbodur	3	Sikadur 30	0.63	
9-SKWP-Sk300	Sikawrap Hex	9	Sikadur 300	0.63	
1-CBDR-6-SKWP	Carbodur + SikaWrap	1 + 6	Sikadur 30 + Sikadur 300	0.63	Hybrid patch

Table 5.2 Material Properties

Material	Modulus of elasticity 'E' (GPa)	Tensile Strength (MPa)	Shear Strength (MPa)
Steel	200	450	-
Sika Carbodur	165	2400	-
SikaWrap HEX 103C	65	800	-
Sikadur 30	5	24	17
Sikadur 300	1.724	55	-
Sikadur 330	4.5*	35	-

* Not provided in the supplier's data, obtained from Julia De Castro (2005)

Table 5.3 Test results of ETR 0.21 group; Fatigue life and repair efficiency

Specimens	Fatigue Life		Repair Effectiveness
	Pre-Crack	Repaired	Test / Control
Control-1	28015	16150	1
Control-2	30700	14330	1
1CBDR-Sk-300	27500	47873	3
1CBDR-Sk-30	29020	171992	11
1CBDR-Hf-Sk-30	28000	150336	9
1CBDR-Sk-330	29050	147530	9*
3SKWRP-Sk300	27800	188375	12
3SKWRP-Sk330	28050	229260	14

* Not failed completely

Table 5.4 Test results of ETR 0.42 group; Fatigue life and repair efficiency

Specimens	Fatigue Life		Repair Effectiveness
	Pre-Crack	Repaired	Test / Control
Control-1	28015	16150	1
Control-2	30700	14330	1
2CBDR-Sk-30	2800	56500	3
1-CBDR+ 3SKWRP	27500	137417	9
6SKWRP-Sk300-A	30051	423156	26
6SKWRP-Sk300-B	27800	450559	28

Table 5.5 Test results of ETR 0.63 group; Fatigue life and repair efficiency

Specimens	Fatigue Life		Repair Effectiveness
	Pre-Crack	Repaired	Test / Control
Control-1	28015	16150	1
Control-2	30700	14330	1
3CBDR-Sk-30	27800	61257	4
1CBDR-Sk30 + 6SKWRP	28050	115393	7
9SKWRP-Sk300-A	2800	181490	11
9SKWRP-Sk300-B	27500	1154118	71

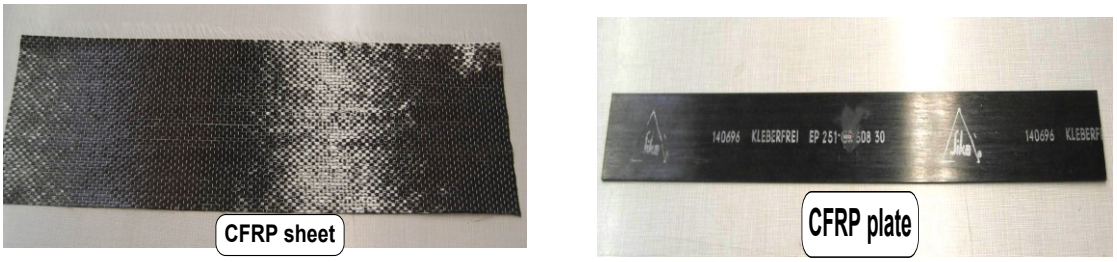

Figure 5.1. Two types of CFRP (a) Lower E_{FRP} CFRP SikaWrap Sheet, (b) Higher E_{FRP} CFRP Sika Carbodur Plate (Source: Lam et al. 2008)

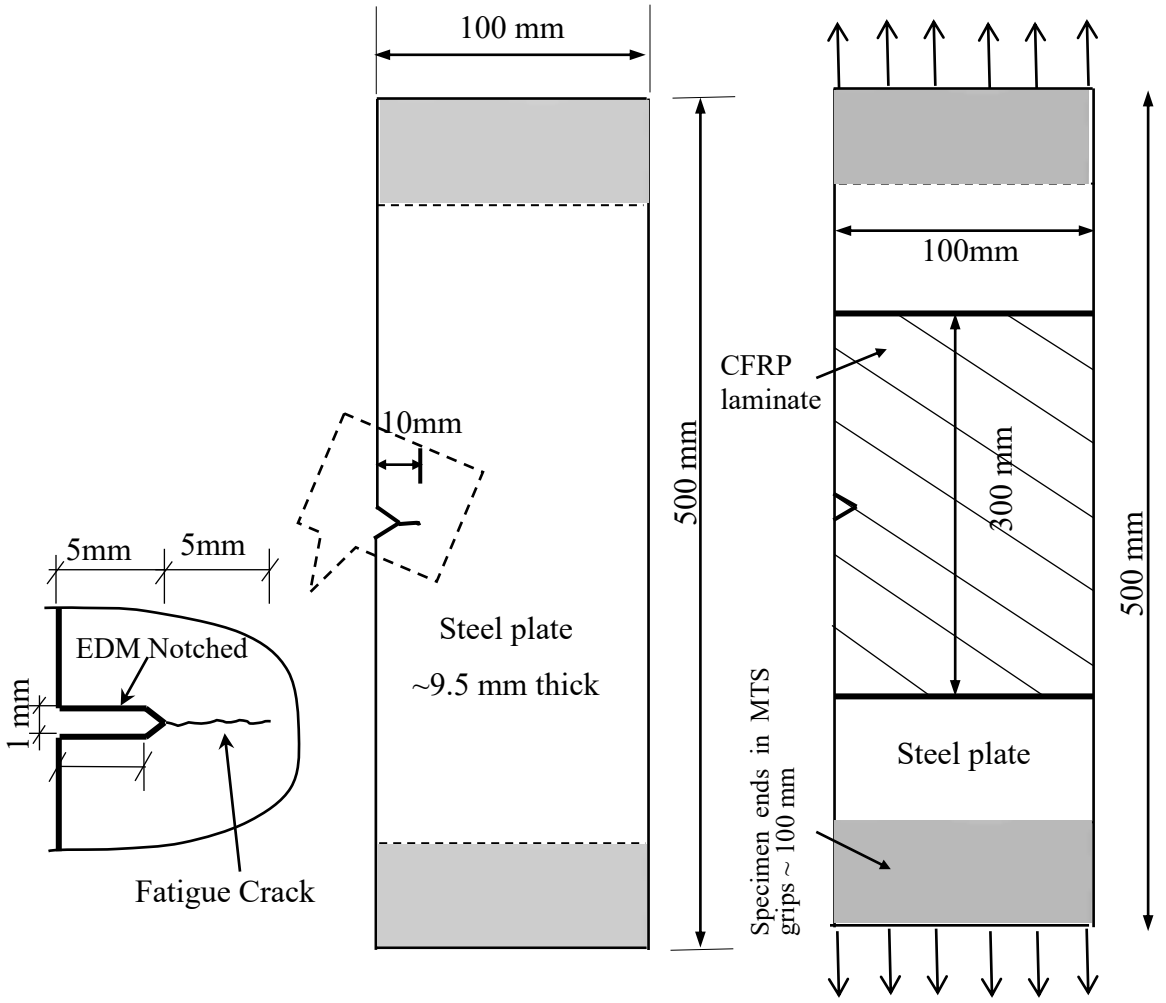

Figure 5.2. Specimen's detail, with and without CFRP patch along with the notch

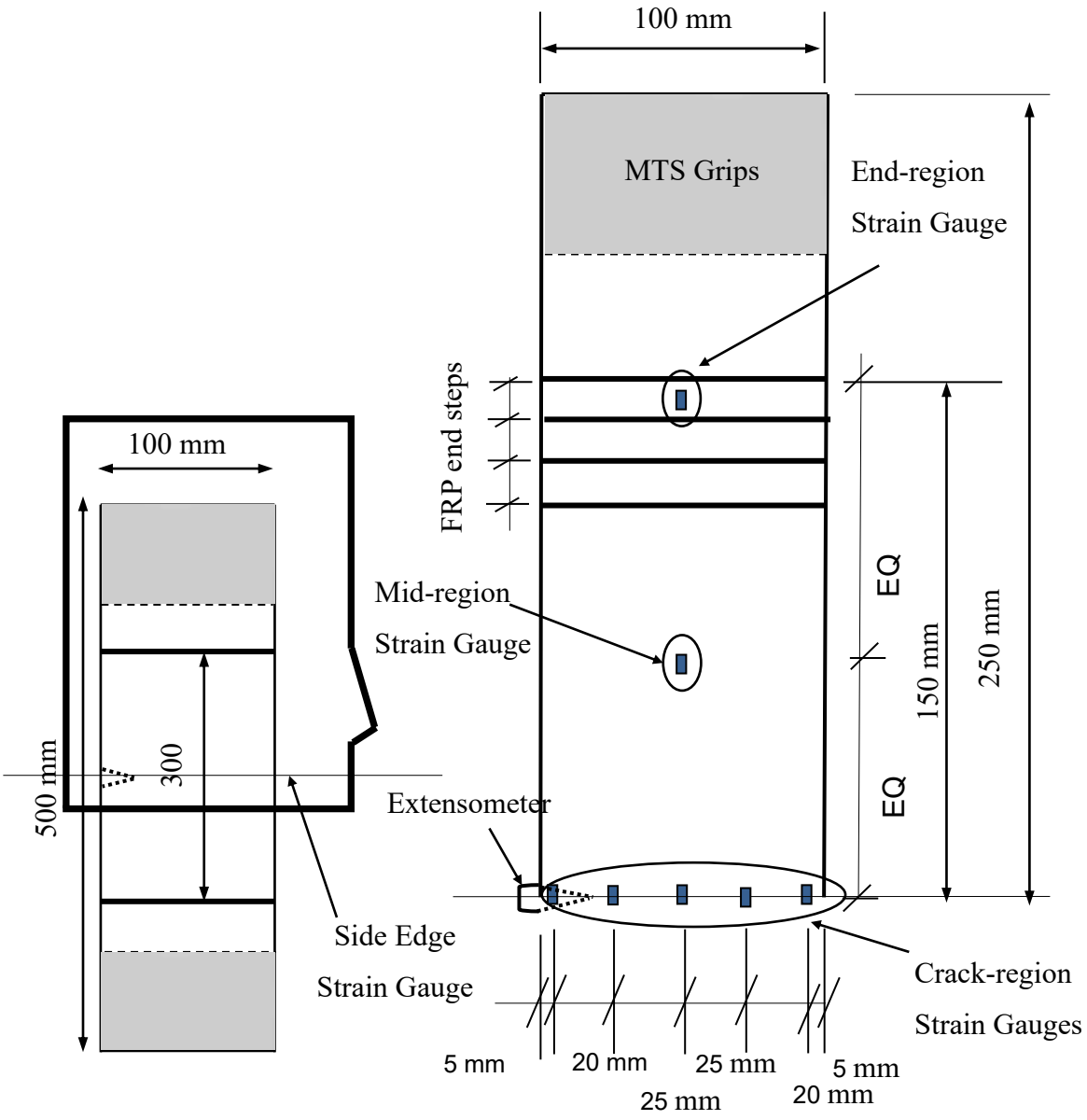

Figure 5.3 Instrumentation of the test specimen

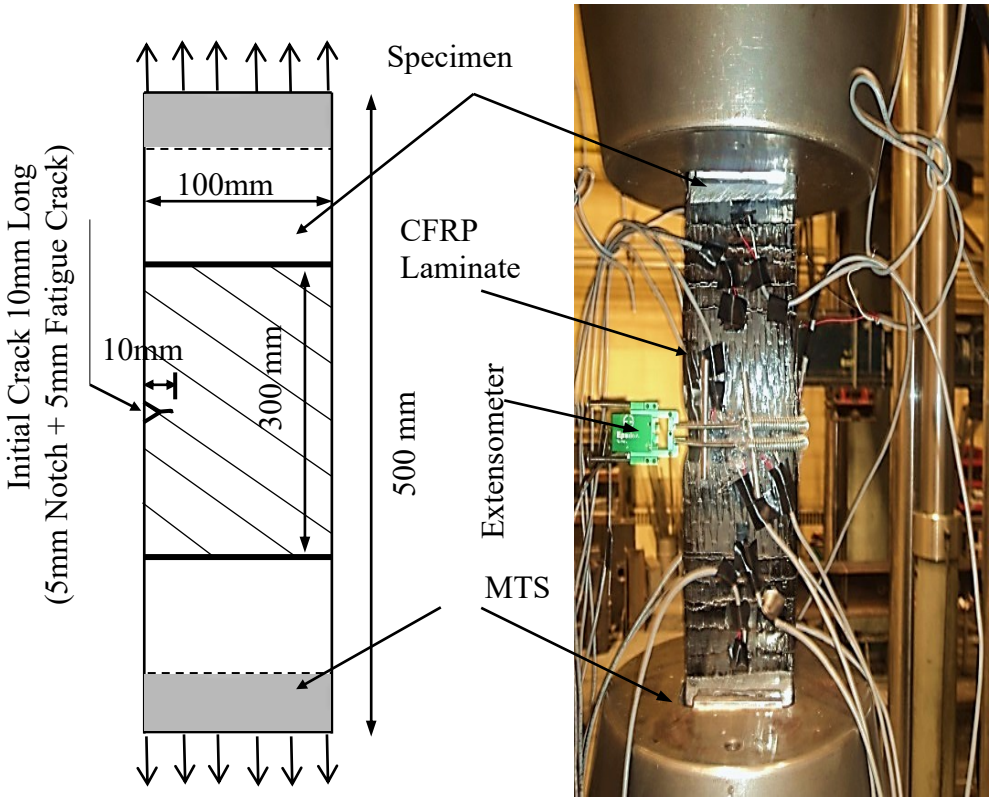

Figure 5.4 Test setup showing an instrumented specimen gripped in MTS

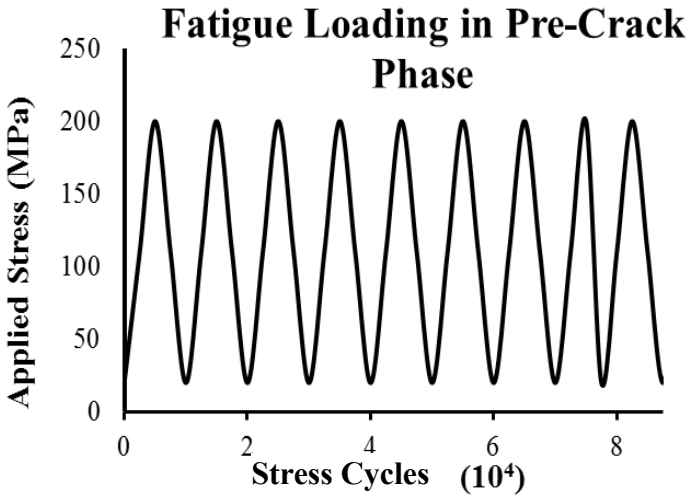

Figure 5.5 Fatigue stress range used in pre-crack phase

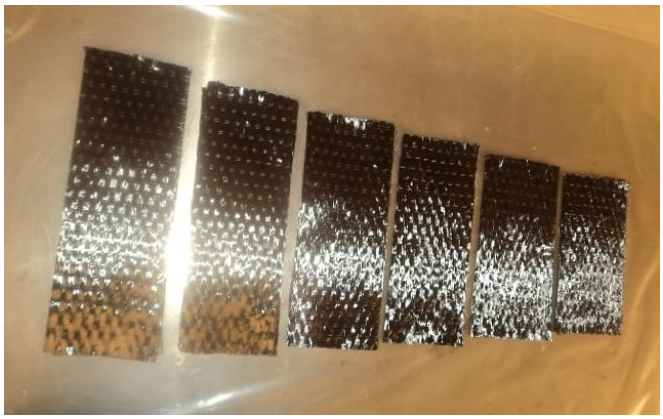

Figure 5.6 Varying lengths of lower modulus CFRP layers to provide tapering at the patch-end

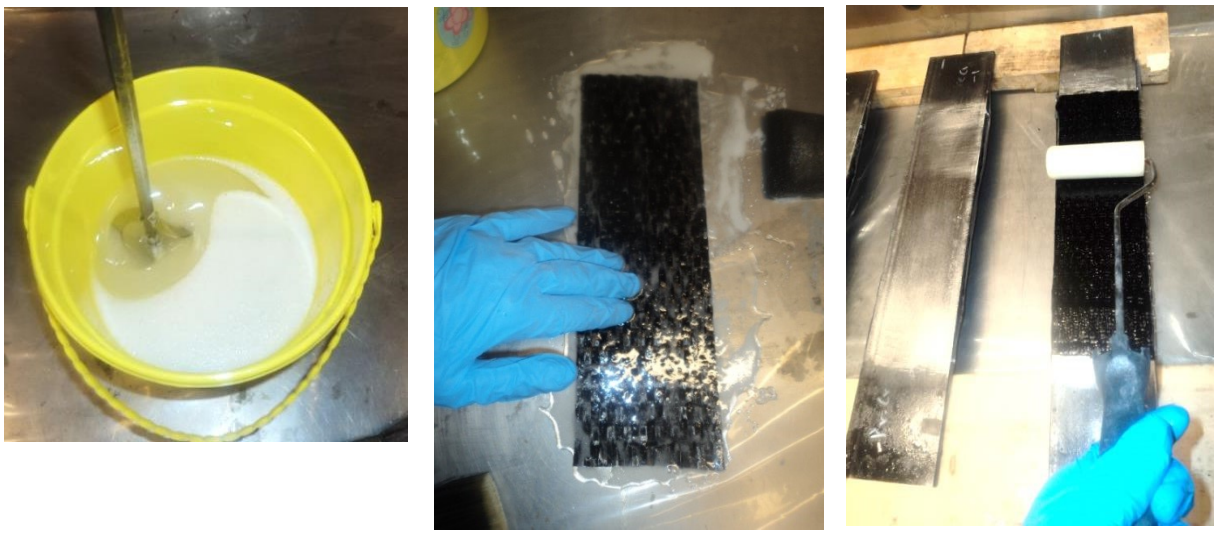

Figure 5.7 Different steps involved during specimen preparation; epoxy mixing; wet-on-wet layering of the CFRP and; rolling to remove air bubbles

Figure 5.8 Tapered end of Sika Carbodur formed by grinding

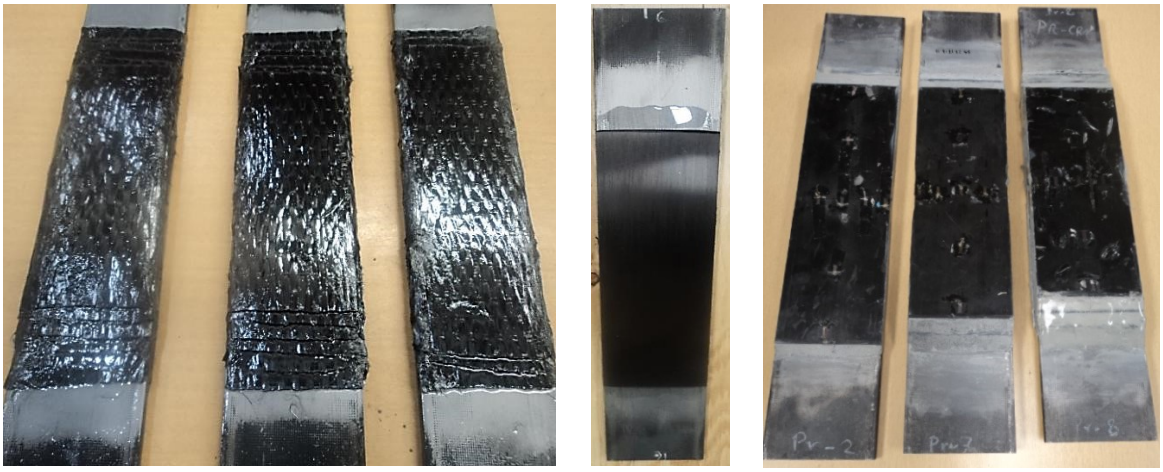

Lower E_{FRP} specimens Higher E_{FRP} specimens

Figure 5.9 Prepared test specimens using two types of CFRP

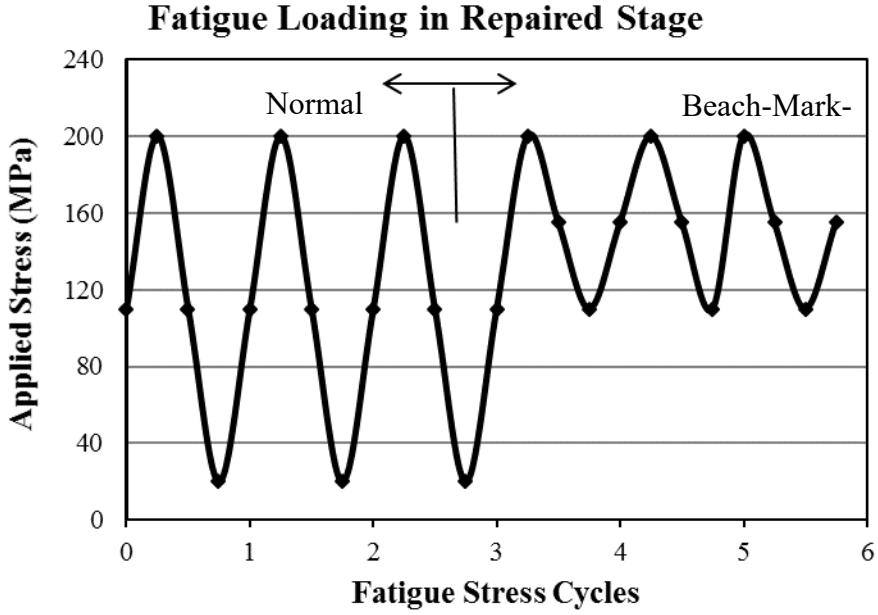

Figure 5.10 Fatigue loading applied in repaired phase including beach-mark cycles

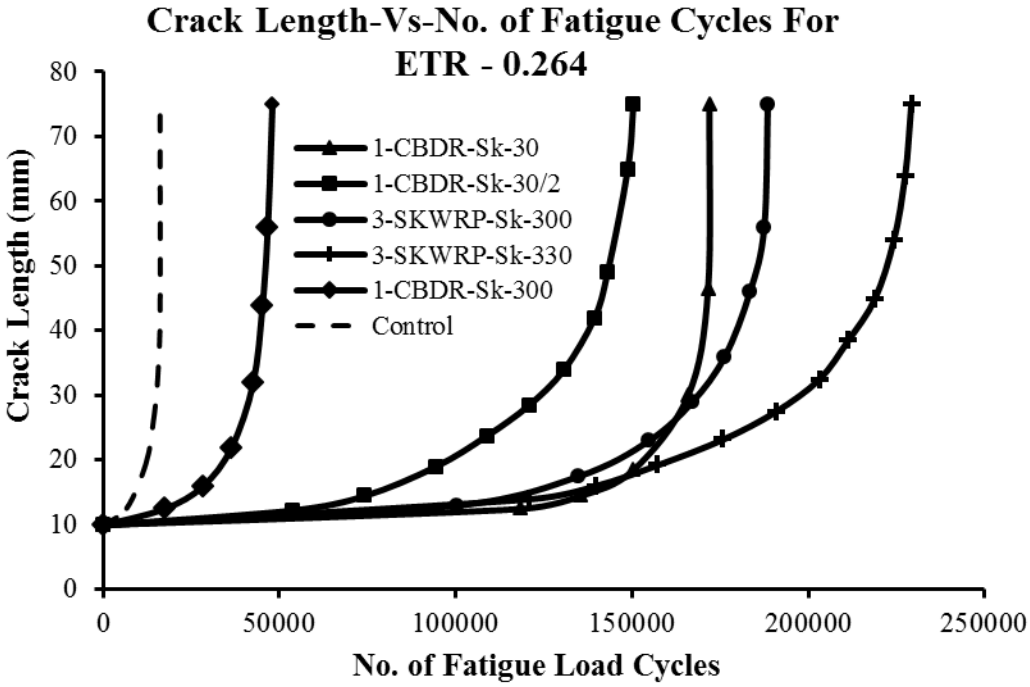

Figure 5.11 Crack-length variations with fatigue cycles (a-N curves) for ETR 0.21 specimens

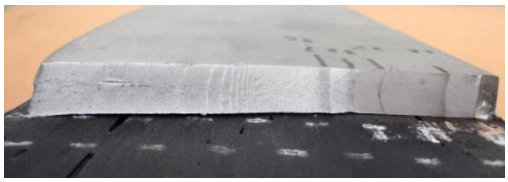

3-Sikawrap-Sk-300

1-CBDR-Sk-30

1-CBDR-Sk-300

1-CBDR-Hf-Sk-30

3-Sikawrap-Sk-330

Figure 5.12 Failed surfaces of steel in specimens of ETR 0.21 showing the beach marks

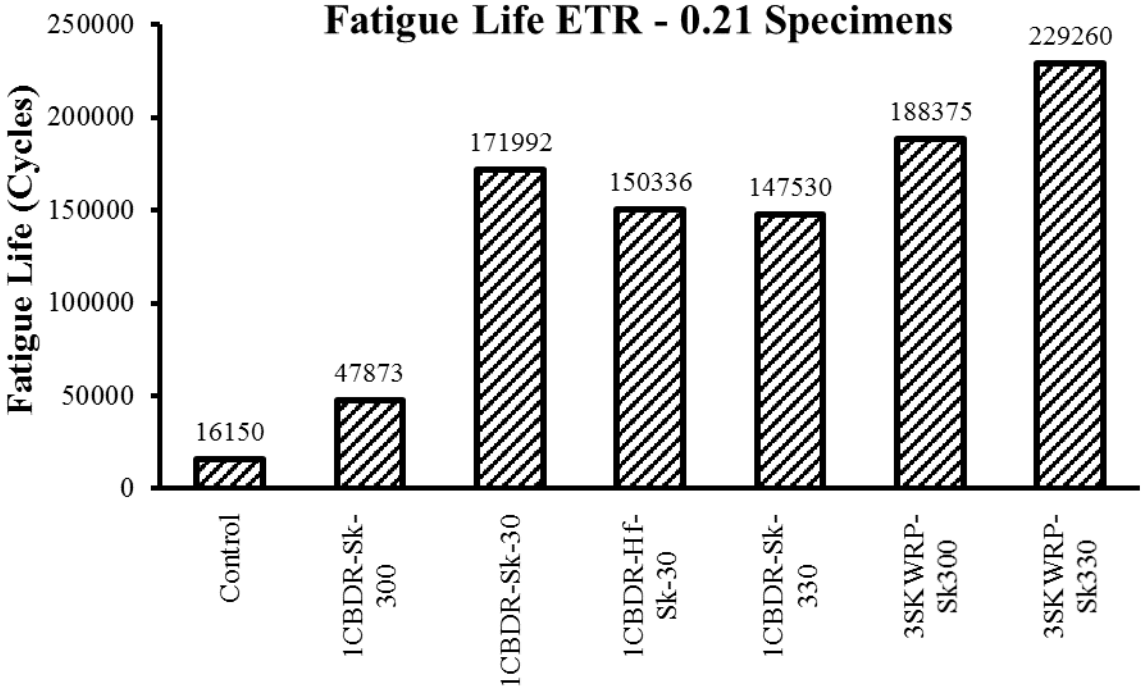

Figure 5.13 Fatigue life of specimens of ETR 0.21 group

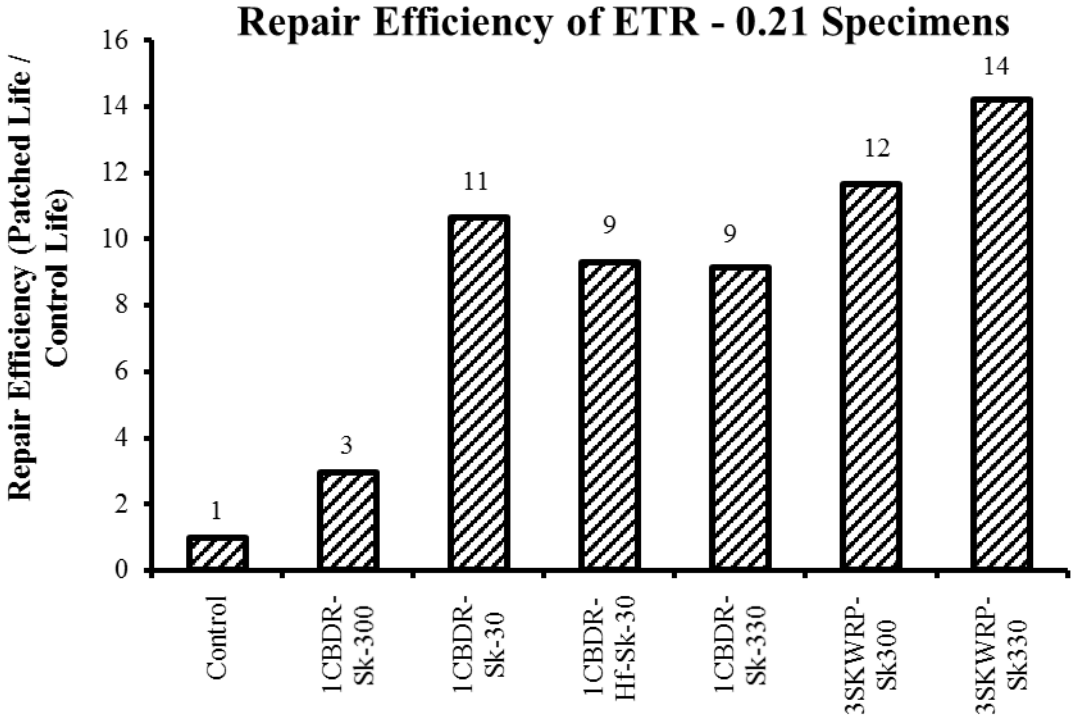

Figure 5.14 Repair efficiency of specimens of ETR 0.21 group

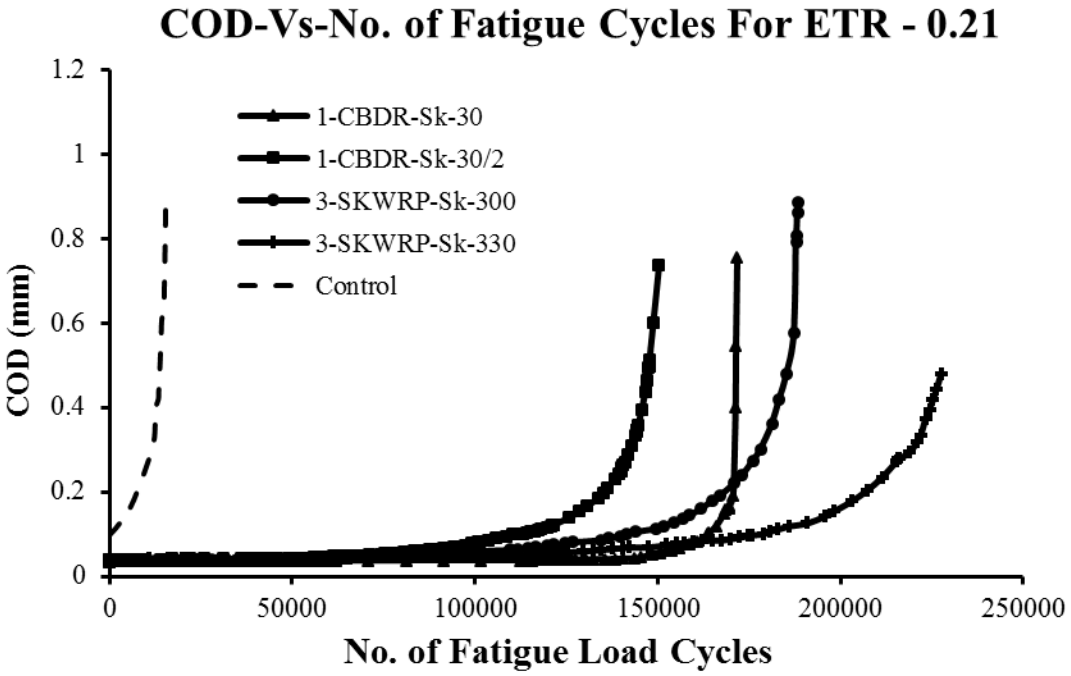

Figure 5.15 COD variations of specimens of ETR 0.21

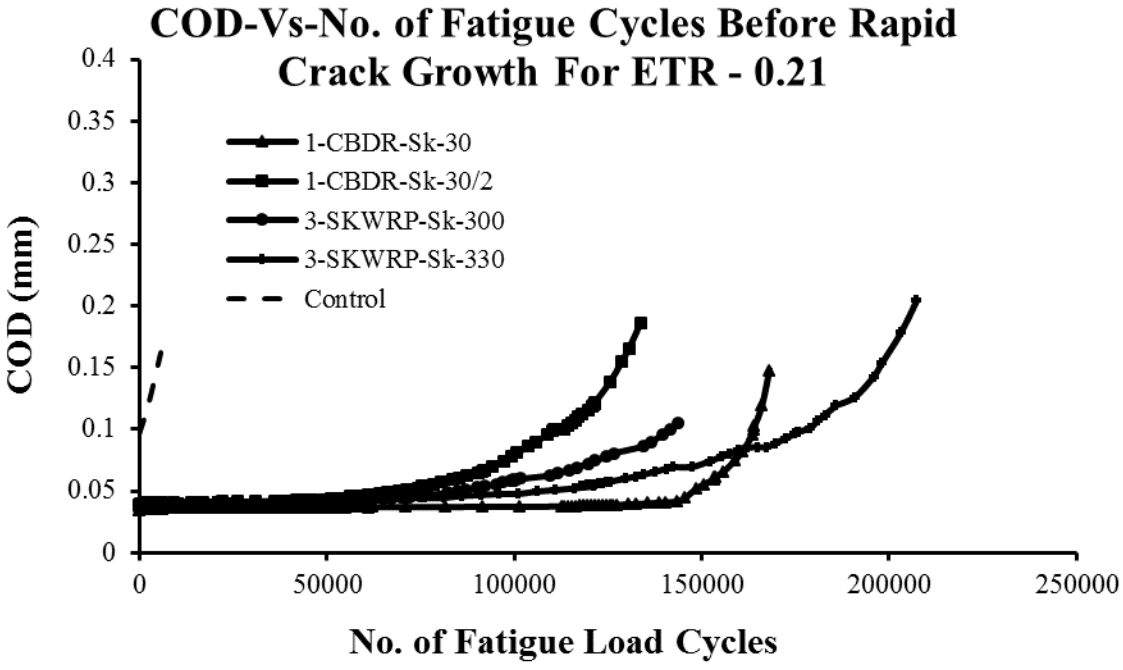

Figure 5.16 COD variations of specimens of ETR 0.21 group before rapid crack growth

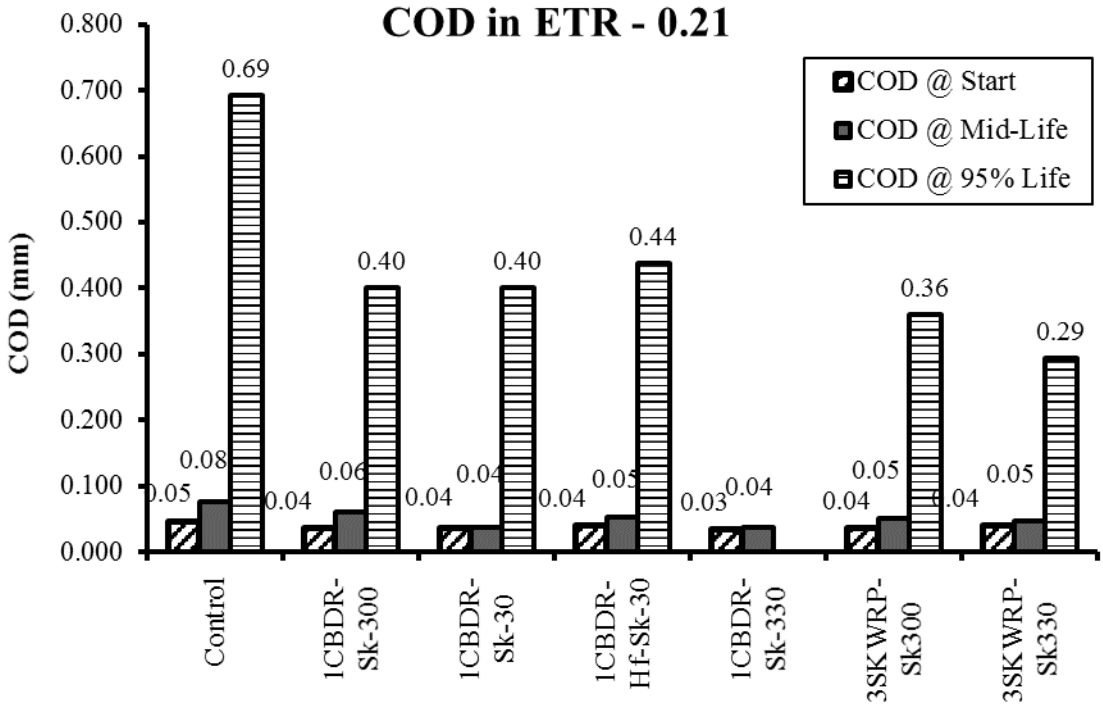

Figure 5.17 COD of specimens of ETR 0.21 group at the three stages of fatigue life

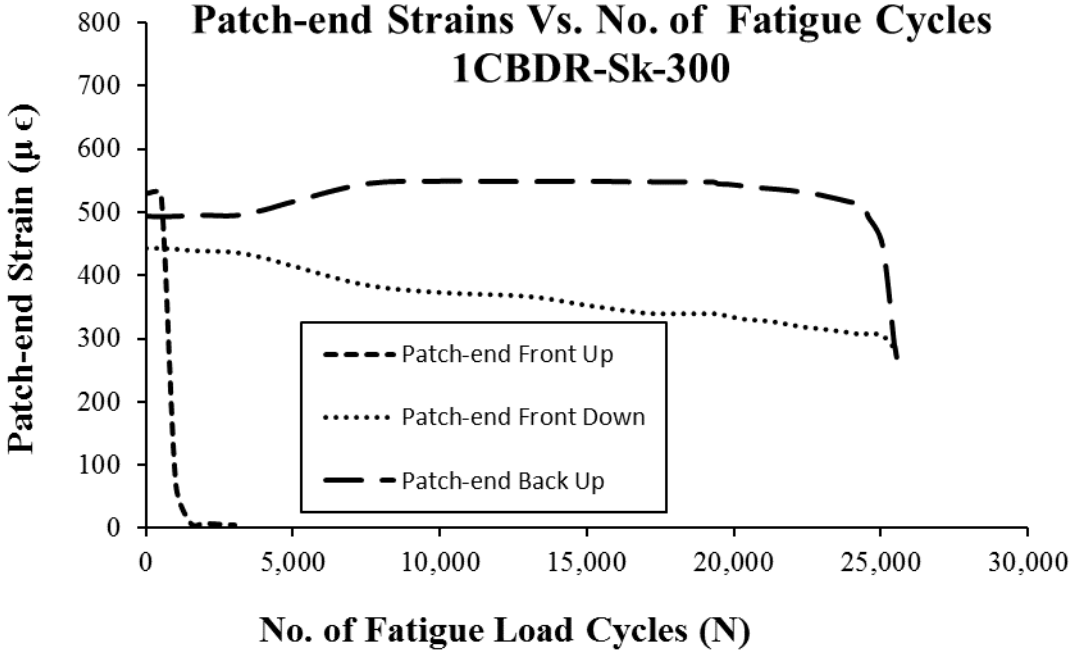

Figure 5.18 Strain outputs of patch-end strain gauges of 1-CBDR-Sk-300

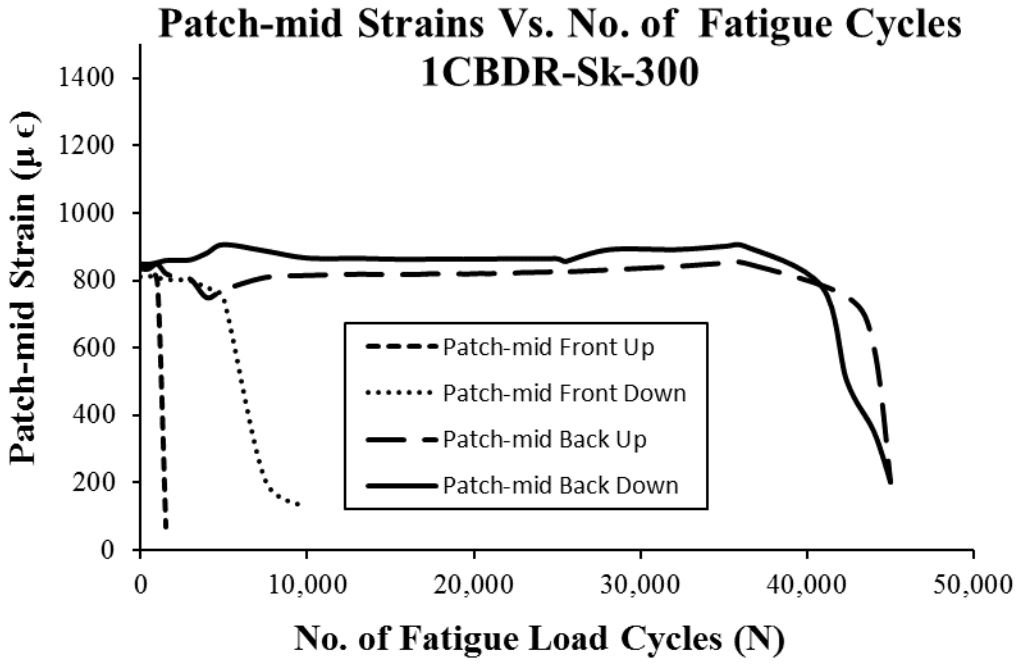

Figure 5.19 Strain outputs of patch-mid strain gauges of 1-CBDR-Sk-300

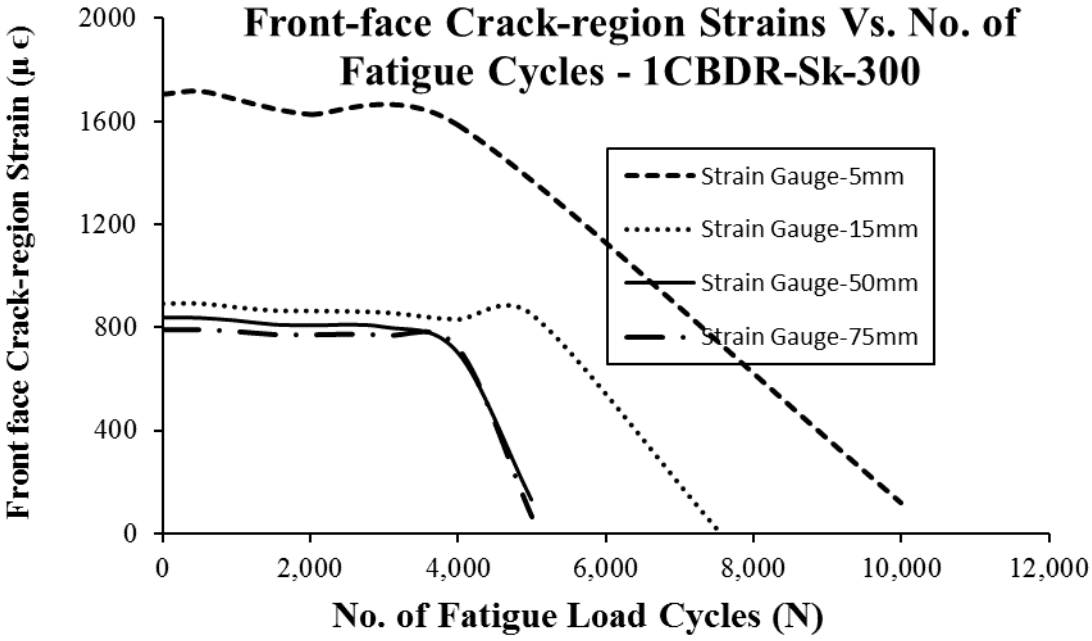

Figure 5.20 Strain outputs of front face crack region strain gauges of 1-CBDR-Sk-300

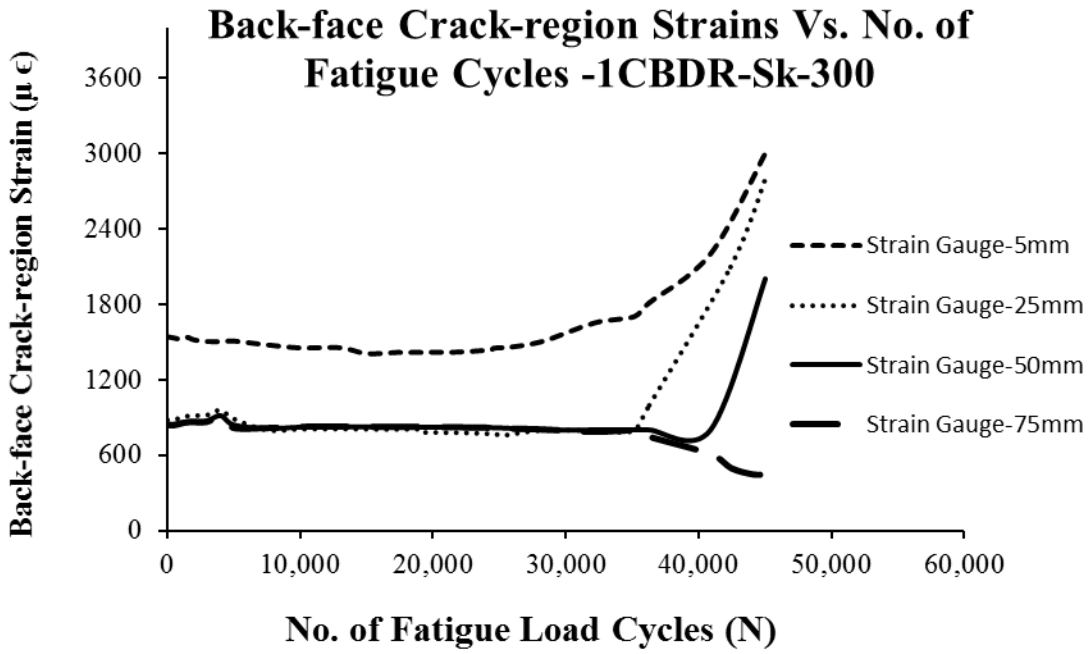

Figure 5.21 Strain outputs of back face crack region strain gauges of 1-CBDR-Sk-300

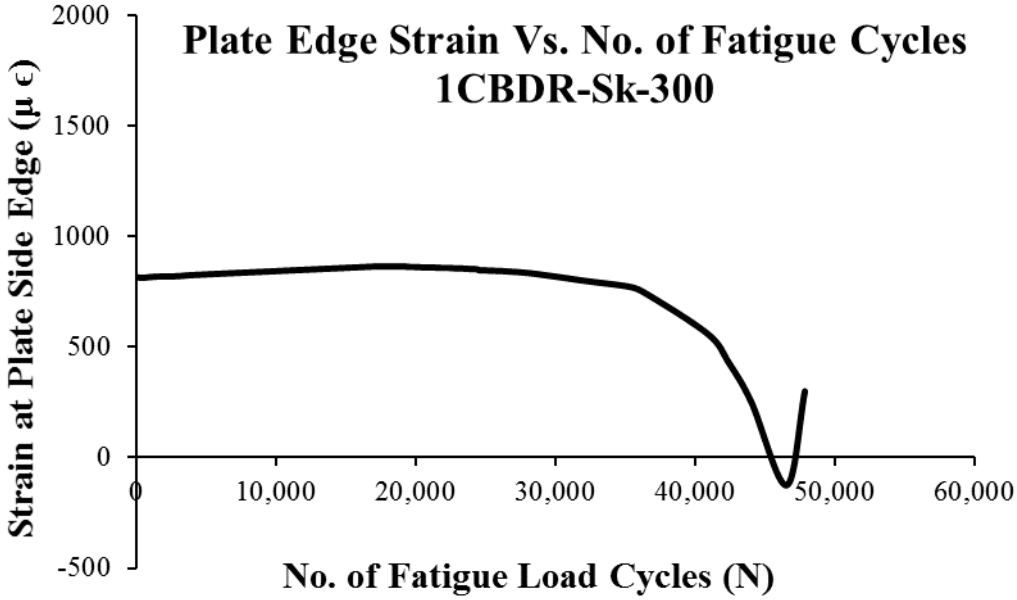

Figure 5.22 Strain outputs of plate edge strain gauge of 1-CBDR-Sk-300

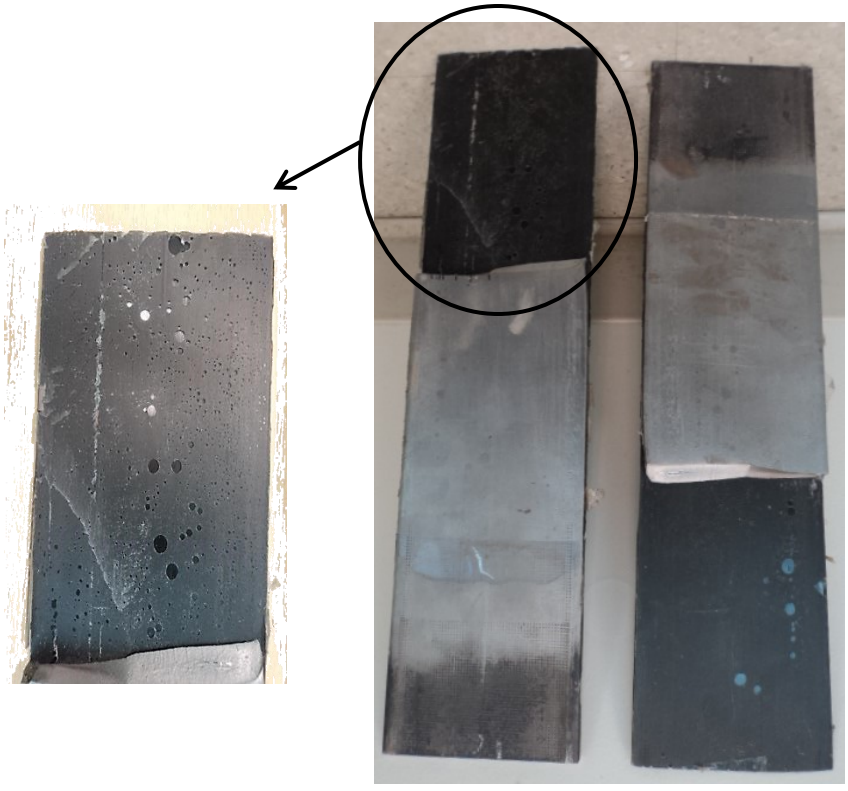

Figure 5.23 Delaminated CFRP surface showing air bubbles marks and the failed specimen 1CBDR-Sk-300

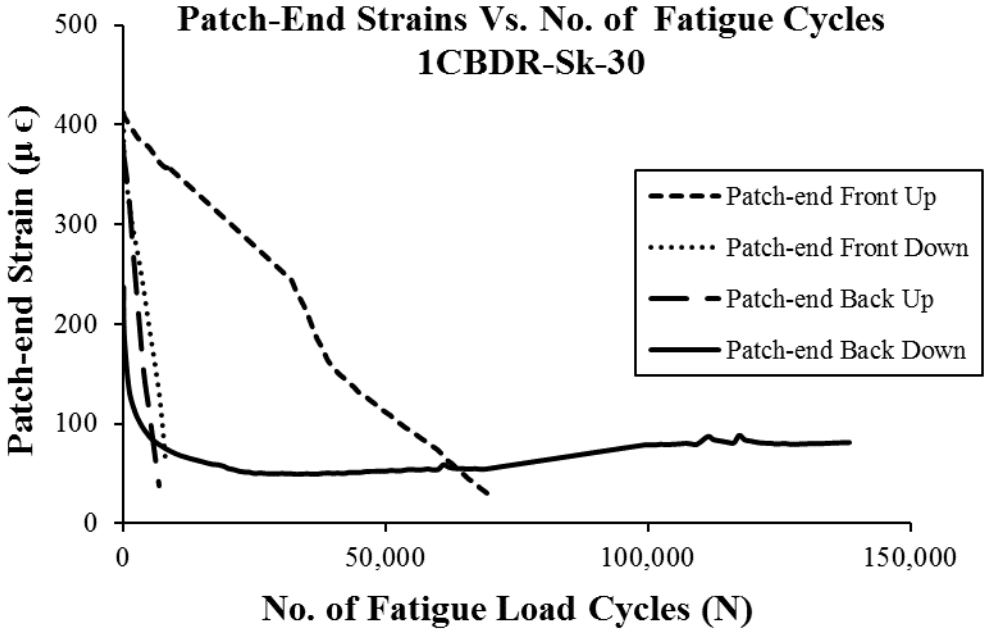

Figure 5.24 Strain outputs of patch-end strain gauges of 1-CBDR-Sk-30

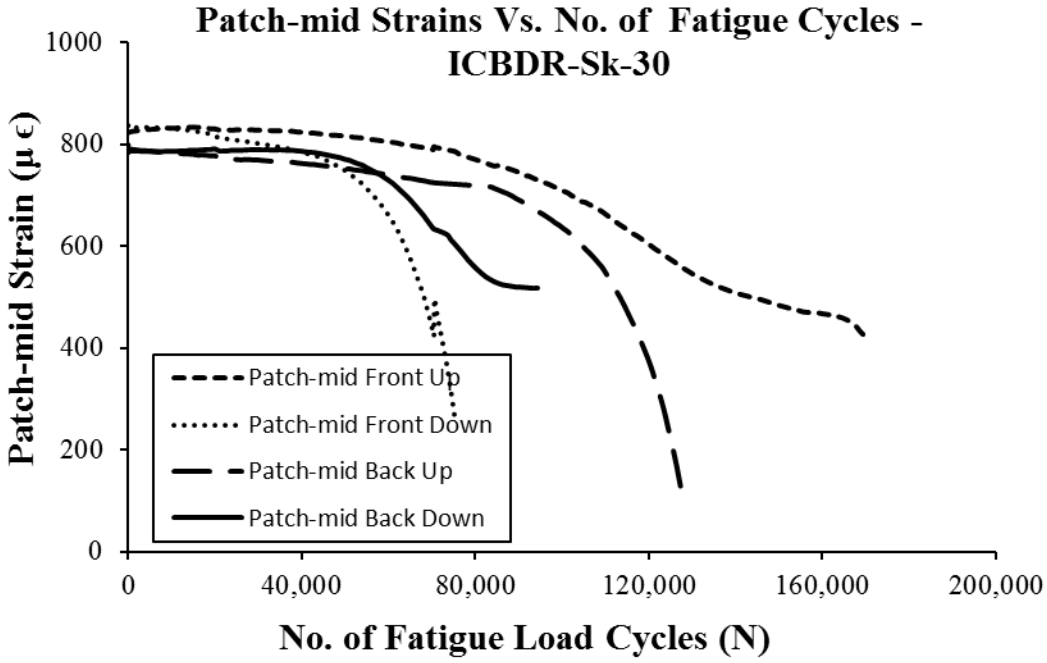

Figure 5.25 Strain outputs of mid bond-length strain gauges of 1-CBDR-Sk-30

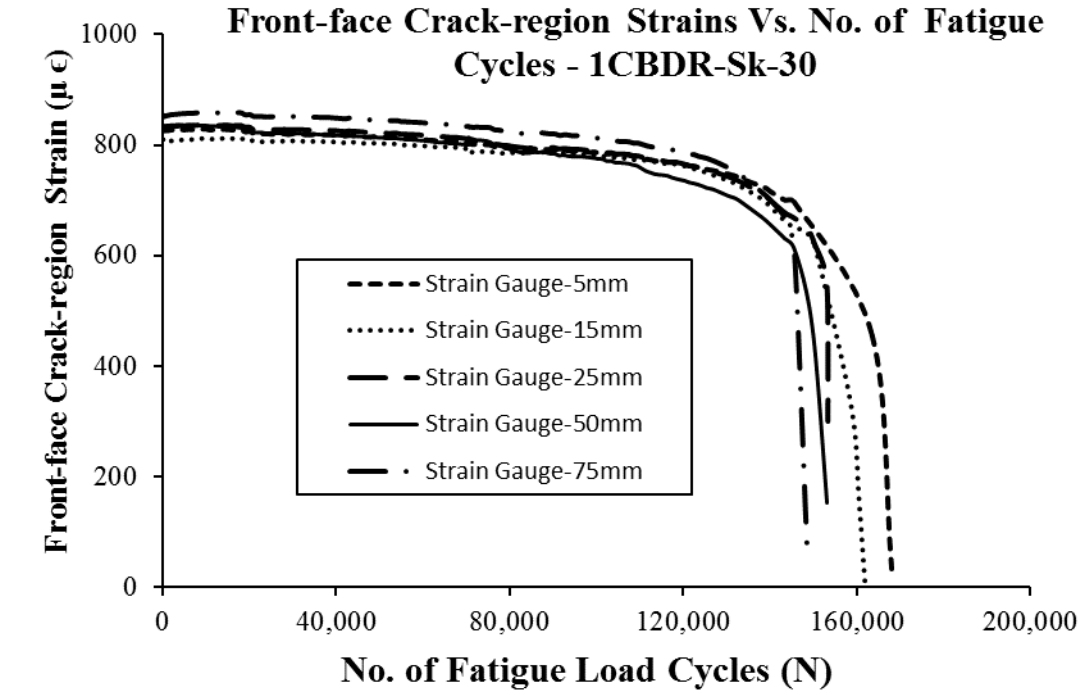

Figure 5.26 Strain outputs of front face crack region strain gauges of 1-CBDR-Sk-30

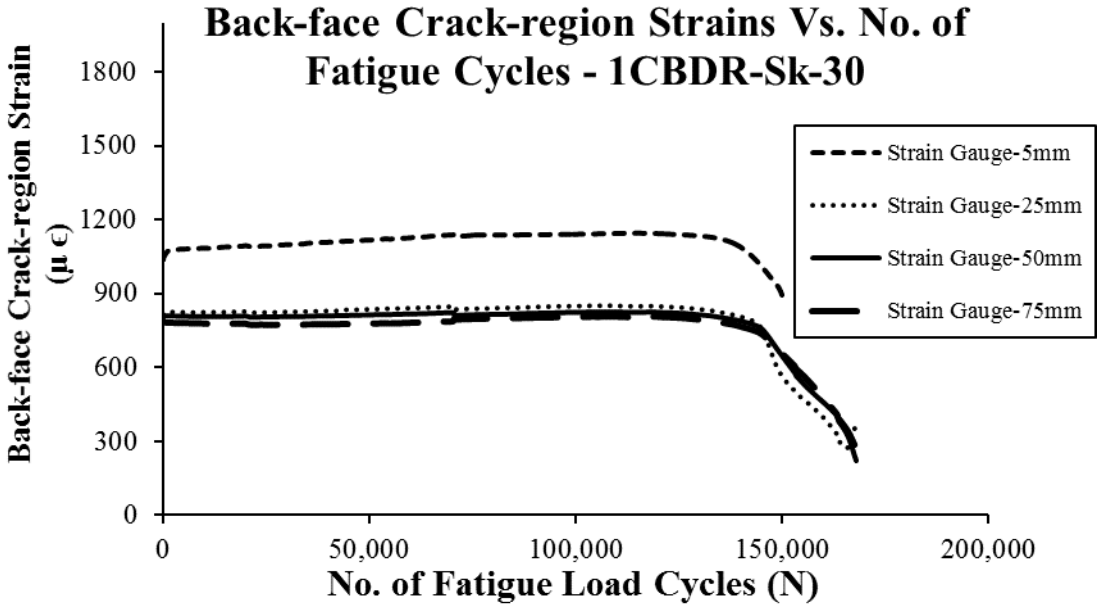

Figure 5.27 Strain outputs of back face crack region strain gauges of 1-CBDR-Sk-30

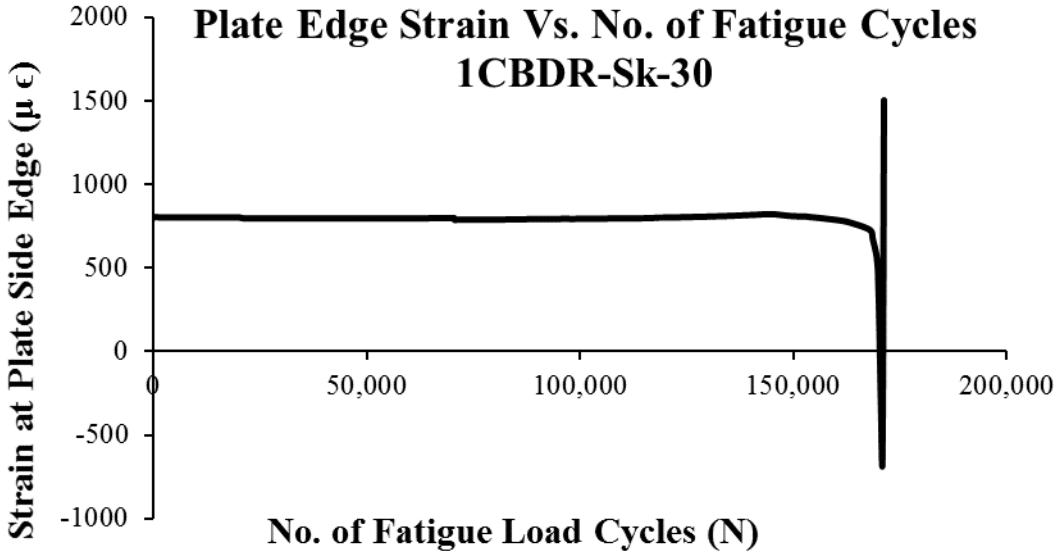

Figure 5.28 Strain outputs of plate edge strain gauge of 1-CBDR-Sk-30

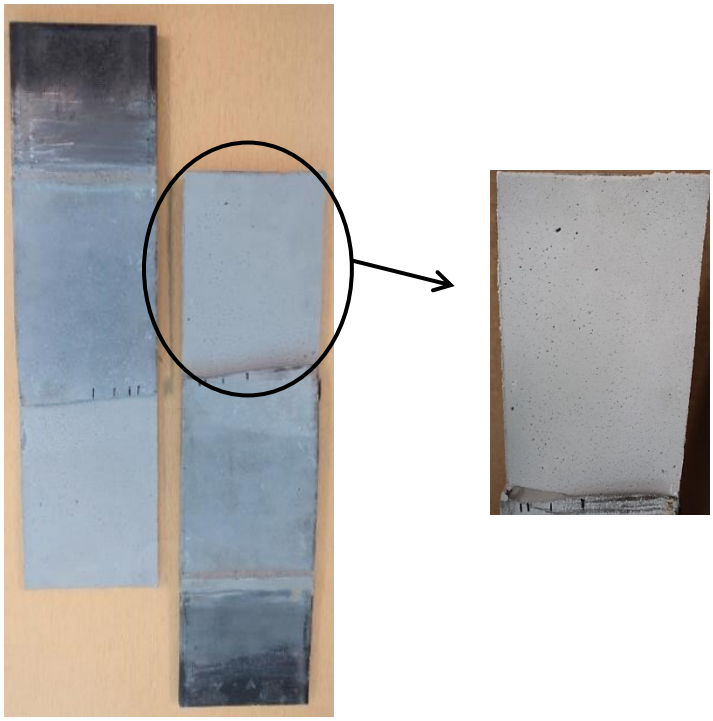

Figure 5.29 Delaminated CFRP surface and the failed specimen 1CBDR-Sk-30

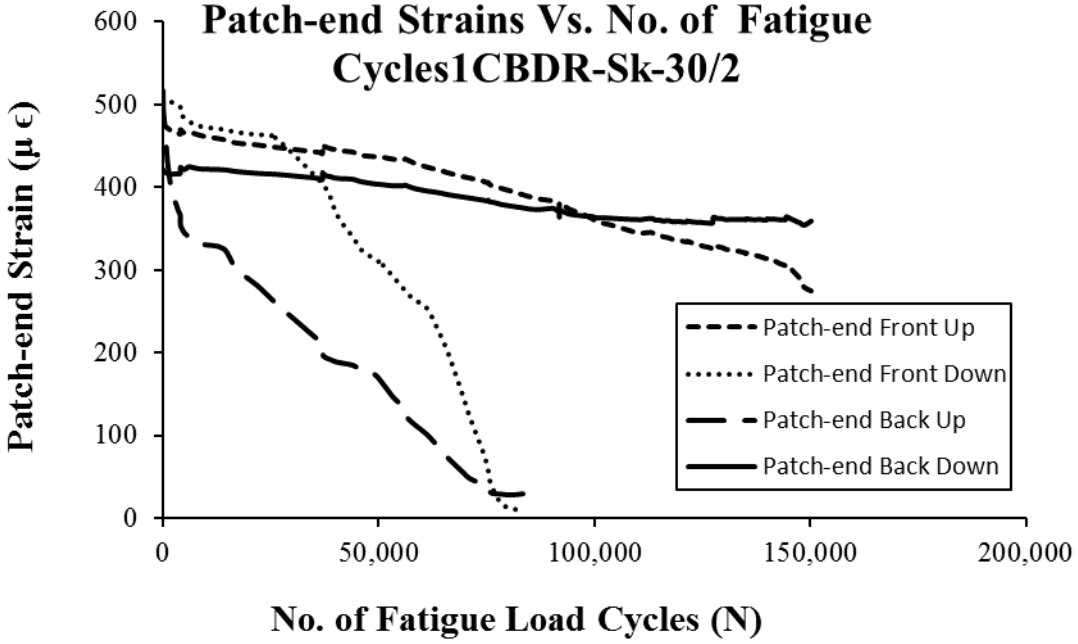

Figure 5.30 Strain outputs of patch-end strain gauges of 1-CBDR-Half-Th-Sk-30

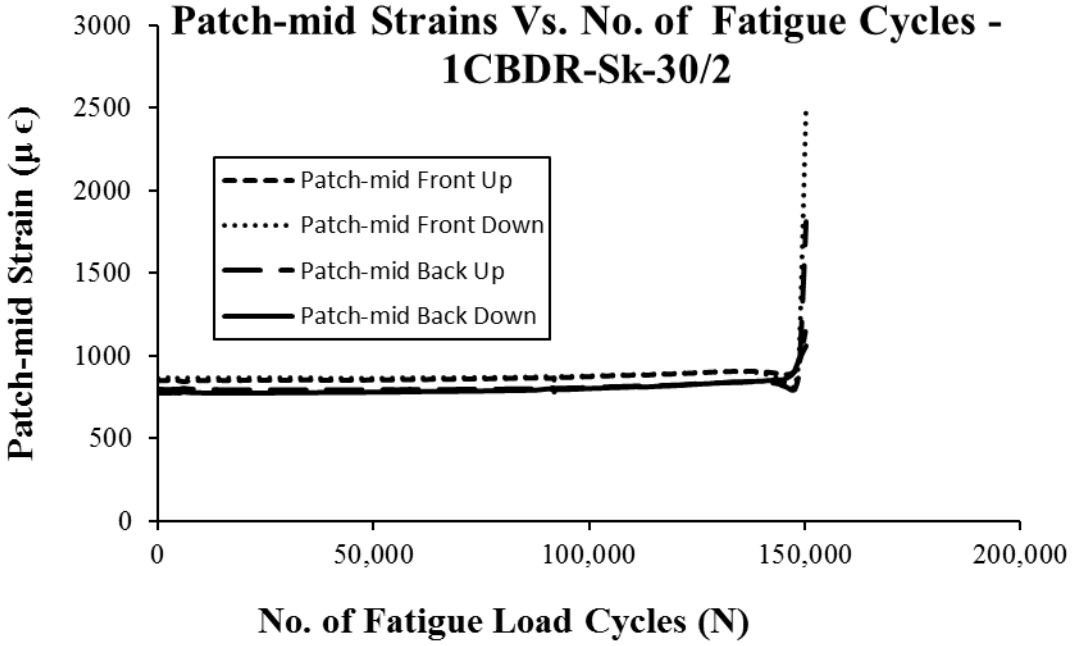

Figure 5.31 Strain outputs of mid bond-length strain gauges of 1-CBDR-Half-Th-Sk-30

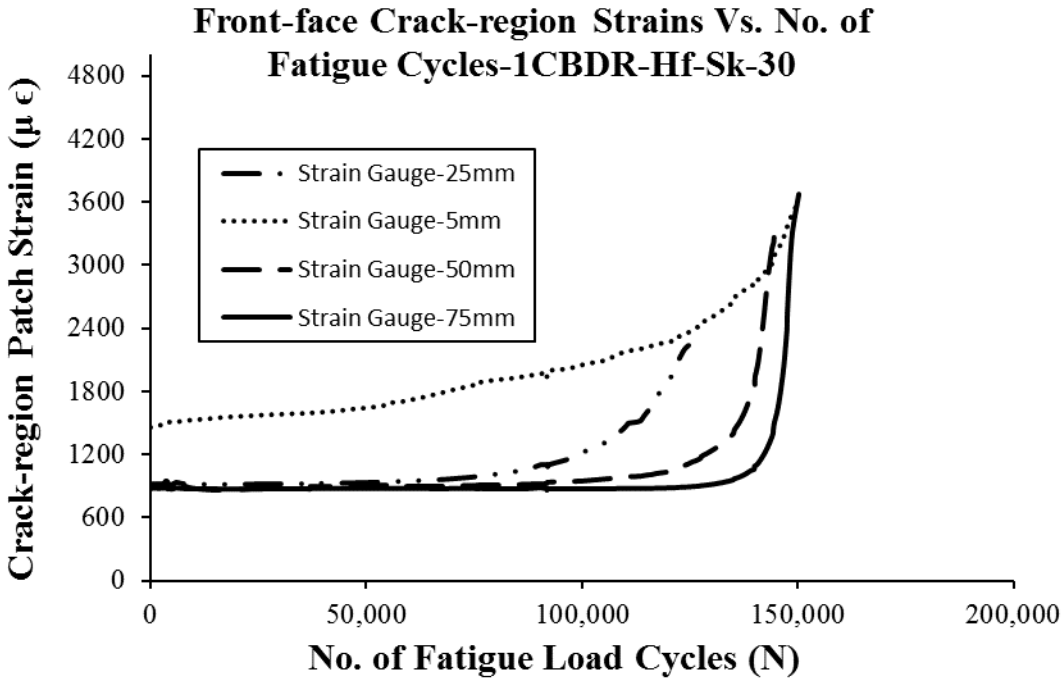

Figure 5.32 Strain outputs of front face crack region strain gauges of 1-CBDR-Half-Th-Sk-30

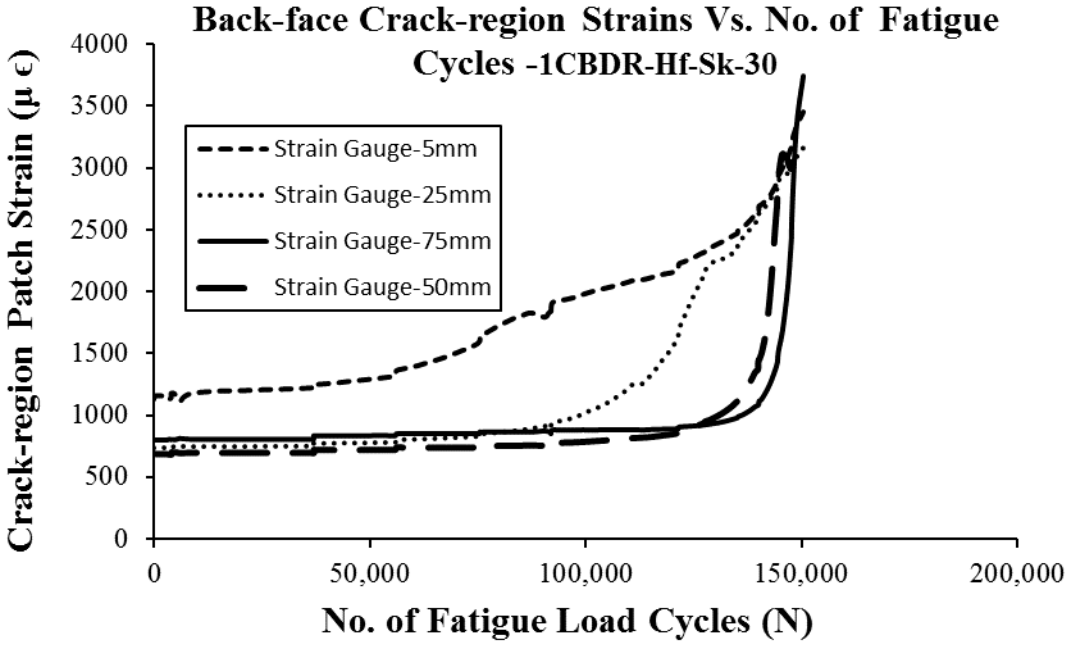

Figure 5.33 Strain outputs of back face crack region strain gauges of 1-CBDR-Half-Th-Sk-30

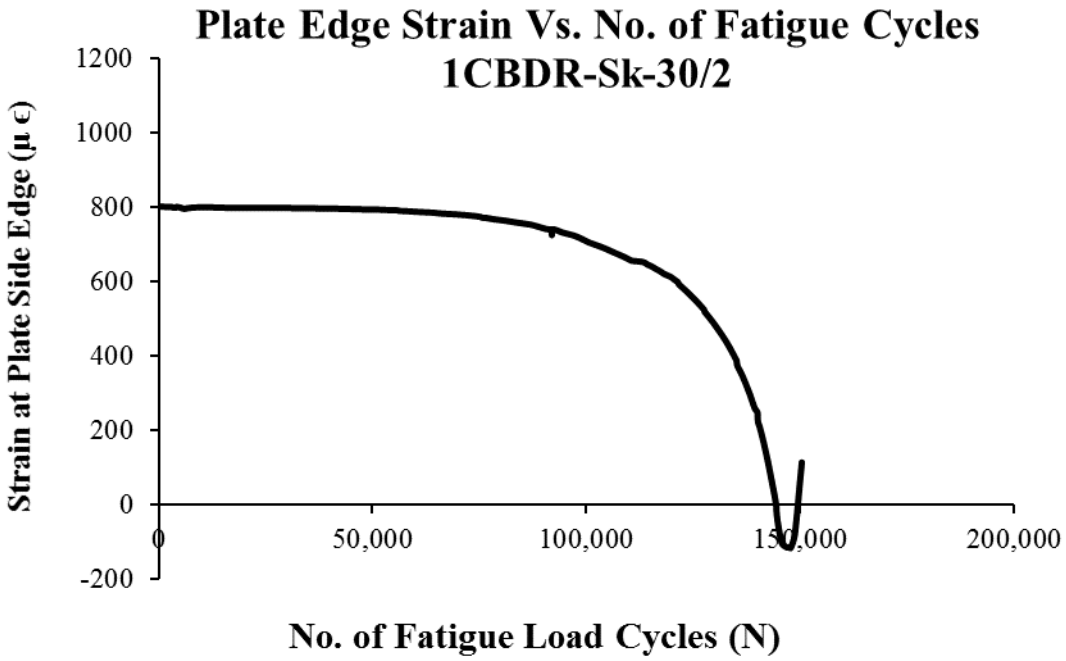

Figure 5.34 Strain outputs of plate edge strain gauge of 1-CBDR-Half-Th-Sk-30

Figure 5.35 Delaminated CFRP surface and the failed specimen
1-CBDR-Half-Th-Sk-30

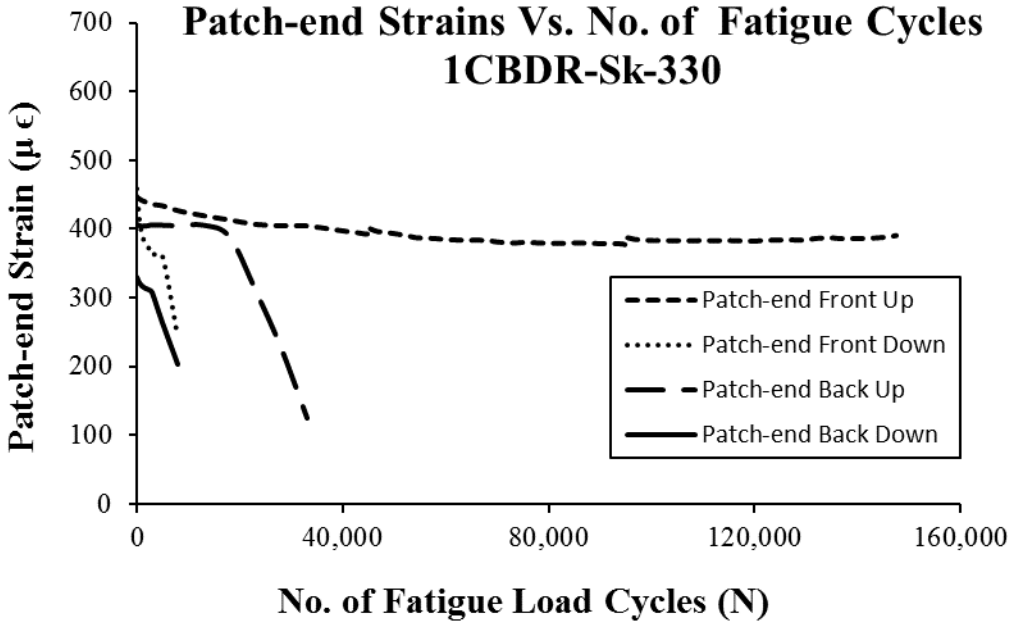

Figure 5.36 Strain outputs of patch-end strain gauges of 1-CBDR-Sk-330

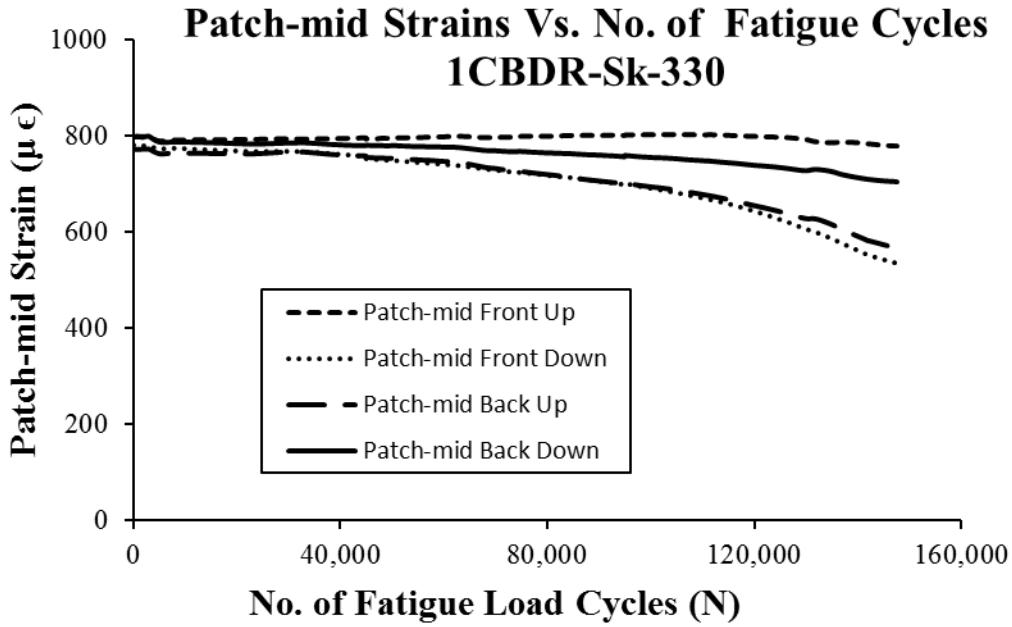

Figure 5.37 Strain outputs of mid bond-length strain gauges of 1-CBDR-Sk-330

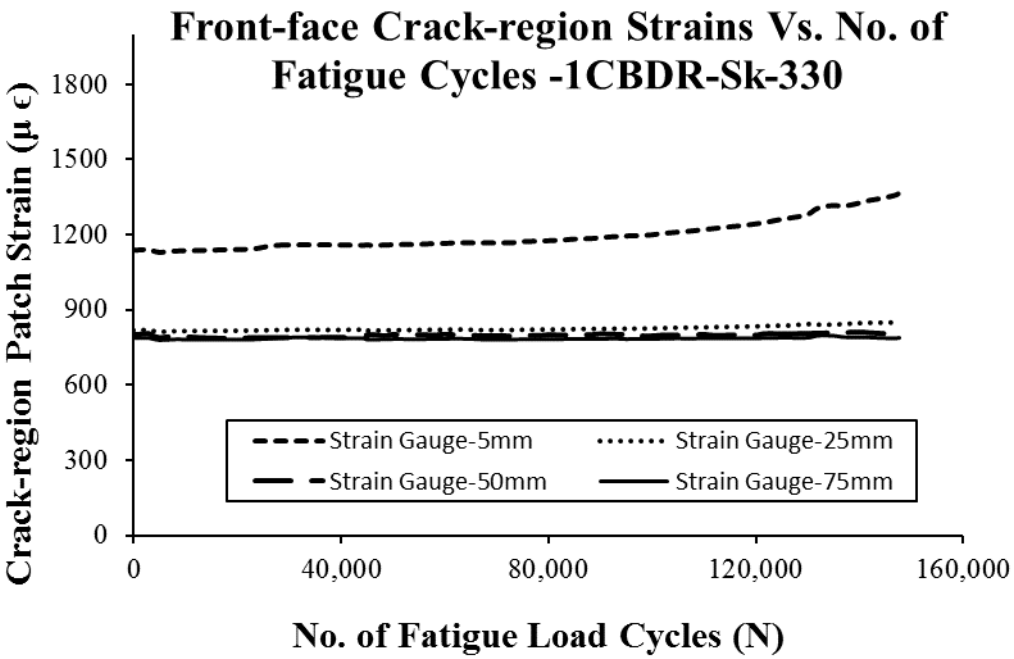

Figure 5.38 Strain outputs of front face crack region strain gauges of 1-CBDR-Sk-330

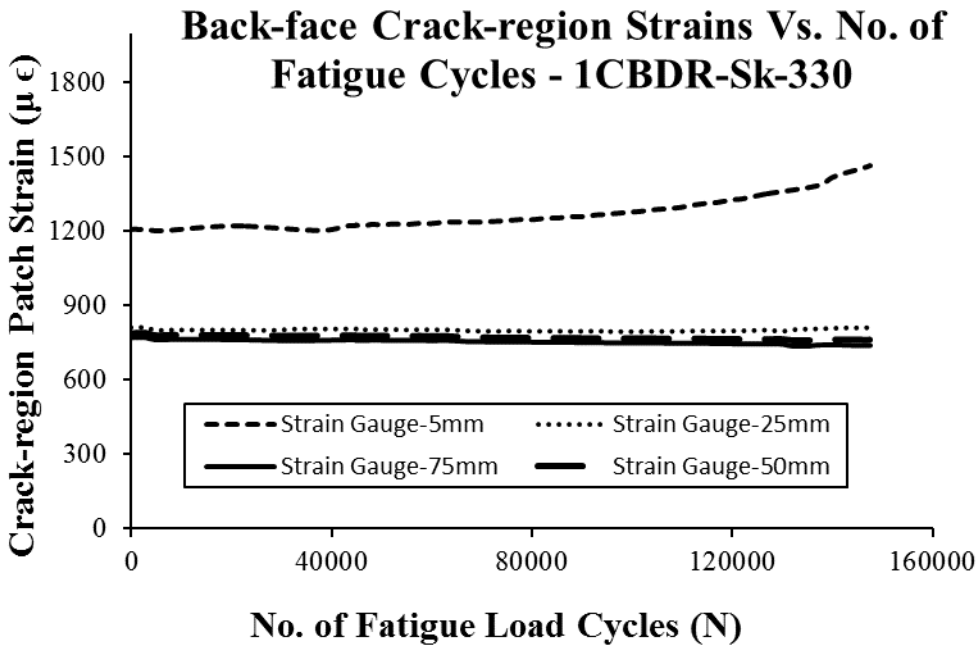

Figure 5.39 Strain outputs of back face crack region strain gauges of 1-CBDR-Sk-330

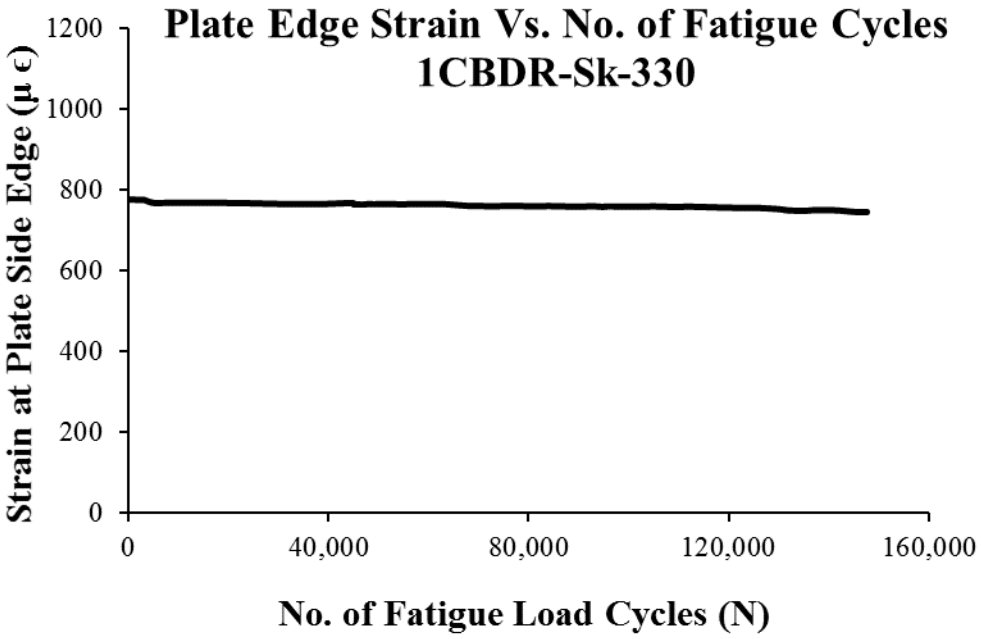

Figure 5.40 Strain outputs of plate edge strain gauge of 1-CBDR-Sk-330

Figure 5.41 Unbroken specimen 1-CBDR-Sk-330

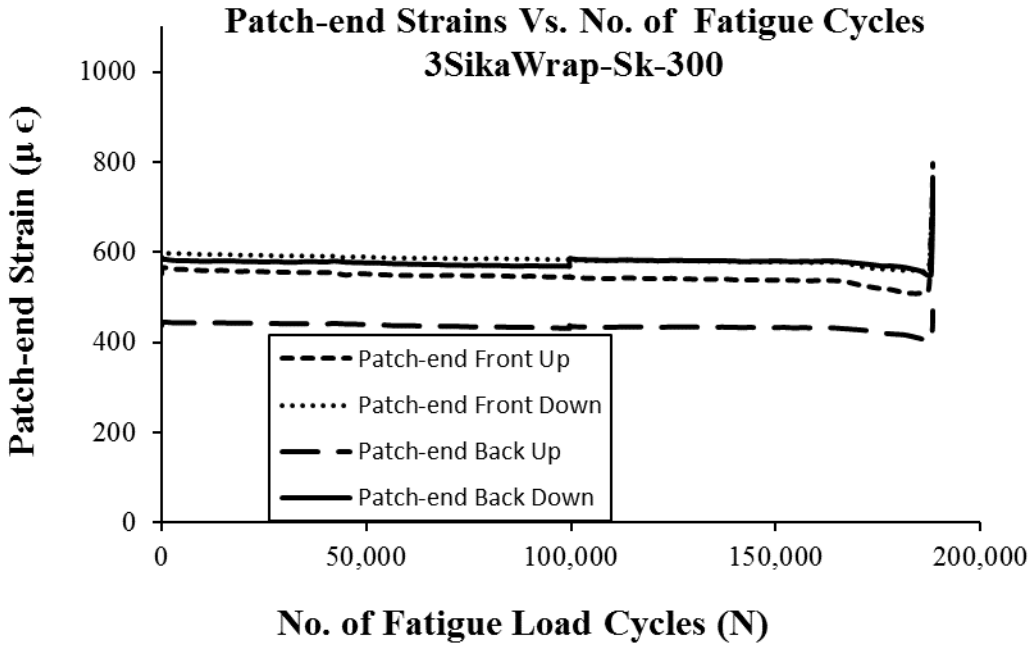

Figure 5.42 Strain outputs of patch-end strain gauges of 3-SikaWrap-Sk-300

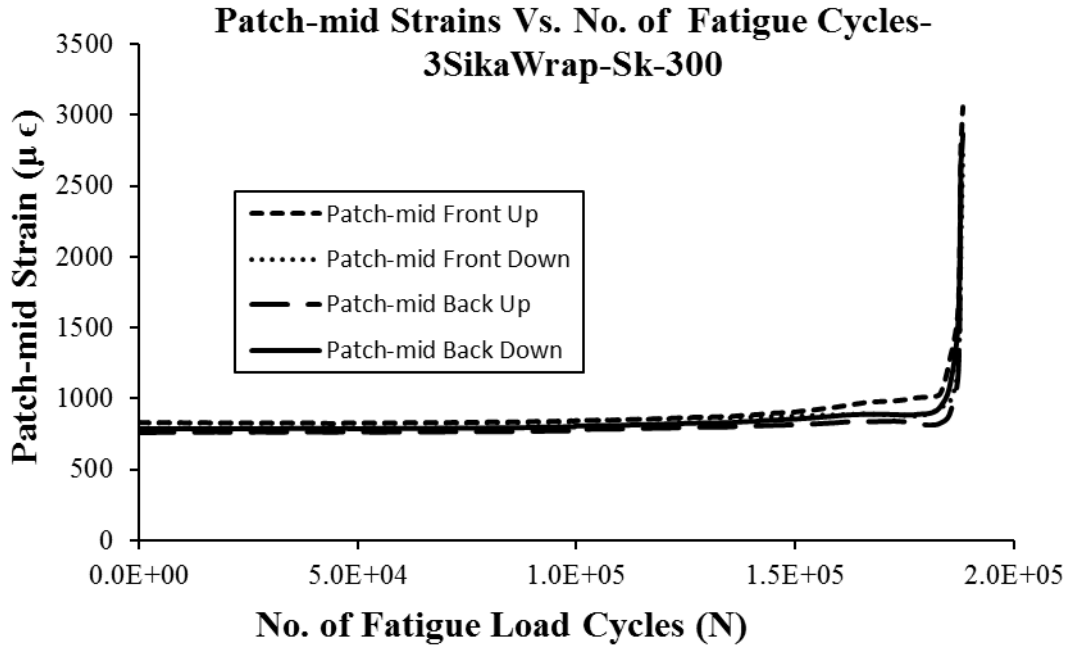

Figure 5.43 Strain outputs of mid bond-length strain gauges of 3-SikaWrap-Sk-300

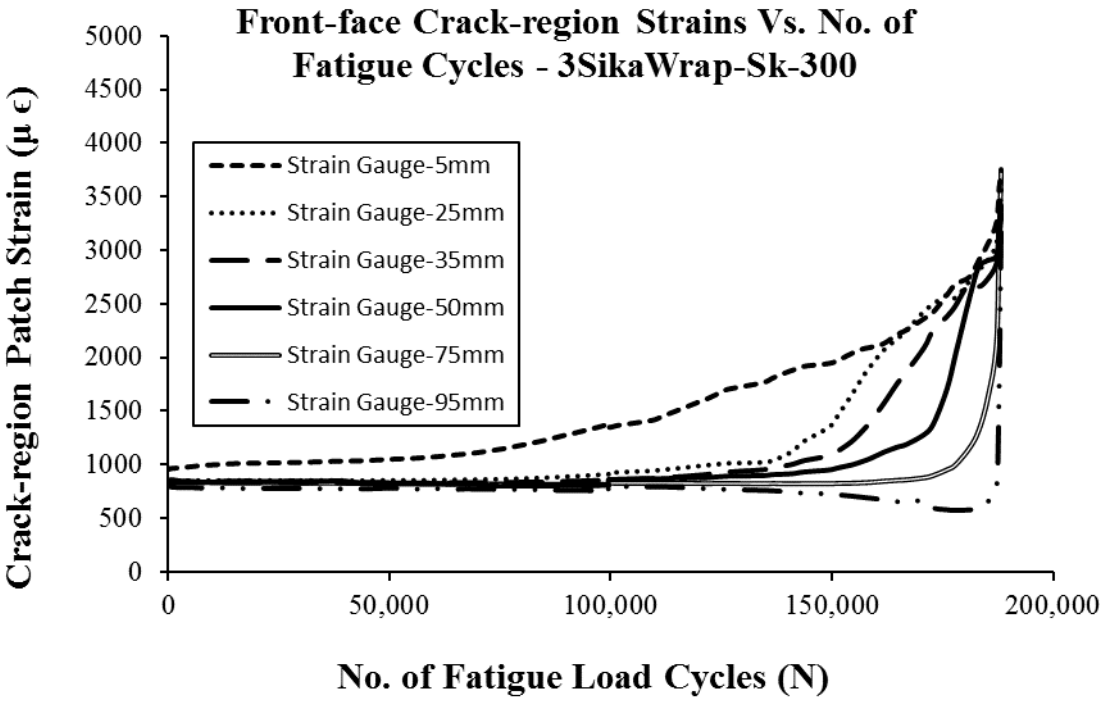

Figure 5.44 Strain outputs of front face crack region strain gauges of 3-SikaWrap-Sk-300

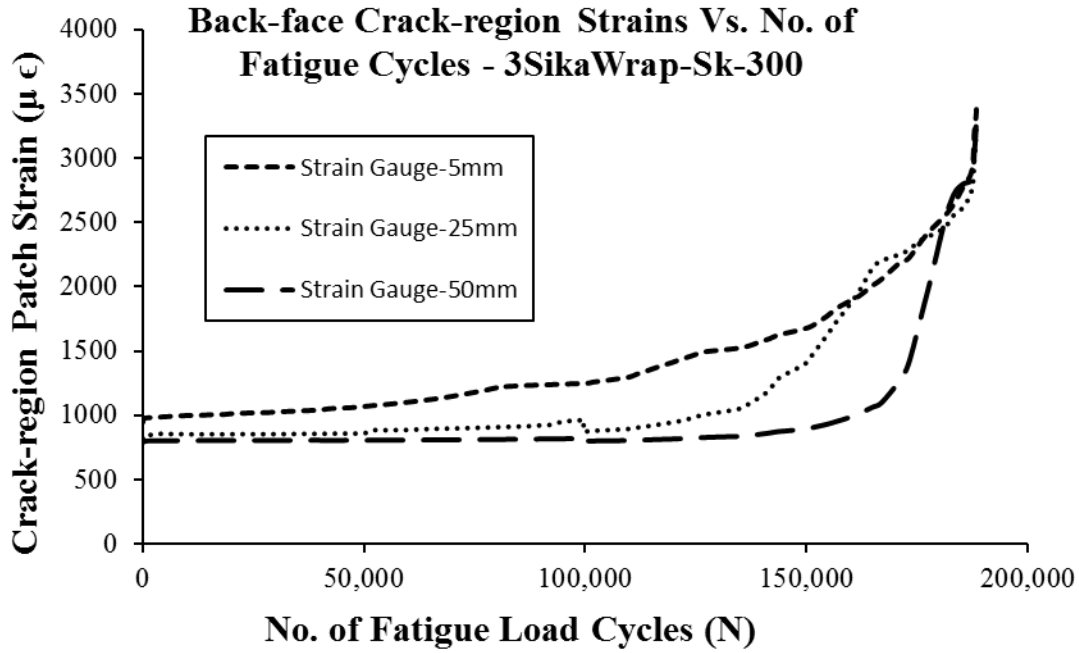

Figure 5.45 Strain outputs of back face crack region strain gauges of 3-SikaWrap-Sk-300

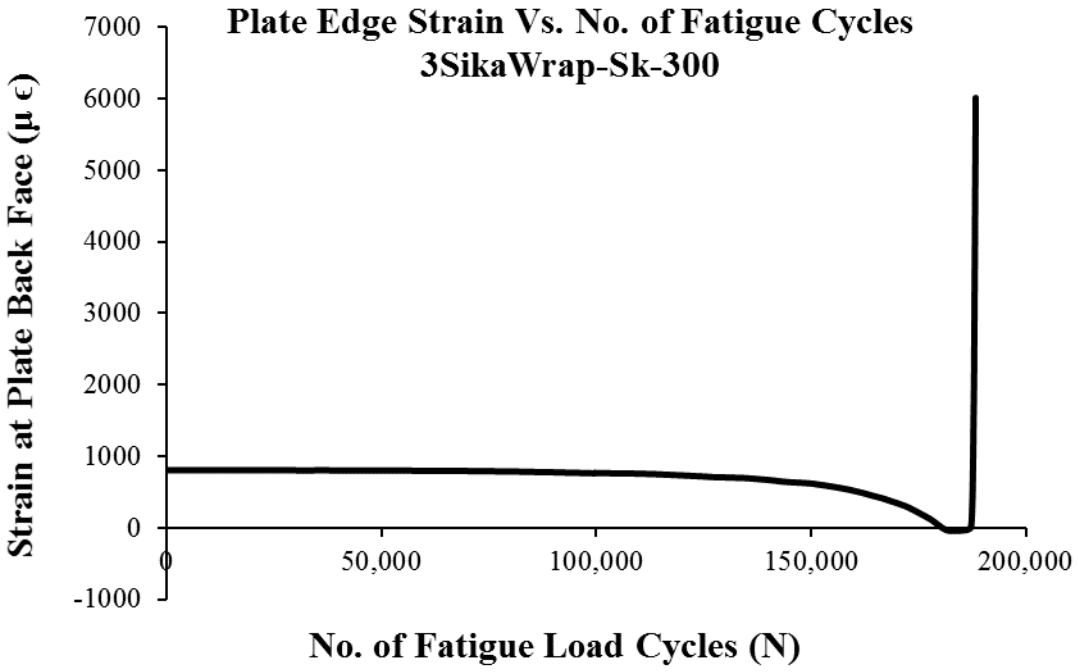

Figure 5.46 Strain outputs of plate edge strain gauge of 3-SikaWrap-Sk-300

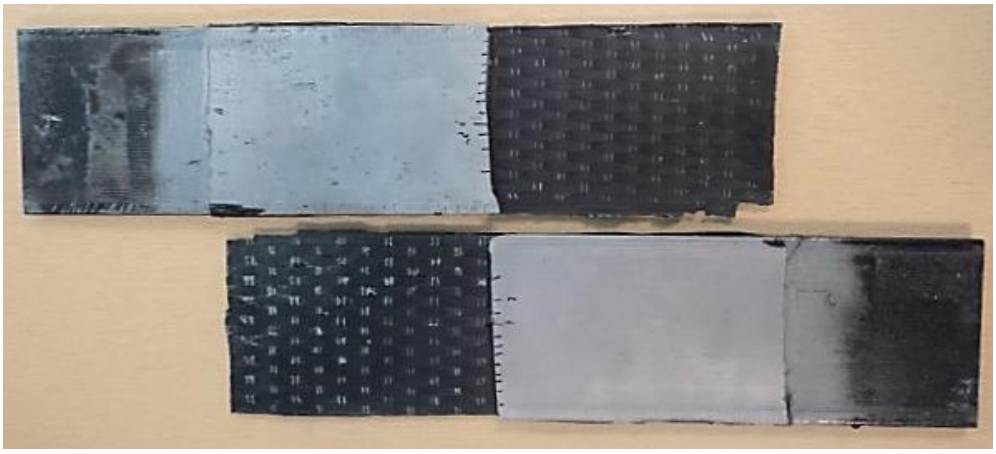

Figure 5.47 Delaminated CFRP surface and the failed specimen 3-Sikwrap-Sk-300

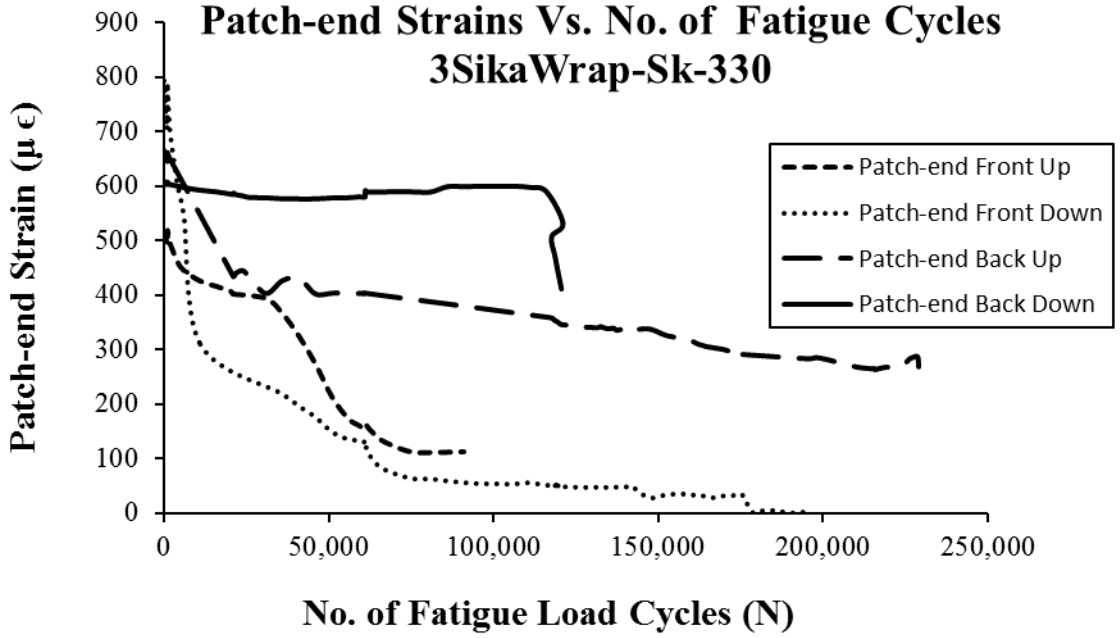

Figure 5.48 Strain outputs of patch-end strain gauges of 3-SikaWrap-Sk-330

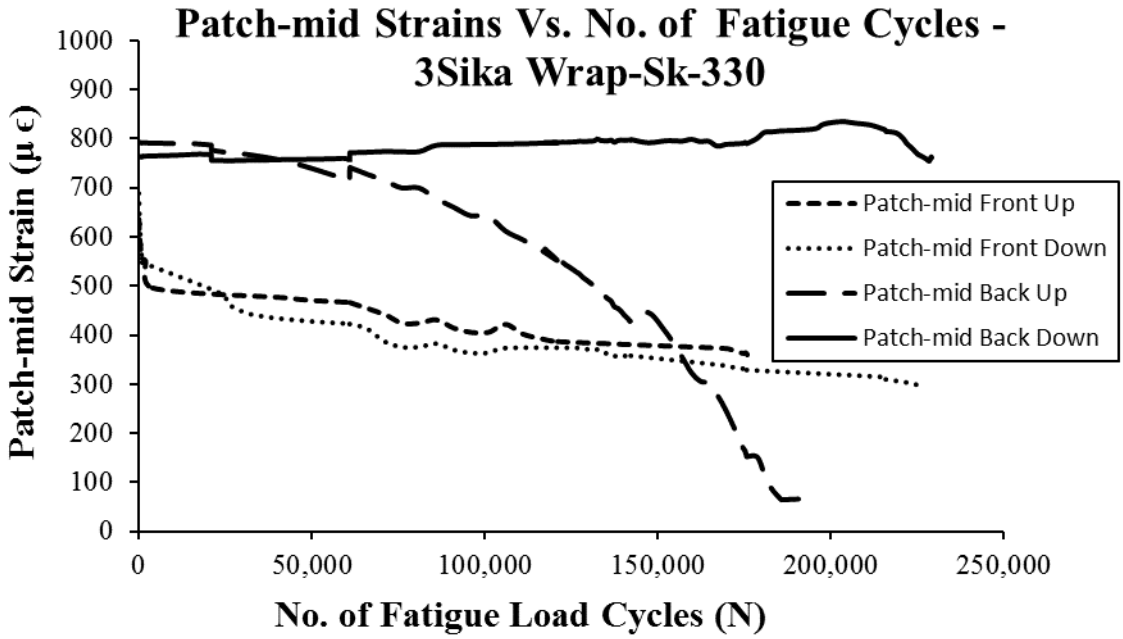

Figure 5.49 Strain outputs of mid bond-length strain gauges of 3-SikaWrap-Sk-330

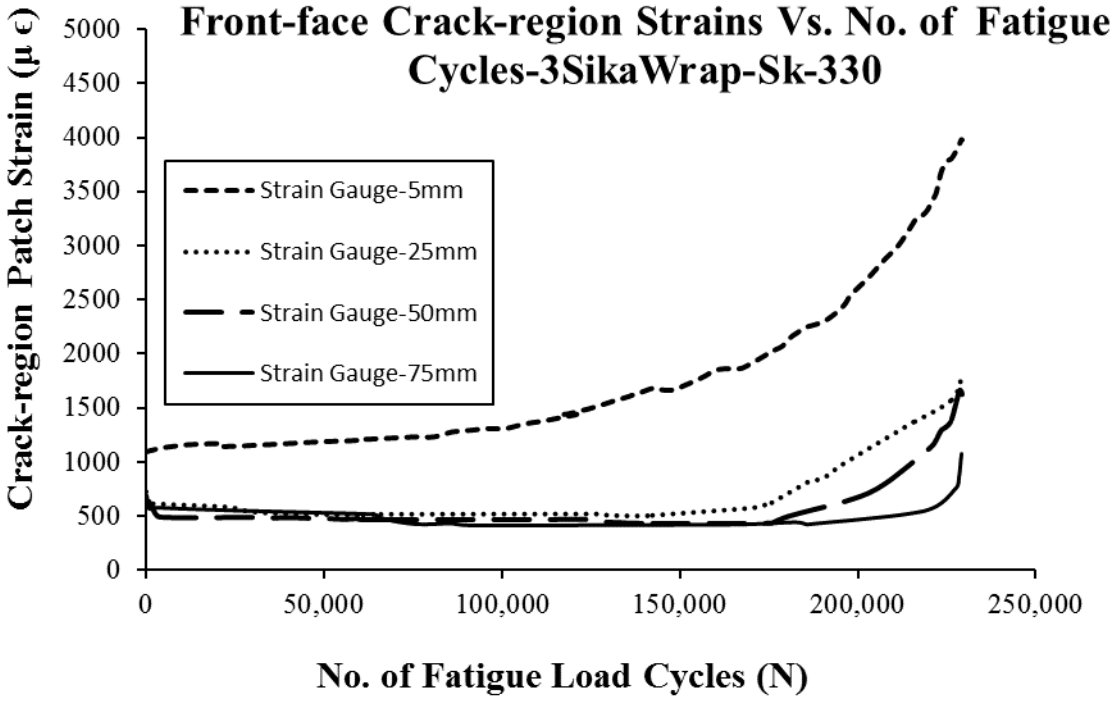

Figure 5.50 Strain at front face crack region strain gauges of 3-SikaWrap-Sk-330

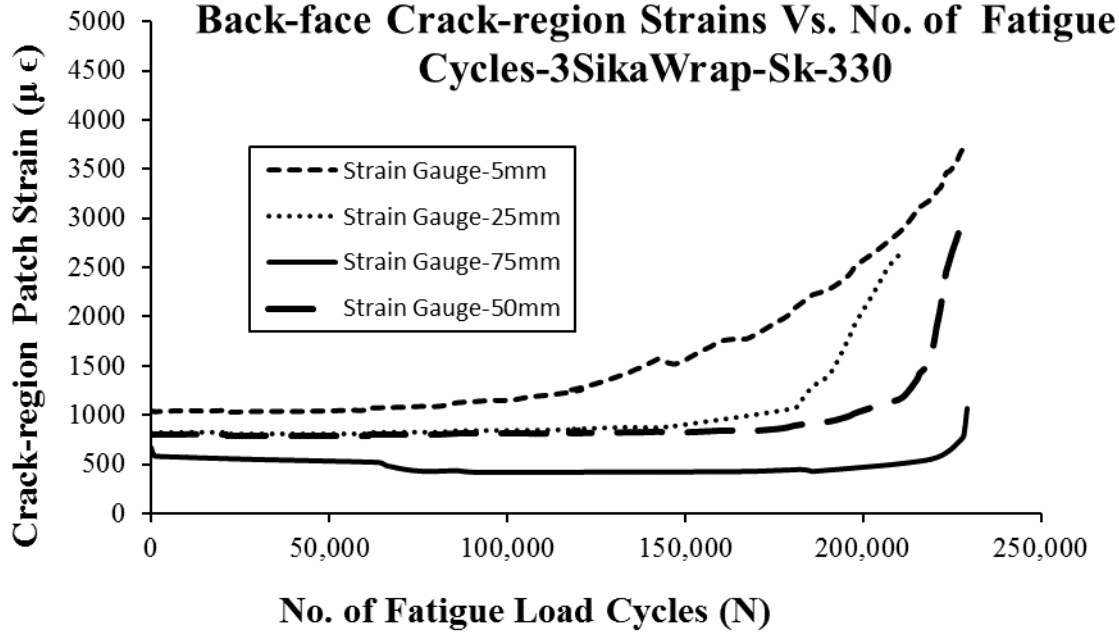

Figure 5.51 Strain outputs of back face crack region strain gauges of 3-SikaWrap-Sk-330

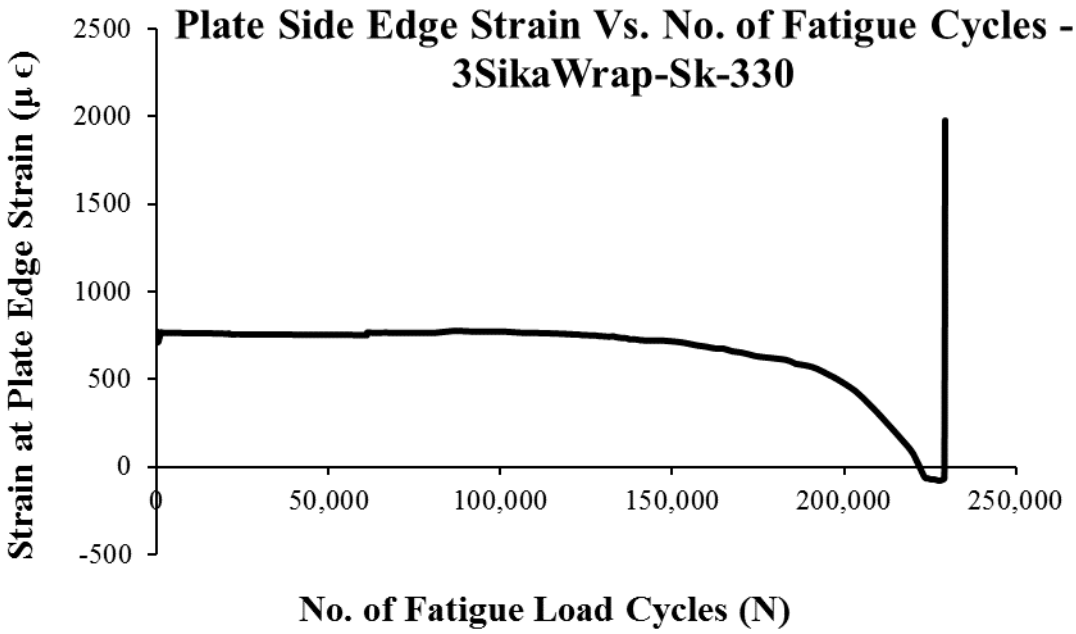

Figure 5.52 Strain outputs of plate edge strain gauge of 3-SikaWrap-Sk-330

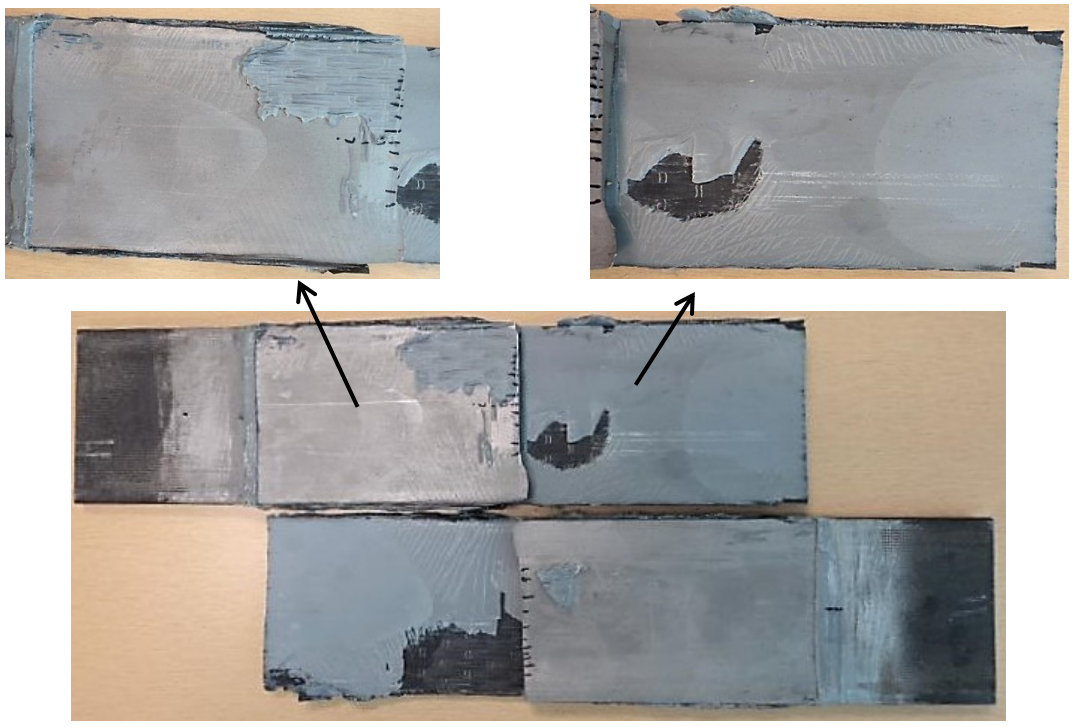

Figure 5.53 Delaminated CFRP surface and the failed specimen 3-Sikwrap-Sk-330

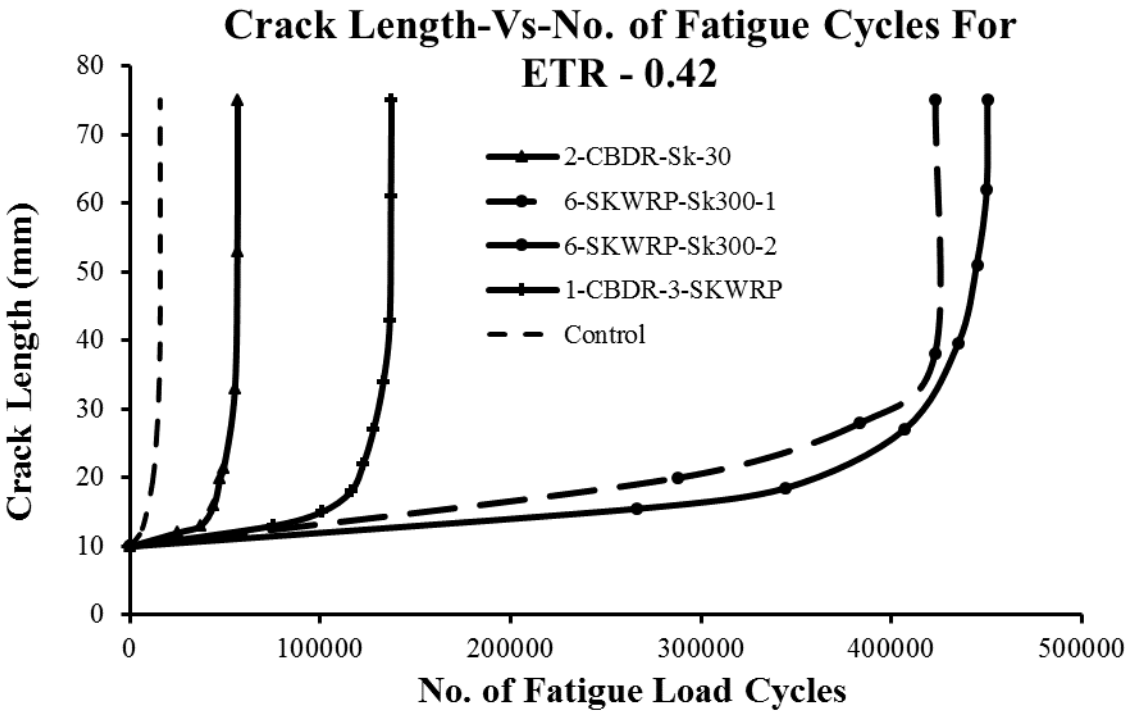

Figure 5.54 Crack-length variations with fatigue cycles (a-N curves) of ETR 0.42 specimens

6-Sikawrap-Sk-300-A

1-CBDR-3-SKWRP

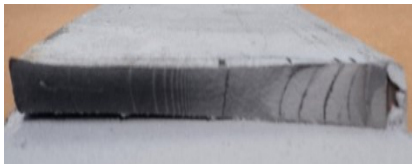

2-CBDR-Sk-30

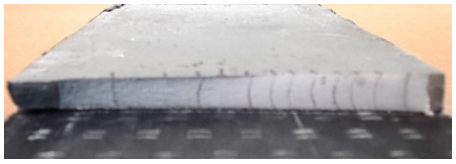

6-Sikawrap-Sk-300-B

Figure 5.55 Failed steel surfaces in specimens of ETR 0.42 showing the beach marks

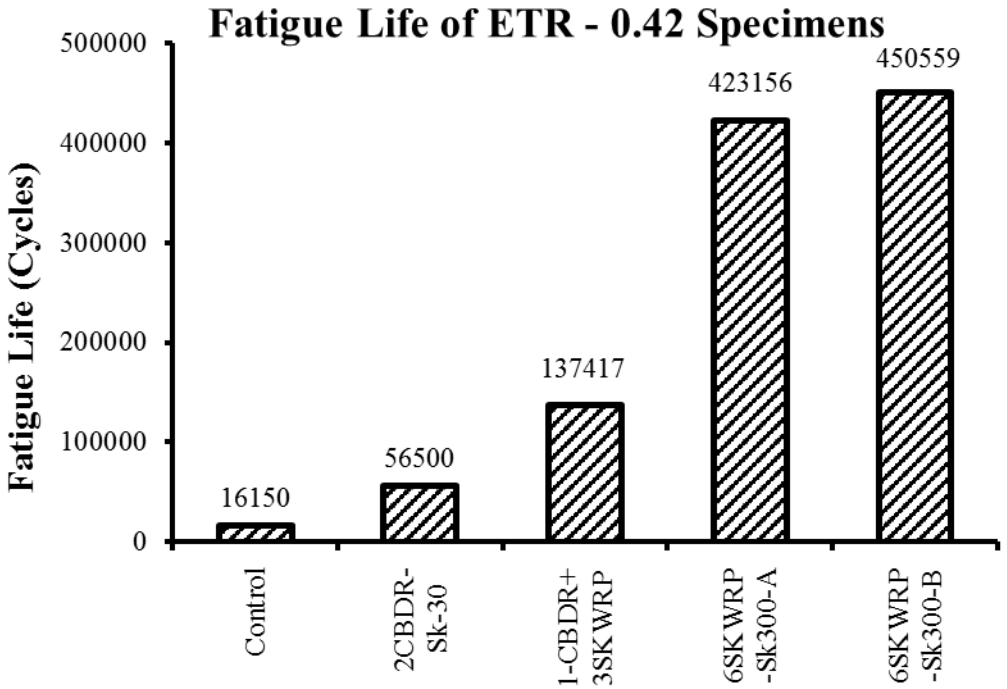

Figure 5.56 Fatigue life of specimens of ETR 0.42 group

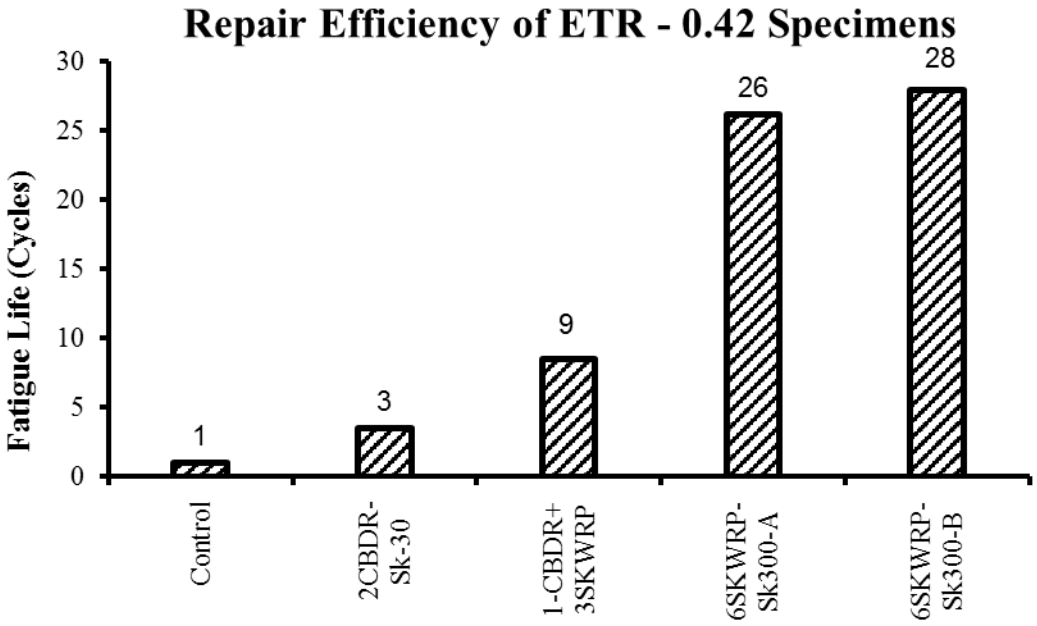

Figure 5.57 Repair efficiency of specimens of ETR 0.42 group

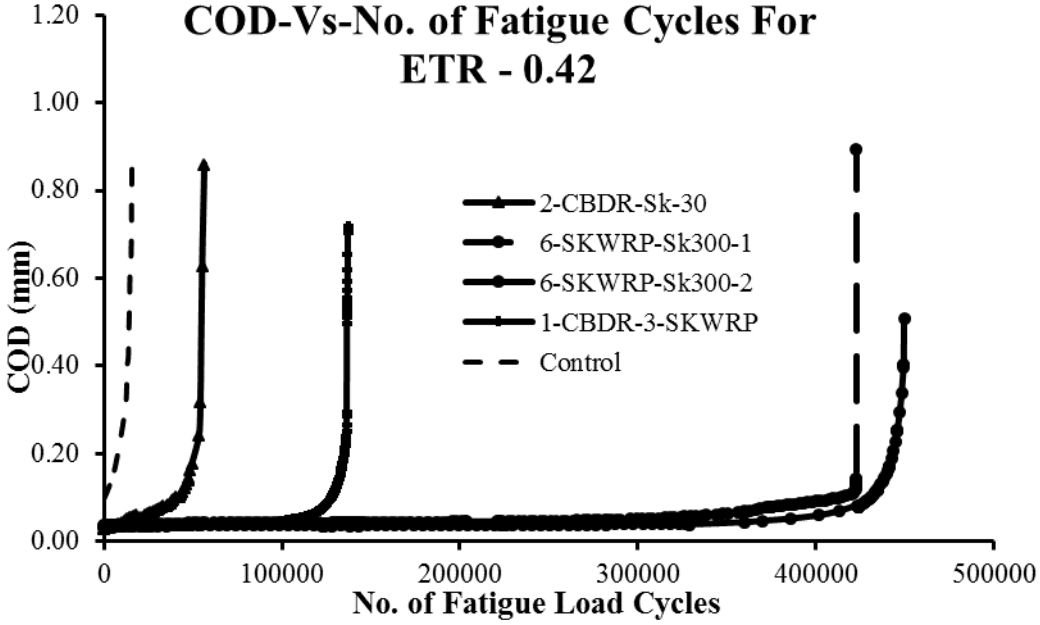

Figure 5.58 COD variations of specimens of ETR 0.42 group

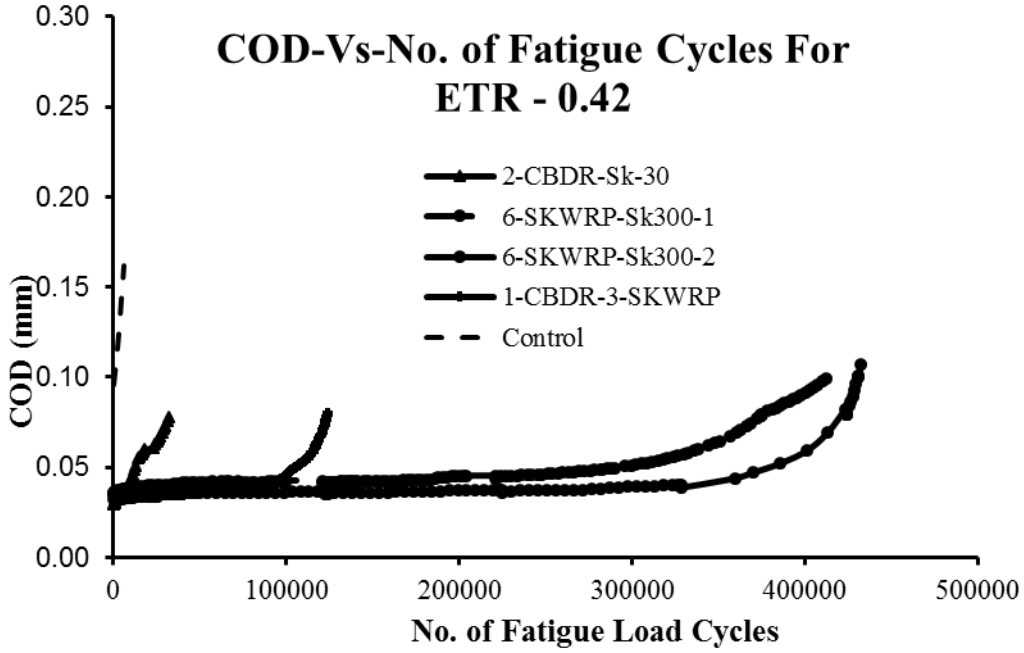

Figure 5.59 COD variations of specimens of ETR 0.42 group before rapid crack growth

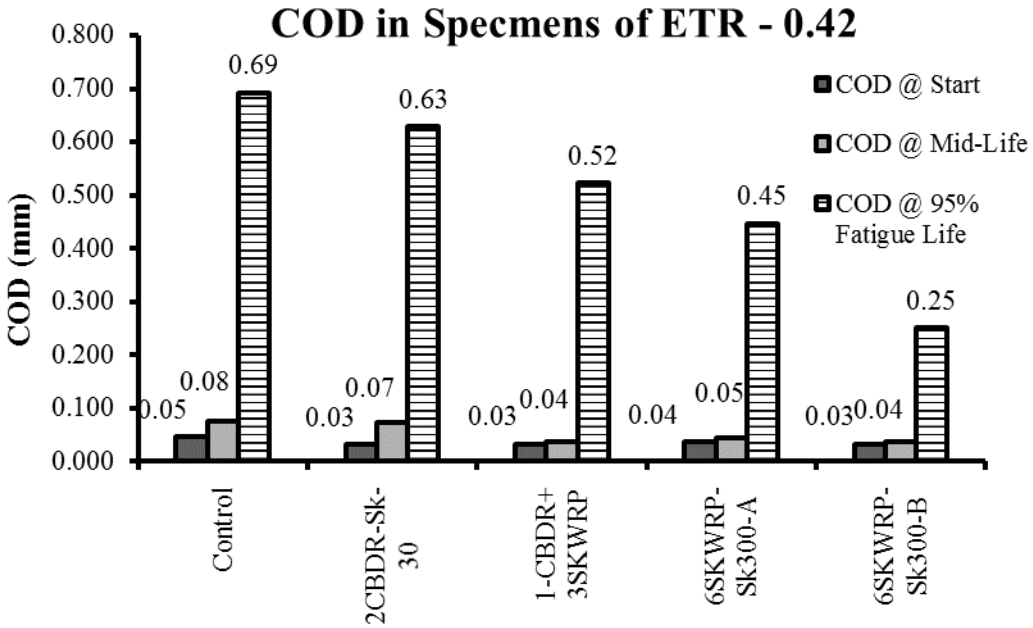

Figure 5.60 COD of specimens of ETR 0.42 group at the three stages of fatigue life

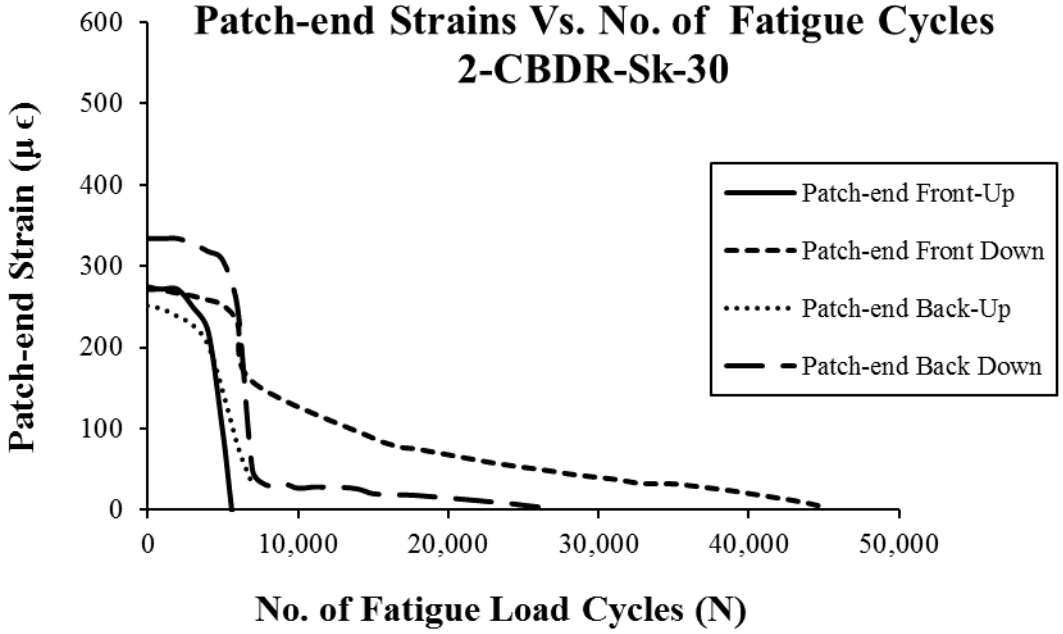

Figure 5.61 Strain outputs of patch-end strain gauges of 2-CBDR-Sk-30

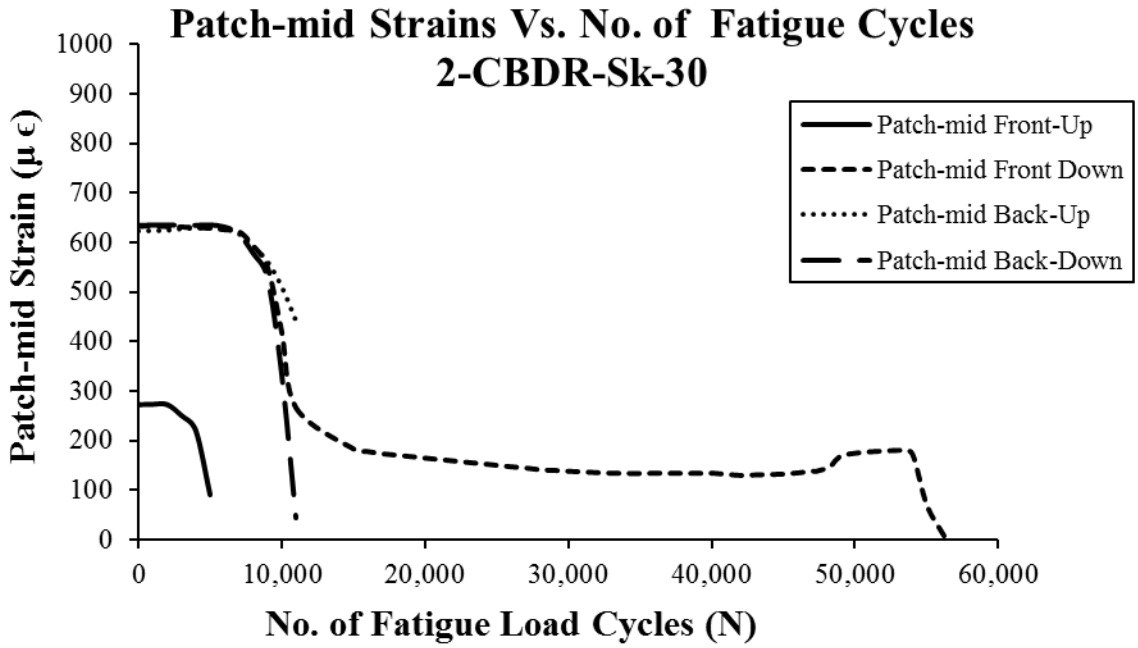

Figure 5.62 Strain outputs of mid bond-length strain gauges of 2-CBDR-Sk-30

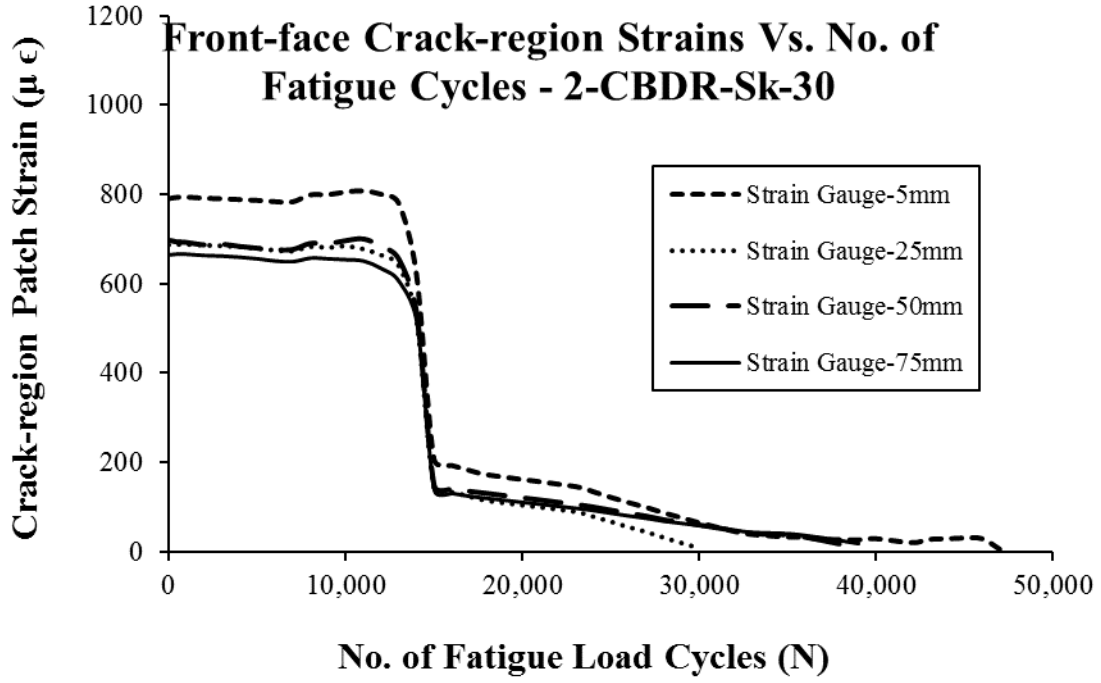

Figure 5.63 Strain outputs of front face crack region strain gauges of 2-CBDR-Sk-30

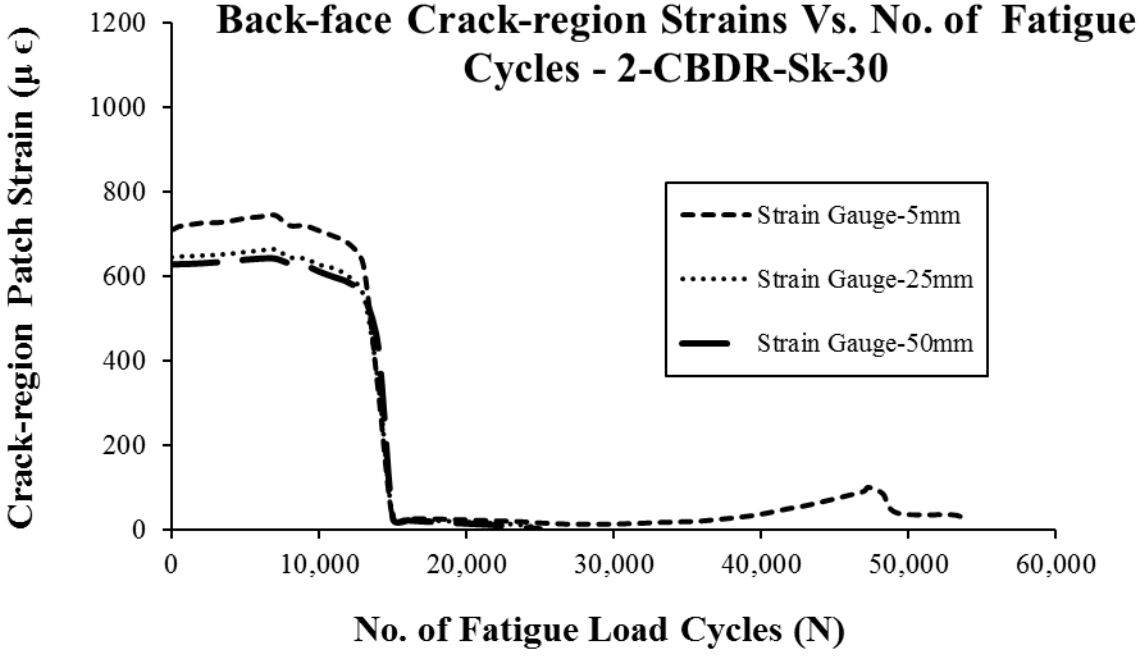

Figure 5.64 Strain outputs of back face crack region strain gauges of 2-CBDR-Sk-30

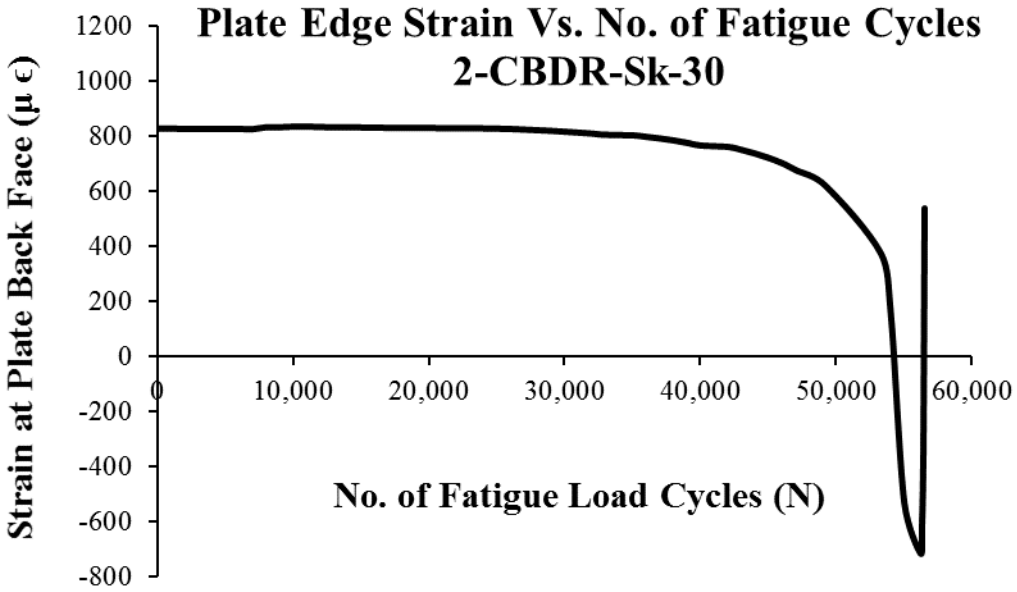

Figure 5.65 Strain outputs of plate edge strain gauge of 2-CBDR-Sk-30

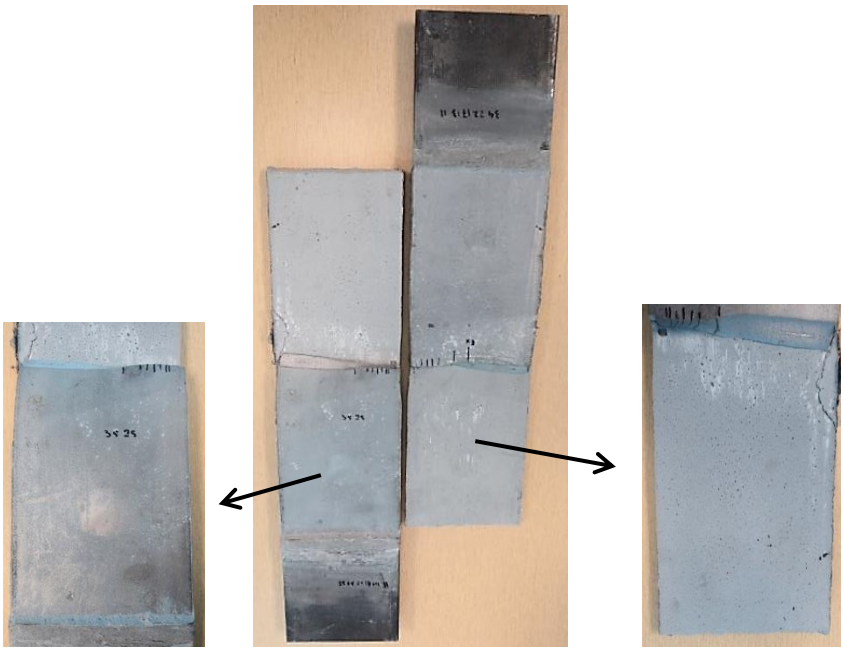

Figure 5.66 Delaminated CFRP surface and the failed specimen 2-CBDR-Sk-30

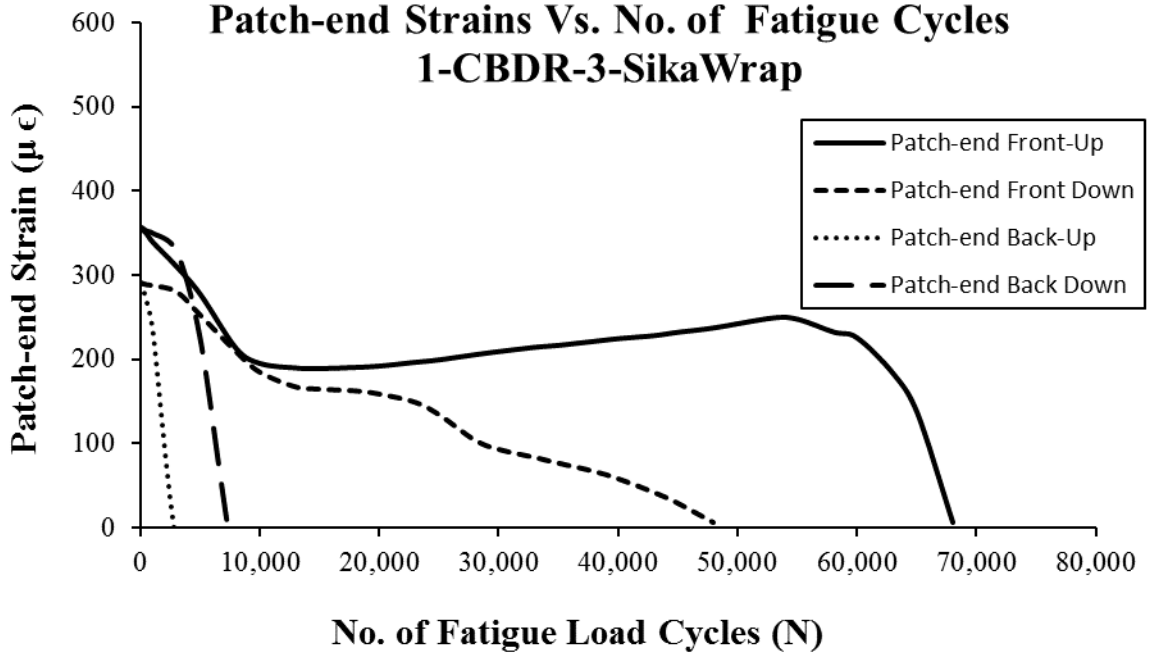

Figure 5.67 Strain outputs of patch-end strain gauges of 1-CBDR-3-SKWRP

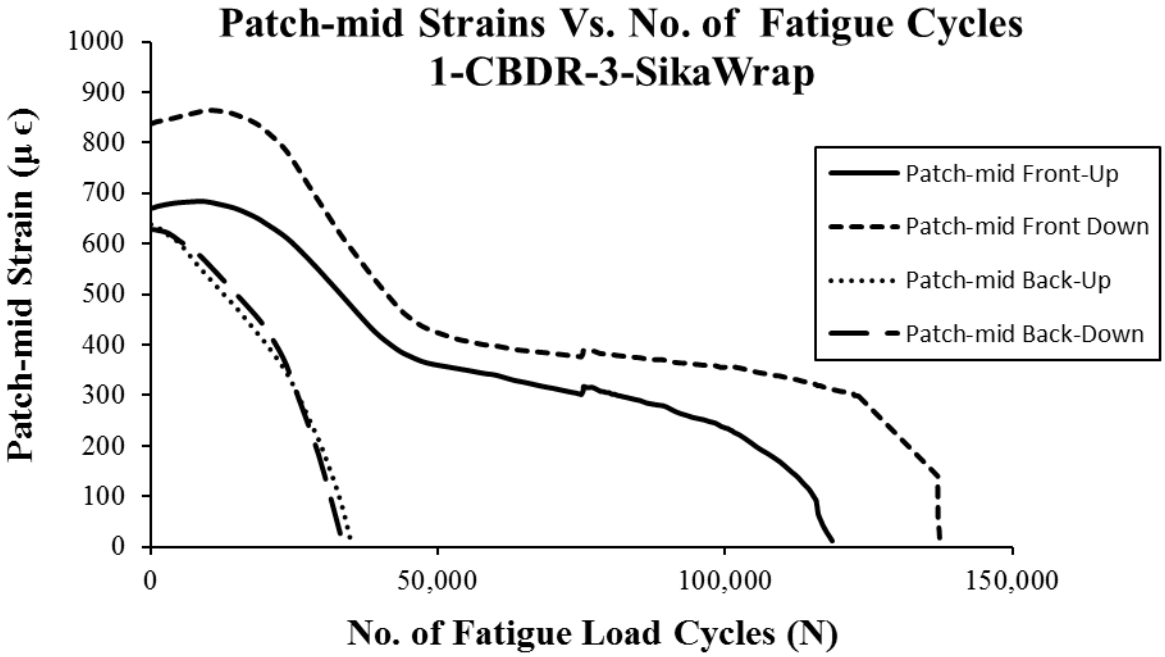

Figure 5.68 Strain outputs of mid bond-length strain gauges of 1-CBDR-3-SKWRP

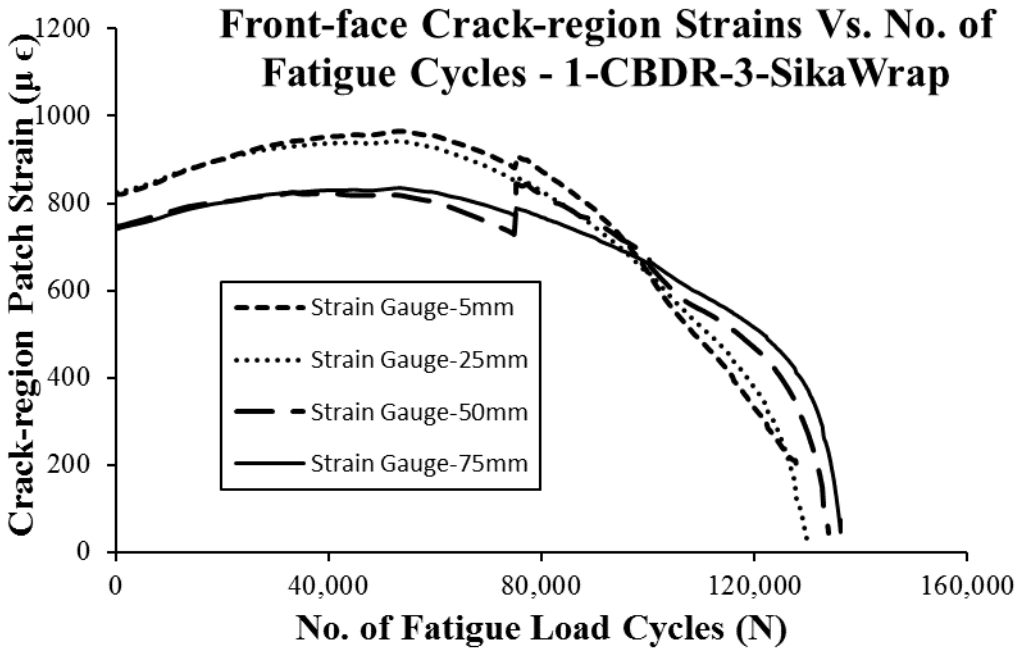

Figure 5.69 Strain outputs of front face crack region strain gauges of 1-CBDR-3-SKWRP

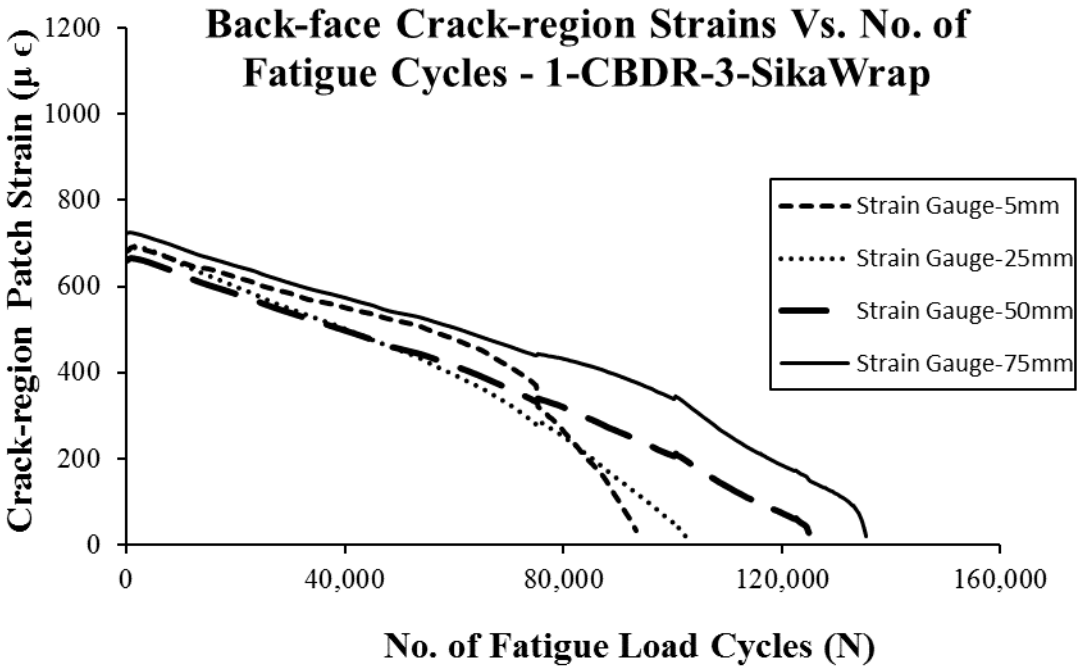

Figure 5.70 Strain outputs of back face crack region strain gauges of 1-CBDR-3-SKWRP

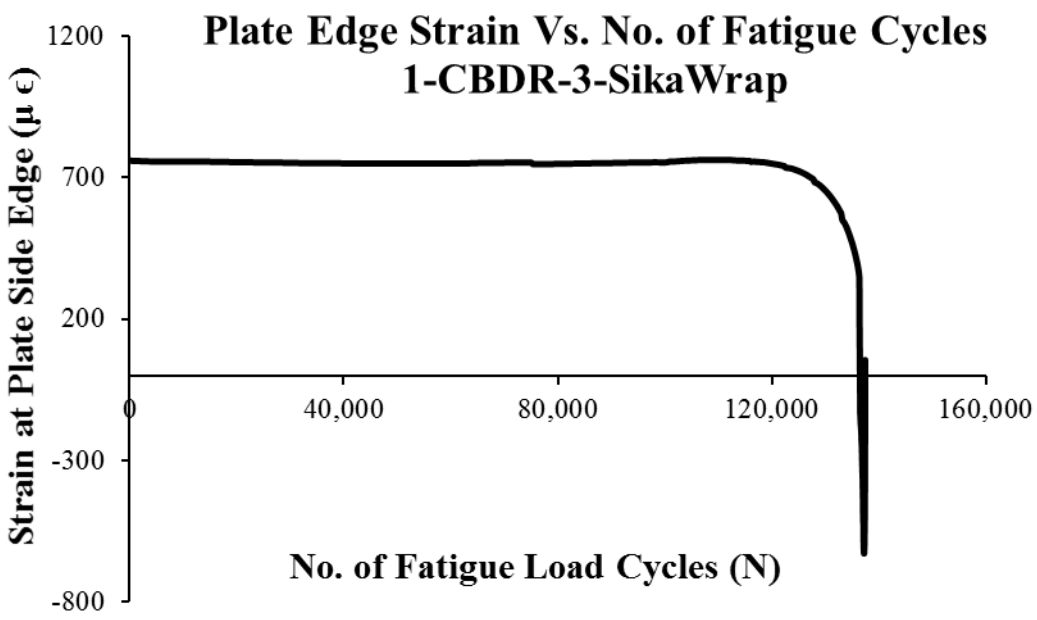

Figure 5.71 Strain outputs of plate edge strain gauge of 1-CBDR-3-SKWRP

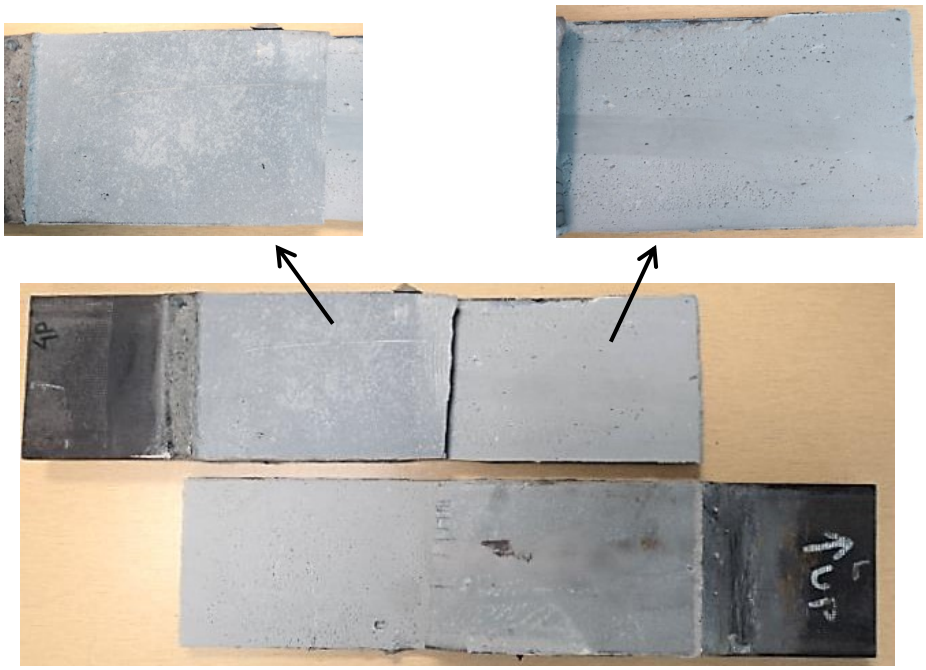

Figure 5.72 Delaminated CFRP surface and the failed specimen 1-CBDR-3-SKWRP

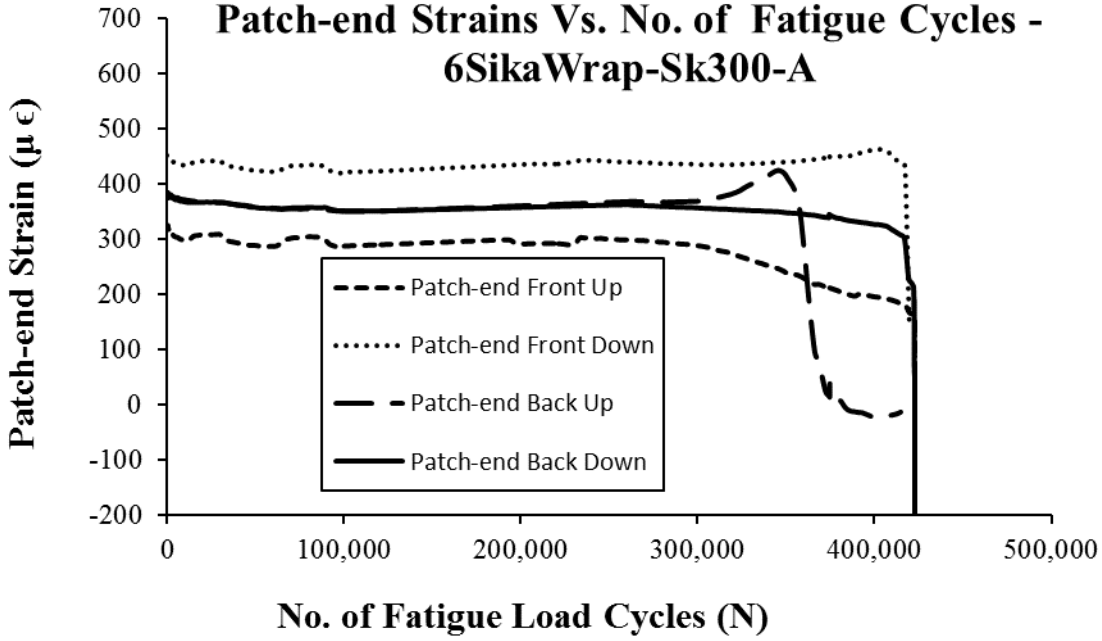

Figure 5.73 Strain outputs of patch-end strain gauges of 6-SKWRP-Sk-300-A

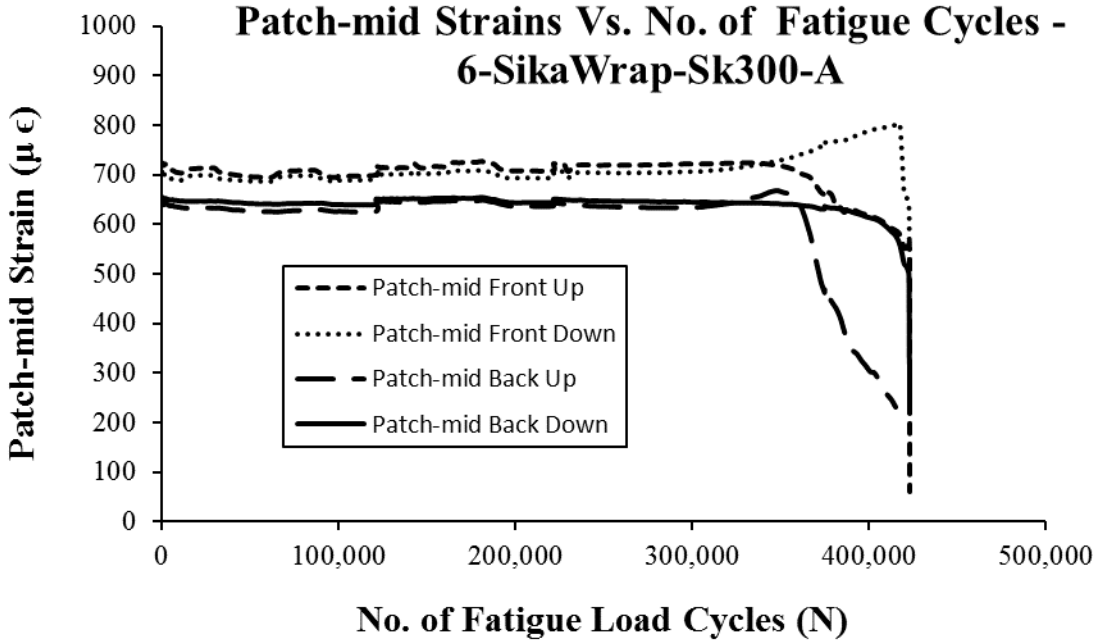

Figure 5.74 Strain outputs of mid bond-length strain gauges of 6-SKWRP-Sk-300-A

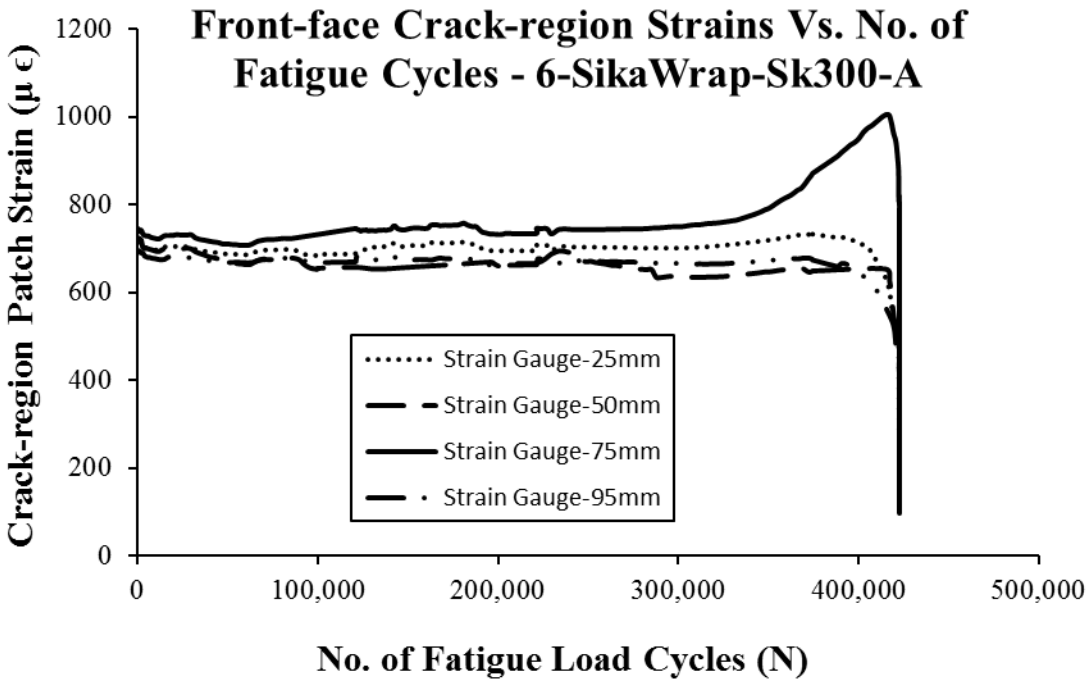

Figure 5.75 Strain outputs of front face crack region strain gauges of 6-SKWRP-Sk-300-A

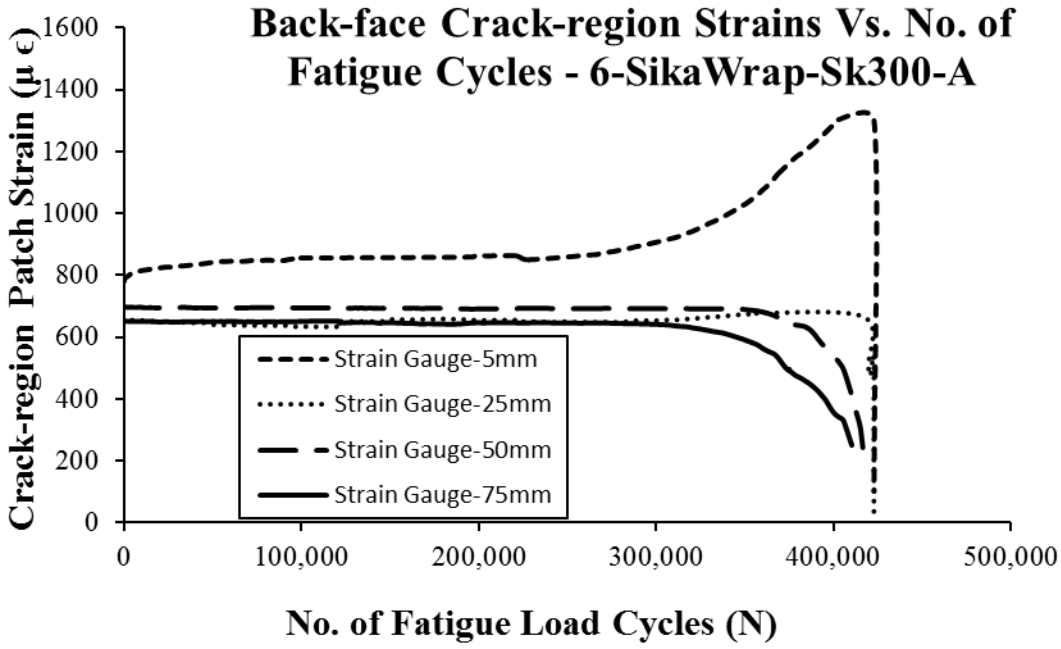

Figure 5.76 Strain outputs of back face crack region strain gauges of 6-SKWRP-Sk-300-A

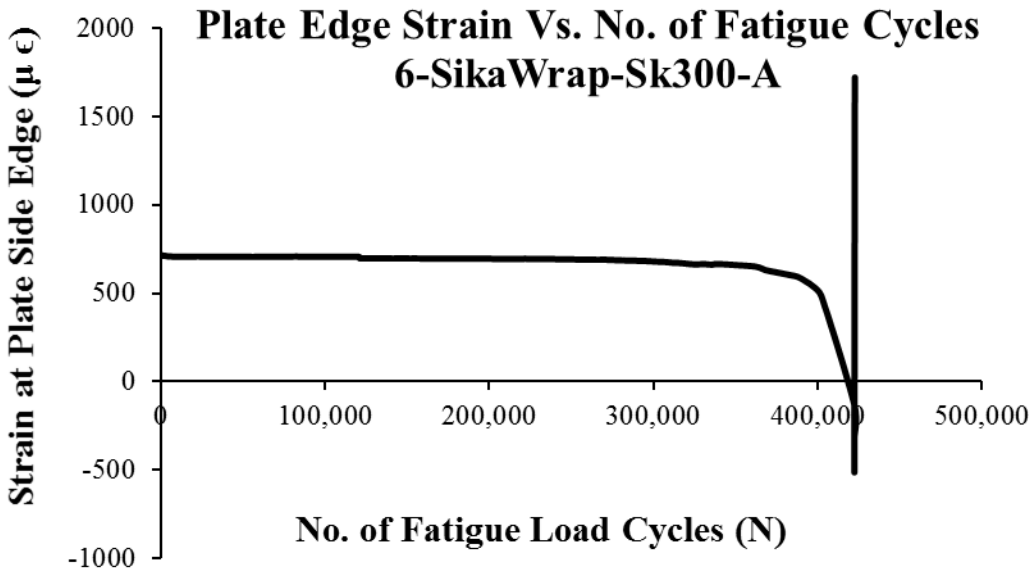

Figure 5.77 Strain outputs of plate edge strain gauge of 6-SKWRP-Sk-300-A

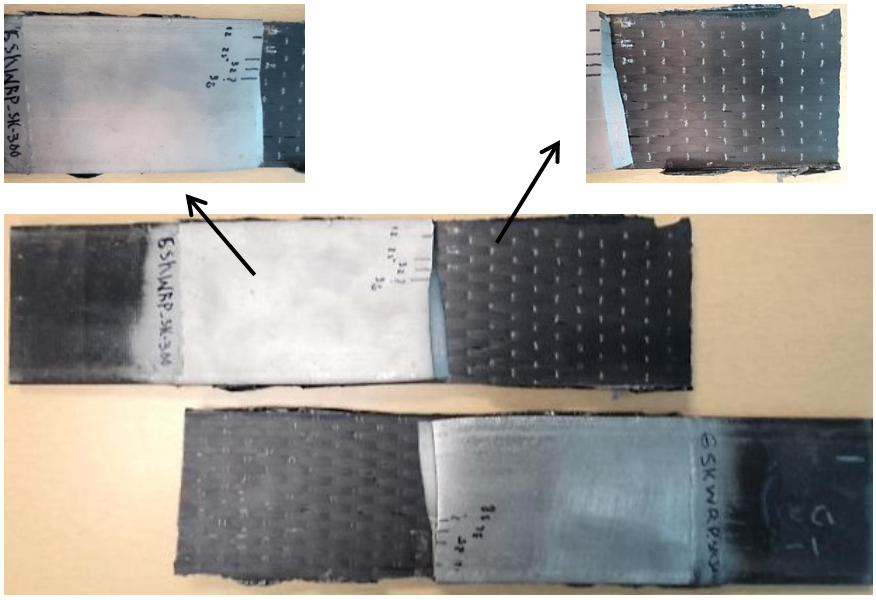

Figure 5.78 Delaminated CFRP surface and the failed specimen 6-SKWRP-Sk-300-A

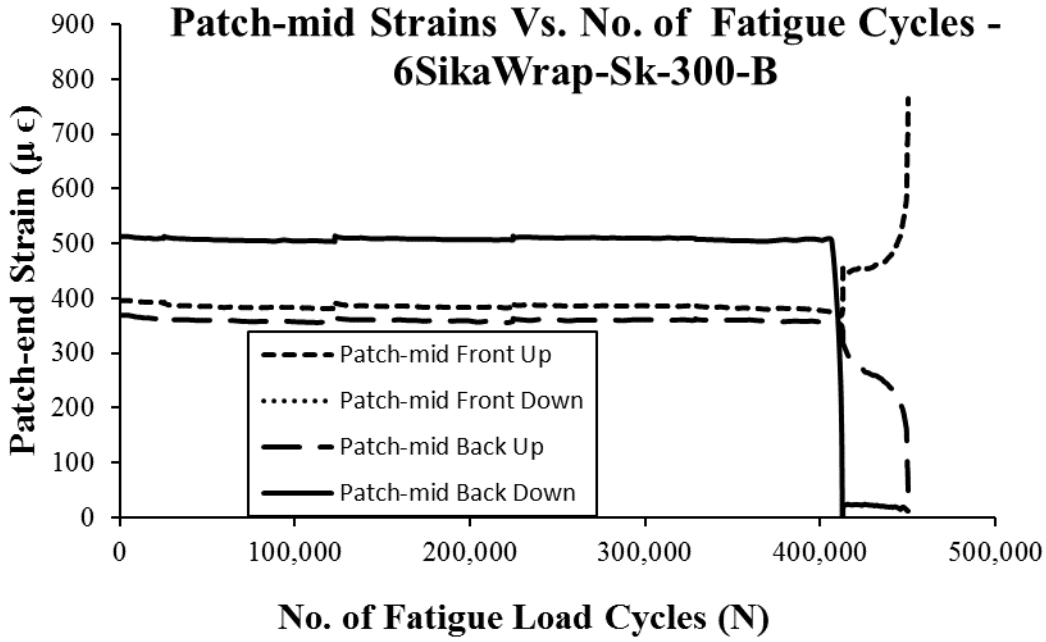

Figure 5.79 Strain outputs of patch-end strain gauges of 6-SKWRP-Sk-300-B

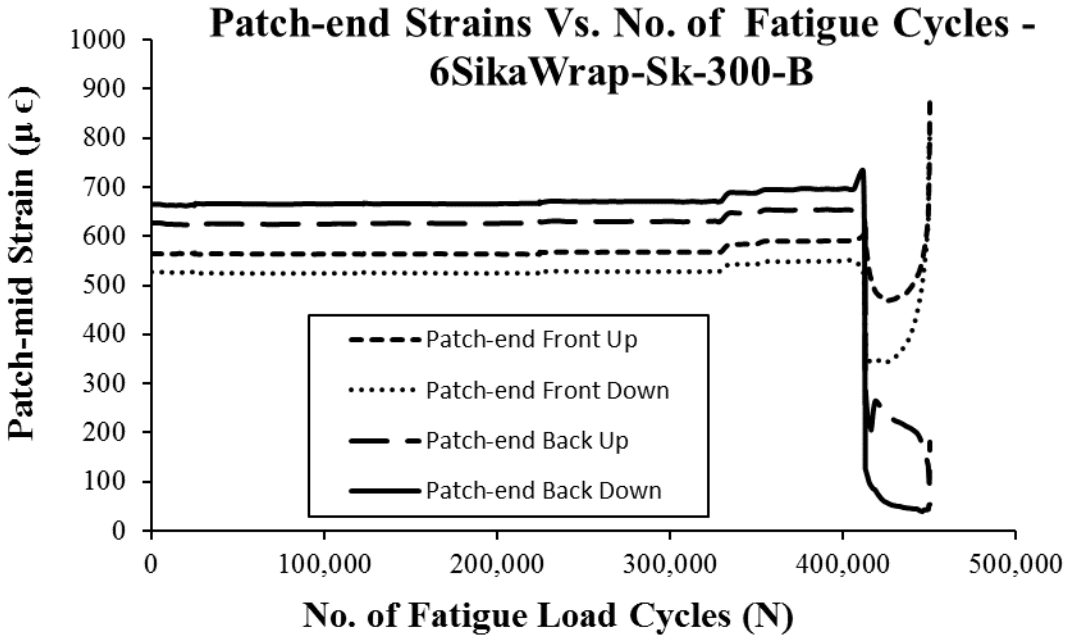

Figure 5.80 Strain outputs of mid bond-length strain gauges of 6-SKWRP-Sk-300-B

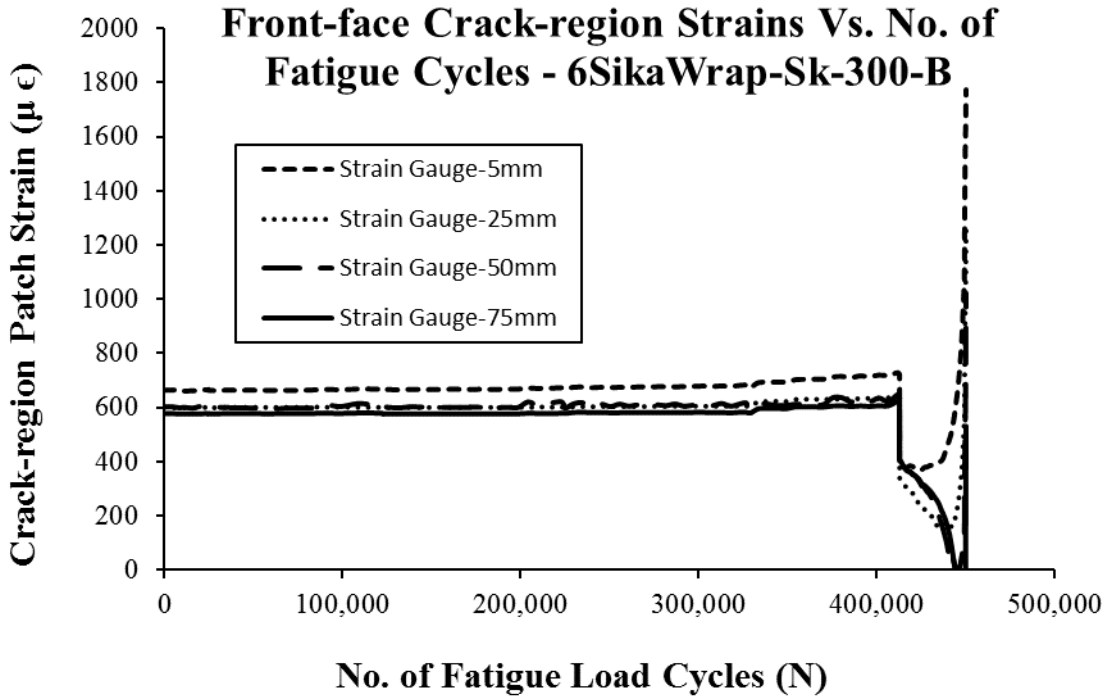

Figure 5.81 Strain outputs of front face crack region strain gauges of 6-SKWRP-Sk-300-B

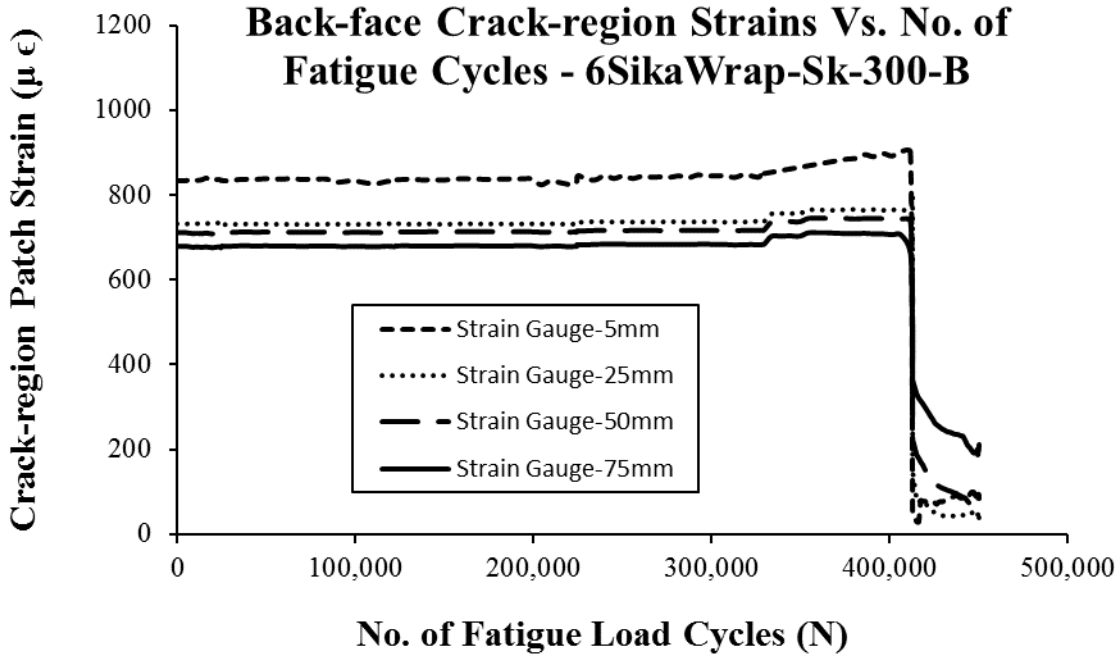

Figure 5.82 Strain outputs of back face crack region strain gauges of 6-SKWRP-Sk-300-B

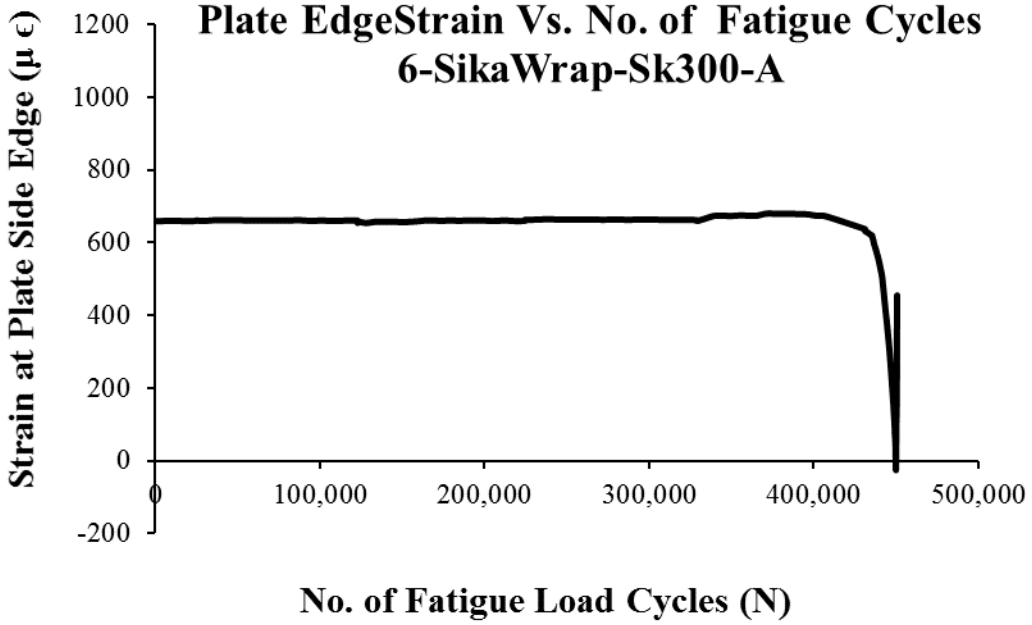

Figure 5.83 Strain outputs of plate edge strain gauge of 6-SKWRP-Sk-300-B

Figure 5.84 Delaminated CFRP surface and the failed specimen 6-SKWRP-Sk-300-B

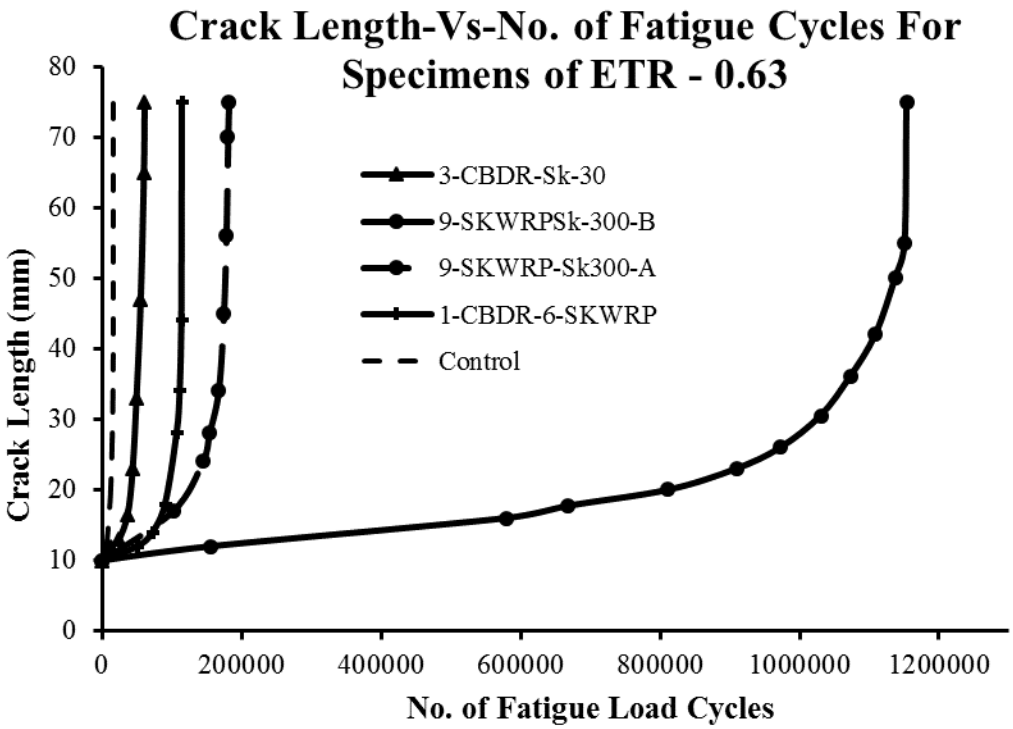

Figure 5.85 Crack-length variation with fatigue cycles (a-N curves) in ETR 0.63 specimens

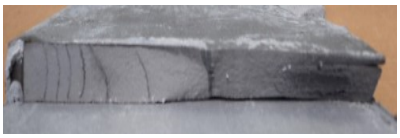

3-CBDR-Sk-30

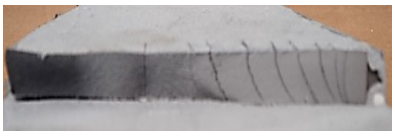

1-CBDR-6-SKWRP

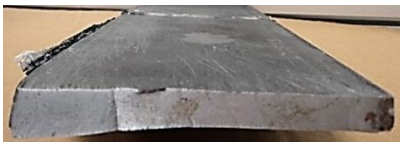

9-SKWRP-Sk-300-A

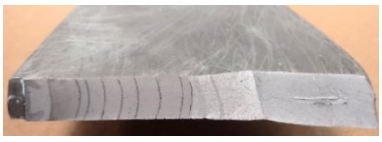

9-SKWRP-Sk-300-B

Figure 5.86 Failed steel surfaces in specimens of ETR 0.63 showing the beach marks

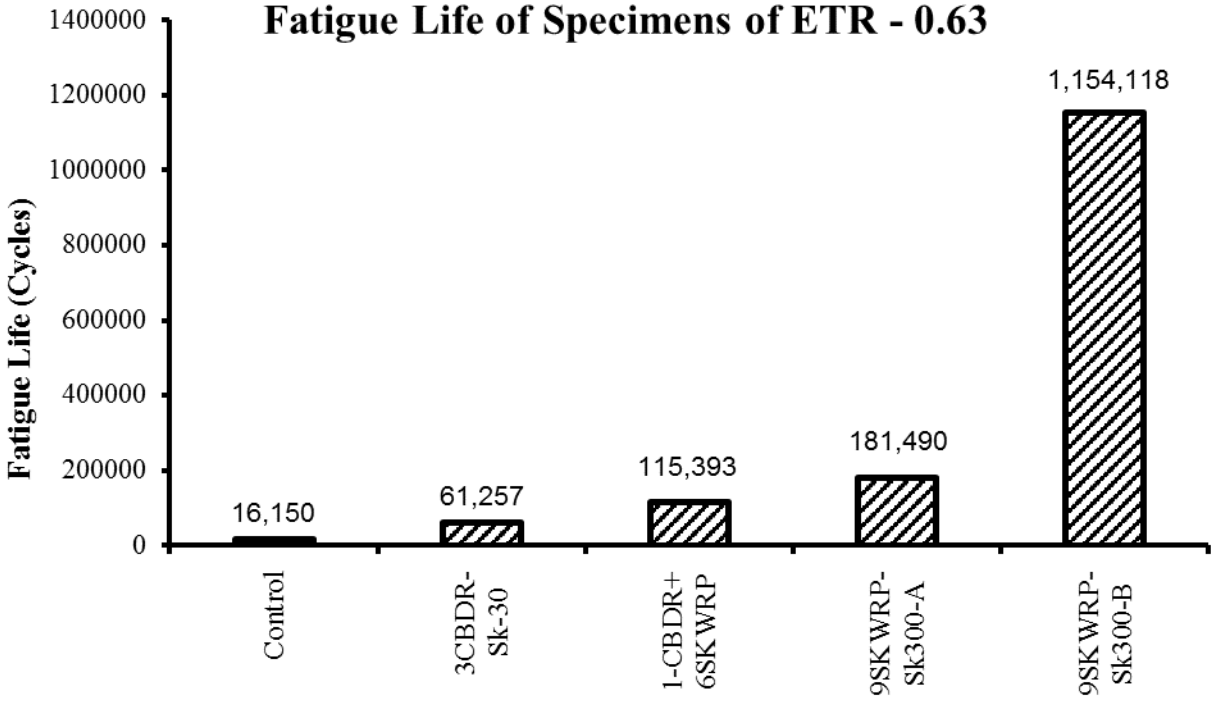

Figure 5.87 Fatigue life of specimens of ETR 0.63 group

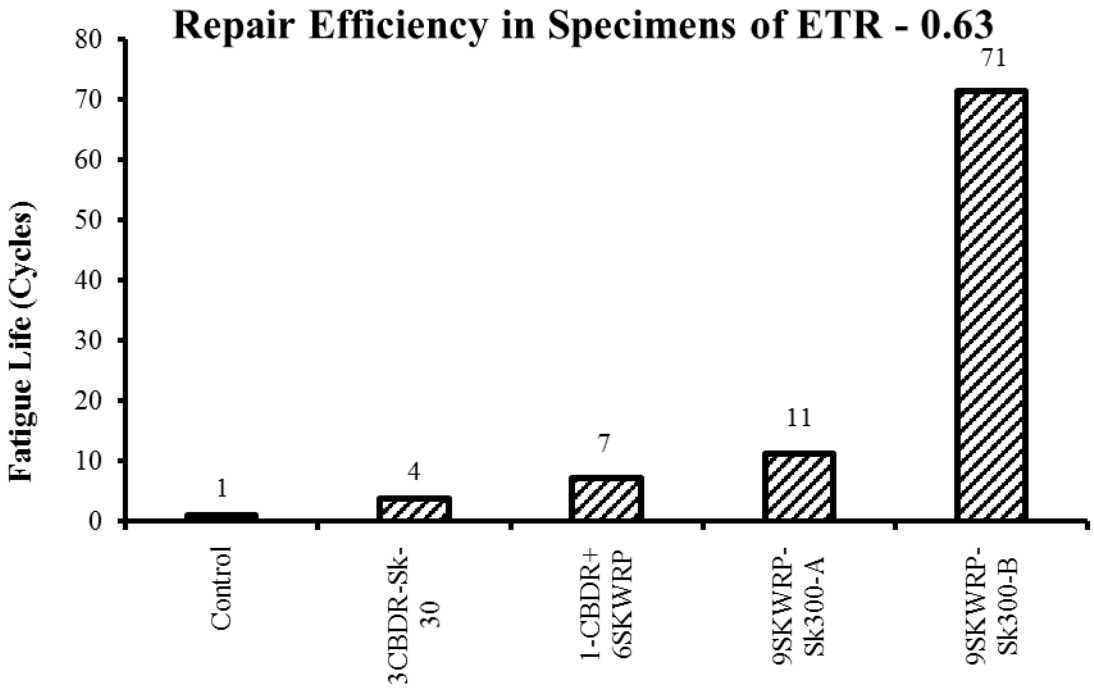

Figure 5.88 Repair efficiency of specimens of ETR 0.63

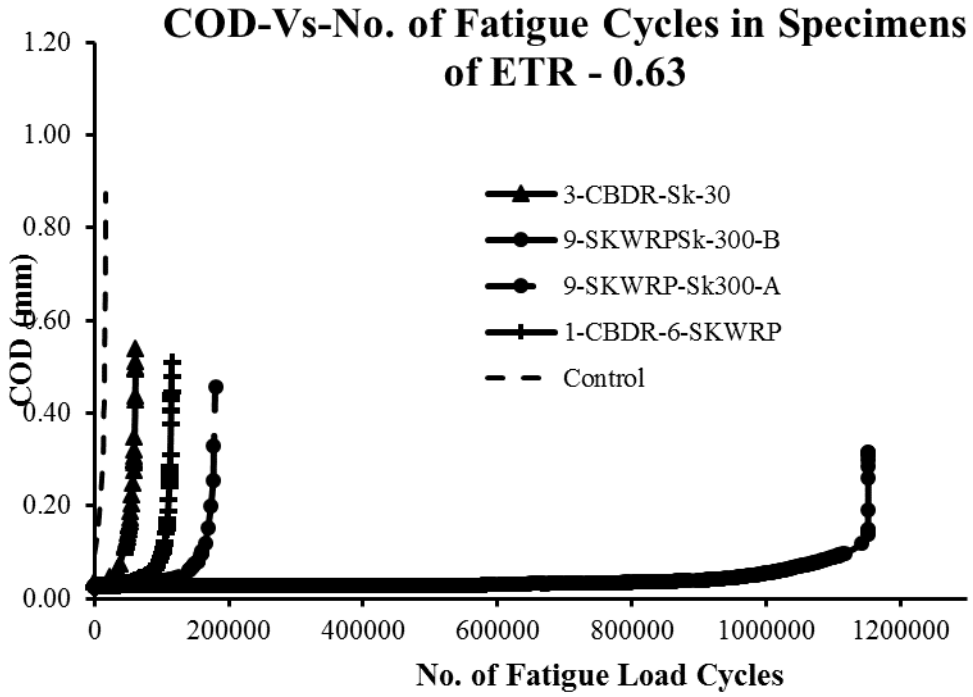

Figure 5.89 COD of specimens of ETR 0.63 group

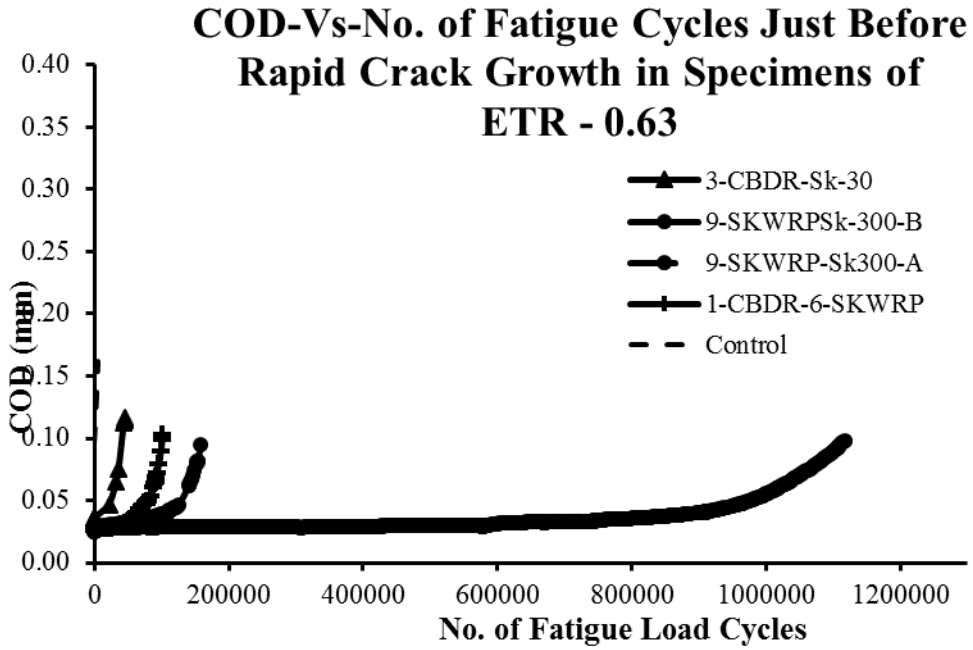

Figure 5.90 COD of specimens of ETR 0.63 group just before rapid crack growth

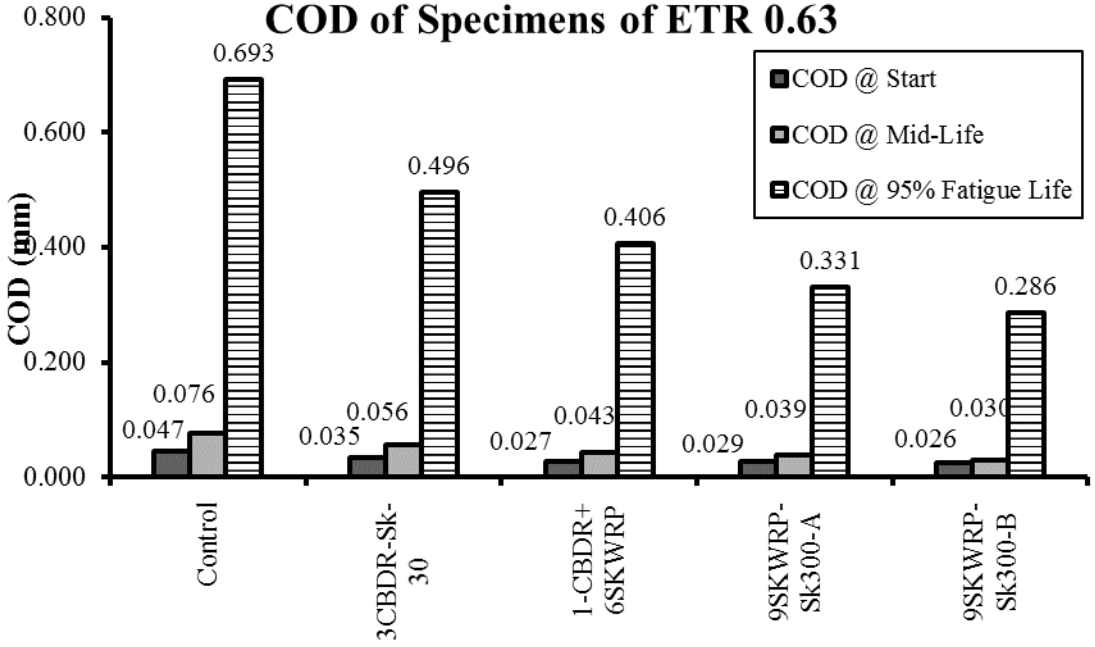

Figure 5.91 COD of specimens of ETR 0.63 group at the three stages of fatigue life

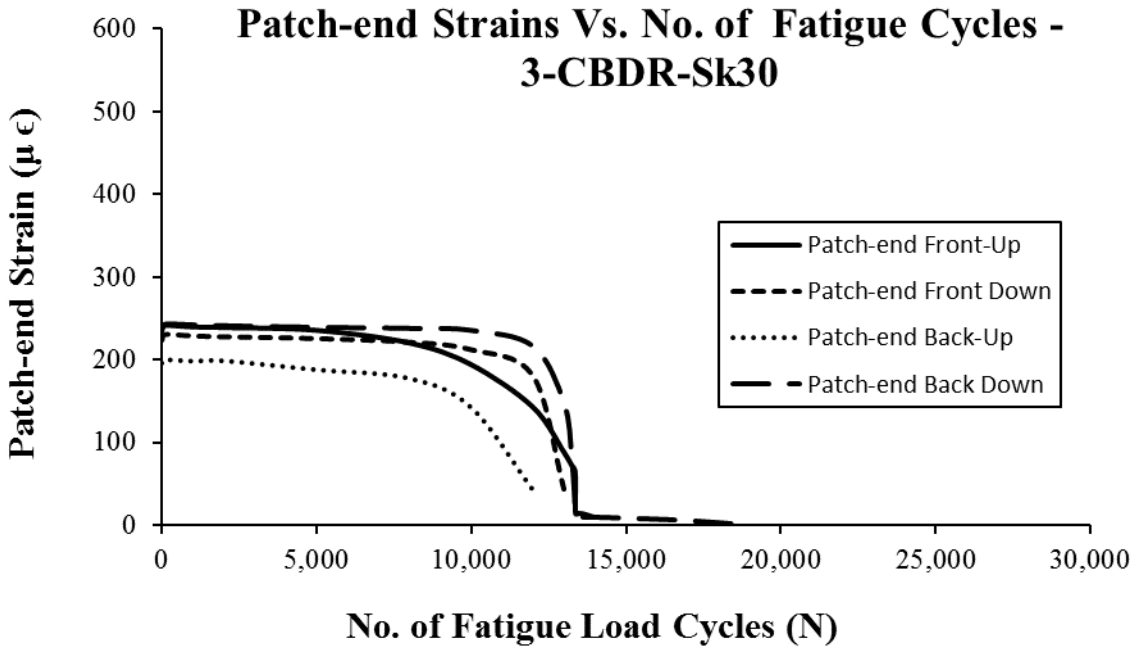

Figure 5.92 Strain outputs of patch-end strain gauges of 3-CBDR-Sk-30

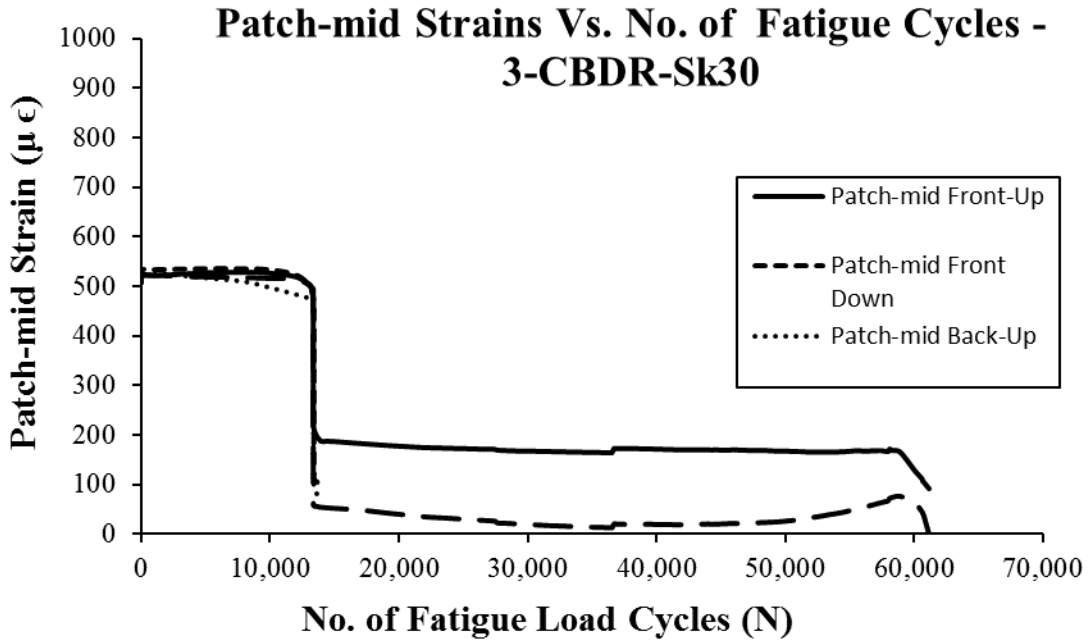

Figure 5.93 Strain outputs of mid bond-length strain gauges of 3-CBDR-Sk-30

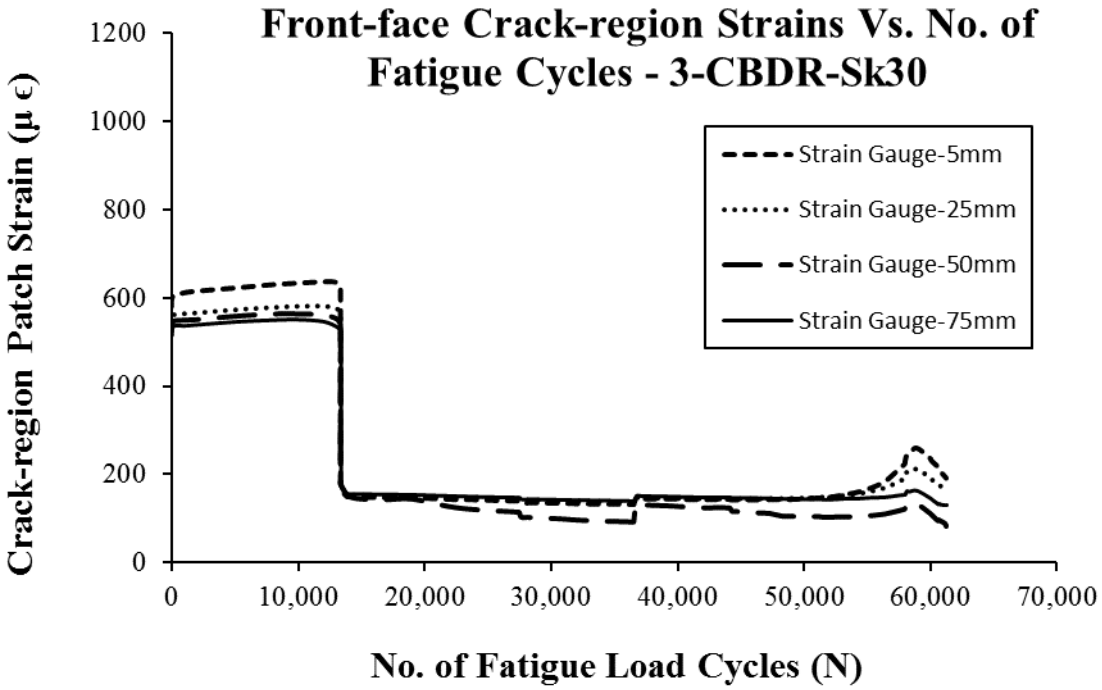

Figure 5.94 Strain outputs of front face crack region strain gauges of 3-CBDR-Sk-30

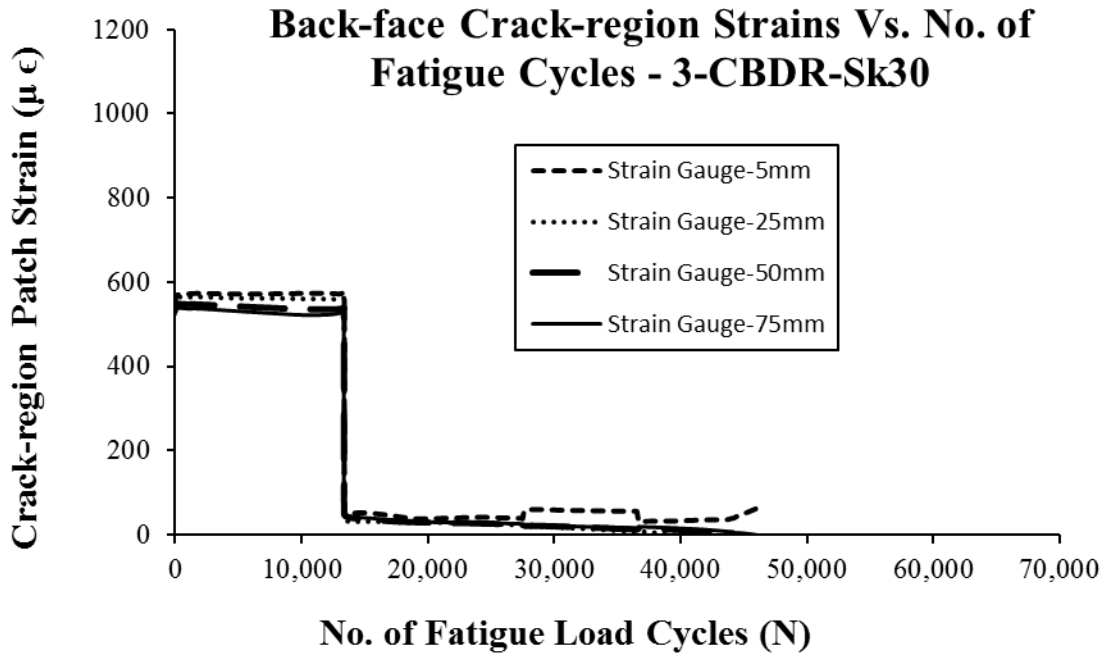

Figure 5.95 Strain outputs of back face crack region strain gauges of 3-CBDR-Sk-30

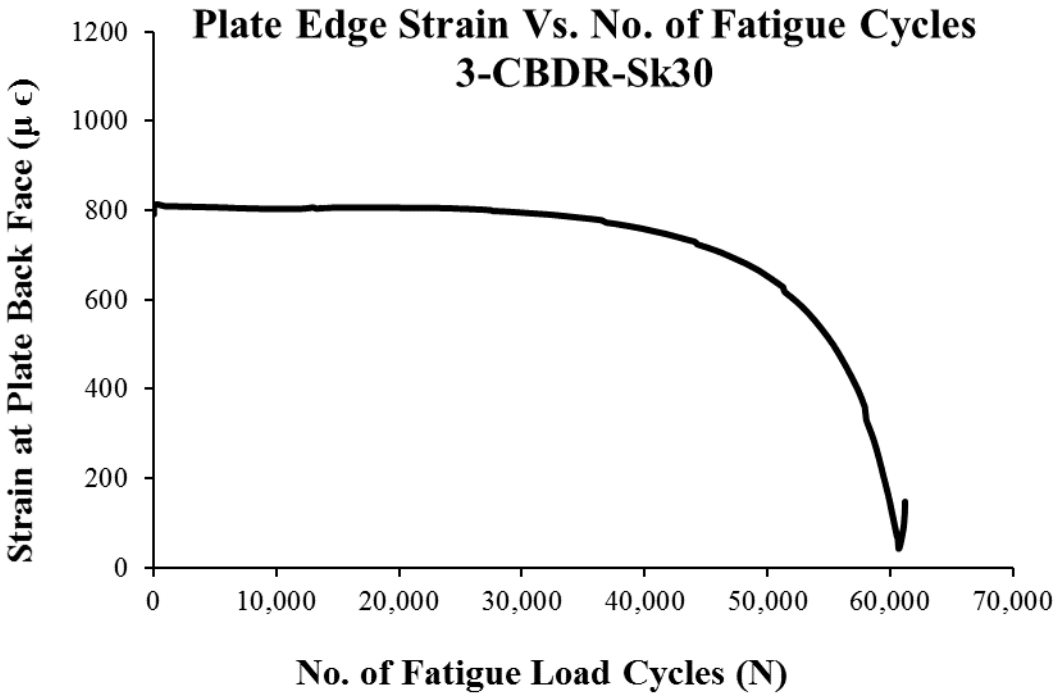

Figure 5.96 Strain outputs of plate side edge strain gauge of 3-CBDR-Sk-30

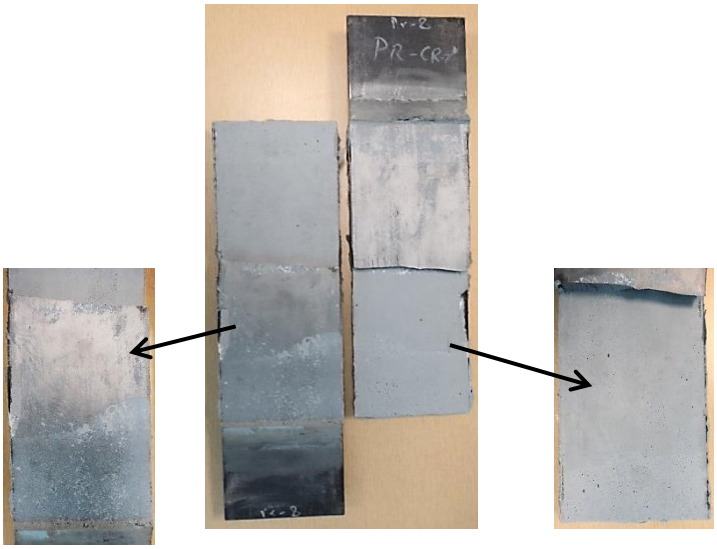

Figure 5.97 Delaminated CFRP surface and the failed specimen 3-CBDR-Sk-30

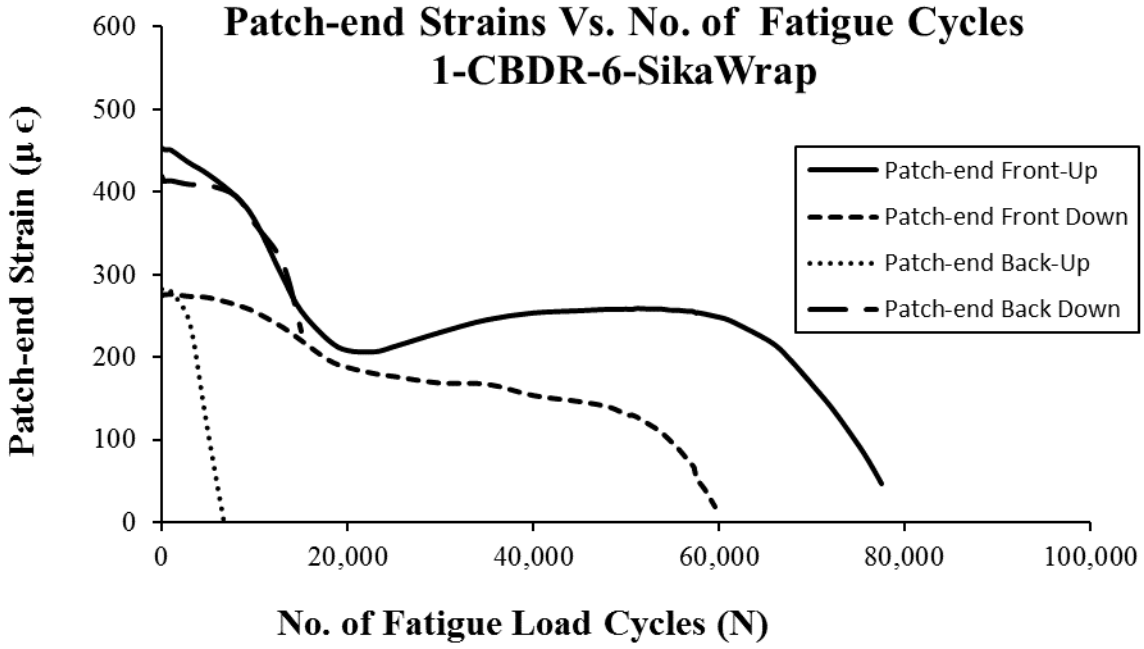

Figure 5.98 Strain outputs of patch-end strain gauges of 1-CBDR-6-SKWRP

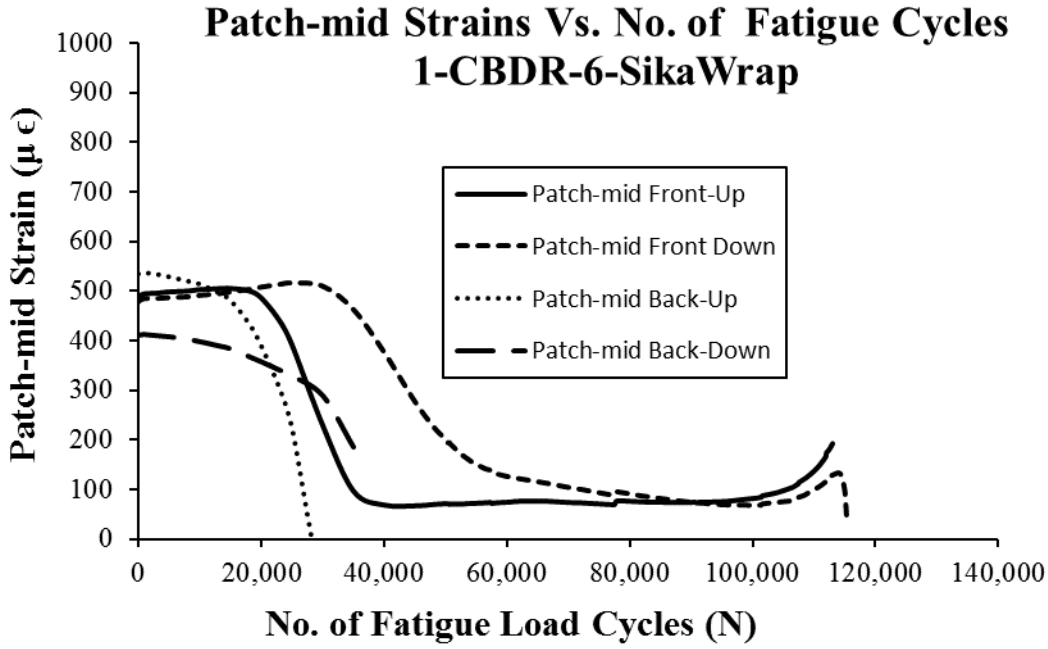

Figure 5.99 Strain outputs of mid bond-length strain gauges of 1-CBDR-6-SKWRP

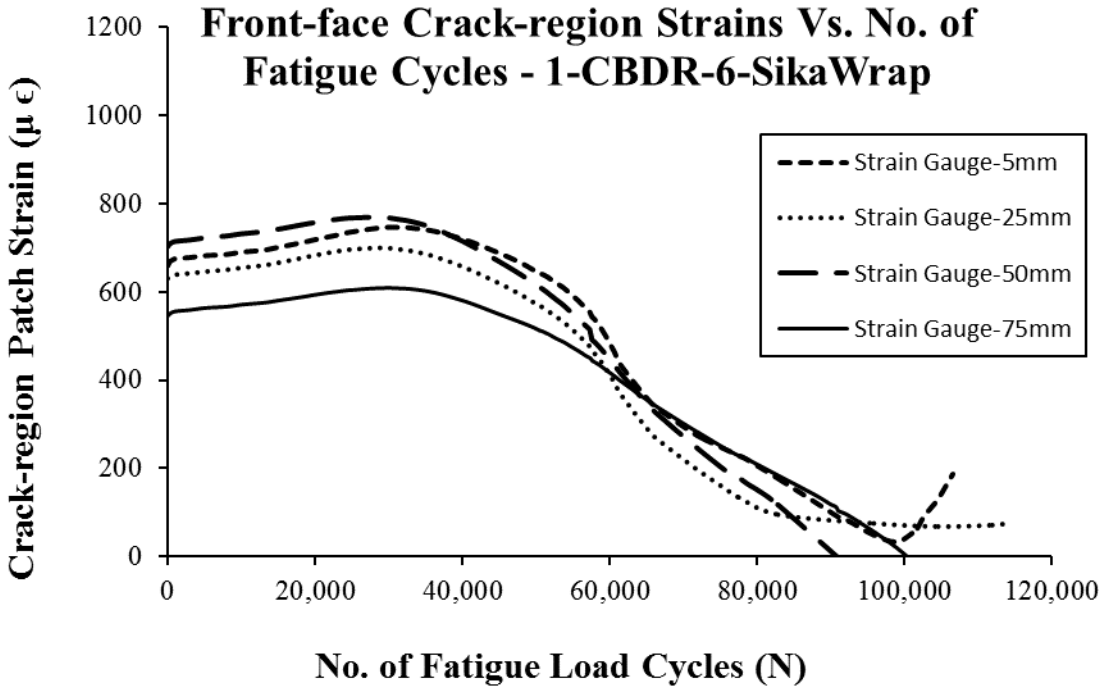

Figure 5.100 Strain outputs of front face crack region strain gauges of 1-CBDR-6-SKWRP

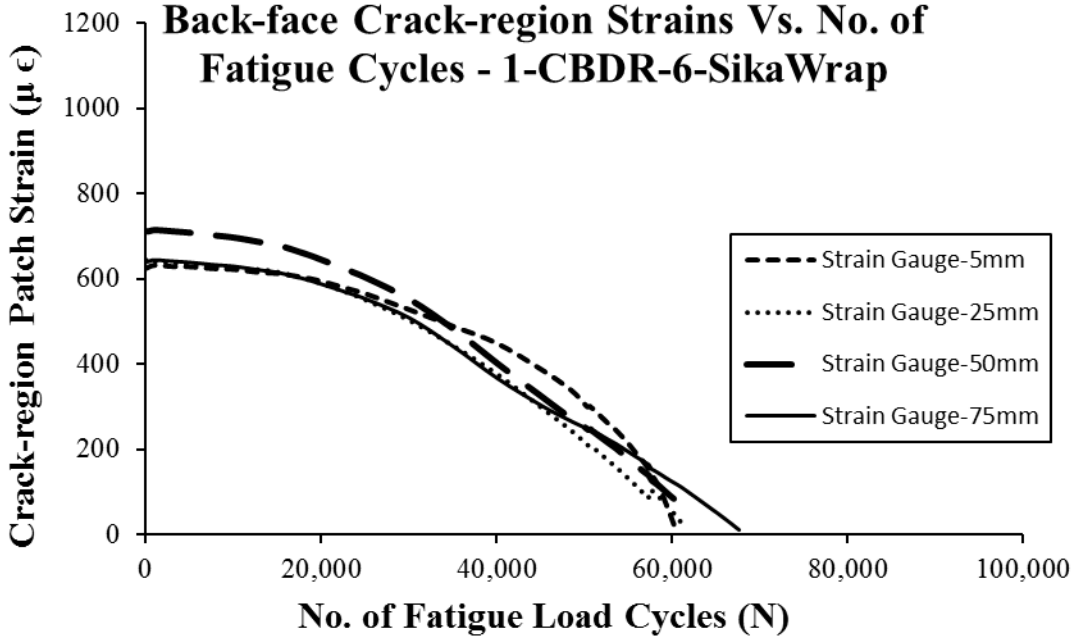

Figure 5.101 Strain outputs of back face crack region strain gauges of 1-CBDR-6-SKWRP

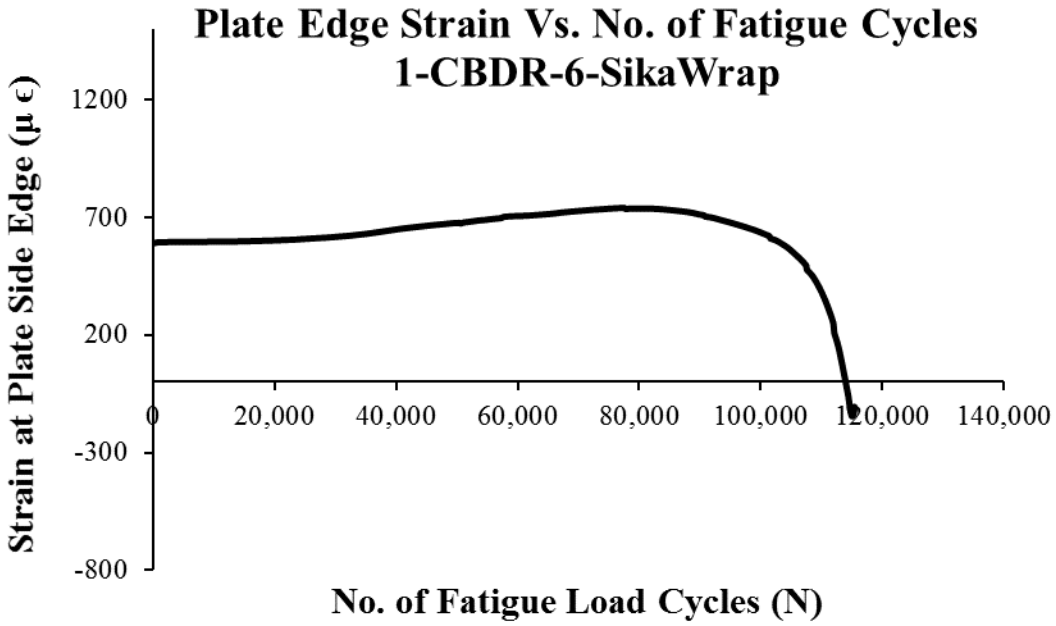

Figure 5.102 Strain outputs of plate side edge strain gauge of 1-CBDR-6-SKWRP

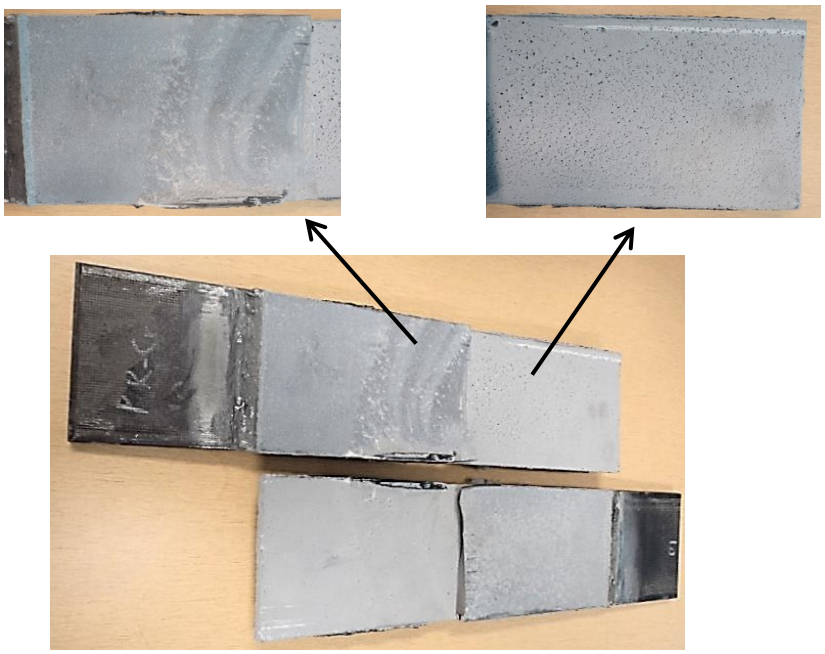

Figure 5.103 Delaminated CFRP surface and the failed specimen 1-CBDR-6-SKWRP

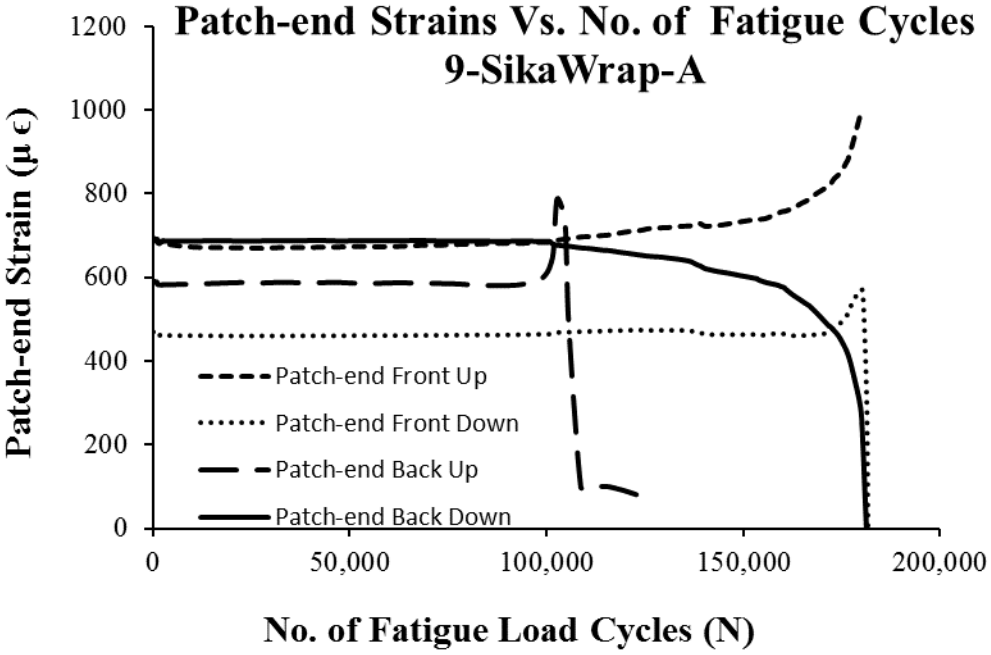

Figure 5.104 Strain outputs of patch-end strain gauges of 9-SKWRP-Sk300-A

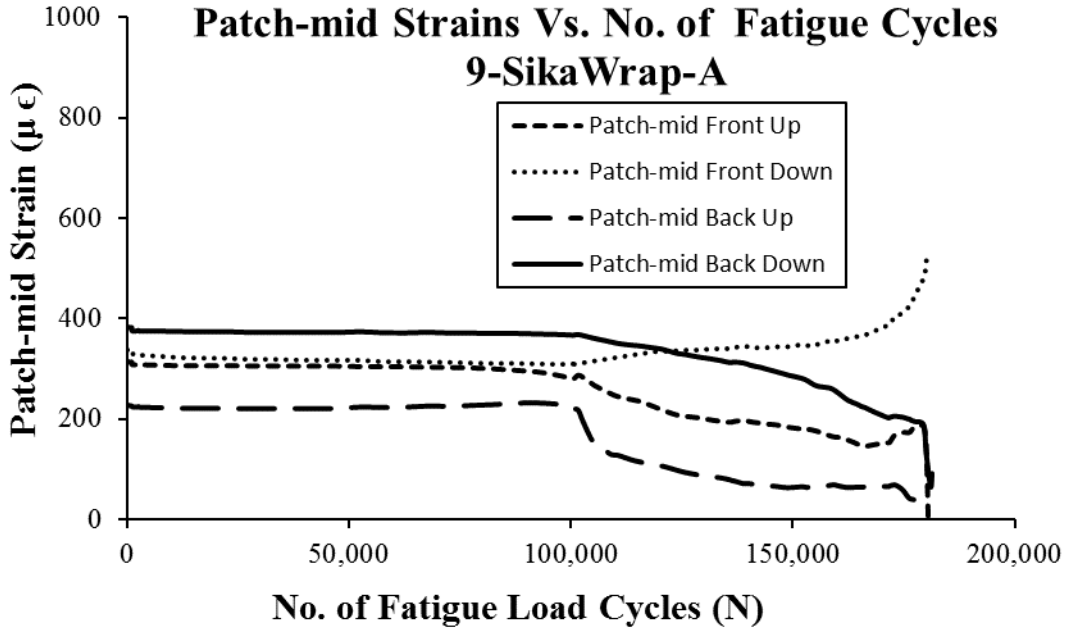

Figure 5.105 Strain outputs of mid bond-length strain gauges of 9-SKWRP-Sk300-A

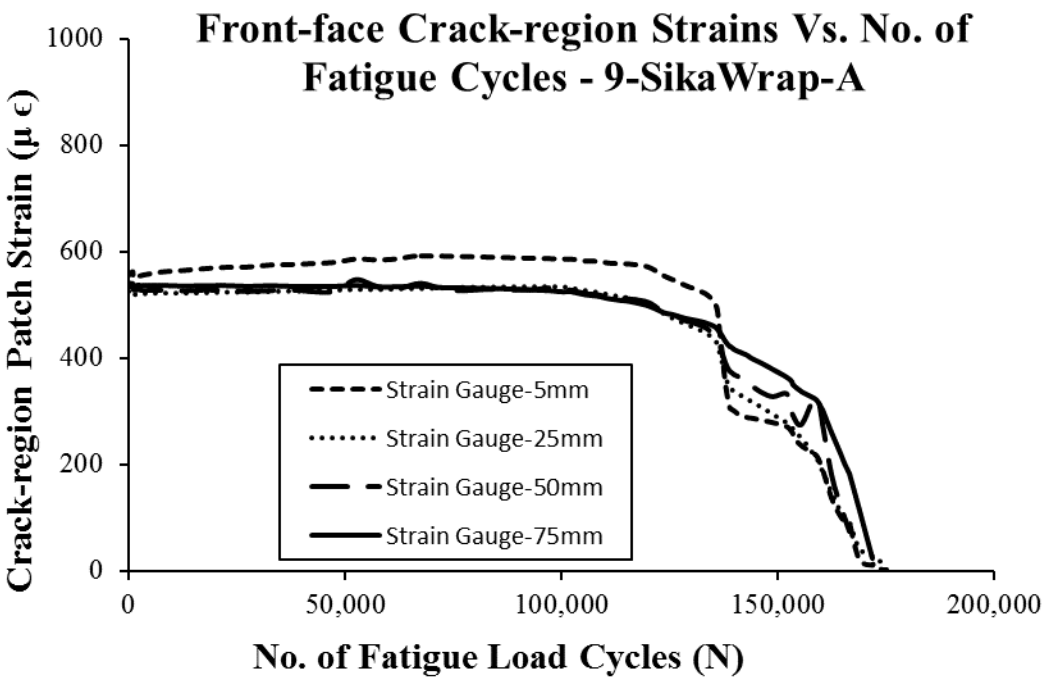

Figure 5.106 Strain outputs of front face crack region strain gauges of 9-SKWRP-Sk300-A

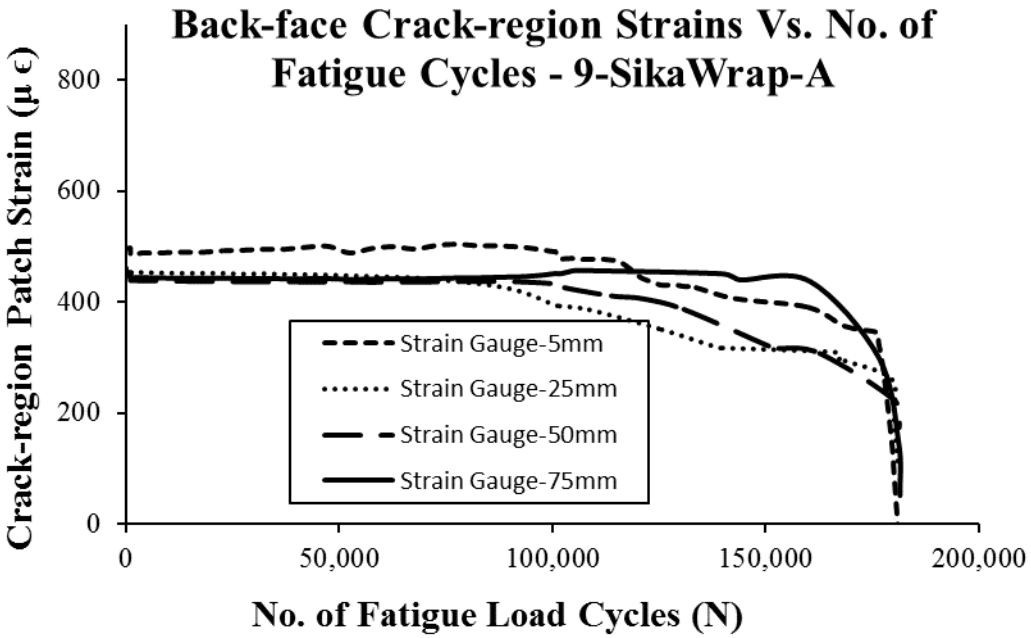

Figure 5.107 Strain outputs of back face crack region strain gauges of 9-SKWRP-Sk300-A

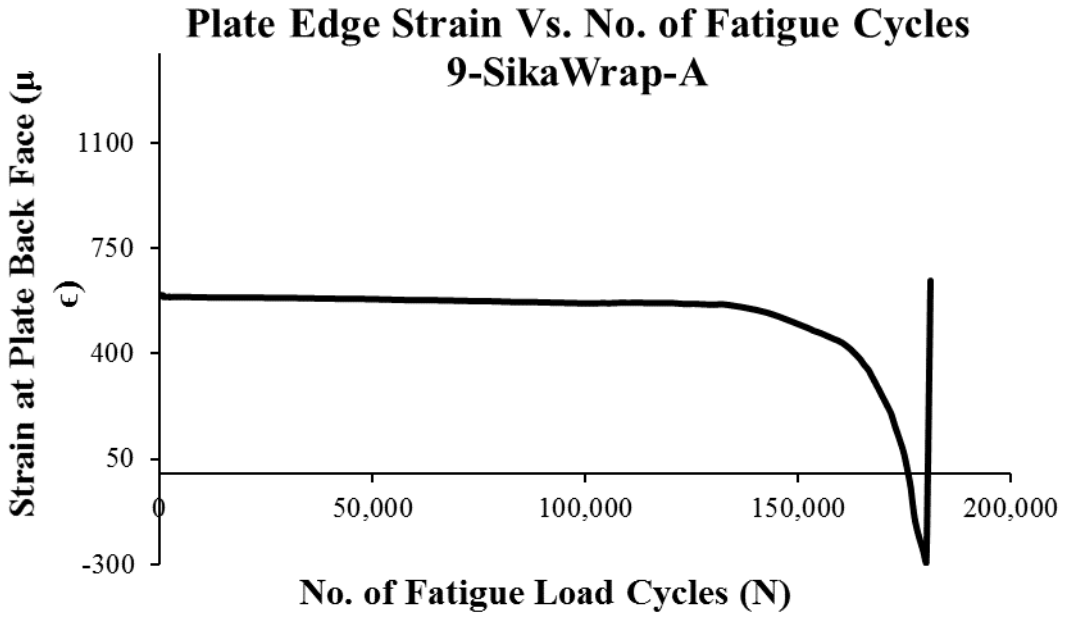

Figure 5.108 Strain outputs of plate side edge strain gauge of 9-SKWRP-Sk300-A

Figure 5.109 Delaminated CFRP surface and the failed specimen 9-SKWRP-Sk300-A

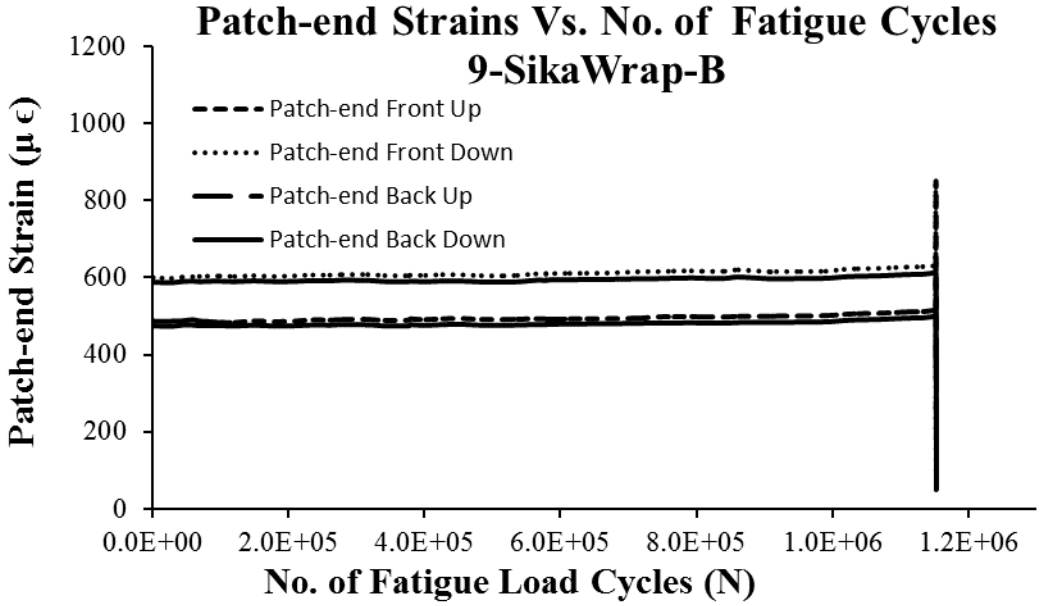

Figure 5.110 Strain outputs of patch-end strain gauges of 9-SKWRP-Sk300-B

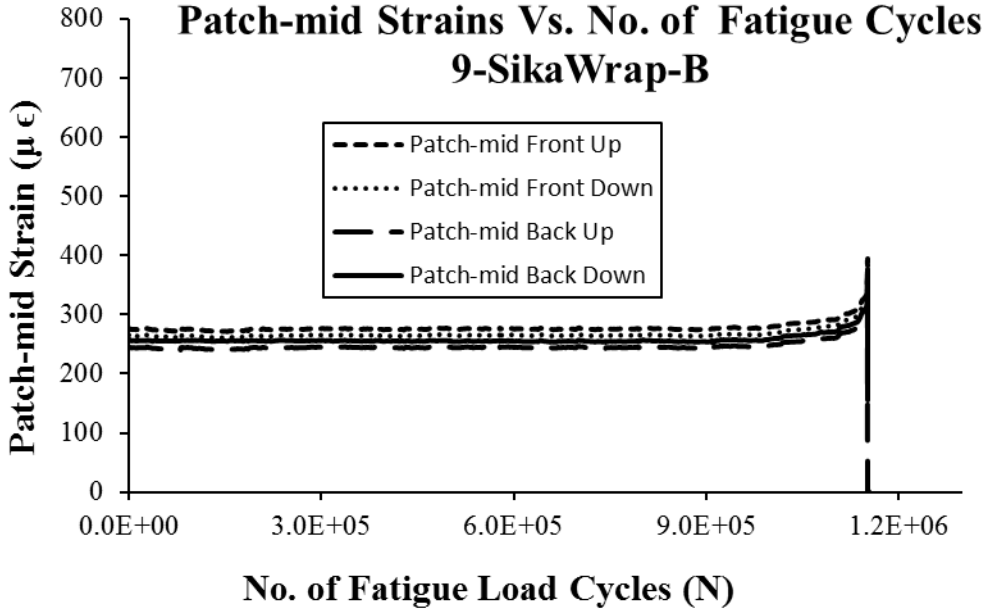

Figure 5.111 Strain outputs of mid bond-length strain gauges of 9-SKWRP-Sk300-B

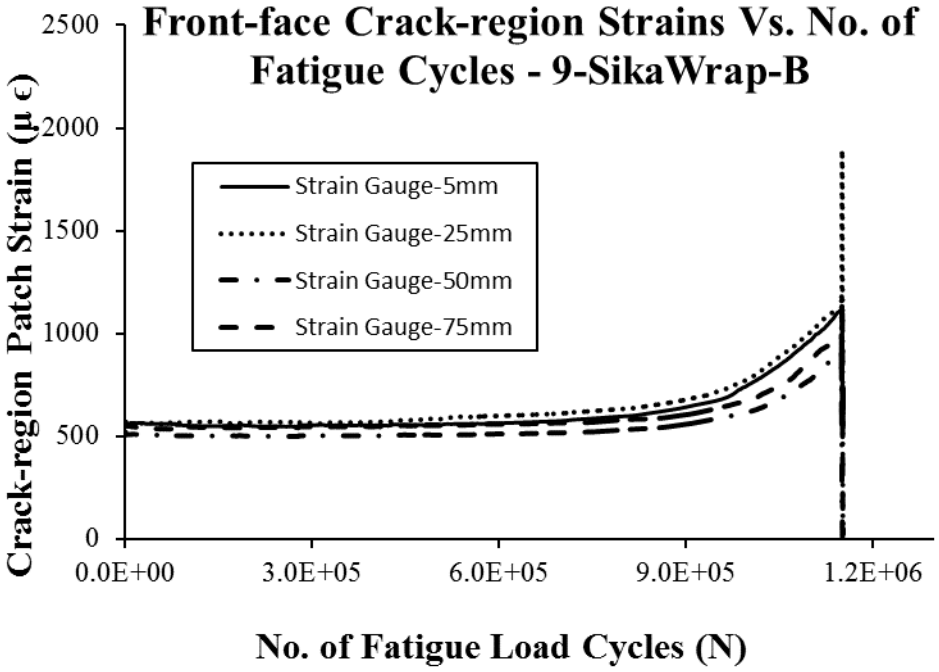

Figure 5.112 Strain outputs of front face crack region strain gauges of 9-SKWRP-Sk300-B

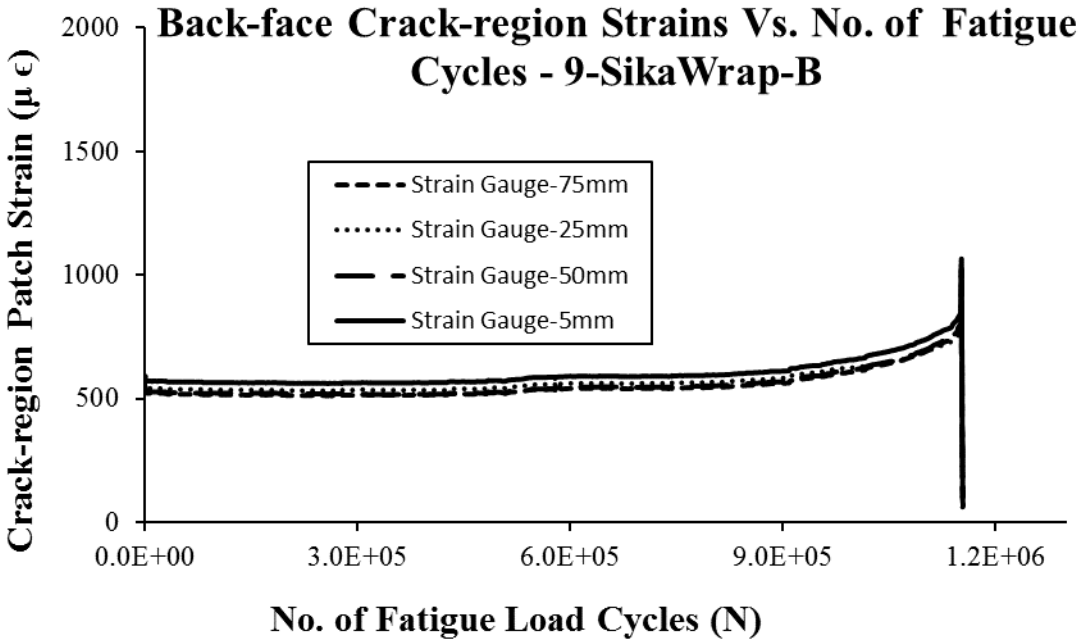

Figure 5.113 Strain outputs of back face crack region strain gauges of 9-SKWRP-Sk300-B

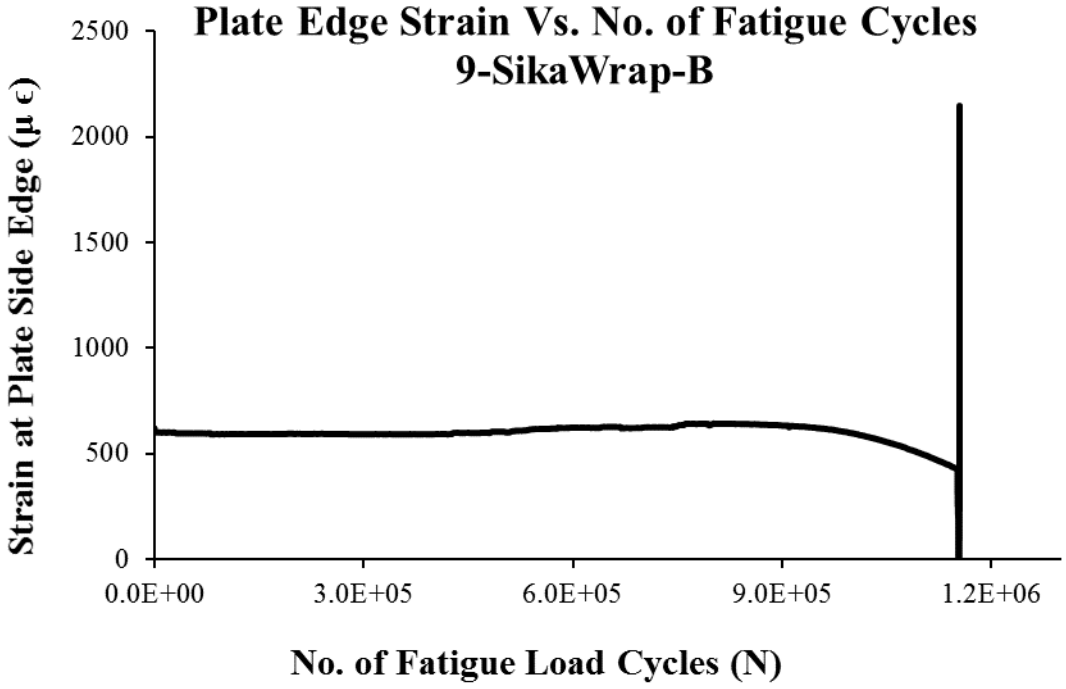

Figure 5.114 Strain outputs of plate side edge strain gauge of 9-SKWRP-Sk300-B

Figure 5.115 Delaminated CFRP surface and the failed specimen 9-SKWRP-Sk300-B

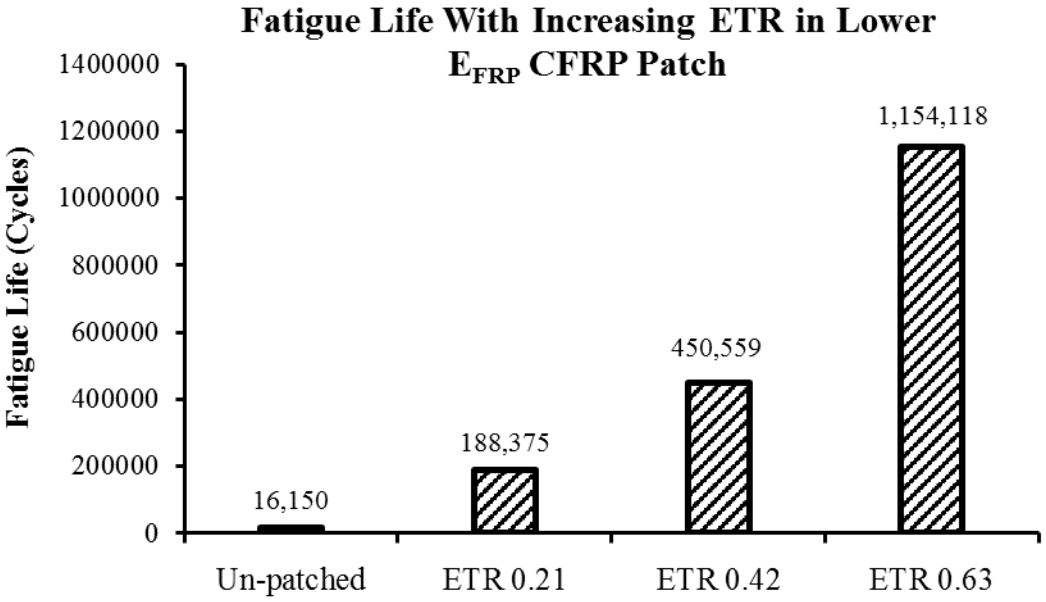

Figure 5.116 Impact of ETR on fatigue life of lower E_{FRP} CFRP specimens

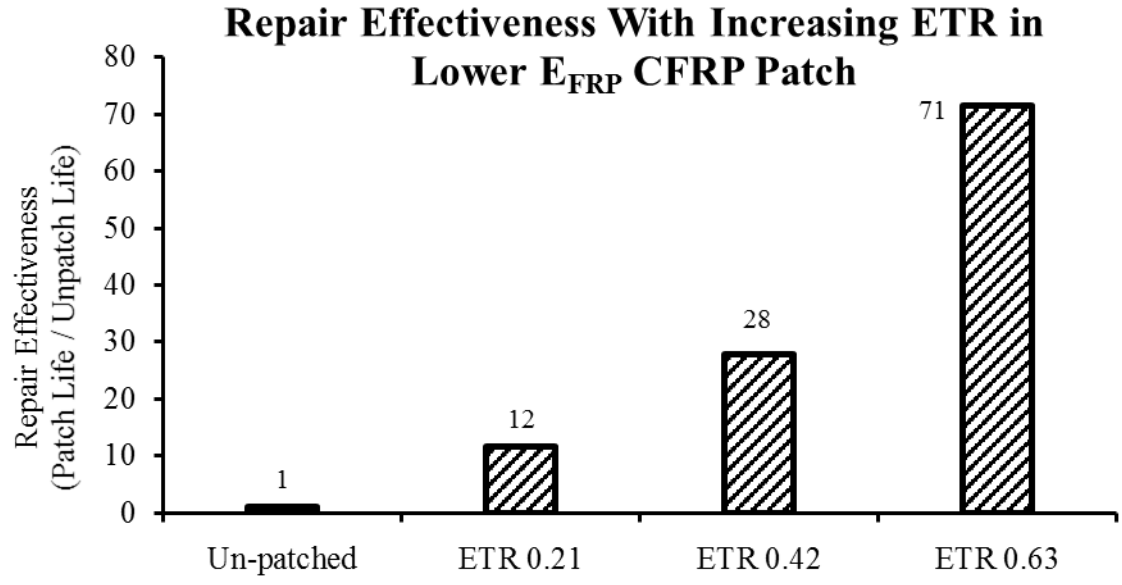

Figure 5.117 Impact of ETR on repair effectiveness of lower E_{FRP} CFRP specimens

6. Numerical evaluation of fatigue life of the tested specimens

6.1 Introduction and Background

After analyzing results of the experimental phase of current research work, the next task was intended towards the development of methodology for predicting the fatigue life of tested specimens using analytical and numerical tools, which became the focus of current chapter. The predictive procedure was developed through augmentation of application of linear elastic fracture mechanics and finite element analysis (FEA). As already shown in chapters 3 and 4 that FEA successfully predicted the SIF (K_I) at the crack tip of the cracked steel or metal plate with bonded CFRP patches, therefore, the knowledge of SIF at different crack lengths can further be used to predict the fatigue life (N) of the repaired plate for any given increase in the crack length. Detail of development of the predictive procedure using FEA and linear elastic fracture mechanics is provided in section 6.3 of this chapter.

Discussion on the development and use of finite element model (FEM) to evaluate SIF at the crack tip has already been presented in detail in chapters 3 and 4, and, therefore, it will only be discussed briefly in the current chapter for any changes in specimen geometry or loading etc. Similarly, the experimental results have been presented in detail in chapter 5, therefore, these will be summarized here for a quick reference. Successful achievement of the aim of current chapter was helpful in several ways in the current research work. It served as the validation model for the experimental results and it was also helpful in conducting the detail parametric study, presented in the last part of the current research work.

6.2 Background and summary of the experimental work

Detail description of the experimental phase of current research work, along with the test results, has already been presented in chapter 5. Therefore, for quick reference here, some of the related information would be reproduced. Main parameters of the experimental work included ETR, modulus of elasticity and type of CFRP (E_{FRP}), hybrid CFRP patches, modulus of elasticity of adhesive (E_a), thickness of adhesive (t_a) and the shear strength of adhesive (τ). Specimen's details and the test parameters, which were already shown in Table 5.1, are again

shown here in Table 6.1, being helpful in the development of respective finite element models. Table 6.1 additionally shows the governing failure mode of each specimen which was helpful in understanding the differences in the predicted and the tested fatigue life. Similarly, material properties of steel, CFRP and adhesive used in the experimental work are also reproduced in Table 6.2.

In summary, the tested specimens were divided into three main groups with increasing ETR values of 0.21, 0.42 and 0.63. Higher ETR groups of 0.42 and 0.63 were simply formed by doubling and triplicating the number of CFRP layers of the first ETR group of 0.21. In each ETR group two different types of CFRP, with different modulus of elasticity (E_{FRP}) and thickness (t_{FRP}), were used which are also mentioned in Table 6.2. Nominal thicknesses of one cured layer of the lower and higher E_{FRP} CFRP, as mentioned in the supplier's information were 1.016 mm and 1.2 mm, respectively. It has also been shown in chapter 5 that the ETR of a patch with three layers of lower modulus CFRP was approximately equal to the ETR of one layer of the higher modulus CFRP.

Within each ETR group further distinction between specimens was created by using different E_{FRP} and E_A. Additionally, in the first ETR group of 0.21, impact of varying adhesive shear strength (τ) and thickness (t_A) was also tested. Nominal dimensions of cracked steel plate used in the experiments were 500 mm x 100 mm x 9.5 mm thick while the length of double sided CFRP patch used was 300 mm. A typical test specimen is schematically shown in Figure 6.1. All the specimens were tested under the fatigue loading with stress range ($\Delta\sigma$) of 180 MPa and with σ_{max} and σ_{max} of 200 MPa and 20 MPa, respectively. The test results have already been presented in detail in section 5.4 but here only the fatigue life and the fatigue crack growth with number of fatigue cycles (a-N curve) for each specimen, are reproduced in Tables 6.3, 6.4 and 6.5 and Figures 6.2, 6.3 and 6.4.

In summary failure mode of all tested specimens was progressive patch delamination from the steel plate, occurred mainly at the steel-adhesive interface. But the delamination initiation and propagation was observed to be either from the path-end or from the crack surrounding or combination of the two. Patch-end delamination resulted in unexpectedly reduced fatigue life while near-crack patch delamination resulted in stable crack growth and higher fatigue life.

Majority of the ETR 0.21 specimens were failed in the near-crack or the combined delamination failure mode. The specimens of ETR 0.21, fabricated with the lower E_{FRP} CFRP, were failed in the near-crack delamination mode, while the specimens fabricated with the higher E_{FRP} CFRP were mostly failed in the combined delamination failure mode. Fatigue life enhancement in the specimens of ETR 0.21 was ranging between 9 to 11 times, compared to the fatigue life of unrepaired specimen.

Specimens of ETR 0.42 and 0.63 groups with higher E_{FRP} CFRP suffered with early patch-end delamination and resulted in unexpected reduced fatigue life. The expected reasons were the combined impact of peel and shear stresses at the patch-ends, especially in thicker patches of higher ETR groups, and the weaker adhesive strength. Specimens fabricated with lower E_{FRP} CFRP type in all ETR groups showed stable fatigue behavior and didn't suffered with patch-end delamination as well as resulted in higher fatigue life. Main reason for their higher fatigue life was expected to be the stronger and smooth-finish adhesive with high shear and bond strengths. Fatigue life enhancements in the lower E_{FRP} specimens of ETR 0.42 and 0.63 were found to be 28 and 72 times, respectively, compared to the fatigue life of unrepaired specimen. Their failure was governed by near-crack patch delamination mode.

In the ETR of 0.21, the impact of adhesive layer thickness was also studied by providing 40% reduced adhesive thickness in one of the specimen having the higher E_{FRP} CFRP. The specimen achieved 14% lesser fatigue life than the specimen provided with the full nominal adhesive thickness. Adhesives of the lower and higher E_{FRP} CFRP patches were also interchanged within some specimens of lower and higher E_{FRP} CFRP patches in the ETR 0.21 group, but it resulted in improper bonding of patch with the steel plate and caused premature patch delamination of the whole CFRP patch.

6.3 Methodology for evaluation of fatigue life of the tested specimens

Procedure developed for evaluation of fatigue life of cracked steel plate, repaired with bonded CFRP patch, mainly involved linear elastic fracture mechanics approach under constant amplitude fatigue load cycles. Fatigue crack growth rate can be predicted in metals through the knowledge of applied stress intensity factor range and the power law like the Paris Erdogan relation, as most authors suggest (Broek 1986, Barsome 2000 and Anderson 1994). A

simpler form of the Paris Erdogan relation (Paris and Erdogan 1963) is shown in Equation 6.1 below

$$\frac{da}{dN} = C\Delta K_I{}^m \qquad \text{Eq. 6.1}$$

Where C and m are material constants and da/dN is the rate of fatigue crack growth with respect to the number of fatigue load cycles. ΔK_I in the above equation is the applied stress intensity factor range and is given by the Equation 6.2 below (Anderson 2005). It can be noted that Equation 6.2 is similar to the Equation 3.4 because both are used to evaluate the SIF.

$$\Delta K_I = f_{(a/b)}\Delta\sigma\sqrt{\pi a} \qquad \text{Eq. 6.2}$$

Where a is the initial crack length, $\Delta\sigma$ is the applied stress range given by $\sigma_{max} - \sigma_{min}$ and $f_{(a/b)}$ is the geometric factor that usually accounts for the geometry of specimen, crack shape, crack location and stress concentration etc. The geometric factor has also been notated by different symbols in previous literature, like β, F, f and g etc. A detailed discussion about the stress intensity factor (SIF) and the geometric factor have already been provided in section 3.4. The geometric factor $f_{(a/b)}$ for an infinitely long and wide plate, with a central crack of length 2a, approaches 1.0. The geometric factor for a semi-infinite plate is usually formulated in the form of a polynomial or trigonometric function of the non-dimensionlized crack length (a/b).

It has also been shown in several numerical research works that the SIF (K_I) near the crack tip of the cracked plate has been reduced significantly by application of the bonded FRP patch on plate faces (Lam et al. 2008, Madani et al. 2008, Ellyin et al. 2006, Tsouvalis et al. 2009, Aglan et al. 2001, Liu et al. 2009, Jones and Callinan 1979, Taljsten et al. 2009, Lin et al. 1995). Similar results have also been obtained in section 4.4 of the current thesis. Therefore, in a way, the patch effect can be interpreted through evaluation of a reduced geometric factor which ultimately reduces the SIF of unpatched plate through Equation 6.2.

The geometric factor $f_{(a/b)}$ for any given crack and applied stress can be evaluated using the resulting reduced SIF values at the crack tip from any numerical analysis tool (like finite element analysis) and rearranging the Equation 6.2 for $f_{(a/b)}$ as shown in Equation 6.2a below.

$$f_{(a/b)} = \Delta K_I / \Delta\sigma\sqrt{\pi a} \qquad \text{Eq. 6.2a}$$

Lam et al (2008) successfully predicted the fatigue life of single sided bonded cracked steel plates by numerically evaluating the reduced geometric factor $f_{(a/b)}$ and using Equations 6.1 and 6.2. He also proposed the geometric factors for the double sided bonded steel plates for different ETR. But those geometric factors $f_{(a/b)}$ did not consider the patch delamination effect in their evaluation. It has already been shown in chapter 4 that the SIF was enhanced by introduction of patch delamination in the numerical analysis. Therefore, it can be interpreted that the patch delamination would also affect the corresponding geometric factor, evaluated using the results of the corresponding numerical analysis. Therefore, the geometric factors $f_{(a/b)}$, evaluated by Lam et al (2008) would predict closer fatigue life of a bonded steel plate if the shear strength of adhesive is much higher to minimize patch delamination.

The reduced geometric factors $f_{(a/b)}$ for each tested specimen were evaluated through the ΔK_I obtained from FEA and further use of Equation 6.2a. It is important to mention that the FEA carried out to evaluate the $f_{(a/b)}$ was also incorporating the impact of progressive patch delamination through modelling of adhesive shear failure in the corresponding FEA, as already demonstrated in chapter 4. Four finite element models were developed for each tested specimen, corresponding to the four crack lengths of 10 mm, 20 mm, 30 mm and 40 mm (a/b 0.1, 0.2, 0.3 and 0.4). It was carried out to develop $f_{(a/b)}$ as a continuous function of the non-dimensionalized crack length a/b which is described in detail in subsequent sections.

Another important phenomenon which has been observed during previous experiments, affecting the ΔK_I, is the crack closure. It was therefore needed to incorporate the crack closure impact in the current predictive methodology. Crack closure is the closing of crack before the load actually reaches zero in the down part of the stress cycle. Elber (1971) was among the pioneers who noticed the crack closure in aluminum plates, before complete removal of the tensile load from the plate. He found the reason being the remains of plastic deformations on the wake of crack surface which resulted in closure of the crack during unloading part of cyclic load before the load was still in tensile zone. Further bringing of the load down to zero then resulted in transfer of compressive stress through crack surfaces. He concluded that the actual stress intensity range exists at the crack tip is lower than the applied stress intensity range because of the crack closure before reaching the minimum stress limit σ_{min} of the fatigue cycle, and the full applied stress intensity range is not responsible for further crack growth. He also proposed the concept of effective SIF range (ΔK_{eff}) as the difference between K_{max} and

K_{op}, where K_{max} is the SIF corresponding to the σ_{max} and K_{op} is the SIF corresponding to the opening stress σ_{op}, (σ_{op} being higher than the σ_{min}). He then used the concept of ΔK_{eff} in validating the crack growth rate in several previous experiments and found that the use of ΔK_{eff} brought the crack growth rate closer to the material characteristic crack growth rate, which was, otherwise, not conforming well by using the applied stress intensity factor range ΔK_I. Link (1990) also used the concept of ΔK_{eff} to verify the crack growth rate in the fatigue tests of steel weldments and found it working better than using the applied ΔK_I.

Therefore, the impact of crack closure was also incorporated in the fatigue life prediction methodology by using ΔK_{eff} instead of applied ΔK_I in the Equation 6.1 (Paris and Erdogan 1963). The rearranged form of Equation 6.1 for the required number of fatigue load cycles (N) is shown in Equation 6.1a, in which it is obvious that the applied stress intensity factor range ΔK_I is replaced by the effective stress intensity factor range ΔK_{eff} for incorporating the crack closure effect, while a_i and a_f are the initial and final crack lengths.

$$N = \int_{a_f}^{a_i} \frac{1}{C(\Delta K_{eff})^m} \, da \qquad \text{Eq. 6.1a}$$

ΔK_{eff} in the above equation was calculated using more elaborated and modified form of the Equation 6.2 incorporating the crack closure effect and it is shown in Equation 6.3.

$$\Delta K_{eff} = (\sigma_{max} - \sigma_{op}) \, f_{(a/b)} \sqrt{\pi a} \qquad \text{Eq. 6.3}$$

Where $f_{(a/b)}$ is the geometric factor that accounts for the crack and specimen's geometry, loading as well as for the bonded patch effect, and it could be obtained through Equation 6.2a. σ_{max} in Equation 6.3 is the maximum stress of the applied stress range and σ_{op} is the opening stress and it must be higher than the minimum stress σ_{min} because of crack closure effect. Lam et al. (2008) calculated the σ_{op} for the fatigue crack growth in weldments with bonded FRP patch by superimposing the impact of crack closure and the FRP patch on the weldment. Here only the impact of CFRP patch was needed to be incorporated, therefore, σ_{op} was formulated for the patch impact and is given below in Equation 6.4, which is similar to that used by Lam et al. (2008).

$$\sigma_{op} = \left(\frac{E_s t_s + E_{frp} t_{frp}}{E_s t_s} \right) \sigma_{min} \qquad \text{Eq. 6.4}$$

In the above equation σ_{op} is the applied minimum stress to open the crack in the steel plate in the presence of bonded FRP patch. Equation 6.4 shows the sharing of stress by the FRP patch through its axial stiffness and it shows the situation of a bonded FRP plate in which the minimum applied stress required to open the crack is higher than the minimum stress required to open the same crack in the plate without the FRP patch by at least an amount equal to the stress which is being shared or drawn out of the plate by the patch.

Therefore, fatigue life of the tested specimens was predicted by performing numerical integration of Equation 6.1a, as shown in Equation 6.1b. ΔK_{eff} in Equation 6.1b was computed using Equation 6.3 and the interval Δa was needed to be kept very small so that ΔK_{eff} remained constant within the interval Δa. The fatigue life was then finally evaluated through numerical integration of Equation 6.1b and using Δa of 0.5 mm with the crack length variation was selected from 10 mm to 100 mm, which were the initial and final crack lengths in the experiments.

$$N = \sum_{10}^{100} \frac{\Delta a}{C\,(\Delta K_{eff})^m} \qquad \text{Eq. 6.1b}$$

It is important to note that in order to perform integration or numerical integration in Equation 6.1 ΔK_{eff} needs to be a continuous function of the crack length (a/b). It was accomplished by making the geometric factor $f_{(a/b)}$ in the Equation 6.3 a continuous function of (a/b). It was accomplished by first evaluating at least four discrete $f_{(a/b)}$ values from the ΔK_I results of the four FEM of each test specimen, corresponding to the four crack lengths of 10 mm, 20 mm, 30 mm and 40 mm. The four $f_{(a/b)}$ values were then plotted with the non-dimensionalized crack length a/b and then using curve fitting technique a continuous polynomial function of $f_{(a/b)}$was developed. Similar procedure had been adopted by Lam et al. (2008) to develop $f_{(a/b)}$ function for the single sided bonded CFRP repairs. In the current work, all the tested specimens were double sided patched and the assumption of equal crack growth on both the faces seemed reasonable and therefore the crack growth in these specimens can be modelled by developing several finite element models of each repaired specimen with different crack

lengths and then the impact of any parameter with varying crack length can be studied by joining the results of all those sub-models.

6.4 Finite element analysis of the tested specimens

A detailed description on the development of finite element model and the use of finite element analysis to evaluate the stress intensity factor has already been provided in chapter 3 of the thesis. Chapter 4 further extended the procedure to incorporate the patch delamination in the finite element analysis and it also showed the impact of patch delamination on the SIF (K_I). Similar methodology was also followed in the FEA of the tested specimens to incorporate the patch delamination impact on the resulting K_I obtained from their FEA analysis. The size and dimensions of the cracked steel plate and the CFRP patch selected to develop the respective finite element models were exactly same as that used in the experiments.

A typical test specimen is already shown in Figure 6.1 having the plate size of 500 mm x 100 mm x 9.5 mm thick, whose finite element analysis was required to be carried out. By using the plane of symmetries in the specimen, one quarter of the original specimen was modeled using ABAQUS Standard finite element code, similar to the model developed in section 3.5. 20 nodes Brick elements C3D20R were used to define the steel plate, adhesive and the CFRP layers. Realizing the evaluation of SIF (K_I) from the finite element analysis a finer meshed region was defined around the crack tip while a relatively coarser mesh region was used in the remaining portion of steel plate, adhesive and CFRP layers.

A typical one-quarter finite element model of plain steel specimen is shown in Figure 6.5 along with the planes of symmetry used to develop it. To include crack tip singularity in the analysis, collapsed node elements were defined by shifting the mid-length nodes of the elements surrounding the crack tip to their quarter length, through which the stress/strain singularity could be achieved at the crack tip (Barsome 1976). To reduce model size and analysis time in thicker patches the outcome of section 3.5.4 was used, which has shown that while keeping the ETR constant, providing the CFRP patch in multi layers will not affect the SIF at the crack tip of crack in steel plate, unless properties of the first adhesive layer change.

Therefore, the test specimens having more number of CFRP layers could be modelled using lesser number of equivalent CFRP layers by keeping their actual ETR and the first adhesive layer properties identical to that of the actual specimen. It was then followed thorough out in the current study that the specimens with more than three CFRP layers on each face were modelled with equivalent three-layered patch on each face of the cracked steel plate. Thickness of the equivalent CFRP layers (t_{FRP}) and their elastic modulus (E_{FRP}) were then set to achieve the actual ETR of the tested CFRP patch.

It is important to mention here the fatigue life of the specimens of ETR 0.42 and 0.63, failed in the governing patch-end delamination failure mode could not be predicted using the current methodology because of having different delamination failure mode. The other reason is that it has already been shown in section 4.5 that the patch end delamination does not affect the SIF (K_I) at the crack tip. Therefore, the fatigue life prediction of those specimens was just adopted from the other specimen's model having identical ETR but failed in the near-crack patch delamination failure mode. Although their prediction would not be accurate because of the difference in the failure mode as well as their different patch properties with the adopted model but at least it will provide a close estimate about their expected fatigue life. It is also important to mention here that the repairs whose predictive finite element analyses have not been carried out specifically here (because of their different failure modes) will automatically be covered later on in the parametric study part of the thesis, but considering only the near-patch delamination failure mode.

Four finite element models of each tested specimen of Table 6.1 were developed for the four non-dimensionlized crack lengths of 0.1, 0.2, 0.3 and 0.4, following the procedure already described in section 3.5. Steel plate was defined with two distinct regions of finer and coarser mesh and the crack tip was defined as a straight crack front through the steel plate thickness. Adhesive and CFRP layers were applied by imposing the identical displacement constraint to the two adjacent surfaces at all interfaces, as described in detail in section 3.5 which serve as a perfect bond between the two adjacent layers of different material. Material properties for adhesive, CFRP and steel were assigned according to Table 6.2 and the first analyses cycle was performed for each FEM under the far field applied maximum and minimum stress of 200 Mpa and 20 MPa, respectively to achieve the results of applying $\Delta\sigma$ of 180 MPa ($\Delta\sigma$ = 200 – 20 = 180 MPa).

Removal of failed adhesive region was carried out after analyzing the results of first analysis cycle, and reanalysis cycles were performed for the modified and reduced geometry of first adhesive layer. The process of removal of failed adhesive region and reanalysis of the models, with modified or reduced adhesive geometry, were continued for each crack length model until convergence in the progressive delamination procedure achieved as per the convergence criteria of section 4.2. The convergence in adhesive removal process, according to section 4.2, could assumed to be achieve if the failed adhesive region in any analysis cycle is found to be less than 1% of the initial bonded area of the patch. Similar procedure has already been carried out and demonstrated in sections 4.4.1.1, 4.4.2.1 and 4.4.3.1.

It is important to mention here that if in any model the convergence criterion was found fulfilled in the very first analysis cycle then two separate cases of analysis were carried out in those models. In the first case convergence was assumed to be achieved and the adhesive removal was not performed in those models. SIF range ΔK_I obtained for the un-delaminated case was considered to be valid after the delamination also. In the second case convergence criteria was modified to 0.5 % instead of 1 %, just to have the impact of a smaller delamination on the ΔK_I (or on the fatigue life) of the specimen. Only one adhesive removal cycle was performed in those models to achieve ΔK_I after incorporating that small delamination.

Finite element analysis of each specimen of Table 6.1 is individually discussed in the next section along with the process of introduction of patch delamination in their FEA as well as the details of reaching at their predictive fatigue life through the results of the FEA, and following the methodology presented in section 6.3.

6.4.1 Finite element analysis and results of control specimen

Finite element analysis of control specimen was carried out to validate and compare its SIF results with the standard case of the edge cracked specimen with applied uniform tensile far field stress. Five models of the control specimen with varying crack lengths were developed following the guide lines provided in sections 3.5 and 6.3. FEA of these models was carried out under the far filed applied stresses σ_{max} and σ_{min} of 200 MPa and 20 MPa respectively. The selected five crack lengths were 10 mm (a/b = 0.1), 20 mm (a/b = 0.2), 30 mm (a/b = 0.3), 35

mm (a/b = 0.35) and 40 mm (a/b = 0.4). A typical FEM of plain steel specimen has already been shown in Figure 6.5 for the crack length of 20 mm (or a/b = 0.2) with highlighted near-crack densely meshed region compared to the rest of the model. Figure 6.6 shows deformed geometry of the same FEM under the applied far-field tensile stress σ_{max} of 200 MPa.

After analyzing the five FEM of the control specimen, stress intensity factor (K_I) was obtained for each model, near the plate surface, because it has already been shown in section 3.5.1 that the SIF values obtained from FEA, close to the plate surface, correlated well with the SIF provided by Tada et al. (2000). ΔK_I was then evaluated from the SIF results of the five FEMs, corresponding to the applied stresses of 200 MPa and 20 MPa (by using $\Delta K_I = K_{I\,200} - K_{I\,20}$). The geometric factors $f_{(a/b)}$ were then evaluated by dividing these obtained ΔK_I with ($\Delta\sigma \sqrt{\pi}\, a$) and using the equation 6.2a. As already discussed in section 6.3 that a continuous function of geometric factor $f_{(a/b)}$ is required to be used in the Equation 6.1b to evaluate fatigue life of the specimens. Therefore the five obtained geometric factors $f_{(a/b)}$ were first plotted with the non-dimensionalized crack length a/b as shown in Figure 6.7. A polynomial curve was closely fitted to that $f_{(a/b)}$ distribution, which is also shown in the Figure 6.7. The equation of polynomial function of the curve shown in Figure 6.7 is reproduced in Equation 6.5.

$$f_{(a/b)} = 1.119 + 0.6038\left(\frac{a}{b}\right) + 3.4658\left(\frac{a}{b}\right)^2 + 2.7843\left(\frac{a}{b}\right)^3 + 2.1356\left(\frac{a}{b}\right)^4 \qquad \text{Eq. 6.5}$$

Figure 6.7, also shows the $f_{(a/b)}$ provided by Tada et al. (2000) for the edge crack plate with uniform far field applied stress. Its equation has already shown in Equation 3.12, but for convenience it is again reproduced below.

$$f_{(a/b)} = 1.12 - 0.231\left(\frac{a}{b}\right) + 10.55\left(\frac{a}{b}\right)^2 - 21.72\left(\frac{a}{b}\right)^3 + 30.39\left(\frac{a}{b}\right)^4 \qquad \text{Eq. 3.12}$$

Figure 6.7 shows that the $f_{(a/b)}$ obtained from FEA correlated closely with that provided by Tada et al. (2000) through Equation 3.12. It provided a good level of confidence in using the finite element results in further analyses. Fatigue life of control specimen was then evaluated using the obtained $f_{(a/b)}$ function of Equation 6.5, along with Equations 6.1, 6.1a and 6.1b, with ΔK_{eff} replaced by the applied ΔK because of the unpatched specimen. Material constants C and m were taken as 6.89×10^{-9} and 3, respectively as provided by Dowling, 2007, which were internally referred from Barsome (2000) for the ferrite pearlite steels. Note that these values were provided for the units of da/dN in mm/cycle and ΔK in MPa.$\sqrt{m}$. Crack length

versus number of fatigue cycles (a-N curve) of the control specimen was developed using the selected material constants and Equations 6.1, 6.1a and 6.1b with Δa selected to be 0.5 mm in Equation 6.1b. Initial crack length used to develop the curve was 10 mm because at this crack length the CFRP patch was bonded to the cracked steel plates in all repaired specimens. Crack length versus number of fatigue cycles (a-N curve) of the control specimen obtained through Equation 6.1b is shown in Figure 6.8 along with the experimental a-N values. Figure 6.8 also shows the a-N curve obtained using the $f_{(a/b)}$ values from Equation 3.12 provided by Tada et al. (2000). It can be seen from Figure 6.8 that all of these correlated closely. The control specimen actually took 16,150 fatigue cycles for the crack growth from 10mm till complete failure of the specimen. The predicted number of fatigue cycles for the same crack growth using the above procedure was found to be 17,296 cycles, which thus provided the test to predicted ratio of 0.95 for the control specimen. Further validation of the crack opening displacement (COD) obtained during the test was also carried out using the COD predictive equation provided by Tada et al. (2000) as reproduce below in Equation 6.6

$$COD = \left(\frac{4\sigma a}{E'}\right) V_{(a/b)} \qquad \text{Eq. 6.6}$$

With $V_{(a/b)}$ is given by Equation 6.7 below which is also taken from Tada et al. (2000)

$$V_{(a/b)} = \left(\frac{1.46 + 3.42\,(1 - \mathrm{Cos}(\lambda a / 2b)}{(\mathrm{Cos}(\lambda a / 2b))^2}\right) \qquad \text{Eq. 6.7}$$

Using σ as σ_{max} of 200 Mpa in Equation 6.6 above and E' as $E / (1-\nu^2)$ with ν as 0.3 for steel, the COD variation with a/b was evaluated. With the help of already developed a-N curve of the specimen (as shown in Figure 6.8) the COD values were then correlated with and plotted with the number of fatigue load cycles as shown in Figure 6.9. The experimentally obtained COD from the extensometer readings at the crack mouth, at different stages of the test, are also shown in Figure 6.9. The figure shows that the experimentally obtained COD are lying close to the predicted COD at different stages of fatigue load cycles.

After validating the working of the developed FEM of the plain steel specimen the process of evaluation of the $f_{(a/b)}$ for all the test specimens was carried out following the methodology of section 6.3 and is presented in subsequent sections of this chapter.

6.4.2 Finite element analysis of specimens failed by the near-crack patch delamination failure mode

As already mentioned in section 6.4 that FEA to develop the predicted model was carried out for the specimens failed in the governing near-crack patch delamination mode during the test. For the specimens failed in the governing patch-end delamination mode current methodology could not be used because of its less sensitivity on the SIF at the crack tip. The predictive fatigue life of those specimens was therefore adopted from the specimens with identical patch ETR and had failed in the near-crack patch delamination failure mode. Table 6.1 shows that nearly all specimens of higher elastic modulus E_{FRP} CFRP were failed in the patch-end delamination failure mode, except the two in the ETR group of 0.21 which were failed in the near-crack patch delamination failure mode. The predicted fatigue life of all specimens of higher elastic modulus E_{FRP}, failed in patch-end delamination mode, were adopted from the specimens of lower elastic modulus E_{FRP} CFRP, but having identical ETR. In the following sub-sections the details of finite element analysis of all the specimens failed in the near-crack patch delamination failure mode is presented, highlighting the impact of patch delamination on the resulting SIF and the predictive fatigue life.

6.4.2.1 Specimen 3-SKWRP-Adh-Sikudr-300

The specimen 3-SKWRP-Sk300 was the first specimen provided with the lower E_{FRP} sheets SikaWrap Hex 103C and it has already been mentioned before in sections 3.42, 4.42 and 5.34 that in order to make the ETR of the CFRP patch 0.21 three sheets of Sika Wrap Hex 103C were required on each face. It can also be seen in Table 6.2 that the recommended adhesive for this CFRP was Sikadur 300, which was comparatively thinner, flexible and less viscous compared to the adhesive Sikadur 30 used in the CFRP Sika Carbodur.

Four finite element models of 3-SKWRP-Sk300, corresponding to the four crack lengths, were developed by applying the adhesive and CFRP layers to the faces of control specimen, following the methodology summarized in sections 6.3 and 3.5. A typical FEM of 3-SKWRP-Sk300 for the crack length of 20 mm is shown in Figure 6.10. All four FEM were identical except that the crack length was different in these. Material properties were assigned to the steel, adhesive and the CFRP layers according to Table 6.2. The thickness of adhesive Sikadur 300 was provided to be 0.1mm, which was not provided separately in the supplier's data sheet and it was noted from the difference of the measured thicknesses of cured and uncured CFRP sheets during the specimen fabrication in the lab. Similarly, the elastic modulus and thickness of the SikaWrap Hex sheet (E_{FRP} and t_{FRP}) were selected so as to develop the same axial stiffness (E_{FRP} x t_{FRP}) provided in the supplier's data sheet for one cured sheet of SikaWrap Hex and these were 81 GPa and 0.816 mm respectively. Linear elastic analysis was performed for the applied far-field stresses of 200 MPa and 20 MPa (σ_{max} and σ_{min}), applied at the end faces of the specimen.

After performing the first analysis cycle, shear stress distribution in the interface adhesive layers of the four FEMs of 3-SKWRP-Sk300 were extracted and these are shown in Figures 6.11 through 6.14. Knowing the shear strength of adhesive from Table 6.2 the extent of adhesive failure was then determined within the shear stress distributions of Figures 6.11 through 6.14, and the resulting failed adhesive regions are shown in Figure 6.15.

Comparison of the shear stresses distribution and the corresponding failed adhesive regions could be understood by using the conclusions of chapter 3 and 4. Chapter 3 concluded that within identical ETR patches the developed peak shear stress in the interface adhesive layer will be higher in the patch having higher adhesive G/t ratio with a simultaneous reduction in SIF at the crack tip in the steel plate. Chapter 4 concluded that the failure of adhesive depends upon the magnitude and distribution of the developed shear stress as well as on the shear strength of the adhesive. Therefore, if the adhesive G/t is high then the developed shear stresses will be higher in adhesive near the crack, but at the same time, if the adhesive shear strength is also higher (than the developed shear) then there won't be any adhesive failure and no patch delamination will be needed to induce in the FEA.

Similar conditions existed for specimen 3-SKWRP-Sk300, its adhesive shear stiffness (G/t) was quite high (approximately 9 times) than that of adhesive Sikadur 30 therefore the

developed shear stress was much higher in it which is obvious from the Figures 6.11 to 6.14. But at the same time the SIF at crack tip was also lower in it, before induction of any adhesive failure. On the other hand, the shear strength of adhesive Sikadur 300 was also much higher (approximately 100%) than the adhesive Sikadur 30. Therefore, the combined impact of the two supporting adhesive properties finally resulted in reduced SIF (K_I) and a smaller adhesive failure region.

Analysis of area of the failed adhesive regions of Figure 6.14 showed that the adhesive failure and removal criterion of section 6.4 was fulfilled for the crack lengths 0.3 and 0.4. But for the crack lengths 0.1 and 0.2 it was not fulfilled, as shown in Figure 6.15, because of being less than 1 % of the total bond area. Therefore, following the procedure mentioned in section 6.4, two separate cases of analysis were required for the FEMs of crack lengths 0.1 and 0.2. In the first case convergence was assumed in adhesive failure process and no further re-analysis was carried out. In the second case, a one-step re-analysis was carried out for the removal of small failed adhesive region, whose area was lying between 0.5 % and 1 % of the total initial bonded area of patch.

For the first case, failure analysis of adhesive layer was performed in the FEMs of crack length 0.3 and 0.4 and these models were successively re-analyzed after progressive removal of the failed adhesive region from their geometry until the convergence criterion of section 6.4 was achieved. Figure 6.16 shows the failed adhesive regions obtained after convergence and Figures 6.17 and 6.18 show the modified and reduced geometry of the interface adhesive layers in their respective FEMs. To show the working of finite element models, Figure 6.19 shows deformed geometry of the FEM of crack length 30mm with the reduced interface adhesive layer after converged failure analysis.

SIF (K_I) values were then evaluated from the results of FEA of the models of crack length 0.3 and 0.4, both before and after induction of the patch delamination. For the crack lengths of 0.1 and 0.2, as obtained from Figure 6.14, the adhesive failure requirement was found below the criterion of section 6.4. Therefore, as first case, these were supposed to have achieved the convergence and were not required the adhesive failure process. The K_I values obtained from the FEA of the basic models of crack lengths a/b of 0.1 and 0.2 and from the converged FEMs of crack lengths 0.3 and 0.4 were plotted with the non-dimensionlized crack length a/b, as shown in Figure 6.20.

It is important to mention here that the K_I values shown in Figure 6.20 were corresponding to the applied σ_{max}, because of being larger than those obtained for the σ_{min}. It can be noted in Figure 6.20 that the SIF was enhanced after the introduction of patch delamination in the FEMs of crack lengths 0.3 and 0.4, by 36% and 90 %, respectively, but no impact of delamination observed on the crack lengths of 0.1 and 0.2 because no delamination was provided in these FEMs (as a first case). It is also important to note that the K_I values after delamination for the bigger crack length of 0.4 was very close to the fracture toughness (K_{IC}) of steel of 55 MPa.$m^{1/2}$ but not for the lower crack length values. Therefore, unstable fracture could not be expected below the crack length of 0.4. Using the resulting K_I values for both far-field applied stresses (σ_{max} and σ_{min}), ΔK_I was evaluated and was divided with the applied $\Delta\sigma$ of 180 MPa. The results are plotted with the non-dimensionlized crack length a/b as shown in Figure 6.21, which shows similar trend of variation as for K_I in Figure 6.20. The obtained $\Delta K/\Delta\sigma$ values for each crack length were then finally divided with the factor ($\sqrt{\pi}a$) to achieve the required geometric factors $f_{(a/b)}$, using the Equation 6.2a. These geometric factors $f_{(a/b)}$ were also plotted with the non-dimensionlized crack length a/b and shown in Figure 6.22. Figure 6.22 shows the K_I values both before and after the patch delamination.

In order to obtain $f_{(a/b)}$ a continuous function of the crack length, polynomial curves were fitted to the $f_{(a/b)}$ distributions of Figure 6.22 and these curves are also shown in Figure 6.22, along with their equations. In order to compare the obtained $f_{(a/b)}$ functions with the $f_{(a/b)}$ of standard edge crack plain plate without bonded CFRP patch the $f_{(a/b)}$ functions of Figure 6.22 were again plotted with the $f_{(a/b)}$ of the plain edge crack plate provided by Tada et al. (2000) using Equation 3.12 and these are shown in Figure 6.23. Figure 6.23 shows that the bonded CFRP patch initially reduced the $f_{(a/b)}$ values by a huge proportion, but, after introduction of patch delamination the $f_{(a/b)}$ again rose up by up to 90% (maximum), because of increase in the corresponding K_I values. The polynomial functions of $f_{(a/b)}$ shown in the Figures 6.22 and 6.23 are again reproduced in Equations 6.8 and 6.9 below, respectively for the case of before and after the patch delamination, with the coefficient of variation of 1 and 0.964, respectively.

$$f_{(a/b)} = 0.8312 - 1.9933\left(\frac{a}{b}\right) + 3.79\left(\frac{a}{b}\right)^2 - 3.335\left(\frac{a}{b}\right)^3 \quad \text{Eq. 6.8}$$

$$f_{(a/b)} = 0.8695 - 2.7751\left(\frac{a}{b}\right) + 6.658\left(\frac{a}{b}\right)^2 \quad \text{Eq. 6.9}$$

After developing the $f_{(a/b)}$ functions, the next step was to evaluate fatigue life and the a-N curve of specimen 3-SKWRP-Adh-Sikudr300, using Equations 6.1a, 6.1b and 6.3. In order to evaluate ΔK_{eff} from Equation 6.3, σ_{op} was calculated using Equation 6.4 using the given CFRP properties, and it came out to be 25.3 MPa, which was expectedly higher than the σ_{min} of 20 MPa. Fatigue life of 3-SKWRP-Sk300 was then evaluated using Equation 6.1b, both before and after the introduction of patch delamination, with ΔK_{eff} evaluated from Equation 6.3 and using the $f_{(a/b)}$ functions obtained in Equations 6.8 and 6.9. The crack increment Δa of 0.5 mm was used in Equation 6.1b and the material constants 'C' and 'm' were provided to be 6.89 x 10^{-9} and 3 respectively, as already mentioned in section 6.4.1.

The predicted a-N curves of the specimen 3-SKWRP- Sk300, finally obtained using the $f_{(a/b)}$ functions of Equations 6.8 and 6.9, are shown in Figure 6.24 along with its a-N curve obtained in the test and already shown in the Figure 6.2. It can be noted in Figure 6.24 that the predicted a-N curve of the specimen, before introduction of the patch delamination, was curtailed because of reaching quite large value. Total fatigue life of this specimen, evaluated using the developed $f_{(a/b)}$ functions of Equations 6.8 and 6.9, were 6,14,332 and 2,05,702 cycles, respectively, before and after the induction of patch delamination. This specimen had actually taken 1,88,375 fatigue cycles in the test, before its complete failure. Therefore, the test to predicted ratio for this specimen was evaluated to be 0.92 if predicting the fatigue life with consideration of patch delamination. But if the patch delamination impact was not considered or introduced in FEA then the evaluated fatigue life would be 6,14,332 cycles. In that case the test to predict ratio became 0.30, which shows a big deviation from the experimental results. The above comparison of predicted fatigue life shows that without considering the impact of patch delamination in the corresponding FEA the predicted fatigue life would deviate by a large amount and it would also be towards non-conservative side.

In the last phase of predicted analysis, fatigue life of specimen 3-SKWRP-Sk300 was re-evaluated, as the second case, with consideration of small delamination impact in the FEA of crack lengths 0.1 and 0.2, which was not considered in the above completed phase. As per the discussion of section 6.4, and as a second case, the adhesive failed regions shown in the Figure 6.15 were also introduced in the crack length models of 0.1 and 0.2. The process of evaluation of $f_{(a/b)}$ function was repeated for the new values of K_I for crack lengths 0.1 and 0.2 and the revised K_I and $f_{(a/b)}$ distribution were obtained as shown in Figures 6.25 and 6.26. The

polynomial function obtained after curve fitting of the revised $f_{(a/b)}$ values of Figure 6.26, is also shown in the same figure. The coefficient of variation for the new $f_{(a/b)}$ function was found to be 0.998 and the corresponding equation of new $f_{(a/b)}$ function is also reproduced in Equation 6.10 below.

$$f_{(a/b)} = 0.9317 - 2.7118\left(\frac{a}{b}\right) + 6.0549\left(\frac{a}{b}\right)^2 \qquad \text{Eq. 6.10}$$

The fatigue life and a-N curve were again evaluated for the revised $f_{(a/b)}$ distribution of Equation 6.10 and the resulting a-N curve is shown in Figure 6.27, along with the previously obtained a-N curve of the same specimen. As expected from the increased $f_{(a/b)}$ distribution the reduced fatigue life thus obtained was 1,75,529 which was reduced by approximately 14% from the previously evaluated predicted fatigue life when the delamination provided in only two crack lengths of 0.3 and 0.4. The test to predict ratio for this case was found to be 1.07. Figure 6.27 shows the impact of smaller patch delamination provided in the finite element analysis, even less than 1% of the initial bond area, to obtain the $f_{(a/b)}$ distribution. Therefore, the fatigue life evaluation using numerically evaluated geometric factors was found to be much sensitive to the level of patch delamination provided in the numerical or finite element analysis.

6.4.2.2 Specimen 3-SKWRP-Adh-Sikudr-330

The specimen 3-SKWRP-Sk330 was provided with the same type and number of CFRP layers as provided in the specimen 3-SKWRP-Sk300 but with different adhesive (Sikadur 330). The Tensile modulus of elasticity (E_A) of this adhesive was not provided in the supplier's data sheet so it was adopted from other research work (Julia de Castro 2005), which provided it to be 4.5 GPa. Similarly, the thickness of this adhesive was also not mentioned in any form in the supplier's data sheet and it was noted to be ranging between 0.1 mm and 0.2 mm in the experimental work. It was taken as 0.1 mm in the current study, i.e. same as that used for the Sikadur 300 before. Methodology of obtaining the required geometric factor $f_{(a/b)}$, through evaluation of SIF or K_I from FEA, and the procedure of invoking patch delamination in FEA, was followed from the specimen 3-SKWRP-Sk300. Similar procedure was adopted in

development of the required geometric factor $f_{(a/b)}$ in all the specimens. Therefore, for the current specimen and also for the rest of specimens only the results of FEA including the K_I distribution and the corresponding $f_{(a/b)}$ functions will be provided with brief discussion and explanation.

After performing the first cycle of FEA in the four crack-length models of specimen 3-SKWRP-Sk300, the shear stress in the interface adhesive layer was studied for the applied σ_{max} of 200 MPa, as shown in Figures 6.28 to 6.31. Using the shear strength of adhesive from Table 6.2, the extent of adhesive failure was determined in each adhesive layer of Figures 6.28 through 6.31, and the resulting failed adhesive regions are shown in Figure 6.32. Analysis of the failed adhesive regions of Figure 6.32 showed that the adhesive failure in crack lengths of 0.1 and 0.2 already fulfilled the convergence criteria and therefore, as a first case, no adhesive failure was required to be introduced in these models. But analysis of the failed adhesive regions of crack lengths 0.3 and 0.4 (from Figure 6.32) showed that these required the progressive failure process in their interface adhesive layer.

Progressive adhesive failure process was carried out in the FEA of crack lengths 0.3 and 0.4 until the convergence achieved according to the criterion of section 6.4 and the failed adhesive regions after convergence are also shown in Figure 6.33. Figures 6.34 and 6.35 show the reduced interface adhesive layers of the crack lengths 0.3 and 0.4, after convergence, in their respective finite element models. Comparing the failed adhesive regions in specimens 3-SKWRP-Sk300 and 3-SKWRP-Sk-330 (from Figures 6.16 and 6.33), it can be noted that the adhesive layer in specimen 3-SKWRP- Sk-330 suffered with 20% more failure, or in other words, the patch delamination would be more in this specimen. It could be understood by using the conclusions of chapter 4, because the adhesive Sikadur 330 had the G/t ratio three times greater than adhesive Sikadur 300. Its shear strength was also approximately 65% of the adhesive Sikadur 300. Therefore, because of very high adhesive G/t ratio the developed shear stress in this adhesive was high but its shear strength was, although lower than that of Sikadur 300, but not very low. Therefore, the net result was comparatively more adhesive failure in adhesive Sikadur 330.

The resulting $\Delta K/\Delta\sigma$ and $f_{(a/b)}$ distributions developed using the K_I from the results of FEA are shown in Figures 6.36 and 6.37. It is obvious from Figures 6.36 and 6.37 that the resulting $\Delta K/\Delta\sigma$ and $f_{(a/b)}$ values were enhanced by 92 % and 180 % after the patch delamination,

respectively in the FEA of crack lengths of 0.3 and 0.4. Comparing Figures 6.21 and 6.22 with 6.36 and 6.37 it can be seen that the $\Delta K/\Delta\sigma$ or the $f_{(a/b)}$ values in this specimen were enhanced more after the patch delamination than the specimen 3-SKWRP-Sk-300. But the final delaminated values of $\Delta K/\Delta\sigma$ or $f_{(a/b)}$ in Sikadur 330 specimen were only 11 % to 14 % higher than those in the Sikadur 300 specimen. It was because of very high adhesive G/t ratio in Sikadur 330 specimen, which initially brought down the K_I values to very low values, such that, even after getting two to three times more enhancement in K_I values, than the Sikadur 300 specimen after the patch delamination, the final values of K_I just exceeded that of Sikadur 300 specimen. Another important thing noted from the comparison of the $f_{(a/b)}$ between specimens 3-SKWRP-Sk-300 and 3-SKWRP-Sk-330 that the $f_{(a/b)}$ values after patch delamination were 11 % to 14 % higher in the crack length of 0.3 and 0.4 in the specimen 3-SKWRP-Sk-330, but these were quite low in the crack lengths of 0.1 and 0.2.

Polynomial functions were then fitted to the $f_{(a/b)}$ distributions shown in Figure 6.37 and these functions are also shown in Figure 6.37. The equations of the fitted polynomial functions to the $f_{(a/b)}$ distribution are again reproduced in Equations 6.11 and 6.12 below, respectively for the case of before and after the patch delamination. Note that the coefficients of variation determined for these two cases were 1 and 0.91 respectively. Figure 6.38 again shows the $f_{(a/b)}$ functions shown in Figure 6.37, but, additionally it includes the $f_{(a/b)}$ of the plain edge crack plate obtained from Tada et al. (2000) using Equation 3.12.

$$f_{(a/b)} = 0.7601 - 2.3466\left(\frac{a}{b}\right) + 4.9622\left(\frac{a}{b}\right)^2 - 4.4116\left(\frac{a}{b}\right)^3 \qquad \text{Eq. 6.11}$$

$$f_{(a/b)} = 0.7231 - 2.5555\left(\frac{a}{b}\right) + 7.8745\left(\frac{a}{b}\right)^2 \qquad \text{Eq. 6.12}$$

Fatigue life and a-N curves for specimen 3-SKWRP-Sk330 were evaluated, following the methodology defined in section 6.3, and using the $f_{(a/b)}$ functions of Equations 6.11 and 6.12. The resulting a-N curve is shown in Figure 6.39, along with the a-N curve of the specimen already obtained in the test and shown in the Figure 6.2. Fatigue life of specimen 3-SKWRP-Sk330, evaluated using the developed $f_{(a/b)}$ function of equations 6.11 and 6.12, were found to be 9,48,857 and 2,69,213, respectively before and after the patch delamination. This specimen had actually taken 2,29,260 fatigue cycles in the test. Therefore, test to predicted ratio for this

specimen was evaluated to be 0.85, if the patch delamination was considered in predicted fatigue life evaluation. If the impact of patch delamination is not considered in the FEA then the predicted fatigue life of this specimen would be 9,48,857, with test to predict ratio of 0.24. It shows that if the patch delamination was not introduced in FEA then the predicted fatigue life would be very high towards un-conservative side. If the patch delamination is introduced in FEA, then the corresponding predicted fatigue life would become more realistic and close to the experimental.

Last part of analysis, carried out for the current specimen, was the re-evaluation of its predicted fatigue life, with consideration of small delamination in the crack lengths 0.1 and 0.2, which was not considered in the above completed phase because of being converged in their first analysis cycles.

FEA of crack lengths 0.1 and 0.2 (10 mm and 20 mm) was then repeated with the introduction of patch delamination, through removal of the failed regions of their interface adhesive layers, as shown in Figure 6.32. After re-analysis, the $f_{(a/b)}$ values were re-evaluated using the revised K_I values in crack lengths of 0.1 and 0.2 but keeping the old K_I values in crack lengths of 0.3 and 0.4. The revised $f_{(a/b)}$ distribution obtained is shown in Figure 6.40, along with the fitted polynomial function for the revised $f_{(a/b)}$ distribution. The polynomial function is again reproduced in Equation 6.13 below. It is obvious from Figure 6.40 that due to increased patch delamination, the $f_{(a/b)}$ values were increased and the resulting fatigue life was expected to be shorter. The coefficient of variation obtained for the fitted polynomial function shown in Figure 6.40 was 0.95.

$$f_{(a/b)} = 0.814 - 2.5576\left(\frac{a}{b}\right) + 7.2425\left(\frac{a}{b}\right)^2 \qquad \text{Eq. 6.13}$$

Fatigue life and the a-N curve were again evaluated for the revised $f_{(a/b)}$ distribution of Equation 6.13 and the revised a-N curve is shown in Figure 6.41, along with the previously obtained a-N curve of the same specimen. As expected from the increased $f_{(a/b)}$ distribution, the reduced fatigue life, obtained using the revised $f_{(a/b}$ functions of Equation 6.13, was 2,01,776. It was reduced by approximately 11 %, compared to the previously predicted fatigue life, when the patch delamination was considered in its crack lengths of 0.3 and 0.4 only. The

test to predict ratio for the revised fatigue life was evaluated to be 1.12, which was higher from the test but on a conservative side.

6.4.2.3 Specimen 1-CBDR-Adh-Sikudr-30

The specimen 1-CBDR-Sk-30 was the first specimen in ETR 0.21 group provided with the higher modulus CFRP plate, with commercial designation 'Sika Carbodur'. One layer of the CFRP plate was provided on each face of the steel plate so as to make its patch ETR of 0.21. Material properties of CFRP plate and adhesive Sikadur 30 were assigned in the FEA according to Table 6.2. Thicknesses of the CFRP plate and adhesive were provided to be 1.2 mm and 2.5 mm respectively, as provided in the supplier's data sheets. FEA of this specimen was performed following the methodology provided in section 6.3 under far field applied σ_{max} of 200 MPa. The required geometric factors $f_{(a/b)}$ were developed through evaluation of SIF or K_I from the FEA and the patch delamination was introduced in the FEA, following procedures of sections 4.4, 6.4.2.1 and 6.4.2.2.

After the first analysis cycle in the finite element models of four crack-lengths of this specimen shear stress was studied in the interface adhesive layers of all models. Figures 6.42 to 6.45 show the resulting shear stress distribution in the interface adhesive layer of the four crack-length models. Using shear strength of adhesive from Table 6.2 the extent of adhesive failure was determined in each adhesive layer of Figures 6.42 through 6.45 and the resulting failed adhesive regions are shown in Figure 6.46. Analysis of the failed adhesive regions of Figure 6.46 showed that the adhesive failure in crack lengths of 0.1, 0.2 and 0.3 was much less and has already fulfilled the convergence criteria of section 6.4. Therefore, as a first case, no interface adhesive failure was introduced in their FEA.

Comparing the adhesive failure in this specimen with that obtained in the specimen 3-SKWRP-Sk300 or 3-SKWRP-Sk330, it can be noted that lesser adhesive failure occurred in this specimen. It is important to note that the shear strength of adhesive in this specimen was lesser than the adhesive of other two specimens. But lesser adhesive failed regions obtained in it. It was because of comparatively lower magnitude of shear stresses developed in this specimen.

Lower magnitude of adhesive shear stresses in this specimen could be understood using the conclusions of chapter 3. Adhesive Sikadur 30 had very small G/t ratio because of its large

thickness (approximately 25 times thicker than that of adhesive Sikadur 300). Therefore, lower adhesive shear stress was expected at its interface. Failure process in adhesive layer was then performed only in the model of crack length 0.4, until the convergence achieved according to the criterion of section 6.4. Failed adhesive region obtained after convergence in the FEM of crack length of 0.4 is shown in Figure 6.47 and the reduced interface adhesive layer of crack length 0.4 in its finite element model is also shown in Figure 6.48.

Using the resulting SIF (K_I) from the FEA, before and after the patch delamination, the $\Delta K/\Delta\sigma$ and $f_{(a/b)}$ distributions were developed and these are shown in Figures 6.49 and 6.50. It is obvious from these figures that the resulting $\Delta K/\Delta\sigma$ and $f_{(a/b)}$ values were enhanced by 76% after the patch delamination in the FEM of crack length 0.4. There is no change in SIF (K_I) or the $f_{(a/b)}$ values in the crack lengths 0.1, 0.2 and 0.3 because of no patch delamination or adhesive failure found in these.

Polynomial curves were then fitted to the $f_{(a/b)}$ distribution of Figure 6.50 and ther functions are also shown in same figure. The equations of the fitted polynomial functions to the $f_{(a/b)}$ distribution are again reproduced in Equations 6.14 and 6.15 below, respectively before and after induction of patch delamination. Note that the coefficients of variation found in these two fitted polynomials were 1.0 and 0.884, respectively. Figure 6.51 shows the $f_{(a/b)}$ functions already developed and shown in Figure 6.50 but it additionally includes the $f_{(a/b)}$ of the plain edge crack plate obtained from Tada et al. (2000) using Equation 3.12.

$$f_{(a/b)} = 0.8278 - 1.1644\left(\frac{a}{b}\right) + 1.697\left(\frac{a}{b}\right)^2 - 1.6568\left(\frac{a}{b}\right)^3 \qquad \text{Eq. 6.14}$$

$$f_{(a/b)} = 1.1094 - 4.675\left(\frac{a}{b}\right) + 10.421\left(\frac{a}{b}\right)^2 \qquad \text{Eq. 6.15}$$

Fatigue life and a-N curves for specimen 1-CBDR-Sk30 were evaluated, following the methodology of section 6.3, as demonstrated in section 6.4.2.1 or 6.4.2.2, and the resulting a-N curve is shown in Figure 6.52. The a-N curve of this specimen obtained during the test is also shown in Figure 6.52. Fatigue life of this specimen was then evaluated using the $f_{(a/b)}$ distribution of Equations 6.14 and 6.15 and following the procedure of section 6.3. The evaluated fatigue life of this specimen, before and after the induction of patch delamination, was found to be 4,46,360 and 1,79,400, respectively. This specimen had taken 1,71,992

fatigue cycles during the test, as mentioned in chapter 5. Therefore, test to predicted ratio for this specimen was evaluated to be 0.96, if considering the impact of patch delamination. If the impact of adhesive failure or the corresponding patch delamination is not considered in the FEA then obviously the predicted fatigue life would be 4,46,360 and the respective test to predict ratio becomes 0.39. It shows that if introduction of patch delamination was not considered in the FEA then the predicted fatigue life would be very high and towards un-conservative side. If patch delamination was considered in the FEA then the corresponding predicted fatigue life would become more realistic and close to the actual.

Last part of analysis performed for this specimen was the re-evaluation of its predicted fatigue life with consideration of small delamination in the FEA of crack lengths 0.1, 0.2 and 0.3. It was not considered in the above completed phase because of being found converged in their first analysis cycles. Finite element analysis of crack lengths 0.1, 0.2 and 0.3 was repeated with the introduction of small adhesive failure in their interface adhesive layers, as shown in the Figure 6.46. After the re-analysis, $f_{(a/b)}$ values were re-evaluated in the models of crack lengths 0.1, 0.2 and 0.3, using the revised K_I values. The resulted revised $f_{(a/b)}$ distribution is shown in Figure 6.53. Figure 6.53 shows that, due to increased patch delamination, the $f_{(a/b)}$ values were increased and the resulting fatigue life was expected to be smaller. The polynomial function fitted for the revised $f_{(a/b)}$ distribution in Figure 6.53 is also reproduced below in Equation 6.16. The corresponding coefficient of variation for the revised $f_{(a/b)}$ function of Equation 6.16 was found to be 0.998.

$$f_{(a/b)} = 0.8953 - 2.2524\left(\frac{a}{b}\right) + 5.8143\left(\frac{a}{b}\right)^2 \qquad \text{Eq. 6.16}$$

Fatigue life and a-N curve of this specimen were again evaluated for the revised $f_{(a/b)}$ function of Equation 6.16 and the revised a-N curve of this specimen is shown in Figure 6.54. This figure also shows the previous a-N curve, when no delamination was considered in the three models of crack lengths 0.1, 0.2 and 0.3. The revised and reduced fatigue life obtained from the increased $f_{(a/b)}$ values was 1,43,123, which was reduced by approximately 17 %, compared to the previous predicted fatigue life when delamination was provided in only one crack

length of 0.4. The test to predict ratio for the revised fatigue life of 1,43,123 was evaluated to be 1.2, which was 20 % higher from the test but towards conservative side.

6.4.2.4 Specimen 1-CBDR-Adh-Sikudr-30/2

The specimen 1-CBDR-Sk-30/2 was identical to the specimen 1-CBDR-Sk30 except that it was provided with half the adhesive thickness of 1-CBDR-Sk30. The main intension was to study the role of reduced adhesive thickness on the resulting fatigue life of the repair. FEA of this specimen was carried out, following the methodology of sections 3.5, 4.2 and 6.3. Patch delamination was also introduced in FEA, following the methodology of sections 4.2, 4.4 and 6.4.2. After the first analysis cycle of finite element analysis in the models of four crack-lengths (0.1, 0.2, 0.3 and 0.4) of this specimen, shear stress was studied in the interface adhesive layers of all models, which is also shown in Figures 6.55 through 6.58. Comparing these shear stress distributions with those obtained in specimen 1-CBDR-Sk-30, it can be concluded that the peak shear stress values were higher in this specimen.

Using the shear strength of adhesive from Table 6.2, the extent of adhesive failure was determined in each adhesive layer of Figures 6.55 through 6.58, and the resulting failed adhesive regions are shown in Figure 6.59. Analysis of the failed adhesive regions of Figure 6.59 showed that in this specimen shear strength failure criteria was fulfilled in the two crack length models of 0.1 and 0.2, compared to three crack lengths fulfilling in the specimen 1-CBDR-Sk-30. It showed that the shear stresses were higher in this specimen, although the adhesive shear strength was same in the two. These results could be understood by using the conclusions of chapter 3. Because of half adhesive thickness in this specimen the adhesive G/t ratio was almost double in it, compared to 1-CBDR-Sk-30, which resulted in higher adhesive shear stresses and more adhesive failure in this specimen.

As a first case, the models of crack lengths 0.1 and 0.2 were not re-analyzed for the adhesive failure and were assumed to have achieved convergence in their first analysis cycle. These models were then re-analyzed separately for their small adhesive failure, as a second case, after evaluation of fatigue life of the specimen for the first case. Failure analysis in adhesive layer was then performed in the models of crack length 0.3 and 0.4, through progressive removal of the failed adhesive region until the convergence criterion of section 4.2 or section

6.4 was achieved. Failed adhesive regions obtained after convergence in the models of crack lengths 0.3 and 0.4 are shown in Figure 6.60, and these are also shown in their finite element models in Figures 6.61 and 6.62.

K_I values were extracted from the results of FEA of all crack lengths, both before and after the patch delamination. The corresponding $\Delta K/\Delta\sigma$ and $f_{(a/b)}$ distributions were developed, following the methodology of section 6.4.2, and these are shown in Figures 6.63 and 6.64. It can be seen from Figure 6.63 that the resulting $\Delta K/\Delta\sigma$ values were enhanced by 40 % and 104 %, respectively for the crack lengths of 0.3 and 0.4, due to the impact of patch delamination. It is also important to note that the 104 % enhancement of $\Delta K/\Delta\sigma$ in crack length of 0.4 was itself 10 % higher than that obtained in the specimen 1-CBDR-Sk-30 for the same crack length. Similar impact of the patch delamination could be seen from the enhancement in the $f_{(a/b)}$ distribution in Figure 6.64 after the patch delamination.

Figure 6.64 also shows the corresponding equations of fitted polynomial functions to the $f_{(a/b)}$ distributions. These polynomial functions are again reproduced in Equations 6.17 and 6.18 below, respectively for the cases of before and after the introduction of patch delamination. The coefficients of variation of these equations were found to be 1.0 and 0.98, respectively. In order to assess the patch effectiveness of current specimen, the f(a/b) functions already developed and shown in Figure 6.64 were again plotted in Figure 6.65 along with the $f_{(a/b)}$ of plain edge cracked plate provided Tada et al. (2000) using Equation 3.12.

$$f_{(a/b)} = 0.8354 - 1.4286\left(\frac{a}{b}\right) + 2.2076\left(\frac{a}{b}\right)^2 - 1.9442\left(\frac{a}{b}\right)^3 \quad \text{Eq. 6.17}$$

$$f_{(a/b)} = 0.9166 - 2.9124\left(\frac{a}{b}\right) + 7.8641\left(\frac{a}{b}\right)^2 \quad \text{Eq. 6.18}$$

Fatigue life and a-N curves of specimen 1-CBDR-Sk-30/2 were evaluated, following the methodology of section 6.3, which has also been demonstrated in sections 6.4.2.1 and 6.4.2.2. The resulting a-N curve is shown in Figure 6.66 along with the a-N curve of the specimen obtained in the test. Fatigue life of this specimen was evaluated using the $f_{(a/b)}$ functions of Equations 6.17 and 6.18 and following the methodology of section 6.3. The resulting fatigue life was found to be 2,48,676 and 1,52,852, respectively before and after the patch delamination in FEA. This specimen had actually taken 1,50,336 fatigue cycles before its

complete failure in the test. The test to predicted ratio for this specimen was evaluated to be 0.97, if using the predicted fatigue life of 1,52,852, which was evaluated considering the impact of patch delamination. If patch delamination was not considered in the FEA then obviously the predicted fatigue life would be 2,48,676, and the corresponding test to predict ratio becomes 0.60. It shows great impact of considering the patch delamination in FEA on the predicted fatigue life.

Last part of analysis performed for this specimen was the re-evaluation of its predicted fatigue life with consideration of small delamination in the FEA of crack lengths 0.1 and 0.2, which was not considered in the above completed phase, because of being found converged in their first analysis cycles. Finite element analysis of models of crack lengths 0.1 and 0.2 was then repeated with the introduction of adhesive failure in their interface adhesive layers, as shown in the Figure 6.59. After the re-analysis, $f_{(a/b)}$ values were re-evaluated in the models of crack lengths 0.1 and 0.2 using the revised K_I values, and the resulted revised $f_{(a/b)}$ distribution is shown in Figure 6.67. It can be seen in Figure 6.67 that due to increased patch delamination, the $f_{(a/b)}$ values were higher than before and the resulting fatigue life was expected to be shorter. The polynomial function fitted for the revised $f_{(a/b)}$ distribution is also shown in Figure 6.67, and it is also reproduced below in Equation 6.19. The corresponding coefficient of variation for the revised $f_{(a/b)}$ function of Equation 6.19 was found to be 0.99.

$$f_{(a/b)} = 0.9492 - 2.5423\left(\frac{a}{b}\right) + 6.6609\left(\frac{a}{b}\right)^2 \qquad \text{Eq. 6.19}$$

The fatigue life and the a-N curve for this specimen were re-evaluated for the revised $f_{(a/b)}$ function of Equation 6.19. The resulting a-N curve is shown in Figure 6.68, along with the previous a-N curve, in which no delamination was considered in the two crack lengths of 0.1 and 0.2. The revised and reduced fatigue life obtained from the increased $f_{(a/b)}$ function was evaluated to be 1,24,678. It was reduced by approximately 17 % compared to the previous predicted fatigue life when the delamination was provided in the crack lengths of 0.3 and 0.4 only. The test to predict ratio for the revised predicted fatigue life was found to be 1.18, which was 18 % higher from the test results but on a conservative side.

6.4.2.5 Specimen 6-SKWRP-Adh-Sikudr-300

This specimen was provided with 6 layers of the CFRP SikaWrap Hex-103C on its each face in the test, which made its ETR double of the specimen 3-SKWRP-Si300. Finite element analysis of this specimen was carried out similar to all the previous specimens provided in section 6.4.2. Using conclusions of section 3.5.4, its FEM was developed with three equivalent CFRP layers, instead of the six actual layers in order to reduce the file size and the run-time. The CFRP elastic modulus (E_{FRP}) was then defined double of the specimen 3-SKWRP-Si300, so that the resulting overall patch ETR became 0.42. A typical FEM of this specimen, with crack length of 0.3, is also shown in Figure 6.69.

After the first cycle of FEA of its four crack-length models, the resulting shear stress distribution in interface adhesive layers of each model was studied and it is also shown in Figures 6.70 through 6.73. Using shear strength of the adhesive from Table 6.2, the extent of adhesive failure was determined in each adhesive layer of Figures 6.70 through 6.73. The resulting failed adhesive regions in the four interface adhesive layers are shown in Figure 6.74. Analysis of these failed regions for the convergence criteria of section 6.2 showed that the adhesive failure in the crack lengths of 0.1 and 0.2 have already fulfilled the convergence criteria. The adhesive failure in rack lengths of 0.3 and 0.4 were found to be exceeding the convergence limit and thus required the adhesive failure process.

Adhesive failure analysis was performed in the models of crack length 0.3 and 0.4 and these models were successively re-analyzed after progressive removal of the failed adhesive region until the convergence achieved. Figure 6.75 shows the reduced adhesive layers in models of crack lengths 0.3 and 0.4, after convergence, and these are also shown in their respective finite element models in Figures 6.76 and 6.77. It is obvious from the failed adhesive regions of Figures 6.74 and 6.75 that these were lesser than the specimen 3-SKWRP-Sik300 because of higher patch ETR of the current patch. It can be noted that the models of crack lengths 0.1, 0.2 were not provided with the adhesive failure analysis in the current analysis phase, as a first case, because these were assumed to be converged in their first analysis cycles.

The $\Delta K/\Delta\sigma$ and $f_{(a/b)}$ distributions, developed from the resulting SIF (K_I) values from FEA, are shown in Figure 6.78 and 6.79, respectively. Figures 6.78 and 6.79 show that the resulting $\Delta K/\Delta\sigma$ and $f_{(a/b)}$ values for the crack lengths of 0.3 and 0.4 were enhanced by 33% and 68%, respectively, after introduction of patch delamination in their FEA. Comparing Figures 6.78

and 6.79 with 6.21 and 6.22 it can be concluded that little lesser impact of patch delamination on $\Delta K/\Delta\sigma$ or the $f_{(a/b)}$ values was existed in the current specimen compared to the 3-SKWRP-Sk300 because of higher ETR.

The polynomial functions fitted to the $f_{(a/b)}$ distributions of Figure 6.79 are also shown in the same figure. These polynomial functions are again reproduced in Equations 6.20 and 6.21 below, respectively before and after the introduction of patch delamination. The corresponding coefficients of variation for the two cases were found to be 1 and 0.816, respectively. In order to assess the patch effectiveness in current specimen, its $f_{(a/b)}$ functions, which were already developed and shown in Figure 6.79, were again plotted in Figure 6.80 along with the $f_{(a/b)}$ of plain edge cracked steel plate, provided by Tada et al. (2000) and shown in Equation 3.12.

$$f_{(a/b)} = 0.7062 - 2.1777\left(\frac{a}{b}\right) + 4.5671\left(\frac{a}{b}\right)^2 - 4.0097\left(\frac{a}{b}\right)^3 \quad \text{Eq. 6.20}$$

$$f_{(a/b)} = 0.6377 - 1.5199\left(\frac{a}{b}\right) + 3.1497\left(\frac{a}{b}\right)^2 \quad \text{Eq. 6.21}$$

Fatigue life and a-N curves of specimen 6-SKWRP-Sk300 were evaluated following the methodology of section 6.3, and the resulting a-N curve is shown in Figure 6.81. The a-N curve of the tested specimen, obtained during the test, is also shown in the Figure 6.81. Fatigue life of this specimen was then evaluated using the $f_{(a/b)}$ functions of Equations 6.20 and 6.21 and following the methodology of section 6.3. The resulting predicted fatigue life of this specimen was found to be 10,22,684 and 4,95,187, respectively before and after the introduction of patch delamination in the analysis. It can be noted from Figure 6.81 that it shows two a-N curves of tested specimen. It was because of having two specimens tested for this CFRP patch, as already discussed in section 5.4.2.3. Fatigue life of the two tested specimens of 6-SKWRP-S300 were 4,23,156 and 4,50,559, respectively. The test to predicted ratio for this specimen was evaluated to be 0.91 if using the predicted fatigue life with consideration of patch delamination. If patch delamination not considered in the FEA then the predicted fatigue life will be 10,22,684, and the corresponding test to predict ratio becomes 0.44, which shows great impact of patch delamination, on the predicted fatigue life.

Last part of analysis performed for this specimen was the re-evaluation of its predicted fatigue life with consideration of small delamination in the FEA of crack lengths 0.1 and 0.2, which was not considered in the above completed phase because of being found converged in their first analysis cycles. Finite element analysis of models of crack lengths 0.1 and 0.2 was then repeated with the introduction of adhesive failure in their interface adhesive layers as shown in the Figure 6.74. After re-analysis of the models of crack lengths 0.1 and 0.2, the geometric factors $f_{(a/b)}$ were re-evaluated using the revised K_I values. The resulted $f_{(a/b)}$ distribution is shown in Figure 6.82. It can be noted in Figure 6.82 that the $f_{(a/b)}$ values of crack lengths 0.3 and 0.4 were same as taken before. It is obvious from Figure 6.82 that due to increased patch delamination in the two crack lengths of 0.1 and 0.2, the $f_{(a/b)}$ values were higher than before and the resulting fatigue life was expected to be shorter. The polynomial function fitted for the revised $f_{(a/b)}$ distribution is shown in Figure 6.82 and it is also reproduced below in Equation 6.22. The corresponding coefficient of variation for the revised $f_{(a/b)}$ function was found to be 0.99.

$$f_{(a/b)} = 0.675 - 1.3501\left(\frac{a}{b}\right) + 2.4409\left(\frac{a}{b}\right)^2 \qquad \text{Eq. 6.22}$$

The fatigue life and the a-N curve were re-evaluated for the revised $f_{(a/b)}$ function of Equation 6.22 and the resulting a-N curve is shown in Figure 6.83. This figure also shows the previous a-N curve when no delamination was considered in the two models of crack lengths 0.1 and 0.2. The reduced fatigue life obtained from the increased $f_{(a/b)}$ function was evaluated to be 4,10,453. It was reduced by approximately 17% compared to the previously predicted fatigue life, when the delamination was provided in only two models of crack lengths 0.3 and 0.4. The revised test to predict ratio, corresponding to the reduced fatigue life was evaluated to be 1.09 which was 9% higher from the test but on a conservative side.

6.4.2.6 Specimen 9-SKWRP-Adh-Sikudr300

This specimen was provided with 9 layers of the CFRP Sika Wrap Hex-103C sheets on its each face in the test, which was three times of 3-SKWRP-Sk300 and that was why its ETR was 0.63. Finite element analysis of this specimen was carried out similar to all the previous

specimens provided in this chapter. Similar to the specimen 6-SKWRP-Sk300 and using the conclusions of section 3.5.4, the FEM of the specimen 9-SKWRP-Sk300 was defined with three equivalent CFRP layers instead of actual nine layers, in order to reduce the file size and the run-time. The CFRP thickness (t_{FRP}) and modulus (E_{FRP}) of the three equivalent CFRP layers were provided to be 1.6 mm and 124 GPa, so that its final patch ETR became 0.63.

Five FEMs, corresponding to the crack lengths of 0.1, 0.2, 0.3, 0.35 and 0.4, were developed for this specimen, instead of four used in all previous specimens, to improve the accuracy of polynomial curve fitting for the geometric factor $f_{(a/b)}$.

After the first cycles of analysis in its five crack-length models, the resulting shear stress distributions in interface adhesive layers were studied and these are shown in Figures 6.84 through 6.88. Using the shear strength of adhesive from Table 6.2, the extent of adhesive failure was determined in each adhesive layer of Figures 6.84 through 6.88. The resulting failed adhesive regions are shown in Figure 6.89. Analysis of these failed adhesive regions for the convergence criteria of section 6.2 showed that the adhesive failure in the crack lengths of 0.1, 0.2 and 0.3 have already fulfilled the convergence criteria. Failed adhesive regions of crack lengths 0.35 and 0.4 were found to be exceeding the convergence criteria, and thus required the adhesive failure analysis in their FEA. Adhesive failure analysis was then performed in the models of crack length 0.35 and 0.4 and these models were successively re-analyzed after progressive removal of the failed adhesive region until the convergence achieved. Figures 6.90 and 6.91 show the reduced adhesive layers of crack lengths 0.35 and 0.4, after achieving the convergence and these are also shown in their respective finite element models in Figures 6.92 and 6.93.

Comparing the failed adhesive regions of Figures 6.89, 6.90 and 6.91 with the failed adhesive regions of 6-SKWRP-Sk300 and other specimens, it can be seen that least patch delaminated regions (or failed adhesive regions) were found in the current specimen. It was mainly because of the highest patch ETR and high adhesive shear strength used in this specimen.

The $\Delta K/\Delta\sigma$ and $f_{(a/b)}$ distributions, developed from the resulting SIF (K_I) values from the FEA, are shown in Figures 6.94 and 6.95, respectively. It can be seen in Figures 6.94 and 6.95 that the resulting $\Delta K/\Delta\sigma$ and $f_{(a/b)}$ values were enhanced by 12% and 25%, respectively for the crack lengths of 0.35 and 0.4, due to the impact of patch delamination in the models. Comparing Figures 6.94 and 6.95 with 6.78 and 6.79, it can be concluded that little lesser

impact of patch delamination on $\Delta K/\Delta\sigma$ and $f_{(a/b)}$ values was existed in the current specimen compared to the 6-SKWRP-Sk300, because of highest patch ETR.

The polynomial functions fitted to the $f_{(a/b)}$ distributions of Figure 6.95 are also shown in the same figure. These polynomial functions are again reproduced in Equations 6.23 and 6.24 below, respectively for the cases of before and after the patch delamination. The coefficients of variation for the two cases were found to be 1 and 0.994, respectively. In order to assess the patch effectiveness in current specimen, its f(a/b) functions, which were already developed and shown in Figure 6.95, were again plotted in Figure 6.96, along with the f(a/b) of plain edge cracked steel plate, provided by Tada et al. (2000) and shown in Equation 3.12.

$$f_{(a/b)} = 0.5664 - 1.2546\left(\frac{a}{b}\right) + 1.2436\left(\frac{a}{b}\right)^2 \quad \text{Eq. 6.23}$$

$$f_{(a/b)} = 0.6151 - 1.8741\left(\frac{a}{b}\right) - 2.8814\left(\frac{a}{b}\right)^2 \quad \text{Eq. 6.24}$$

Fatigue life and a-N curves of specimen 9-SKWRP-Sk300 were evaluated, following the methodology of section 6.3 and using the $f_{(a/b)}$ functions of Equations 6.23 and 6.24. The resulting predicted a-N curve of this specimen is shown in Figure 6.97, along with the a-N curve of the specimen obtained in the test. It can be noted from Figure 6.97 that it shows two a-N curves of tested specimen. It was because of having two specimens were tested for this CFRP patch, as already discussed in section 5.5.2.1. Fatigue life of specimen 9-SKWRP-Skr300 was evaluated through the numerically developed $f_{(a/b)}$ distribution equations 6.23 and 6.24 and the procedure of section 6.3 were found to be 19,20,784 and 12,08,405, respectively before and after the induction of patch delamination in the analysis. This specimen had actually taken 11,54,118 fatigue cycles before its complete failure during the test, as mentioned in chapter 5. Therefore, test to predicted ratio for this specimen was evaluated to be 0.96, if using the predicted fatigue life with consideration of patch delamination. If the impact of adhesive failure or the corresponding patch delamination is not considered in the FEA then the predicted fatigue life would be 19,20,784 and the respective test to predict ratio becomes 0.60, which shows great impact of the inclusion of patch delamination in the analysis tool on the resulting fatigue life.

The last phase of analysis performed for the current specimen was the re-evaluation of its predicted fatigue life with consideration of small delamination impact in the FEA of crack lengths 0.1, 0.2 and 0.3. It was not considered in the above completed phase because of being found converged in their first analysis cycles. Finite element analyses of models of crack lengths 0.1, 0.2 and 0.3 was then repeated with the introduction of patch delamination by removing the failed regions of their interface adhesive layers, as already shown in Figure 6.89. After re-analysis of the models of crack lengths 0.1, 0.2 and 0.3, the process of evaluation of $f_{(a/b)}$ values, using the revised K_I values, was repeated and the resulted revised $f_{(a/b)}$ distribution is shown in Figure 6.98. The revised polynomial function, shown in Figure 6.89, is also shown below in Equation 6.25.

$$f_{(a/b)} = 0.6079 - 1.6291\left(\frac{a}{b}\right) - 2.2981\left(\frac{a}{b}\right)^2 \qquad \text{Eq. 6.25}$$

Coefficient of variation for the revised f(a/b) polynomial function was evaluated to be 0.999. Fatigue life and the a-N curve were re-evaluated for the revised $f_{(a/b)}$ distribution of Equation 6.25, and the resulting a-N curve is shown in Figure 6.99. This figure also shows the previously obtained a-N curve of the same specimen but with no delamination iin the three models of crack lengths 0.1, 0.2 and 0.3. As expected from the increased $f_{(a/b)}$ distribution, the reduced fatigue life thus obtained was 11,39,928, which was approximately reduced by 6 %, compared to the previously predicted fatigue life, with delamination provided in only two crack lengths of 0.35 and 0.4. The revised test to predict ratio for the revised and reduced predicted fatigue life of 11,39,928 was found to be 1.02. Very small patch delamination in the three crack length models of crack lengths 0.1, 0.2 and 0.3 of this specimen resulted in only 6 % further reduction in the fatigue life, compared to case when patch delamination was not provided in these crack lengths. Lesser patch delamination in all the crack length models of this specimen was mainly because of high shear strength of its adhesive as well as high patch ETR.

6.4.3 Fatigue life prediction of specimens failed by the patch-end delamination failure mode

As already mentioned in sections 6.2 and 6.4 that the detailed finite element analysis of the specimens failed in the governing patch-end delamination mode or in premature failure mode (due to fabrication errors) was not carried out separately because of different failure mode and inapplicability of the current methodology on those modes. Therefore, their predictive fatigue life was taken from other specimen having identical patch ETR and failed under the near-crack patch delamination failure mode. Table 6.1 shows that nearly all the specimens fabricated with the higher E_{FRP} CFRP were failed by the governing patch-end delamination mode except the two in the ETR group of 0.21.

There were two specimens of ETR 0.21 group, failed prematurely; 1-CBDR-Sk-300 and 1-CBDR-Sk-330. The specimen 1-CBDR-Sk-300 was failed due to improper CFRP bonding while the specimen 1-CBDR-Sk-330 was failed due to an accidental overload. The accidental overload occurred even before the start of the beach mark cycles and therefore its complete a-N curve was also not available. Fatigue life prediction for specimen 1-CBDR-Sk-300 could be taken from the specimen 3-SKWRP-Sk-300 because of having identical ETR and adhesive. Similarly, the fatigue life prediction for specimen 1-CBDR-Sk-330 could be taken from the specimen 3-SKWRP-Sk-330 because of having identical ETR and adhesive.

In the ETR 0.42 group two specimens with higher E_{FRP} CFRP were failed by the governing patch-end delamination failure mode; 2-CBDR-Sk-30 and 1-CBDR-3-SKWRP (hybrid patch). Their predicted fatigue life could be taken from the specimen 6-SKWRP-Sk-300, which although had different adhesive but it was the only one specimen in this ETR group which had failed in the near-crack patch delamination mode. Similarly, in ETR 0.63 group, the two specimens with higher E_{FRP} CFRP were failed by the governing patch-end failure mode; 3-CBDR-Sk-30 and; 1-CBDR-6-SKWRP. The predicted fatigue life for these specimens could be taken from the specimen 9-SKWRP-Sk300, which although had different adhesive but it was the only one specimen in this ETR group failed in the near-crack delamination mode.

Figure 6.100 shows the a-N curves of the tested specimens of the ETR 0.42 group failed in the patch-end delamination mode, along with their adopted predicted a-N curve of 6-SKWRP-Adh-Sikudr300. It can be seen from the Figure 6.100 that the impact of patch-end delamination was more highlighted in the specimen 2-CBDR-Adh-Sikadur-30 than 1-CBDR-

3-SKWRP. Comparatively better behaviour of the hybrid-patch specimen 1-CBDR-3-SKWRP was because of its lesser thickness than the specimen 2-CBDR-Adh-Sikadur-30. Figure 6.100 also shows that the fatigue life of specimens 2-CBDR-Adh-Sikadur-30 and 1-CBDR-3-SKWRP were respectively reduced by 8 and 3 times from their predicted fatigue life due to the governing patch end delamination failure mode.

Figure 6.101 shows the a-N curves of the specimens of ETR 0.63 group, failed in the patch-end delamination mode, along with the a-N curve of their adopted predictive specimen 9-SKWRP-Sk-300. It is obvious from Figure 6.101 that the patch-end delamination had greatly affect the fatigue life of these specimen, even more than any previous specimen failed in this failure mode. It can also be seen from Figure 6.101 that the fatigue life of specimens 3-CBDR-Sk-30 and 1-CBDR-6-SKWRP were reduced by 18 and 10 times, respectively, from the predicted. It shows that the impact of patch-end delamination was more highlighted in the specimen 3-CBDR-Sk-30 than 1-CBDR-6-SKWRP, which was most likely because of more patch thickness in it.

6.5 Summary and conclusions

In this chapter, finite element analyses of the tested specimens of current research work were performed to develop their predictive fatigue life models. Finite element models of the tested specimens were developed following the procedure already presented in detail in chapter 3 using ABAQUS finite element code, version 6.10. Patch delamination due to adhesive shear failure around the crack was introduced in the finite element analyses through progressive removal of the failed adhesive regions. It was carried out following the procedure already presented in chapter 4 and using the failure convergence criterion of section 4.2. These procedures and failure criteria were also summarized in sections 6.3 and 6.4 of this chapter. Four to five FEM of each specimen were developed with increasing crack length. In nearly all FEA, the failed adhesive regions in smaller crack lengths were found smaller than the adhesive removal criteria and therefore these were not removed and the corresponding crack lengths models were considered to be converged, as a first case.

SIF (K_I) was studied from the results of FEA, both before and after the introduction of patch delamination, in FEA of all crack length models of each specimen. The geometric factors $f_{(a/b)}$ were then developed for each crack length by non-dimensionalizing the ΔK_I, obtained from

FEA, with the applied stress range ($\Delta\sigma$) and the crack length (a). Continuous functions of the geometric factors $f_{(a/b)}$ for each specimen were then developed by fitting polynomial functions on the resulting geometric factors $f_{(a/b)}$ distributions, obtained from all crack length models. Fatigue life (N) of each tested specimen was then predicted using the developed geometric factors $f_{(a/b)}$ functions and the procedure of section 6.3, both before and after the patch delamination. Fatigue behavior of each specimen was also developed in the form of a-N curves and compared with their test results. It was found that the fatigue life of tested specimens could be closely predicted through the numerically developed geometric factors $f_{(a/b)}$, if near-crack patch delamination was introduced in the FEA. The test to predict ratio for all tested specimen, failed in the near-crack patch delamination failure mode, was ranging between 0.85 and 0.97. If the geometric factors were developed, without considering the near-crack patch delamination in FEA, then the fatigue life (N) of the tested specimens were found to be largely over predicted and the test-to-predicted ratios dropped to the range of 0.24 to 0.60.

Additionally, in a separate analysis phase, just to study the impact of small patch delamination on the resulting geometric factors, adhesive failure was also provided in those smaller crack length models which were not provided with it because of fulfilling the failure criteria in their first analysis cycle. It was found that using the revised geometric factors, the predicted fatigue life further reduced from 6 % to 17 % from the previously predicted because of enhanced $f_{(a/b)}$ functions. But the reduced predicted life can be considered more conservative from practical design point of view. The reduction in fatigue life, caused by induction of smaller near-crack patch delamination in small crack length models, was found more in the specimens having smaller adhesive shear strength because of comparatively larger adhesive failure regions.

Fatigue life of those specimens failed in the governing patch-end delamination mode in their actual tests could not be predicted by using the currently developed methodology because of different failure mode and the insensitivity of SIF (K_I) on the patch-end delamination (concluded in chapter 4). Therefore, considering the patch-end delamination as an undesired failure mode, the predictive fatigue life models of those specimens were not developed. Their fatigue life was then adopted from the specimen having identical patch ETR but failed under the governing near-crack patch delamination failure mode in its actual test. The adopted predictive fatigue life of these specimens was expected not to be much accurate because of

different interface adhesive properties in their adopted models but at least it could provide a 70 % close estimate of their fatigue life because of having identical ETR. It was found that the fatigue life of these specimens was highly over-predicted by the predictive models and it was ranging between 8 to 18 times because of the undesired and fast proceeding end-delamination failure mode.

Finite element models of hybrid-patch specimens were also not developed separately because of being failed in the governing patch-end delamination failure mode in their actual tests. Their predictive models were also adopted from the specimen having identical patch ETR but failed under the governing near-crack patch delamination failure mode in its actual test. Fatigue life of hybrid-patch specimens were also found to be over-predicted by the predictive models and it was ranging between 3 to 10 times because of the undesired governing patch-end delamination failure mode in their actual tests.

Table 6.1 Specimen details used in the experimental program

Specimen Id.	CFRP	CFRP layers each face	Adhesive	ETR	Governing Failure Mode
Plain Steel	—	—		—	Unrepaired specimen
1-CBDR-Sk30	Carbodur	1	Sikadur 30	0.21	Near-crack delamination
1-CBDR-Hf-Sk30	Carbodur	1	Sikadur 30	0.21	Near-crack delamination
1-CBDR-Sk300	Carbodur	1	Sikadur 300	0.21	Improper bond
1-CBDR-Sk330	Carbodur	1	Sikadur 330	0.21	Accidental overload
3-SKWP-Sk-300	Sikawrap Hex	3	Sikadur 300	0.21	Near-crack delamination
3-SKWP-Sk-330	Sikawrap Hex	3	Sikadur 330	0.21	Near-crack delamination
2-CBDR-Sk-30	Carbodur	2	Sikadur 30	0.42	Patch-end delamination
6-SKWP-Sk-300	Sikawrap Hex	6	Sikadur 300	0.42	Near-crack delamination
1-CBDR-3-SKWP	Carbodur + SikaWrap	1 + 3	Sikadur 30 + Sikadur 300	0.42	Patch-end delamination
3-CBDR-Sk-30	Carbodur	3	Sikadur 30	0.63	Patch-end delamination
9-SKWP-Sk300	Sikawrap Hex	9	Sikadur 300	0.63	Near-crack delamination
1-CBDR-6-SKWP	Carbodur + SikaWrap	1 + 6	Sikadur 30 + Sikadur 300	0.63	Patch-end delamination

Table 6.2 Material properties used in the experimental program

Material	Modulus of elasticity 'E' (GPa)	Tensile Strength (MPa)	Shear Strength (MPa)
Steel	200	450	-
Sika Carbodur	165	2400	-
SikaWrap HEX 103C	65	800	-
Sikadur 30	4.5	24	17
Sikadur 300	1.724	55	33**
Sikadur 330	4.5*	35	21**

* Not provided in the supplier's data, obtained from Julia De Castro (2005)
** Not provided in the supplier's data and taken to be 60% of the tensile strength

Table 6.3 Test results of ETR 0.21 group; Fatigue life & repair efficiency

Specimens	Fatigue Life		Repair Effectiveness
	Pre-Crack	Repaired	Test / Control
Control-1	28015	16150	1
Control-2	30700	14330	1
1CBDR-Sk-300	27500	47873	3
1CBDR-Sk-30	29020	171992	11
1CBDR-Hf-Sk-30	28000	150336	9
1CBDR-Sk-330	29050	147530	9*
3SKWRP-Sk300	27800	188375	12
3SKWRP-Sk330	28050	229260	14

* Not failed completely

Table 6.4 Test results of ETR 0.42 group; Fatigue life & repair efficiency

Specimens	Fatigue Life		Repair Effectiveness
	Pre-Crack	Repaired	Test / Control
Control-1	28015	16150	1
Control-2	30700	14330	1
2CBDR-Sk-30	2800	56500	3
1-CBDR+ 3SKWRP	27500	137417	9
6SKWRP-Sk300-A	30051	423156	26
6SKWRP-Sk300-B	27800	450559	28

Table 6.5 Test results of ETR 0.63 group; Fatigue life & repair efficiency

Specimens	Fatigue Life		Repair Effectiveness
	Pre-Crack	Repaired	Test / Control
Control-1	28015	16150	1
Control-2	30700	14330	1
3CBDR-Sk-30	27800	61257	4
1CBDR-Sk30 + 6SKWRP	28050	115393	7
9SKWRP-Sk300-A	2800	181490	11
9SKWRP-Sk300-B	27500	1154118	71

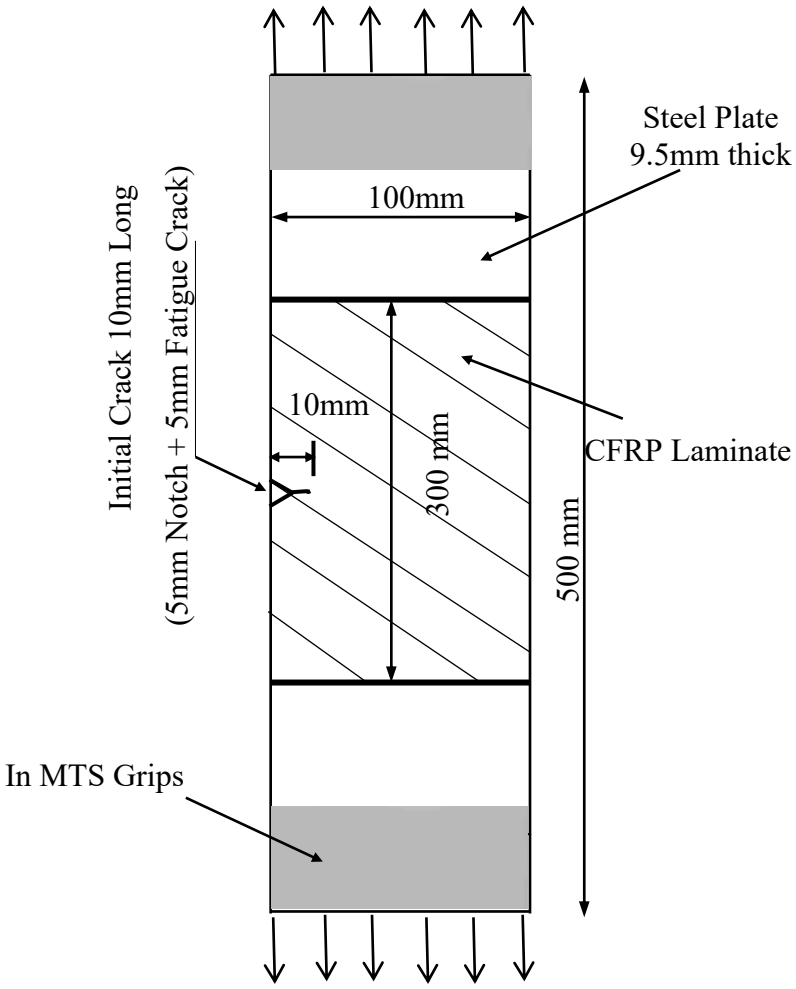

Figure 6.1. Schematic of a typical tested specimen

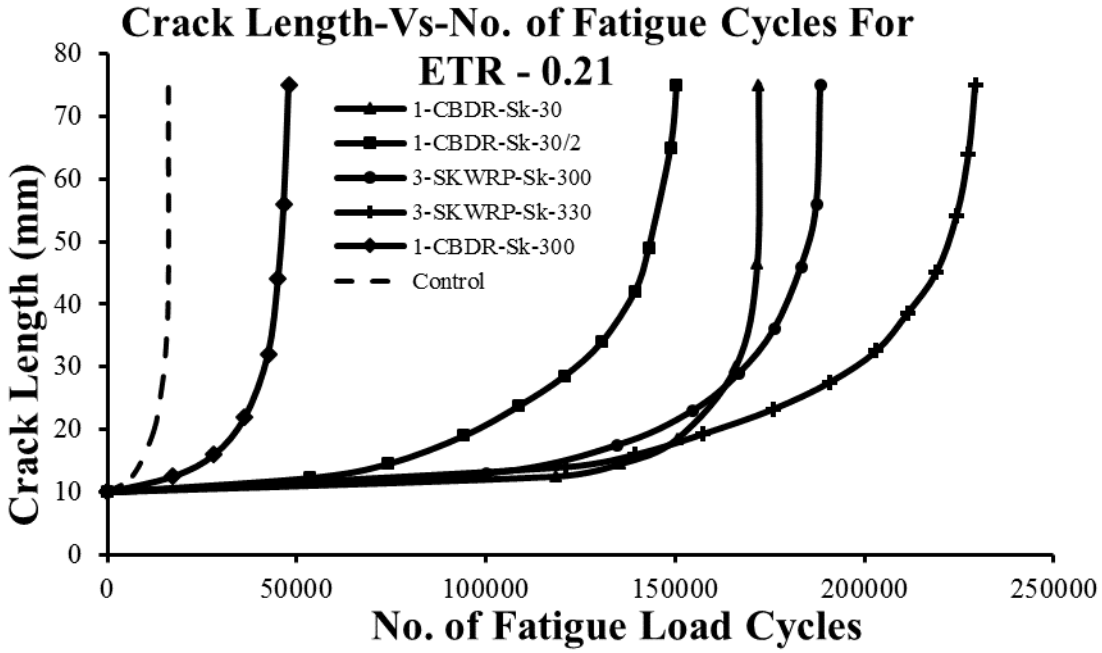

Figure 6.2 Crack-length variation with fatigue cycles (a-N curves) for ETR 0.2 specimens

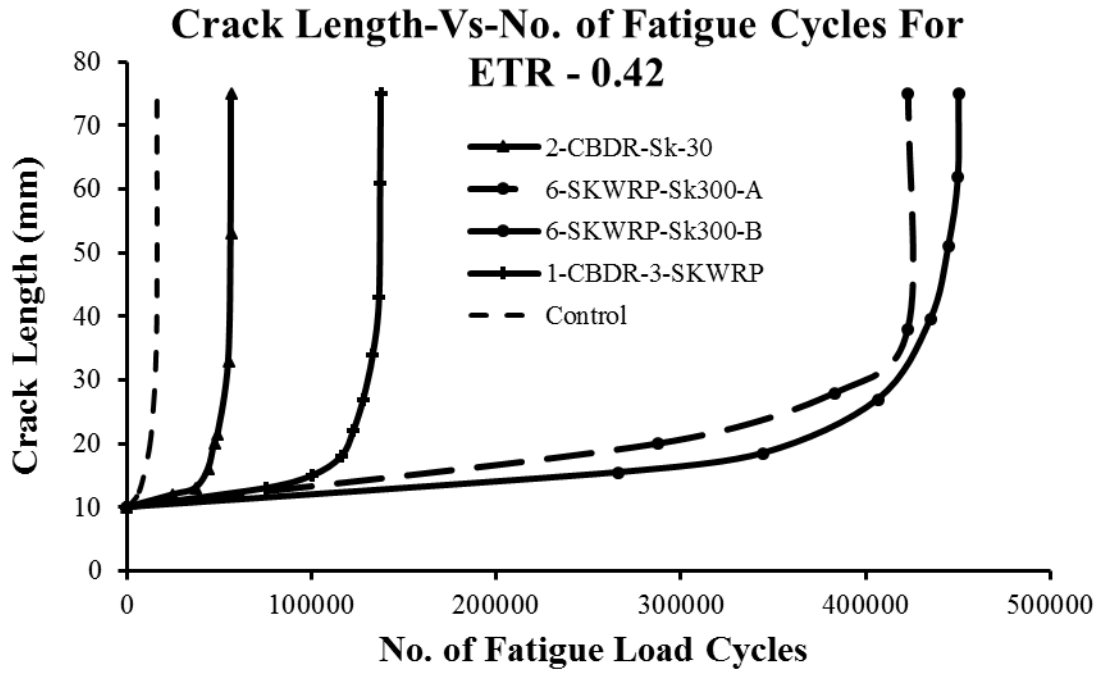

Figure 6.3 Crack-length variation with fatigue cycles (a-N curves) for ETR 0.4 specimens

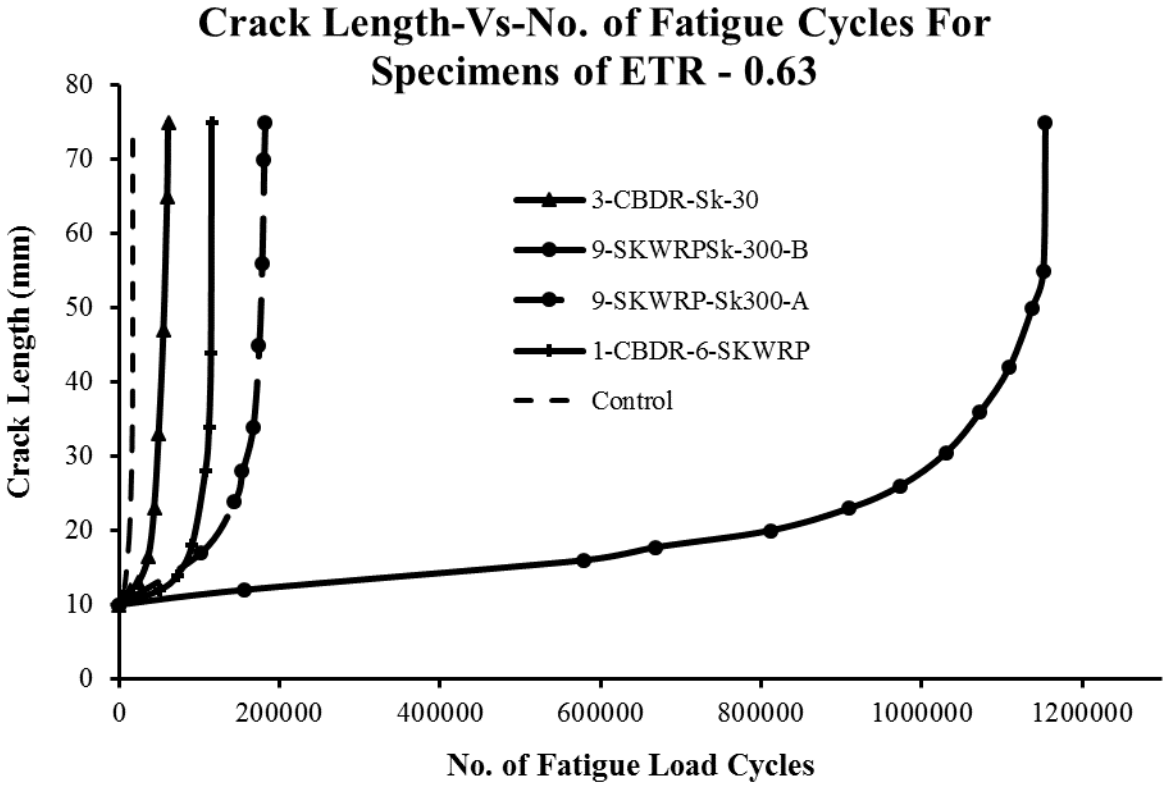

Figure 6.4 Crack-length variation with fatigue cycles (a-N curves) for ETR 0.6 specimens

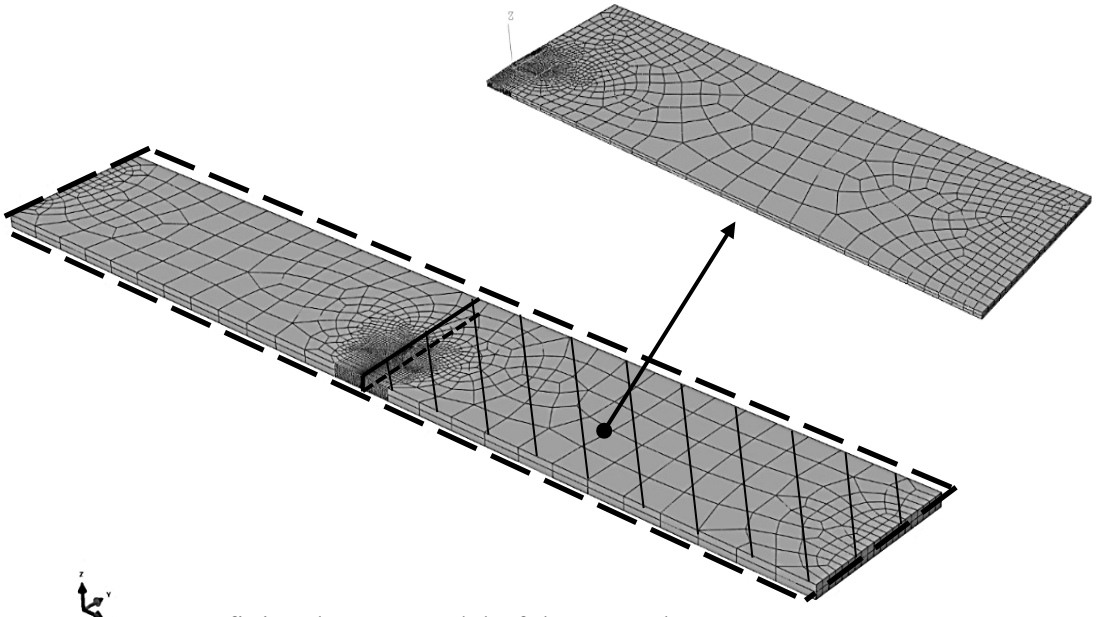

Figure 6.5 One-quarter finite element model of the control specimen and the planes of symmetries

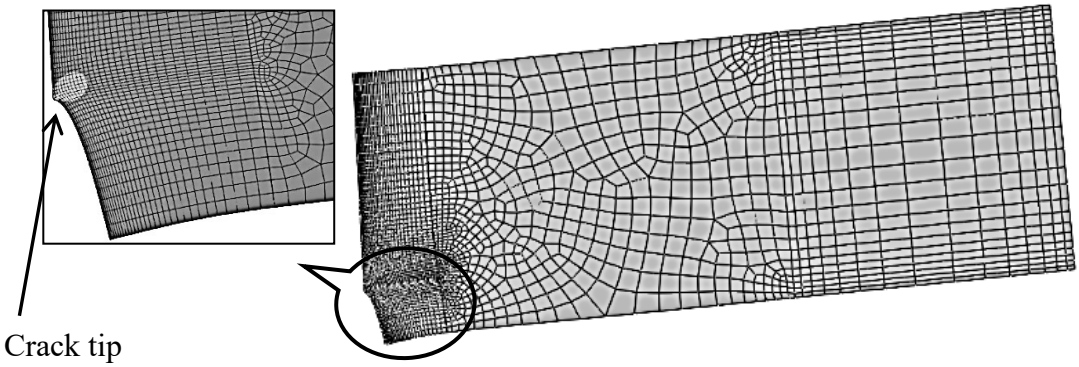

Figure 6.6 Typical deformed geometry of finite element model of control specimen

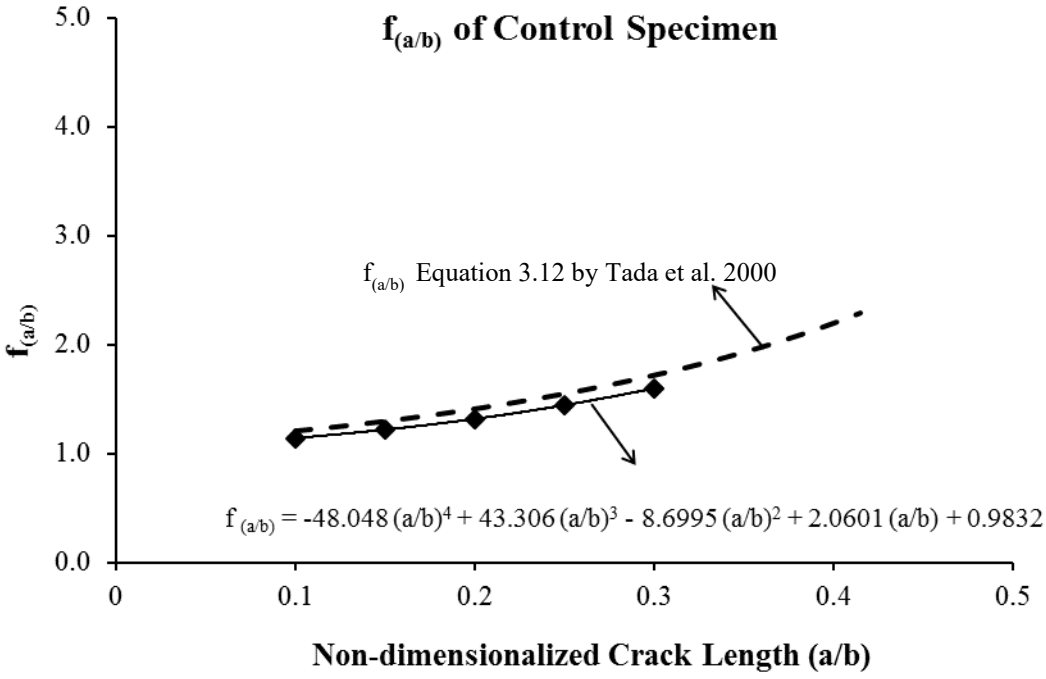

Figure 6.7 Developed geometric factor $f_{(a/b)}$ for control specimen

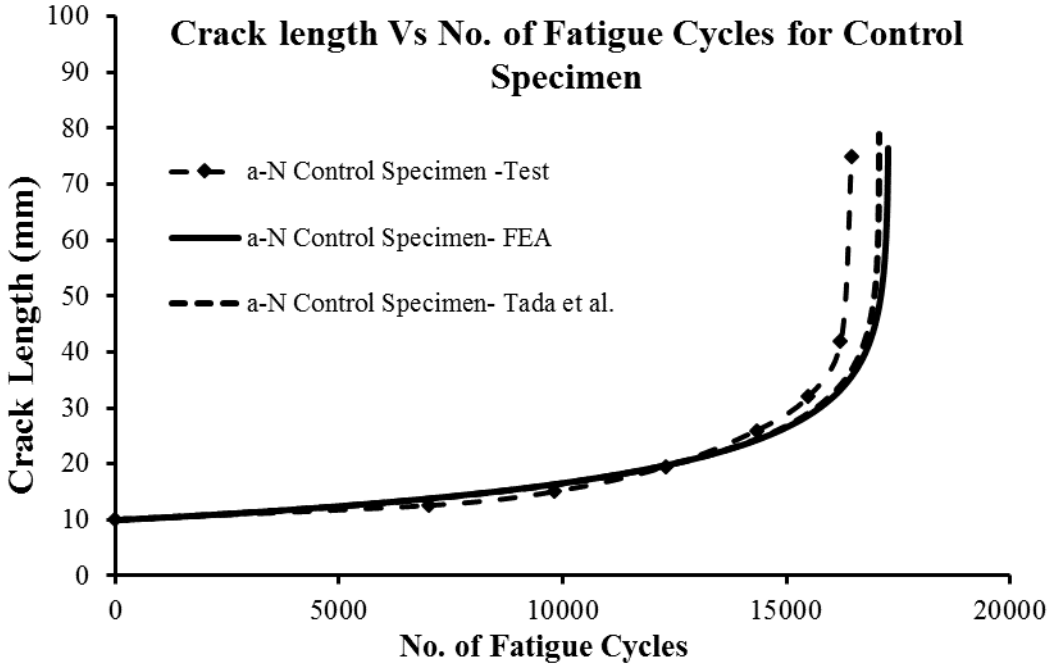

Figure 6.8 Crack length versus number of fatigue cycles for control specimen

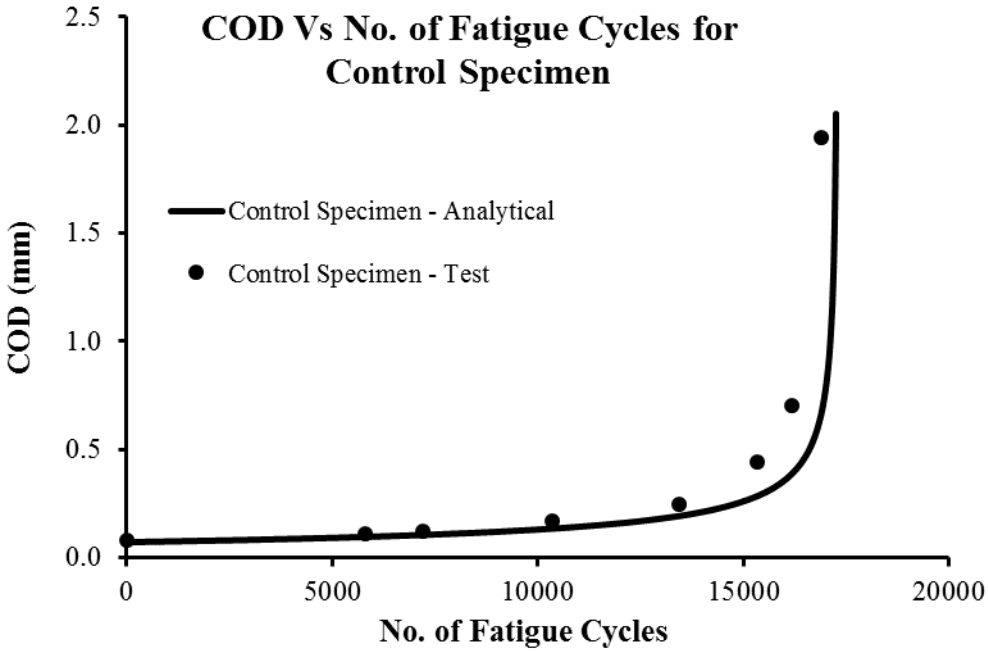

Figure 6.9 COD versus number of fatigue cycles for control specimen

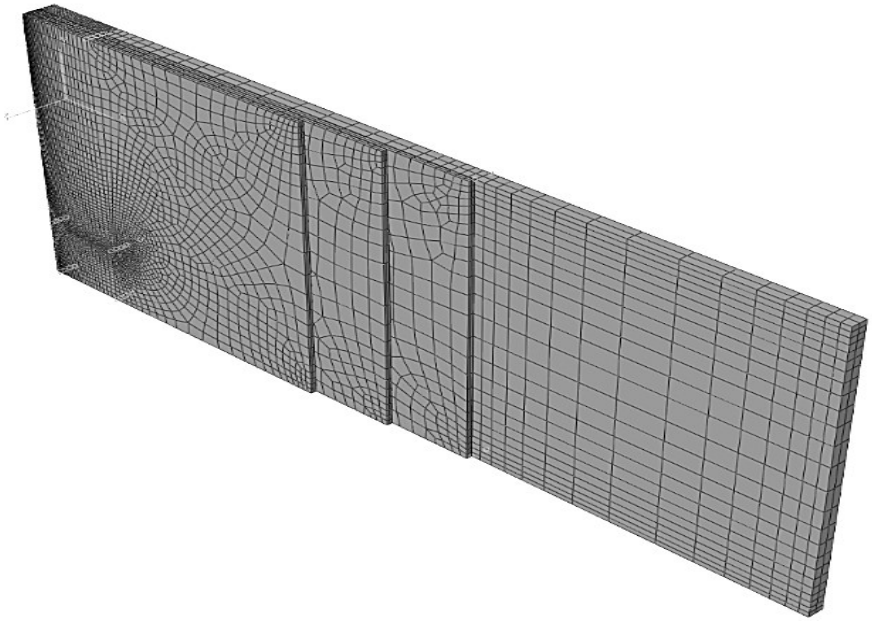

Figure 6.10 Finite element model of 3-SKWRP-Adh-Sikadur-300

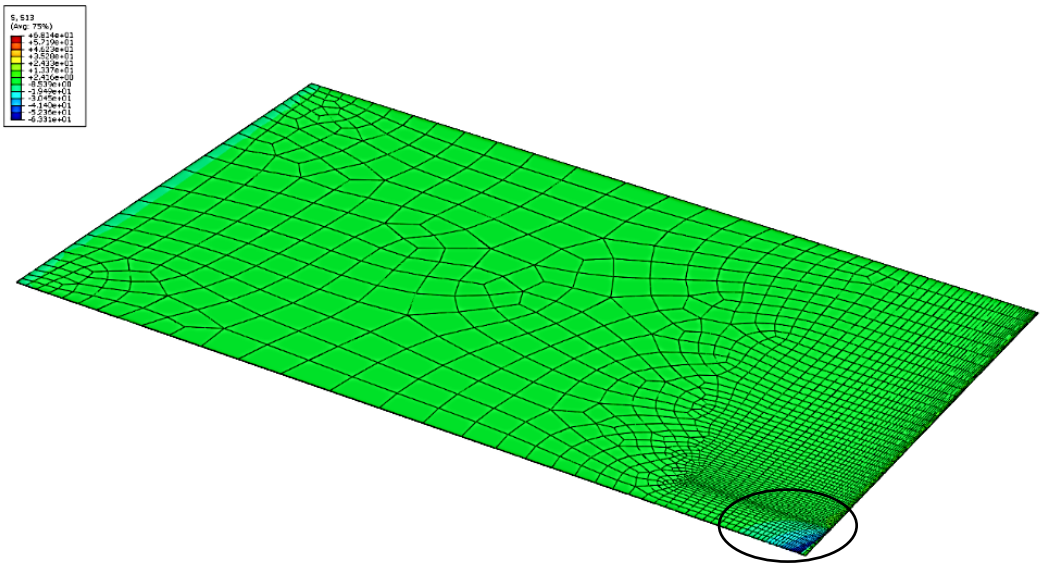

Figure 6.11 Shear stress distribution in interface adhesive layer of FEM of 3-SKWRP-Sk-300 for crack length 0.1 (10mm)

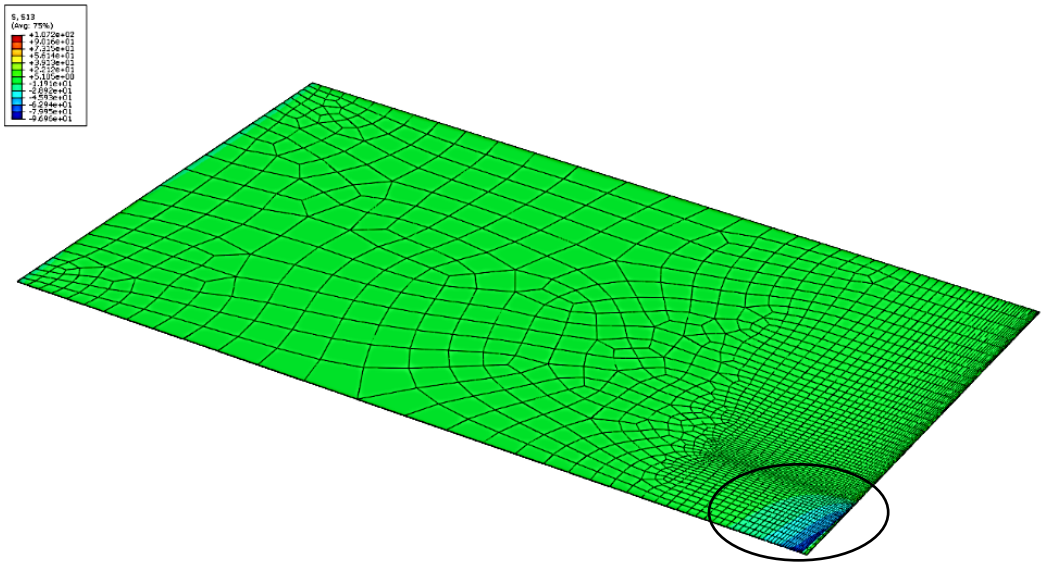

Figure 6.12 Shear stress distribution in interface adhesive layer of FEM of 3-SKWRP-Sk-300 for crack length 0.2 (20mm)

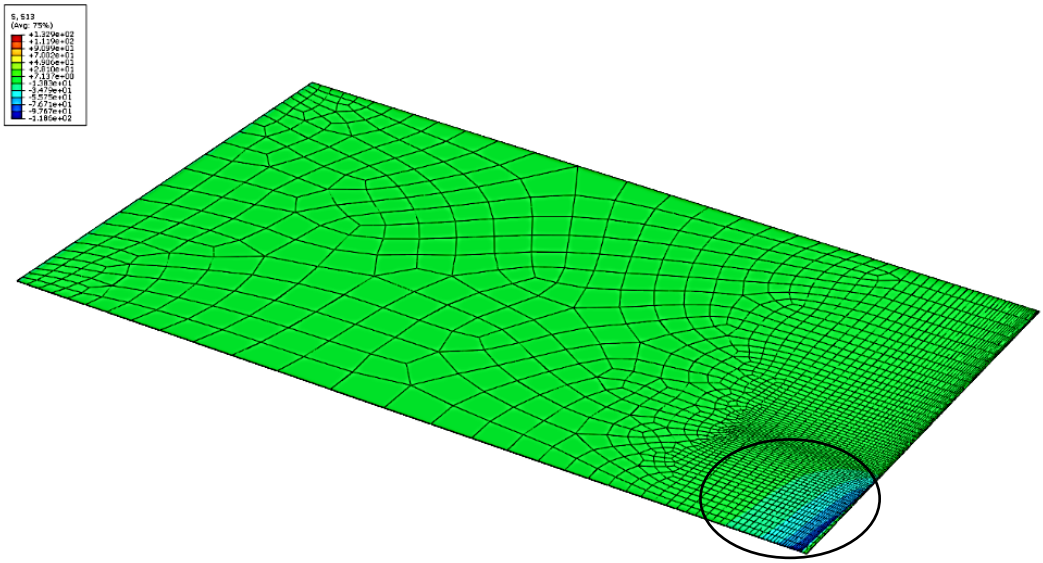

Figure 6.13 Shear stress distribution in interface adhesive layer of FEM of 3-SKWRP-Sk-300 for crack length 0.3 (30mm)

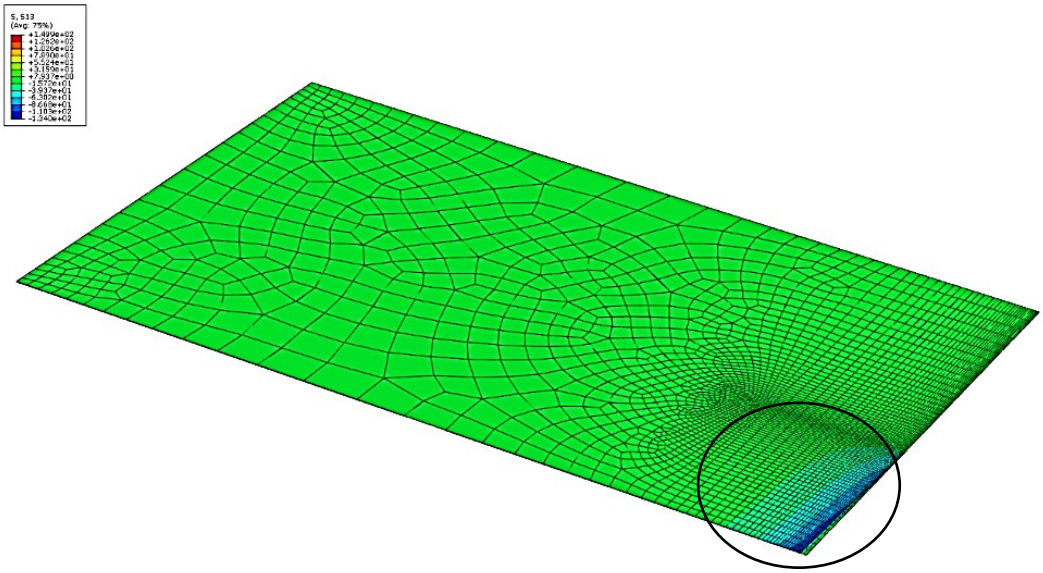

Figure 6.14 Shear stress distribution in interface adhesive layer of FEM of 3-SKWRP-Sk-300 for crack length 0.4 (40mm)

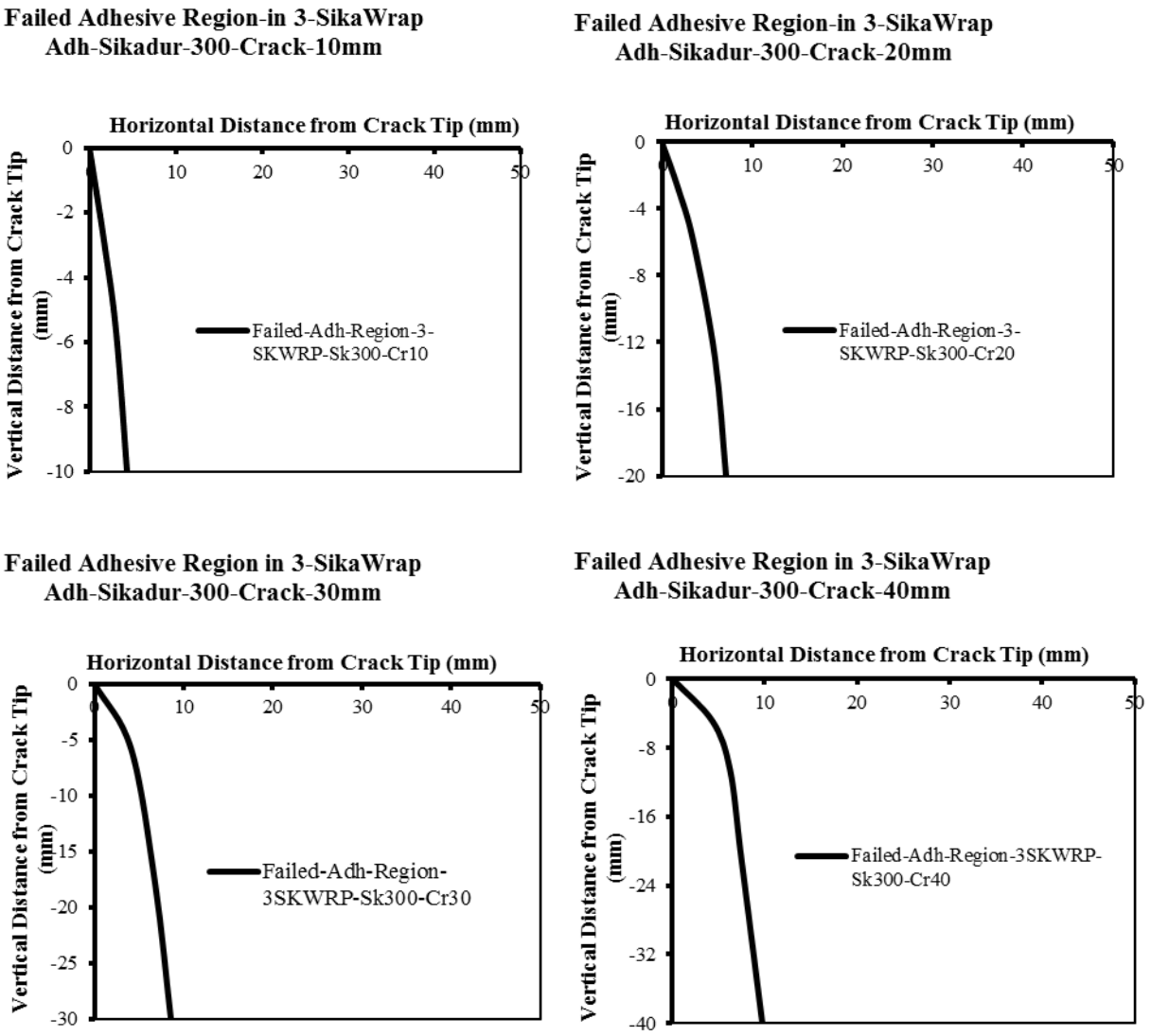

Figure 6.15 Failed adhesive regions in interface adhesive layer of FEM of 3-SKWRP-Sk-300 in its four crack lengths; 0.1, 0.2, 0.3 and 0.4 (10mm, 20mm, 30mm, and 40mm)

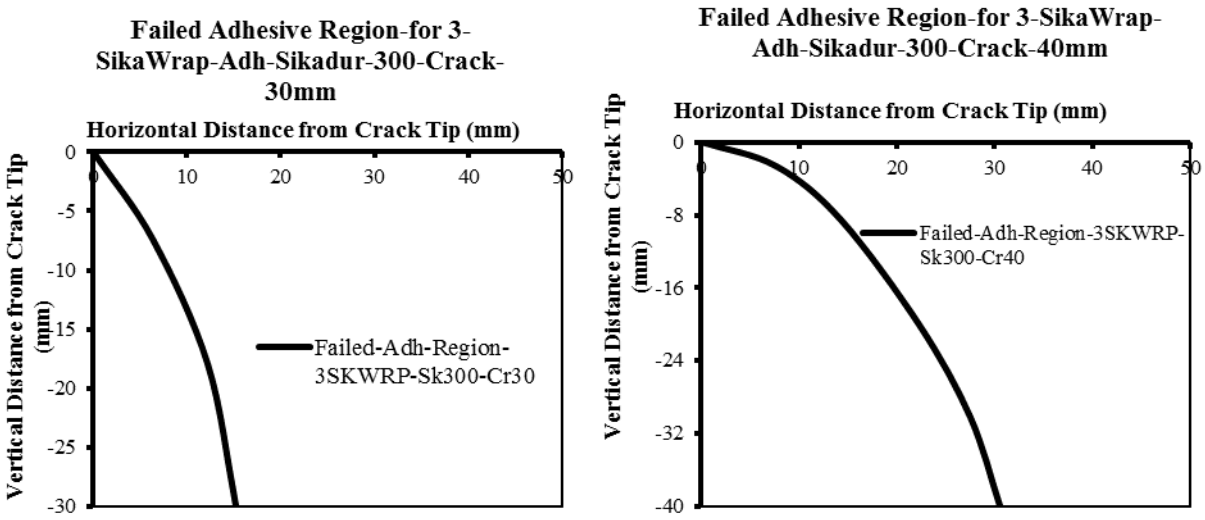

Figure 6.16 Failed adhesive regions in interface adhesive layer of FEM of 3-SKWRP-Sk-300 in crack lengths of 0.3 and 0.4 (30mm and 40mm) after Convergence

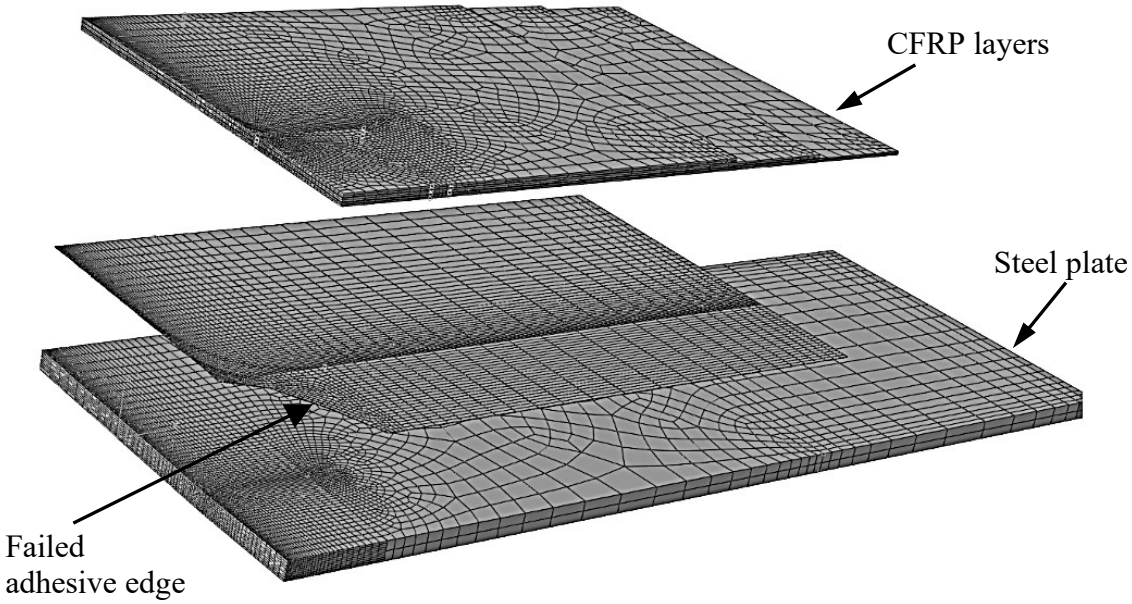

Figure 6.17 Interface adhesive layer with failed region removed in the FEM of 3-SKWRP-Sk-300.in crack length 30mm (0.3) after convergence

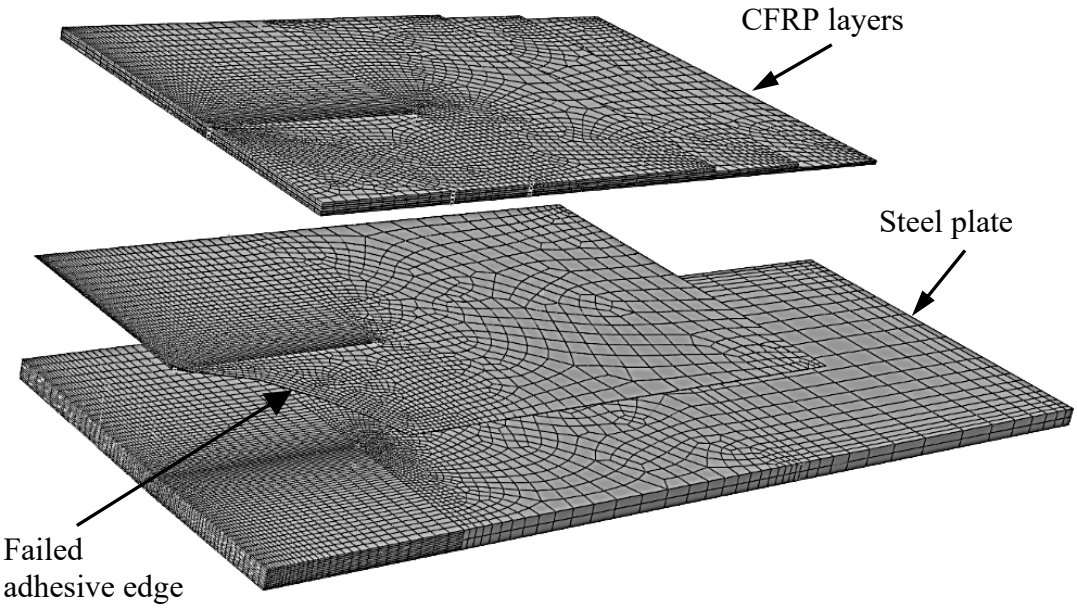

Figure 6.18 Interface adhesive layer with failed region removed in the FEM of 3-SKWRP-Sk-300.in crack length 40mm (0.4) after convergence

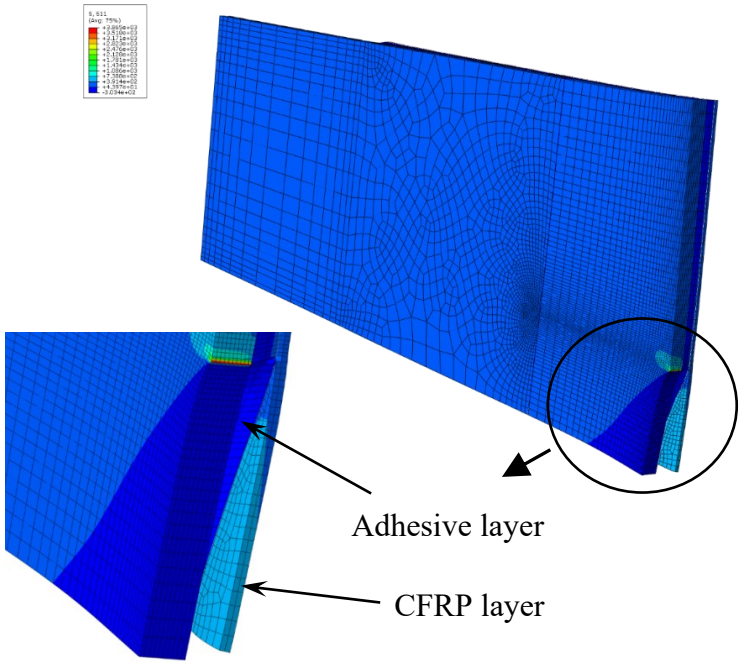

Figure 6.19 Deformed geometry of FEM of crack length (0.4) 40mm of 1-CBDR-Adh-Sk-30 with converged failed interface adhesive layer

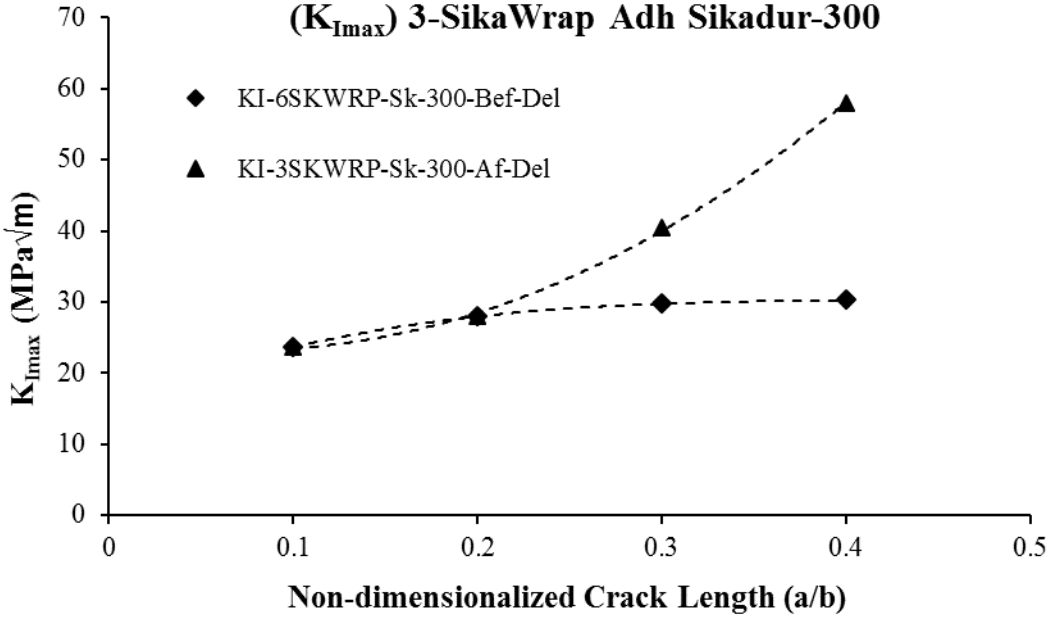

Figure 6.20 K_{Imax} variation with non-dimensionalized crack length obtained from FEA of 3-SKWRP-Sk-300

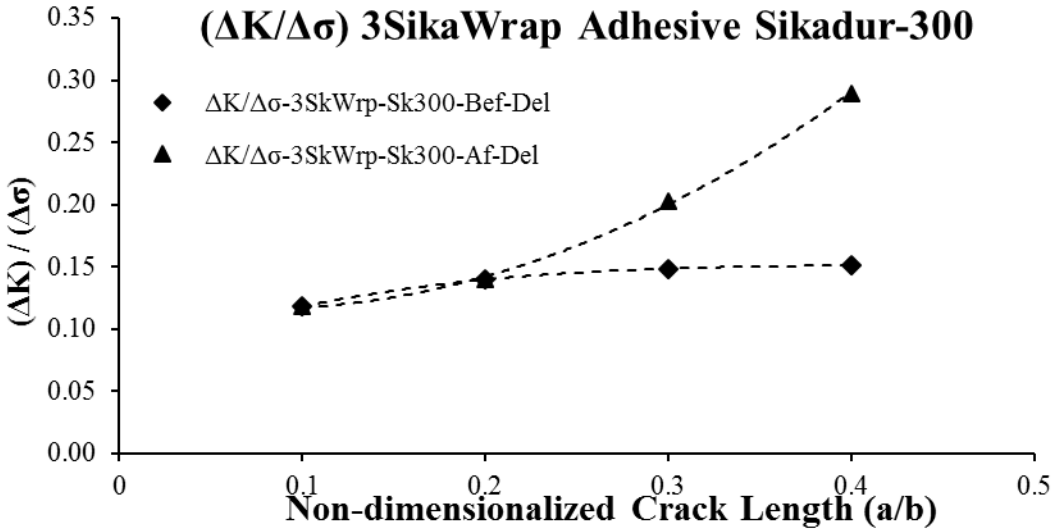

Figure 6.21 ΔK/Δσ variation with non-dimensionalized crack length obtained from FEA of 3-SKWRP-Sk-300

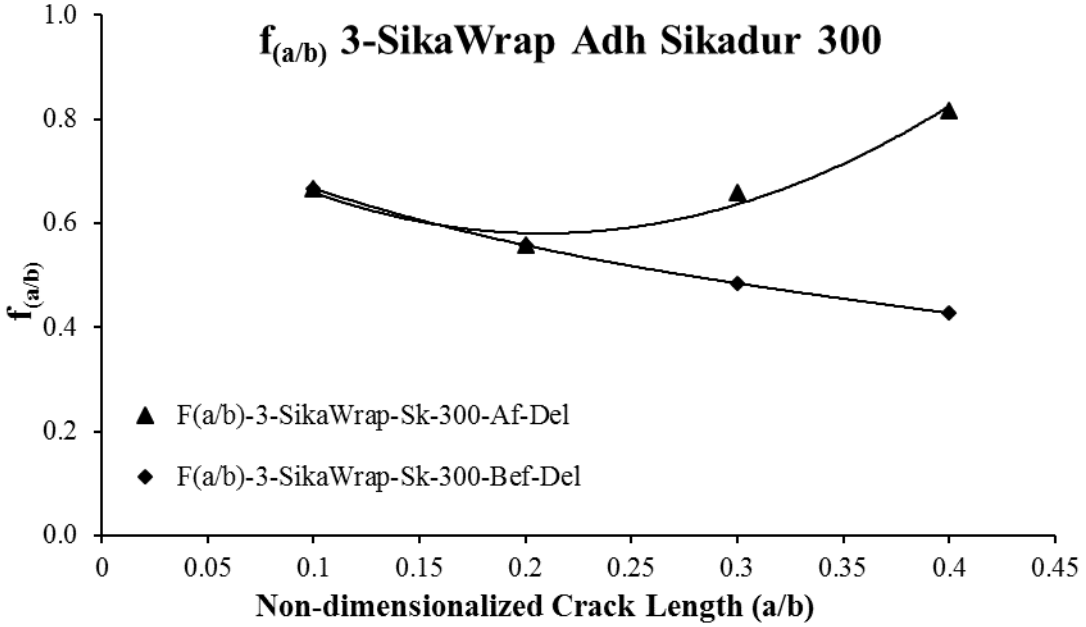

Figure 6.22 Geometric factor $f_{(a/b)}$ variation with non-dimensionalized crack length developed from SIF results of 3-SKWRP-Sk-300

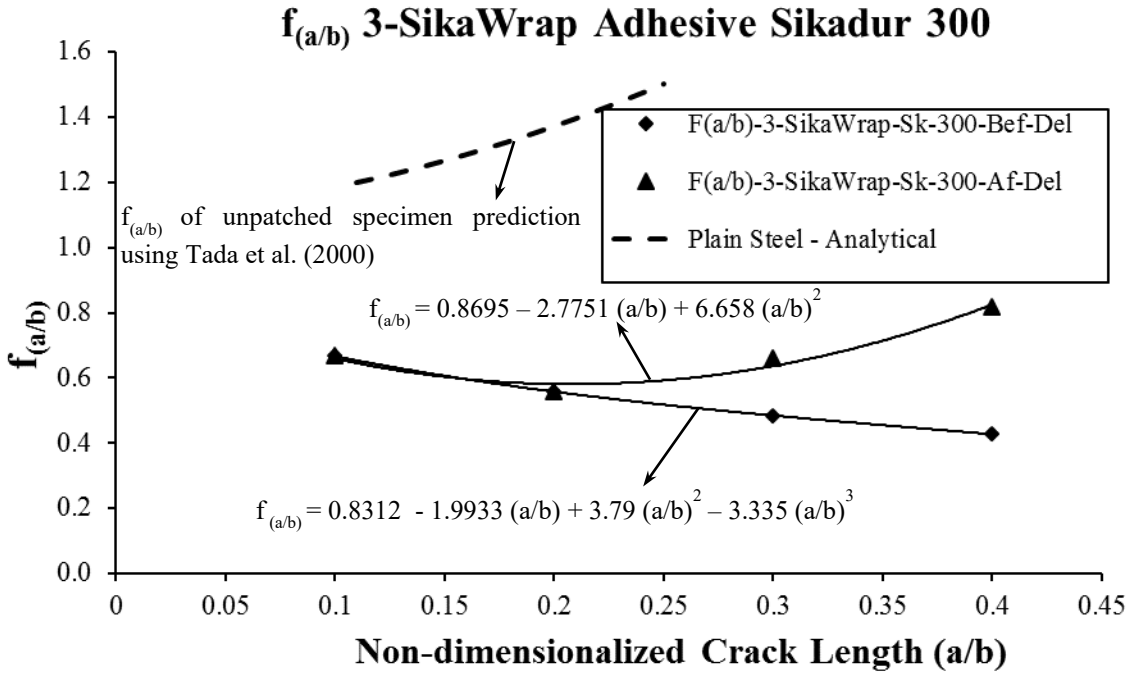

Figure 6.23 Geometric factor $f_{(a/b)}$ variation with non-dimensionalized crack length developed from SIF results of 3-SKWRP-Sk-300 including plain specimen

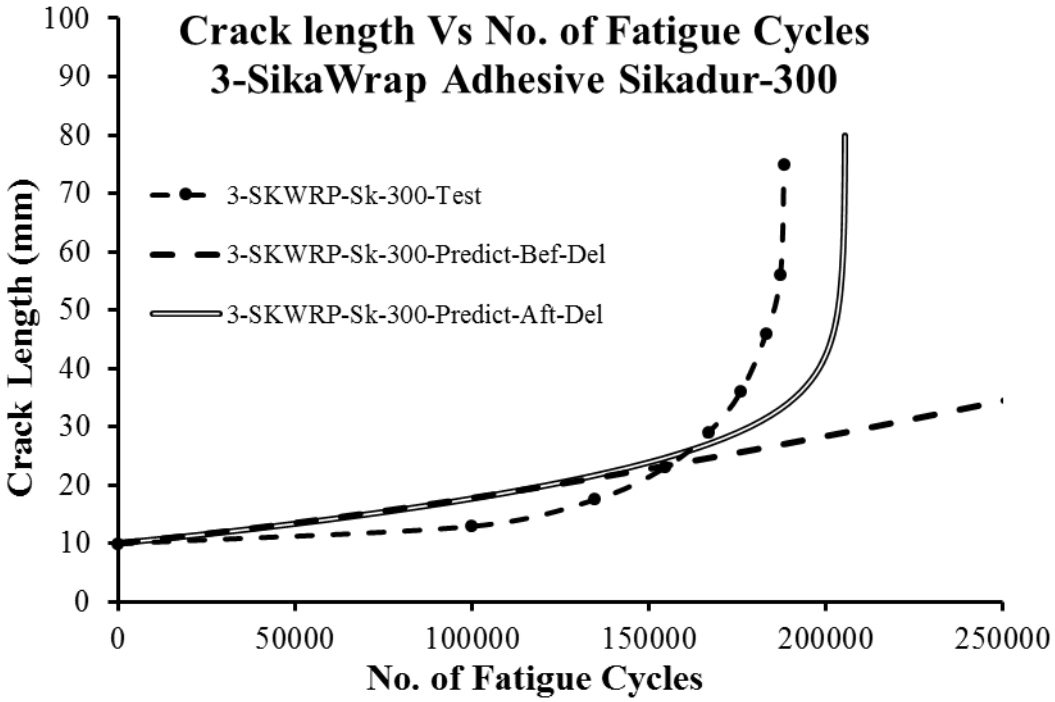

Figure 6.24 Predicted crack length versus number of fatigue cycles for 3-SKWRP-Sk-300

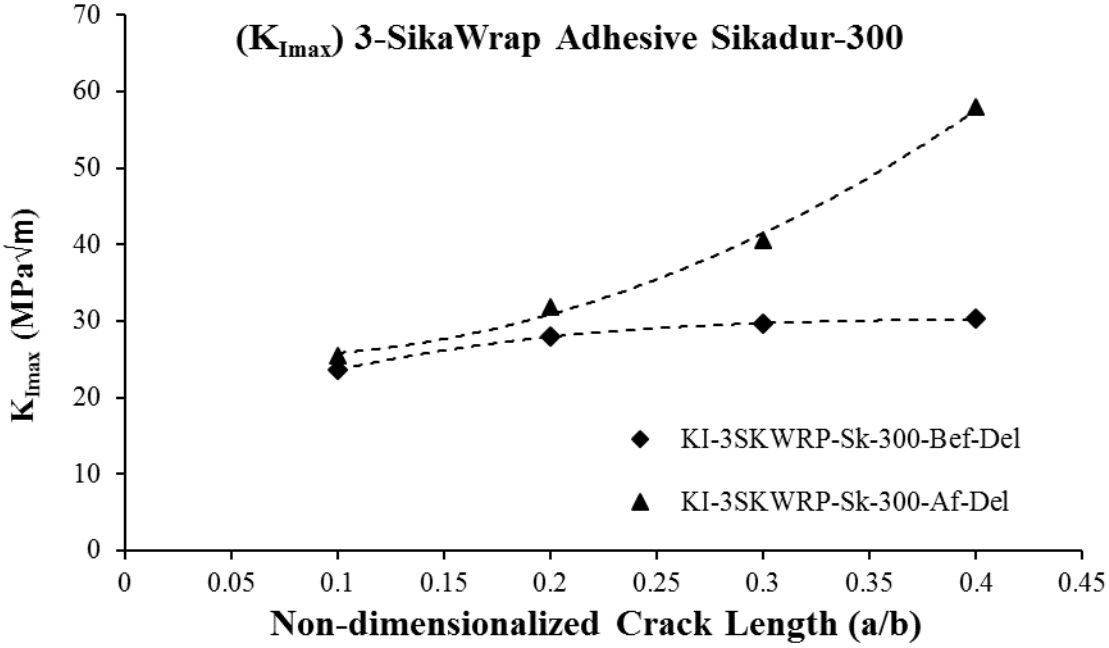

Figure 6.25 K_{Imax} variation with non-dimensionalized crack length developed from SIF results of 3-SKWRP-Sk-300 with the provided delamination case

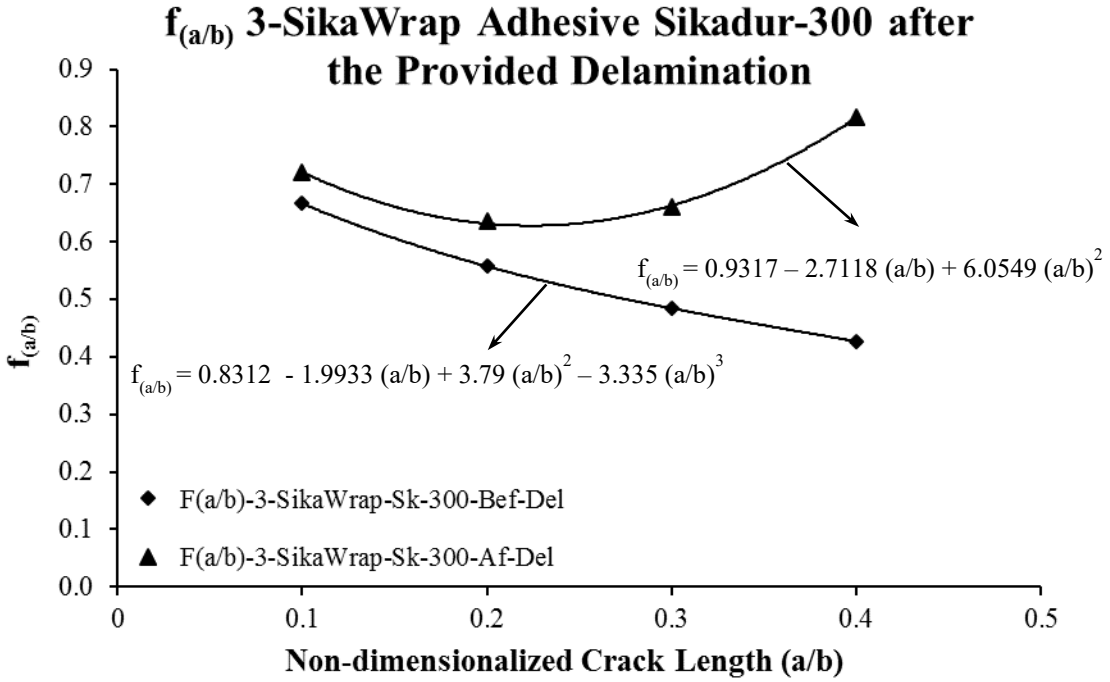

Figure 6.26 $f_{(a/b)}$ variation with non-dimensionalized crack length developed from SIF results of 3-SKWRP-Sk-300 with the provided delamination case

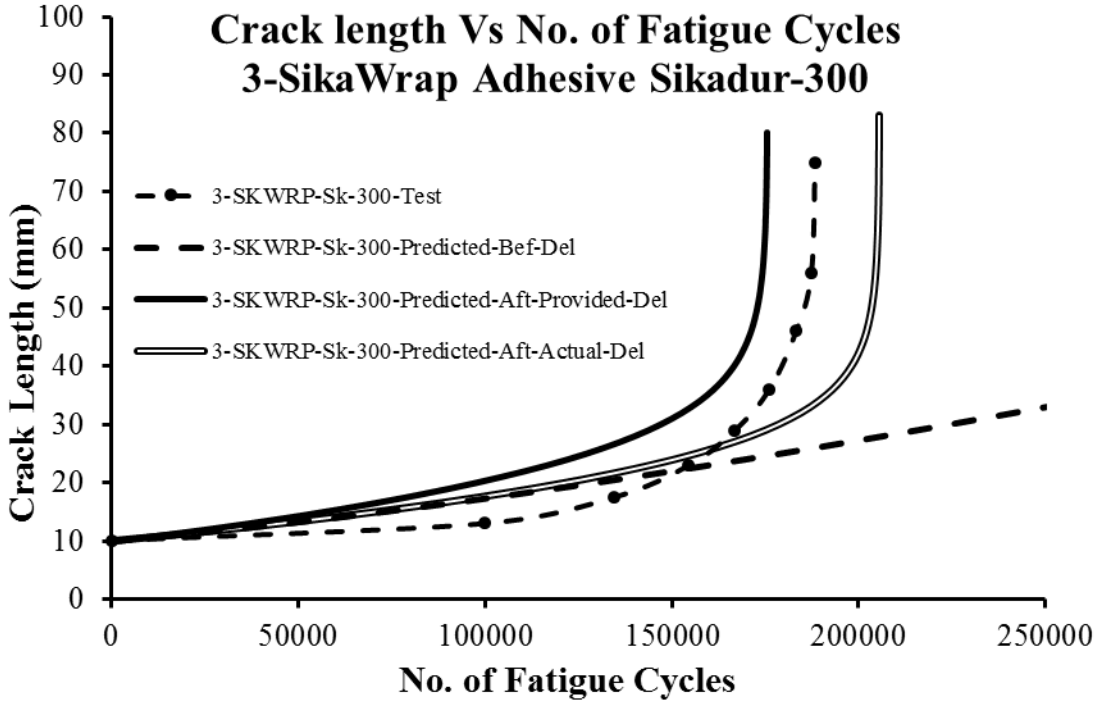

Figure 6.27 Predicted crack length versus number of fatigue cycles for 3-SKWRP-Sk-300 including the provided delamination case

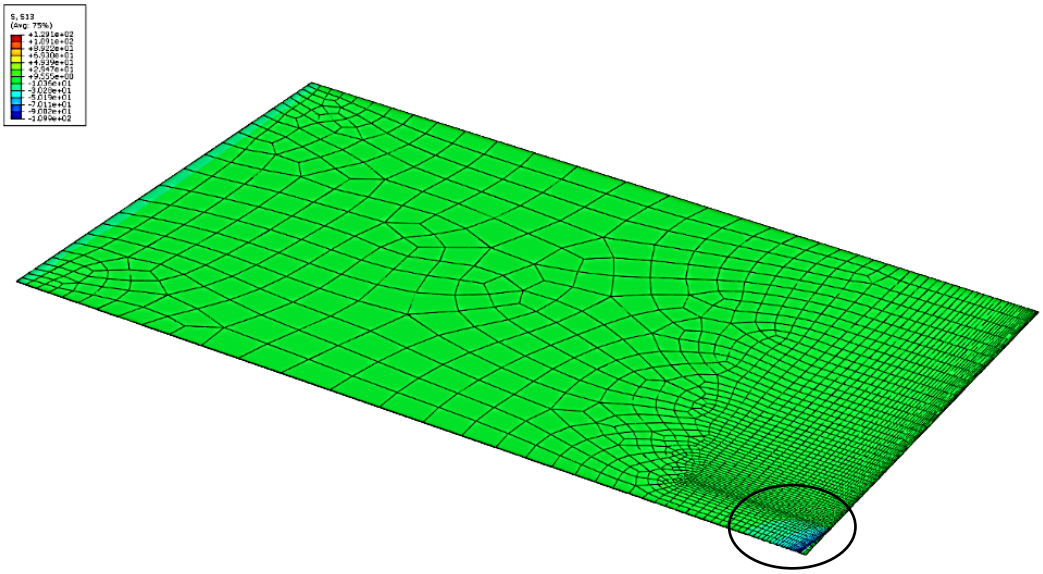

Figure 6.28 Shear stress distribution in interface adhesive layer of FEM of 3-SKWRP-Sk-330 for crack length 0.1 (10mm)

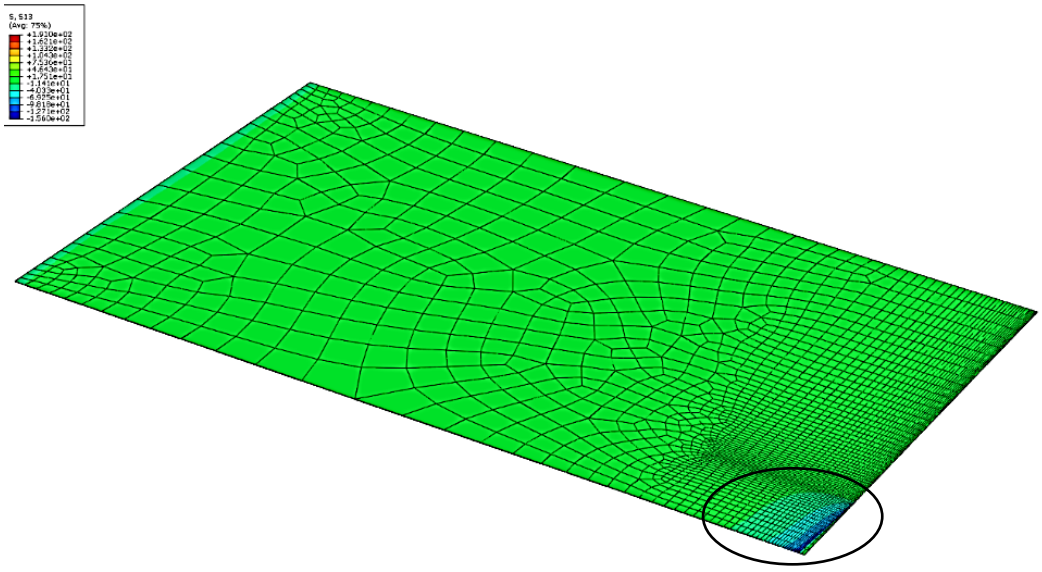

Figure 6.29 Shear stress distribution in interface adhesive layer of FEM of 3-SKWRP-Sk-330 for crack length 0.2 (20mm)

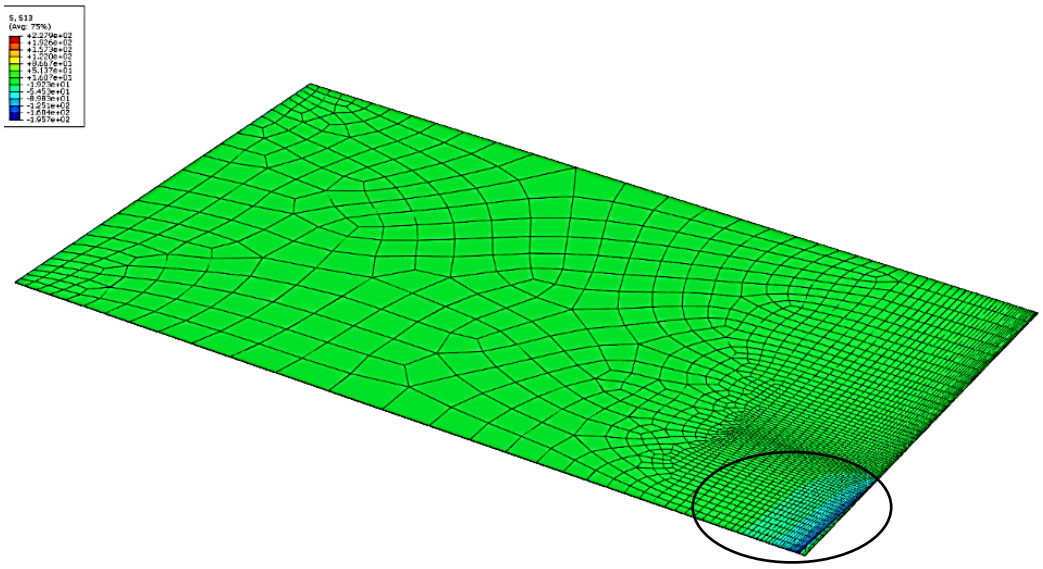

Figure 6.30 Shear stress distribution in interface adhesive layer of FEM of 3-SKWRP-Sk-330 for crack length 0.3 (30mm)

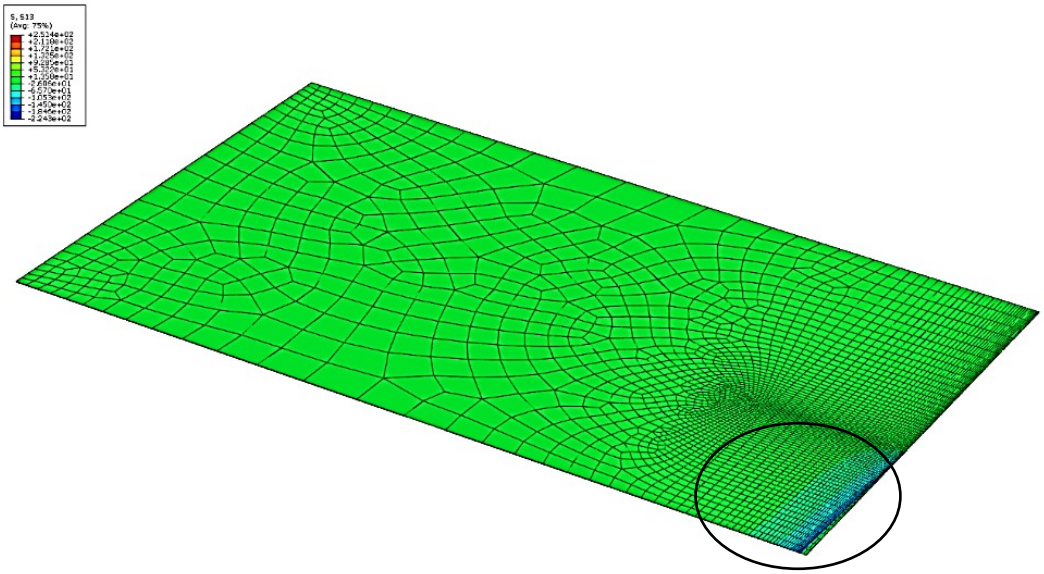

Figure 6.31 Shear stress distribution in interface adhesive layer of FEM of 3-SKWRP-Sk-330 for crack length 0.4 (40mm)

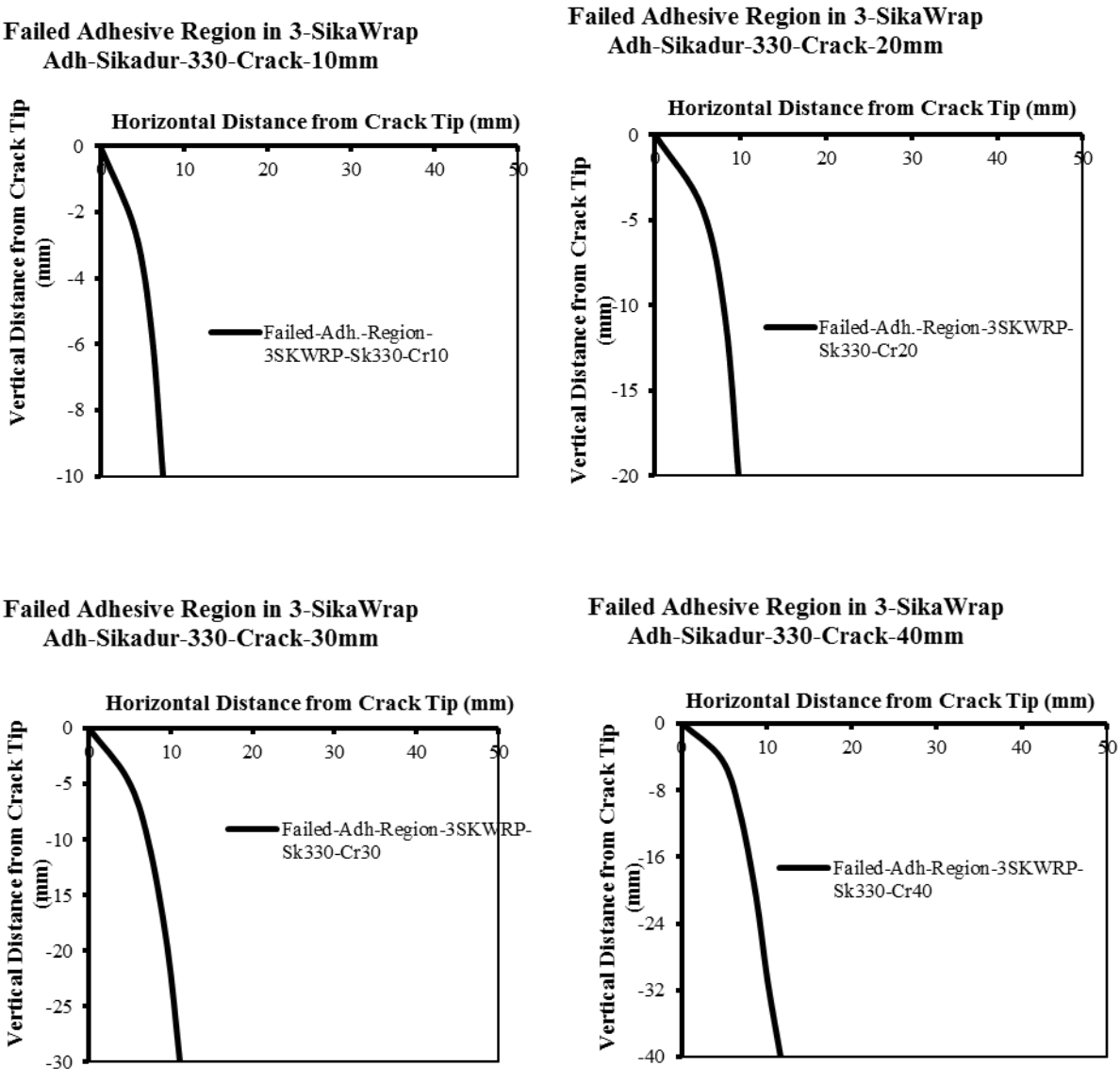

Figure 6.32 Failed regions in interface adhesive layer of FEM of 3-SKWRP-Sk-330 in its four crack lengths; 0.1, 0.2, 0.3 and 0.4 (10mm, 20mm, 30mm, and 40mm)

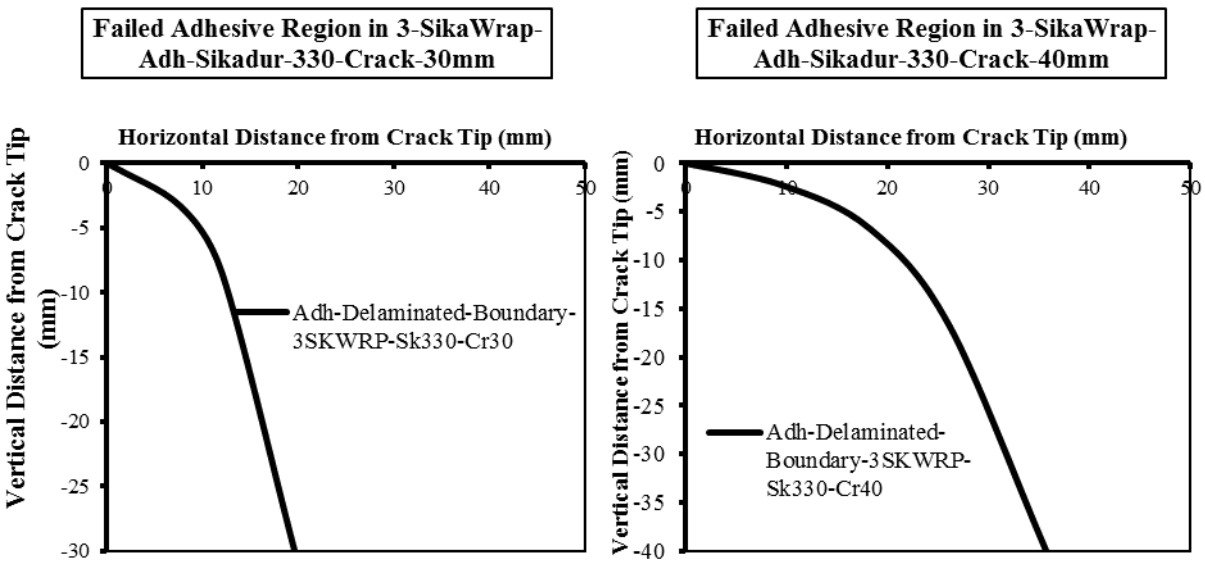

Figure 6.33 Failed adhesive regions in interface adhesive layer of FEM of 3-SKWRP-Sk-330 in crack lengths of 0.3 and 0.4 (30mm and 40mm) after convergence

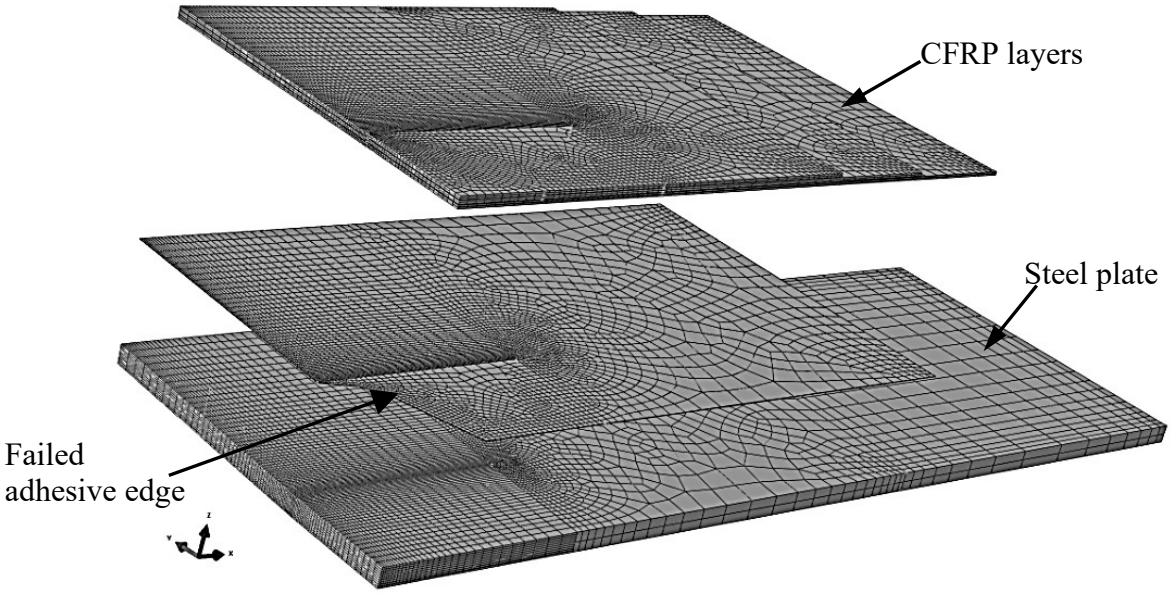

Figure 6.34 Interface adhesive layer with converged failed region removed in the FEM of 3-SKWRP-Sk-330 in crack length 30mm (0.3)

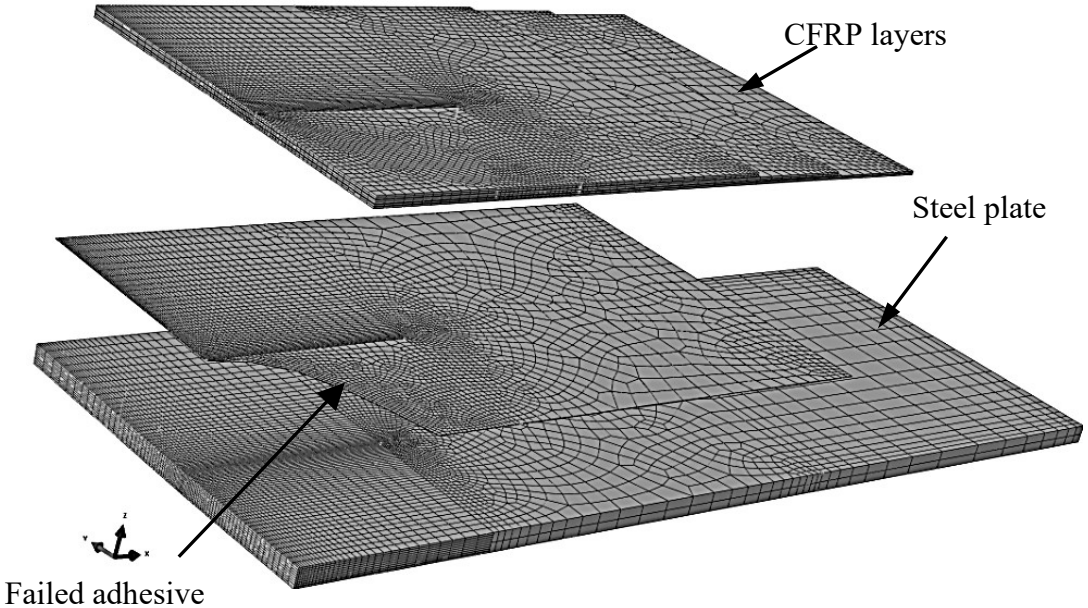

Figure 6.35 Interface adhesive layer with failed region removed in the FEM of 3-SKWRP-Sk-330.in crack length 40mm (0.4) after convergence

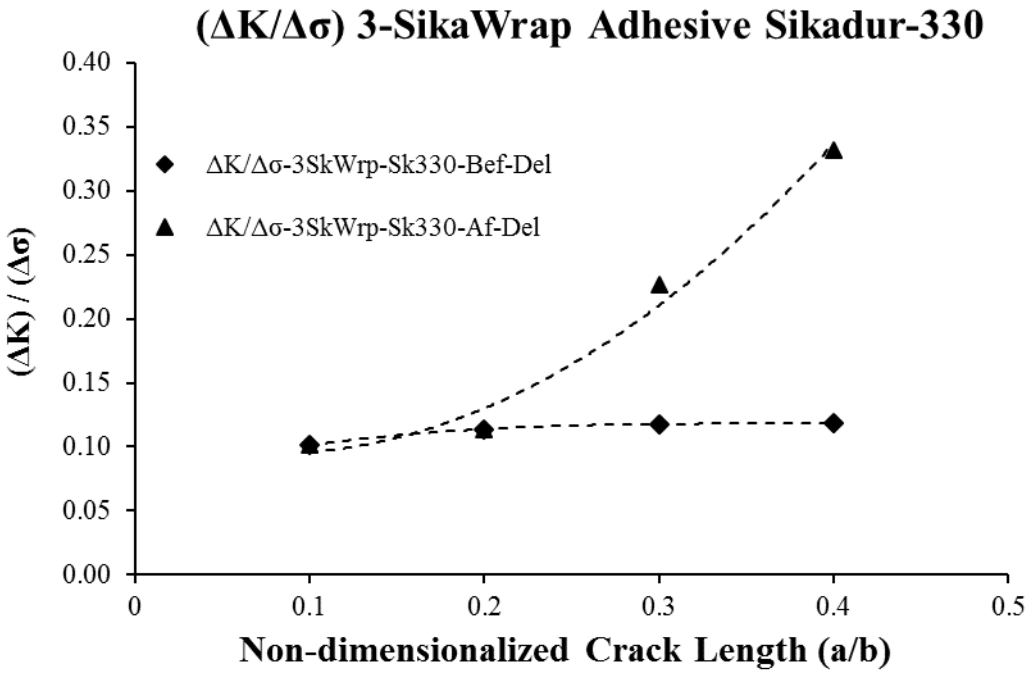

Figure 6.36 ΔK/Δσ variation with non-dimensionalized crack length obtained from FEA of 3-SKWRP-Sk-330 after actual delamination

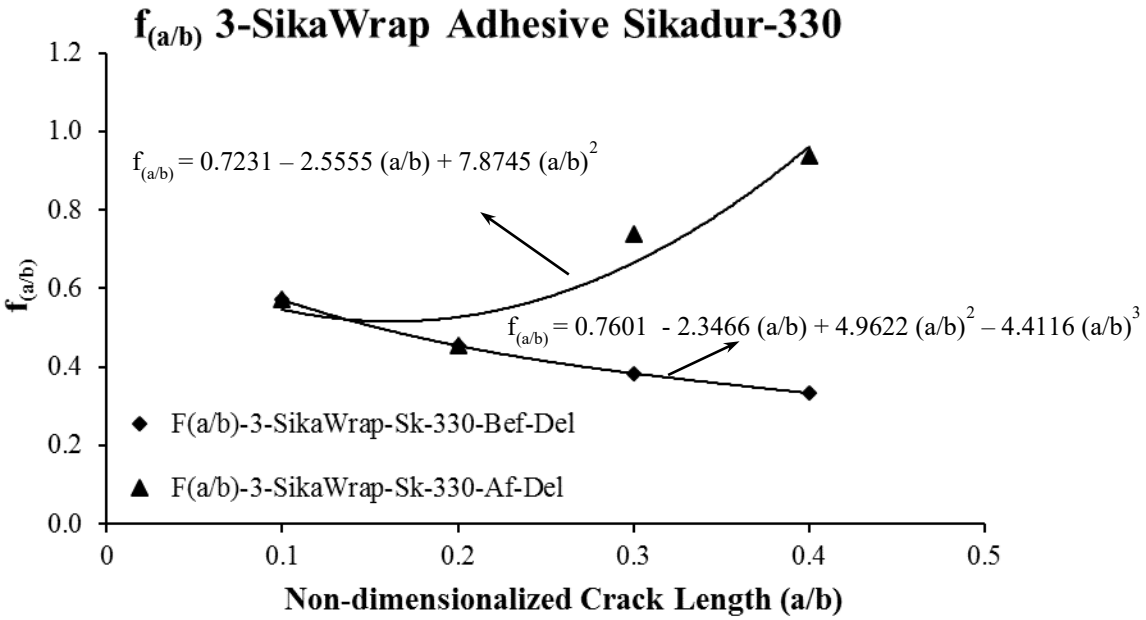

Figure 6.37 Geometric factor $f_{(a/b)}$ variation with non-dimensionalized crack length developed from SIF results of 3-SKWRP-Sk-330

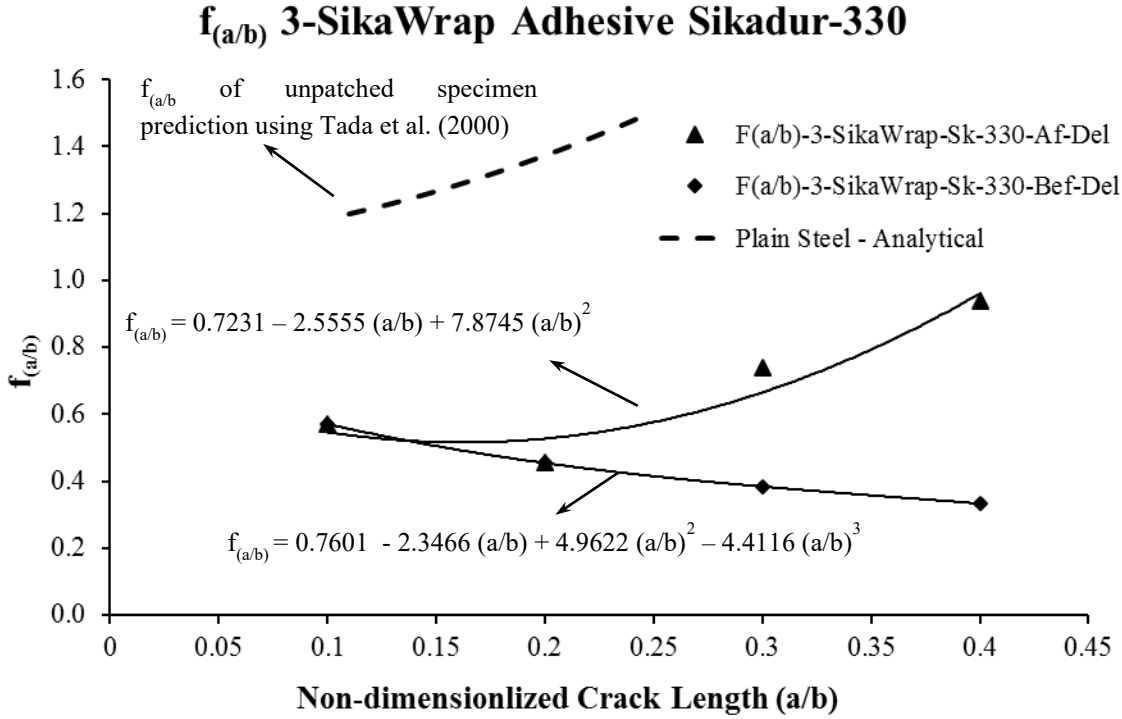

Figure 6.38 Geometric factor $f_{(a/b)}$ variation with non-dimensionalized crack length developed from SIF results of 3-SKWRP-Sk-330 including plain specimen

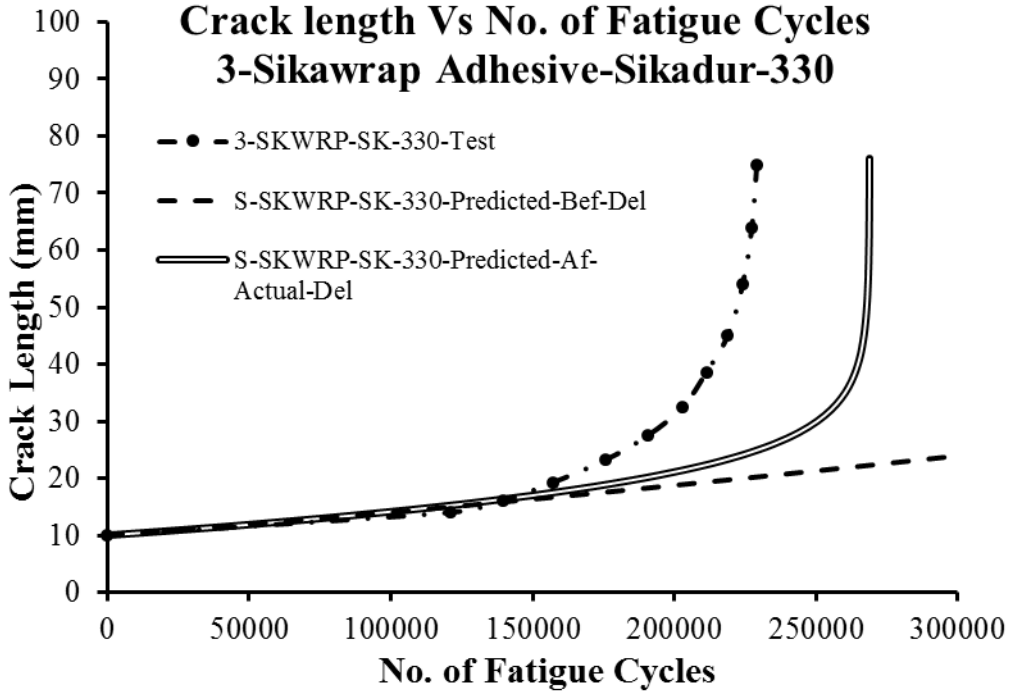

Figure 6.39 Predicted crack length versus number of fatigue cycles for Adhesive 3-SKWRP-Sk-330

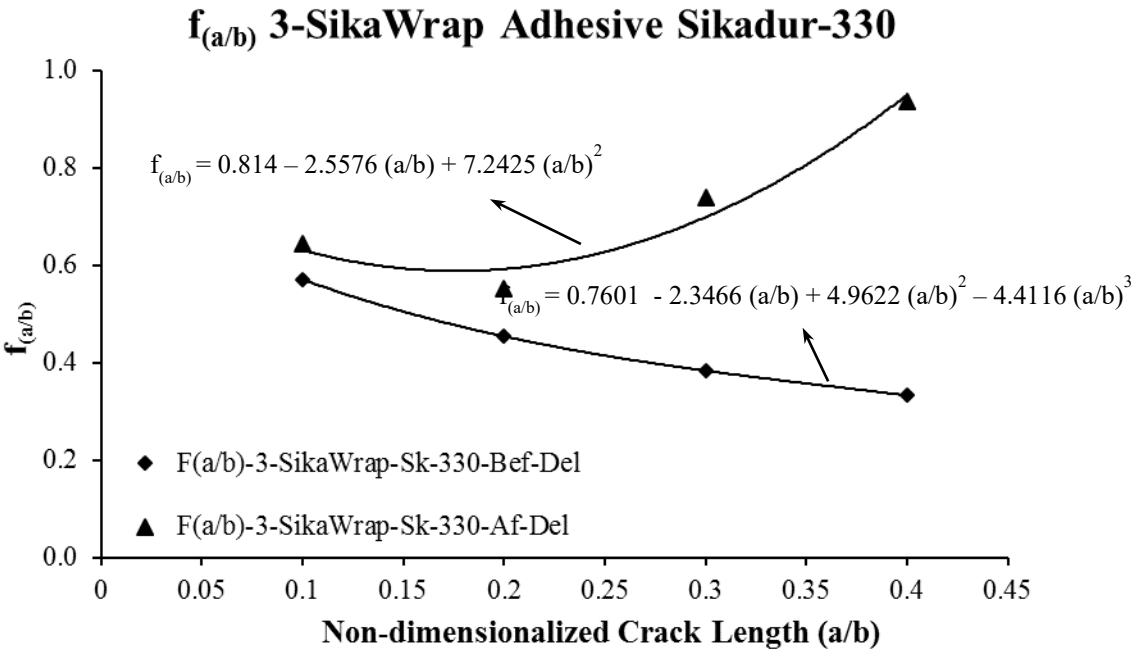

Figure 6.40 f $_{(a/b)}$ variation with non-dimensionalized crack length developed from SIF results of 3-SKWRP-Sk-330 with provided delamination

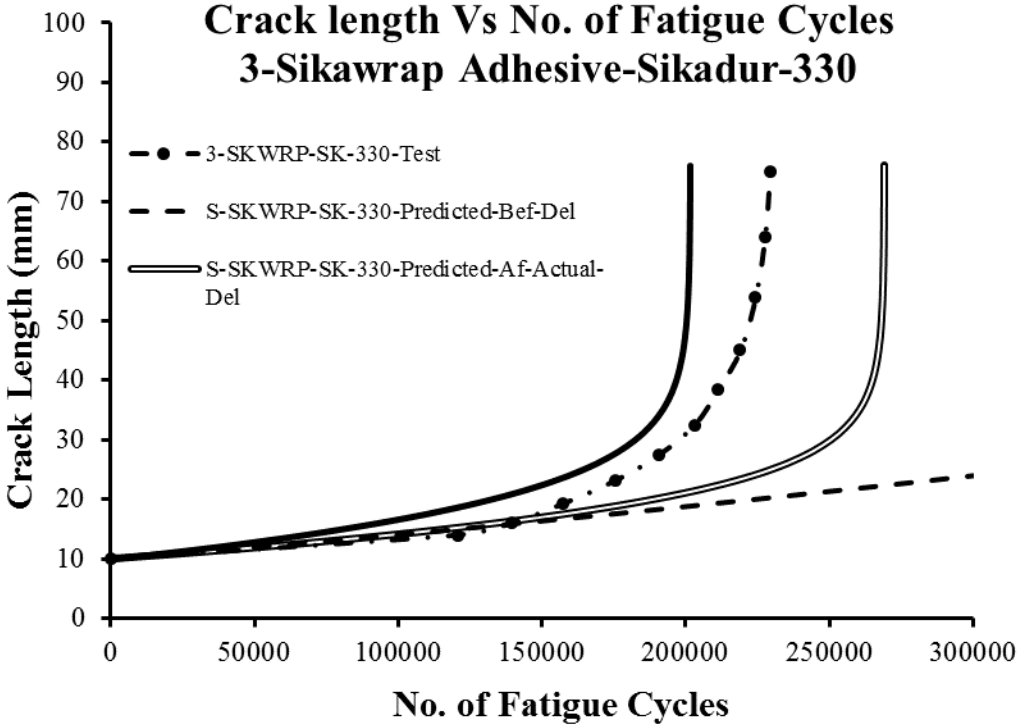

Figure 6.41 Predicted crack length versus number of fatigue cycles for 3-SKWRP-Sk-330 including the provided delamination case

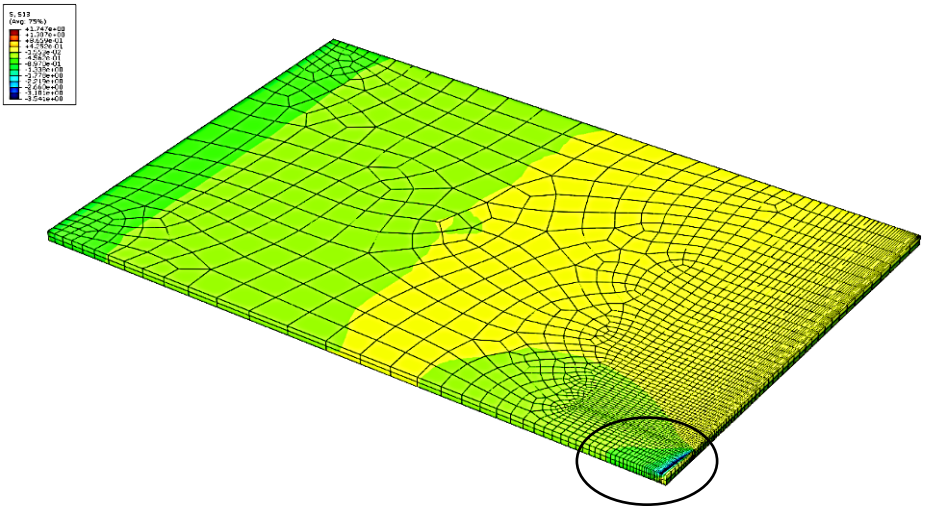

Figure 6.42 Shear stress distribution in interface adhesive layer of FEM of 1-CBDR-Adh-Sk-30 for crack length 0.1 (10mm)

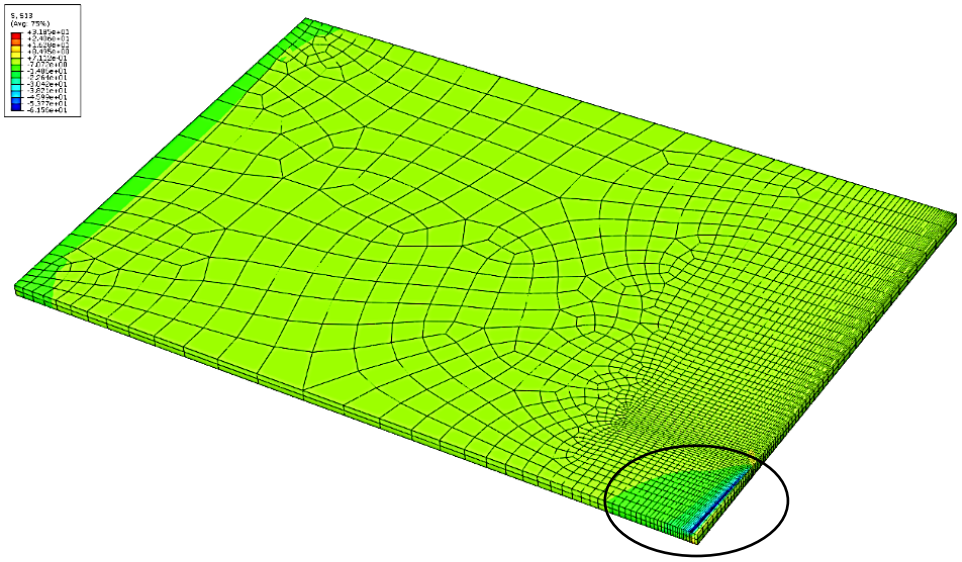

Figure 6.43 Shear stress distribution in interface adhesive layer of FEM of 1-CBDR-Adh-Sk-30 for crack length 0.2 (20mm)

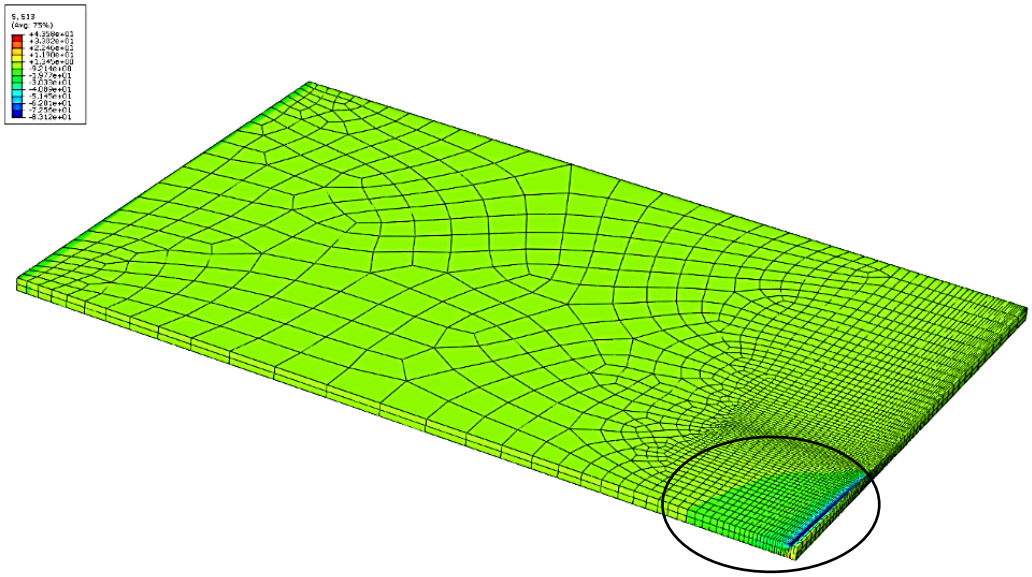

Figure 6.44 Shear stress distribution in interface adhesive layer of FEM of 1-CBDR-Adh-Sk-30 for crack length 0.3 (30mm)

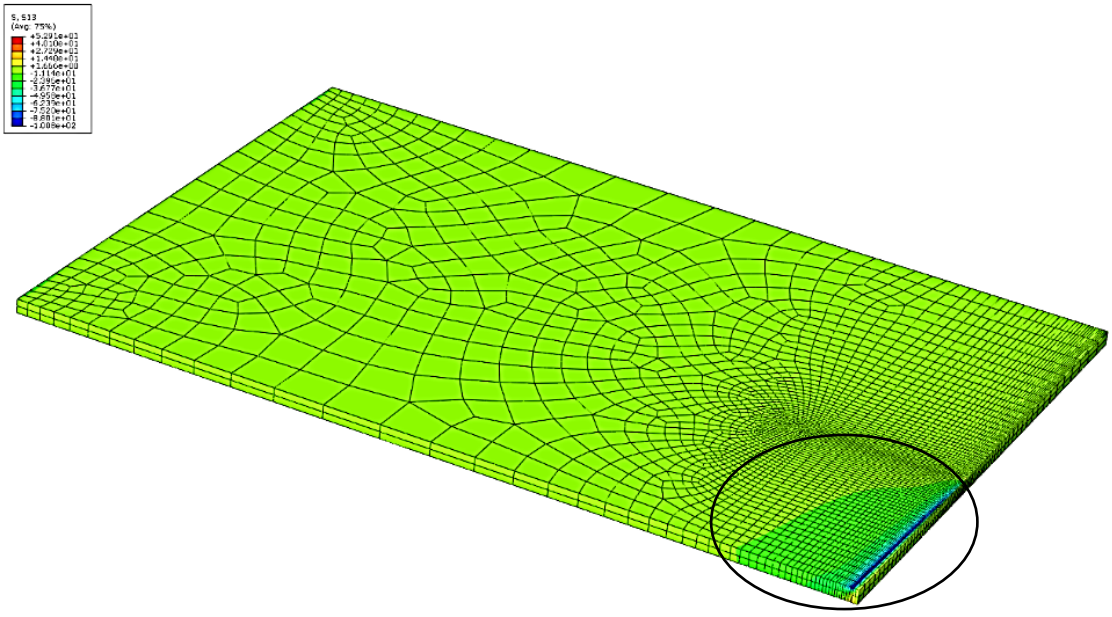

Figure 6.45 Shear stress distribution in interface adhesive layer of FEM of 1-CBDR-Adh-Sk-30 for crack length 0.4 (40mm)

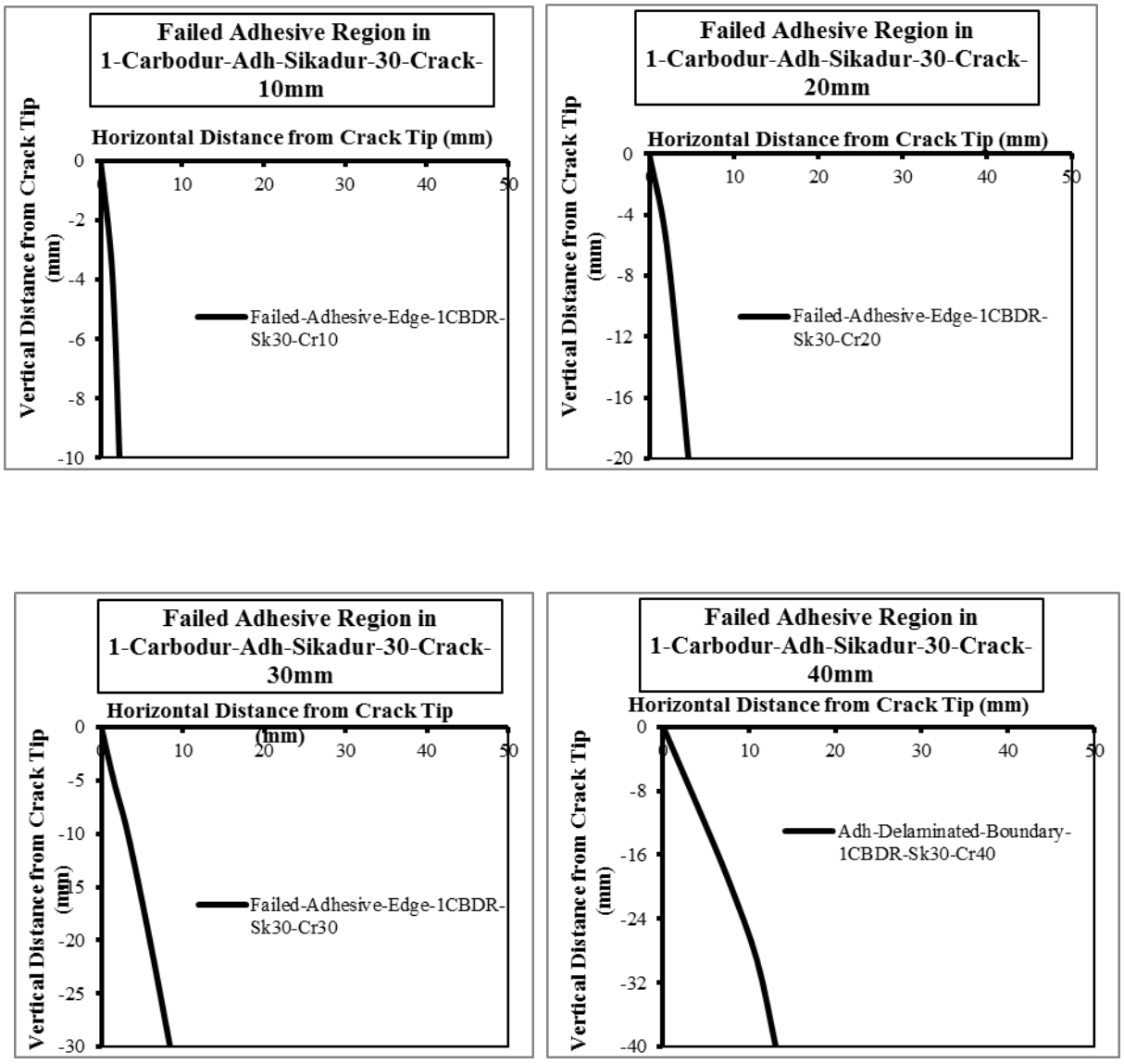

Figure 6.46 Adhesive failed regions in FEM of 1-CBDR-Adh-Sk-30 in its four crack lengths; 0.1, 0.2, 0.3 and 0.4 (10mm, 20mm, 30mm, and 40mm)

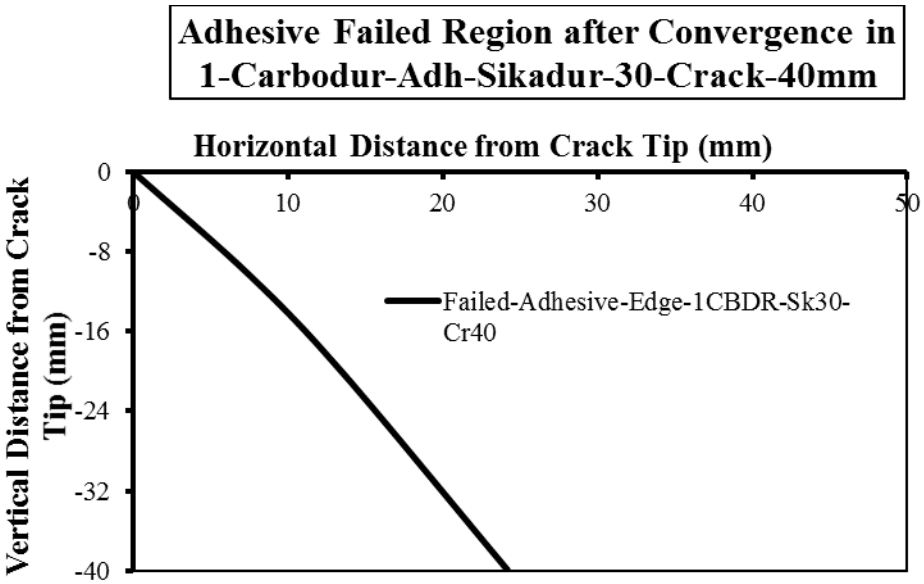

Figure 6.47 Failed regions in interface adhesive layer of FEM of 1-CBDR-Adh-Sk-30 for crack length 0.4 (40mm) after Convergence

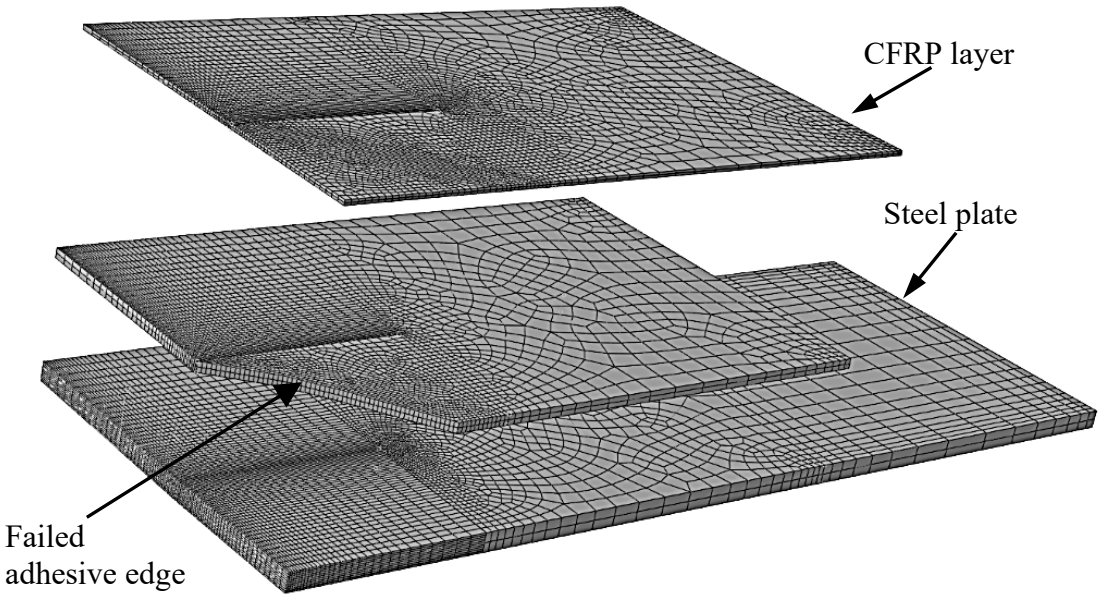

Figure 6.48 Interface adhesive layer with its failed region removed in the FEM of 1-CBDR-Adh-Sk-30-crack length 40mm (0.4) after convergence

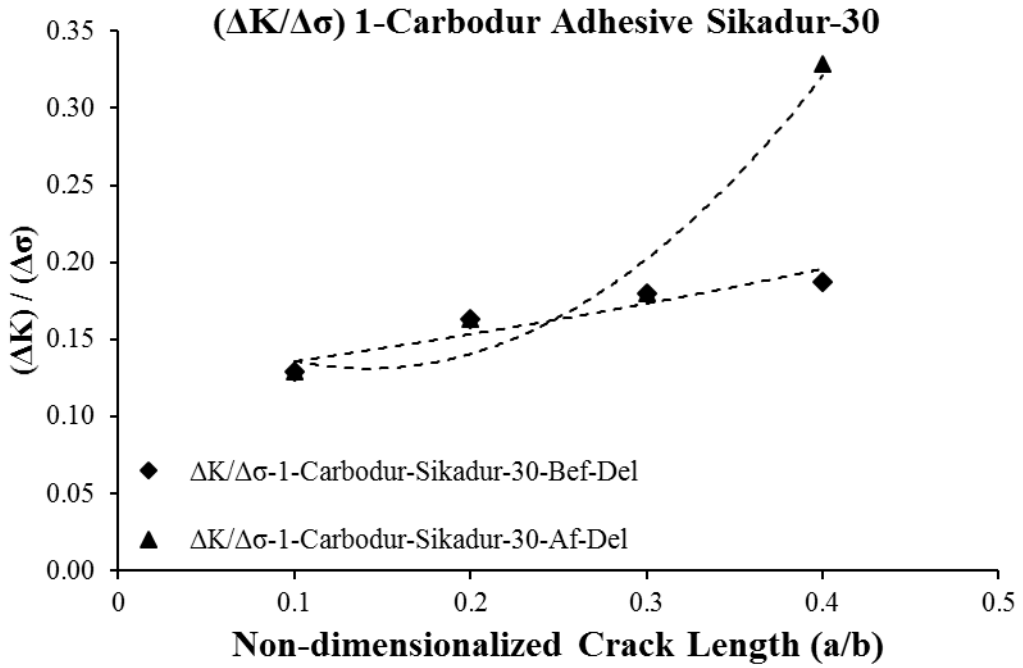

Figure 6.49 ΔK/Δσ variation with non-dimensionalized crack length obtained from FEA of 1-CBDR-Adh-Sk-30

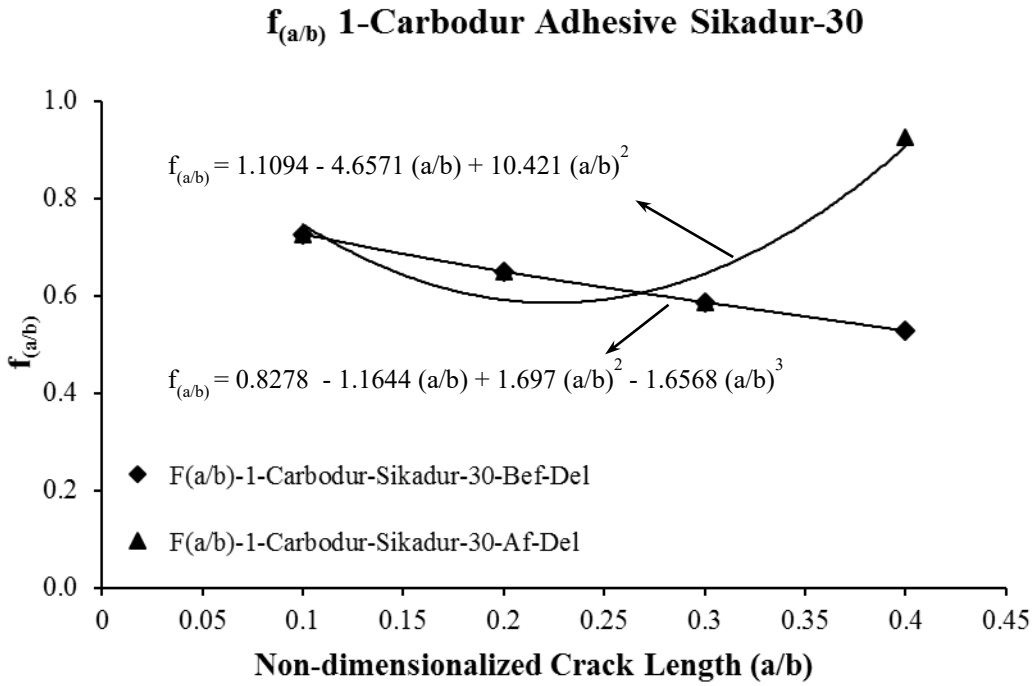

Figure 6.50 Geometric factor $f_{(a/b)}$ variation with non-dimensionalized crack length developed from SIF results of 1-CBDR-Adh-Sk-30

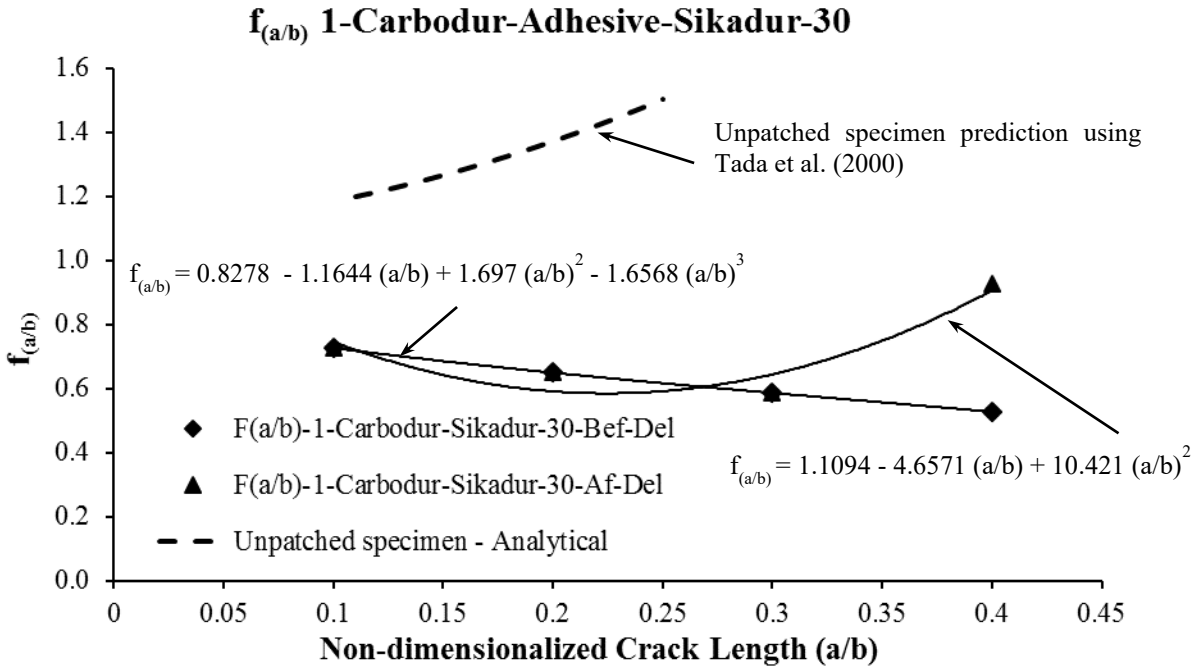

Figure 6.51 Geometric factor $f_{(a/b)}$ variation with non-dimensionalized crack length developed from SIF results of 1-CBDR-Adh-Sk-30 including unpatched specimen

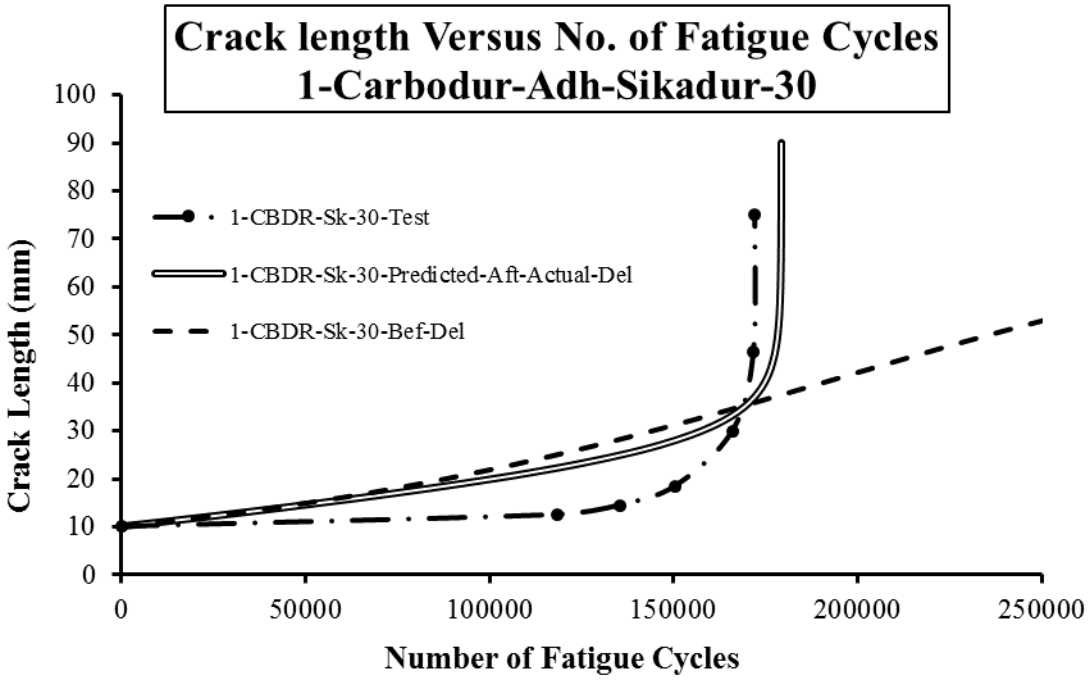

Figure 6.52 Predicted crack length versus number of fatigue cycles for 1-CBDR-Sk-30

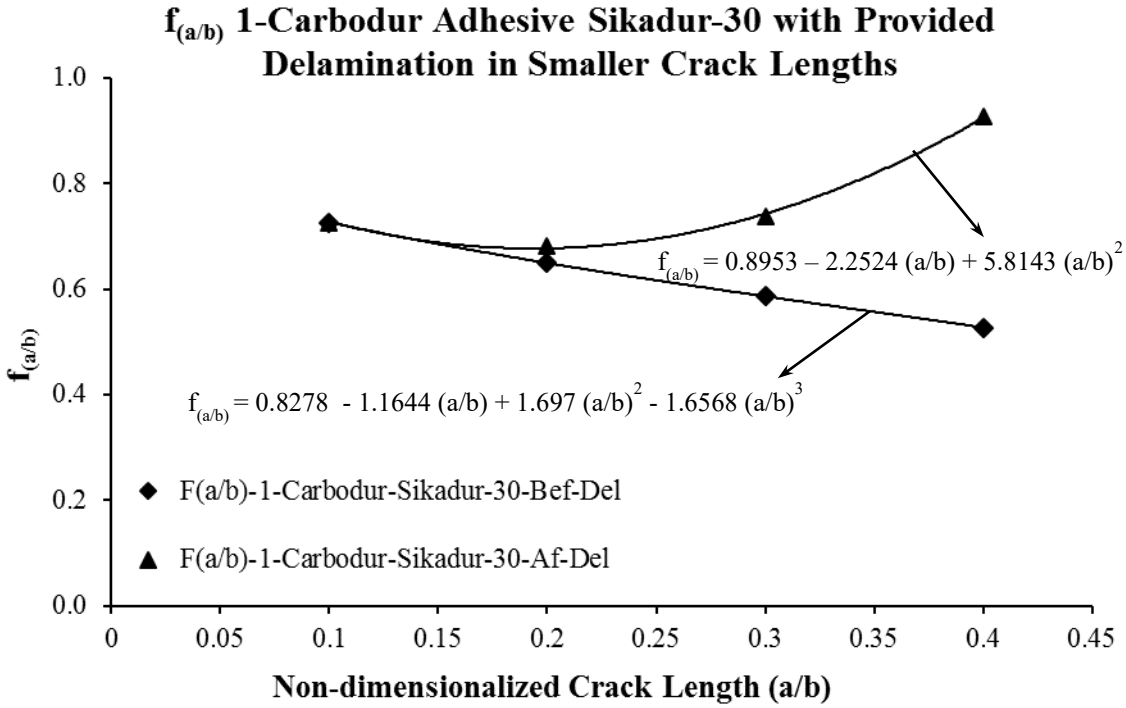

Figure 6.53 $f_{(a/b)}$ variation with non-dimensionalized crack length developed from SIF results of 1-CBDR-Adh-Sk-30 with provided delamination

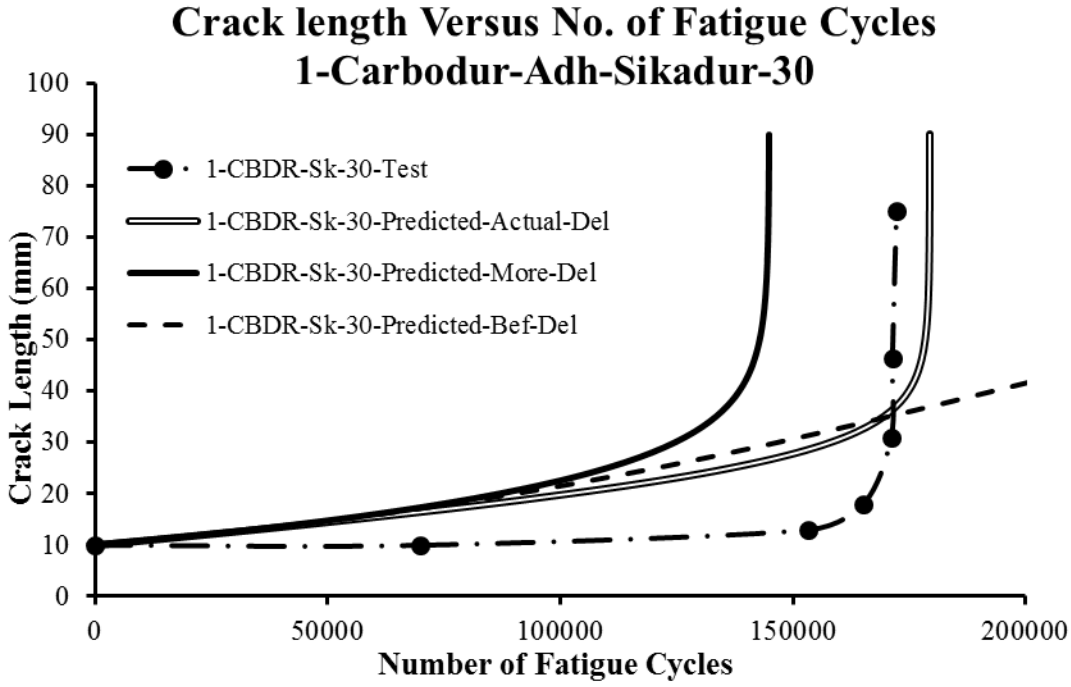

Figure 6.54 Crack length versus number of fatigue cycles for 1-CBDR-Sk-30 including the provided delamination case

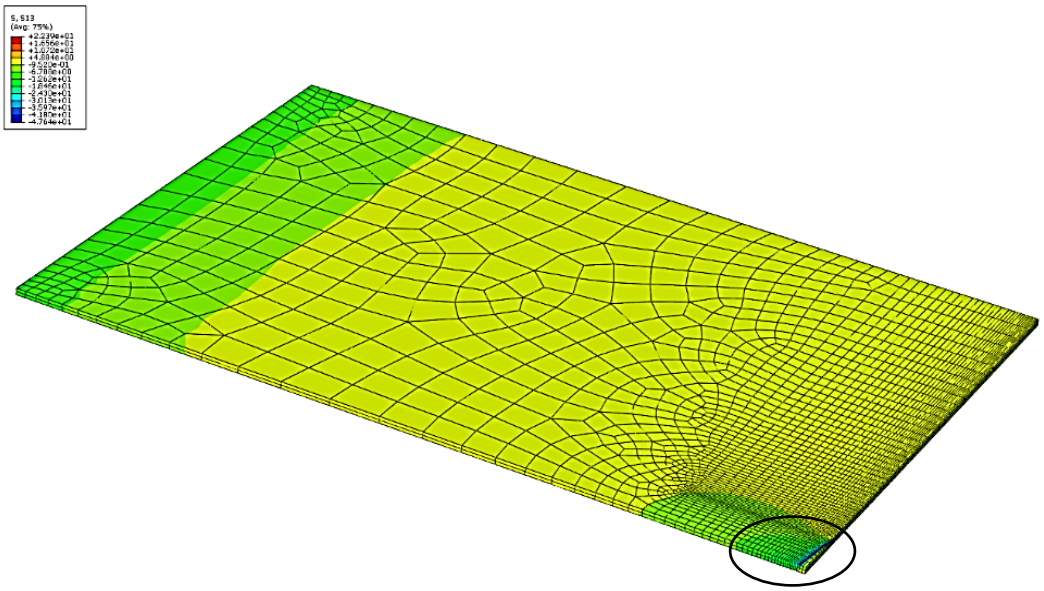

Figure 6.55 Shear stress distribution in interface adhesive layer of FEM of 1-CBDR-Adh-Sk-30/2 for crack length 0.1 (10mm)

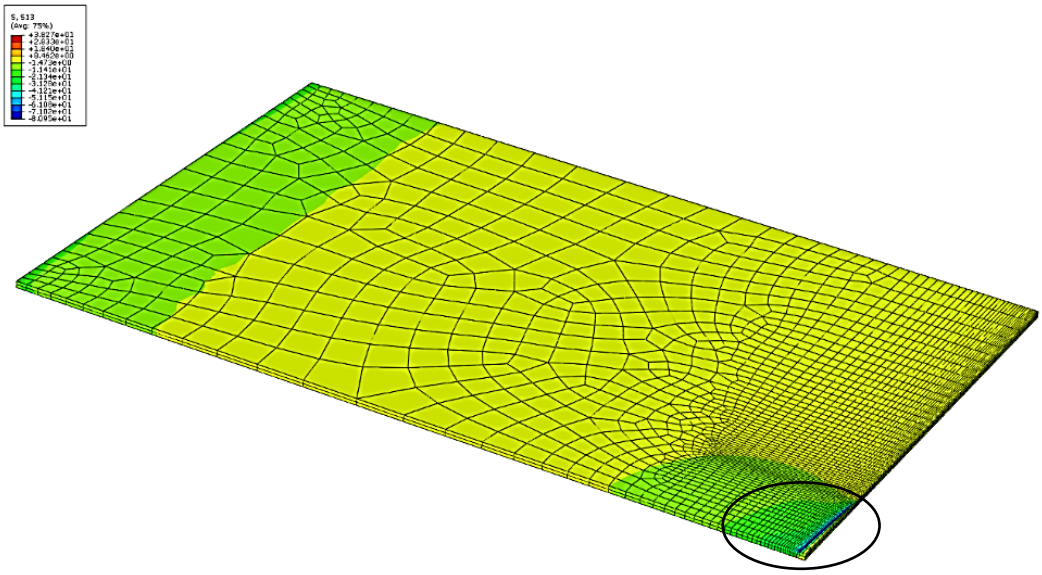

Figure 6.56 Shear stress distribution in interface adhesive layer of FEM of 1-CBDR-Adh-Sk-30/2 for crack length 0.2 (20mm)

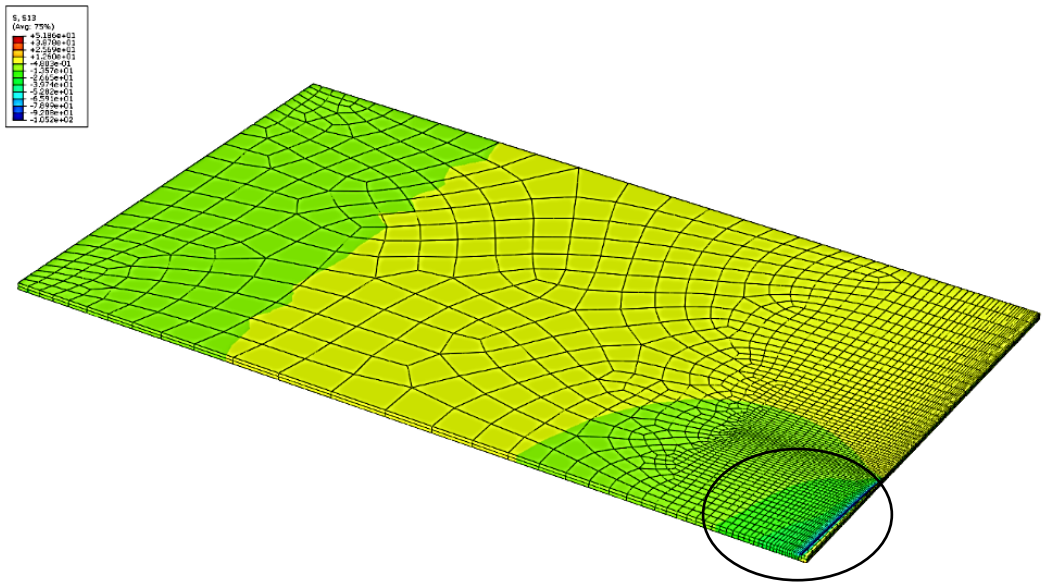

Figure 6.57 Shear stress distribution in interface adhesive layer of FEM of 1-CBDR-Adh-Sk-30/2 for crack length 0.3 (30mm)

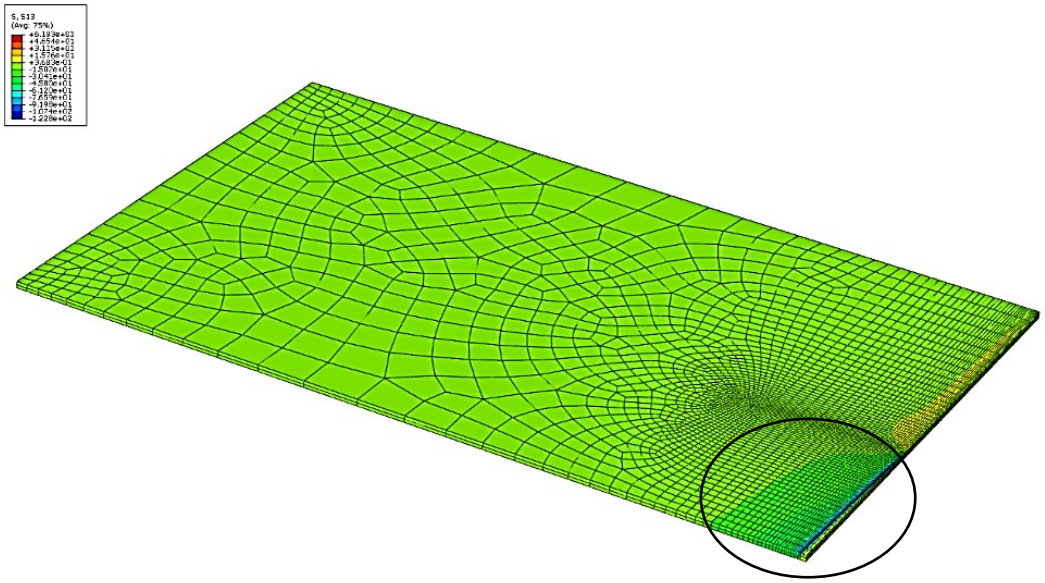

Figure 6.58 Shear stress distribution in interface adhesive layer of FEM of 1-CBDR-Adh-Sk-30/2 for crack length 0.4 (40mm)

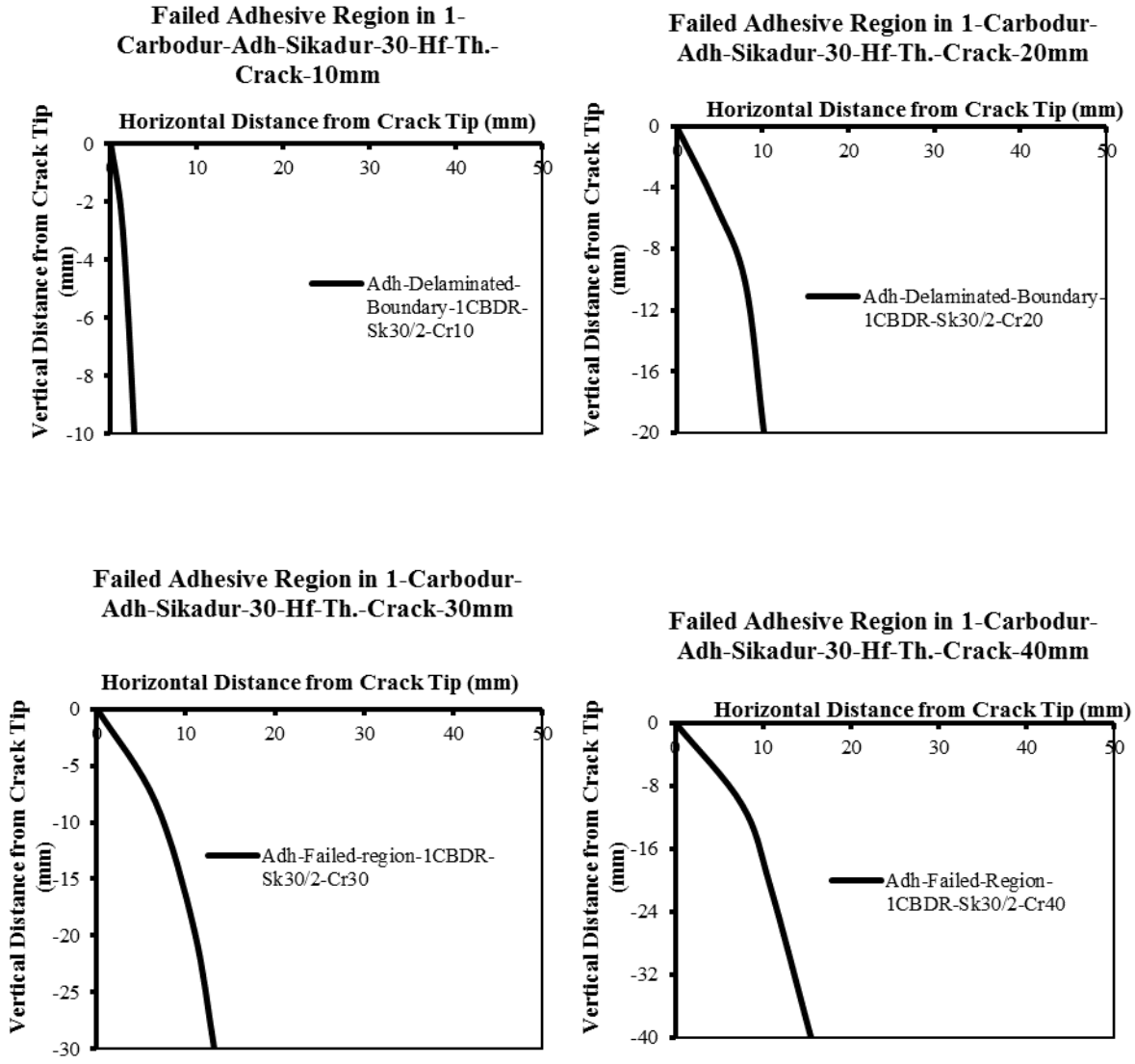

Figure 6.59 Adhesive failed regions in FEM of 1-CBDR-Adh-Sk-30-Hf. Th. in its four crack lengths; 0.1, 0.2, 0.3 and 0.4 (10mm, 20mm, 30mm, and 40mm)

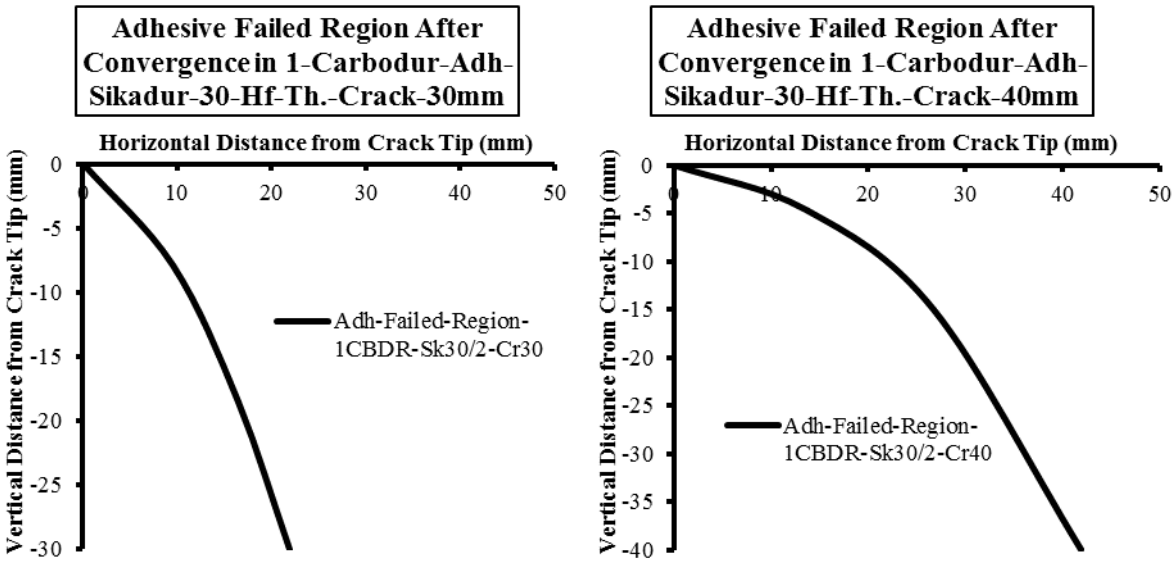

Figure 6.60 Failed regions in interface adhesive layers in FEM of 1-CBDR-Adh-Sk-30-Hf. Th. in crack lengths 30mm and 40mm (30mm & 40mm) after convergence

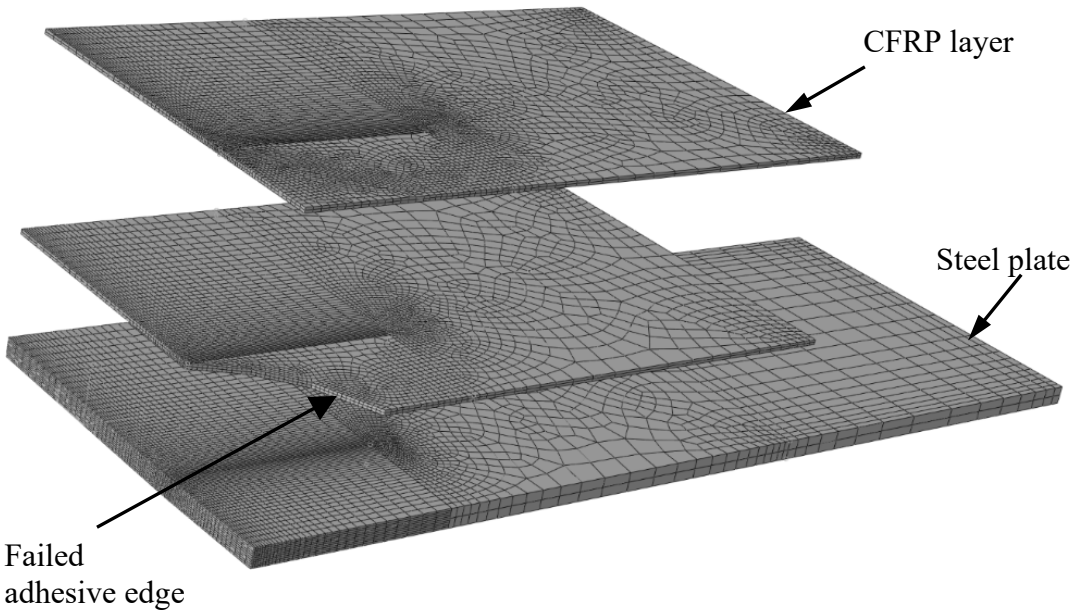

Figure 6.61 Interface adhesive layer with failed region removed in the FEM of 1-CBDR-Adh-Sk-30-Hf. Th.-crack lengths 30mm (0.3) after convergence

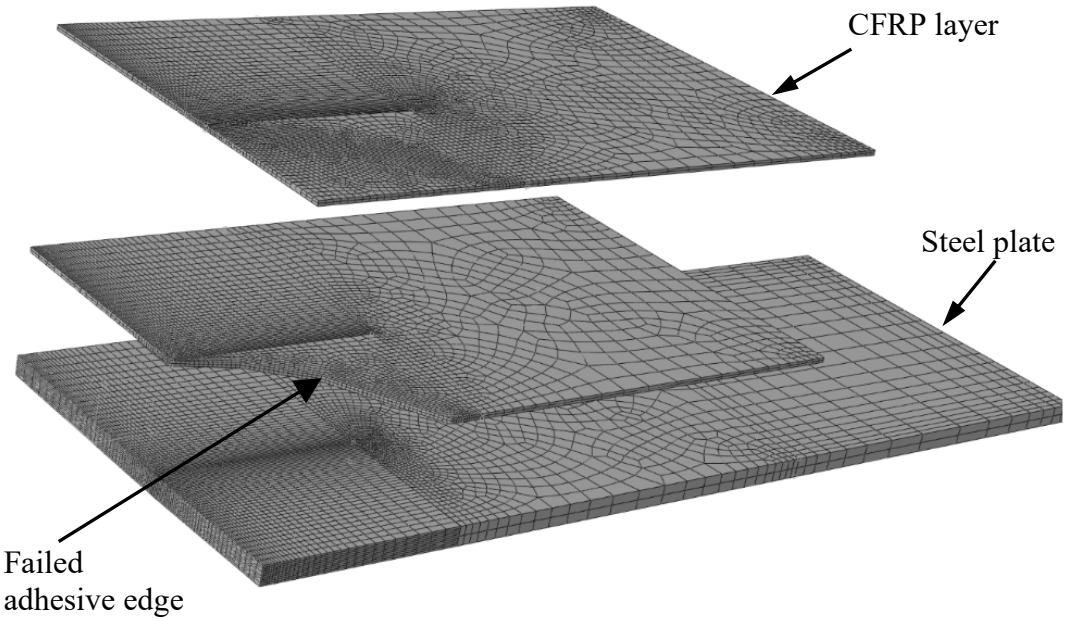

Figure 6.62 Interface adhesive layer with failed region removed in the FEM of 1-CBDR-Adh-Sk-30-Hf. Th.-crack lengths 40mm (0.4) after convergence

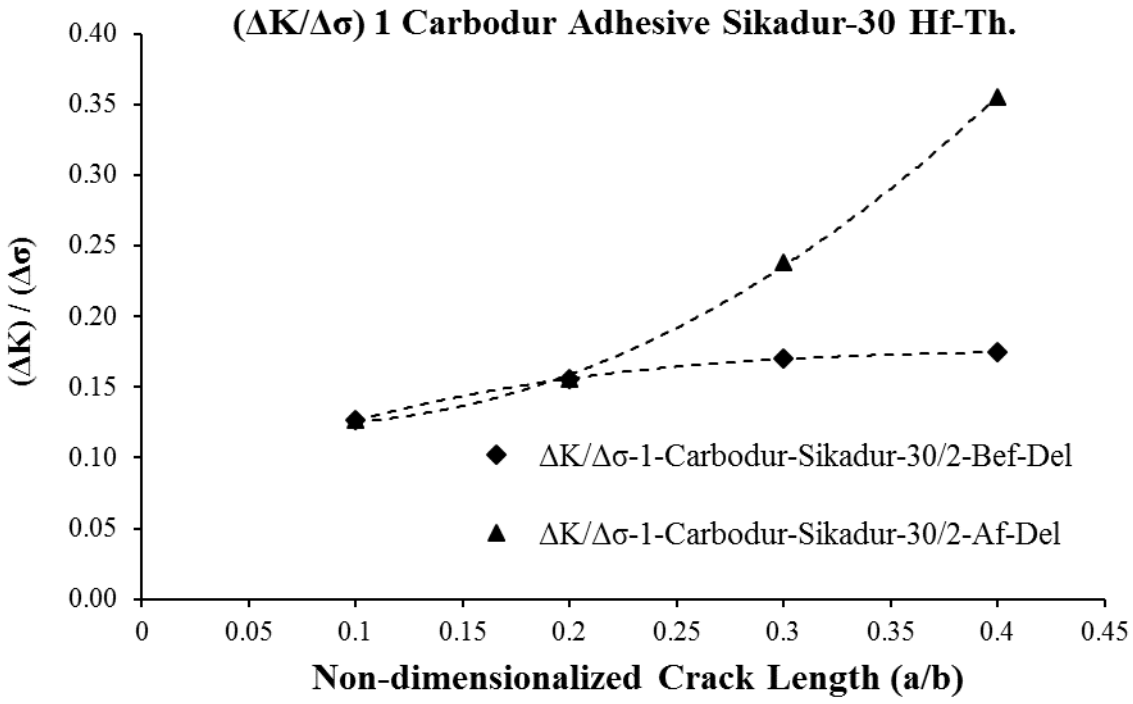

Figure 6.63 ΔK/Δσ variation with non-dimensionalized crack length obtained from FEA of 1-CBDR-Adh-Sk-30-Hf.Th.

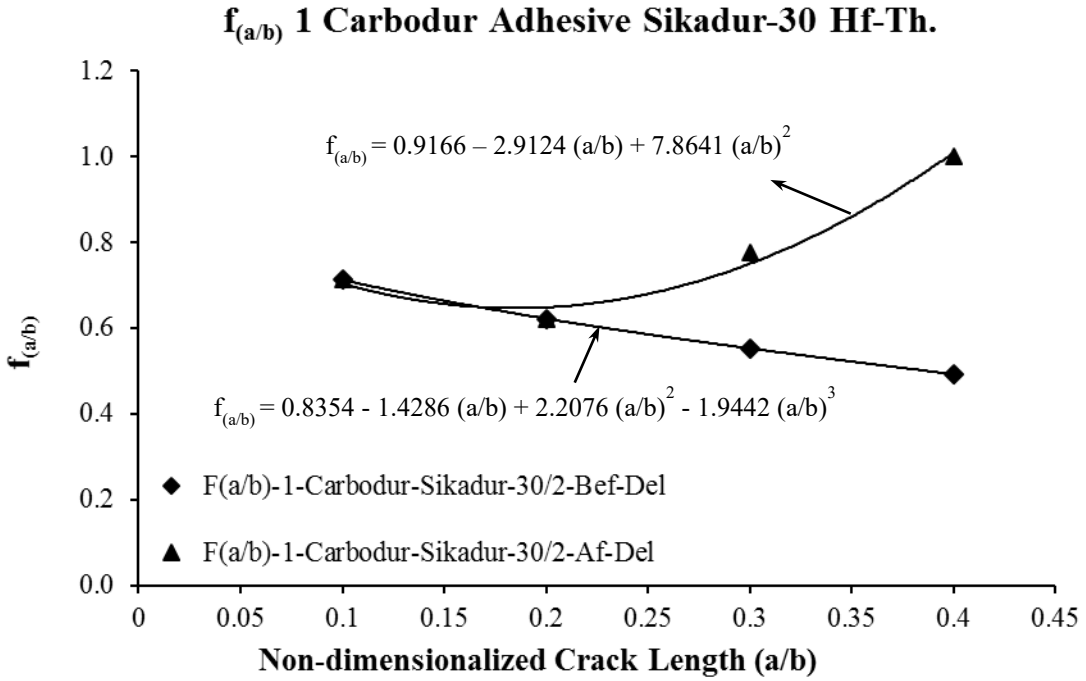

Figure 6.64 Geometric factor $f_{(a/b)}$ variation with non-dimensionalized crack length developed from SIF results of 1-CBDR-Adh-Sk-30-Hf.Th.

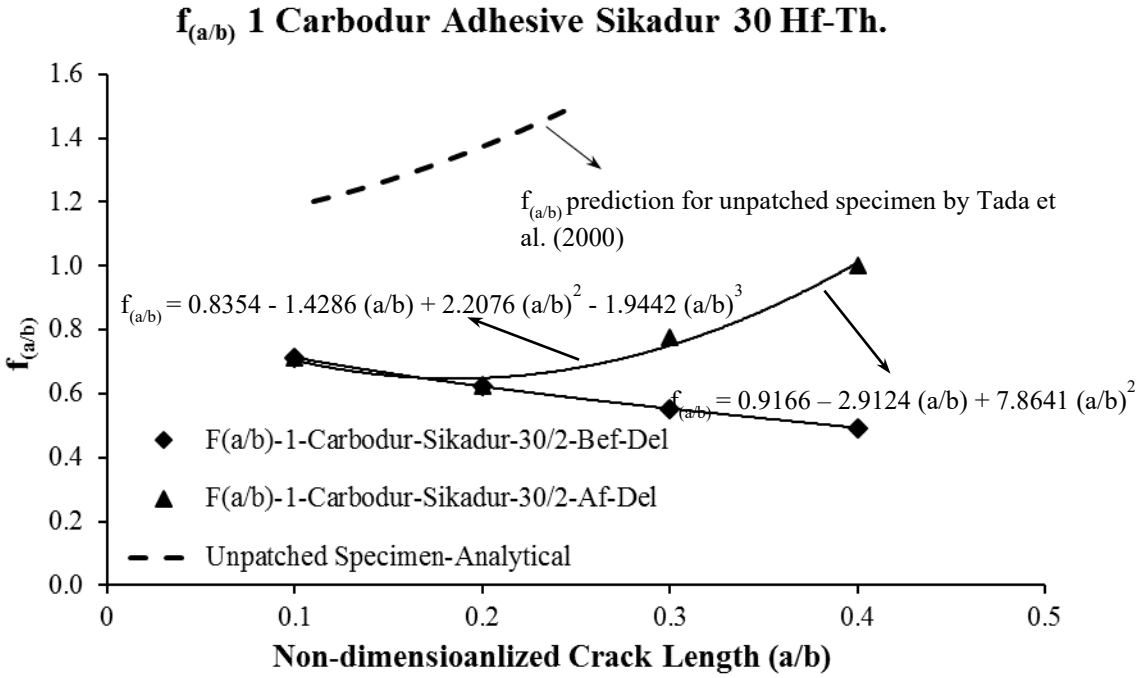

Figure 6.65 Geometric factor $f_{(a/b)}$ variation with non-dimensionalized crack length from SIF results of 1-CBDR-Adh-Sk-30-Hf-Th including plain specimen

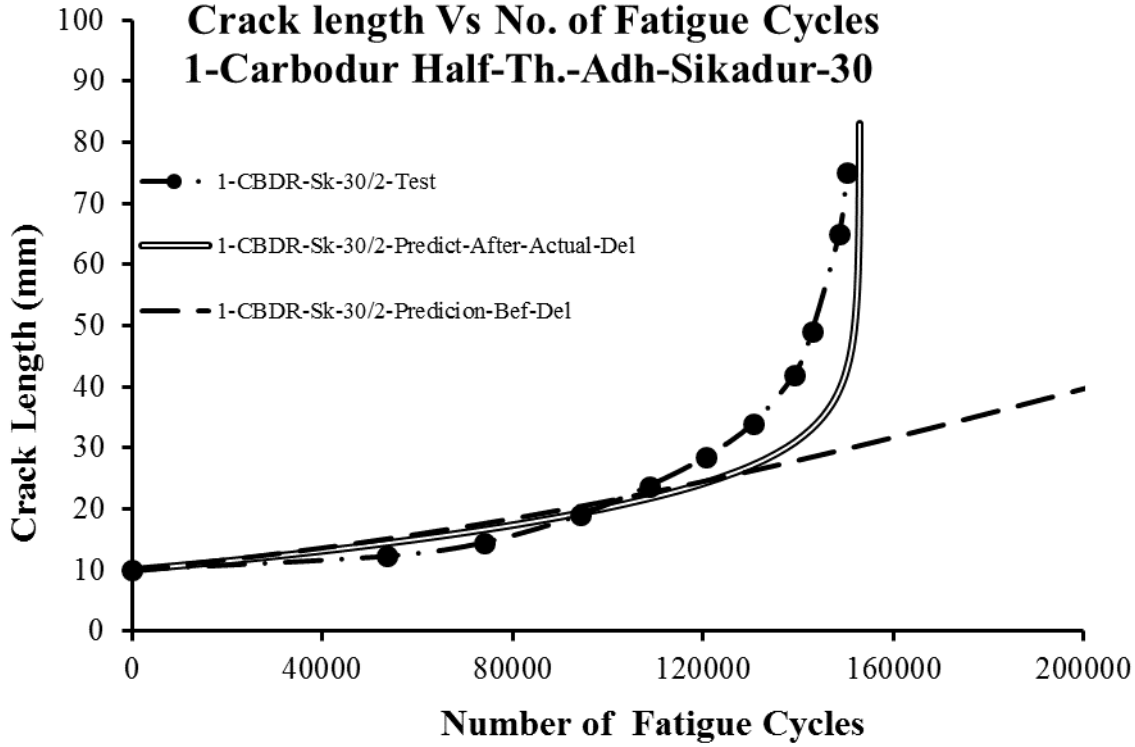

Figure 6.66 Predicted crack length versus number of fatigue cycles for 1-CBDR-Sk-30-Hf.-Th.

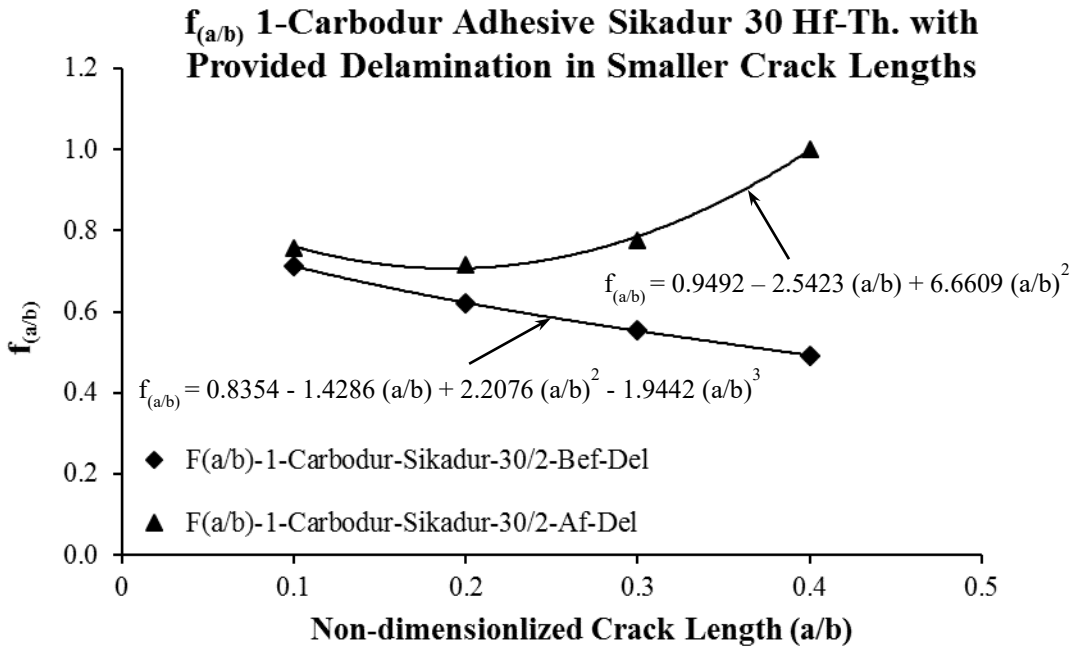

Figure 6.67 $f_{(a/b)}$ variation with non-dimensionalized crack length developed from SIF results of 1-CBDR-Adh-Sk-30-Hf.-Th. with provided delamination

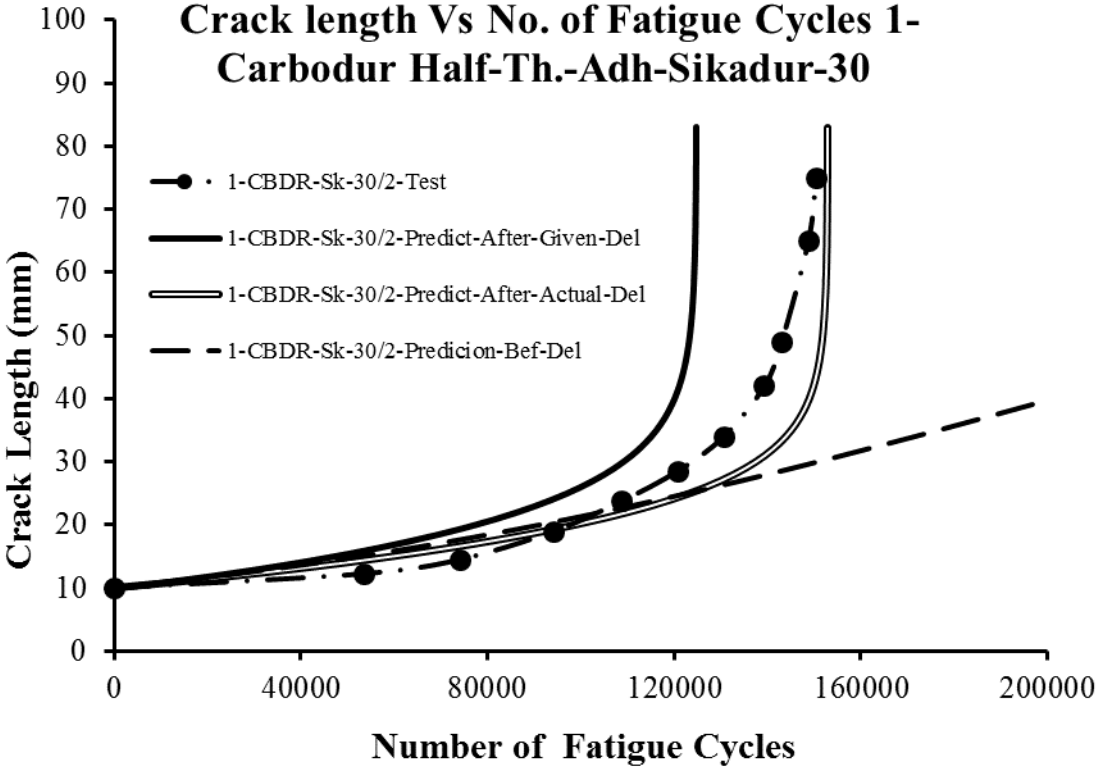

Figure 6.68 Predicted crack length versus number of fatigue cycles for 1-CBDR-Sk-Hf-Th including provided delamination case

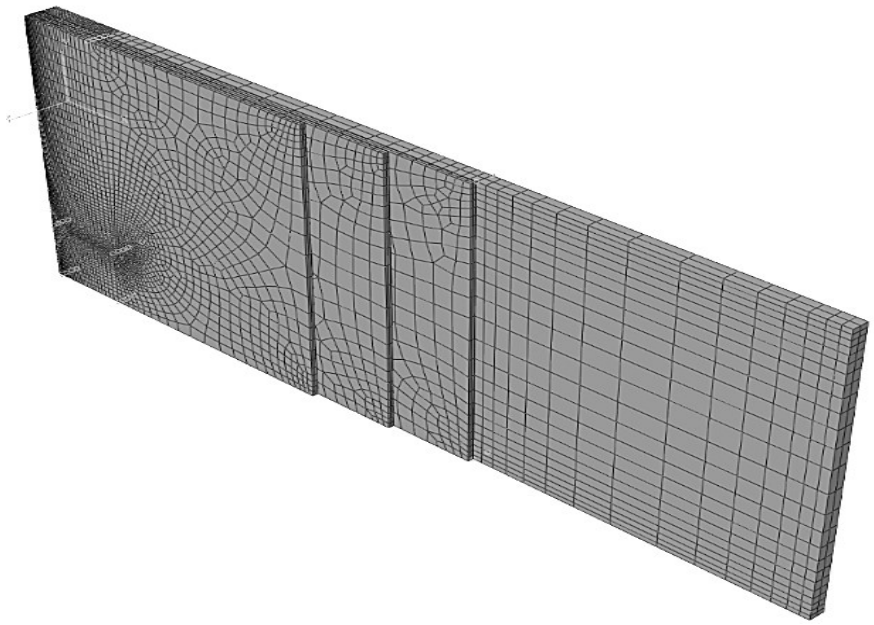

Figure 6.69 Finite element model of 6-Sikawrap Hex showing adhesive and CFRP layers

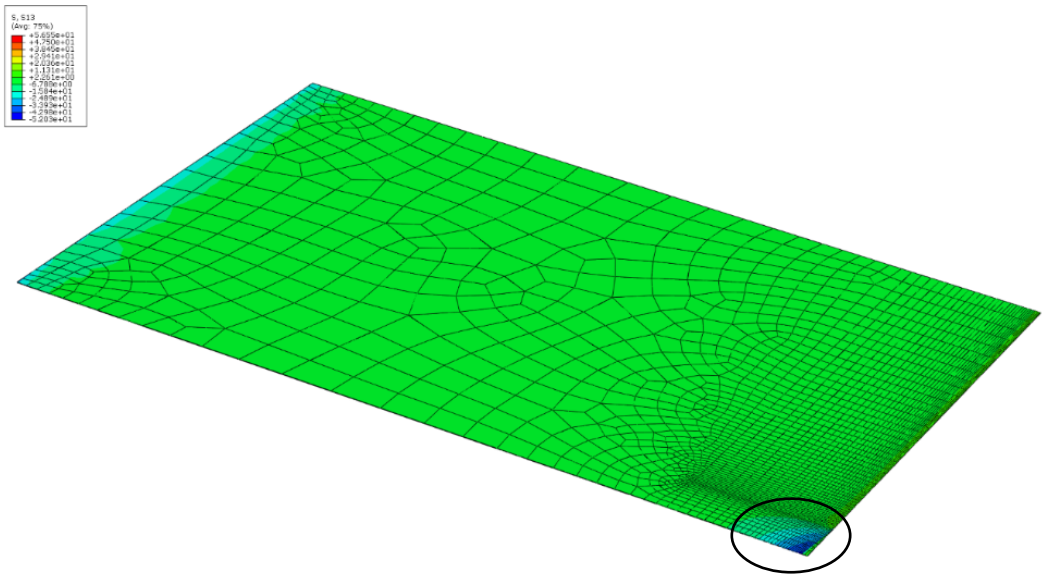

Figure 6.70 Shear stress distribution in interface adhesive layer of FEM of 6-SKWRP-Sk-300 for crack length 0.1 (10mm)

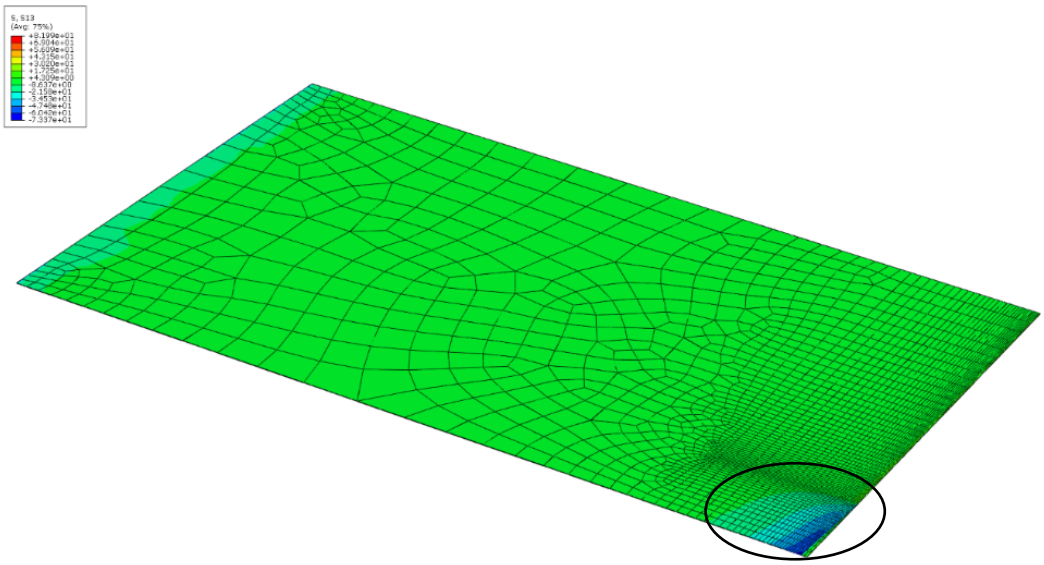

Figure 6.71 Shear stress distribution in interface adhesive layer of FEM of 6-SKWRP-Sk-300 for crack length 0.2 (20mm)

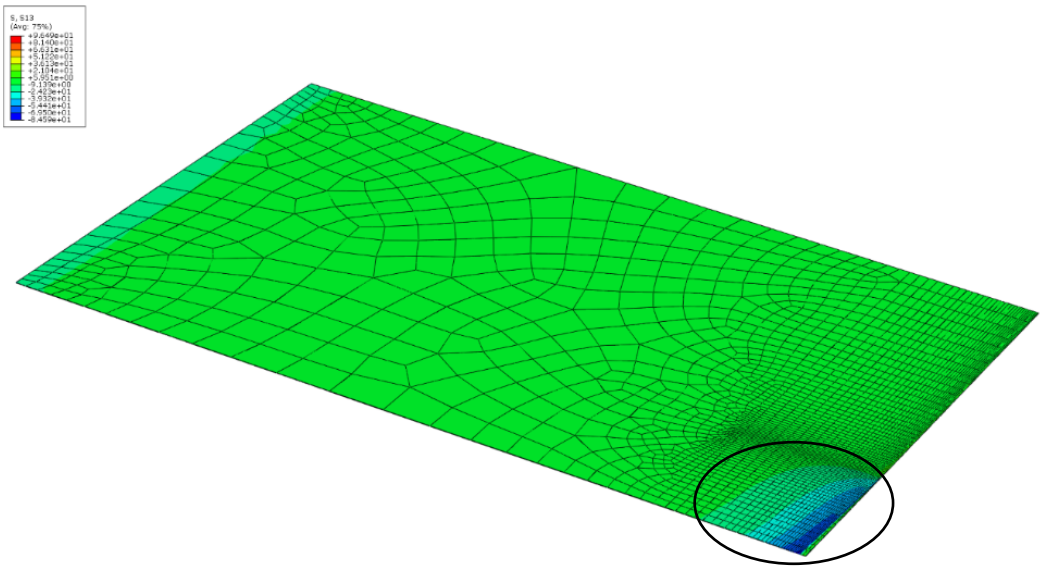

Figure 6.72 Shear stress distribution in interface adhesive layer of FEM of 6-SKWRP-Sk-300 for crack length 0.3 (30mm)

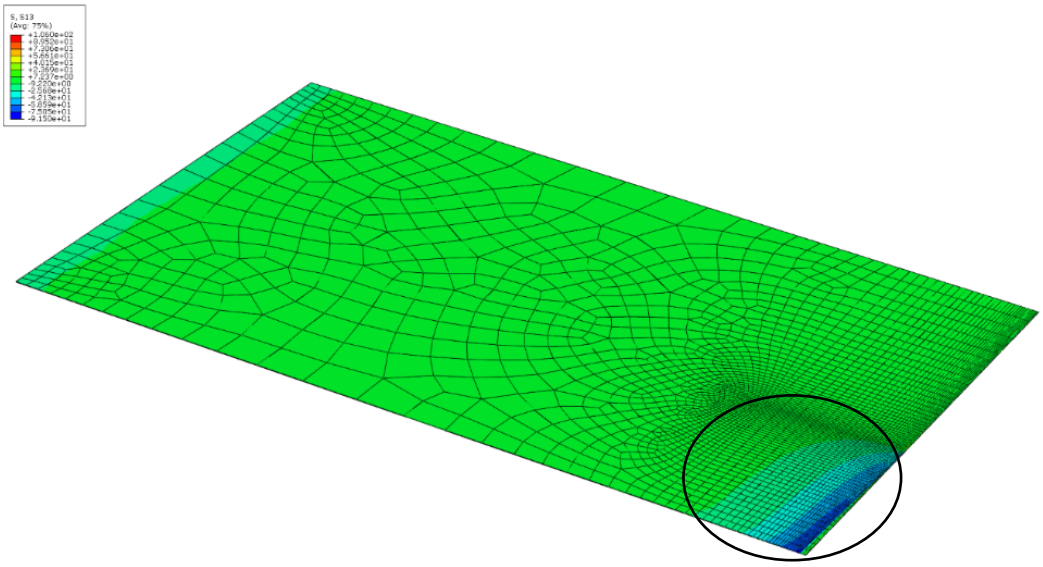

Figure 6.73 Shear stress distribution in interface adhesive layer of FEM of 6-SKWRP-Sk-300 for crack length 0.4 (40mm)

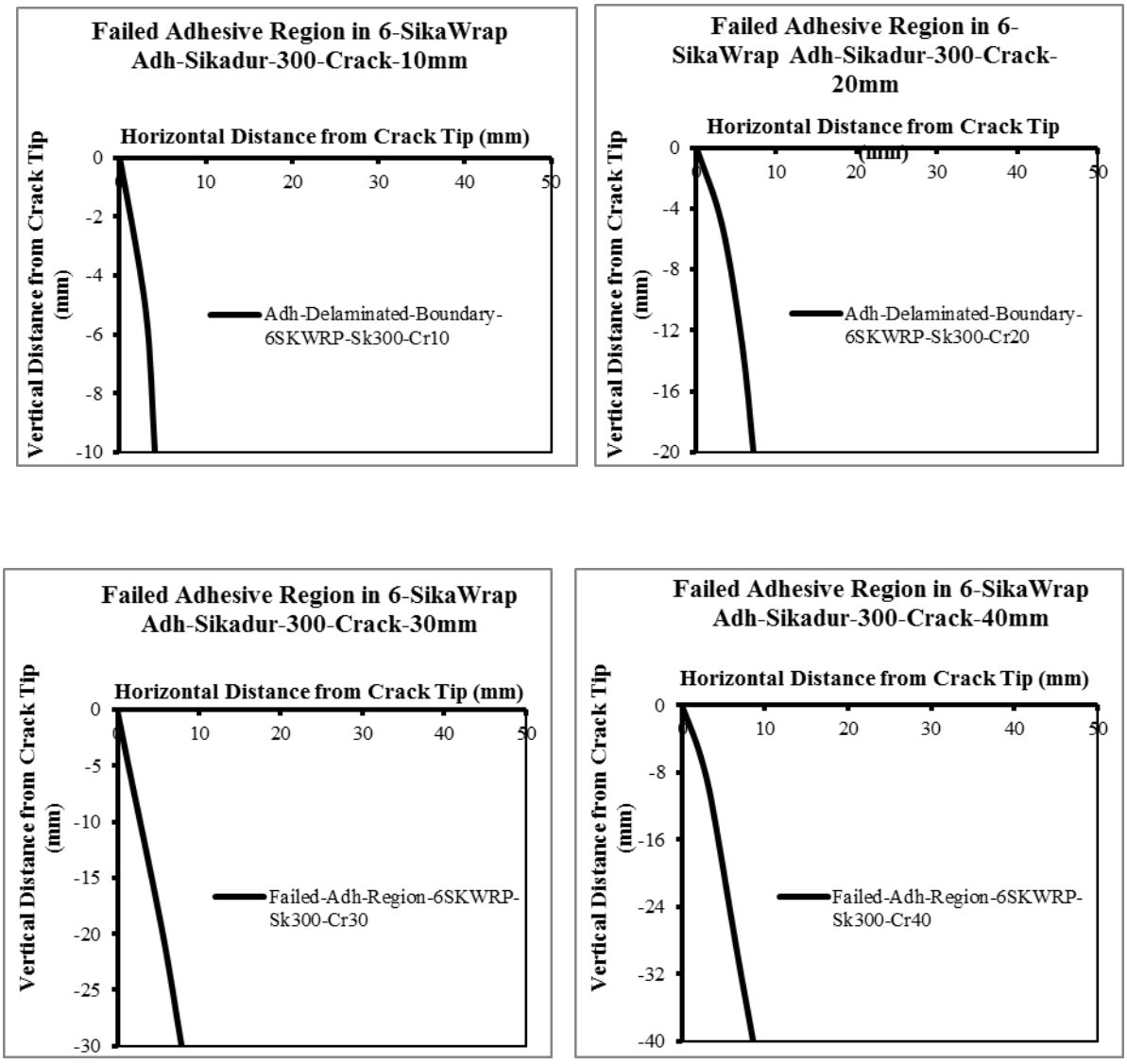

Figure 6.74 Failed regions in interface adhesive layer of FEM of 6-SKWRP-Sk-300 in its four crack lengths; 10mm, 20mm, 30mm and 40mm (a/b = 0.1, 0.2, 0.3 and 0.4)

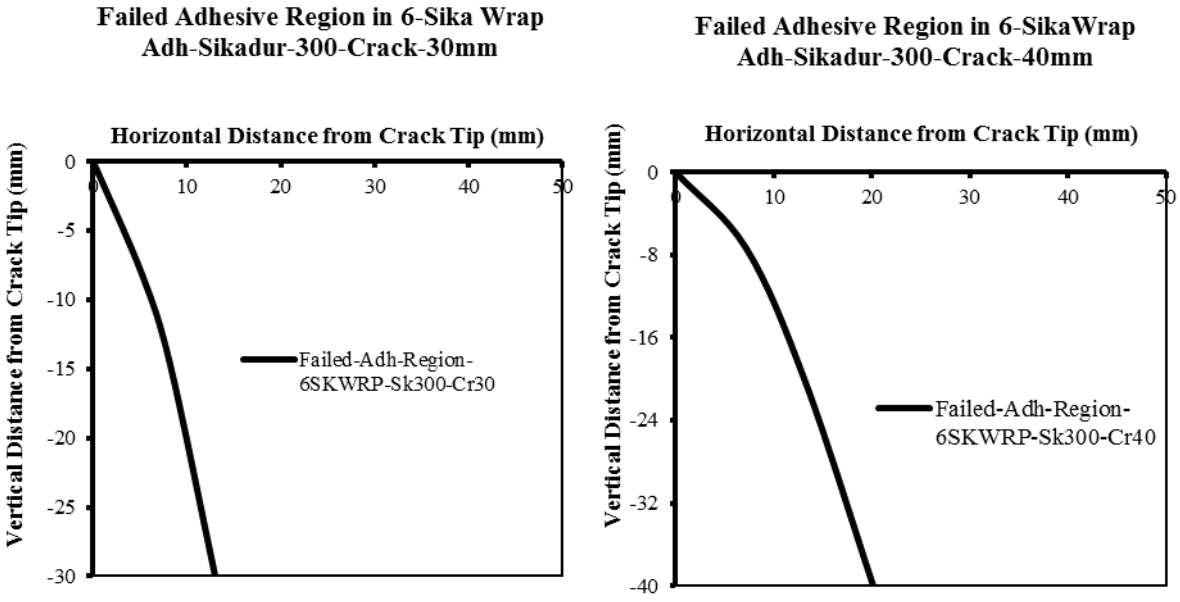

Figure 6.75 Failed adhesive regions in the interface adhesive layer of FEM of 6-SKWRP-Sk-300 in its crack lengths of 30mm and 40mm (a/b = 0.3 and 0.4) after convergence

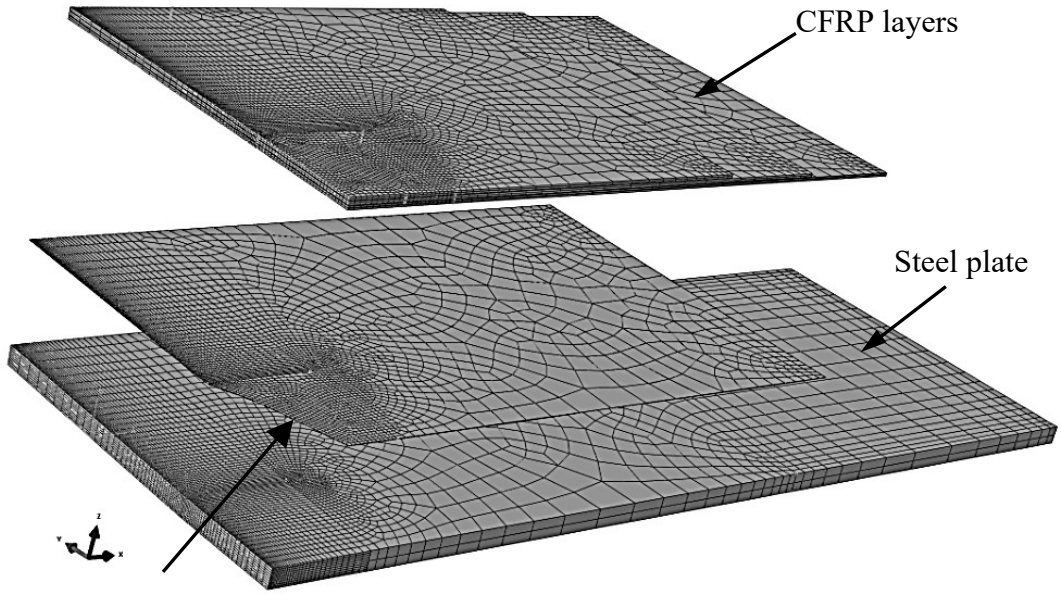

Figure 6.76 Interface adhesive layer with failed region removed in the FEM of 6-SKWRP-Sk-300.in crack length 30mm (a/b = 0.3) after convergence

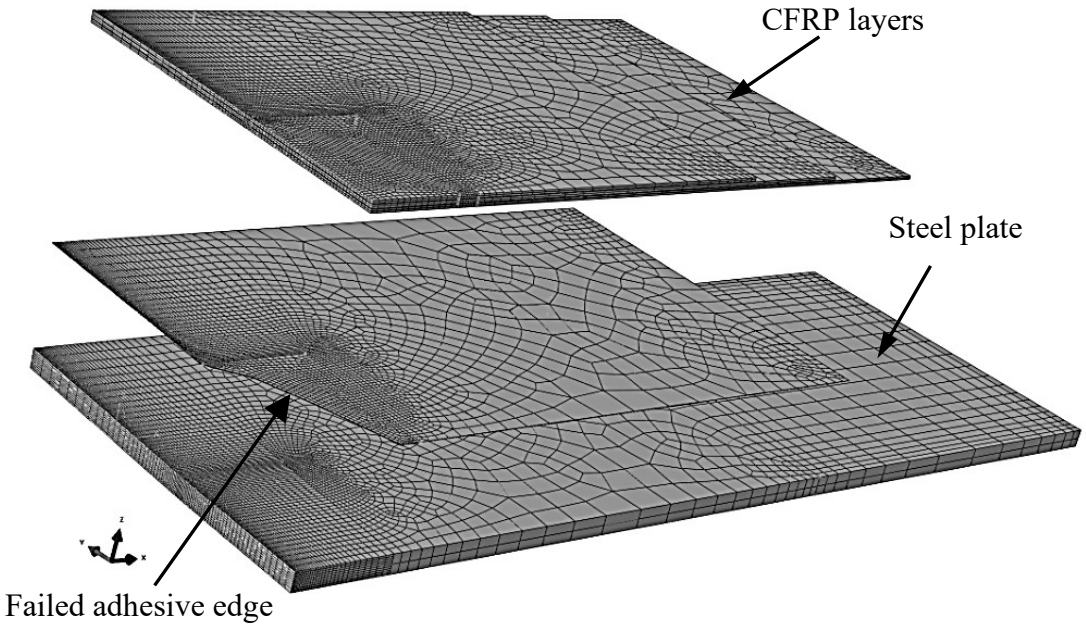

Figure 6.77 Interface adhesive layer with failed region removed in the FEM of 6-SKWRP-Sk-300.in crack length 40mm (a/b = 0.4) after convergence

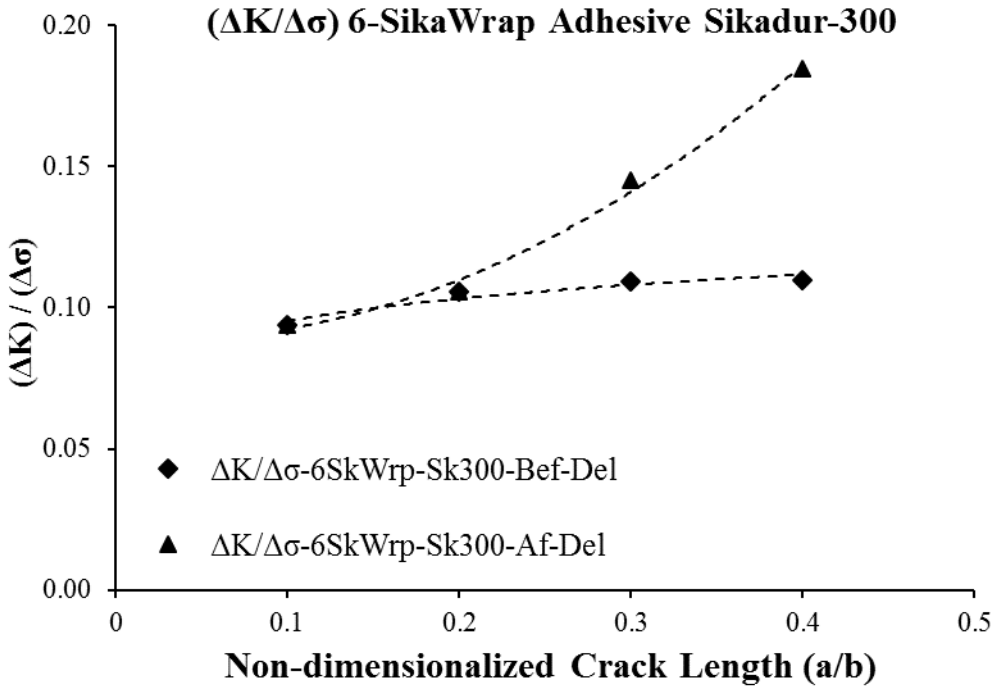

Figure 6.78 ΔK/Δσ variation with non-dimensionalized crack length obtained from FEA of 6-SKWRP-Sk-300

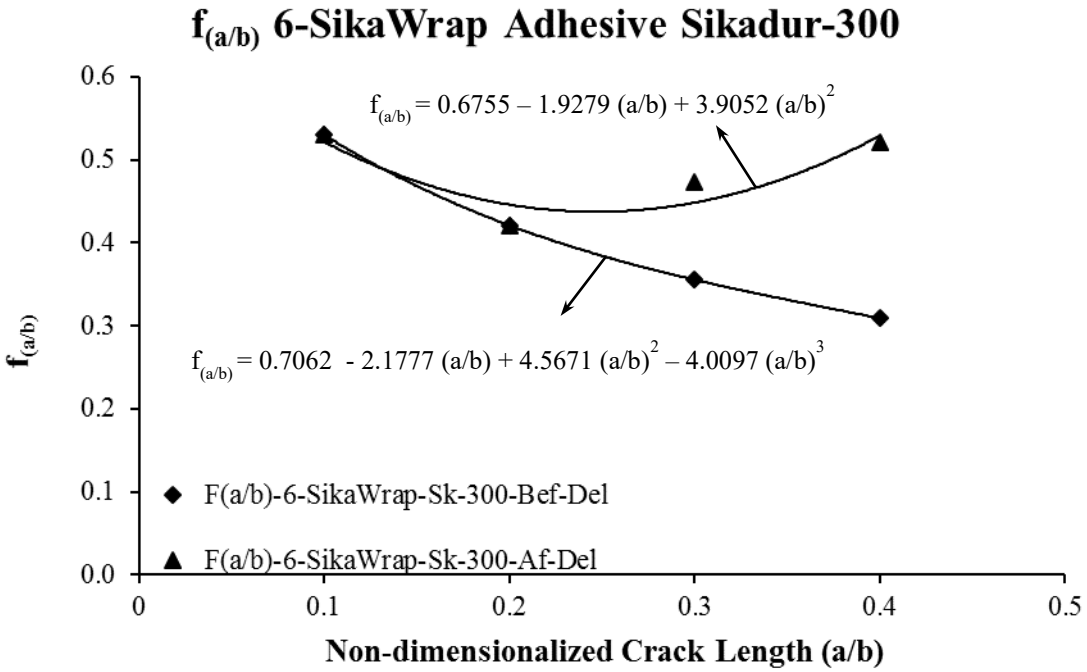

Figure 6.79 Geometric factor $f_{(a/b)}$ variation with non-dimensionalized crack length developed from SIF results of 6-SKWRP-Sk-300

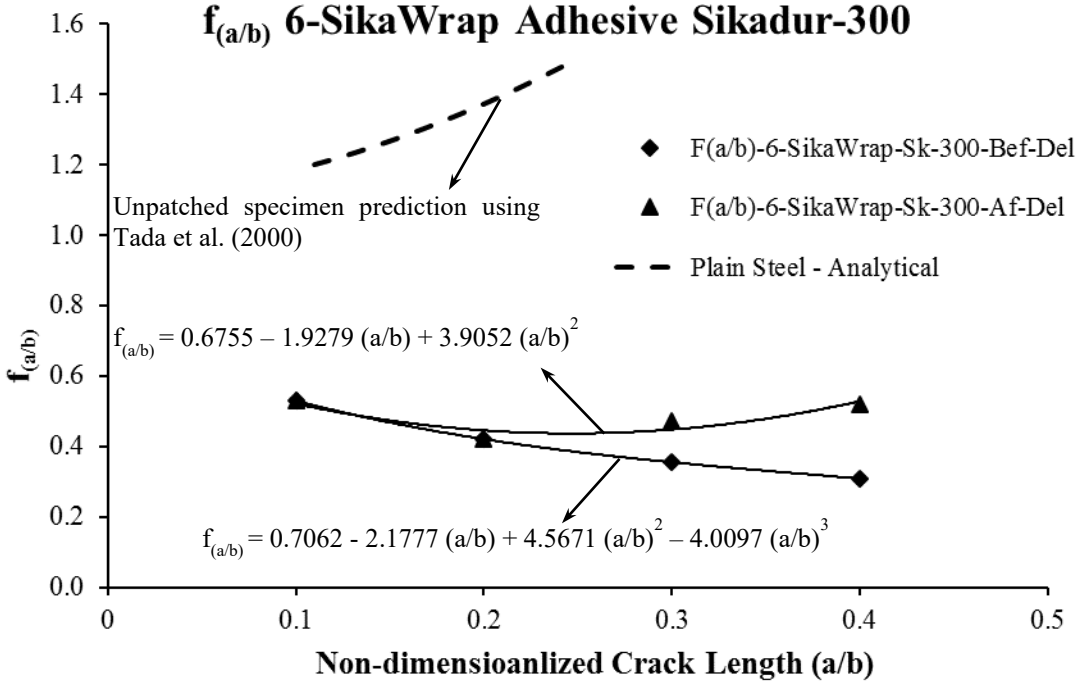

Figure 6.80 Geometric factor $f_{(a/b)}$ variation with non-dimensionalized crack length developed from SIF results of 6-SKWRP-Sk-300 including plain specimen

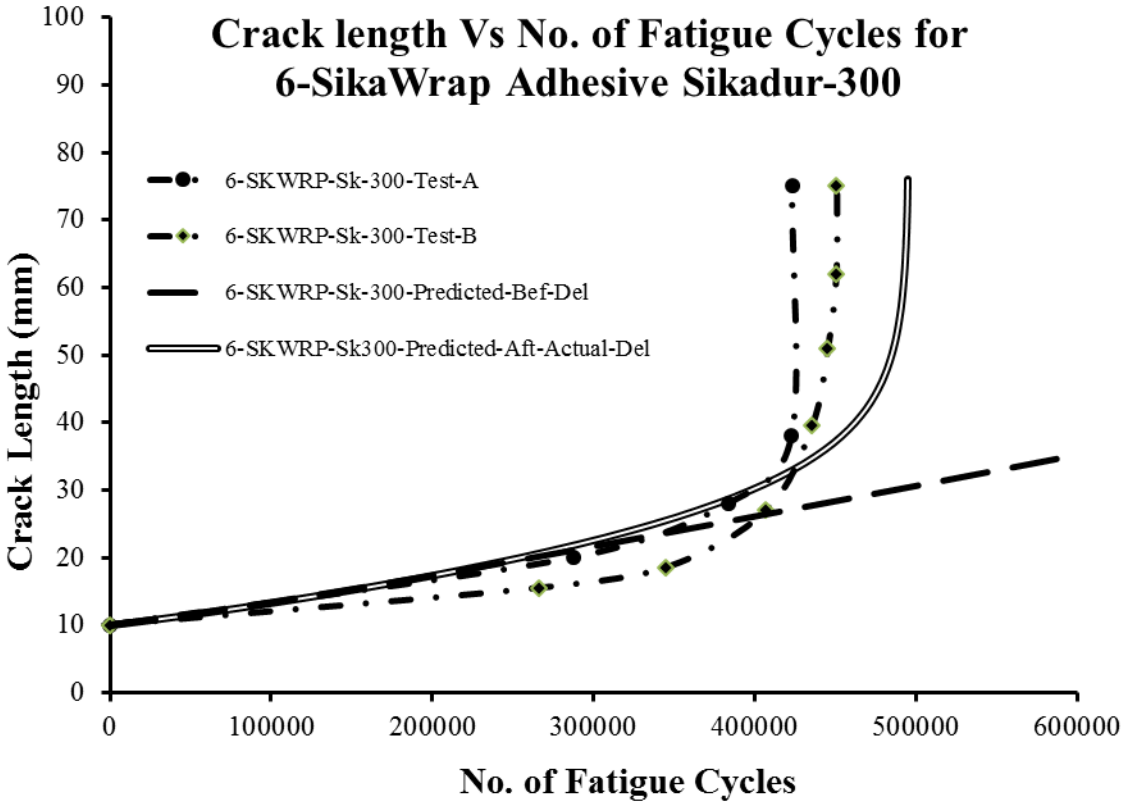

Figure 6.81 Predicted crack length versus number of fatigue cycles for 6-SKWRP-Sk-300

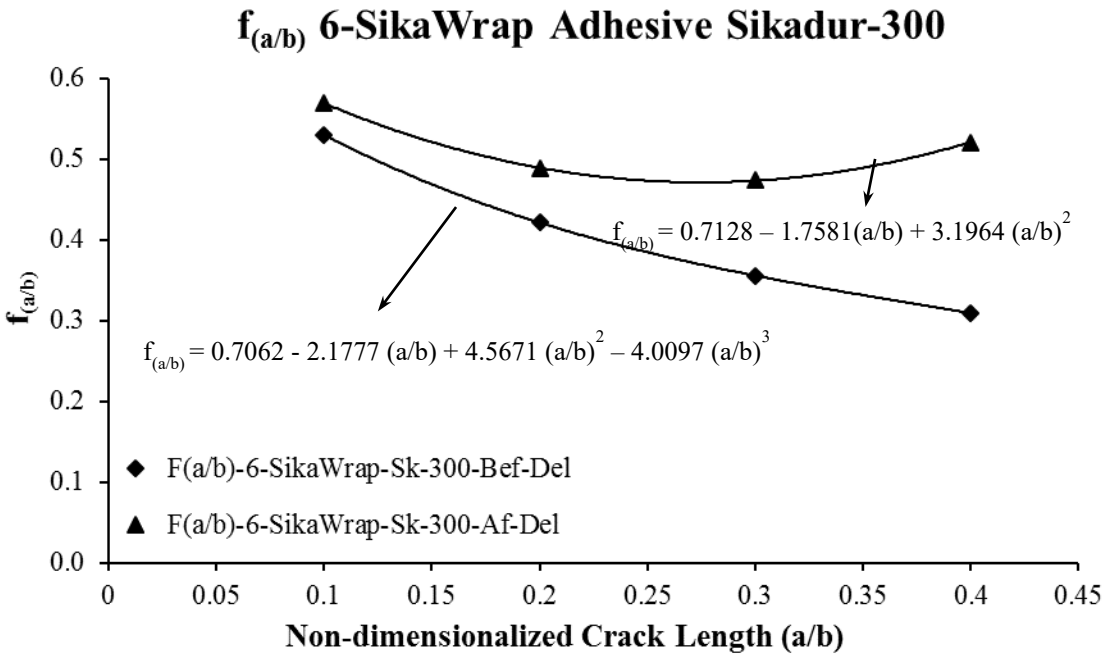

Figure 6.82 $f_{(a/b)}$ variation with non-dimensionalized crack length developed from SIF results of 6-SKWRP-Sk-300 with provided delamination

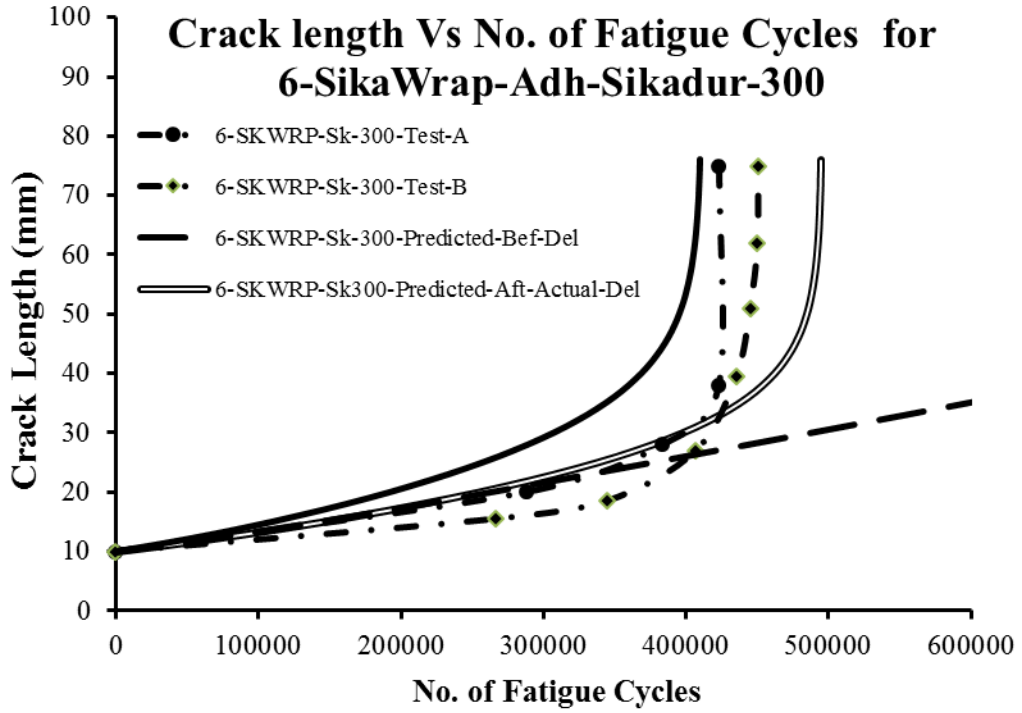

Figure 6.83 Predicted crack length versus number of fatigue cycles for 6-SKWRP Adhesive-Skidur-300 including the provided delamination case

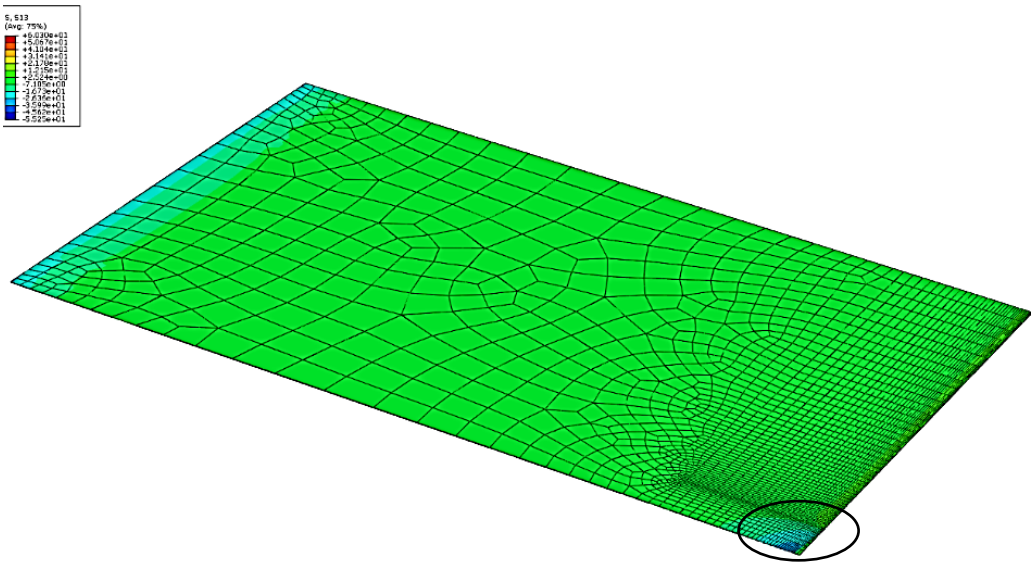

Figure 6.84 Shear stress distribution in interface adhesive layer of FEM of 9-SKWRP-Sk-300 for crack length 0.1 (10mm)

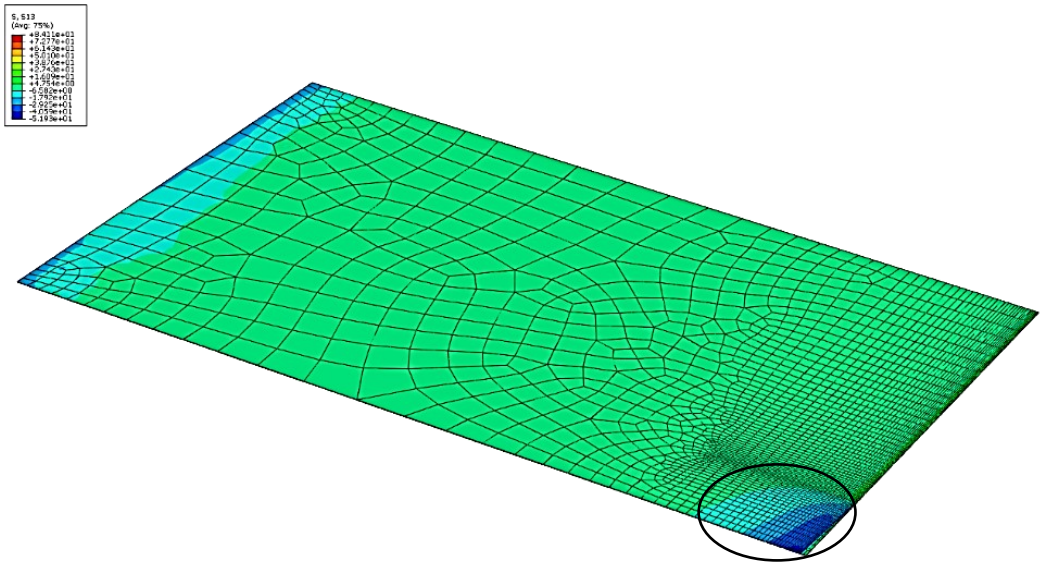

Figure 6.85 Shear stress distribution in interface adhesive layer of FEM of 9-SKWRP-Sk-300 for crack length 0.2 (20mm)

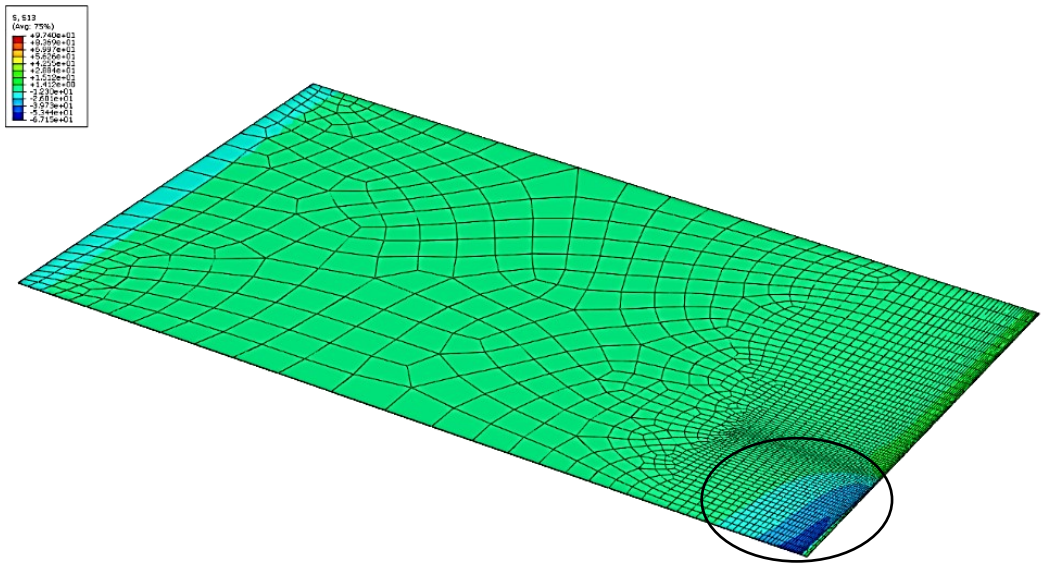

Figure 6.86 Shear stress distribution in interface adhesive layer of FEM of 9-SKWRP-Sk-300 for crack length 0.3 (30mm)

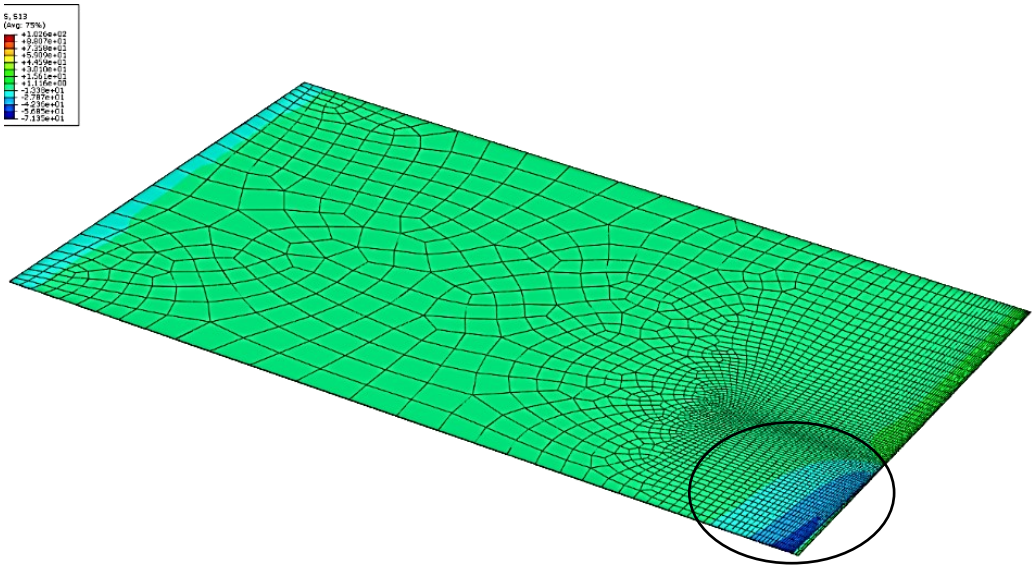

Figure 6.87 Shear stress distribution in interface adhesive layer of FEM of 9-SKWRP-Sk-300 for crack length 0.35 (35mm)

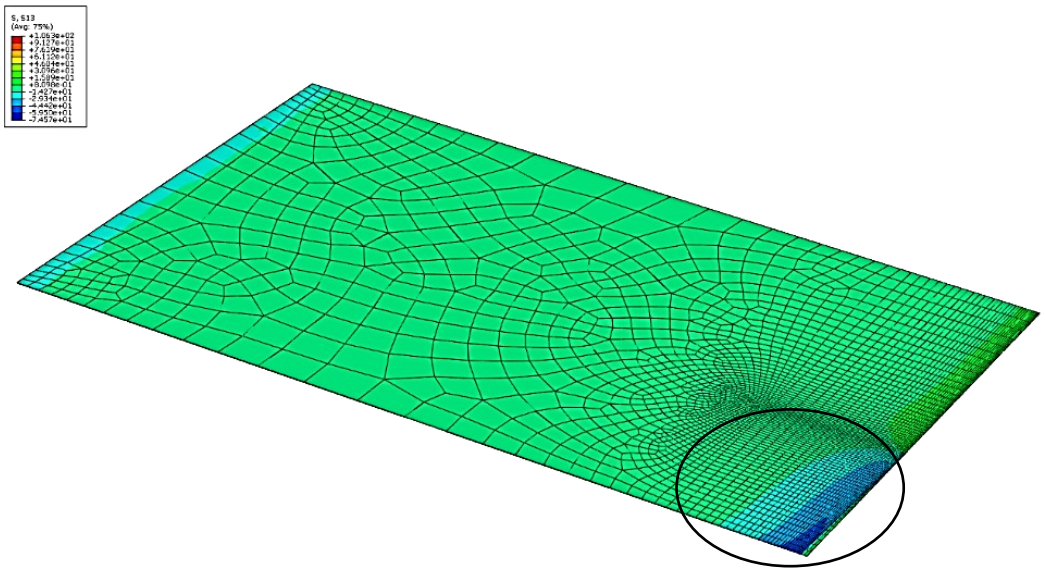

Figure 6.88 Shear stress distribution in interface adhesive layer of FEM of 9-SKWRP-Sk-300 for crack length 0.4 (40mm)

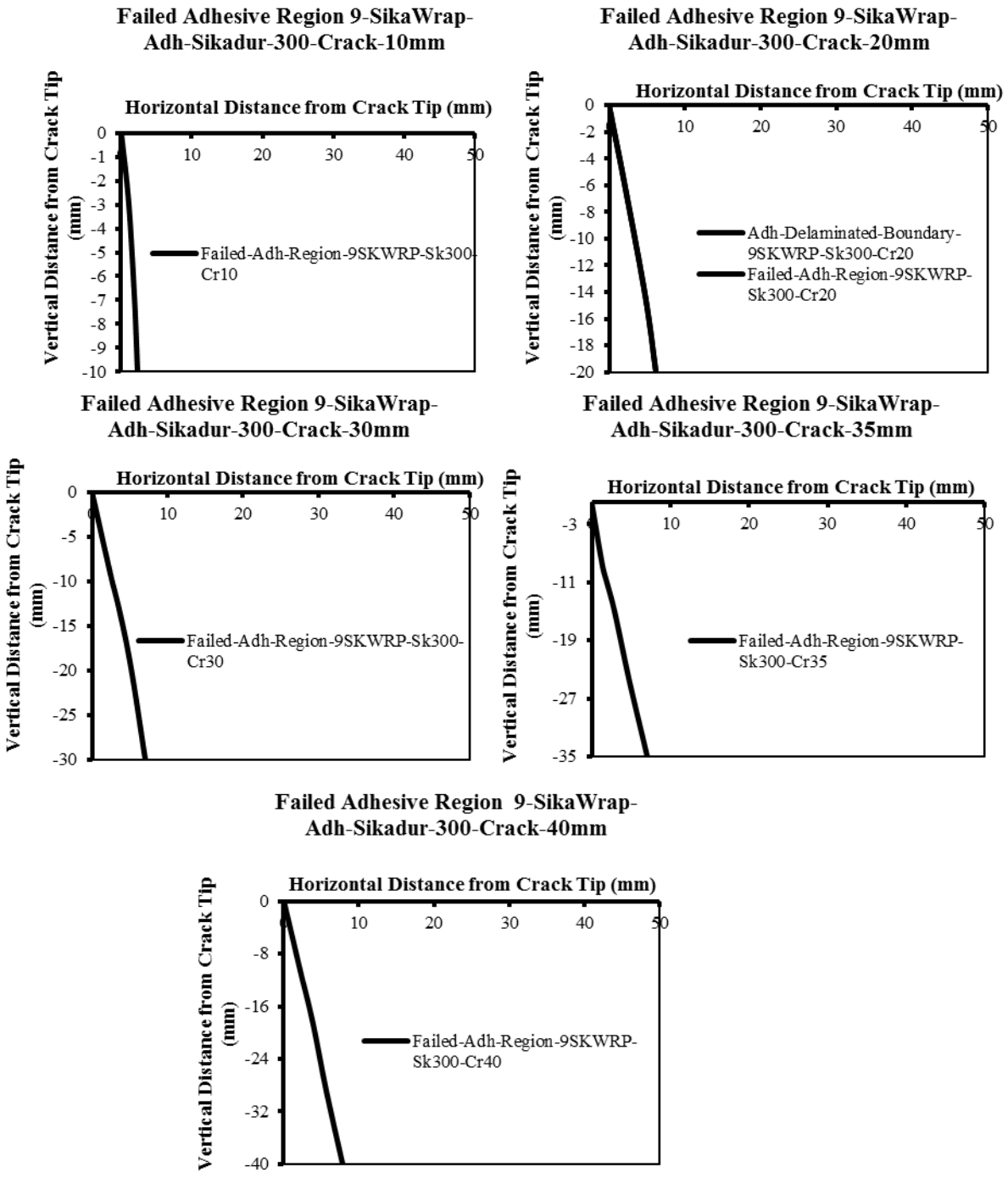

Figure 6.89 Failed regions in interface adhesive layer in FEM of 9-SKWRP-Sk-300 in its five crack lengths; 10mm, 20mm, 30mm, 35mm, 40mm (a/b = 0.1, 0.2, 0.3, 0.35 and 0.4)

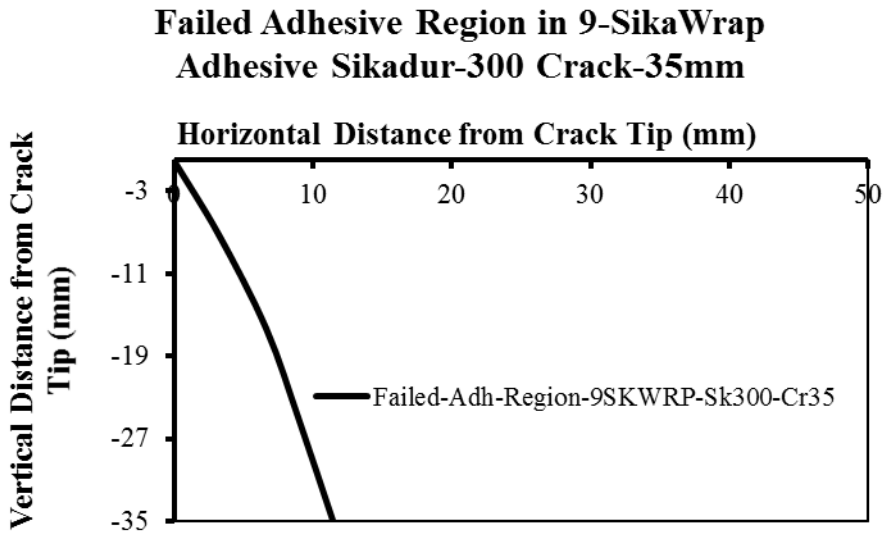

Figure 6.90 Failed adhesive regions in interface adhesive layer in FEM of 9-SKWRP-Sk-300 in its crack length of 0.35 (35mm) after convergence

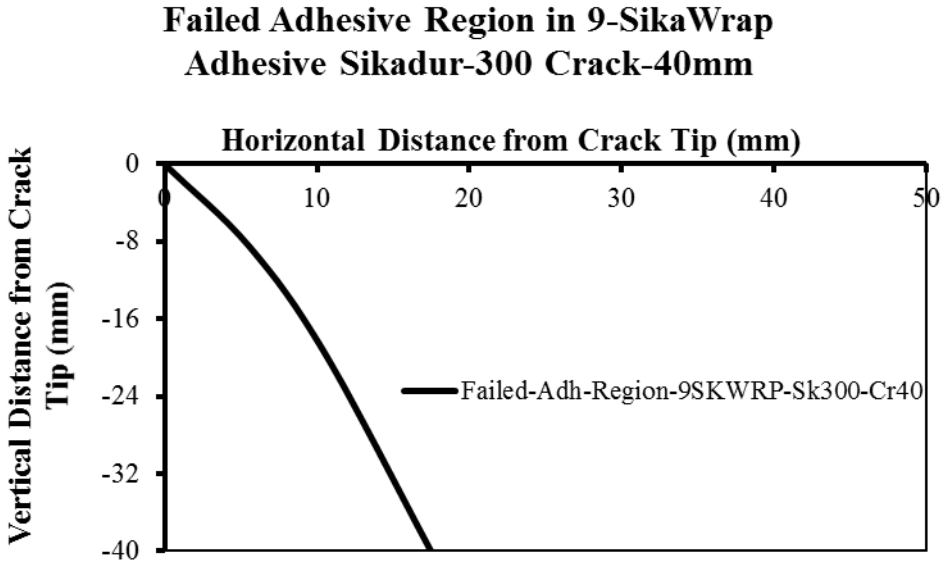

Figure 6.91 Failed adhesive regions in interface adhesive layer in FEM of 9-SKWRP-Sk-300 in its crack length of 0.40 (40mm) after convergence

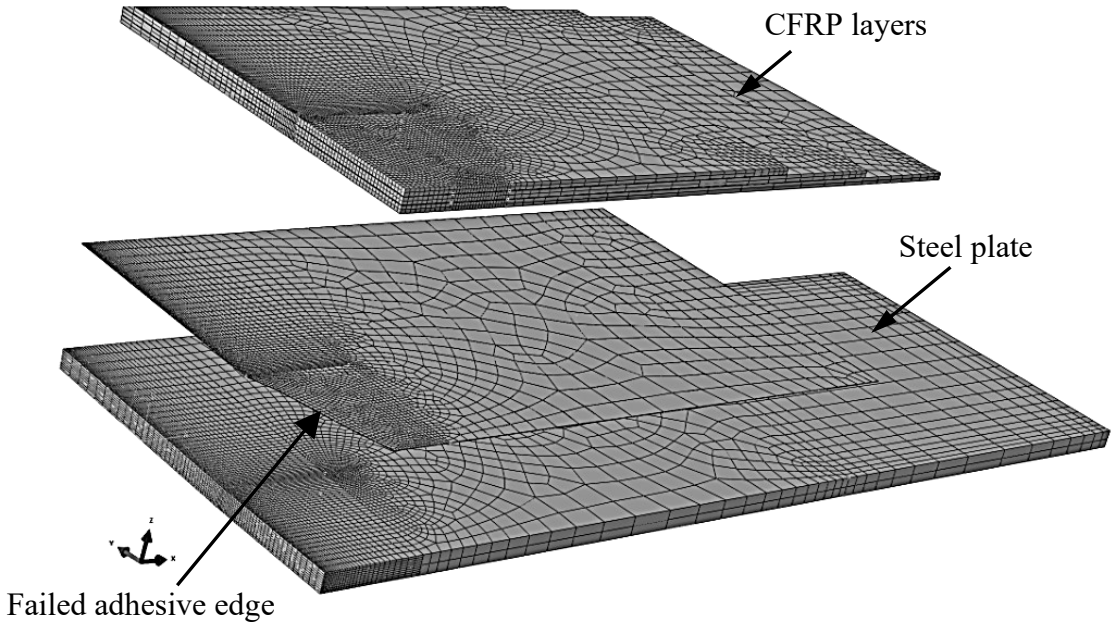

Figure 6.92 Interface adhesive layer with its failed region removed in FEM of 9-SKWRP-Sk-300 in its crack length of 35mm (0.35) after convergence

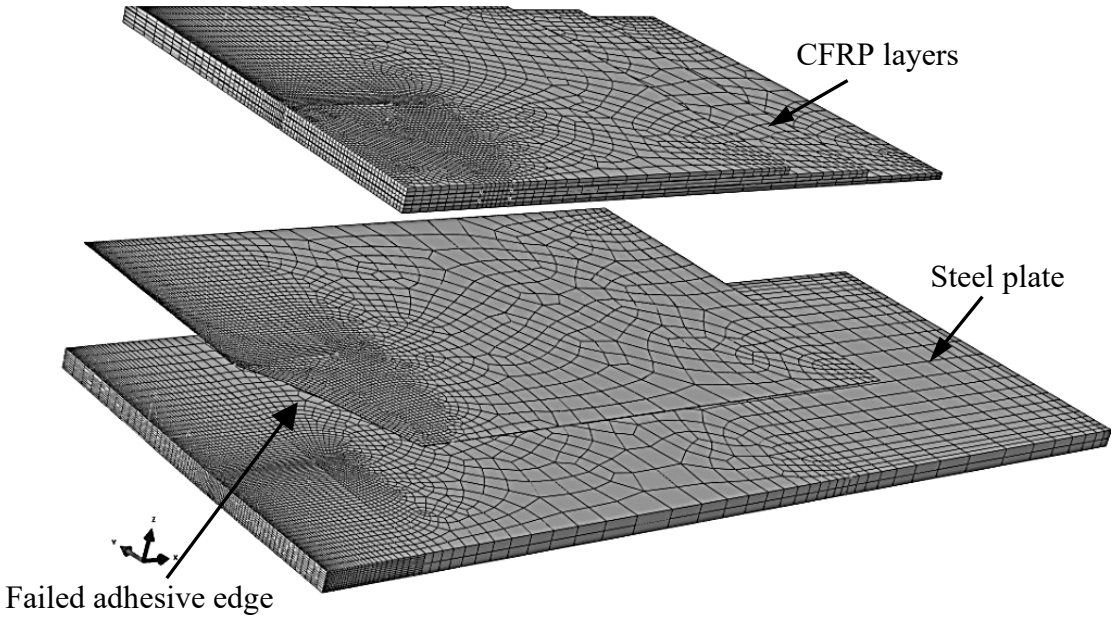

Figure 6.93 Interface adhesive layer with its failed region removed in FEM of 9-SKWRP-Sk-300 in its crack length of 40mm (0.40) after convergence

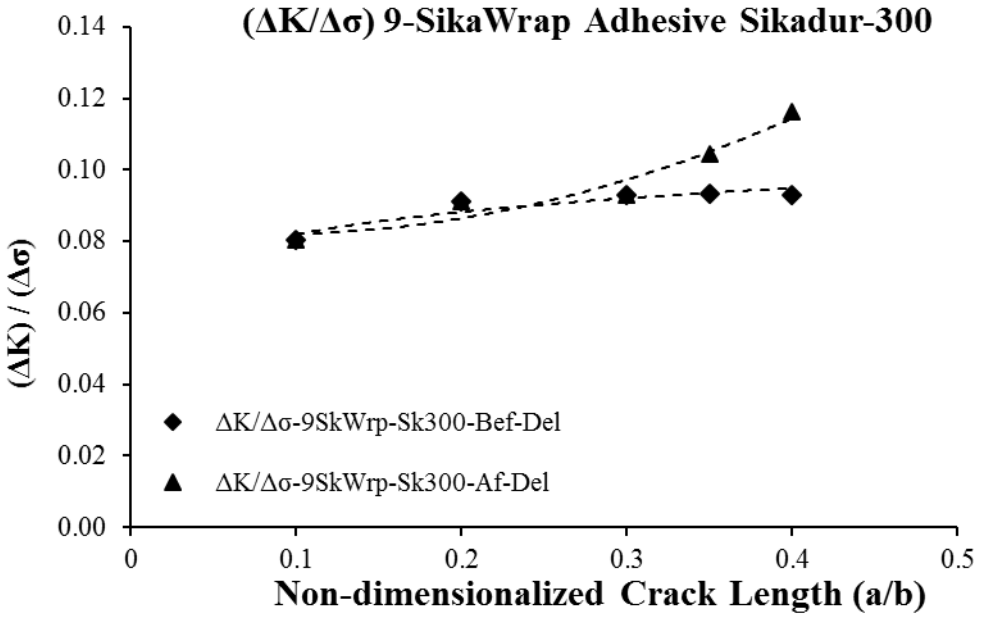

Figure 6.94 ΔK/Δσ variation with non-dimensionalized crack length obtained from FEA of 9-SKWRP-Sk-300

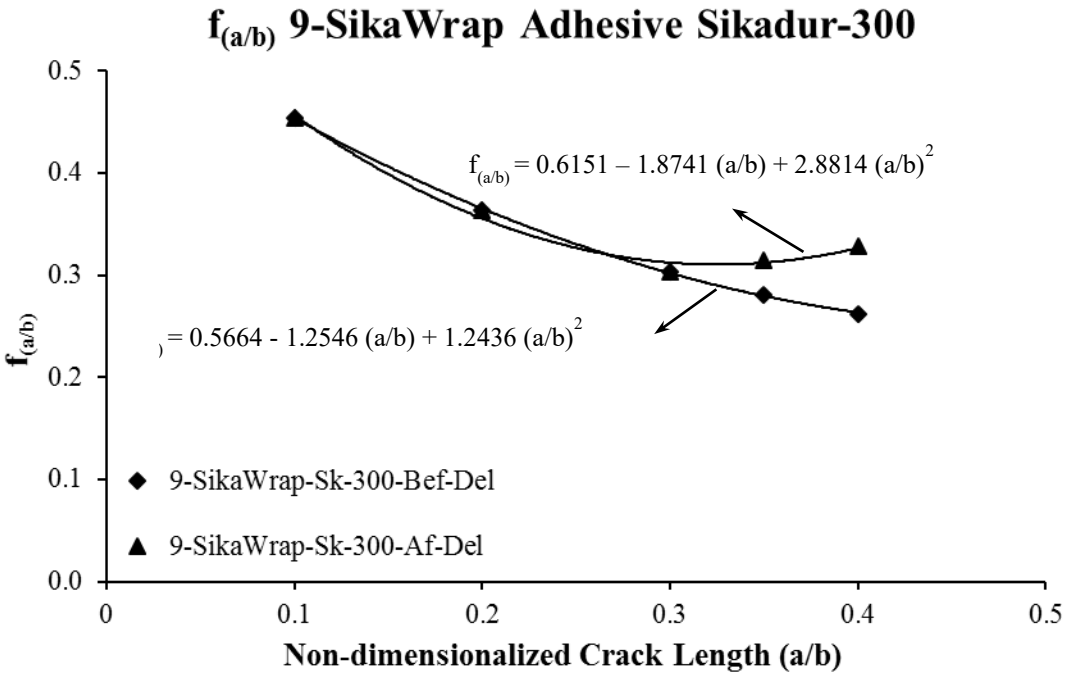

Figure 6.95 Geometric factor $f_{(a/b)}$ variation with non-dimensionalized crack length developed from SIF results of 9-SKWRP-Sk-300

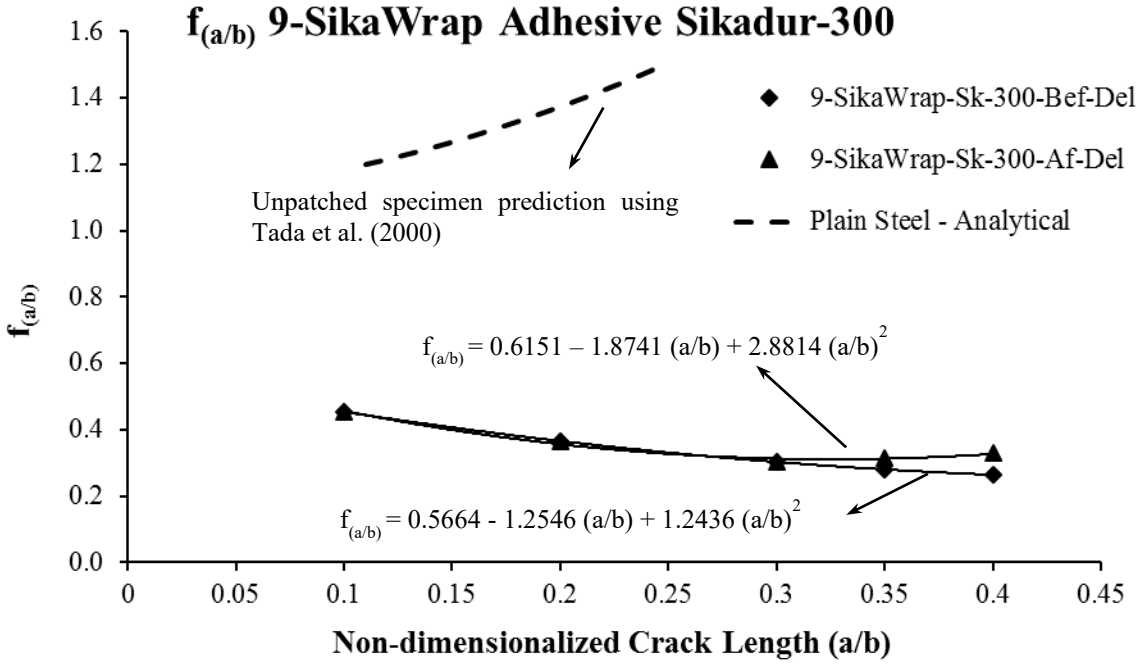

Figure 6.96 Geometric factor $f_{(a/b)}$ variation with non-dimensionalized crack length developed from SIF results of 9-SKWRP-Sk-300 including plain specimen

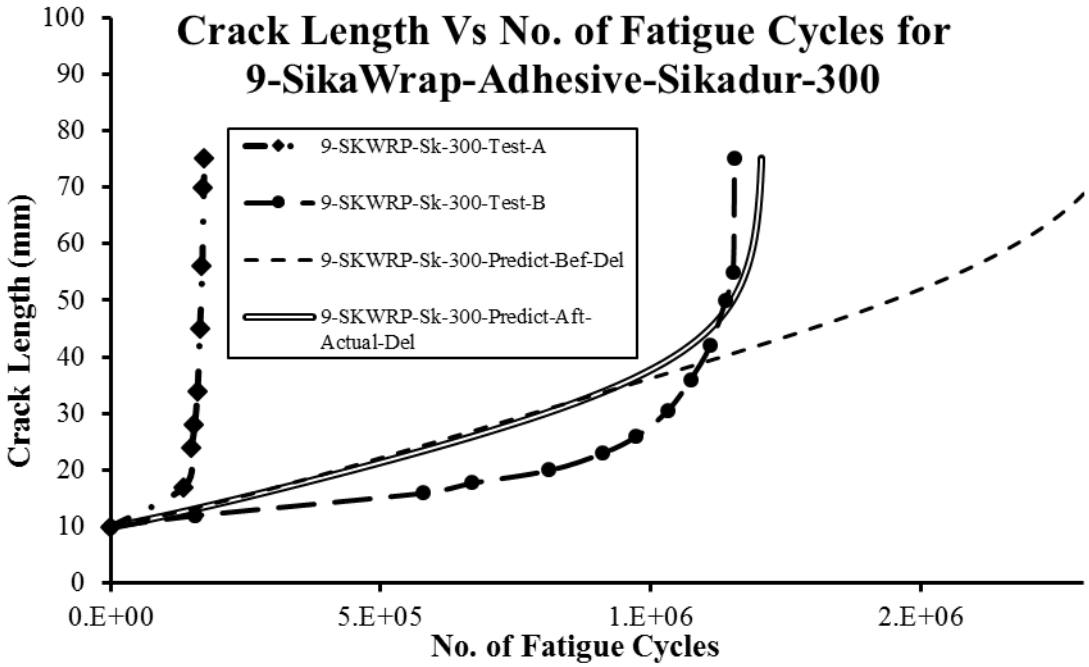

Figure 6.97 Predicted crack length versus number of fatigue cycles for 9-SKWRP-Sk-300

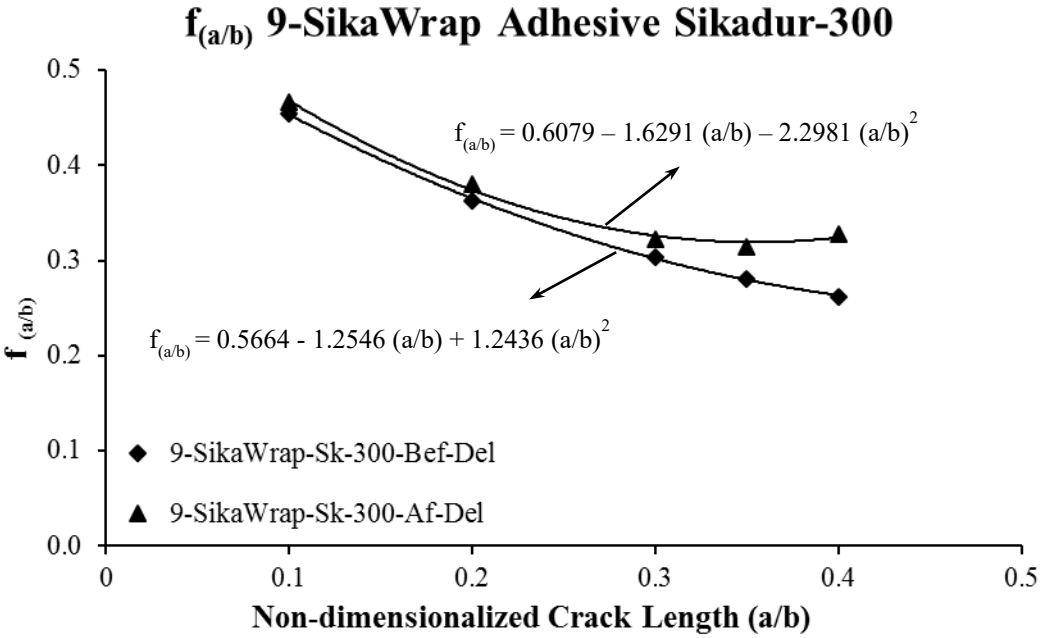

Figure 6.98 $f_{(a/b)}$ variation with non-dimensionalized crack length developed from SIF results of 9-SKWRP-Sk-300 with the provided delamination

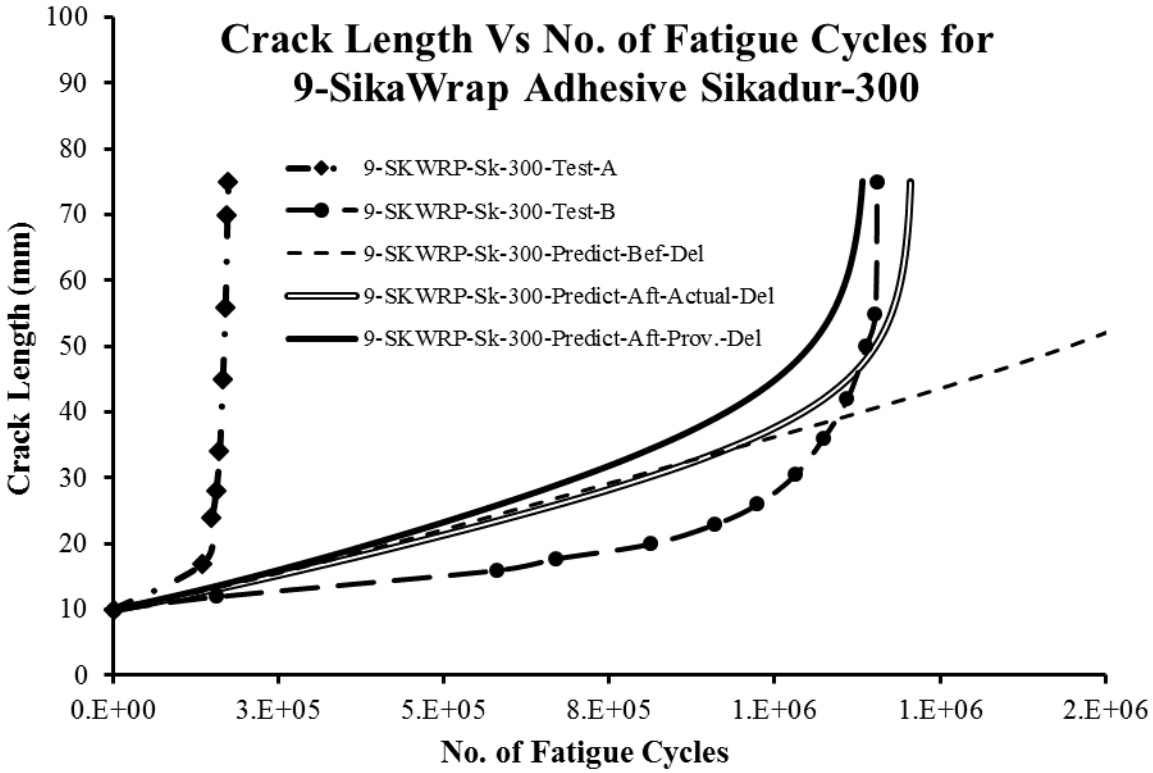

Figure 6.99 Predicted crack length versus number of fatigue cycles for 9-SKWRP-Sk-300 including the additional provided delamination case

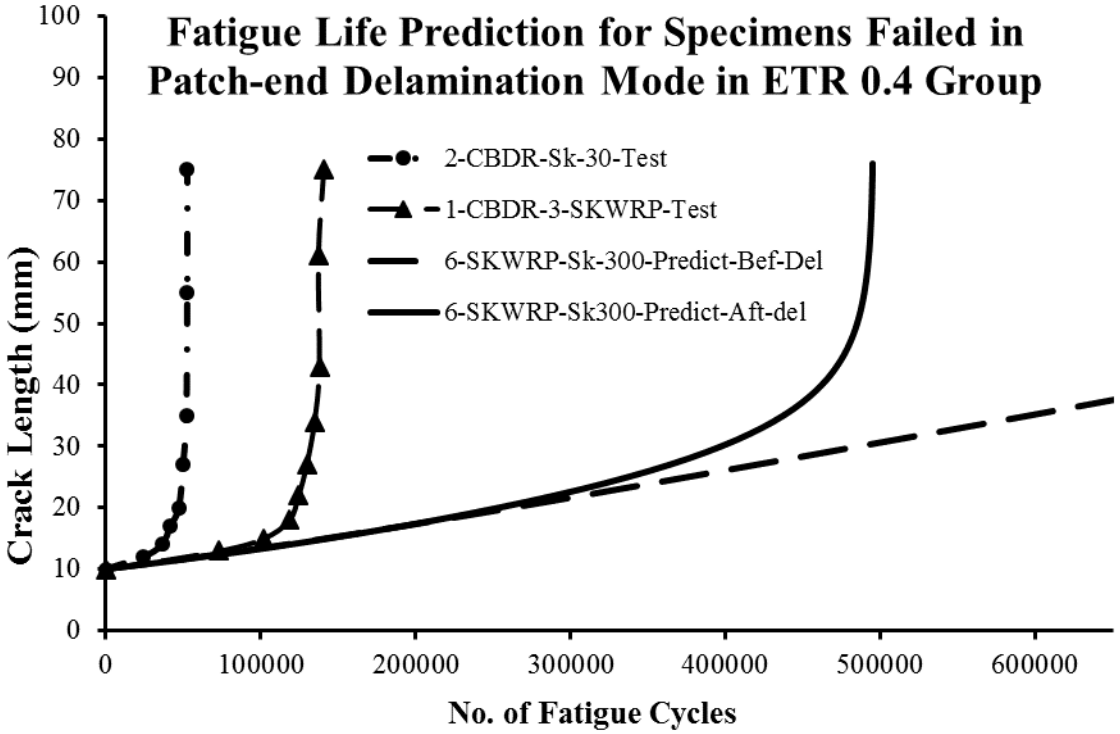

Figure 6.100 Predicted crack length versus number of fatigue cycles for the specimens of ETR 0.4 group failed in patch-end delamination mode

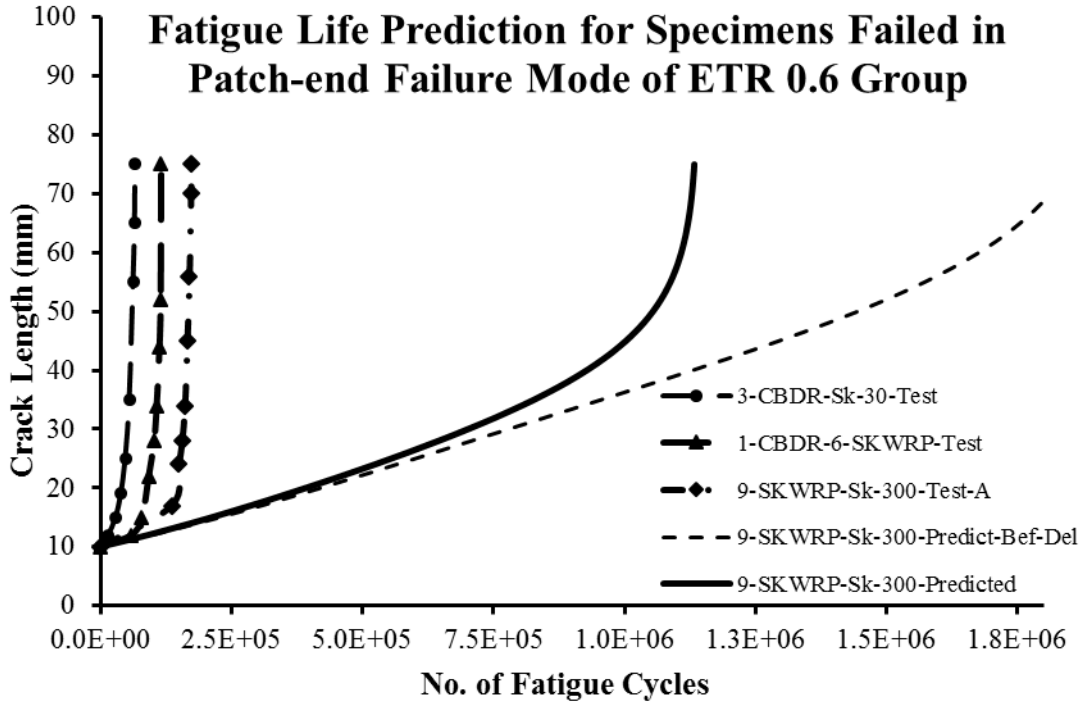

Figure 6.101 Predicted crack length versus number of fatigue cycles for the specimens of ETR 0.6 group failed in patch-end delamination mode

7. Parametric Study

7.1 Introduction and back ground

Previous research works have shown that under fatigue loading, FRP patch delamination was the governing failure mode of cracked or un-cracked metallic plates (specifically steel) with bonded FRP patches (Alawi and Saleh 1992, Schubbe and Mall 1999a, Colombi et al. 2003a, Lenwari et al. 2006, Papanikos et al. 2007, Taljsten et al. 2009, Bocciarelli et al. 2009, Liu et al. 2009, Kennedy and Cheng 1998, Ahmed Al-Shawaf 2011, Holden 2012, Mobeen et al. 2012, Mobeen and Cheng 2015). The same failure mode was also observed in the experimental phase of current testing program, in which all specimens were failed in progressive patch delamination mode, from the patch-steel interface (test results have already been presented in detail in chapter 5).

It has also been shown in chapters 3 and 4 that both the geometric and material properties of adhesive and the FRP (or CFRP) greatly affects the interface stresses that can lead to the patch delamination, and similar conclusions have also been achieved in several other research works (Madani et al. 2008, Ahmad Al-Shawaf 2011). On the other hand, the use of bonded FRP is growing fast in practical engineering applications, including repair, strengthening and re-strengthening of small to large engineering structures because of its advantages over other methods and materials (section 1.3). Due to which there has also been an increase in the variety of commercially available FRP and adhesives, bearing different geometric and mechanical properties.

It has already been shown in chapter 6 that the fatigue life of CFRP repaired cracked steel plates can successfully be predicted using numerically developed geometric factors $f_{(a/b)}$, incorporating the impact of patch delamination through introduction of adhesive failure in the respective finite element analyses. Therefore, a numerical parametric study deemed suitable and equally important to evaluate geometric factors corresponding to available ranges of adhesive and FRP properties. The focus of current chapter was then intended towards development of the geometric factors, corresponding to various CFRP patches, bearing different adhesive and FRP properties, which are discussed below in detail.

7.2 Details of parameters selected for the parametric study

The parameters selected in the current parametric study included those which have already been found impacting the two main phenomena occurring during the fatigue loading and leading towards the failure of FRP bonded cracked metallic plates. Those two phenomena are the FRP patch delamination and the crack growth in the repaired plate. It has already been shown in chapter 3 that within identical ETR CFRP patches, modulus of elasticity of CFRP (E_{FRP}) does not affect the interface adhesive shear stress distribution near the crack or the SIF at the crack tip, if the adhesive shear stiffness (G_A /t_A) is kept constant. These would be affected when the patch ETR varied.

Similarly, it has also been shown in chapter 3 and 4 that within identical ETR CFRP repairs, adhesive shear stiffness (G_A/t_A) found to be the main parameter, affecting the near-crack adhesive shear stress distribution and the SIF at the crack tip. When the adhesive shear stress near the crack exceeds shear strength of the adhesive, it can cause patch delamination there, which can result in little release of restriction to the crack opening by the CFRP patch. Therefore, SIF at the crack tip could increase and further crack growth is expected. Therefore, main parameters selected in the current parametric study included patch ETR, adhesive shear stiffness (G_A/t_A) and adhesive shear strength. Advantage of using adhesive shear stiffness (G_A /t_A) is that it includes impact of both geometric and material properties, which covers properties of variety of commercially available adhesive as well as the variation of adhesive thickness due to different fabrication procedures. It is also important to mention that at some points in the current chapter, adhesive shear strength was non-dimensionalized with the applied far-field normal stress. The reason being that within an elastic analysis adhesive shear stress distribution around the crack is expected to be proportional to the applied far-filed stress. Therefore, adhesive failed regions (in shear) are also expected to be proportional to the applied far-filed stress.

Keeping in view the above discussion, test matrix was developed for the current parametric study and is shown in Table 7.1. The table shows that the specimen were arranged into three main groups of the patch ETR, and, within each ETR group, further discretization was made with the adhesive shear stiffness (G_A/t_A) parameter. For each specimen of any ETR group, with a given adhesive shear stiffness (G_A/t_A), further discretization was made using the adhesive shear strength (T) or the non-dimensionalized adhesive shear strength parameter

(τ_A/σ_o). The adhesive or CFRP properties, including elastic modulus, thickness and shear strengths, were selected from a range of commercially available CFRP and adhesives, except in some cases, in which the parameters were selected to achieve upper or lower bound of the study. Summarizing the test matrix for the parametric study, it was broadly divided into three ETR groups; 0.21, 0.42 and 0.63, and within each ETR group the specimen were differentiated with respect to four adhesive shear stiffness (G_A/t_A) of 0.1, 1.0, 10 and 20. For each specimen, four adhesive shear strengths (τ_A) were selected; 7.5 MPa, 15 MPa, 25 MPa and 35 MPa. These shear strengths were then non-dimensionalized by the applied maximum far-filed stress (σ_{max}) of 200 MPa, and the corresponding ratios (τ_A/σ_o) became 3.75 %, 7.5 %, 12.5 % and 17.5 %. It is also important to mention that the parametric study was carried out for the two more common cases of central cracked and edge cracked steel plates, under the far applied stresses of 200 MPa and 20 MPa, which were also the upper and lower stress limits of the applied stress range of 180 MPa in the experimental phase of research.

7.3 Methodology

Methodology used in developing the required geometric factors for the two crack locations, with varying patch parameters, was similar to that already described and demonstrated in sections 6.3 and 6.4. The procedure is again described here in detail in the subsequent sections of this chapter. Steel plate selected in this study for the edge crack case was similar to that used in sections 6.3 and 6.4, with dimensions 500 mm long x 100 mm wide x 9.5 mm thick, because results of its SIF and COD from finite element analysis (FEA) have already been validated in chapter 6. Plate dimensions selected for the central crack plate were 500 mm long x 200 mm wide x 9.5 mm thick, which were similar to the edge crack plate except that its width (2b) was double than the width of edge crack plate (b), because the crack length being doubled in it (2a). But the ratio of total crack length to total plate width remained same in the two cases, i.e. a/b in the edge crack case and 2a/2b in the central crack case. The edge cracked and the central cracked steel plates are schematically shown in Figures 7.1 and 7.2, respectively.

Four finite element models (FEM) of each specimen with varying crack lengths of 0.1, 0.2, 0.3 and 0.4 (10 mm, 20 mm, 30 mm and 40 mm) were analyzed and the resulting K_I at the

crack tip, as well as the interface adhesive shear stress distribution were extracted from the FEA results. Process of progressive patch delamination was carried out for each specimen of Table 7.1 by performing failure analysis of the interface adhesive layer around the crack, similar to that already carried out in sections 4.4 and 6.4. After achieving the adhesive failure convergence, K_I was again extracted from the FEA, which was expected to bear the impact of patch delamination or the adhesive failure. It is also important to mention that in the current parametric study if the adhesive removal criterion, as mentioned in section 4.2, for any FEM was not fulfilled after analyzing its failed adhesive region, then the delamination criterion was set to 0.5 % instead of the 1 %. It was carried out because it has shown to be providing better and conservative distribution of the geometric factor $f_{(a/b)}$ in chapter 6. In this way the impact of small adhesive failure region, less than 1%, could also be incorporated in the evaluation of the geometric factor $f_{(a/b)}$. To evaluate geometric factor $f_{(a/b)}$ of any specimen, the values of ΔK_I from the converged FEA were extracted for the four crack lengths (a/b); 0.1, 0.2, 0.3 and 0.4, and, these were non-dimensionalized by dividing with factor $\Delta\sigma\sqrt{(\pi a)}$ to achieve the desired geometric factor $f_{(a/b)}$. These geometric factors were then plotted with the non-dimensionalized crack length (a/b). Finally, the required continuous function of geometric factor $f_{(a/b)}$ was obtained by fitting a suitable polynomial function on the distribution of geometric factors, developed from the results of ΔK_I from FEA of the four crack length models. This procedure of obtaining $f_{(a/b)}$ was similar to that adopted in section 6.3 before.

7.4 Finite element analysis

Specimens with two different crack locations, were analyzed using ABAQUS finite element analysis code (version 6.10), including an edge cracked and a central cracked steel plate. FEA of these cracked plates was carried out, following the methodology described and demonstrated in sections 3.5, 4.2 and 6.4. One-quarter FEM of four non-dimensionalized crack lengths of 0.1, 0.2, 0.3 and 0.4 was developed for each specimen of Table 7.1. The dimensions of a typical one-quarter edge cracked steel plate FEM were 250 mm long x 100 mm wide x 4.75 mm thick. A typical FEM of an edge cracked specimen is also shown in Figure 7.3, highlighting the planes of symmetry in it. FEA of the central cracked plate was conducted similar to the edge cracked plate, except that three planes of symmetries were used,

instead of two, each plane passed through the center line of each side of the plate. Therefore, the FEM of central crack steel plate was one-eighth of the actual plate size. Dimensions of a typical one-eight model of central cracked steel plate were 250 mm long x 100 mm wide x 4.75 mm thick. A typical FEM of a central cracked specimen is also shown in Figure 7.4, highlighting the planes of symmetry.

Steps involved in the development of three-dimensional FEM, for the current parametric study, were similar to that described in detail in sections 3.5, 4.2 and 6.4. These are again briefly described in this chapter. Steel plate was provided with two distinct regions; a near-crack fine-meshed region and; a coarser-meshed remaining region. 20 nodes brick elements C3D20R were used to define the steel plate, adhesive and the CFRP layers. Crack tip singularity was achieved in the analysis by providing collapsed node elements surrounding the crack tip. Adhesive and CFRP layers were applied to the steel plate by imposing the identical displacement constraint to the two adjacent surfaces at all interfaces, as already described in detail in sections 3.5, 4.2 and 6.4. It simulated perfect bond between the two adjacent layers of different material.

Four FEM of each specimen of Table 7.1 were developed for four non-dimensionalized crack lengths of 0.1, 0.2, 0.3 and 0.4. FEA was performed for the far filed applied stresses of 200 MPa and 20 MPa, which were the σ_{max} and σ_{min} of selected fatigue loading. K_I was extracted from the FEA results and the ΔK_I was evaluated by performing the $K_{I\,max}$ - $K_{I\,min}$, which were the K_I corresponding to the applied σ_{max} and σ_{min}. To reduce the model size and analysis time only three layers of CFRP were applied to each side of the steel plate and the patch ETR was controlled by varying the CFRP layer's thickness (t_{FRP}) or modulus (E_{FRP}). Progressive failure of adhesive interface layer or the progressive patch delamination was introduced in FEA of each specimen of Table 7.1, corresponding to the selected adhesive shear strength. The iterative process of progressive removal of failed adhesive region and the re-analysis continued until the convergence achieved, as per the convergence criteria mentioned in section 4.2. Figure 7.5 shows a typical three-layered specimen used in the parametric study with its interface adhesive layer reduced after removal of the failed region.

7.5 Results of finite element analysis and corresponding geometric factors $f_{(a/b)}$

As already defined in section 7.1 that the focus of current parametric study is the development of geometric factors $f_{(a/b)}$, corresponding to different patch parameters and including the impact of patch delamination. The procedure of developing the geometric factor has already been described and demonstrated in chapter 6, while predicting the fatigue life of the tested specimens. Similar procedure has also been summarized in section 7.3 and the same is followed in the current chapter. Results of FEA of the parametric study are presented in the later part of the chapter with respect to the two crack locations; edge crack and central crack. Within each crack case, the K_I variation, before and after the introduction of patch delamination was studied. It is also important to mention that due to variation of K_I through the steel plate thickness the K_I values close to the CFRP patched face have been used to develop the $f_{(a/b)}$ functions. The SIF (K_I) for this location have already been found successful in predicting the fatigue life of the tested specimens in chapter 6 and these were also found to be closely correlating with Tada et al. (2000) in section 6.4.1. The K_I values were extracted from results of the finite element analysis of each specimen, both before and after the introduction of patch delamination. The geometric factors $f_{(a/b)}$ were evaluated from the results of ΔK_I, obtained from FEA and following the methodology of section 7.3.

7.5.1 Edge cracked plate with patch ETR 0.21 before delamination

The stress intensity factors, K_I, for the edge cracked specimens of Table 7.1, with patch ETR of 0.21, were extracted from the results of FEA of the four-crack models of each specimen. These K_I values were corresponding to the applied σ_{max} and σ_{min} and these were extracted before the introduction of patch delamination in the FEA. The $K_{I\,max}$ for the specimens of ETR 0.21, is plotted with the non-dimensionalized crack length (a/b) in Figure 7.6. It can be noted in Figure 7.6 that the ETR, modulus of elasticity of the CFRP (E_{FRP}), and its thickness (t_{FRP}), were identical in all specimens. The only difference within these specimens was the adhesive shear stiffness (G_A/t_A), which made the difference in the SIF variation between these specimens. Figure 7.6 shows that the K_I was higher in the specimen having smaller adhesive G_A/t_A and lower in the specimen with higher G_A/t_A and the difference increases with the crack length. Similar variations and conclusion were also obtained in section 3.4.3.4 and shown in

Figure 3.25, for identical ETR specimens. Another important thing that can be noted from the Figure 7.6 that the SIF variation for the specimens, with adhesive G_A /t_A less than 1, fall closer to each other. Similarly, the SIF variation for the other two specimens, with adhesive G_A /t_A greater than 10, also fall close to each other. It shows that the SIF variation was much sensitive to the adhesive G_A /t_A within the range from 1 to 10, but it was not much affected by further increase or decrease in the adhesive G_A /t_A, either above 10 or below 1. It was also not expected to have the G_A/t_A values much higher than 20 or much below 0.25 because these were already selected to be practical upper and lower bounds. Therefore, it was expected to be difficult to have more flexible or further stiffer adhesive beyond these bounds.

7.5.2 Edge cracked plate with patch ETR 0.21 after delamination

The above discussed SIF variation was based upon the situation before any adhesive failure or the CFRP patch delamination was introduced in the FEA. After introduction of patch delamination in the analysis the comparison between different repairs could not be simply based upon the patch ETR or the adhesive G_A /t_A. The comparison could become more complex because of its dependency on adhesive shear strength (τ), in addition to the adhesive G_A/t_A. Therefore, to avoid much complexity in the further comparative analysis, the SIF variation and the corresponding geometric factor $f_{(a/b)}$ are presented and discussed separately for the specimens with identical ETR and adhesive G_A/t_A, but with varying adhesive shear strengths.

7.5.2.1 Edge cracked plate with patch ETR 0.21 and adhesive G_A /t_A of 20

Figure 7.7 shows the $K_{I\,max}$ variation in the edge cracked specimens, with patch ETR 0.21 and adhesive G_A /t_A of 20, before and after the introduction of patch delamination in the analysis. Figure 7.7 shows that within the group of specimens having identical ETR and identical adhesive G_A/t_A, the K_{Imax} variation was different in each specimen after the introduction of the patch delamination. The K_{Imax} variation varied with the adhesive shear strength and it showed to be higher for weaker adhesive shear strength and vice versa. Most possible reason for getting such variation was expected to be because of variation in the failed and removed adhesive region around the crack in these specimens, which was more in the case of weaker

adhesive and less with stronger adhesive. It is also important to mention that the adhesive shear strengths shown in Figure 7.7 could also be non-dimensionalized using the applied far filed stress σ_o. Therefore, the shear strengths of 7.5 MPa, 15 MPa, 25 MPa and 35 MPa could be replaced with parameter τ/σ_o of 3.75 %, 7.5 %, 12.5 % and 17.5 %, respectively. Where τ is the adhesive shear strength and σ_o is the applied far filed maximum stress. ΔK_I was then evaluated for each specimen using the difference of K_{Imax} and $K_{Imin.}$ ΔK_I was further divided with applied stress range $\Delta\sigma$ to generalize it for any applied stress range and its variation with non-dimensionalized crack length (a/b) is shown in Figure 7.8.

The trend of variations of generalized ΔK_I shown in Figure 7.8 is similar to the trend of variation of the K_{Imax} already shown in Figure 7.7. The required geometric factor $f_{(a/b)}$ or the non-dimensionalized ΔK_I for each specimen was obtained by using Equation 6.2a and further dividing the generalized $\Delta K_I / \Delta\sigma$ obtained in Figure 7.8 with $\sqrt{(\pi a)}$. The resulting variation of the $f_{(a/b)}$ with non-dimensionalized crack length (a/b) is finally shown in Figure 7.9. In Figure 7.9 the $f_{(a/b)}$ of an unpatched edge cracked plate with uniform far filed applied stress is also shown for the reference, which was obtained using the Equation 3.12 provided by Tada et al. (2000) and is again reproduced below for convenience

$$f_{(a/b)} = 1.12 - 0.231\left(\frac{a}{b}\right) + 10.55\left(\frac{a}{b}\right)^2 - 21.72\left(\frac{a}{b}\right)^3 + 30.39\left(\frac{a}{b}\right)^4 \qquad 3.12$$

Figure 7.9 shows that the CFRP patch of ETR 0.2 with adhesive G_A / t_A of 20 was effective in reducing the $f_{(a/b)}$ of an unpatched steel plate by more than 100% before consideration of patch delamination. But after the patch delamination introduced in FEA, the $f_{(a/b)}$ increased with respect to the shear strength of adhesive in specimen. The variation of $f_{(a/b)}$ was, in turn, corresponded to the magnitude of adhesive shear failure around the crack. Figure 7.9 also shows that for the weakest adhesive shear strength of 7.5 MPa (or the lowest value of τ / σ_o of 3.5 %) the $f_{(a/b)}$ values after patch delamination, were found to be 11 % to 25 % below the lowest value of the $f_{(a/b)}$ of an unpatched plate. The polynomial functions for $f_{(a/b)}$ for different specimens was obtained by fitting suitable polynomial curve to the $f_{(a/b)}$ distributions, which are also shown in Figure 7.9. These $f_{(a/b)}$ functions are also reproduced below in equations 7.1 through 7.5, respectively for the un-delaminated patch, and the four cases of patch

delamination, corresponding to the four adhesive shear strengths ratios (τ/σ_o) of 3.75 %, 7.5 %, 12.5 % and 17.5 % . These strength ratios were also corresponded to the four adhesive shear strengths of 7.5 MPa, 15 MPa, 25 MPa and 35 MPa).

$$f_{(a/b)} = -4.5258\,(a/b)^3 + 5.0778\,(a/b)^2 - 2.3713\,(a/b) + 0.7446 \quad 7.1$$

$$f_{(a/b)} = 3.3848\,(a/b)^2 - 0.6198\,(a/b) + 0.8351 \quad 7.2$$

$$f_{(a/b)} = 2.6226\,(a/b)^2 - 0.5457\,(a/b) + 0.7523 \quad 7.3$$

$$f_{(a/b)} = 2.5908\,(a/b)^2 - 0.8723\,(a/b) + 0.6558 \quad 7.4$$

$$f_{(a/b)} = 2.9446\,(a/b)^2 - 1.3413\,(a/b) + 0.6568 \quad 7.5$$

Figure 7.9 highlighted the role of the adhesive shear strength (τ) on the resulting $f_{(a/b)}$ distribution, caused by the corresponding adhesive failures around the crack. These results would equally be applicable to any other form of failure occurred at the patch-plate interface around the crack, that results in patch delamination.

7.5.2.2 Edge cracked plate with patch ETR 0.21 and adhesive G_A/t_A of 10 after delamination

Procedure for obtaining the $f_{(a/b)}$ was repeated for the specimens of ETR 0.2 group with the adhesive shear stiffness (G_A/t_A) of 10, similar to that carried out for the specimens with adhesive G_A/t_A of 20. The resulting $K_{I\ max}$, $\Delta K_I/\Delta\sigma$ and the $f_{(a/b)}$ variations for the four adhesive shear strength ratios (τ/σ_o) of 3.75 %, 7.5 %, 12.5 % and 17.5 % (corresponded to the four adhesive shear strengths of 7.5 MPa, 15 MPa, 25 MPa and 35 MPa) are shown in Figures 7.10, 7.11 and 7.12 respectively. Comparing the K_{Imax} variation of Figure 7.10 with those previously obtained for the specimens of adhesive G_A/t_A of 20, it can be concluded that the K_{Imax} values before the introduction of patch delamination were 5 % to 17 % higher in the specimens of adhesive G_A/t_A of 20 than in the specimens with G_A/t_A of 10. It could be understood by using the conclusions of the chapter 4 for the difference in the adhesive G_A/t_A ratio.

But after the introduction of patch delamination the comparison becomes complex and it was expected to depend upon the combination of two parameters, instead of only one. These

parameters include adhesive shear stiffness G_A/t_A and adhesive shear strength τ. Higher adhesive G_A/t_A reduces the K_I values, before introduction of the patch delamination, but at the same time develop higher shear stresses around the crack. Therefore, if the adhesive shear strength is high then lesser or negligible adhesive shear failure would occur around the crack and lesser would be the corresponding patch delamination. But if the adhesive has weaker shear strength, then large patch delamination would result and K_I values would rise up markedly after the patch delamination. If the K_{Imax} values, after patch delamination, are compared between the specimens of adhesive G_A/t_A of 20 and 10, for the identical adhesive shear strength of 7.5 MPa (or the τ/σ_o of 3.75 %), then it is found that the difference in the two reduced to overall 5 %. It was because of very little variation in the SIF values between the specimens of G_A/t_A of 10 and 20. But the difference was expected to be more while comparing the results of specimens with adhesive G_A/t_A of 1 and 10, which is discussed in the later sections.

Figure 7.12 shows the $f_{(a/b)}$ variation with non-dimensionalized crack length (a/b), for the specimens of ETR 0.2, with adhesive G_A/t_A of 10. The results are shown for varying adhesive shear strengths. $f_{(a/b)}$ for an unpatched plate, obtained using Equation 3.12, as provided by Tada et al. (2000), is also shown in Figure 7.12. This figure shows that the $f_{(a/b)}$ values were higher for weaker adhesive shear strength and vice versa. The polynomial functions for $f_{(a/b)}$ variation for all the specimens, as shown in Figure 7.12, are again reproduced below in equations 7.6 through 7.10, respectively, for the un-delaminated patch and for the four adhesive shear strengths ratios (τ/σ_o) of 3.75 %, 7.5 %, 12.5 % and 17.5 % (which also corresponded to the four adhesive shear strengths of 7.5 MPa, 15 MPa, 25 MPa and 35 MPa).

$$f_{(a/b)} = -3.8843\,(a/b)^3 + 4.4119\,(a/b)^2 - 2.1967\,(a/b) + 0.8016 \quad (7.6)$$

$$f_{(a/b)} = 3.4963\,(a/b)^2 - 0.8506\,(a/b) + 0.8819 \quad (7.7)$$

$$f_{(a/b)} = 2.6201\,(a/b)^2 - 0.6112\,(a/b) + 0.7721 \quad (7.8)$$

$$f_{(a/b)} = 2.6516\,(a/b)^2 - 0.9966\,(a/b) + 0.723 \quad (7.9)$$

$$f_{(a/b)} = 2.9841\,(a/b)^2 - 1.5144\,(a/b) + 0.7429 \quad (7.10)$$

7.5.2.3 Edge cracked plate with patch ETR 0.21 and adhesive G_A/t_A of 1 after delamination

Following the same procedure carried out for the specimens of the ETR 0.21 with adhesive G_A/t_A of 20 and 10, the $f_{(a/b)}$ for the specimens of ETR 0.2 group, with adhesive shear stiffness (G_A/t_A) of 1, was also evaluated. The resulting K_{Imax}, $\Delta K_I / \Delta\sigma$ and the $f_{(a/b)}$ variations for the four adhesive shear strength ratios (τ/σ_o) of 3.75 %, 7.5 %, 12.5 % and 17.5 % (corresponded to the four adhesive shear strengths of 7.5 MPa, 15 MPa, 25 MPa and 35 MPa), are shown in Figures 7.13, 7.14 and 7.15 respectively. It can be noted in Figure 7.13 that there was lesser difference in the K_{Imax} values, before and after the patch delamination, for the higher shear strengths of 25 MPa and 35 MPa (or the τ/σ_o of 12.5 % and 17.5 %). It was because of very small delamination in these specimens, especially in their smaller crack length models. Only the specimen with lowest adhesive shear strength of 7.5 MPa (or the τ/σ_o of 3.75 %) suffered with the delamination in all of its crack length models. The FEM of smaller crack lengths, with adhesive shear strength of 15 MPa, 25 MPa and 35 MPa (or with τ/σ_o of 7.5 %, 12.5 % and 17.5 %), did not suffer with the patch delamination because of no or negligible adhesive shear failure.

Lesser adhesive failures in the specimens with adhesive G_A/t_A of 1, compared to the specimens of adhesive G_A/t_A of 10 and 20, could be justified using the conclusions of chapters 3 and 4. Therefore, it can be concluded that if the adhesive shear strength is higher, as in the case of adhesive shear strengths of 25 MPa and 35 MPa, then there would be lesser or no adhesive shear failure expected. The same has been found in the FEM of smaller crack of the two specimens with the adhesive shear strengths of 25 MPa and 35 MPa. Comparing the K_{Imax} variation of Figure 7.13 with that previously obtained for the specimens of adhesive G_A/t_A of 10, it can be concluded that the K_{Imax} values before the introduction of patch delamination were around 30 % to 80 % higher in the specimens of adhesive G_A/t_A of 10, which could be understand by using the conclusions of the chapter 3.

Comparing the K_{Imax} variation, after the patch delamination, between the specimens of Figure 7.13 and Figure 7.10, it can be seen that when the adhesive shear strength was low the K_{Imax} values of specimens with adhesive G_A/t_A of 10 were little higher than those of the specimens with adhesive G_A/t_A of 1, mainly because of more delamination in these. But if the adhesive

shear strength became higher above 15 MPa then the specimens with adhesive G_A/t_A of 10 showed lesser K_{Imax} values, which was again because of lesser patch delamination in these. Therefore, in case of lesser adhesive failures, as obvious in higher adhesive shear strengths, the K_{Imax} values after the delamination would fall closer to their values before the introduction of delamination. But the K_{Imax} values before the introduction of patch delamination were already higher in the specimens having lower adhesive G_A/t_A.

Figure 7.15 shows the $f_{(a/b)}$ variation with non-dimensionlized crack length (a/b) for the specimens of ETR 0.2 with adhesive G_A/t_A of 1 and with adhesive shear strengths of 7.5 MPa, 15 MPa, 25 MPa and 35 MPa (or τ/σ_o of 3.75 %, 7.5 %, 12.5 % and 17.5 %). Figure 7.15 also shows the $f_{(a/b)}$ of an unpatched plate, obtained using Equation 3.12, provided by Tada et al. (2000). The figure shows that the $f_{(a/b)}$ values were higher for weaker adhesive shear strength than the stronger ones. The polynomial functions for $f_{(a/b)}$ variation of all the specimens shown in Figure 7.15, are again reproduced below in Equations 7.11 through 7.15, respectively, for the un-delaminated case as well as for the four adhesive shear strength ratios (τ/σ_o), corresponded to the four adhesive shear strengths.

$$f_{(a/b)} = -0.115\,(a/b)^2 - 0.397\,(a/b) + 0.862 \quad 7.11$$

$$f_{(a/b)} = 3.857\,(a/b)^2 - 1.169\,(a/b) + 0.926 \quad 7.12$$

$$f_{(a/b)} = 2.650\,(a/b)^2 - 1.028\,(a/b) + 0.898 \quad 7.13$$

$$f_{(a/b)} = 1.303\,(a/b)^2 - 0.818\,(a/b) + 0.890 \quad 7.14$$

$$f_{(a/b)} = 0.626\,(a/b)^2 - 0.649\,(a/b) + 0.880 \quad 7.15$$

7.5.2.4 Edge cracked plate with patch ETR 0.21 and adhesive G_A/t_A of 0.25 after delamination

Following the same procedure carried out for the previous specimens of the ETR 0.21 group, the geometric factors $f_{(a/b)}$ were evaluated for the specimens of adhesive shear stiffness (G_A/t_A) of 0.25. The resulting K_{Imax}, $\Delta K_I / \Delta\sigma$ and the $f_{(a/b)}$ variations for the adhesive shear strength ratios (τ / σ_o) of 3.75 %, 7.5 %, 12.5 % and 17.5 % (or the adhesive shear strengths of 7.5 MPa, 15 MPa, 25 MPa and 35 MPa respectively), are shown in Figures 7.16, 7.17 and 7.18, respectively. These figures show that the K_{Imax} or the $f_{(a/b)}$ values were not much enhanced

after the introduction of patch delamination in the analysis, similar to the case of the specimens of the adhesive G_A/t_A of 1.0. The main reason was again lesser adhesive failure found in these specimens because of which the corresponding K_{Imax} values were not increased by a large amount after the delamination. lesser adhesive failures in the specimens of adhesive G_A/t_A of 0.25, compared to the previous specimens with adhesive G_A/t_A of 1, 10 and 20, could be justified using the conclusions of chapters 3 and 4, in which, it was shown that the adhesive shear stresses around the crack would be lesser in magnitude in specimen with lesser adhesive G_A/t_A. Therefore, if the adhesive shear strength was higher in those specimens, as the case with specimens having adhesive shear strengths of 15 MPa, 25 MPa and 35 MPa, then there would be lesser or no adhesive shear failure expected (especially in the smaller crack lengths). Figure 7.18 shows the corresponding $f_{(a/b)}$ variation with non-dimensionalized crack length (a/b) of the specimens of ETR 0.2 having adhesive G_A/t_A of 0.25 and with adhesive shear strengths of 7.5 MPa, 15 MPa, 25 MPa and 35 MPa (or τ/σ_o of 3.75 %, 7.5 %, 12.5 % and 17.5 %). Figure 7.18 also shows the $f_{(a/b)}$ of an unpatched plate, obtained using Equation 3.12, provided by Tada et al. (2000). The polynomial functions for $f_{(a/b)}$ variations of all the specimens shown in Figure 7.15, are again reproduced below in Equations 7.16, 7.17, 7.18, 7.19 and 7.20, respectively, for the un-delaminated case as well as for the four adhesive shear strength ratio τ/σ_o of 3.75 %, 7.5 %, 12.5 % and 17.5 % (or for the corresponding adhesive shear strength of 7.5 MPa, 15 MPa, 25 MPa and 35 MPa).

$$f_{(a/b)} = -0.4635\,(a/b)^2 + 0.0956\,(a/b) + 0.8432 \quad 7.16$$

$$f_{(a/b)} = 3.7485\,(a/b)^2 - 1.223\,(a/b) + 0.939 \quad 7.17$$

$$f_{(a/b)} = 1.1337\,(a/b)^2 - 0.4114\,(a/b) + 0.8787 \quad 7.18$$

$$f_{(a/b)} = 0.7402\,(a/b)^2 - 0.3285\,(a/b) + 0.8752 \quad 7.19$$

$$f_{(a/b)} = 0.1456\,(a/b)^2 - 0.0956\,(a/b) + 0.8432 \quad 7.20$$

7.5.3 Edge cracked plate with patch ETR 0.42 before delamination

Finite element analysis of the edge cracked plate with patch ETR of 0.42 was carried out similar to that of ETR 0.21 specimens by doubling the modulus of elasticity of the CFRP to make the ETR of 0.42. The stress intensity factor K_I for the edge cracked specimens of Table

7.1, with patch ETR of 0.42, corresponding to applied σ_{max}, was extracted from the results of FEA of the four-crack models for each specimen of the ETR 0.42 group, before the introduction of patch delamination in the analysis, and it is plotted with the non-dimensionalized crack length (a/b) in Figure 7.19. This figure shows that the K_{Imax} values were higher in the specimen having smaller adhesive G_A /t_A and lower in the specimen with higher adhesive G_A /t_A, and the difference increases with increasing crack length. The trends of variation of K_{Imax} in the specimens of ETR 0.42 were also similar to that of the ETR 0.21 specimens, with the difference that the magnitudes are comparatively lesser here because of higher patch ETR.

Probable reasons for such K_{Imax} distributions had already been discussed in detail in sections 3.4.3.4 and 7.5.1. Comparing the absolute K_{Imax} values from Figures 7.19 and 7.6 it was found that due to higher patch ETR the K_{Imax} values were 13 % to 30 % lower in the specimens of ETR 0.42 than in the specimens of ETR 0.21. The other conclusion obtained from Figure 7.19 was that the difference in the K_{Imax} values is not high between the specimens of adhesive G_A /t_A of 10 and 20 or with G_A /t_A of 1 and 0.25. Similar conclusions were also obtained in specimens of ETR 0.21.

7.5.4 Edge cracked plate with patch ETR 0.42 after delamination

Patch delamination was introduced in the FEA of specimens of patch ETR of 0.42, through modelling the failure of interface adhesive layer, as already mentioned and demonstrated in sections 4.4 and 6.4. The adhesive failure was corresponding to the four adhesive shear strength ratios of (τ/σ_o) of 3.75 %, 7.5 %, 12.5 % and 17.5 % (which also corresponded to the four adhesive shear strengths of 7.5 MPa, 15 MPa, 25 MPa and 35 MPa). As already mentioned and shown in section 7.5.2, that after the introduction of adhesive failure in FEA, the comparison of K_{Imax} or the $f_{(a/b)}$ variation became more complex because of their dependency on the adhesive shear strength also, in addition to the adhesive G_A /t_A. It was also shown in section 7.5.2 that a better way of presenting and comparing the K_{Imax} or the $f_{(a/b)}$ variation of specimens, with different adhesive G_A /t_A and strength T, was to draw comparison within sub-groups of specimens. Those sub-groups have identical adhesive G_A /t_A and ETR,

but have varying adhesive shear strengths. Therefore, the K_{Imax} and the $f_{(a/b)}$ variation are presented in a similar way for the specimens of ETR 0.42 in the next section.

7.5.4.1 Edge cracked plate with patch ETR 0.42 and adhesive G_A/t_A of 20 after delamination after delamination

After introduction of the patch delamination in the four FEMs of ETR 0.42 and adhesive G_A/t_A of 20, through modelling the progressive adhesive failure, corresponding to four adhesive shear strengths or four strengths ratios (T/σ_o), the resulting K_I values corresponding to the applied σ_{max} were extracted from the results of corresponding FEA. The corresponding geometric factors $f_{(a/b)}$ were evaluated, following the procedure of section 7.3. The K_{Imax}, $\Delta K_I/\Delta\sigma$ and the evaluated $f_{(a/b)}$ functions for the four adhesive shear strength ratios (T/σ_o) of 3.75 %, 7.5 %, 12.5 % and 17.5 % are shown in Figures 7.20, 7.21 and 7.22, respectively. These shear strength ratios were corresponded to the four adhesive shear strengths of 7.5 MPa, 15 MPa, 25 MPa and 35 MPa.

It can be seen from these figures that the trends of variation of K_{Imax} and $f_{(a/b)}$ were similar to the ETR 0.21 specimens but their magnitudes were lesser by 18 % to 25 % because of higher patch ETR. The K_{Imax} distribution in Figure 7.20 is found to be varying with respect to the adhesive G_A/t_A, similar to that found in all the specimens of ETR 0.21. Figure 7.22 shows the $f_{(a/b)}$ variation of the specimens of ETR 0.42, with adhesive G_A/t_A of 20, with varying adhesive shear strengths. Figure 7.22 also shows the $f_{(a/b)}$ variation of an unpatched plain steel plate, obtained using Equation 3.12, provided by Tada et al. (2000). It can also be seen in Figure 7.22 that the $f_{(a/b)}$ values were higher for weaker adhesive shear strength and vice versa. The polynomial functions for $f_{(a/b)}$ variation of all the specimens, shown in Figure 7.22, are again reproduced below in Equations 7.21 through 7.25, respectively for the un-delaminated case and for four adhesive shear strengths ratios (T/σ_o) of 3.75 %, 7.5 %, 12.5 % and 17.5 % (which also corresponded to the four adhesive shear strengths of 7.5 MPa, 15 MPa, 25 MPa and 35 MPa respectively).

$$f_{(a/b)} = -4.9691\,(a/b)^3 + 5.4395\,(a/b)^2 - 2.3407\,(a/b) + 0.6109 \qquad 7.21$$

$f_{(a/b)} = 1.9998\ (a/b)^2 - 0.0695\ (a/b) + 0.6143$ 7.22

$f_{(a/b)} = 2.8029\ (a/b)^2 - 0.6765\ (a/b) + 0.5768$ 7.23

$f_{(a/b)} = 3.5768\ (a/b)^2 - 1.4162\ (a/b) + 0.5591$ 7.24

$f_{(a/b)} = 3.226\ (a/b)^2 - 1.5649\ (a/b) + 0.5487$ 7.25

7.5.4.2 Edge cracked plate with patch ETR 0.42 and adhesive G_A/t_A of 10 after delamination

After introducing the patch delamination in specimens of ETR 0.42, with adhesive G_A/t_A of 10, the resulting $K_{I\ max}$, $\Delta K_I / \Delta\sigma$ and the evaluated $f_{(a/b)}$ functions, for the four adhesive shear strength ratios (T/σ_o) of 3.75 %, 7.5 %, 12.5 % and 17.5 % are shown in Figures 7.23, 7.24 and 7.25 respectively. These strength ratios were also corresponded to the four adhesive shear strengths of 7.5 MPa, 15 MPa, 25 MPa and 35 MPa. It can be seen in these figures that the trend of variation of K_{Imax}, $\Delta K_I/\Delta\sigma$ and the geometric factors $f_{(a/b)}$ were similar to the specimens with G_A/t_A of 20, with minor differences in their numerical values because of the reduced adhesive G_A/t_A. Figure 7.25 shows the $f_{(a/b)}$ variation for the specimens of ETR 0.42, with adhesive G_A/t_A of 10, with varying adhesive shear strengths. Figure 7.25 also shows the $f_{(a/b)}$ of an unpatched plate, obtained using Equation 3.12, provided by Tada et al. (2000). It can be seen in Figure 7.25 that the $f_{(a/b)}$ values were higher for weaker adhesive shear strength and vice versa. The polynomial functions for $f_{(a/b)}$ variation for all the specimens of Figure 7.25 are again reproduced below in Equations 7.26 through 7.30, respectively for the un-delaminated case and for the four adhesive shear strengths ratios (T / σ_o) of 3.75 %, 7.5 %, 12.5 % and 17.5 % (which also corresponded to the four adhesive shear strengths of 7.5 MPa, 15 MPa, 25 MPa and 35 MPa respectively).

$f_{(a/b)} = -4.5691\ (a/b)^3 + 5.0981\ (a/b)^2 - 2.3068\ (a/b) + 0.6732$ 7.26

$f_{(a/b)} = 1.8113\ (a/b)^2 - 0.0078\ (a/b) + 0.6169$ 7.27

$f_{(a/b)} = 2.570\ (a/b)^2 - 0.6946\ (a/b) + 0.6125$ 7.28

$f_{(a/b)} = 3.3518\ (a/b)^2 - 1.3977\ (a/b) + 0.6056$ 7.29

$f_{(a/b)} = 3.4899\ (a/b)^2 - 1.8486\ (a/b) + 0.6381$ 7.30

7.5.4.3 Edge cracked plate with patch ETR 0.42 and adhesive G_A/t_A of 1 after delamination

Following the same procedure of introduction of patch delamination, carried out for all previous specimens of the ETR 0.21 and 0.42 groups, the $f_{(a/b)}$ of the specimens of ETR 0.42 group, with adhesive shear stiffness (G_A/t_A) of 1, were also evaluated. The extracted $K_{I\ max}$ values and the evaluated $\Delta K_I / \Delta\sigma$ and the $f_{(a/b)}$ distributions, for the four adhesive shear strength ratios (T / σ_o) of 3.75 %, 7.5 %, 12.5 % and 17.5 %, are shown in Figures 7.26, 7.27 and 7.28, respectively. These shear strength ratios also corresponded to the four adhesive shear strengths of 7.5 MPa, 15 MPa, 25 MPa and 35 MPa, It can be noted from these figures that the trends of variations in $K_{I\ max}$ and $f_{(a/b)}$ distributions in these figures were similar to the specimens of ETR 0.21 with G_A/t_A of 1, except that the numerical values of these parameters were lesser in current specimens because of higher patch ETR.

The results were following the conclusion of chapters 3 and 4, which showed that due to lesser adhesive G_A/t_A and higher ETR the patch delamination was lesser, especially in the smaller crack length models of higher adhesive shear strengths. Figure 7.28 shows the $f_{(a/b)}$ variation for the specimens of ETR 0.42, with adhesive G_A/t_A of 1, along with the $f_{(a/b)}$ for an unpatched plate, obtained using Equation 3.12, provided by Tada et al. (2000). Figure 7.28 shows that the $f_{(a/b)}$ values were higher for weaker adhesive shear strength and vice versa. The polynomial functions for $f_{(a/b)}$ variation for all the specimens shown in Figure 7.28 are again reproduced in Equations 7.31 through 7.35, respectively for the un-delaminated case as well as for the four adhesive shear strengths ratios (T/σ_o) of 3.75 %, 7.5 %, 12.5 % and 17.5 %..

$$f_{(a/b)} = 0.330\ (a/b)^2 - 0.746\ (a/b) + 0.753 \quad 7.31$$

$$f_{(a/b)} = 3.346\ (a/b)^2 - 1.096\ (a/b) + 0.785 \quad 7.32$$

$$f_{(a/b)} = 3.07\ (a/b)^2 - 1.398\ (a/b) + 0.789 \quad 7.33$$

$$f_{(a/b)} = 2.24\ (a/b)^2 - 1.383\ (a/b) + 0.799 \quad 7.34$$

$$f_{(a/b)} = 1.05\ (a/b)^2 - 0.953\ (a/b) + 0.766 \quad 7.35$$

7.5.4.4 Edge cracked plate with patch ETR 0.42 and adhesive G_A/t_A of 0.25 after delamination

After performing the patch delamination process for the four adhesive shear strength ratios, the $f_{(a/b)}$ functions for the specimens of ETR 0.42 group, with adhesive shear stiffness (G_A/t_A) of 0.25, were also evaluated. The extracted K_{Imax}, the evaluated $\Delta K_I / \Delta\sigma$ and the $f_{(a/b)}$ distributions, for the four adhesive shear strength ratios (T / σ_o) of 3.75 %, 7.5 %, 12.5 % and 17.5 %, are shown in Figures 7.29, 7.30 and 7.31, respectively. These shear strength ratios were also corresponding to the four adhesive shear strengths of 7.5 MPa, 15 MPa, 25 MPa and 35 MPa. Comparing these figures with the specimens of ETR 0.21, having same adhesive G_A/t_A, it was found that the K_{Imax} or the $f_{(a/b)}$ distributions were similar but with lesser magnitude or numerical values in current specimen because of higher patch ETR.

Main reasons for not having much enhancement in the K_{Imax} values, after the patch delamination in current specimens, was the lesser adhesive failure in these specimens. This matter has already been discussed in detail in section 7.5.24 and in the conclusions of chapters 3 and 4. Combined impact of lesser adhesive G_A/t_A and higher patch ETR resulted in negligible patch delamination in these specimens, especially in its smaller crack length models. Due to very small G_A/t_A in current specimens, lesser patch delamination was also found in the bigger crack length models.

Figure 7.31 shows the $f_{(a/b)}$ variation of all the specimens of ETR 0.42, with adhesive G_A/t_A of 0.25. Additionally, Figure 7.31 also shows the $f_{(a/b)}$ of an unpatched plate, as provided by Tada et al. (2000) through Equation 3.12. The polynomial functions for $f_{(a/b)}$ variation of all the specimens, shown in Figure 7.31, are again reproduced in Equations 7.36 through 7.40, respectively for the un-delaminated case as well as for the four adhesive shear strength ratios (T/σ_o) of 3.75 %, 7.5 %, 12.5 % and 17.5 %. These shear strength ratios were also corresponded to the adhesive shear strengths of 7.5 MPa, 15 MPa, 25 MPa and 15 MPa respectively.

$$f_{(a/b)} = -0.3131\,(a/b)^2 - 0.1809\,(a/b) + 0.7577 \quad 7.36$$

$$f_{(a/b)} = 3.4281\,(a/b)^2 - 1.3293\,(a/b) + 0.8386 \quad 7.37$$

$$f_{(a/b)} = 0.991\,(a/b)^2 - 0.6224\,(a/b) + 0.7901 \quad 7.38$$

$$f_{(a/b)} = 0.4653\,(a/b)^2 - 0.4361\,(a/b) + 0.776 \quad 7.39$$

$$f_{(a/b)} = 0.1191\,(a/b)^2 - 0.3127\,(a/b) + 0.7666 \quad 7.40$$

7.5.5 Edge cracked plate with patch ETR 0.63 before delamination

Finite element analysis of the edge cracked plate, with patch ETR of 0.63 was also carried out similar to the ETR 0.21 and 0.42 specimens. Modulus of elasticity and thickness of the CFRP (E_{FRP} and t_{FRP}) were provided to be 124 GPa and 1.6 mm, respectively, to make the overall patch ETR of 0.63. FEA of four crack models of each specimen of the ETR 0.63 group was carried out under the applied stresses of σ_{max} and σ_{min},, without consideration of patch delamination. The SIF (K_I), corresponding to applied σ_{max}, were extracted from the results of FEA and plotted with the non-dimensionalized crack length (a/b) in Figure 7.32. This figure shows that the trend of variation of K_{Imax} in the specimens of ETR 0.63 was similar to the specimens of the ETR 0.21 and 0.42, but their magnitudes were least in the current ETR group, because of highest patch ETR. Figure 7.32 also shows that K_{Imax} was higher in the specimen having smaller adhesive G_A/t_A and lower in the specimen with higher G_A/t_A, and the difference increases with increase in the crack length. Similar results have already been achieved in the specimens of ETR 0.21 and 0.42 and these were already found to be according to the conclusions of section 3.4.3.4.

Comparing the $K_{I\ max}$ values of specimens of ETR 0.63 and 0.42, it was found that due to higher patch ETR the K_{Imax} values were 5 % to 16 % lower in the specimens of ETR 0.63. Figure 7.32 also shows that the difference in the $K_{I\ max}$ values were not noticeable between the specimens of adhesive G_A/t_A of 10 and 20 or between 1 and 0.25. This finding also existed in other ETR groups.

7.5.6 Edge cracked plate with patch ETR 0.63 after delamination

Patch delamination was introduced in the FEA of specimens of patch ETR of 0.63, through the introducing the failure of interface adhesive layer, corresponding to the four adhesive shear strengths ratios of (τ/σ_o) of 3.75 %, 7.5 %, 12.5 % and 17.5 %, which indirectly corresponded to the adhesive shear strengths of 7.5 MPa, 15 MPa, 25 MPa and 35 MPa, respectively. But, as mentioned and shown in sections 7.5.2 and 7.5.4, after introduction of the adhesive failure in FEA, the comparison of K_{Imax} or the $f_{(a/b)}$ became more complex because of their dependency on the adhesive shear strength, in addition to the adhesive G_A/t_A. It has shown in sections 7.5.2 and 7.5.4 that a better way of presenting and comparing the K_{Imax} or the $f_{(a/b)}$ variation of specimens, with different adhesive G_A/t_A and shear strength T, was to draw comparison within sub-groups of specimens. Those sub-groups have identical adhesive G_A/t_A and ETR, but with varying adhesive shear strengths. Therefore, the K_{Imax} and the $f_{(a/b)}$ variation are presented in a similar way for the specimens of ETR 0.63 in the nest section.

7.5.6.1 Edge cracked plate with patch ETR 0.63 and adhesive G_A/t_A of 20 after delamination

Patch delamination, through adhesive failure, for the four adhesive shear strengths of 7.5MPa, 15MPa, 25MPa and 35MPa, was introduced in the FEA of the specimens of patch ETR 0.63, with adhesive G_A/t_A of 20, similar to the previous specimens of Table 7.1. These four adhesive shear strengths were corresponding to the four non-dimensionalized shear strength ratios (T/σ_o) of 3.75 %, 7.5 %, 12.5 % and 17.5 %. The K_I values, corresponding to the applied σ_{max}, were extracted from the results of FEA of the four crack-length models of each specimen of this group and the geometric factors $f_{(a/b)}$ were evaluated following the procedure of section 7.3. The $K_{I\,max}$, $\Delta K_I/\Delta\sigma$ and the evaluated $f_{(a/b)}$ functions for the four adhesive shear strength ratios (T/σ_o) are shown in Figures 7.33, 7.34 and 7.35 respectively. It is obvious from these figures that the trend of variation of K_{Imax} and the geometric factors $f_{(a/b)}$ were similar to the specimens of ETR 0.21 and 0.42 but their magnitudes were further reduced by 15 % to 30 %, compared to the specimens of ETR 0.42. It was because of higher patch ETR.

The K_{Imax} distribution in Figure 7.33 is found to be varying with respect to the adhesive shear strength or T/σ_o, similar to the specimens of ETR 0.21 and 0.42. Figure 7.35 shows the $f_{(a/b)}$

variation with non-dimensionlized crack length (a/b) of the specimens of ETR 0.63, with adhesive G_A/t_A of 20, after the patch delamination and corresponding to the four adhesive shear strengths (or T/σ_o). It also shows the $f_{(a/b)}$ function for an unpatched plate, obtained from Tada et al. (2000) and given through Equation 3.12. It can be seen in Figure 7.35 that the $f_{(a/b)}$ values were higher for weaker adhesive shear strength and vice versa. The polynomial functions for $f_{(a/b)}$ variation of all the specimens, as shown in Figure 7.35, are again reproduced below in Equations 7.41 through 7.45, respectively for the un-delaminated patch case and for the four adhesive shear strengths ratios (T / σ_o) of 3.75 %, 7.5 %, 12.5 % and 17.5 %. These shear strength ratios (T / σ_o) indirectly corresponded to the four adhesive shear strengths of 7.5 MPa, 15 MPa, 25 MPa and 35 MPa respectively.

$$f_{(a/b)} = -4.8845\,(a/b)^3 + 5.3265\,(a/b)^2 - 2.2541\,(a/b) + 0.5585 \quad 7.41$$

$$f_{(a/b)} = 2.4177\,(a/b)^2 - 0.2503\,(a/b) + 0.452 \quad 7.42$$

$$f_{(a/b)} = 2..3488\,(a/b)^2 - 0.5776\,(a/b) + 0.452 \quad 7.43$$

$$f_{(a/b)} = 3.3632\,(a/b)^2 - 1.5851\,(a/b) + 0.5149 \quad 7.44$$

$$f_{(a/b)} = 2.4439\,(a/b)^2 - 1.4405\,(a/b) + 0.4987 \quad 7.45$$

7.5.6.2 Edge cracked plate with patch ETR 0.63 and adhesive G_A/t_A of 10 after delamination

Patch delamination, through adhesive failure, for the four adhesive shear strengths of 7.5 MPa, 15 MPa, 25 MPa and 35 MPa, was introduced in the FEA of the specimens of patch ETR 0.63, with adhesive G_A/t_A of 10. The resulting K_{Imin} and K_{Imax} values, corresponding to the applied σ_{max} and σ_{min} were extracted from FEA, before and after the introduction of patch delamination. The geometric factors $f_{(a/b)}$ for these specimens were evaluated using results of the FEA of the four crack-length FEMs, corresponding to the four adhesive shear strengths of 7.5 MPa, 15 MPa, 25 MPa and 35 MPa. The $K_{I\,max}$, $\Delta K_I/\Delta\sigma$ and the evaluated $f_{(a/b)}$ functions for the four adhesive shear strength of 7.5 MPa, 15 MPa, 25 MPa and 35 MPa, are shown in Figures 7.36, 7.37 and 7.38 respectively. These four shear strengths were also corresponded to the four shear strength ratios (T/σ_o) of 3.75 %, 7.5 %, 12.5 % and 17.5 %, respectively.

These figures show that the trend of variation of K_{Imax} and the geometric factors $f_{(a/b)}$ were similar to the specimens of ETR 0.21 and 0.42 but their magnitudes were further reduced by 15 % to 30 %, from the ETR of 0.42, because of higher patch ETR. The K_{Imax} distribution in Figure 7.36 is shown to be varying with the adhesive shear strength T or the shear strength ratio T/σ_o, similar to the specimens of ETR 0.21 and 0.42. Figure 7.38 shows the $f_{(a/b)}$ variation of the specimens of ETR 0.63 and adhesive G_A/t_A of 10, after the patch delamination for the four adhesive shear strengths (or T/σ_o). This figure also shows the $f_{(a/b)}$ function of an unpatched plate, provided by Tada et al. (2000), through Equation 3.12. Figure 7.38 also shows that the $f_{(a/b)}$ values are higher for weaker adhesive shear strength and vice versa. The polynomial functions for $f_{(a/b)}$ variation for all the specimens shown in Figure 7.38 are again reproduced below in Equations 7.46 through 7.50, respectively for the un-delaminated case as well as for the four adhesive shear strengths ratios (T/σ_o) of 3.75 %, 7.5 %, 12.5 % and 17.5 %. These shear strengths ratios (T / σ_o) were also corresponding to the four adhesive shear strengths of 7.5 MPa, 15 MPa, 25 MPa and 35 MPa respectively.

$$f_{(a/b)} = -4.4928\,(a/b)^3 + 5.0017\,(a/b)^2 - 2.219\,(a/b) + 0.6089 \quad 7.46$$

$$f_{(a/b)} = 2.837\,(a/b)^2 - 0.6034\,(a/b) + 0.5109 \quad 7.47$$

$$f_{(a/b)} = 2.5486\,(a/b)^2 - 0.8295\,(a/b) + 0.5109 \quad 7.48$$

$$f_{(a/b)} = 3.5445\,(a/b)^2 - 1.8076\,(a/b) + 0.5821 \quad 7.49$$

$$f_{(a/b)} = 2.4116\,(a/b)^2 - 1.5431\,(a/b) + 0.5607 \quad 7.50$$

7.5.6.3 Edge cracked plate with patch ETR 0.63 and adhesive G_A/t_A of 1 after delamination

Following the procedure carried out above for previous specimens of the ETR 0.21, 0.42 and 0.63 groups with different adhesive G_A/t_A and after performing patch delamination process for the four adhesive shear strength ratios, the $f_{(a/b)}$ for the specimens of ETR 0.63 group with adhesive shear stiffness (G_A/t_A) of 1 was also evaluated. The extracted $K_{I\,max}$ values and the evaluated $\Delta K_I/\Delta\sigma$ and the $f_{(a/b)}$ distributions, for the four adhesive shear strength ratios (T/σ_o) of 3.75 %, 7.5 %, 12.5 % and 17.5 %, are shown in Figures 7.39, 7.40 and 7.41 respectively. It

can be noted in these figures that the trends of variations in $K_{I\ max}$ and $f_{(a/b)}$ distributions in these figures are similar to the specimens of ETR 0.42 or ETR 0.21, with G_A/t_A of 1, except that the numerical values of these parameters were least here because of highest patch ETR. Comparing the K_{Imax} variations and values from Figure 7.39 with the specimen of ETR 0.42, it was found that none of the 10 mm crack length FEMs of all adhesive shear strengths suffered with the patch delamination. The FEMs of 20 mm crack length, with most adhesive shear strengths, was also not suffered by the patch delamination. The K_{Imax} values of current specimens were found to be 15 % to 28 % smaller than the specimens of ETR 0.42 because of the high patch ETR.

Figure 7.41 shows the $f_{(a/b)}$ variation with non-dimensionlized crack length (a/b) of the specimens of ETR 0.63 and adhesive G_A/t_A of 1. It also included $f_{(a/b)}$ of an unpatched plate, provided by Tada et al. (2000), through Equation 3.12. It is obvious from Figure 7.41 that the $f_{(a/b)}$ values were higher for weaker adhesive shear strength and vice versa. The polynomial functions for $f_{(a/b)}$ variations, in all the specimens shown in Figure 7.41, are again reproduced below in Equations 7.51 through 7.55, respectively for the un-delaminated case, as well as, for the four adhesive shear strengths ratios (T / σ_o) of 3.75 %, 7.5 %, 12.5 % and 17.5 %.

$$f_{(a/b)} = -0.8716\,(a/b)^3 + 1.1493\,(a/b)^2 - 0.9728\,(a/b) + 0.6828 \quad 7.51$$

$$f_{(a/b)} = 2.7653\,(a/b)^2 - 0.9703\,(a/b) + 0.6647 \quad 7.52$$

$$f_{(a/b)} = 2.0338\,(a/b)^2 - 1.1631\,(a/b) + 0.6887 \quad 7.53$$

$$f_{(a/b)} = 1.7119\,(a/b)^2 - 1.2141\,(a/b) + 0.7007 \quad 7.54$$

$$f_{(a/b)} = 0.8683\,(a/b)^2 - 0.8936\,(a/b) + 0.6754 \quad 7.55$$

7.5.6.4 Edge cracked plate with patch ETR 0.63 and adhesive G_A/t_A of 0.25 after delamination

$K_{I\,max}$ values, corresponding to the applied σ_{max}, were extracted from the results of FEA of the four crack-length models of ETR 0.63. These FEM were having adhesive G_A/t_A of 0.25 and the $K_{I\,max}$ values were extracted before and after the introduction of patch delamination, corresponding to the four adhesive shear strengths T of 7.5 MPa, 15 MPa, 25 MPa and 35 MPa (or equivalent shear strength ratios T/σ_o) , These extracted $K_{I\,max}$ values are shown in Figure 7.42. This figure shows that there was even no impact of patch delamination on the K_{Imax} values, after the introduction of patch delamination, in most of the smaller crack length models. But little impact of patch delamination was found on the larger crack length models. Comparing the K_{Imax} values of Figure 7.42 and the K_{Imax} values of specimens of ETR 0.42, it can be concluded that these were quite similar and the trend of variation of K_{Imax} was also similar. But the impact of delamination was further reduced in the specimens of ETR 0.63 resulting in 16 % to 18 % lesser magnitudes of K_{Imax}, compared to the specimens of ETR 0.42. Probable reasons of getting such trend have been discussed throughout in sections 7.5.2.4, 7.5.4.4, as well as in the conclusions of chapters 3 and 4. In summary, it was mainly because of very small patch delamination in these specimens, which was because of the least adhesive G_A/t_A and highest patch ETR of the current specimens. Figure 7.43 shows the variation of $\Delta K_I/\Delta\sigma$, before and after the patch delamination, for the adhesive shear strength of 7.5 MPa and its trend was similar to the variation of K_{Imax} in Figure 7.42.

The geometric factors $f_{(a/b)}$ for the specimens of patch ETR 0.63, with adhesive G_A/t_A of 0.25, were evaluated from the K_{Imax} and K_{Imin} results of the respective FEA of their four crack-length models. These $f_{(a/b)}$ were evaluated before and after the introduction of patch delamination and these were corresponding to the four adhesive shear strength ratios (T/σ_o) of 3.75 %, 7.5 %, 12.5 % and 17.5 %. Figure 7.44 shows the developed geometric factors $f_{(a/b)}$ function of all the specimens of ETR 0.63 with adhesive G_A/t_A of 0.25. Figure 7.44 also includes the $f_{(a/b)}$ of an unpatched plate provided by Tada et al. (2000), through Equation 3.12. It can also be seen in this figure that the $f_{(a/b)}$ values increased due to the impact of patch delamination. The increase in $f_{(a/b)}$ values was not huge because of least adhesive G_A/t_A and highest patch ETR. The polynomial functions for $f_{(a/b)}$ distribution of all the specimens shown

in Figure 7.44, are again reproduced below in Equations 7.56 through 7.60, respectively for the un-delaminated case as well as for the four adhesive shear strengths T (or the four equivalent shear stress ratios T/σ_o).

$$f_{(a/b)} = -0.3444\,(a/b)^3 + 0.0961\,(a/b)^2 - 0.3792\,(a/b) + 0.7019 \quad 7.56$$

$$f_{(a/b)} = 2.5905\,(a/b)^2 - 1.1639\,(a/b) + 0.7562 \quad 7.57$$

$$f_{(a/b)} = 1.1639\,(a/b)^2 - 0.755\,(a/b) + 0.7293 \quad 7.58$$

$$f_{(a/b)} = 0.7781\,(a/b)^2 - 0.6555\,(a/b) + 0.7236 \quad 7.59$$

$$f_{(a/b)} = 0.5063\,(a/b)^2 - 0.5522\,(a/b) + 0.7154 \quad 7.60$$

7.5.7 Comparison of impact of patch delamination in the edge cracked specimens - Lower ETR versus higher ETR patch

In the parametric study provided above for the edge cracked specimens, the results have been presented for the specimens having identical patch ETR and adhesive G_A/t_A, but with varying adhesive shear strengths, in order to avoid complexity in their comparison. As mentioned in section 7.5.2 that after introduction of patch delamination in the FEA, the resulting K_I variation was found to be mainly depending upon the adhesive shear strength, in addition to the patch ETR and adhesive G_A/t_A. Therefore, the results have been presented separately for the group of specimens, having identical ETR and adhesive G_A/t_A, but with varying adhesive shear strengths. In this section some comparisons of K_I variation between specimens of different patch ETR, G_A/t_A and adhesive shear strengths is presented in order to highlight and compare the impact of patch delamination in specimens with different ETR and adhesive G_A/t_A.

K_I variation in specimens of ETR 0.63, with adhesive G_A/t_A 20 and adhesive shear strengths of 7.5 MPa and 15 MPa, are compared with specimens of ETR 0.42, with adhesive G_A/t_A 10 and adhesive shear strengths of 25 MPa and 35 MPa. The resulting K_I variations are shown in Figure 7.45. This figure shows that before introduction of patch delamination, the K_I values in ETR 0.63 specimen, with adhesive G_A/t_A 20, were 10% to 28% lower than the specimen of ETR 0.42 with adhesive G_A/t_A 10. It was because of higher patch ETR. But after the

introduction of patch delamination, the resulting K_I values in higher ETR specimen with adhesive shear strength of 7.5 MPa became 20% to 38% higher than the K_I values in the lower ETR specimen, with adhesive shear strength of 7.5 MPa. If the comparison is again drawn between the adhesive shear strength of 35 MPa in lower ETR specimen and 15 MPa in the higher ETR specimen then still it can be seen from Figure 7.45 that the K_I values of the two specimens are falling very close to each other.

Another comparison was drawn between the specimens of patch ETR 0.63 and ETR 0.21 with adhesive G_A/t_A of 20 and it is shown in Figure 7.46. Before patch delamination, the K_I values in lower ETR specimen were 60% higher than the specimen of higher patch ETR, because of the impact of three times lower patch ETR. But after the introduction of patch delamination, the K_I values in some crack lengths of higher ETR specimen, having adhesive shear strength of 7.5 MPa, became 15% to 25% higher than the K_I values in lower ETR specimen, having adhesive shear strength of 35 MPa. Although the K_I values in higher ETR specimen with adhesive shear strength of 15 MPa are found to be lesser than the K_I values in the lower ETR specimen with adhesive shear strength of 35 MPa.

The above comparison highlighted the role of adhesive shear strength in reducing the efficiency of higher ETR patches and showed that a higher ETR patch may become less efficient, even lesser than a lower ETR patch, if its adhesive shear strength is lesser than the shear strength of lower ETR patch. Even if the shear strength of higher ETR patch is not much lower, then, still the efficiencies of the two patches are expected to be close. The higher ETR patch would not be much effective than the lower ETR patch by a big proportion as it would be if the adhesive shear strength is not too low in it.

7.5.8 Central cracked plate with patch ETR 0.21 before delamination

The procedure for development of the required geometric factors $f_{(a/b)}$ in the central crack plate was exactly similar to that of the edge crack plate. It involved extraction of the SIF (K_I) from the results of FEA, before introduction of patch delamination in the four crack-length models of each specimen. The $f_{(a/b}$ were then evaluated following the procedure of section 7.3. The K_I for the central cracked specimens of Table 7.1, with patch ETR of 0.21, corresponding to applied σ_{max} and σ_{min} and for four adhesive G_A/t_A, were extracted from the results of FEA of

the four crack-length models of each specimen. The resulting K_{Imax} values were then plotted with the non-dimensionlized crack length (a/b) in Figure 7.47. Figure 7.47 shows that the K_{Imax} was varied with respect to the adhesive G_A/t_A, similar to that obtained for case of edge cracked specimens, but the K_{Imax} values for central crack specimen were 13% to 24% lesser in magnitude because of having less critical crack location than the edge crack.

Similar to the edge crack case, the K_{Imax} values were higher in the specimen with smaller adhesive G_A/t_A and lower in the specimen with higher G_A/t_A, as shown in Figure 7.47. The difference increases with increase in crack length. As discussed in section 7.5.1, this trend was according to the conclusions of section 3.4.3.4, for identical ETR specimens. Figure 7.47 also shows lesser K_{Imax} difference between the specimens of adhesive G_A/t_A 0.25 and 1 as well as between the specimens of adhesive G_A/t_A of 10 and 20. Similar trend was also found in the results of edge crack specimens in section 7.5.1. It shows that the SIF variation was not much affected by further increase or decrease in the adhesive G_A/t_A, either above 10 or below 1, keeping in view that the G_A/t_A of 20 and 0.25 were the upper and lower bounds of the practically available adhesive properties.

7.5.9 Central cracked plate with patch ETR 0.21 after delamination

Patch delamination was introduced in the FEA of the central cracked plates through the procedure mentioned in section 7.3. The delamination carried out for the four adhesive shear strengths of 7.5 MPa, 15 MPa, 25 MPa and 35 MPa (or their equivalent adhesive shear strengths ratios (τ / σ_o) of 3.75 %, 7.5 %, 12.5 % and 17.5 %, respectively). But as mentioned in sections 7.5.2 and 7.5.4 and 7.5.6 that after introduction of the adhesive failure in the FEA, the comparison of K_{Imax} or the $f_{(a/b)}$ variation became more complex because of their dependency on the adhesive shear strength, in addition to the adhesive G_A/t_A. It has also shown in sections 7.5.2 and 7.5.4 that a better way of presenting and comparing the K_{Imax} or the $f_{(a/b)}$ variation, for the specimens with different adhesive G_A/t_A and strength T, was to draw comparison within sub-groups of specimens. The sub-groups have identical adhesive G_A/t_A and ETR, but have varying adhesive shear strengths. Therefore the K_{Imax} and the $f_{(a/b)}$

variation for the central crack case are presented in a similar way, for the specimens of ETR 0.21, in the following sections.

7.5.9.1 Central cracked plate with patch ETR 0.21 and adhesive G_A/t_A of 20 after delamination

$K_{I\,max}$ values, from the results of FEA of the four crack-length models of central cracked plate, with adhesive G_A/t_A of 20, were extracted, before and after the introduction of patch delamination and are shown in Figure 7.48. The adhesive failure was provided for the four adhesive shear strengths 'T' of 7.5 MPa, 15 MPa, 25 MPa and 35 MPa (or their equivalent shear strength ratios 'T/σ_o' of 3.75 %, 7.5 %, 12.5 % and 17.5 %). The geometric factors $f_{(a/b)}$ of these specimens, corresponding to the applied stresses of σ_{max} and σ_{min}, were evaluated using the results of FEA of the four crack-length models of each specimen and following the procedure mentioned in section 7.3. The developed geometric factors $f_{(a/b)}$ are shown in Figure 7.49. Figures 7.48 and 7.49 show that the trend of variation of K_{Imax} and the geometric factors $f_{(a/b)}$ were similar to those of edge crack specimens of ETR 0.21 with adhesive G_A/t_A of 20, but the magnitude of K_{Imax} were lesser by 20% to 30% in the central crack specimen, because of being less critical crack case.

The K_{Imax} distribution in Figure 7.48 varies with respect to the adhesive shear strength T, similar to that found in the results of all the ETR groups of the edge crack case. Figure 7.49 shows that the $f_{(a/b)}$ values were higher for weaker adhesive shear strength and vice versa, which was also the common findings in the results of all previous specimens. Figure 7.49 also shows the $f_{(a/b)}$ of an unpatched central crack plate, obtained from Tada et al. (2000), and its governing equation is again reproduced as Equation 7.61 below. The polynomial functions for $f_{(a/b)}$ variation, for all specimens shown in Figure 7.49, are again reproduced below in Equations 7.62 through 7.66. These $f_{(a/b)}$ functions are respectively for the un-delaminated case as well as for the four adhesive shear strengths of 7.5 MPa, 15 MPa, 25 MPa and 35 MPa (or their equivalent shear strength ratios T/σ_o of 3.75 %, 7.5 %, 12.5 % and 17.5 % respectively).

$f_{(a/b)} = 1.525\ (a/b)^3 - 0.288\ (a/b)^2 + 0.128\ (a/b) + 1$ 7.61

$f_{(a/b)} = -4.1344\ (a/b)^3 + 4.7998\ (a/b)^2 - 2.232\ (a/b) + 0.6911$ 7.62

$f_{(a/b)} = 2.167\ (a/b)^2 - 0.4488\ (a/b) + 0.6106$ 7.63

$f_{(a/b)} = 3.5737\ (a/b)^2 - 1.3382\ (a/b) + 0.6581$ 7.64

$f_{(a/b)} = 3.7935\ (a/b)^2 - 1.7068\ (a/b) + 0.6583$ 7.65

$f_{(a/b)} = 3.693\ (a/b)^2 - 2.0239\ (a/b) + 0.6802$ 7.66

7.5.9.2 Central cracked plate with patch ETR 0.21 and adhesive G_A/t_A of 10 after delamination

The procedure of introduction of patch delamination in the FEA was carried out in the central cracked specimens of ETR 0.21 and adhesive G_A/t_A of 10, following methodology of section 7.3, and similar to the sections 7.5.2, 7.5.4, 7.5.6 and 7.5.9.1. The required geometric factors $f_{(a/b)}$ were evaluated for each specimen from the results of the FEA of the four crack-length models of each specimen. The extracted K_{Imax} values and the evaluated geometric factors $f_{(a/b)}$, corresponding to the four adhesive shear strengths 'T' of 7.5 MPa, 15 MPa, 25 MPa and 35 MPa, are shown in Figures 7.50 and 7.51 respectively. These figures show that the trend of variation of K_{Imax} and the geometric factors $f_{(a/b)}$ were similar to the edge crack specimens of ETR 0.21, with adhesive G_A/t_A of 10, but the magnitude of K_{Imax} were lesser in the central crack specimen by 17% to 30%, because of being less critical crack location.

The K_{Imax} distribution and the $f_{(a/b)}$ variations in Figures 7.50 and 7.51 were found to be varying with respect to the adhesive shear strength, similar to that found in the results of all the previous ETR groups of the edge crack case. Figure 7.51 shows that the $f_{(a/b)}$ values were higher for weaker adhesive shear strength and vice versa, which was also the common finding in all the specimens of central and edge crack plates. Figure 7.51 also shows the $f_{(a/b)}$ of an unpatched central crack plate, obtained from Tada et al. (2000), and its governing equation has already been shown in Equation 7.61. The polynomial functions for $f_{(a/b)}$ variation, as shown in Figure 7.51, are again reproduced below in Equations 7.67 through 7.71, respectively for the un-delaminated case as well as for the four adhesive shear strengths.

$$f_{(a/b)} = -3.657\,(a/b)^3 + 4.3624\,(a/b)^2 - 2.1319\,(a/b) + 0.7432 \quad 7.67$$

$$f_{(a/b)} = 2.5806\,(a/b)^2 - 0.8454\,(a/b)^2 + 0.6858 \quad 7.68$$

$$f_{(a/b)} = 3.527\,(a/b)^2 - 1.4913\,(a/b) + 0.7122 \quad 7.69$$

$$f_{(a/b)} = 4.1332\,(a/b)^2 - 2.0715\,(a/b) + 0.7486 \quad 7.70$$

$$f_{(a/b)} = 3.826\,(a/b)^2 - 2.2324\,(a/b) + 0.7551 \quad 7.71$$

7.5.9.3 Central cracked plate with patch ETR 0.21 and adhesive G_A/t_A of 1 after delamination

The required geometric factors $f_{(a/b)}$ for the central cracked specimens of ETR 0.21, with adhesive G_A/t_A of 1, were evaluated using the ΔK_I obtained from the FEA of the four crack-length models of each specimen. FEA also included the process of introduction of patch delamination, mentioned in section 7.3, and already shown in sections 7.5.2, 7.5.4, 7.5.6 7.5.9.1 and 7.5.9.2. The patch delamination was carried out for the four adhesive shear strengths 'T' of 7.5 MPa, 15 MPa, 25 MPa and 35 MPa (or their equivalent adhesive shear strength ratios T/σ_o of 3.75 %, 7.5 %, 12.5 % and 17.5 %). The extracted K_{Imax} values from FEA and the evaluated geometric factors $f_{(a/b)}$, corresponding to the four adhesive shear strengths, are shown in Figures 7.52 and 7.53, respectively.

The K_{Imax} distribution and the $f_{(a/b)}$ variations in Figures 7.52 and 7.53 were found to be varying with respect to the adhesive shear strength. These were higher for weaker adhesive shear strength and vice versa, similar to that already found in the results of all the specimens of different ETR groups of the edge crack case. It can be noted in Figure 7.52 that there was lesser difference in the K_{Imax} values before and after the patch delamination especially in the smaller crack lengths and higher adhesive shear strengths. Similar trends, in variation of K_{Imax} and geometric factors $f_{(a/b)}$, have been obtained in the edge cracked specimens, having adhesive G_A/t_A of 1. But the values of K_{Imax} and the $f_{(a/b)}$ are further reduced in the central cracked specimens by 13% to 33%, because of getting comparative lesser delamination. The reasons of getting lesser delamination have already been discussed in detail in section 7.5.2.3 as well as in the conclusions of chapters 3 and 4. Figure 7.53 also shows the $f_{(a/b)}$ of the

unpatched central crack plate, obtained from Tada et al. (2000), and its governing equation has already been shown in Equation 7.61. The polynomial functions of $f_{(a/b)}$ variation for all the specimens shown in Figure 7.53 are again reproduced below in Equations 7.72 through 7.76, respectively for the un-delaminated case as well as for the four adhesive shear strength ratios (T / σ_o).

$$f_{(a/b)} = -0.7572\,(a/b)^3 + 1.3651\,(a/b)^2 - 1.05\,(a/b) + 0.8218 \quad 7.72$$

$$f_{(a/b)} = 2.7211\,(a/b)^2 - 1.3024\,(a/b) + 0.8522 \quad 7.73$$

$$f_{(a/b)} = 2.1656\,(a/b)^2 - 1.271\,(a/b) + 0.8366 \quad 7.74$$

$$f_{(a/b)} = 1.4837\,(a/b)^2 - 1.1114\,(a/b) + 0.8253 \quad 7.75$$

$$f_{(a/b)} = 1.3689\,(a/b)^2 - 1.1408\,(a/b) + 0.831 \quad 7.76$$

7.5.9.4 Central cracked plate with patch ETR 0.21 and adhesive G_A / t_A of 0.25 after delamination

Following similar procedure of evaluating geometric factors $f_{(a/b)}$, already been carried out for all previous specimens, through extraction of the K_{Imin} and K_{Imax} values from the FEA of four crack-length models, the geometric factors $f_{(a/b)}$ for current specimens were also evaluated. The extracted K_{Imax} values and the developed $f_{(a/b)}$ variations, are respectively shown in Figures 7.54 and 7.55, which were corresponding to the four adhesive shear strengths 'T' of 7.5 MPa, 15 MPa, 25 MPa and 35 MPa (or equivalent four adhesive shear strengths ratios T/σ_o of 3.75 %, 7.5 %, 12.5 % and 17.5 %). Figures 7.54 and 7.55 show that the K_{Imax} or the $f_{(a/b)}$ distributions are not much enhanced after the introduction of patch delamination in the analysis. Similar situation existed in the case of the central cracked specimens of adhesive G_A/t_A of 1.0 as well as in the edge cracked specimens of adhesive G_A/t_A of 0.25.

The trend became more prominent in the models of lower crack lengths of higher adhesive shear strengths. The main reasons for getting small delamination impact have already been discussed in detail in sections 7.5.2.3, 7.5.2.4 and also in the conclusions of chapters 3 and 4. Comparing the $K_{I\,max}$ values from Figure 7.54 with the edge crack specimens of ETR 0.21,

having adhesive G_A/t_A of 0.25, it can be seen that the K_{Imax} were lesser in the central crack specimen by 8%, because of being less critical crack location. Figure 7.55 also shows the $f_{(a/b)}$ of an unpatched central crack plate obtained from Tada et al. (2000), whose governing equation has already been shown in Equation 7.61. The polynomial functions for $f_{(a/b)}$ variation for all the specimens shown in Figure 7.55 are again reproduced below in Equations 7.77 through 7.81, respectively for the un-delaminated case as well as for the four adhesive shear strengths (or the equivalent adhesive shear strength ratios T/σ_o).

$$f_{(a/b)} = -0.2928\,(a/b)^3 + 0.7229\,(a/b)^2 - 0.6989\,(a/b) + 0.8101 \quad 7.77$$

$$f_{(a/b)} = 2.0469\,(a/b)^2 - 1.0246\,(a/b) + 0.8303 \quad 7.78$$

$$f_{(a/b)} = 1.1006\,(a/b)^2 - 0.7718\,(a/b) + 0.8118 \quad 7.79$$

$$f_{(a/b)} = 0.9588\,(a/b)^2 - 0.7705\,(a/b) + 0.8141 \quad 7.80$$

$$f_{(a/b)} = 0.9738\,(a/b)^2 - 0.8288\,(a/b) + 0.8211 \quad 7.81$$

7.5.10 Central cracked plate with patch ETR 0.42 before delamination

The required geometric factors $f_{(a/b)}$ of the central cracked specimen of ETR 0.42 group were developed, following the methodology of section 7.3 and using the stress intensity factor K_I, obtained from the results of FEA of the four crack-length models of each specimen. The K_{Imax} for these specimens, obtained from results of their FEA, before introduction of the patch delamination, are plotted with the non-dimensionlized crack length (a/b) in Figure 7.56.

Figure 7.56 shows that K_{Imax} values were varied with respect to the adhesive G_A/t_A, which was similar to that obtained for all specimens of edge cracked and central cracked plates, but the K_{Imax} in current specimen were 11 % to 18 % lesser in magnitude compared to the edge cracked case, because of the less critical crack case. The K_{Imax} values, as obvious in Figure 7.56, were higher in the specimens with smaller adhesive G_A/t_A and lower in the specimen with higher G_A/t_A, and the difference increases with increase in crack length. As already discussed in sections 7.5.1 and 7.5.3, this trend was according to the conclusions of section 3.4.3.4 for identical ETR specimens. Figure 7.56 also shows lesser K_{Imax} difference (5 % to 15 %) between the specimens of adhesive G_A/t_A 0.25 and 1 as well as between the specimens of adhesive G_A/t_A of 10 and 20, which is similar to the results of sections 7.5.1, 7.5.3, 7.5.5 and

7.5.8. It shows that the SIF variation was not much affected by further increase or decrease in the adhesive G_A /t_A, either above 10 or below 1, keeping in view that the G_A/t_A of 20 and 0.25 were the upper and lower bounds of the practically available adhesive properties.

7.5.11 Central cracked plate with patch ETR 0.42 after delamination

Patch delamination was also introduced in the FEA of the central cracked specimens with ETR of 0.42, through the procedure mentioned in section 7.3. It mainly involved progressive failure analysis of the interface adhesive layer around the crack, corresponding to the four adhesive shear strengths of 7.5 MPa, 15 MPa, 25 MPa and 35 MPa. But, as already mentioned in sections 7.5.2, 7.5.4 ,7.5.6 and 7.5.9, that after introduction of the adhesive failure in the FEA, the comparison of K_{Imax} or the $f_{(a/b)}$ variation became more complex because of their dependency on the adhesive shear strength, in addition to the adhesive G_A /t_A. It was shown in sections 7.5.2, 7.5.4, 7.5.6 and 7.5.9 that a better way of presenting and comparing the K_{Imax} or the $f_{(a/b)}$ variation of specimens, with different adhesive G_A /t_A and strength T, was to draw comparison within sub-groups of specimens. The sub-groups have identical adhesive G_A/t_A and ETR, but have varying adhesive shear strengths. Therefore, the K_{Imax} and the $f_{(a/b)}$ variation for the central crack case are presented in a similar way for the specimens of ETR 0.42, in the following sections.

7.5.11.1 Central cracked plate with patch ETR 0.42 and adhesive G_A /t_A of 20 after delamination

The K_I values, corresponding to the applied stresses σ_{max} and σ_{min}, were obtained from the results of FEA of the four-crack models of current specimen, both before and after the patch delamination, and corresponding to the four adhesive shear strengths of 7.5 MPa, 15 MPa, 25 MPa and 35 MPa. The corresponding geometric factors $f_{(a/b)}$ were evaluated following the procedure of section 7.3. The extracted $K_{I\ max}$ values and the evaluated $f_{(a/b)}$ functions for the four adhesive shear strengths ‘T’ (or the four adhesive shear strength ratios T/σ_o), are shown in Figures 7.57 and 7.58, respectively. The trend of $K_{I\ max}$ in Figure 7.57 was similar to that

shown in Figure 7.48 for the specimens of patch ETR 0.2 but the magnitudes were lesser by 12 % to 27 %, because of higher patch ETR.

Figure 7.58 shows the $f_{(a/b)}$ variation of the current specimens, for the four adhesive shear strengths of 7.5 MPa, 15 MPa, 25 MPa and 35 MPa. Figure 7.58 also shows the $f_{(a/b)}$ of an unpatched central crack plate, obtained from Tada et al. (2000), and its governing equation is again shown in Equation 7.61. Figure 7.58 also shows that the $f_{(a/b)}$ values were higher for weaker adhesive shear strength and vice versa, which was also the common finding in results of all edge crack and central crack specimens. The polynomial functions for $f_{(a/b)}$ variation for all the current specimens are shown in Figure 7.58 and these are again reproduced below in Equations 7.82 through 7.86, respectively for the un-delaminated case as well as for the four adhesive shear strengths T (or the four equivalent adhesive shear strength ratios T/σ_o).

$$f_{(a/b)} = 1.6149\,(a/b)^2 - 2.1379\,(a/b) + 0.5671 \quad 7.82$$

$$f_{(a/b)} = 1.6888\,(a/b)^2 - 0.3673\,(a/b) + 0.4673 \quad 7.83$$

$$f_{(a/b)} = 2.7714\,(a/b)^2 - 1.1449\,(a/b) + 0.5101 \quad 7.84$$

$$f_{(a/b)} = 2.6141\,(a/b)^2 - 1.2985\,(a/b) + 0.4976 \quad 7.85$$

$$f_{(a/b)} = 3.3798\,(a/b)^2 - 1.9663\,(a/b) + 0.5608 \quad 7.86$$

7.5.11.2 Central cracked plate with patch ETR 0.42 and adhesive G_A/t_A of 10 after delamination

Repeating the procedure of introducing the patch delamination in the FEA, as mentioned in section 7.3, the K_I values corresponding to the applied stresses σ_{max} and σ_{min} were extracted from the results of FEA of the four crack length models of current specimen, corresponding to the four adhesive shear strengths 'T' of 7.5 MPa, 15 MPa, 25 MPa and 35 MPa. The extracted $K_{I\,max}$ values and the evaluated $f_{(a/b)}$ functions are respectively shown in Figures 7.59 and 7.60. The trend of K_{Imax} variation in Figure 7.59 is shown to be depending upon the adhesive shear strength and it was also similar to that obtained in all ETR groups of edge cracked or central cracked case, after the patch delamination. Comparing the K_{Imax} values of Figure 7.59 with the central crack specimens of patch ETR 0.21, it is obvious that the K_{Imax} magnitudes were lesser in the current case by 18 % to 25 %, because of higher patch ETR.

Figure 7.60 shows the $f_{(a/b)}$ variation for the central crack specimens of ETR 0.42, with adhesive G_A/t_A of 10 and for the four adhesive shear strengths 'T' (or the four equivalent adhesive shear strength ratios T/σ_o). Figure 7.60 also includes the $f_{(a/b)}$ of an unpatched central crack plate, obtained from Tada et al. (2000), with its governing equation also mention in Equation 7.61. Figure 7.60 shows that the $f_{(a/b)}$ values were higher for weaker adhesive shear strength and vice versa, which was a common finding in all the specimens of the edge crack and central crack plate. The polynomial functions for $f_{(a/b)}$ variation for all the specimens shown in Figure 7.60 are again reproduced below in Equations 7.87 through 7.91, respectively for the un-delaminated case as well as for the four adhesive shear strengths 'T' of 7.5 MPa, 15 MPa, 25 MPa and 35 MPa (or the four equivalent adhesive shear strength ratios T/σ_o of 3.75 %, 7.5 %, 12.5 % and 17.5 %).

$$f_{(a/b)} = 1.612\,(a/b)^2 - 1.435\,(a/b) + 0.579 \quad 7.87$$

$$f_{(a/b)} = 1.903\,(a/b)^2 - 0.609\,(a/b) + 0.530 \quad 7.88$$

$$f_{(a/b)} = 2.407\,(a/b)^2 - 1.37\,(a/b) + 0.561 \quad 7.89$$

$$f_{(a/b)} = 2.691\,(a/b)^2 - 1.786\,(a/b) + 0.604 \quad 7.90$$

$$f_{(a/b)} = 2.836\,(a/b)^2 - 1.349\,(a/b) + 0.580 \quad 7.91$$

7.5.11.3 Central cracked plate with patch ETR 0.42 and adhesive G_A/t_A of 1 after delamination

Following similar procedure of evaluating geometric factors $f_{(a/b)}$, as already been carried out with all previous specimens, through extraction of the K_{Imin} and K_{Imax} values from the FEA of four crack-length models, the geometric factors $f_{(a/b)}$, for the central crack specimens of ETR 0.42 and adhesive G_A/t_A of 1, were also evaluated. The extracted K_{Imax} values and the developed $f_{(a/b)}$ variations, following the methodology of section 7.3, are respectively shown in Figures 7.61 and 7.62. These are corresponding to the four adhesive shear strengths 'T' of 7.5 MPa, 15 MPa, 25 MPa and 35 MPa. It is obvious in these figures that the K_{Imax} or the $f_{(a/b)}$ values were not much enhanced after the introduction of patch delamination in the analysis, similar to the central cracked specimens of ETR 0.21, with adhesive G_A/t_A of 1.0 or 0.25. It

was because of very small adhesive failures and it was more highlighted in the models of lower crack lengths, with higher adhesive shear strengths.

The K_{Imax} distribution in Figure 7.61 varies with respect to the adhesive shear strength T, similar to all the specimens of edge crack case. But the impact of patch delamination on the K_{Imax} values was found to be even much lesser in current specimens, especially in the models of smaller crack lengths with higher adhesive shear strengths. The FEM of crack lengths of 10 mm and 20 mm showed even no delamination impact on the K_{Imax} values, because of negligible delamination found in these models. It can be seen from Figure 7.61 that the K_{Imax} of the specimen with adhesive shear strength of 35 MPa was not changed after the introduction of patch delamination because of negligible delamination in any of its crack length model. Similarly, for the adhesive shear strength of 25 MPa, the delamination impact was found only in its 40 mm crack length model. In Figure 7.62 the $f_{(a/b)}$ values were found higher for weaker adhesive shear strength and vice versa, which was also the common finding in the results of all specimens. The lesser enhancement in $f_{(a/b}$ values were also because of the central crack case, resulting in negligible delamination in the smaller crack models of higher adhesive shear strengths. The main reasons for getting small delamination and its impact have already been discussed in detail in sections 7.5.2.3, 7.5.2.4 and also in the conclusions of chapters 3 and 4.

Comparing the $K_{I\ max}$ values from Figure 7.61 with the edge crack specimens of ETR 0.42, with adhesive G_A/t_A of 1, it can be seen that the K_{Imax} were lesser in the central crack specimen by 20 % to 35 %, for the adhesive strength of 7.5 MPa, because of being less critical crack location. Figure 7.62 also shows the $f_{(a/b)}$ of an unpatched central crack plate, obtained from Tada et al. (2000), whose governing equation has been shown in Equation 7.61. The polynomial functions for $f_{(a/b)}$ variation for all the specimens shown in Figure 7.62 are again reproduced below in Equations 7.92 through 7.96, respectively for the un-delaminated case as well as for the four adhesive shear strengths. It can be noted that the $f_{(a/b)}$ Equations 7.92 and 7.96 are identical. It was because of no adhesive failure or patch delamination found in the model of adhesive shear strength of 35 MPa.

$f_{(a/b)} = 0.8531\ (a/b)^2 - 0.9727\ (a/b) + 0.6992$ 7.92

$f_{(a/b)} = 2.1683\ (a/b)^2 - 1.0838\ (a/b) + 0.6986$ 7.93

$f_{(a/b)} = 1.9164\ (a/b)^2 - 1.3185\ (a/b) + 0.7239$ 7.94

$f_{(a/b)} = 1.4111\ (a/b)^2 - 1.1847\ (a/b) + 0.716$ 7.95

$f_{(a/b)} = 0.8531\ (a/b)^2 - 0.9727\ (a/b) + 0.6992$ 7.96

7.5.11.4 Central cracked plate with patch ETR 0.42 and adhesive G_A/t_A of 0.25 after delamination

Following similar procedure of evaluating geometric factors $f_{(a/b)}$, as already been carried out for all previous specimens, the geometric factors $f_{(a/b)}$ for the central crack specimens with patch ETR 0.42 and adhesive G_A/t_A of 0.25 were also evaluated. The procedure involved extraction of the K_{Imin} and K_{Imax} values from the FEA of four crack-length models and following the procedure of section 7.3. The extracted K_{Imax} values and the developed $f_{(a/b)}$ variations, are respectively shown in Figures 7.63 and 7.64. These were corresponding to the four adhesive shear strengths 'T' of 7.5 MPa, 15 MPa, 25 MPa and 35 MPa. The figures show that the K_{Imax} or the $f_{(a/b)}$ values were very less affected by the patch delamination in the analysis. None of the FEM of specimens, with adhesive shear strengths of 25 MPa and 35 MPa, suffered with the patch delamination in any crack length.

Therefore, the K_{Imax} or the $f_{(a/b)}$ values were not changed after the introduction of patch delamination in these specimens. Even in the specimens with adhesive shear strengths of 7.5 MPa and 15 MPa, very small patch delamination found. The FEA of specimen with adhesive shear strength of 15 MPa showed that only the largest crack length of 40 mm suffered with the patch delamination. The main reasons for getting small delamination impact have already been discussed in detail in sections 7.5.2.3, 7.5.2.4 and in the conclusions of chapters 3 and 4. Figure 7.64 also shows the $f_{(a/b)}$ of an unpatched central crack plate, obtained from Tada et al. (2000), whose governing equation has been shown in Equation 7.61. The polynomial functions for $f_{(a/b)}$ variation of all specimens, shown in Figure 7.64, are again reproduced below in Equations 7.97 through 7.101, respectively for the un-delaminated case as well as for the four adhesive shear strengths.

It can be noted that the $f_{(a/b)}$ Equations 7.100 and 7.101, which are for the adhesive shear strengths of 25 MPa and 35 MPa, are identical to the Equation 7.97, which is for the un-delaminated case. It was because of no deamination and no delamination impact in these specimens.

$$f_{(a/b)} = -0.0037\,(a/b)^3 + 0.4572\,(a/b)^2 - 0.6562\,(a/b) + 0.714 \quad 7.97$$

$$f_{(a/b)} = 2.4373\,(a/b)^2 - 1.2975\,(a/b) + 0.7595 \quad 7.98$$

$$f_{(a/b)} = 1.1099\,(a/b)^2 - 0.9047\,(a/b) + 0.7336 \quad 7.99$$

$$f_{(a/b)} = -0.0037\,(a/b)^3 + 0.4572\,(a/b)^2 - 0.6562\,(a/b) + 0.714 \quad 7.100$$

$$f_{(a/b)} = -0.0037\,(a/b)^3 + 0.4572\,(a/b)^2 - 0.6562\,(a/b) + 0.714 \quad 7.101$$

7.5.12 Central cracked plate with patch ETR 0.63 before delamination

The geometric factors $f_{(a/b)}$ were developed for the central cracked specimens of ETR 0.63 group, following the methodology of section 7.3 and the procedure that has been used in all specimens of the current parametric study. The K_{Imax} for the current specimens, were extracted from the results of FEA of the four crack length models of each specimen, before introduction of the patch delamination in the analysis. These are plotted in Figure 7.65 with the non-dimensionlized crack length (a/b). The trend of variation of $K_{I\,max}$ in Figure 7.65 was similar to that found in all ETR groups of edge cracked as well as central cracked specimen. Figure 7.65 shows higher $K_{I\,max}$ values in specimens with lower adhesive G_A /t_A and vice versa and that the difference increases with increase in the crack length. Figure 7.65 also shows lesser K_{Imax} difference (5 % to 12 %) between the specimens of adhesive G_A/t_A 0.25 and 1, and of adhesive G_A /t_A of 10 and 20. This finding was similar to the finding of all ETR groups of edge cracked and central cracked cases. It shows that the SIF variation was not much affected by further increase or decrease in the adhesive G_A /t_A, either above 10 or below 1, keeping in view that the G_A/t_A of 20 and 0.25 were the upper and lower bounds of the practically available adhesive properties.

Comparing the K_{Imax} variations of Figure 7.65 with the K_{Imax} variations in ETR 0.42, it was found that the K_{Imax} values were lesser in current ETR group by 11 % to 15 %, which was as expected because of higher patch ETR.

7.5.13 Central cracked plate with patch ETR 0.63 after delamination

The study of SIF and the geometric factors $f_{(a/b)}$ was carried out in the central crack specimens with ETR of 0.63, before and after the introduction of patch delamination, following the methodology mentioned in section 7.3. But as already mentioned in sections 7.5.2, 7.5.4, 7.5.6, 7.5.9 and 7.5.11, that after introduction of the adhesive failure (or the patch delamination), in the FEA, comparison of $K_{I\ max}$ or $f_{(a/b)}$ variation became more complex. It was shown in sections 7.5.2, 7.5.4, 7.5.6, 7.5.9 and 7.5.11 that a better way of presenting and comparing the K_{Imax} or the $f_{(a/b)}$ of specimens with different adhesive G_A/t_A and adhesive shear strength T, was to draw comparison within sub-groups of specimens. The sub-groups have identical adhesive G_A/t_A and ETR, but have varying adhesive shear strengths. Therefore, the K_{Imax} and the $f_{(a/b)}$ variation for the current ETR group are presented in a similar way for the specimens of ETR 0.63 in the following sections.

7.5.13.1 Central cracked plate with patch ETR 0.63 and adhesive G_A/t_A of 20 after delamination

Repeating the procedure of introduction of patch delamination in the FEA and following section 7.3, the K_I values corresponding to the applied stresses σ_{max} and σ_{min}, were extracted from the results of FEA of the four-crack models of each specimen. The $K_{I\ max}$ was extracted before and after the patch delamination, corresponding to the four adhesive shear strengths T of 7.5 MPa, 15 MPa, 25 MPa and 35 MPa. The extracted $K_{I\ max}$ values and the evaluated $f_{(a/b)}$ functions are respectively shown in Figures 7.66 and 7.67. The trend of K_{Imax} variation in Figure 7.66 is shown to be depending upon the adhesive shear strength, which was also a common finding in all ETR groups of edge cracked or central cracked case.

Comparing the K_{Imax} values of Figure 7.66 with the central crack specimens of patch ETR 0.42, with adhesive G_A/t_A of 20, it is obvious that the K_{Imax} magnitudes are lesser in the

current case by 11 % to 22 % because of higher patch ETR. Only the specimen, with adhesive shear strength of 7.5 MPa, has shown the adhesive failure in all of its crack lengths. Most of the specimens of adhesive shear strengths of 25 MPa and 35 MPa showed no adhesive failure in their smaller crack lengths but showed very small adhesive failure in their lager cracks models. Figure 7.67 shows the $f_{(a/b)}$ variation with non-dimensionlized crack length (a/b) of the central crack specimens of ETR 0.63, with adhesive G_A/t_A of 20 and for four adhesive shear strengths 'T' (or the four equivalent adhesive shear strength ratios T/σ_o). Figure 7.67 also includes the $f_{(a/b)}$ of an unpatched central crack plate, obtained from Tada et al. (2000), with its governing equation mention in Equation 7.61.

Figure 7.67 shows that the $f_{(a/b)}$ values were higher for weaker adhesive shear strength and vice versa, which was the common finding in all the specimens of the edge crack and central crack plate. The polynomial functions for $f_{(a/b)}$ variation, for all specimens shown in Figure 7.67, are again reproduced below in Equations 7.102 through 7.106. These equations are respectively for the un-delaminated case and for the four adhesive shear strengths 'T' of 7.5 MPa, 15 MPa, 25 MPa and 35 MPa.

$$f_{(a/b)} = 1.5327\,(a/b)^2 - 1.3089\,(a/b) + 0.4699 \qquad 7.102$$

$$f_{(a/b)} = 1.71\,(a/b)^2 - 0.4995\,(a/b) + 0.4252 \qquad 7.103$$

$$f_{(a/b)} = 2.1354\,(a/b)^2 - 0.9006\,(a/b) + 0.4216 \qquad 7.104$$

$$f_{(a/b)} = 2.9848\,(a/b)^2 - 1.6184\,(a/b) + 0.4832 \qquad 7.105$$

$$f_{(a/b)} = 2.010\,(a/b)^2 - 1.3764\,(a/b) + 0.470 \qquad 7.106$$

7.5.13.2 Central cracked plate with patch ETR 0.63 and adhesive G_A/t_A of 10 after delamination

Repeating the procedure of introduction of patch delamination in the FEA, as mentioned in section 7.3, the K_I values corresponding to the applied stresses σ_{max} and σ_{min} were extracted from the results of FEA. These K_I values were extracted from the four crack models of each specimen, before and after the patch delamination and corresponding to the four adhesive shear strengths 'T' of 7.5 MPa, 15 MPa, 25 MPa and 35 MPa. The extracted $K_{I\,max}$ values and the evaluated $f_{(a/b)}$ functions are respectively shown in Figures 7.68 and 7.69. The trend of

K_{Imax} variation in Figure 7.68 is shown to be depending upon the adhesive shear strength, which was similar to all ETR groups of edge cracked or central cracked case.

Comparing the K_{Imax} values of Figure 7.68 with the central crack specimens of patch ETR 0.42, with adhesive G_A/t_A of 10, it is obvious that the K_{Imax} magnitudes were lesser in the current case by 17% to 20% because of higher patch ETR. Only the specimen with adhesive shear strength of 7.5 MPa has shown the adhesive failure in all of its crack lengths, while most of the specimens of adhesive shear strengths of 25 MPa and 35 MPa showed the no adhesive failure in their smaller crack length models but showed very small adhesive failure in their lager cracks models. The $f_{(a/b)}$ variations shown in Figure 7.69 are for the four adhesive shear strengths 'T'. Figure 7.69 also includes the $f_{(a/b)}$ of an unpatched central crack plate, obtained from Tada et al. (2000), with its governing equation mention in Equation 7.61. Figure 7.69 also shows that the $f_{(a/b)}$ values are higher for weaker adhesive shear strength and vice versa, which was a common finding in all the specimens of the edge crack and central crack plate. The polynomial functions for $f_{(a/b)}$ variation for all the specimens shown in Figure 7.67 are again reproduced below in Equations 7.107 through 7.111, respectively for the un-delaminated case as well as for the four adhesive shear strengths 'T' of 7.5 MPa, 15 MPa, 25 MPa and 35 MPa.

$$f_{(a/b)} = 1.5274\,(a/b)^2 - 1.3403\,(a/b) + 0.5178 \qquad 7.107$$

$$f_{(a/b)} = 1.7787\,(a/b)^2 - 0.6132\,(a/b) + 0.4663 \qquad 7.108$$

$$f_{(a/b)} = 2.256\,(a/b)^2 - 1.094\,(a/b) + 0.4874 \qquad 7.109$$

$$f_{(a/b)} = 2.4439\,(a/b)^2 - 1.4859(a/b) + 0.52 \qquad 7.110$$

$$f_{(a/b)} = 2.098\,(a/b)^2 - 1.4955\,(a/b) + 0.5273 \qquad 7.111$$

7.5.13.3 Central cracked plate with patch ETR 0.63 and adhesive G_A/t_A of 1 after delamination

The geometric factors $f_{(a/b)}$ of the central crack specimens with patch ETR 0.63 and with adhesive G_A/t_A of 1 were evaluated following the procedure of section 7.3, which has already been demonstrated in all previous edge crack or central crack specimens. The extracted K_{Imax} values and the developed $f_{(a/b)}$ variations, corresponding to the four adhesive shear strengths

'T' of 7.5 MPa, 15 MPa, 25 MPa and 35 MPa, are respectively shown in Figures 7.70 and 7.71. It is obvious in these figures that the K_{Imax} or the $f_{(a/b)}$ values were very less affected by the introduction of patch delamination in the analysis, even lesser than the case of the central cracked specimens of ETR 0.63 group with adhesive G_A/t_A of 1.0. None of the FEM of specimens with adhesive shear strengths of 25 MPa and 35 MPa suffered with the adhesive failure in any crack length.

Therefore, the K_{Imax} or the $f_{(a/b)}$ values were not changed after the introduction of patch delamination in these specimens. Even in the specimens with adhesive shear strengths of 7.5 MPa and 15 MPa, very small patch delamination was found. FEA of specimen with adhesive shear strength of 15 MPa showed that only the crack length of 30 mm and 40 mm were suffered with the patch delamination while the rest of lower crack lengths didn't show any delamination impact. The K_{Imax} values for the specimen with adhesive shear strength of 7.5 MPa in Figure 7.70 was similar to the specimens of patch ETR 0.42, but the magnitudes were lesser by 20 % in Figure 7.70. Main reasons for getting small delamination impact have already been discussed in detail in sections 7.5.2.3, 7.5.2.4, which have also been presented in the conclusions of chapters 3 and 4. Figure 7.71 also shows the $f_{(a/b)}$ of the unpatched central crack plate, obtained from Tada et al. (2000), whose governing equation has been shown in Equation 7.61. The polynomial functions for $f_{(a/b)}$ variation, for all the specimens shown in Figure 7.71, are again reproduced below in Equations 7.112 through 7.116, respectively for the un-delaminated case as well as for the four adhesive shear strengths (or the equivalent adhesive shear strength ratios T/σ_o).

It can be noted that the Equations 7.115 and 7.116 are identical, which were for the un-delaminated adhesive shear strengths of 25 MPa and 35 MPa. It was because no deamination and no delamination impact found in these crack lengths. These equations are also shown to be same as the Equation 7.112 because Equation 7.112 is for the un-delaminated case.

$$f_{(a/b)} = 0.8303\,(a/b)^2 - 0.9339\,(a/b) + 0.6208 \qquad 7.112$$

$$f_{(a/b)} = 2.3282\,(a/b)^2 - 1.2836\,(a/b) + 0.6383 \qquad 7.113$$

$$f_{(a/b)} = 1.2777\,(a/b)^2 - 1.054\,(a/b) + 0.6279 \qquad 7.114$$

$$f_{(a/b)} = 0.8303\,(a/b)^2 - 0.9339\,(a/b) + 0.6208 \qquad 7.115$$

$$f_{(a/b)} = 0.8303\,(a/b)^2 - 0.9339\,(a/b) + 0.6208 \qquad 7.116$$

7.5.13.4 Central cracked plate with patch ETR 0.63 and adhesive G_A/t_A of 0.25 after delamination

The geometric factors $f_{(a/b)}$ for the central crack specimens, with patch ETR of 0.63 and adhesive G_A/t_A of 0.25, were evaluated, following the methodology of section 7.3. The methodology has already been demonstrated in all previous specimens of edge crack and central crack plates. The geometric factors $f_{(a/b)}$ were evaluated through extraction of the K_{Imin} and K_{Imax} values from the FEA of four crack-length FEMs, and following the methodology of section 7.3. The extracted K_{Imax} values and the developed $f_{(a/b)}$ variations, corresponding to the four adhesive shear strengths 'T' of 7.5 MPa, 15 MPa, 25 MPa and 35 MPa, are respectively shown in Figures 7.72 and 7.73. It can be seen in these figures that the K_{Imax} or the $f_{(a/b)}$ values were least affected by patch delamination in the analysis, even lesser than the case of the central cracked specimens of ETR 0.63 group, with adhesive G_A/t_A of 1.0. None of the FEM of adhesive shear strengths of 25 MPa and 35 MPa suffered with the patch delamination in any crack length. Therefore, the K_{Imax} or the $f_{(a/b)}$ values were not changed after the introduction of patch delamination in these specimens.

Even in the specimens with adhesive shear strengths of 7.5 MPa and 15 MPa, very small patch delamination was found. The FEA of specimen with adhesive shear strength of 15 MPa showed that only the largest crack length of 40 mm suffered with the patch delamination. Main reasons for getting small delamination impact have already been discussed in detail in sections 7.5.2.3, 7.5.2.4 and in the conclusions of chapters 3 and 4 as well. Figure 7.73 also shows the $f_{(a/b)}$ of the unpatched central crack plate, obtained from Tada et al. (2000), whose governing equation has been shown in Equation 7.61. The polynomial functions for $f_{(a/b)}$ variation for all the specimens shown in Figure 7.73 are again reproduced below in Equations 7.117 through 7.121, respectively for the un-delaminated case as well as for the four adhesive shear strengths (or the equivalent adhesive shear strength ratios T/σ_o).

It can be noted that the $f_{(a/b)}$ Equations 7.120 and 7.121, which are for the patch delamination cases corresponding to the adhesive shear strengths of 25 MPa and 35 MPa, are exactly same as the Equation 7.117, which is for the un-delaminated case. It was because of no deamination and no delamination impact found in these specimens.

$$f_{(a/b)} = 0.1364\,(a/b)^3 + 0.3271\,(a/b)^2 - 0.6179\,(a/b) + 0.6499 \quad 7.117$$

$$f_{(a/b)} = 1.4456\,(a/b)^2 - 0.8555\,(a/b) + 0.6604 \quad 7.118$$

$$f_{(a/b)} = -2.56\,(a/b)^2 - 0.09\,(a/b) + 0.62 \quad 7.119$$

$$f_{(a/b)} = 0.1364\,(a/b)^3 + 0.3271\,(a/b)^2 - 0.6179\,(a/b) + 0.6499 \quad 7.120$$

$$f_{(a/b)} = 0.1364\,(a/b)^3 + 0.3271\,(a/b)^2 - 0.6179\,(a/b) + 0.6499 \quad 7.121$$

7.5.14 Comparison of impact of patch delamination in the central cracked specimens - Lower patch ETR versus higher patch ETR

In the parametric study provided above for the central cracked specimens, the results have been presented for the specimens of identical patch ETR and adhesive G_A/t_A, but with varying adhesive shear strength, to avoid complexity in the comparison. As already mentioned in section 7.5.2 that after the introduction of patch delamination in the FEA the resulting K_I variation would also depend upon the adhesive shear strength, in addition to the patch ETR and adhesive G_A/t_A. Therefore, the results have been presented separately for a group of specimens having identical ETR and adhesive G_A/t_A, but with varying adhesive shear strength. In that way, it was easier to compare the specimens with different adhesive shear strengths but with identical patch ETR and adhesive G_A/t_A. In this section some comparisons of K_I variation between specimens of different patch ETR, G_A/t_A and adhesive shear strengths, is presented, in order to highlight and compare the impact of the patch delamination in specimens with different ETR and adhesive G_A/t_A.

K_I variation in specimens of ETR of 0.63, with adhesive G_A/t_A 20 and adhesive shear strengths of 7.5 MPa and 15 MPa, are compared with specimens of ETR of 0.42, with adhesive G_A/t_A 10 and adhesive shear strengths of 25 MPa and 35 MPa. The resulting K_I variations are shown in Figure 7.74. It is obvious in Figure 7.74 that, before introduction of patch delamination, the K_I values in the specimen of ETR 0.42 with adhesive G_A/t_A 10 and 20, were 11 % to 40 % higher than the specimen of ETR 0.63 with adhesive G_A/t_A 20. It was because of lower patch ETR. But after the introduction of patch delamination, the resulting K_I values in higher ETR specimen, with adhesive shear strength of 7.5 MPa, became 50 % higher than the lower ETR specimen, with adhesive shear strength of 35 MPa.

Similarly, if the comparison is again drawn between the adhesive shear strengths of 35 MPa in lower ETR specimen and 15 MPa in the higher ETR specimen, then still it can be seen from Figure 7.74 that the K_I values of higher ETR specimen are higher than the K_I values of lower ETR specimen by 15 % to 25 % in the crack lengths of 30 mm and 40 mm (a/b of 0.3 and 0.4).

Another comparison was also drawn between the specimens of patch ETR of 0.63 and ETR of 0.21, with adhesive G_A/t_A of 20, and is shown in Figure 7.75. Before introduction of patch delamination, the K_I values in lower ETR specimen were 40 % to 58 % higher than the specimen of higher patch ETR, because of three times higher patch ETR. But, after the introduction of patch delamination in larger crack length models, the K_I values in higher ETR patch, with adhesive shear strength of 7.5 MPa, became 6 % greater than the lower ETR patch, with adhesive shear strength of 35 MPa. Although, in lower crack lengths, the K_I values in higher ETR patch, were lower than the lower ETR patch.

The above comparison highlighted the role of adhesive shear strength in reducing the efficiency of higher ETR patches and showed that a higher ETR patch may become less efficient, even lesser than a lower ETR patch, if its adhesive shear strength is quite less than the shear strength of lower ETR patch. Even if the adhesive shear strength of higher ETR patch is not significantly lower then still the efficiencies of the two patches are expected to be close, or the higher ETR patch would not be much effective than the lower ETR patch by a big proportion, as it would be, if the adhesive shear strength is not too low in it.

7.6 Summary

The main focus of this chapter was intended towards development of geometric factors $f_{(a/b)}$ for edge cracked and central cracked steel plates, repaired with bonded CFRP patches, having various CFRP and adhesive properties. The methodology of evaluating the geometric factor $f_{(a/b)}$ is described in section 7.3, which has already been presented and demonstrated in detail in chapter 6. Equation 6.2a was used to develop the required geometric factors $f_{(a/b)}$ of the specimens of current study. Equation 6.2a requires that in order to evaluate the $f_{(a/b)}$, SIF (K_I) at the crack tip is required, which was obtained using finite element analysis (FEA). Additionally, impact of patch delamination was also included in the FEA through modeling of

failure of the interface adhesive layer around the crack. Therefore, the K_I obtained from it was also incorporating the effect of the patch delamination. The developed geometric factors can be used to predict or evaluate the fatigue life of the repairs, with varying crack length and applied stresses, and with various CFRP and adhesives properties.

The patch parameters selected in the current parametric study mainly included patch ETR, adhesive shear stiffness (G_A/t_A) and the adhesive shear strength τ_A. It is also important to mention that in order to vary the selected parameters, several basic patch parameters were actually varied. For example, in order to vary patch ETR the CFRP modulus of elasticity E_{frp} or the CFRP thickness t_{frp} were varied. Similarly, in order to vary the adhesive G_A/t_A the adhesive modulus of elasticity (E_A) or the adhesive thickness (t_A) were varied. The adhesive shear strength parameter τ_A/σ_o was varied in the current parametric study by varying the adhesive shear strength τ_A only and not the applied far filed stress σ_o, which was the upper limit of the applied stress range and it was fixed to be 200 MPa, throughout the parametric study.

Three ETR values of 0.2, 0.4 and 0.6 were selected for both the edge crack and central crack plates. Within each ETR group four adhesive shear stiffness (G_A/t_A) of 0.25, 0.1, 10 and 20 were selected, and within each G_A/t_A group four adhesive shear strengths of 7.5 MPa, 15 MPa, 25 MPa and 35 MPa were considered for the delamination study. These adhesive shear strengths were also represented by their non-dimensionlized form of τ_A/σ_o of 3.75 % 7.5 %, 12.5 % and 17.5 % in certain figures and sections. Table 7.1 shows the details of selected parameters (ETR, G_A/t_A and τ_A) used in current study as well as the values of basic parameters (E_{frp}, t_{frp}, E_A and t_A) through which the desired values of the selected parameters were obtained.

Plate dimensions were selected to be 500 mm long x 100 mm wide x 9.5 mm thick for the edge crack specimen and 500 mm long x 200 mm wide x 9.5 mm thick for the central crack specimen. Using planes of symmetry, only one quarter and one eighth model of actual plate dimensions, were developed for the FEA of the edge crack and central crack specimens, respectively. For each specimen of Table 7.1 four finite element models (FEM) were developed, with varying crack lengths of 10 mm, 20 mm, 30 mm and 40 mm, which were also equivalent to the non-dimensionlized crack length (a/b) of 0.1, 0.2, 0.3 and 0.4, respectively. FEA was carried out for each specimen and the resulting K_I were obtained from its results.

The patch delamination procedure was introduced in each FEM, corresponding to the particular adhesive shear strength used in each specimen. The patch delamination was introduced in FEA through incorporation of progressive failure of the interface adhesive layer, around the crack and it was carried out by progressive removal of the failed adhesive region around the crack. This process of introducing the patch delamination in FEA has been described and demonstrated in detail in sections 4.4 and 6.4. The K_I were again obtained from the results of the FEA of each specimen, after the converged stage of the patch delamination process.

The geometric factors $f_{(a/b)}$ were then finally developed, both before and after the induction of patch delamination, by non-dimensionalizing the results of ΔK_I, obtained from the FEA of four FEM of each specimen, by dividing these with factor $\Delta\sigma\sqrt{(\pi a)}$. Finally a continuous function of $f_{(a/b)}$ was developed by fitting a suitable polynomial function on the results of previously obtained non-dimensionalized ΔK_I with varying non-dimensionalized crack length (a/b). The K_I distribution developed from the results of FEA and the corresponding geometric factors $f_{(a/b)}$ for all specimens of Table 7.1, before and after the introduction of patch delamination, were shown in sections 7.5.1 through 7.5.7 for the three ETR groups of the edge cracked specimens. The same are developed and shown in sections 7.5.8 through 7.5.14 for the three ETR groups of the central cracked specimens. Conclusions, obtained from the comparison of K_I and the resulting geometric factors $f_{(a/b)}$, are summarized in the next section.

7.7 Conclusions from the parametric study

Conclusions are mostly based upon the comparison of the resulting K_I or ΔK_I distribution in the specimens of Table 7.1 because the geometric factors $f_{(a/b)}$ were developed on the basis of the same ΔK_I distribution with the only difference that the geometric factors $f_{(a/b)}$ were non-dimensionlized.

Before introduction of patch delamination in the edge crack specimens, the K_I variation within any ETR group, was found to be mainly dependent upon the adhesive G_A/t_A, and it was higher in specimen with lower adhesive G_A/t_A and vice versa. The trend of K_I variation with respect to the adhesive G_A/t_A, within any ETR group was identical in the three ETR groups, but the magnitude of K_I for any particular crack length was reducing with respect to increasing patch

ETR. Therefore, the highest K_I values were found in the specimen of the lowest ETR group, with smallest adhesive G_A/t_A. Within any ETR group of the edge crack specimens, before introduction of patch delamination, the difference in K_I values, between the specimens of highest and lowest adhesive G_A/t_A of 20 and 0.25, was ranging between 50 % and 150 %, but the difference was smaller (5 % to 15 %) if compared between the adhesive G_A/t_A of 0.25 and 1 or 10 and 20. It shows that the further change in adhesive G_A/t_A, below 1 or greater than 10, would not much affect the K_I variation.

In the central crack specimens, in general, the resulting trends of K_I variation, with respect to the adhesive G_A/t_A and patch ETR, were similar to the edge crack specimens but the magnitudes were 11 % to 24 % lower than the edge crack specimens.

After introduction of patch delamination, the K_I comparison could not be easily drawn on the basis of patch ETR and the adhesive G_A/t_A because of its further dependence upon the adhesive shear strength τ_A. Therefore, the ΔK_I variations and the respective $f_{(a/b)}$ functions were mostly presented separately for the specimens, having identical ETR as well as identical adhesive G_A/t_A, but with varying adhesive shear strength τ_A. For a specimen of any particular ETR and adhesive G_A/t_A, the K_I was found to be varying with respect to the adhesive shear strength. Largest K_I values, obtained after delamination in the specimen of lower adhesive shear strength and vice versa, for a given patch ETR and adhesive G_A/t_A.

Within any ETR group of the edge crack specimens, the delamination was found to be reducing with decreasing adhesive G_A/t_A, The SIF (K_I) was found to be reducing with the increase in the patch ETR, both before and after the patch delamination, but within any ETR group, the increase in SIF (K_I) after the patch delamination, compared to the un-delaminated case, was more or less same. It was found to be ranging between 25 % to 200 % for larger crack lengths and 3 % to 50 % for smaller crack lengths.

A comparison of increase in K_I values after the patch delamination in the edge crack specimens of two different ETR groups was drawn in section 7.5.7 and was also shown in Figures 7.45 and 7.46. It can be concluded from Figure 7.45 that for a higher ETR patched specimen, having 10 % to 28 % lesser K_I values than a lower ETR patched specimen, before the patch delamination, become less effective than the lower ETR patched specimen, after the patch delamination. It was due to weaker shear strength of its adhesive which resulted in raising its K_I values 20 % to 38 % higher than that of the lower ETR specimen.

In central crack specimens, before introduction of the patch delamination, the trends of variation of K_I were similar to the edge crack specimens, but the values of K_I for different crack lengths were 11 % to 24 % lesser than the edge crack specimens of identical patch ETR and adhesive G_A/t_A. After the introduction of patch delamination, the trends of variation of K_I were still similar to that of edge crack specimens but the values of K_I were 20 % to 30 % lesser than those of the edge crack specimens of identical ETR, adhesive G_A/t_A and identical adhesive shear strength. A comparison of increase in K_I values, after the patch delamination in the central crack specimens of two different ETR groups, was drawn in section 7.5.14 and also shown in Figures 7.74 and 7.75. It can be concluded from Figure 7.74 that before the patch delamination, the K_I values in specimen of ETR 0.4 with G_A/t_A of 10 were 11 % to 38 % higher than the K_I values in specimen of ETR 0.6, with G_A/t_A of 20, because of the difference in ETR and the adhesive G_A/t_A . But after the patch delamination, the K_I values in specimen of ETR 0.6, with adhesive shear strength of 7.5 MPa, became higher than the K_I values of the specimen of ETR 0.2, with adhesive shear strength of 35 MPa. It shows that weaker adhesive can reduce the efficiency of a higher ETR patch, which was not before the patch delamination occurred.

Table 7.1 Specimen details used in the parametric study

E_{frp}	t_{frp}	ETR	E_A	t_A	G_A/t_A	Adh-Shear Str (τ)	Adh (τ / σ_o) Ratio
(GPa)	(mm)		(GPa)	(mm)	(GPa/mm)	(MPa)	(%)
81	0.816	0.21	1.34	2	0.25	7.5, 15, 25, 35	3.75, 7.5, 12.5, 17.5
81	0.816	0.21	0.268	0.1	1	7.5, 15, 25, 35	3.75, 7.5, 12.5, 17.5
81	0.816	0.21	2.68	0.1	10	7.5, 15, 25, 35	3.75, 7.5, 12.5, 17.5
81	0.816	0.21	5.36	0.1	20	7.5, 15, 25, 35	3.75, 7.5, 12.5, 17.5
162	0.816	0.42	1.34	2	0.25	7.5, 15, 25, 35	3.75, 7.5, 12.5, 17.5
162	0.816	0.42	0.268	0.1	1	7.5, 15, 25, 35	3.75, 7.5, 12.5, 17.5
162	0.816	0.42	2.68	0.1	10	7.5, 15, 25, 35	3.75, 7.5, 12.5, 17.5
162	0.816	0.42	5.36	0.1	20	7.5, 15, 25, 35	3.75, 7.5, 12.5, 17.5
124	1.6	0.63	1.34	2	0.25	7.5, 15, 25, 35	3.75, 7.5, 12.5, 17.5
124	1.6	0.63	0.268	0.1	1	7.5, 15, 25, 35	3.75, 7.5, 12.5, 17.5
124	1.6	0.63	2.68	0.1	10	7.5, 15, 25, 35	3.75, 7.5, 12.5, 17.5
124	1.6	0.63	5.36	0.1	20	7.5, 15, 25, 35	3.75, 7.5, 12.5, 17.5

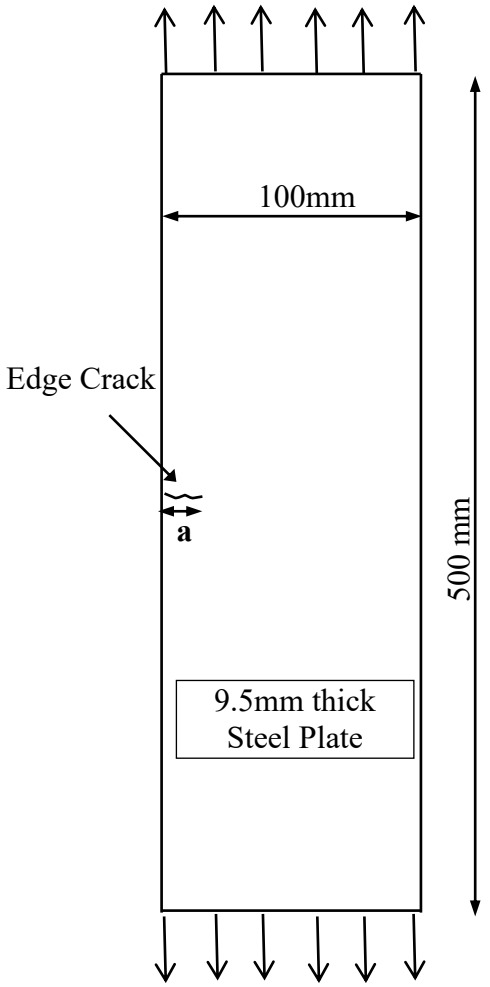

Figure 7.1 Typical edge crack plate

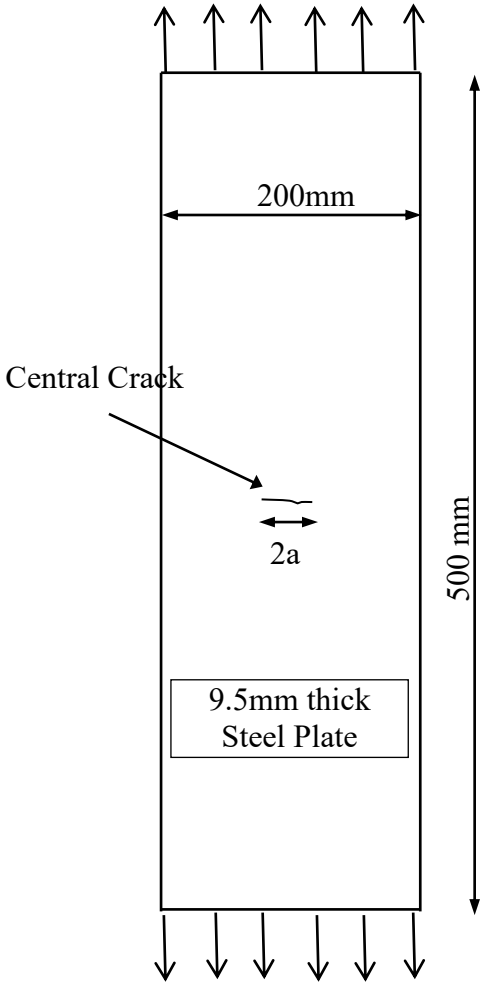

Figure 7.2 Typical central crack plate

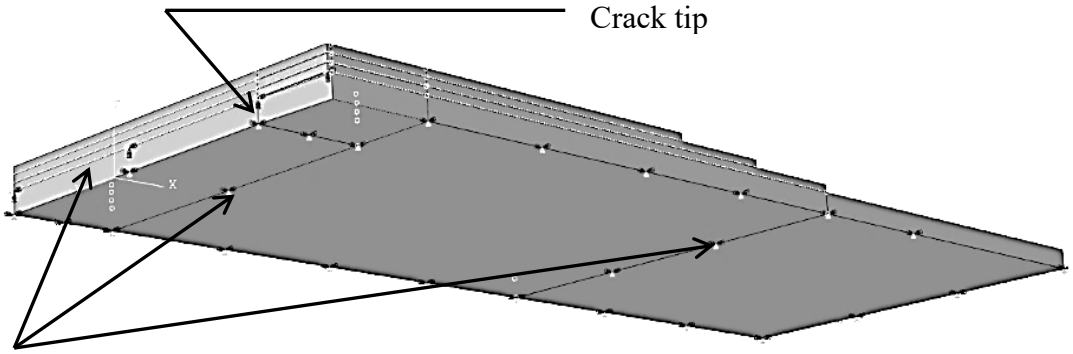

Figure 7.3 Typical edge crack specimen used in finite element analysis

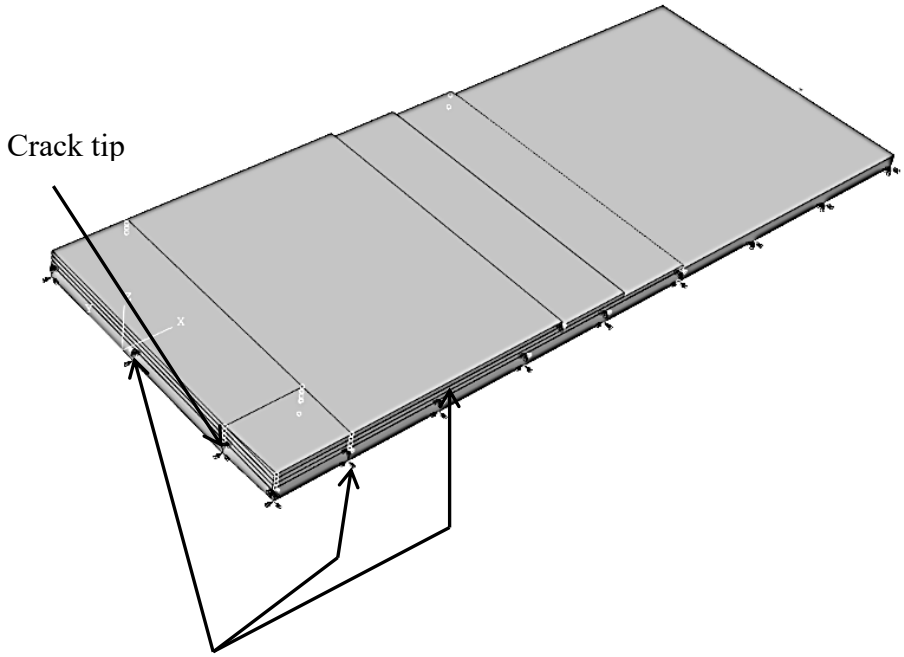

Figure 7.4 Typical central crack specimen used in finite element analysis

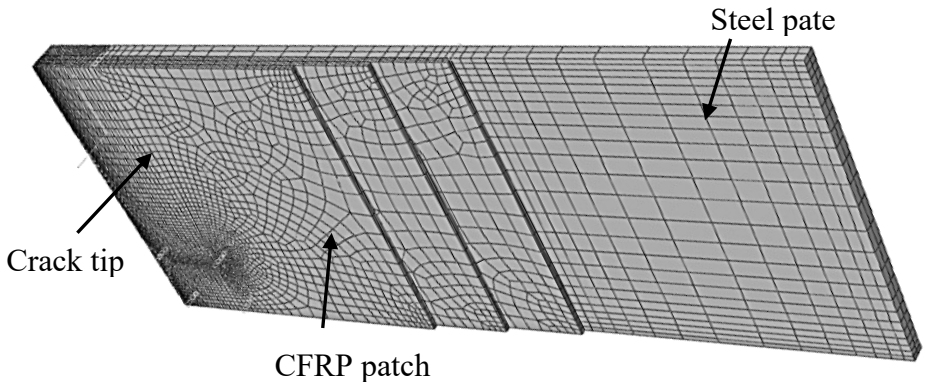

Figure 7.5 Typical three-layered patched specimen used in finite element analysis

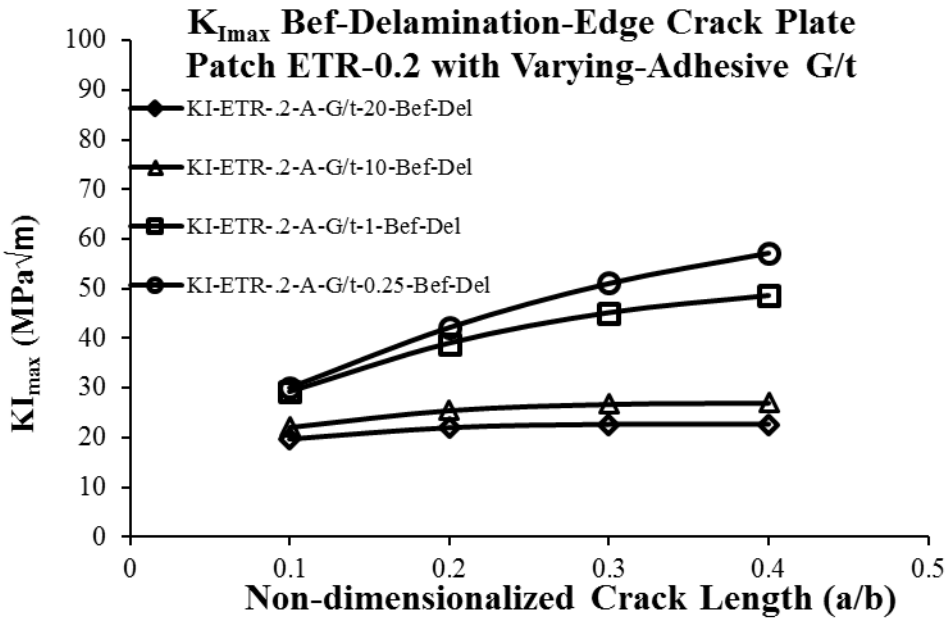

Figure 7.6 Variation of $K_{I\,max}$ in edge cracked specimens of ETR 0.2 with varying adhesive G_A/t_A

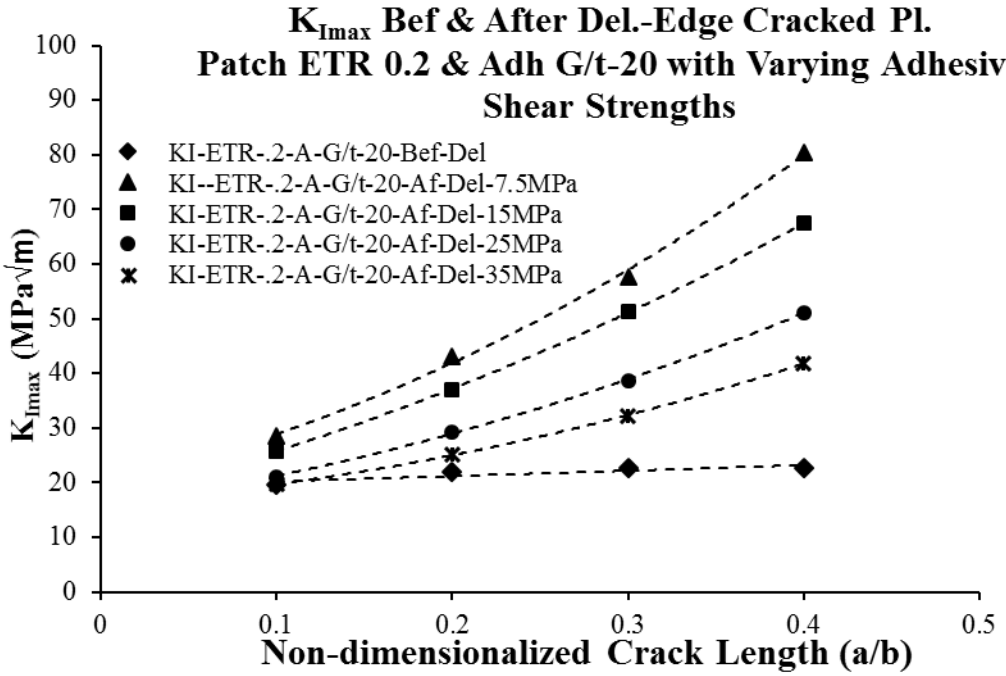

Figure 7.7 Variation of $K_{I\,max}$ in edge cracked specimens of ETR 0.2 and adhesive G_A/t_A 20 with varying adhesive shear strengths

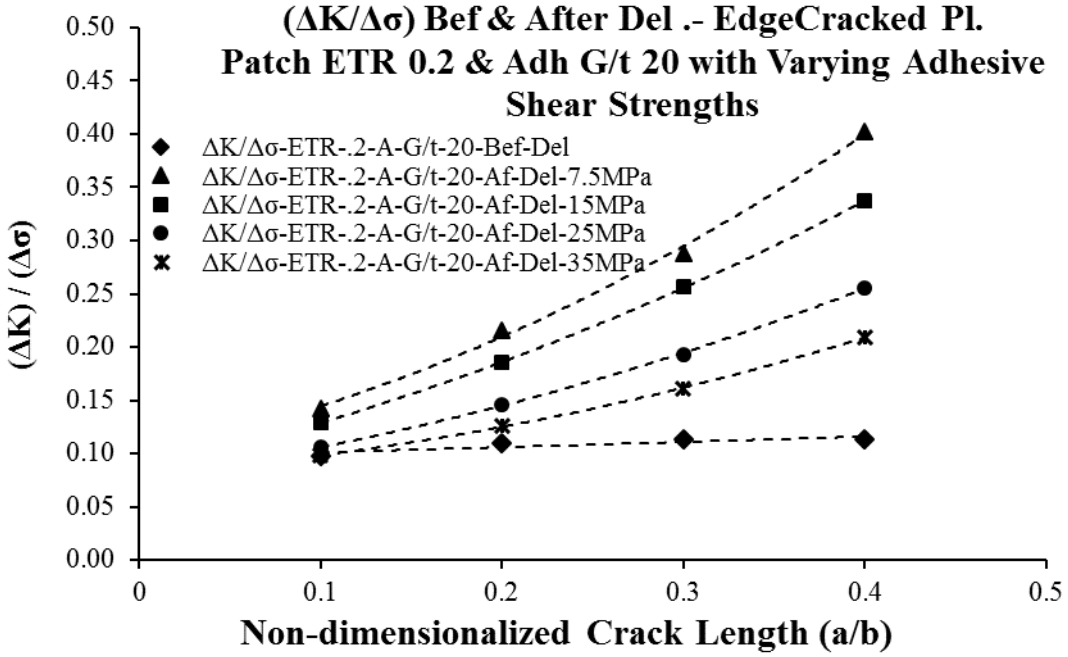

Figure 7.8 Variation of $\Delta K_I/\ \Delta\sigma$ in edge cracked specimens of ETR 0.2 and adhesive G_A/t_A 20 with varying adhesive shear strengths

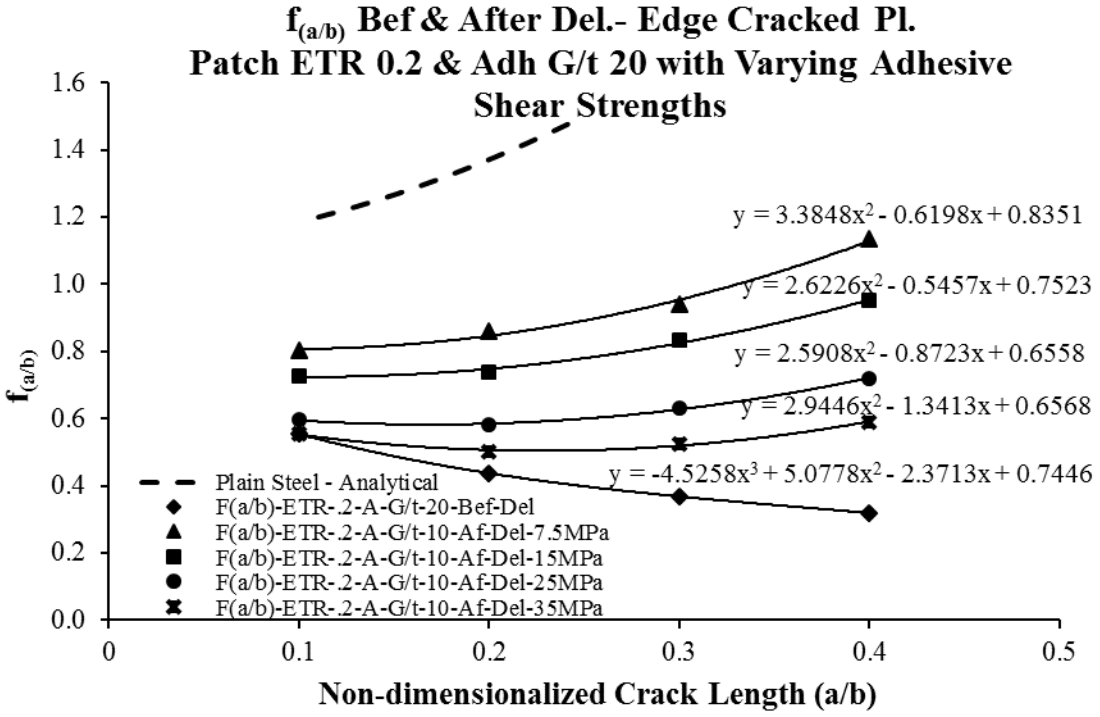

Figure 7.9 Geometric factor $f_{(a/b)}$ for edge cracked specimens of ETR 0.2 and adhesive G_A/t_A 20 with varying adhesive shear strengths

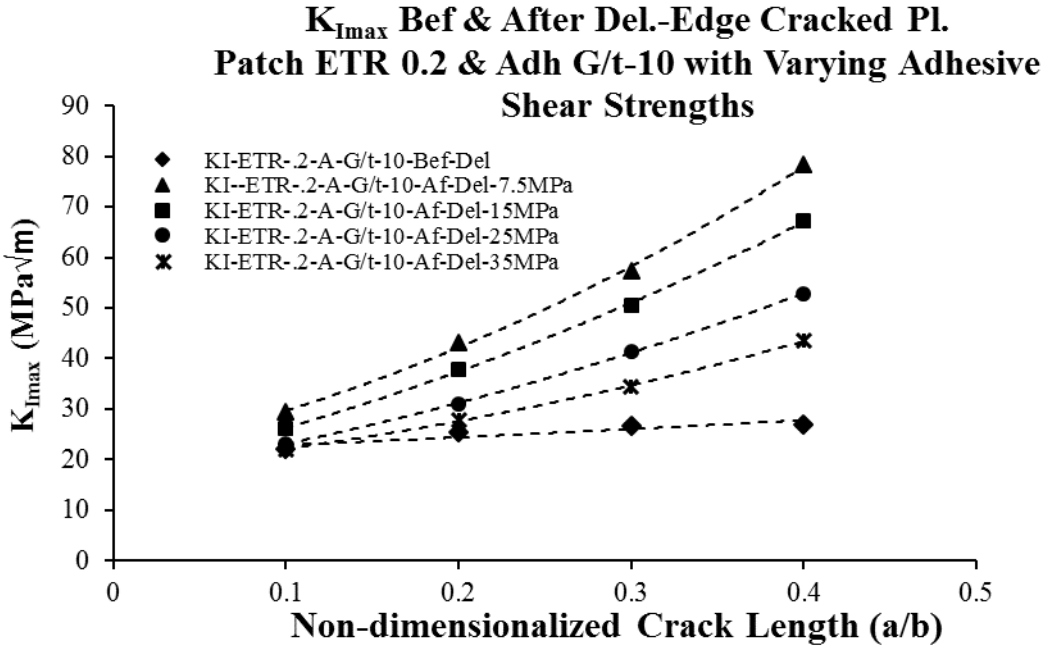

Figure 7.10 Variation of $K_{I\,max}$ in edge cracked specimens of ETR 0.2 and adhesive G_A/t_A 10 with varying adhesive shear strengths

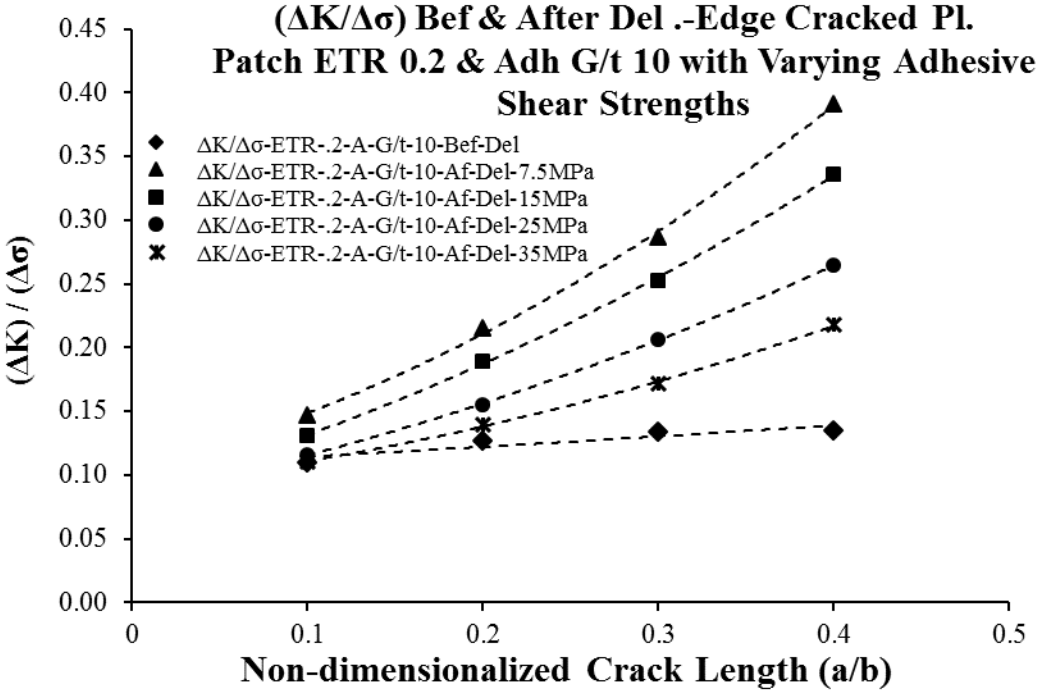

Figure 7.11 Variation of $\Delta K_I/\ \Delta\sigma$ in edge cracked specimens of ETR 0.2 and adhesive G_A/t_A 10 with varying adhesive shear strengths

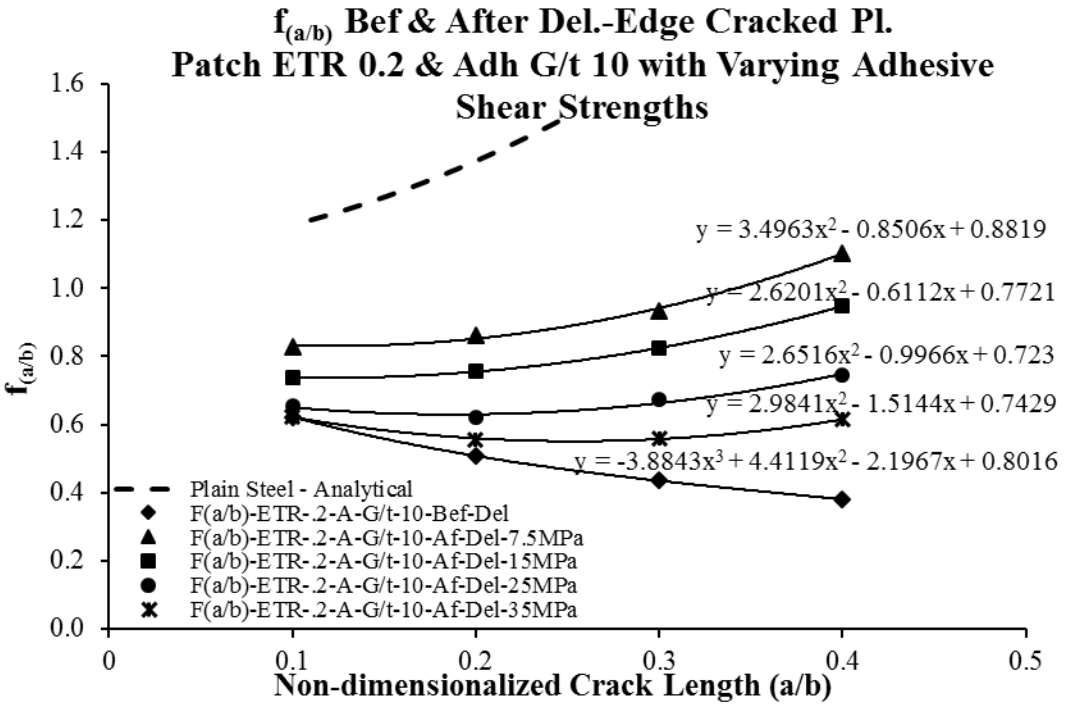

Figure 7.12 Geometric factor $f_{(a/b)}$ for edge cracked specimens of ETR 0.2 and adhesive G_A/t_A 10 with varying adhesive shear strengths

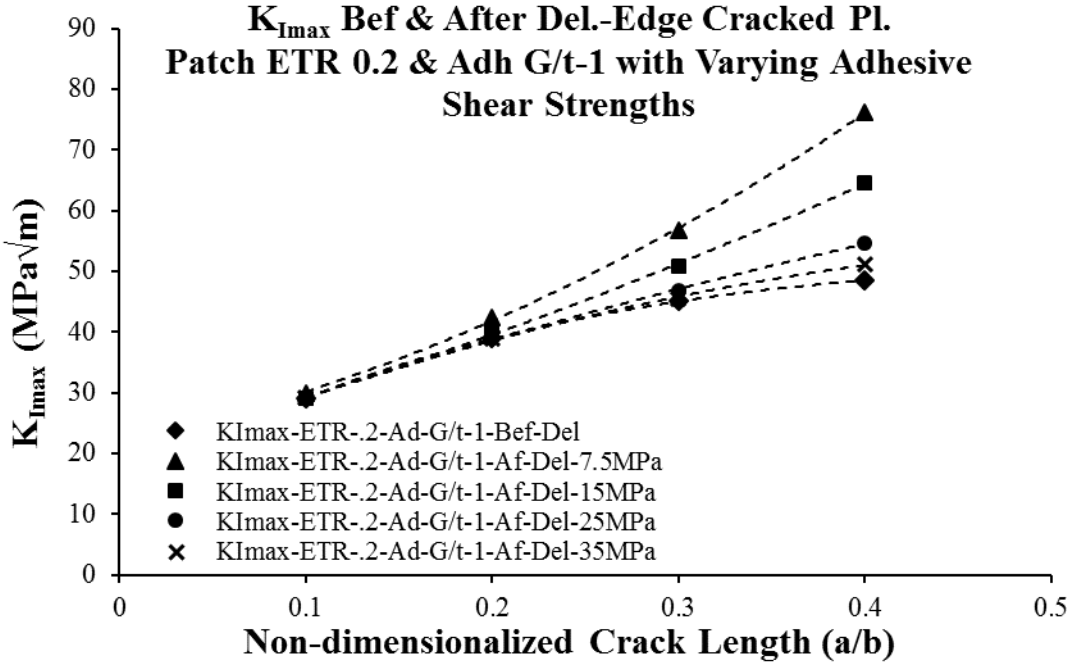

Figure 7.13 Variation of $K_{I\,max}$ in edge cracked specimens of ETR 0.2 and adhesive G_A/t_A 1 with varying adhesive shear strengths

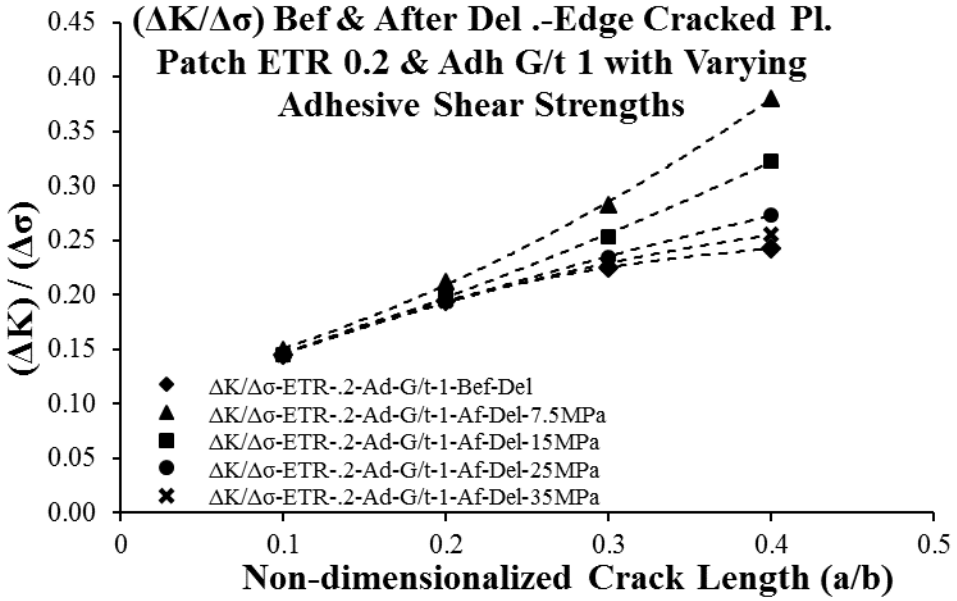

Figure 7.14 Variation of $\Delta K_I/\ \Delta\sigma$ in edge cracked specimens of ETR 0.2 and adhesive G_A/t_A 1 with varying adhesive shear strengths

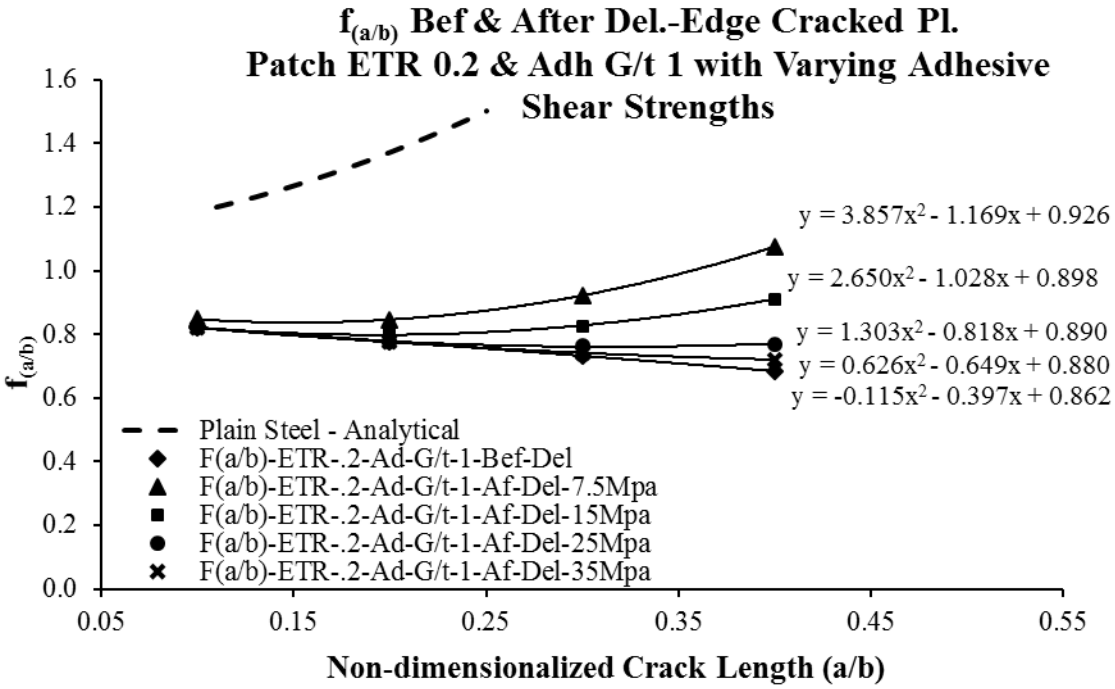

Figure 7.15 Geometric factor $f_{(a/b)}$ for edge cracked specimens of ETR 0.2 and adhesive G_A/t_A 1 with varying adhesive shear strengths

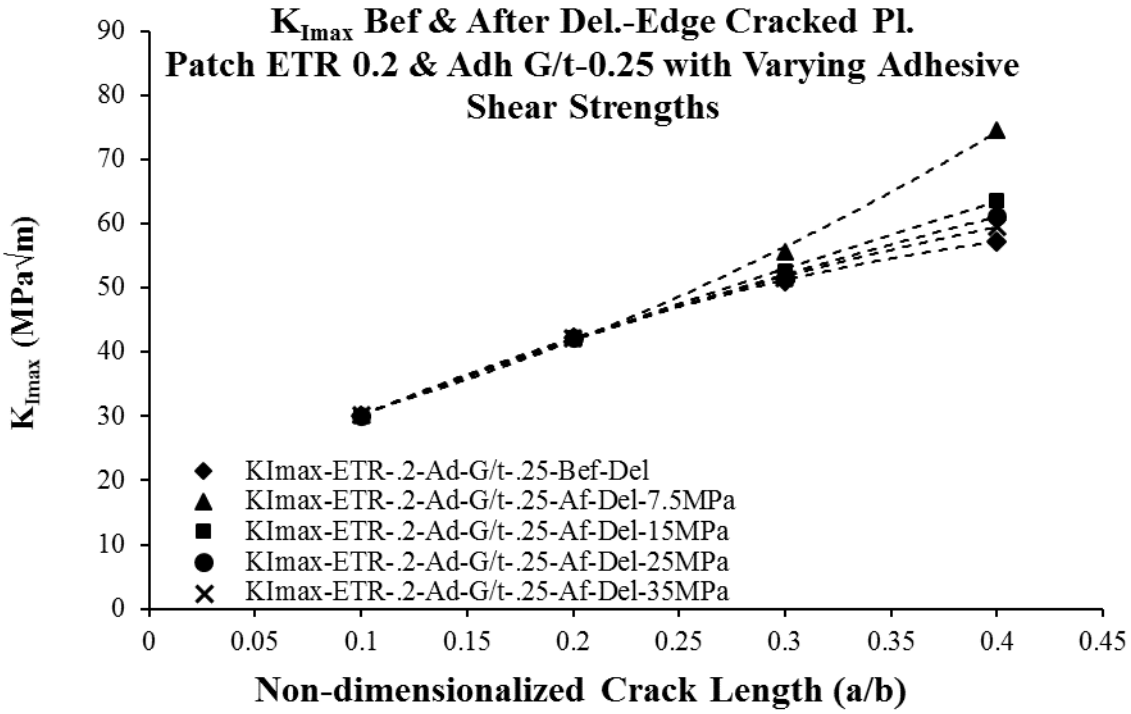

Figure 7.16 Variation of $K_{I\,max}$ in edge cracked specimens of ETR 0.2 and adhesive G_A/t_A 0.25 with varying adhesive shear strengths

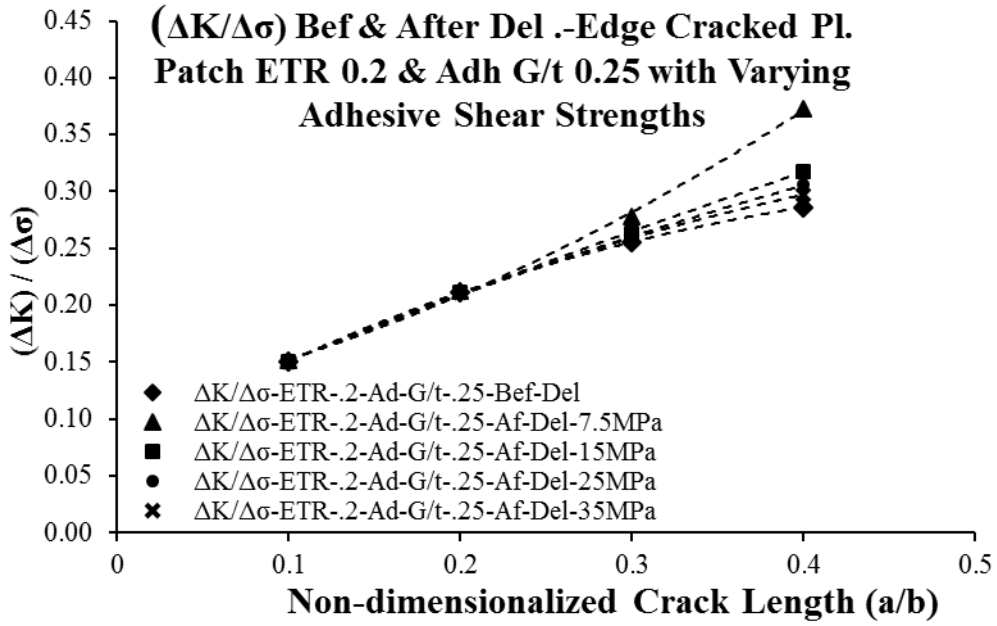

Figure 7.17 Variation of $\Delta K_I/ \Delta\sigma$ in edge cracked specimens of ETR 0.2 and adhesive G_A/t_A 0.25 with varying adhesive shear strengths

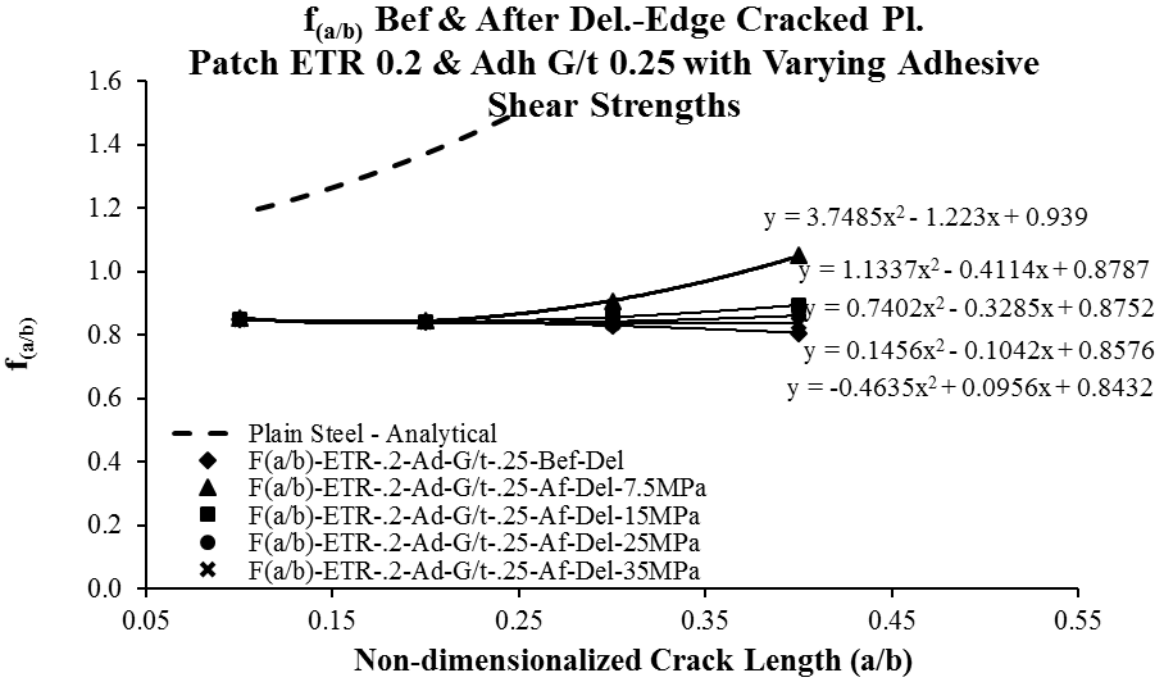

Figure 7.18 Geometric factor $f_{(a/b)}$ for edge cracked specimens of ETR 0.2 and adhesive G_A/t_A 0.25 with varying adhesive shear strengths

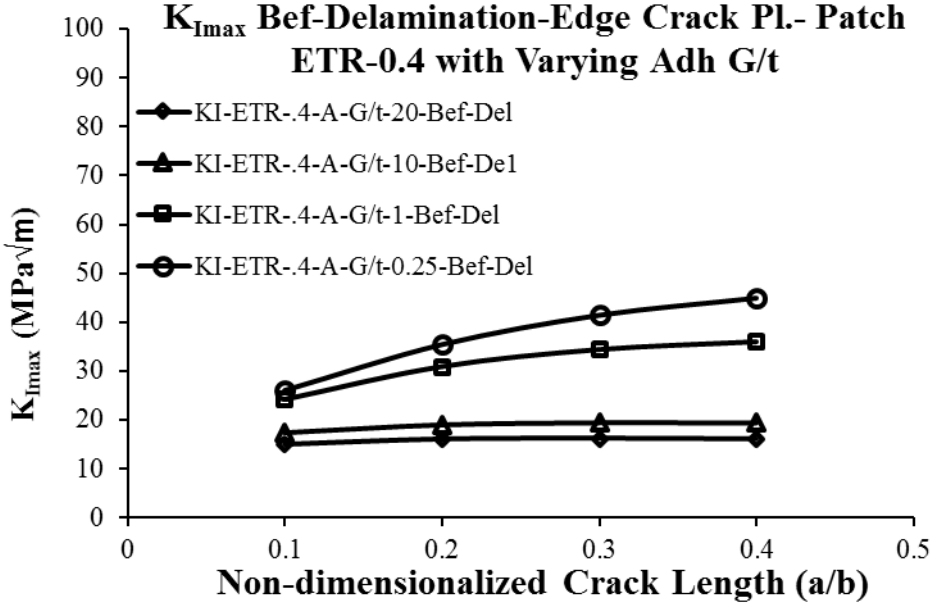

Figure 7.19 Variation of $K_{I\,max}$ in edge cracked specimens of ETR 0.4 with varying adhesive G_A/t_A

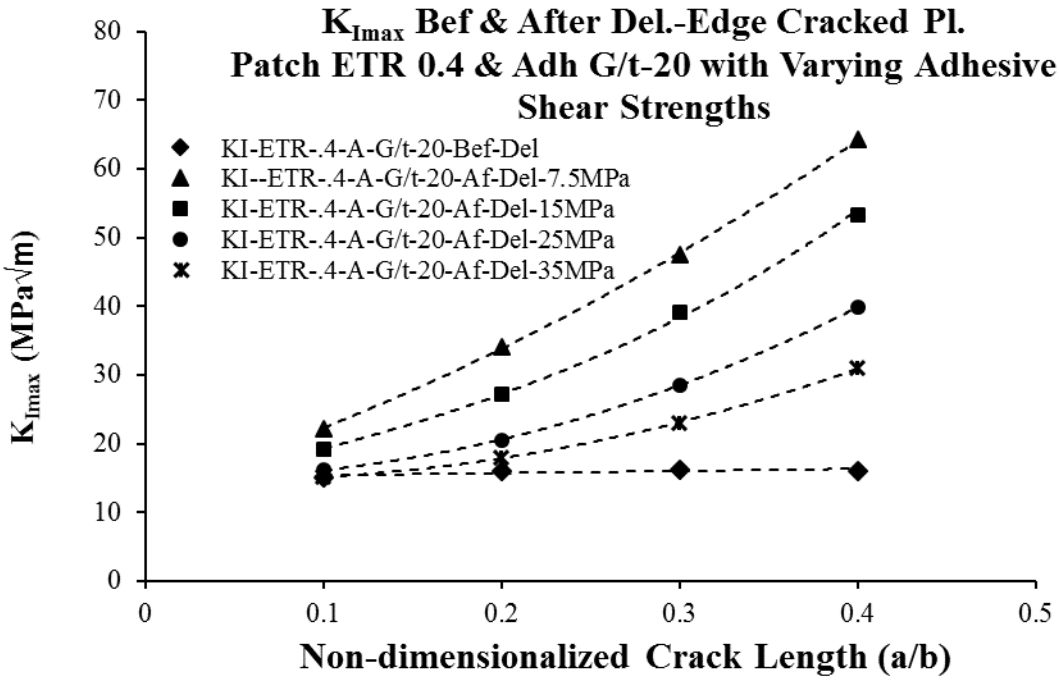

Figure 7.20 Variation of $K_{I\,max}$ in edge cracked specimens of ETR 0.4 and adhesive G_A/t_A 20 with varying adhesive shear strengths

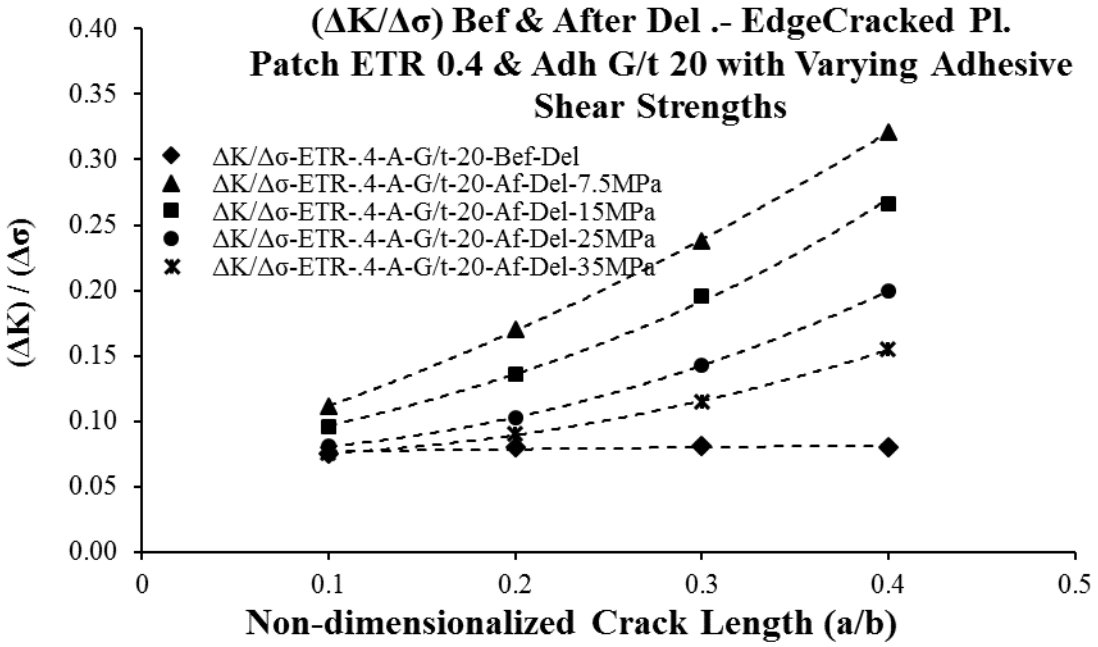

Figure 7.21 Variation of $\Delta K_I/\ \Delta\sigma$ in edge cracked specimens of ETR 0.4 and adhesive G_A/t_A 20 with varying adhesive shear strengths

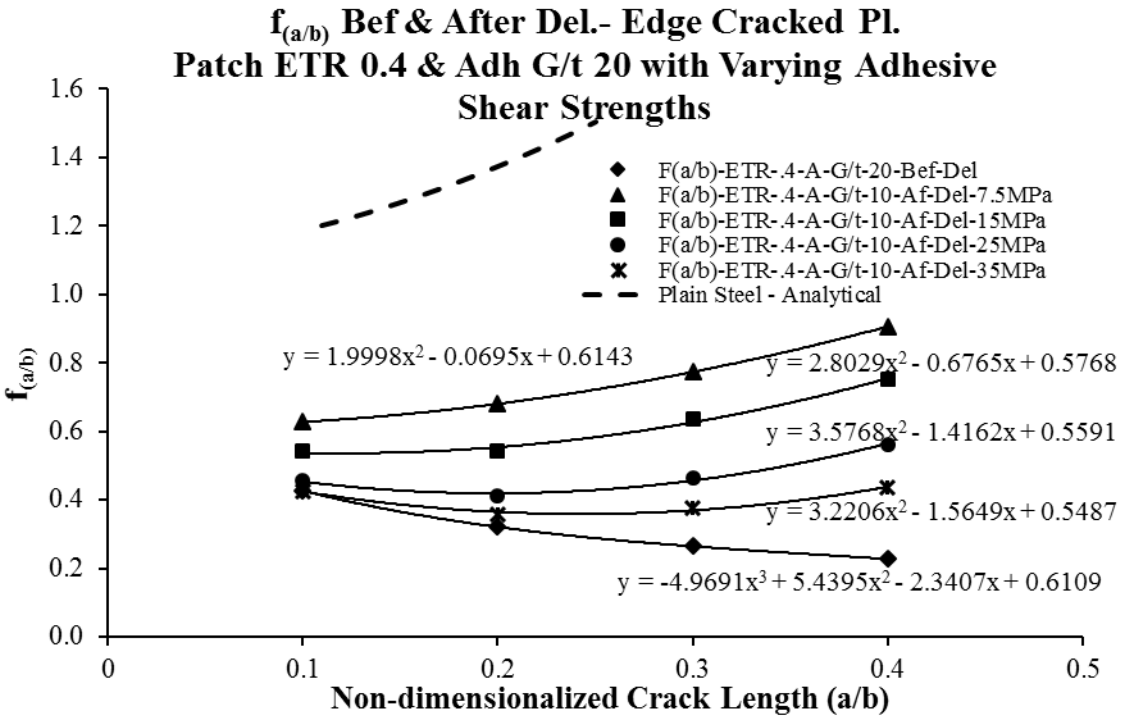

Figure 7.22 Geometric factor $f_{(a/b)}$ for edge cracked specimens of ETR 0.4 and adhesive G_A/t_A 20 with varying adhesive shear strengths

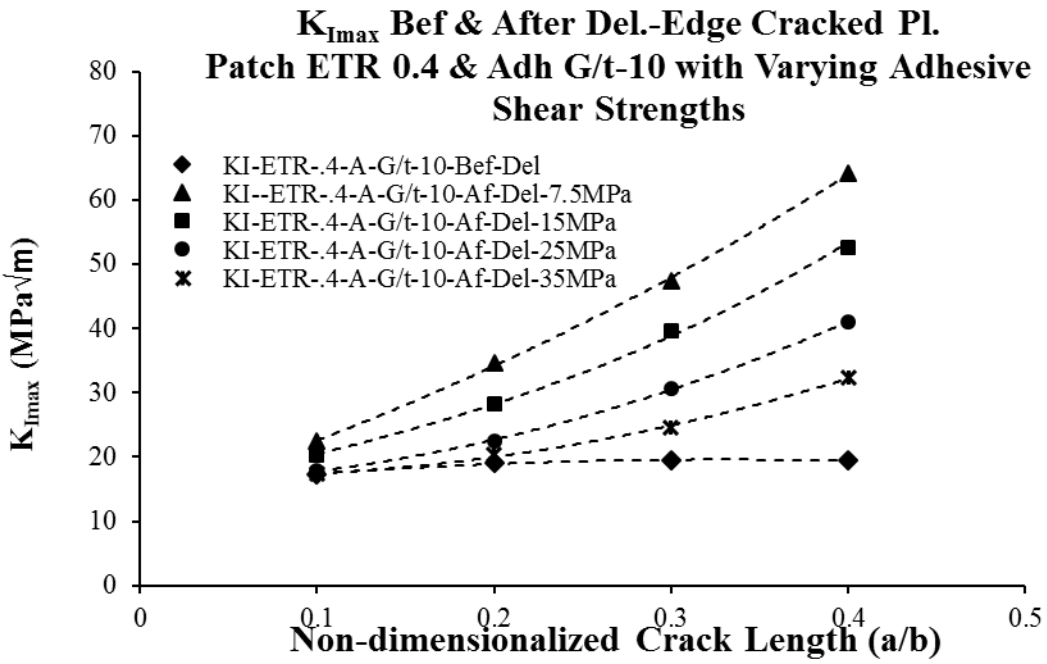

Figure 7.23 Variation of $K_{I\,max}$ in edge cracked specimens of ETR 0.4 and adhesive G_A/t_A 10 with varying adhesive shear strengths

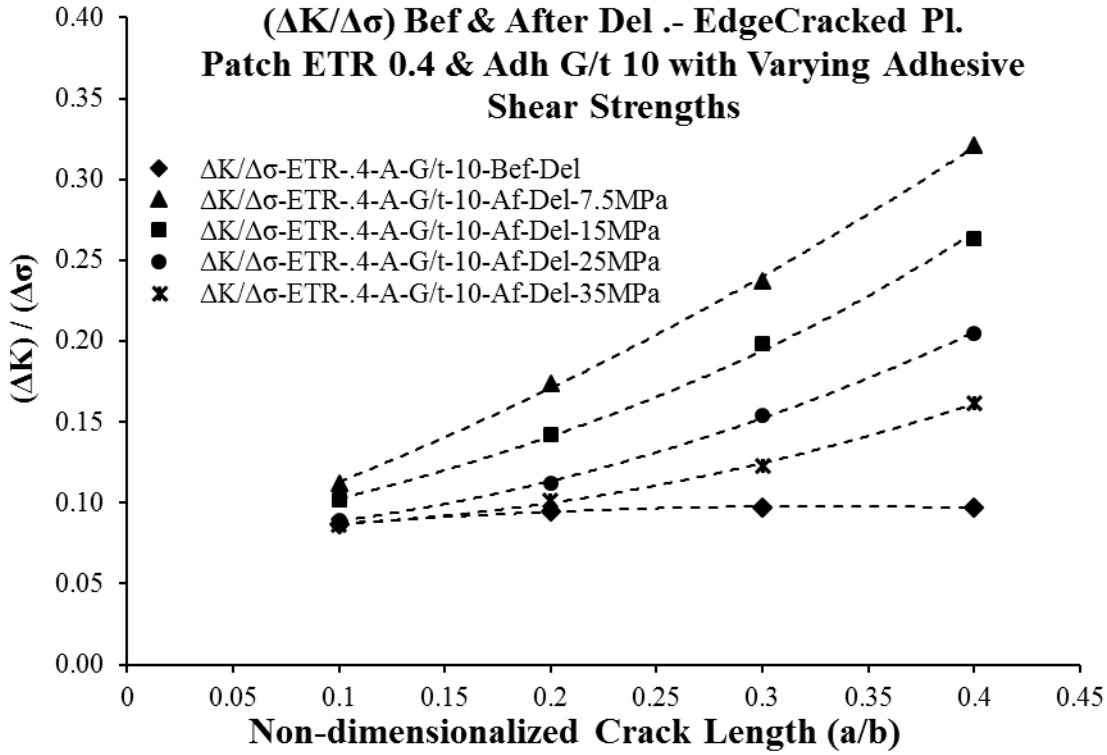

Figure 7.24 Variation of $\Delta K_I/\ \Delta\sigma$ in edge cracked specimens of ETR 0.4 and adhesive G_A/t_A 10 with varying adhesive shear strengths

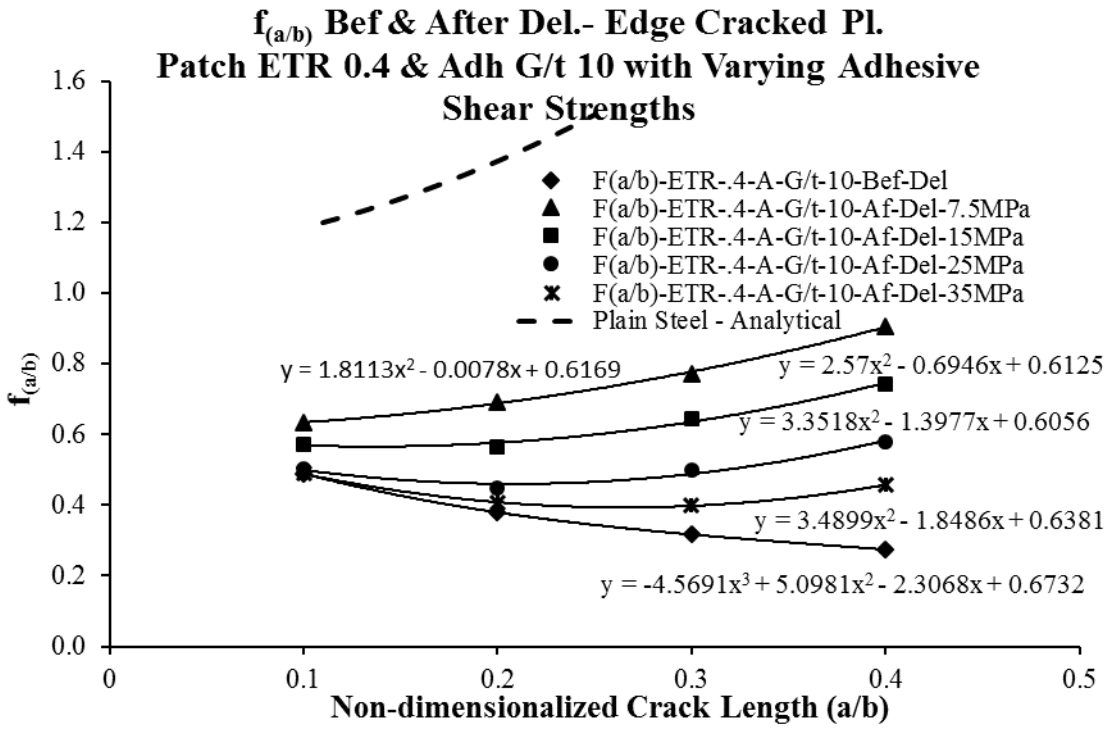

Figure 7.25 Geometric factor $f_{(a/b)}$ for edge cracked specimens of ETR 0.4 and adhesive G_A/t_A 10 with varying adhesive shear strengths

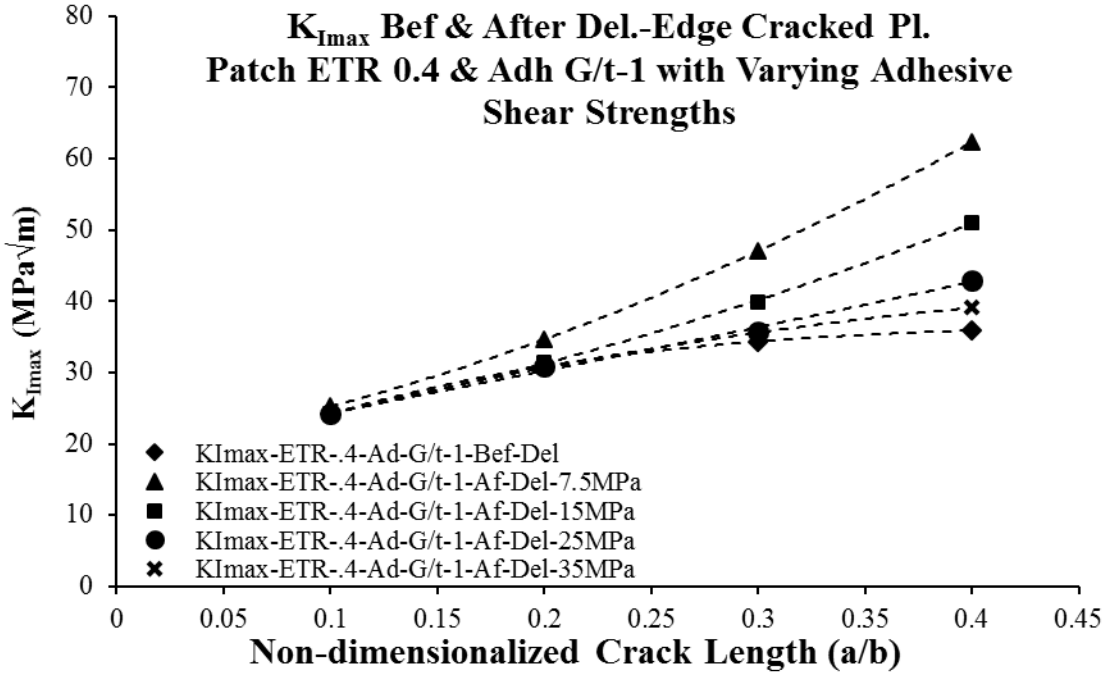

Figure 7.26 Variation of $K_{I\,max}$ in edge cracked specimens of ETR 0.4 and adhesive G_A/t_A 1 with varying adhesive shear strengths

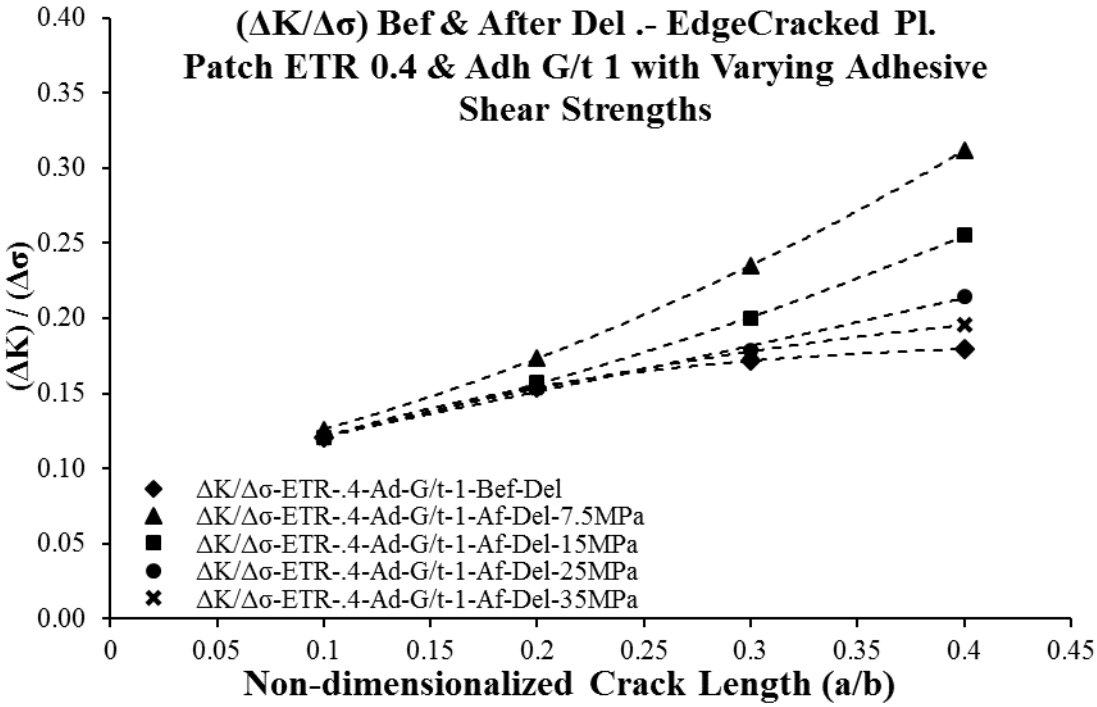

Figure 7.27 Variation of $\Delta K_I/\ \Delta\sigma$ in edge cracked specimens of ETR 0.4 and adhesive G_A/t_A 1 with varying adhesive shear strengths

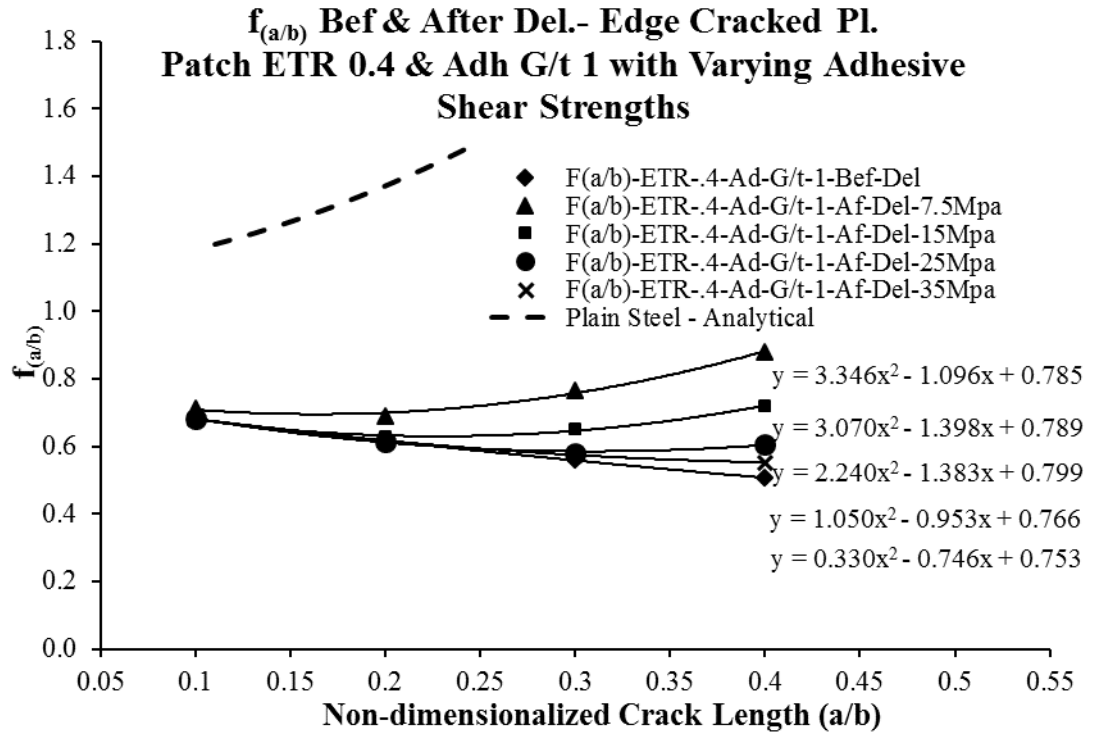

Figure 7.28 Geometric factor $f_{(a/b)}$ for edge cracked specimens of ETR 0.4 and adhesive G_A/t_A 1 with varying adhesive shear strengths

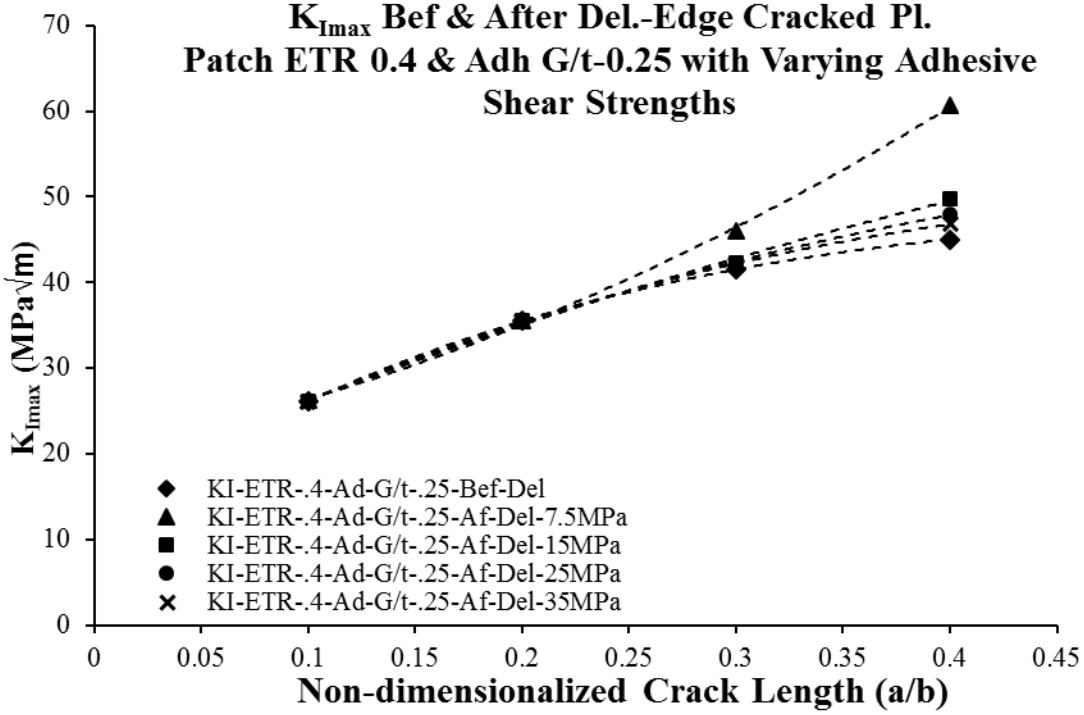

Figure 7.29 Variation of $K_{I\,max}$ in edge cracked specimens of ETR 0.4 and adhesive G_A/t_A 0.25 with varying adhesive shear strengths

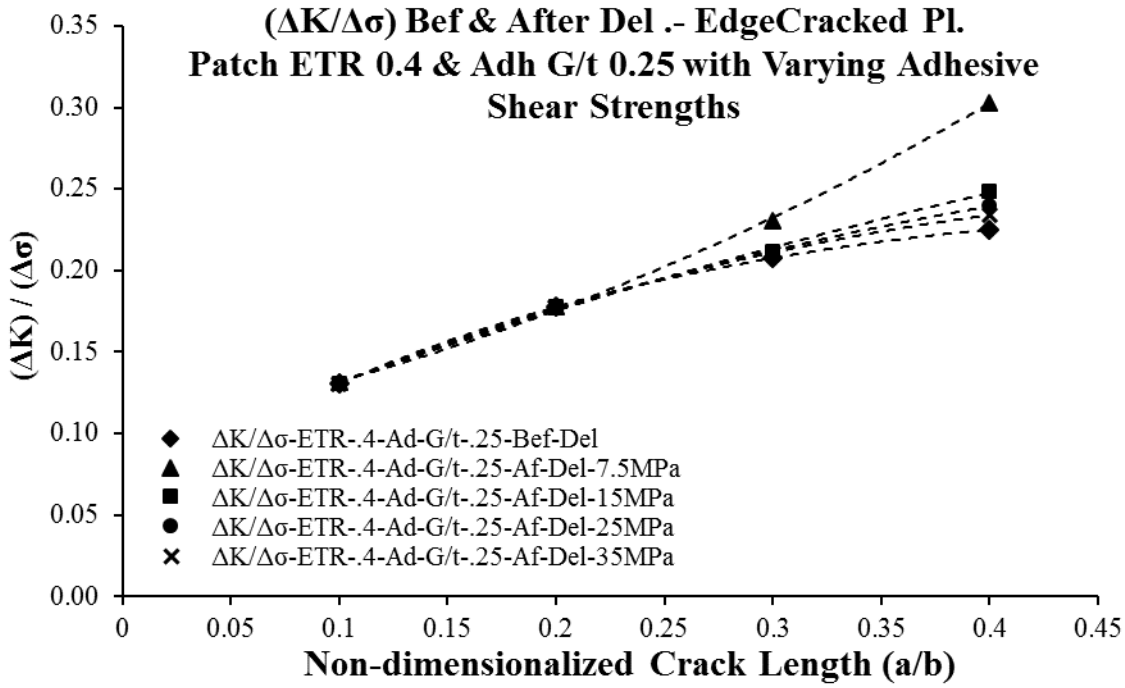

Figure 7.30 Variation of $\Delta K_I/\ \Delta\sigma$ in edge cracked specimens of ETR 0.4 and adhesive G_A/t_A 0.25 with varying adhesive shear strengths

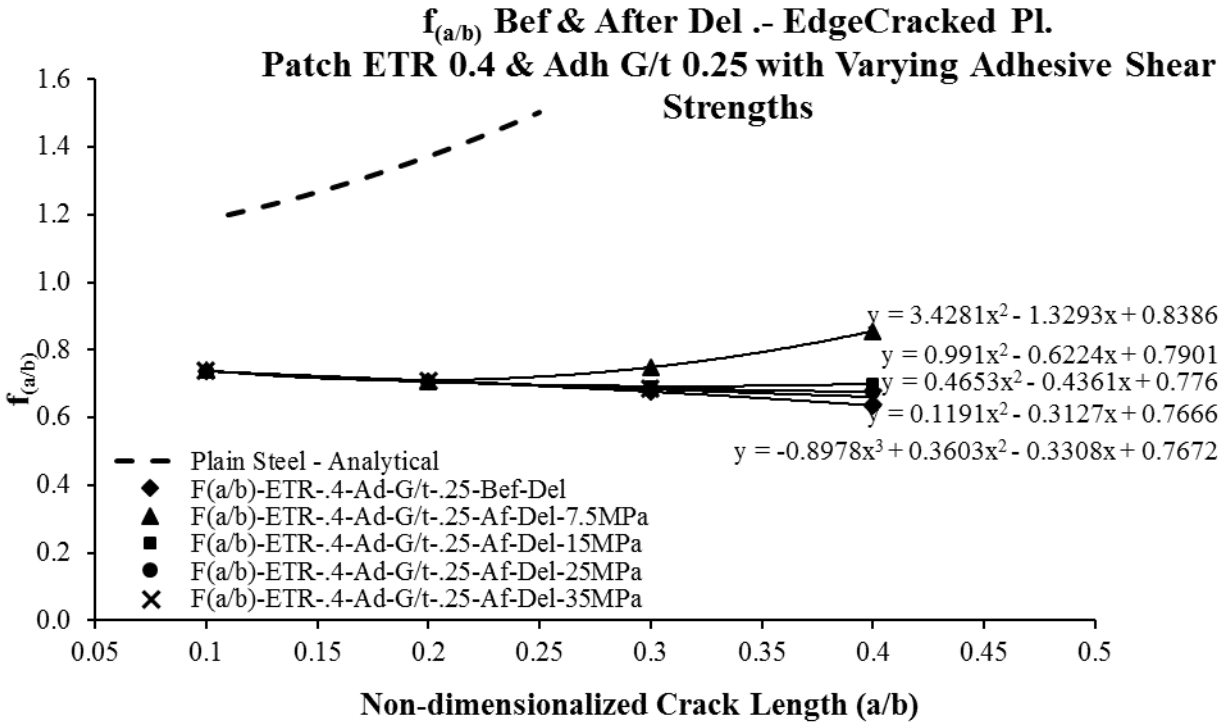

Figure 7.31 Geometric factor $f_{(a/b)}$ for edge cracked specimens of ETR 0.4 and adhesive G_A/t_A 0.25 with varying adhesive shear strengths

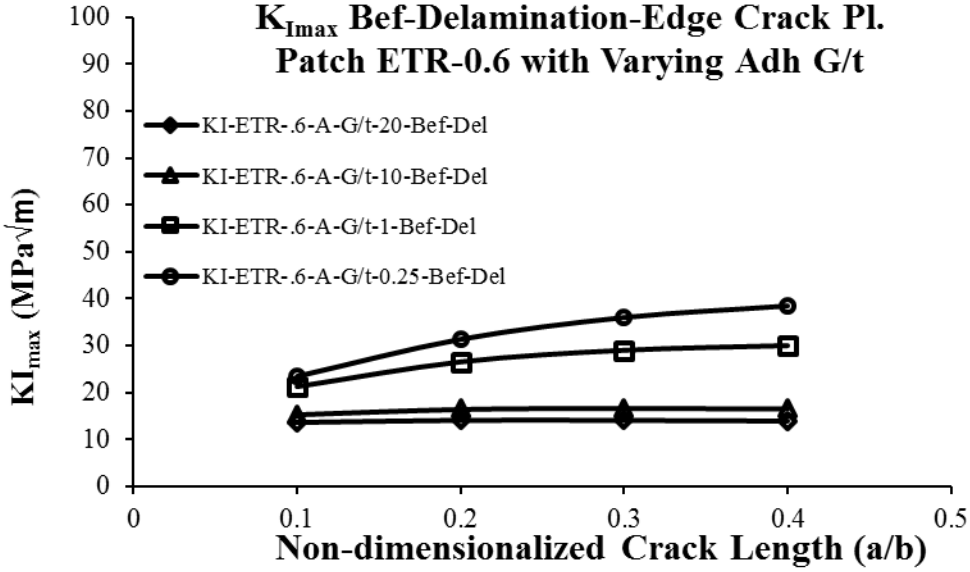

Figure 7.32 Variation of $K_{I\,max}$ in edge cracked specimens of ETR 0.6 with varying adhesive G_A/t_A

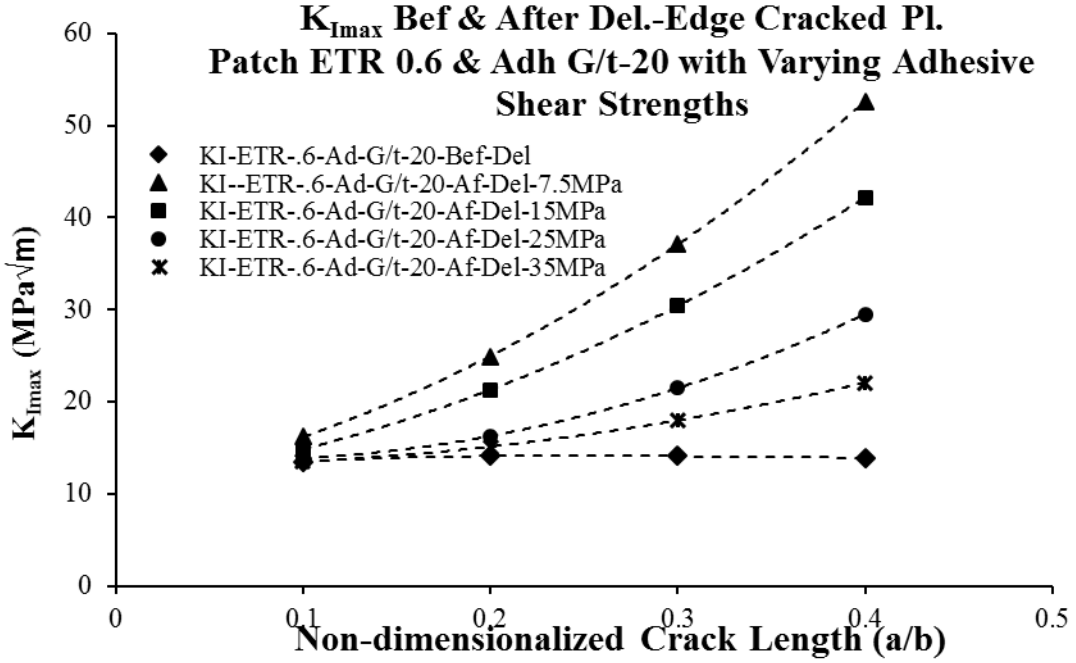

Figure 7.33 Variation of $K_{I\,max}$ in edge cracked specimens of ETR 0.6 and adhesive G_A/t_A 20 with varying adhesive shear strengths

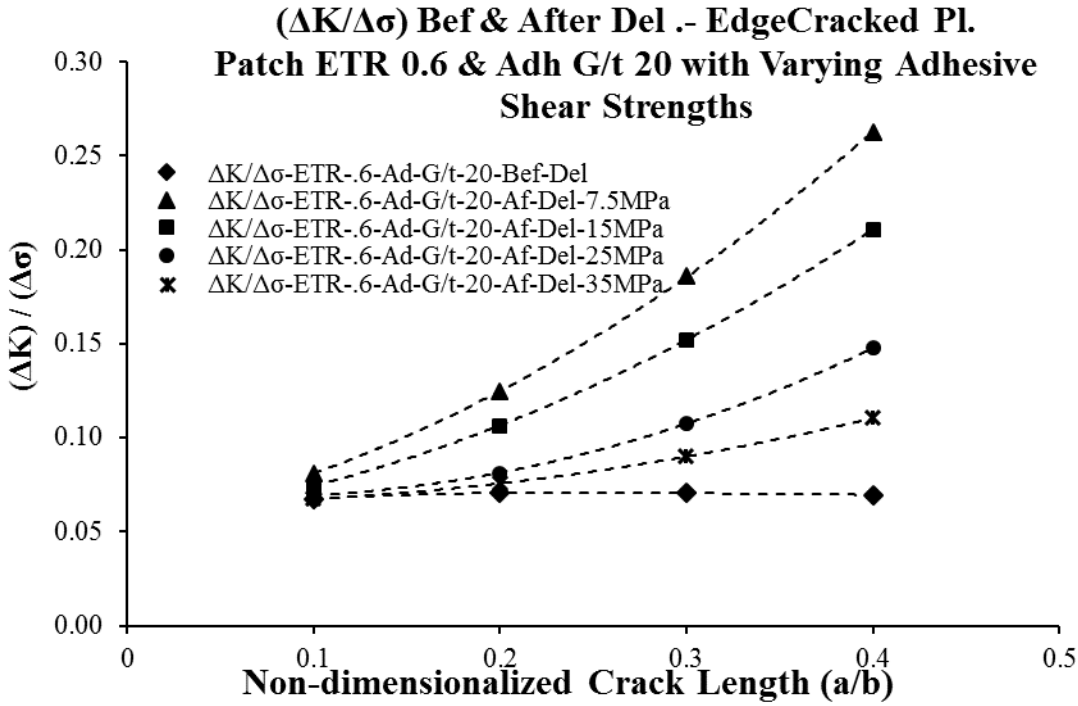

Figure 7.34 Variation of $\Delta K_I/\ \Delta\sigma$ in edge cracked specimens of ETR 0.6 and adhesive G_A/t_A 20 with varying adhesive shear strengths

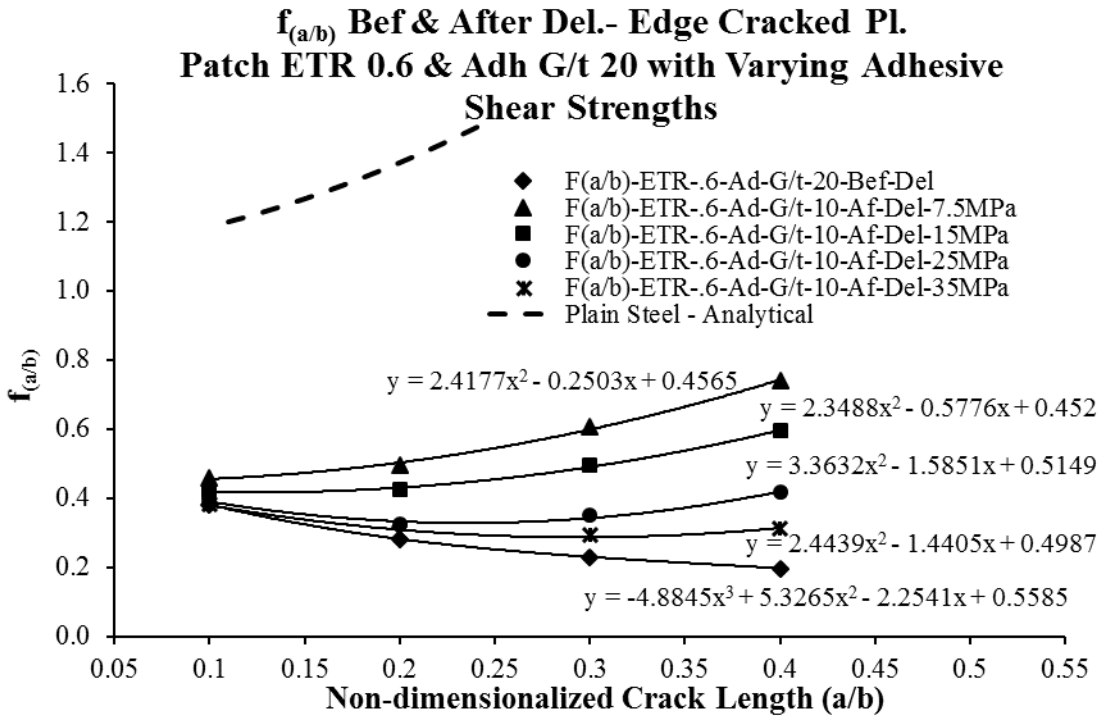

Figure 7.35 Geometric factor $f_{(a/b)}$ for edge cracked specimens of ETR 0.6 and adhesive G_A/t_A 20 with varying adhesive shear strengths

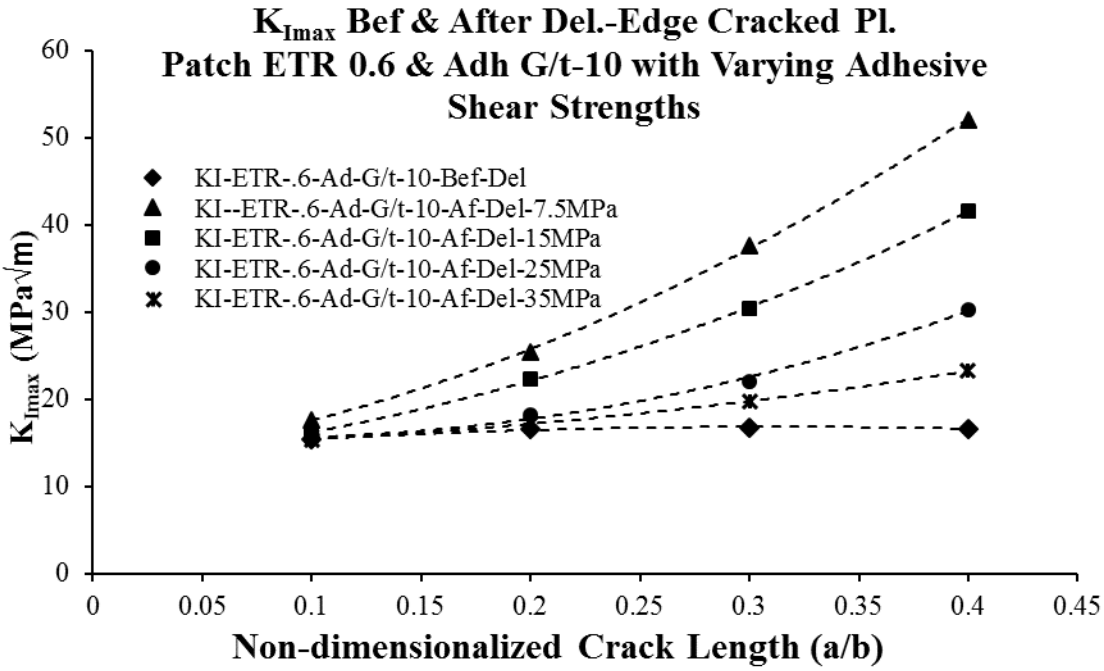

Figure 7.36 Variation of $K_{I\,max}$ in edge cracked specimens of ETR 0.6 and adhesive G_A/t_A 10 with varying adhesive shear strengths

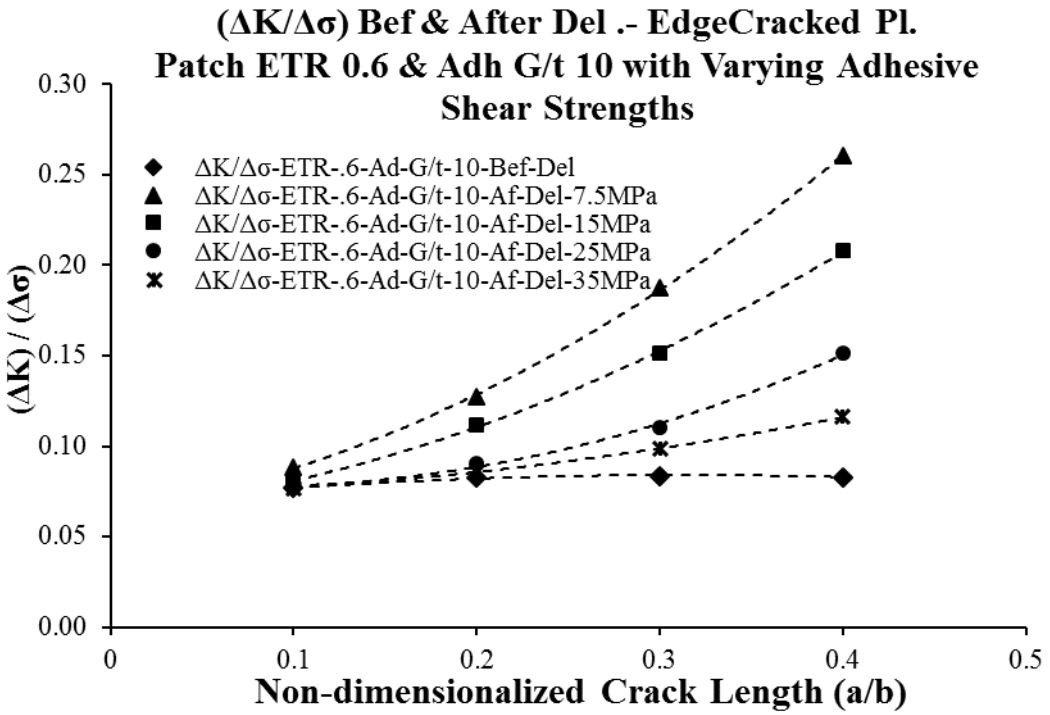

Figure 7.37 Variation of $\Delta K_I/\ \Delta\sigma$ in edge cracked specimens of ETR 0.6 and adhesive G_A/t_A 10 with varying adhesive shear strengths

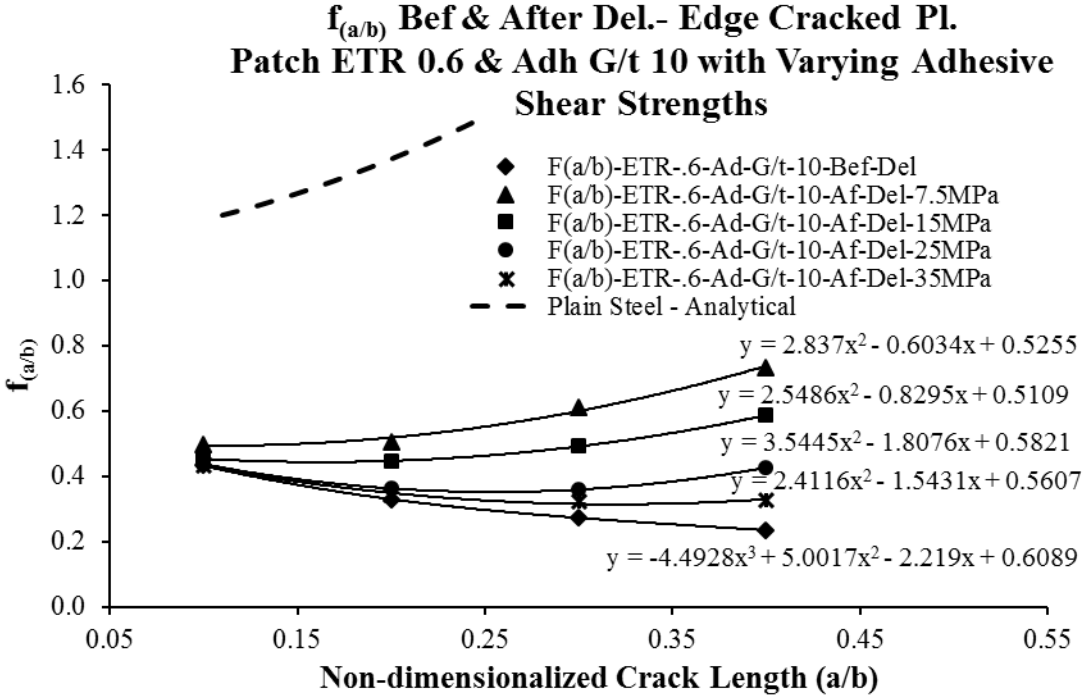

Figure 7.38 Geometric factor $f_{(a/b)}$ for edge cracked specimens of ETR 0.6 and adhesive G_A/t_A 10 with varying adhesive shear strengths

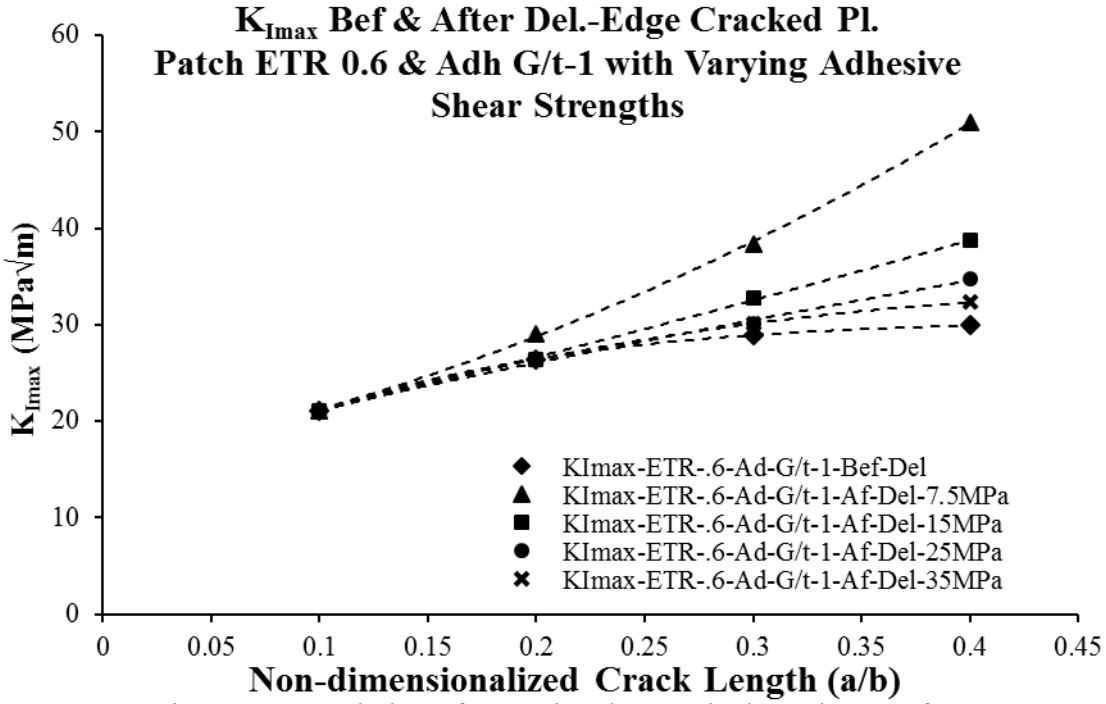

Figure 7.39 Variation of $K_{I\,max}$ in edge cracked specimens of ETR 0.6 and adhesive G_A/t_A 1 with varying adhesive shear strengths

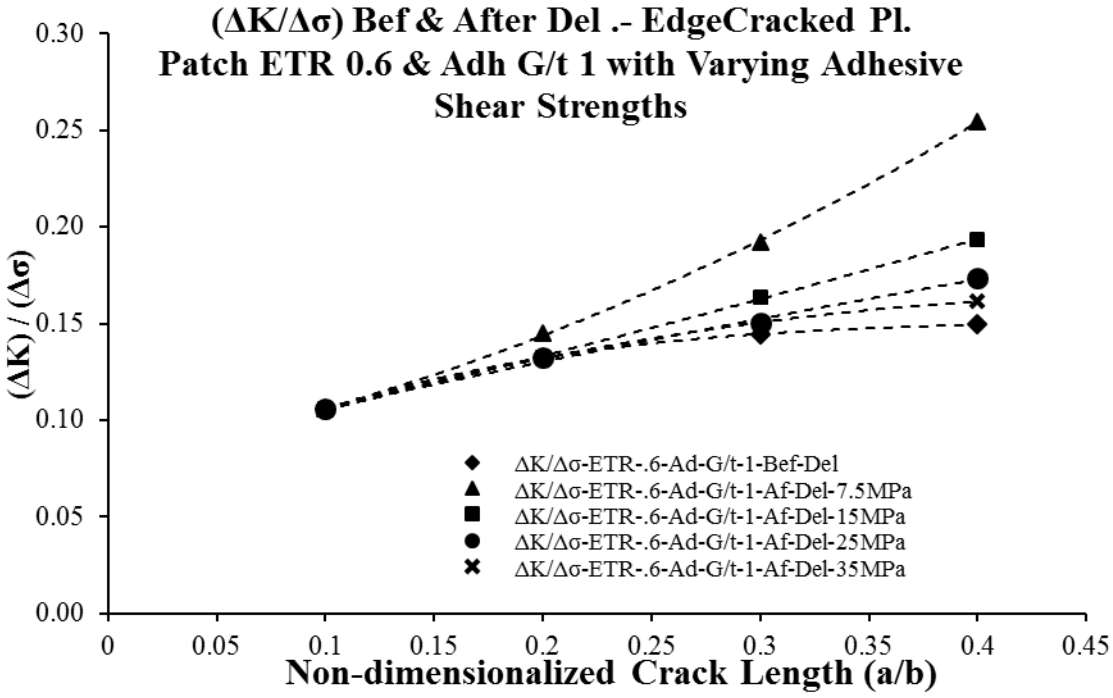

Figure 7.40 Variation of $\Delta K_I/\ \Delta\sigma$ in edge cracked specimens of ETR 0.6 and adhesive G_A/t_A 1 with varying adhesive shear strengths

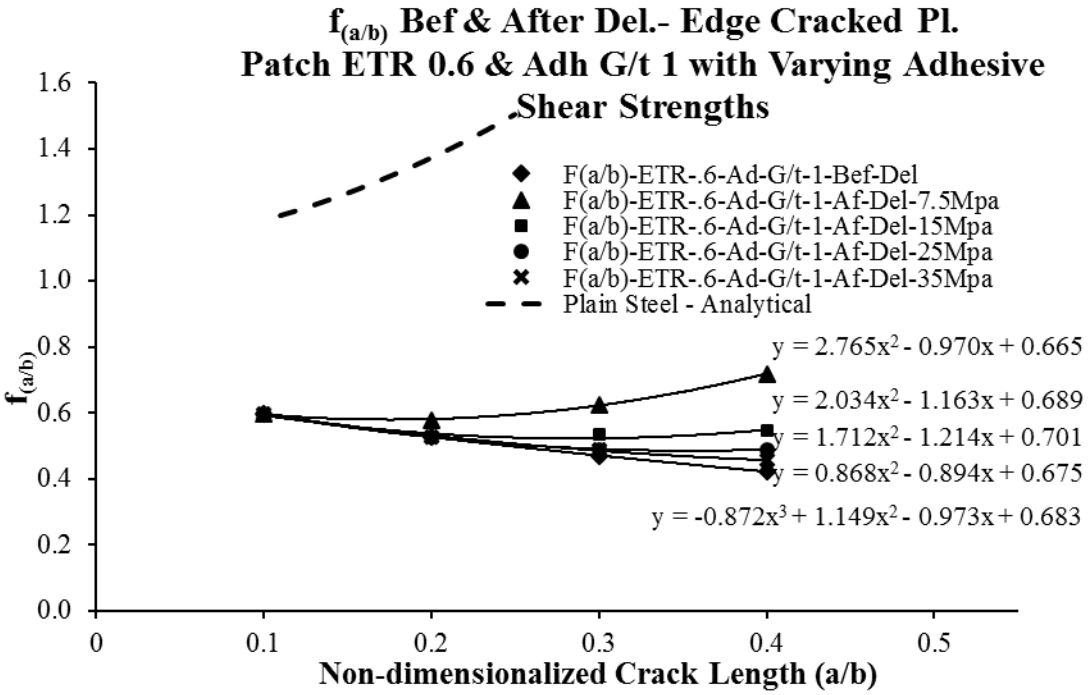

Figure 7.41 Geometric factor $f_{(a/b)}$ for edge cracked specimens of ETR 0.6 and adhesive G_A/t_A 1 with varying adhesive shear strengths

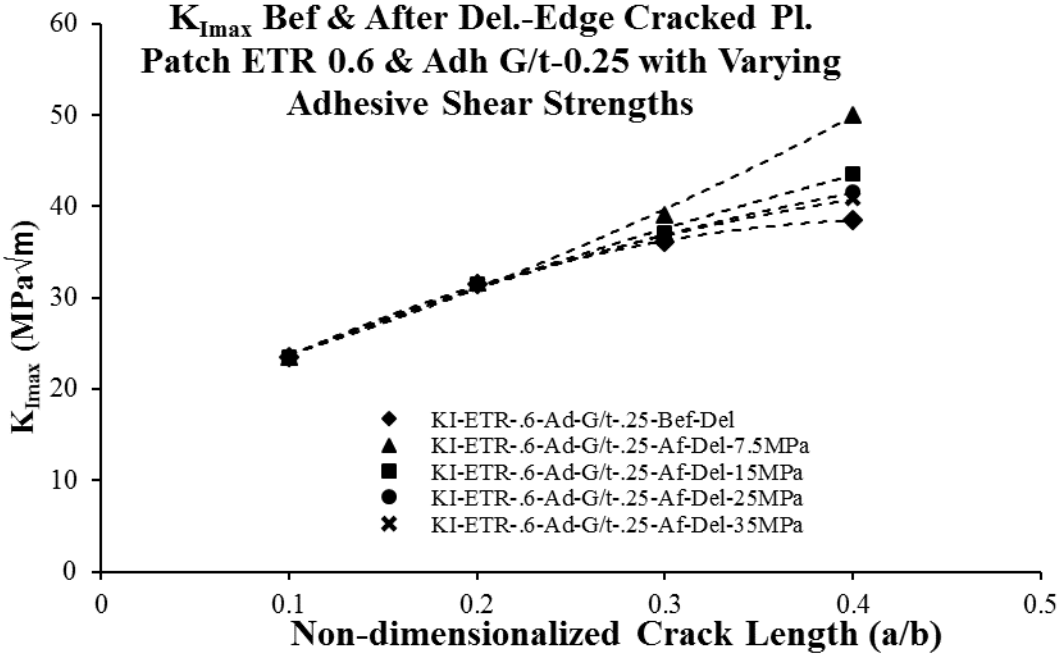

Figure 7.42 Variation of $K_{I\,max}$ in edge cracked specimens of ETR 0.6 and adhesive G_A/t_A 0.25 with varying adhesive shear strengths

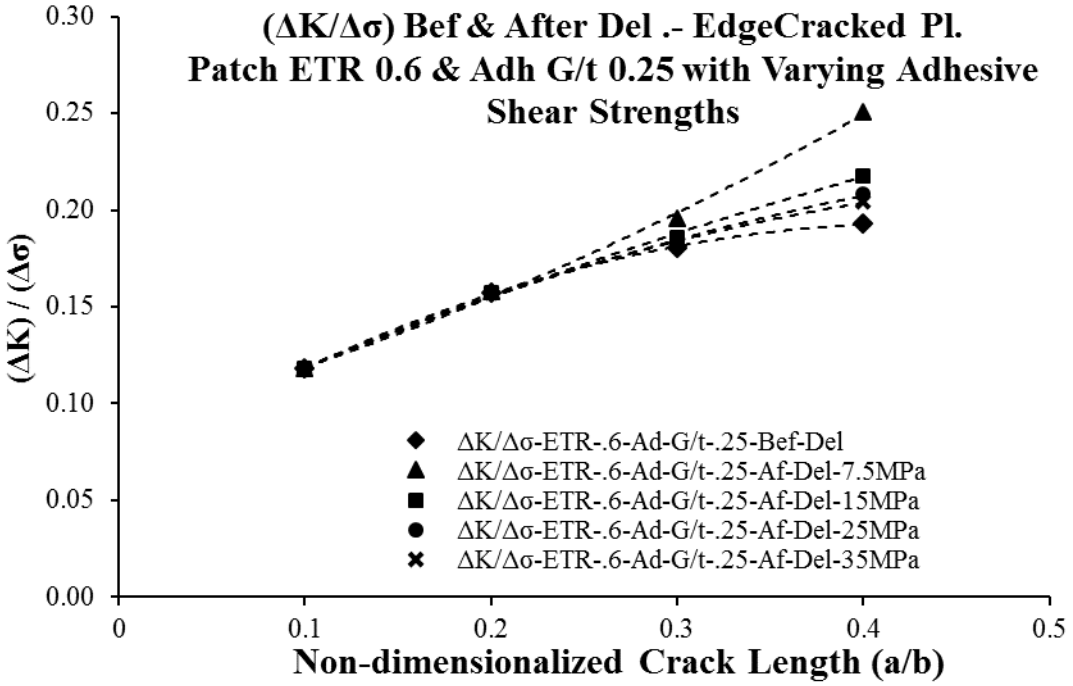

Figure 7.43 Variation of $\Delta K_I/\ \Delta\sigma$ in edge cracked specimens of ETR 0.6 and adhesive G_A/t_A 0.25 with varying adhesive shear strengths

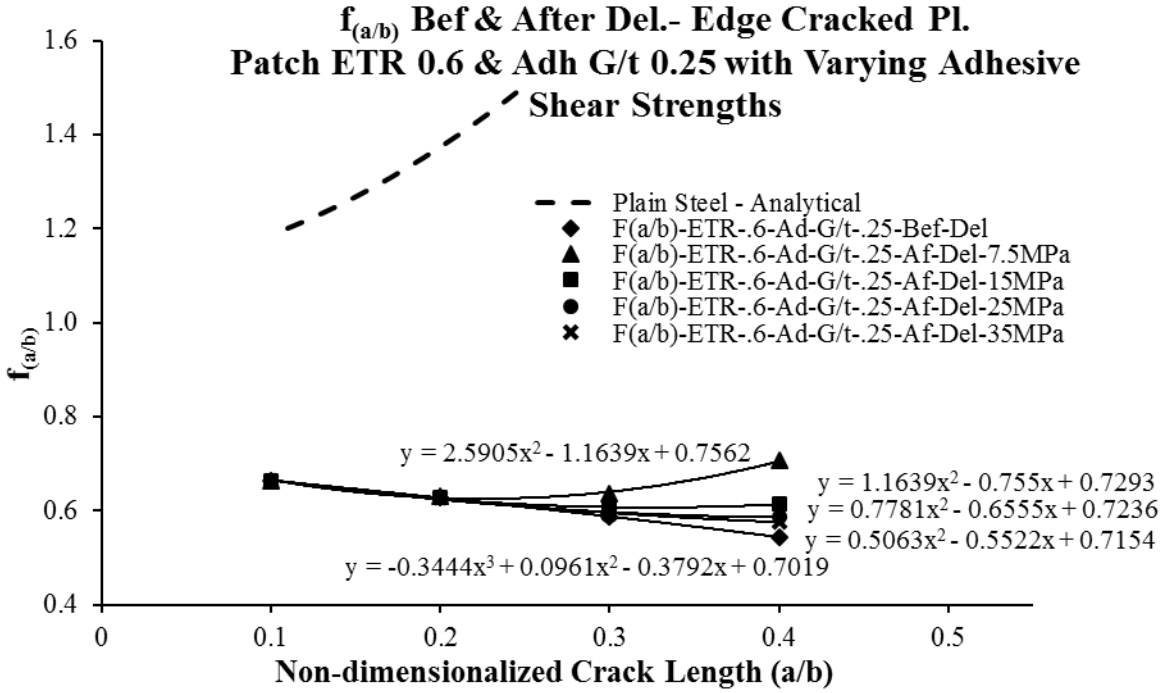

Figure 7.44 Geometric factor $f_{(a/b)}$ for edge cracked specimens of ETR 0.6 and adhesive G_A/t_A 0.25 with varying adhesive shear strengths

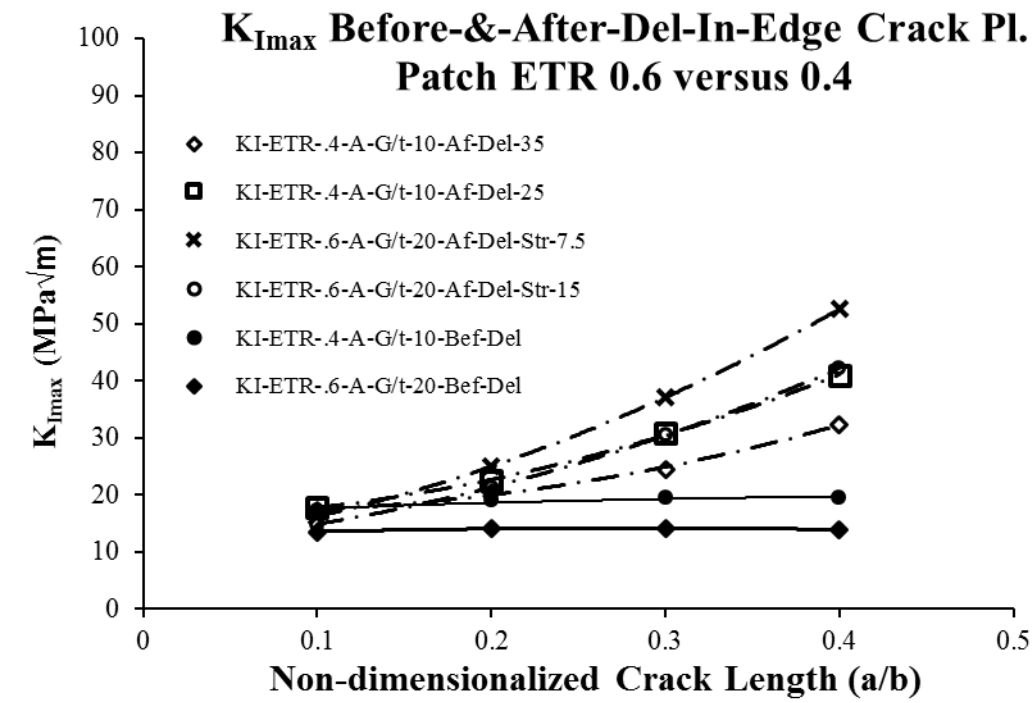

Figure 7.45 Comparison of impact of patch delamination on K_{Imax} between edge cracked specimens of ETR 0.6 and ETR 0.4

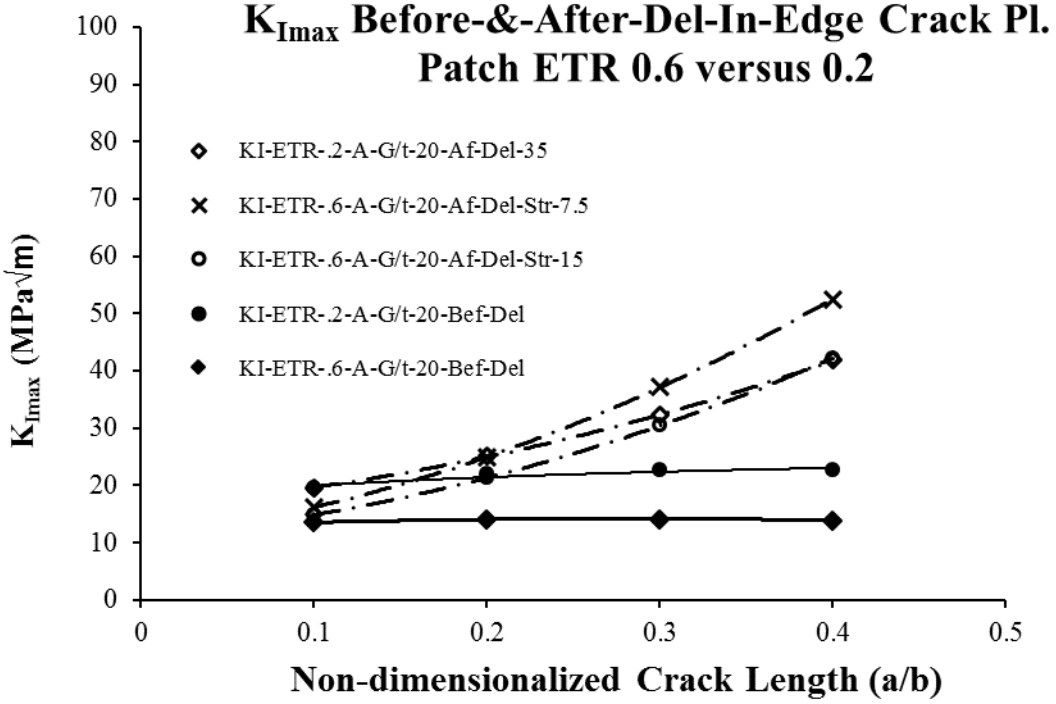

Figure 7.46 Comparison of impact of patch delamination on K_{Imax} between edge cracked specimens of ETR 0.6 and ETR 0.2

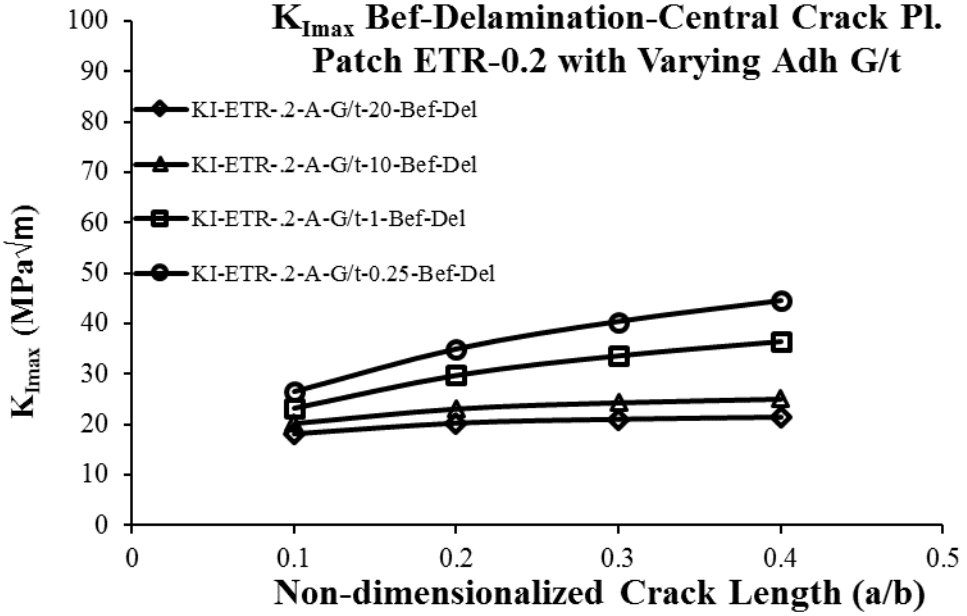

Figure 7.47 Variation of $K_{I\,max}$ in central cracked specimens of ETR 0.2 with varying adhesive G_A/t_A

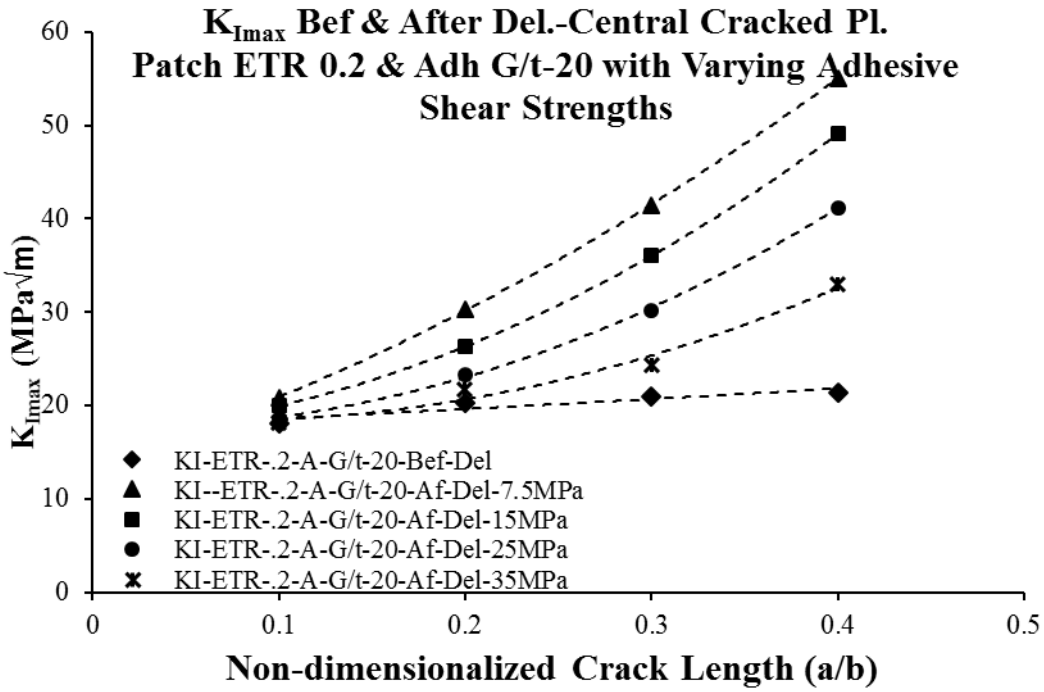

Figure 7.48 Variation of $K_{I\,max}$ in central crack specimens of ETR 0.2 and adhesive G_A/t_A 20 with varying adhesive shear strengths

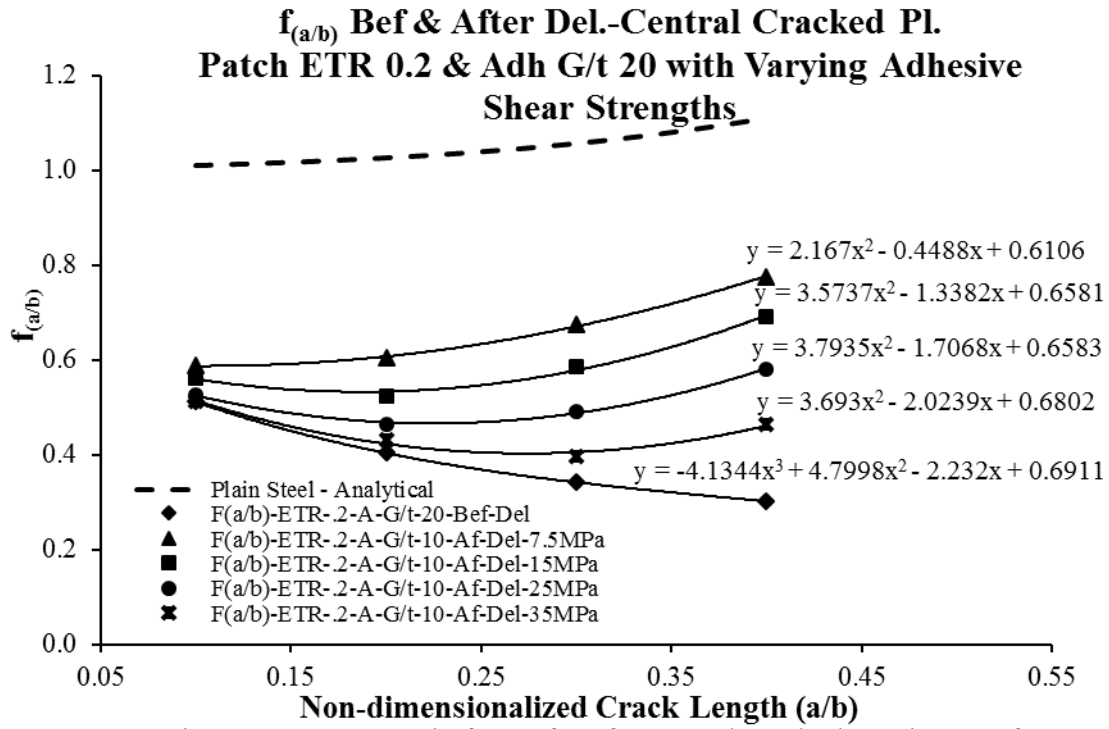

Figure 7.49 Geometric factor $f_{(a/b)}$ for central cracked specimens of ETR 0.2 and adhesive G_A/t_A 20 with varying adhesive shear strengths

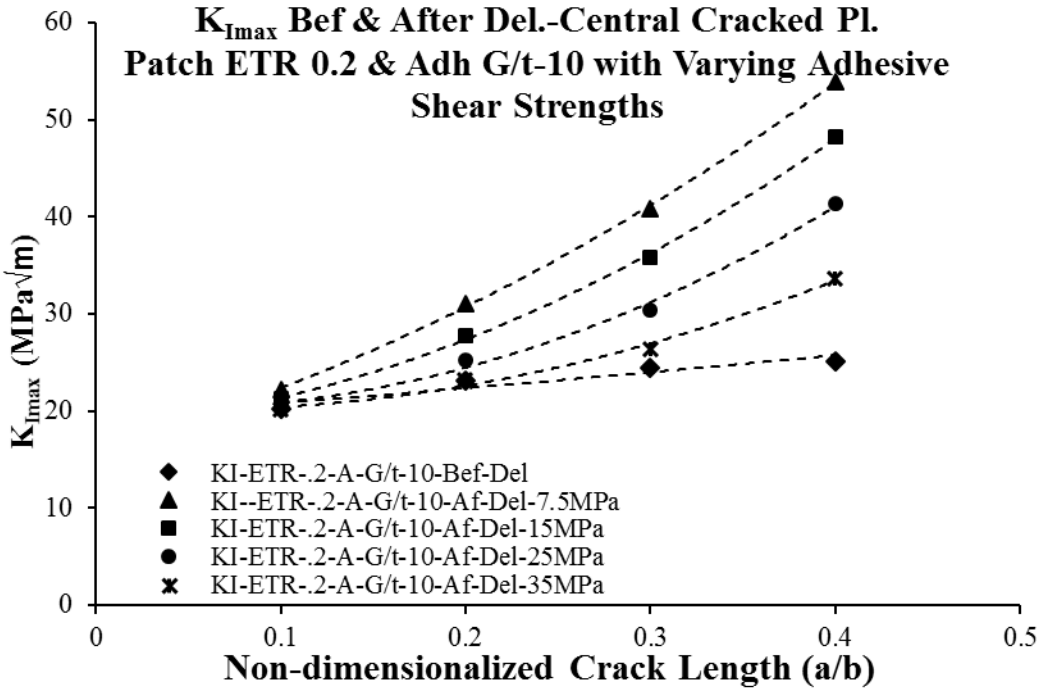

Figure 7.50 Variation of $K_{I\,max}$ in central crack specimens of ETR 0.2 and adhesive G_A/t_A 10 with varying adhesive shear strengths

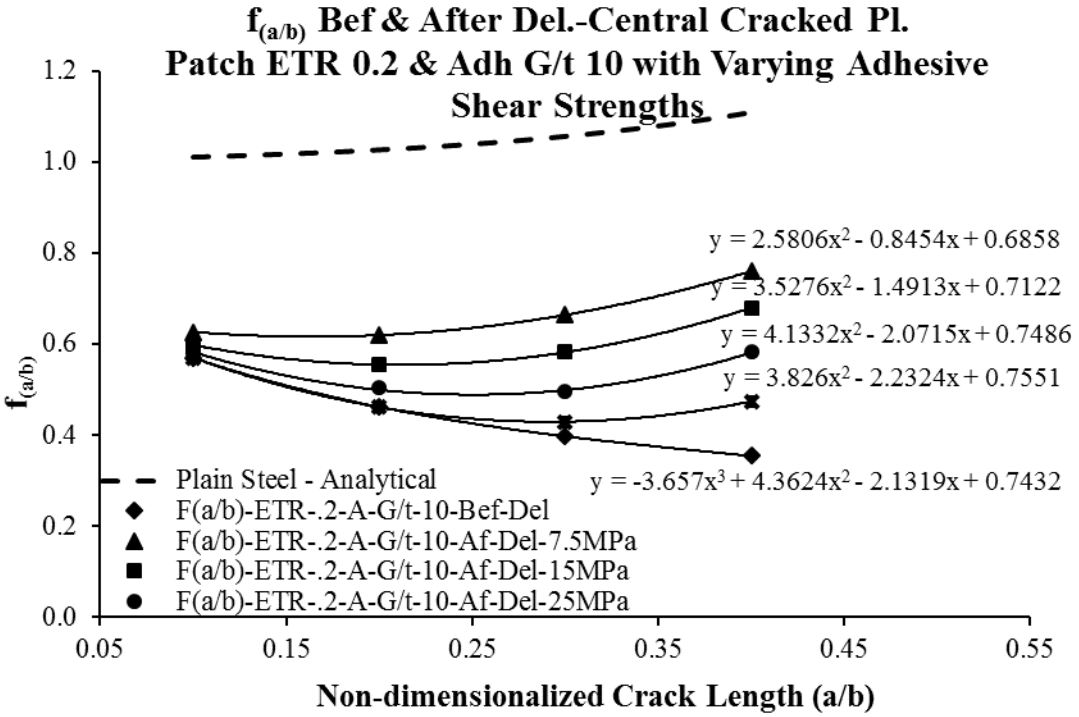

Figure 7.51 Geometric factor $f_{(a/b)}$ for central cracked specimens of ETR 0.2 and adhesive G_A/t_A 10 with varying adhesive shear strengths

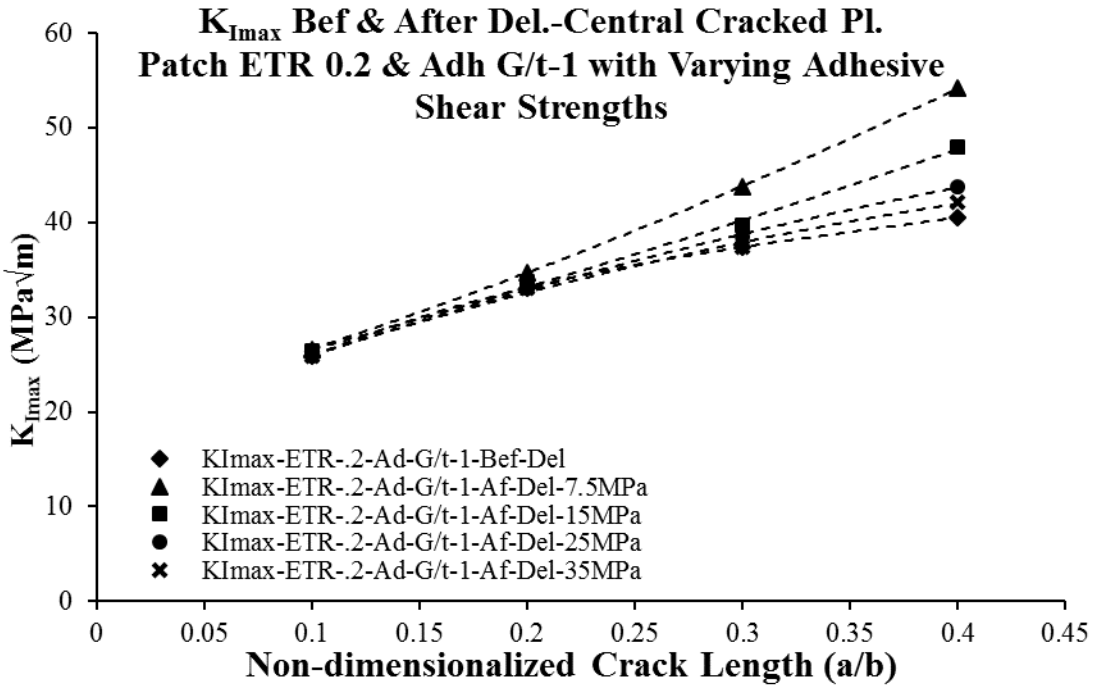

Figure 7.52 Variation of $K_{I\,max}$ in central crack specimens of ETR 0.2 and adhesive G_A/t_A 1 with varying adhesive shear strengths

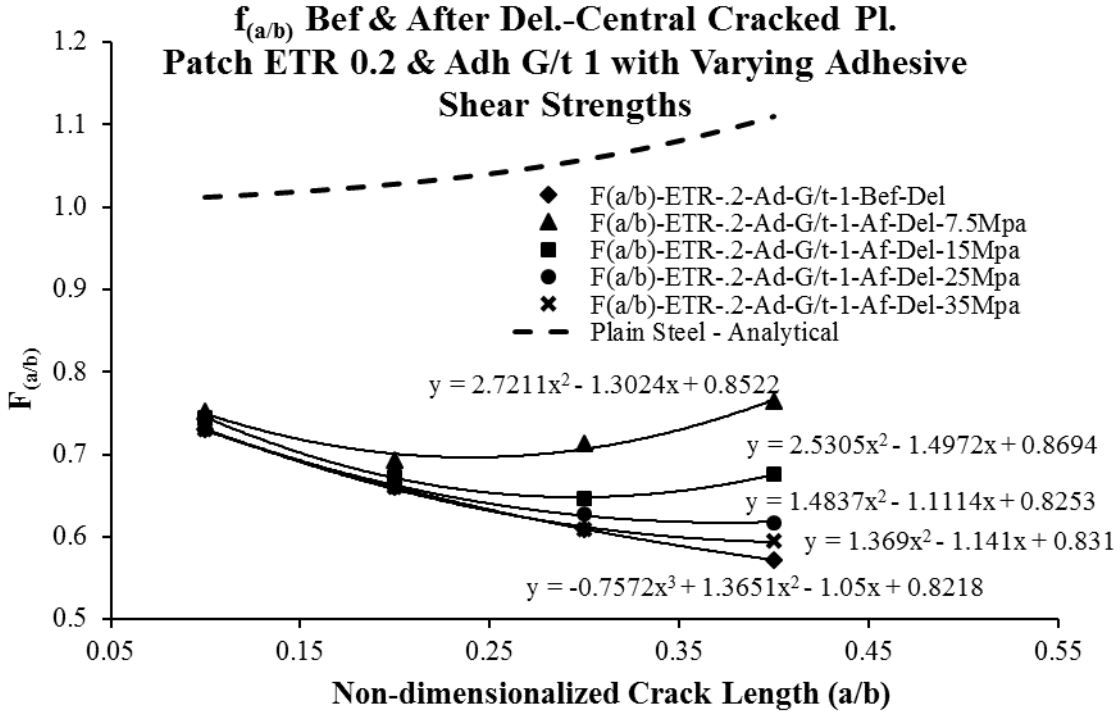

Figure 7.53 Geometric factor $f_{(a/b)}$ for central cracked specimens of ETR 0.2 and adhesive G_A/t_A 1 with varying adhesive shear strengths

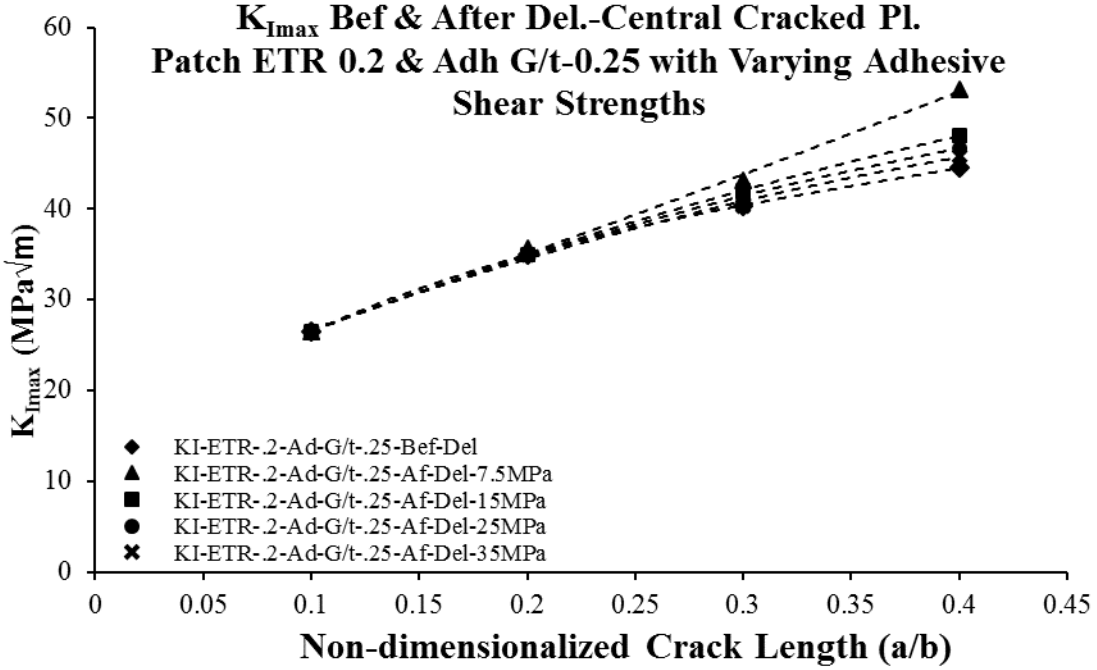

Figure 7.54 Variation of $K_{I\,max}$ in central crack specimens of ETR 0.2 and adhesive G_A/t_A 0.25 with varying adhesive shear strengths

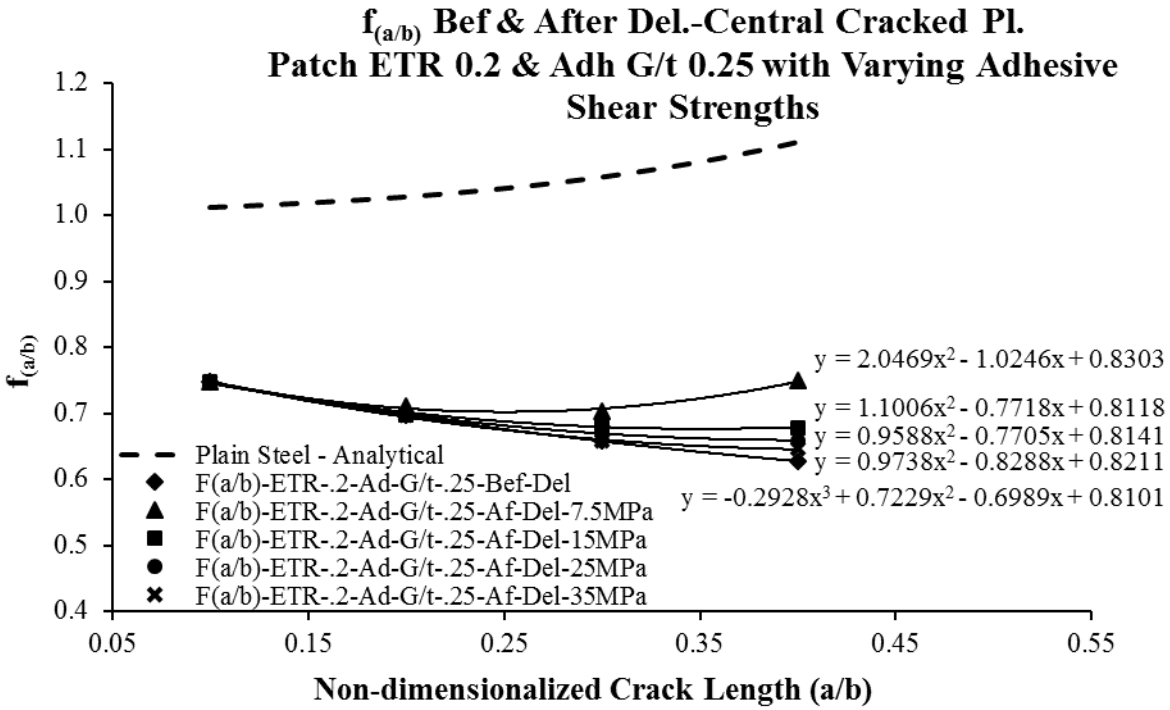

Figure 7.55 Geometric factor $f_{(a/b)}$ for central cracked specimens of ETR 0.2 and adhesive G_A/t_A 0.25 with varying adhesive shear strengths

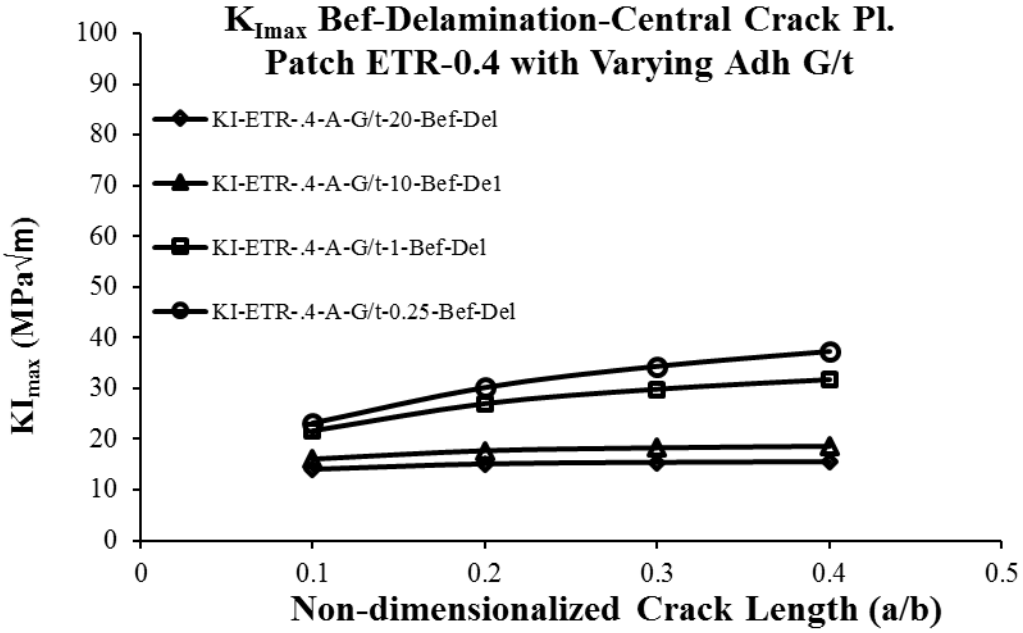

Figure 7.56 Variation of $K_{I\,max}$ in central cracked specimens of ETR 0.4 with varying adhesive G_A/t_A

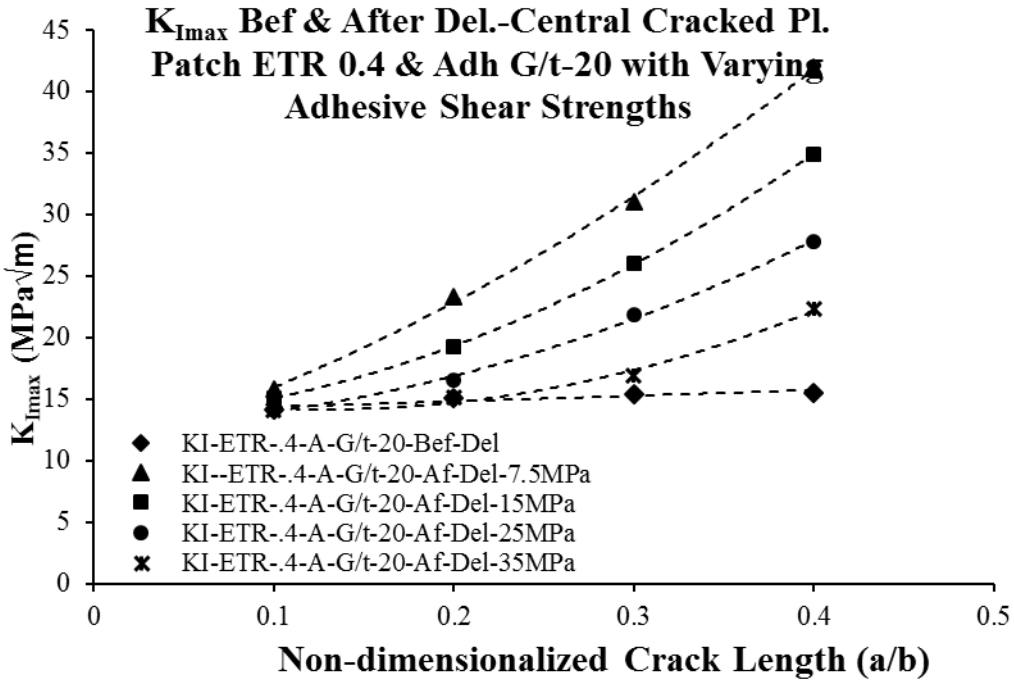

Figure 7.57 Variation of $K_{I\,max}$ in central crack specimens of ETR 0.4 and adhesive G_A/t_A 20 with varying adhesive shear strengths

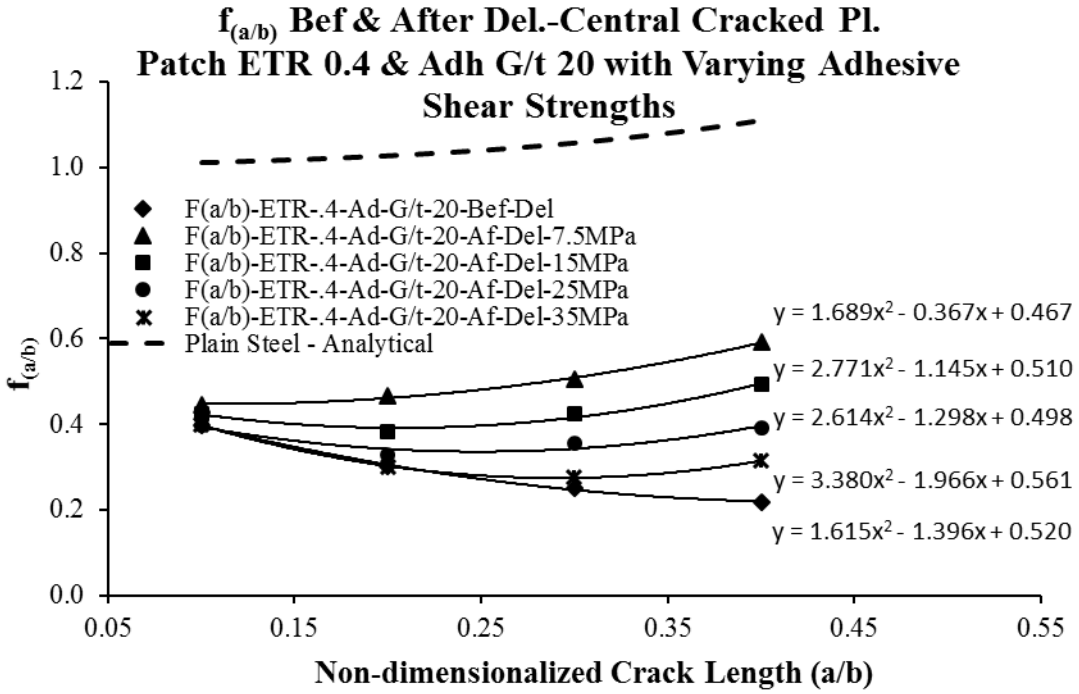

Figure 7.58 Geometric factor $f_{(a/b)}$ for central cracked specimens of ETR 0.4 and adhesive G_A/t_A 20 with varying adhesive shear strengths

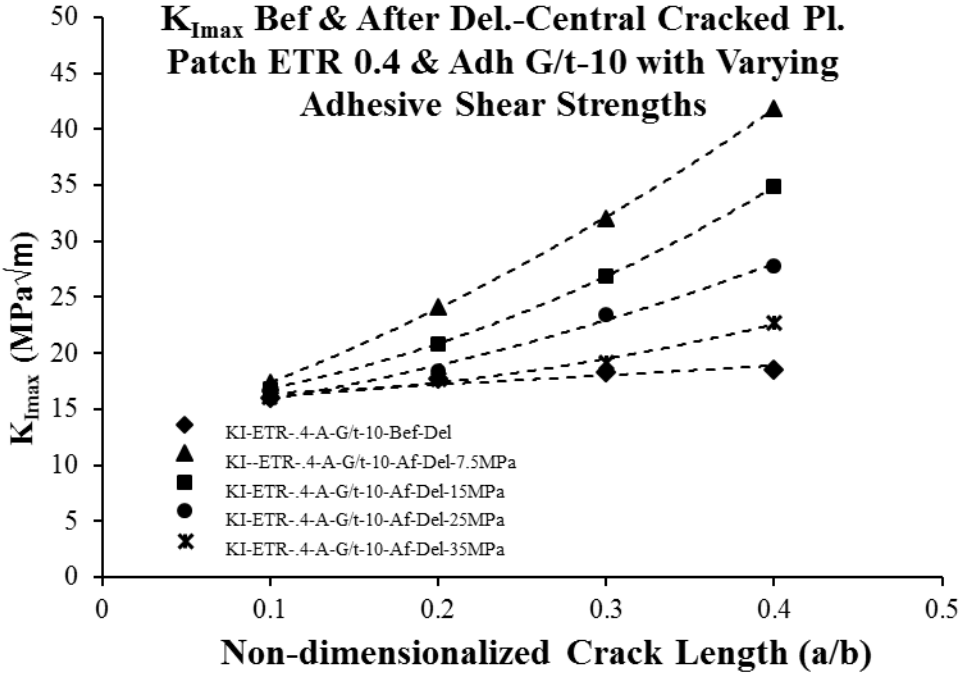

Figure 7.59 Variation of $K_{I\,max}$ in central crack specimens of ETR 0.4 and adhesive G_A/t_A 10 with varying adhesive shear strengths

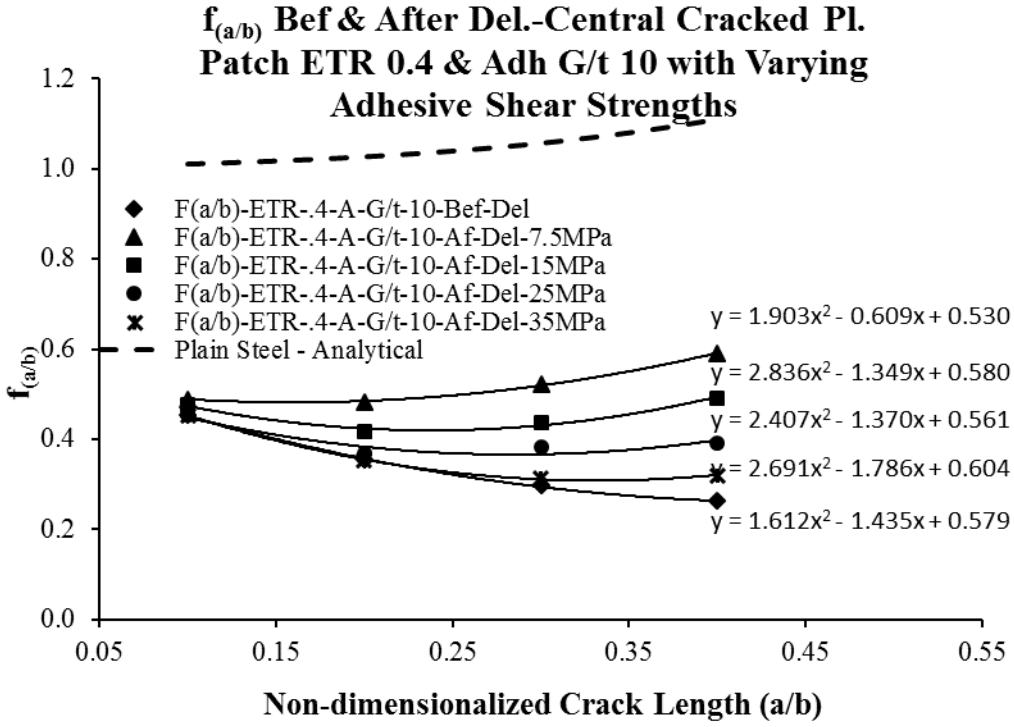

Figure 7.60 Geometric factor $f_{(a/b)}$ for central cracked specimens of ETR 0.4 and adhesive G_A/t_A 10 with varying adhesive shear strengths

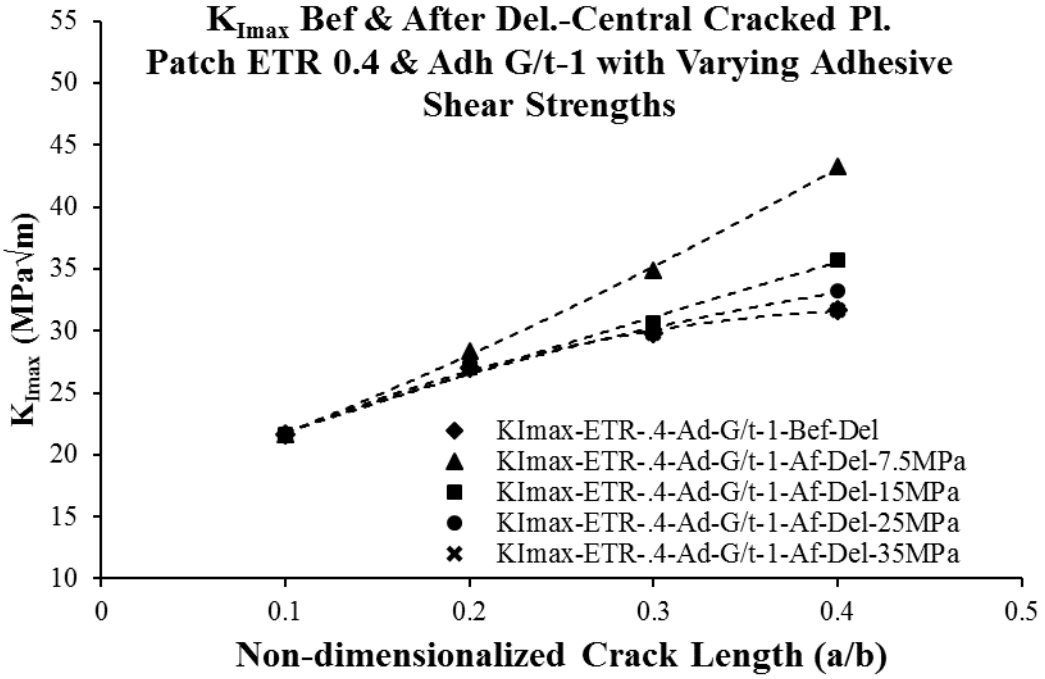

Figure 7.61 Variation of $K_{I\,max}$ in central crack specimens of ETR 0.4 and adhesive G_A/t_A 1 with varying adhesive shear strengths

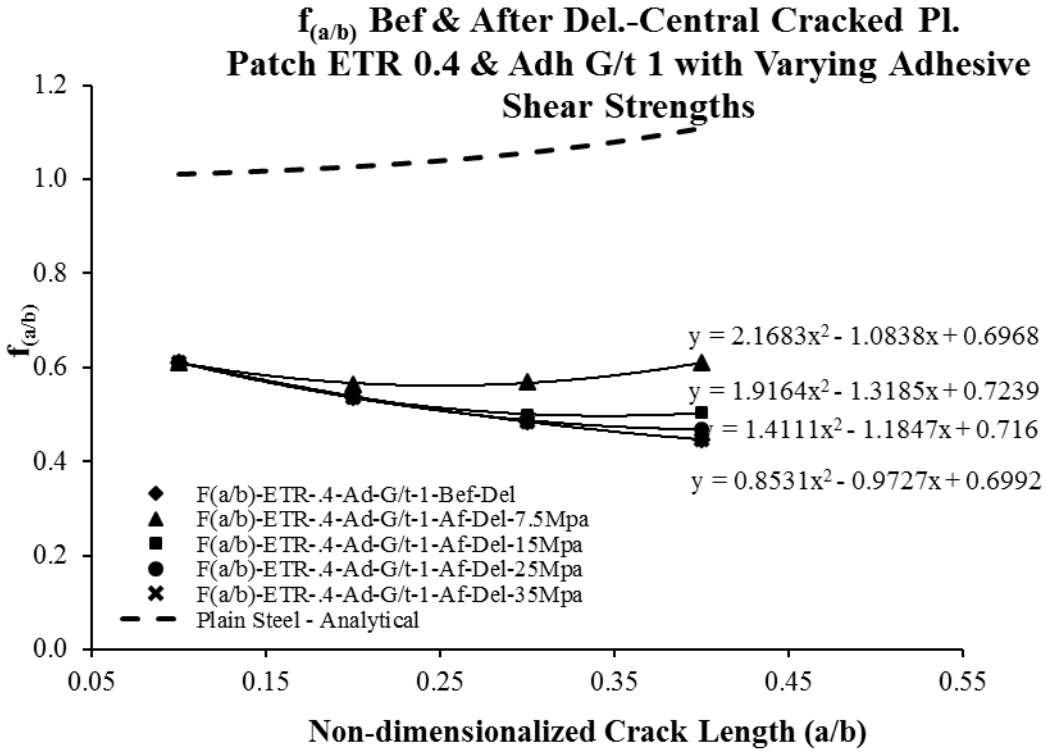

Figure 7.62 Geometric factor $f_{(a/b)}$ for central cracked specimens of ETR 0.4 and adhesive G_A/t_A 1 with varying adhesive shear strengths

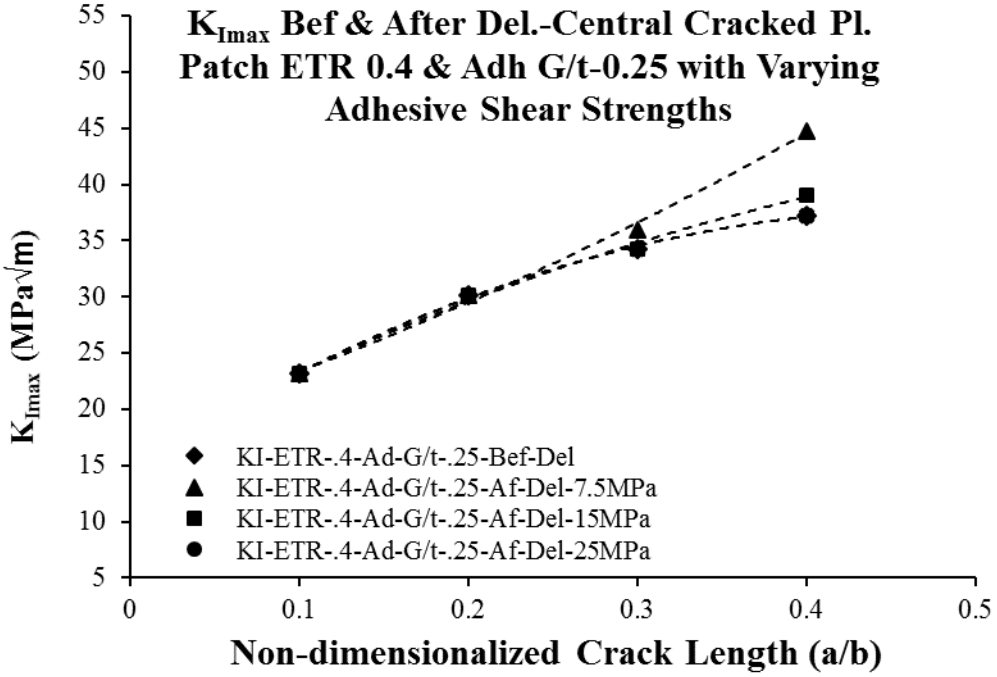

Figure 7.63 Variation of $K_{I\,max}$ in central crack specimens of ETR 0.4 and adhesive G_A/t_A 0.25 with varying adhesive shear strengths

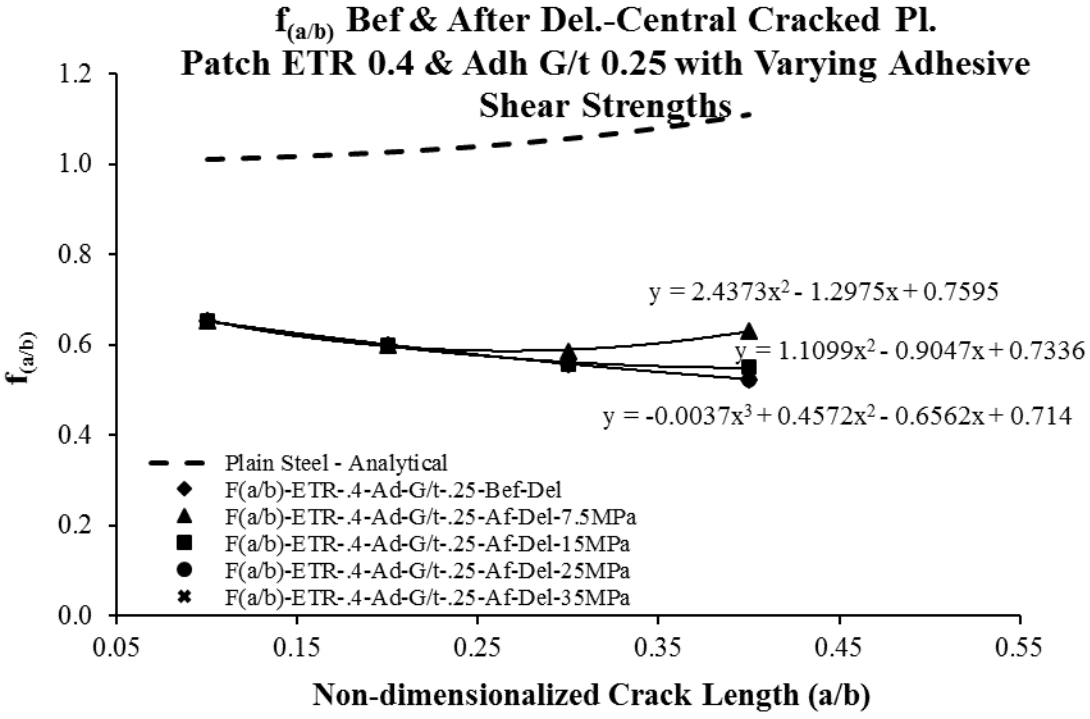

Figure 7.64 Geometric factor $f_{(a/b)}$ for central cracked specimens of ETR 0.4 and adhesive G_A/t_A 0.25 with varying adhesive shear strengths

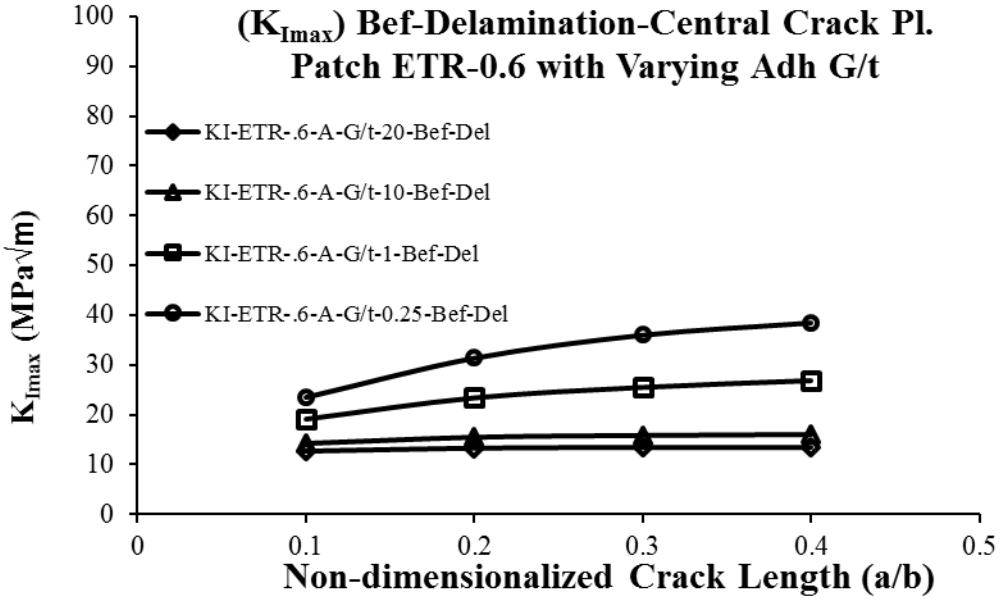

Figure 7.65 Variation of $K_{I\,max}$ in central cracked specimens of ETR 0.6 with varying adhesive G_A/t_A

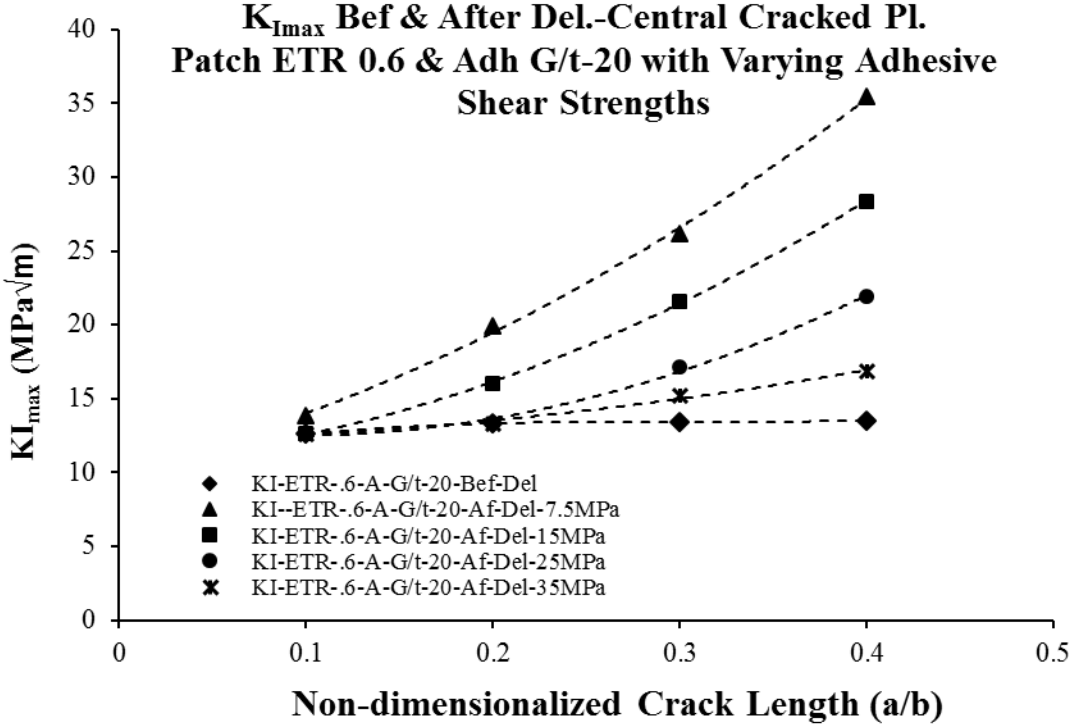

Figure 7.66 Variation of $K_{I\,max}$ in central crack specimens of ETR 0.6 and adhesive G_A/t_A 20 with varying adhesive shear strengths

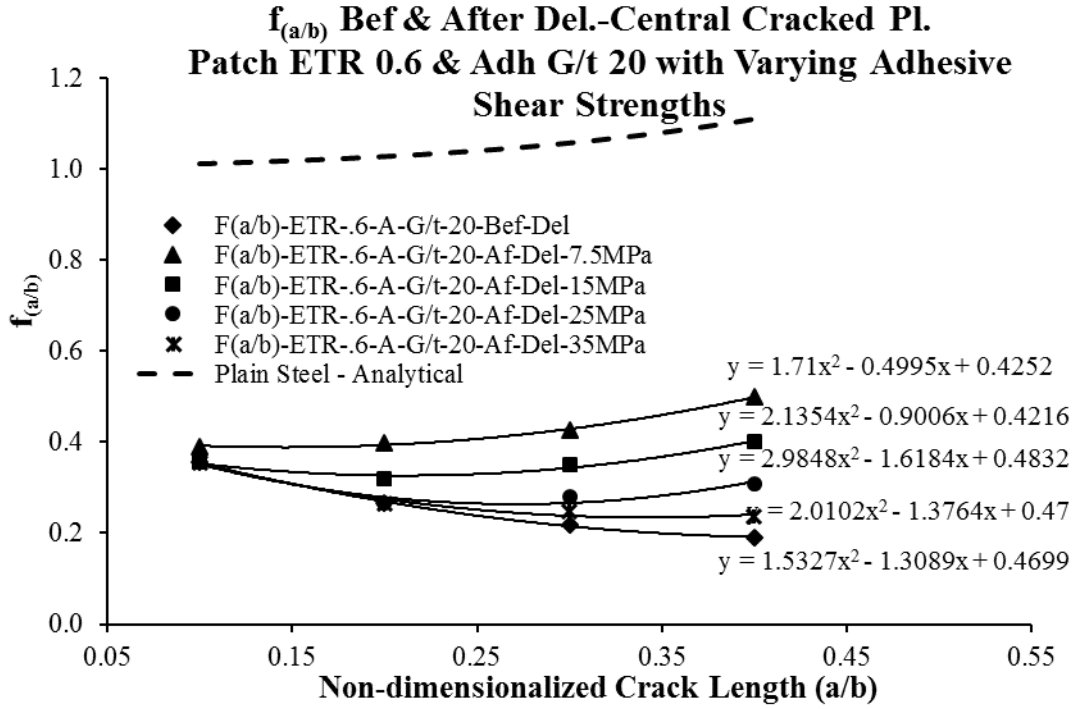

Figure 7.67 Geometric factor $f_{(a/b)}$ for central cracked specimens of ETR 0.6 and adhesive G_A/t_A 20 with varying adhesive shear strengths

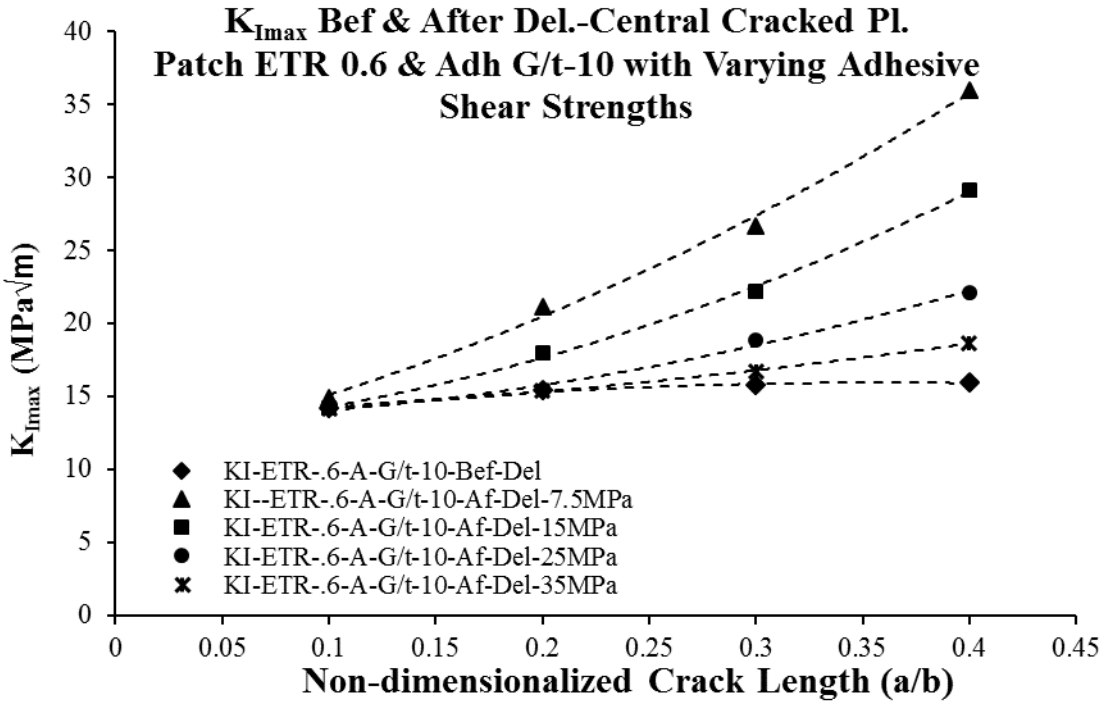

Figure 7.68 Variation of $K_{I\,max}$ in central crack specimens of ETR 0.6 and adhesive G_A/t_A 10 with varying adhesive shear strengths

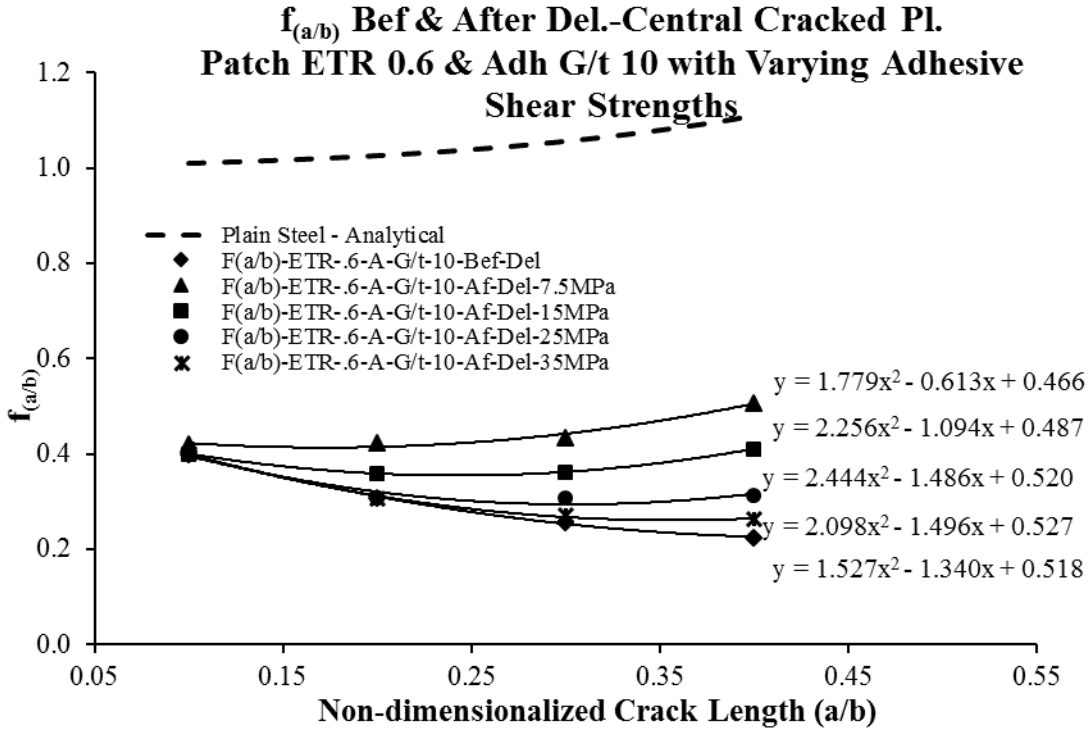

Figure 7.69 Geometric factor $f_{(a/b)}$ for central cracked specimens of ETR 0.6 and adhesive G_A/t_A 10 with varying adhesive shear strengths

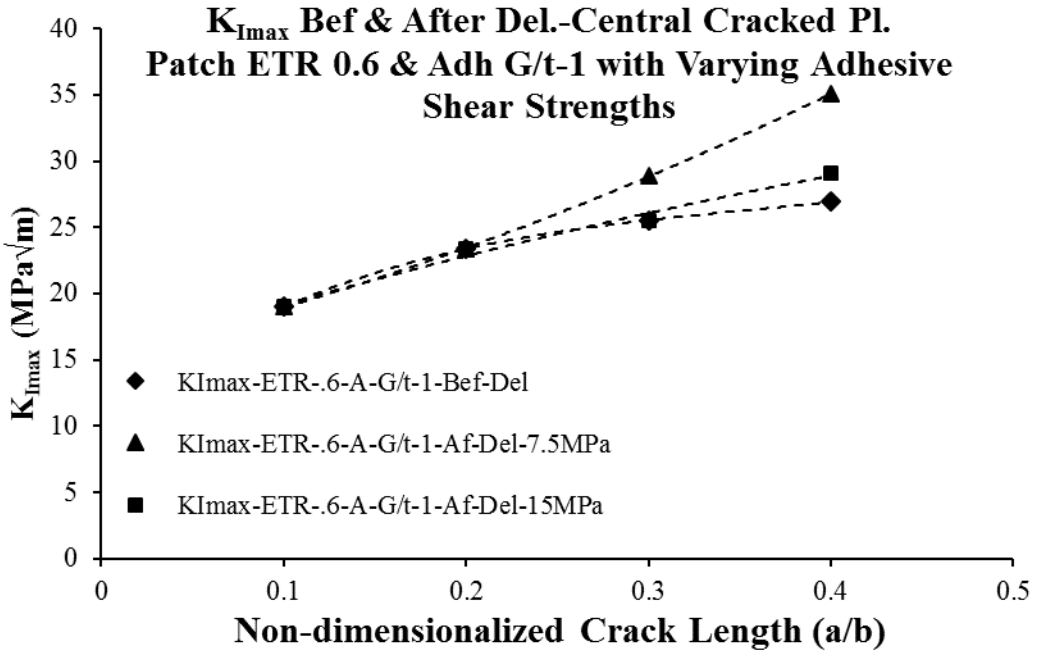

Figure 7.70 Variation of $K_{I\,max}$ in central crack specimens of ETR 0.6 and adhesive G_A/t_A 1 with varying adhesive shear strengths

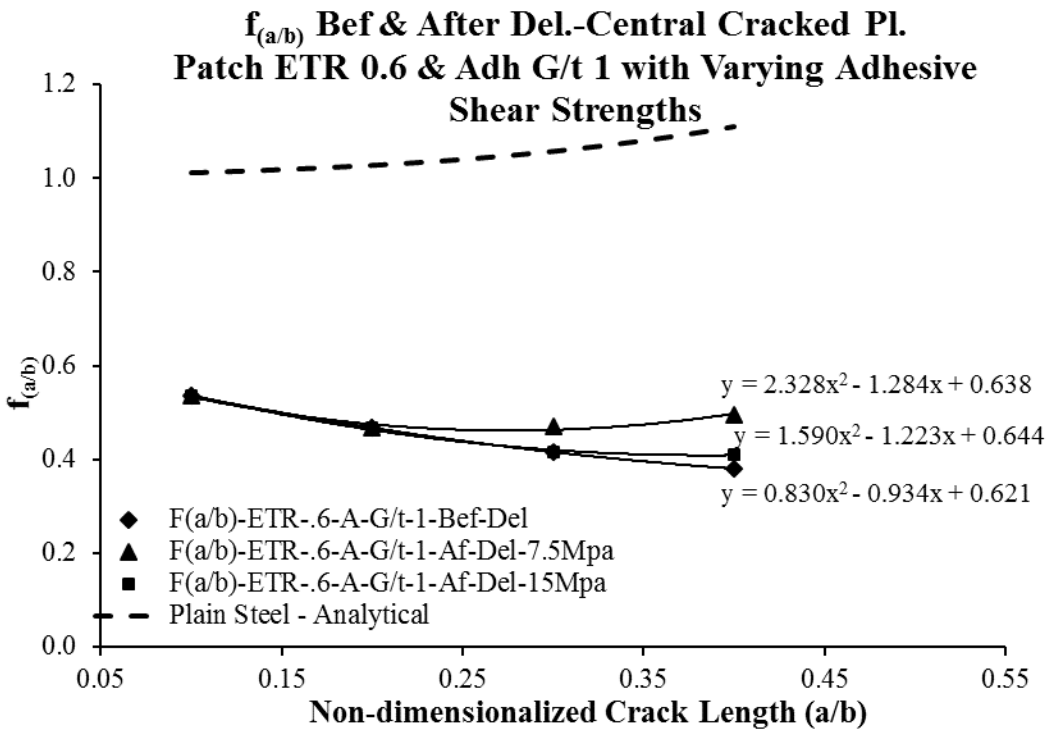

Figure 7.71 Geometric factor $f_{(a/b)}$ for central cracked specimens of ETR 0.6 and adhesive G_A/t_A 1 with varying adhesive shear strengths

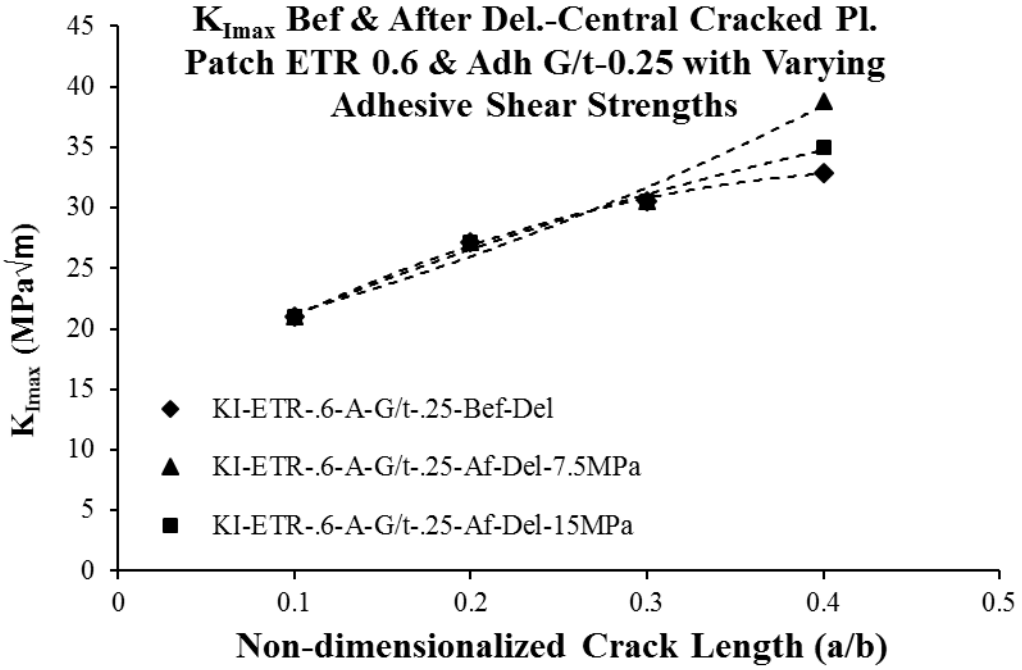

Figure 7.72 Variation of $K_{I\,max}$ in central crack specimens of ETR 0.6 and adhesive G_A/t_A 0.25 with varying adhesive shear strengths

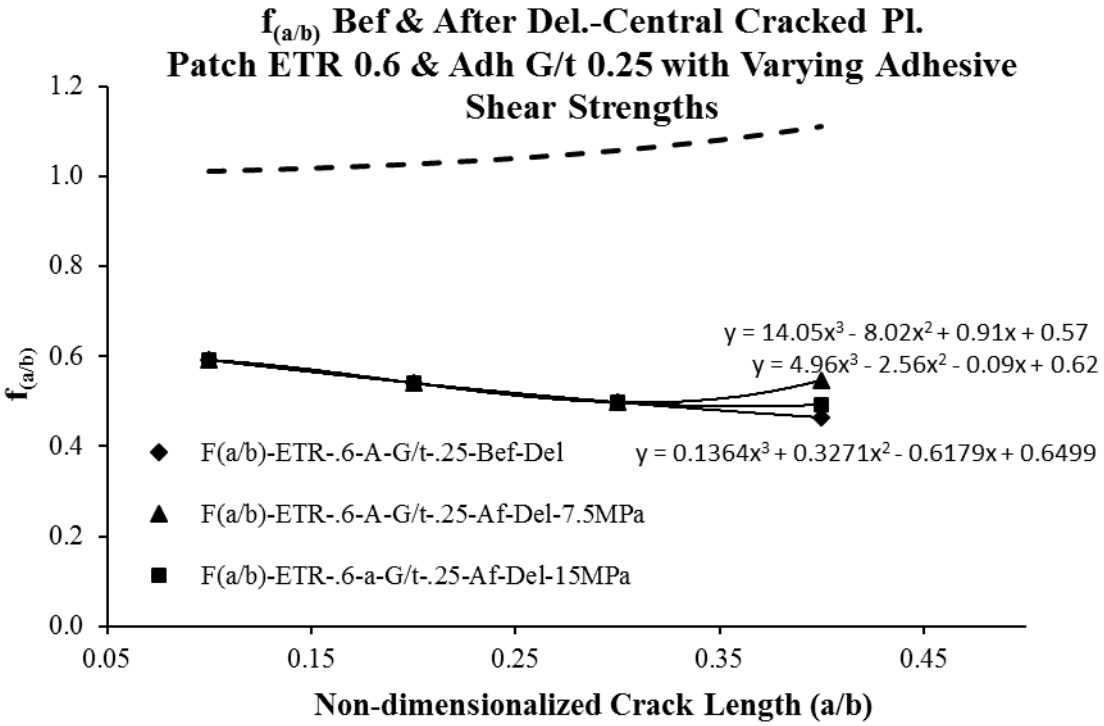

Figure 7.73 Geometric factor $f_{(a/b)}$ for central cracked specimens of ETR 0.6 and adhesive G_A/t_A 0.25 with varying adhesive shear strengths

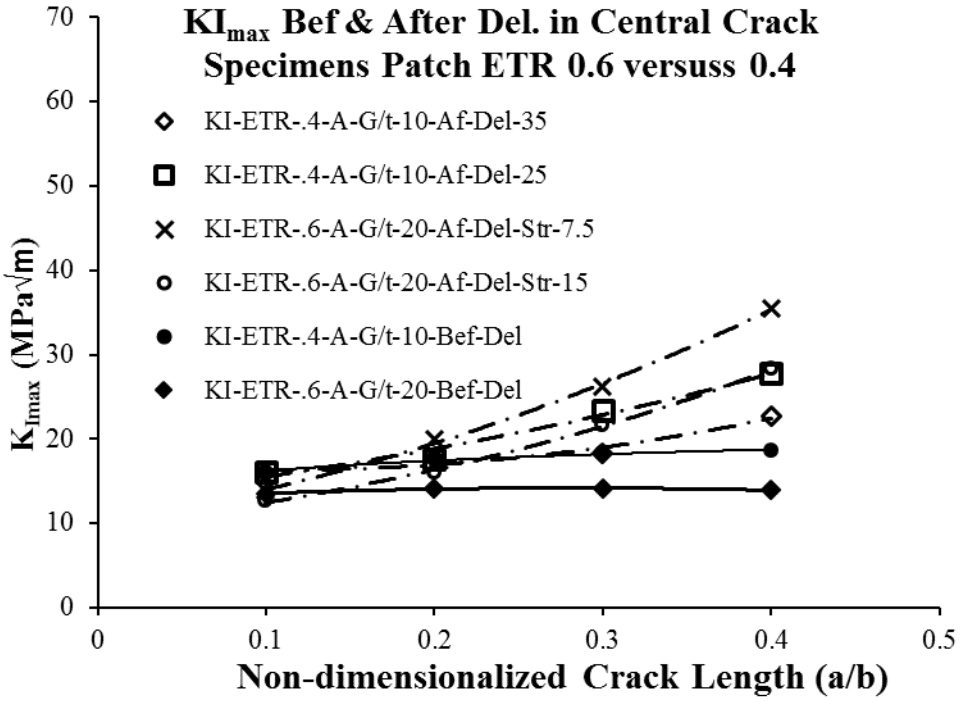

Figure 7.74 Comparison of impact of patch delamination between specimens of ETR 0.6 and ETR 0.4

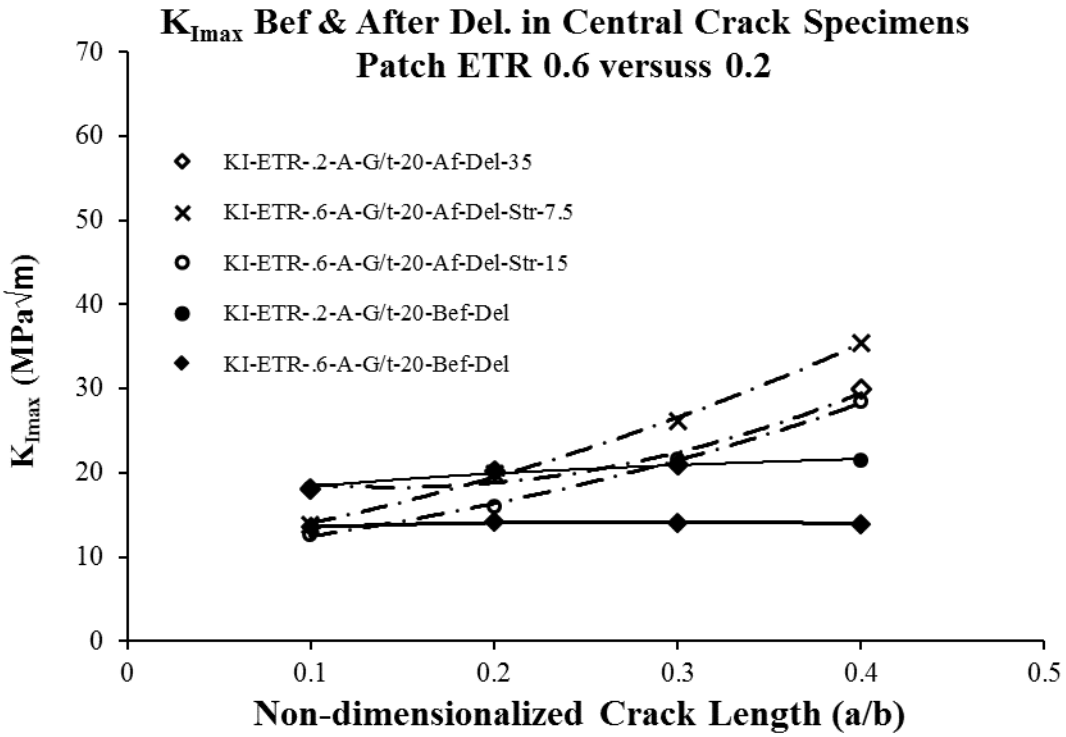

Figure 7.75 Comparison of impact of patch delamination between central cracked specimens of ETR 0.6 and ETR 0.2

8. Summary, conclusions and recommendations

8.1 Summary

Bonding fiber reinforced composites (FRC) or fiber reinforced polymers (FRP) has been successfully used in last three to four decades, in rehabilitation and strengthening of cracked and weak structural elements, made up of metal and concrete, by improving their stiffness, ultimate strength and the remaining fatigue life. Aircraft industry is the most beneficial and pioneered in successful use of FRC in repair of cracked and corroded parts of aircrafts. Use of FRC in repair and strengthening of civil infrastructure is much limited to the concrete structures and its use in repair or strengthening of steel structures has already been started but mostly flourishing in the experimental and research phase. Most of the previous research work considered ETR or the relative axial stiffness of the bonded FRP patch as the main and sole parameter in defining the effectiveness of the bonded FRP patch in enhancing ultimate tensile strength and fatigue life of the structural element with bonded FRP patch. But several experimental works have resulted in quite different fatigue life of cracked metal plates, repaired with bonded FRP patches, having identical or close ETR values, but with different modulus of elasticity (E_{FRP}) and thickness (t_{FRP}) of the FRP used. Some numerical research works also showed that the stress intensity factor (SIF) at the crack tip in steel plate, being repaired with two different moduli FRP (E_{FRP}), was differed by 20% to 24%, although the overall patch ETR was identical in the two (Lam and Cheng, 2008). Therefore, it deemed important to explore the reasons behind the discrepancies in getting different fatigue life or different SIF in identical or close ETR patched elements under same applied loading.

Patch delamination has shown to be the most common failure mode of cracked steel elements with bonded FRP patches under fatigue loading in most of the previous research works, but limited research work is available which explores and highlights the factors affecting initiation and propagation of the patch delamination. Similarly, the predictive tools for evaluation of fatigue life of bonded FRP steel elements, incorporating the impact of patch delamination, are

not available. Although Lam and Cheng (2008) developed the geometric factors $f_{(a/b)}$ that can be used with the application of linear elastic fracture mechanics to predict the fatigue life of bonded FRP steel plates, but those geometric factors did not incorporate the impact of patch delamination. These geometric factors would predict closer fatigue life of the bonded specimens if the adhesive shear strength used is extremely high to avoid the adhesive failure and the respective patch delamination. Therefore, the main objective of current research work was intended towards exploring the factors and patch parameters that can initiate or increase the risk of patch delamination under tensile loading or tensile part of fatigue loading and further to incorporate the impact of patch delamination in the fatigue life evaluation tools, for cracked steel plates with bonded FRP patch.

Initially a detailed numerical study was conducted on cracked steel plate, with bonded CFRP patches on its both faces to explore the factors and patch parameters affecting the distribution and magnitude of stresses in the interface adhesive layer of CFRP bonded repairs. The interface adhesive layer was selected for the study because most of the previous research works showed FRP patch delamination as the most common mode of failure of the FRP bonded steel plates, which occurred through the failure of adhesive or the interface of the FRP patch and the repaired steel plate. The patch parameters selected for that part of study included modulus of elasticity and thickness of adhesive and FRP layers (E_A, t_A, E_{FRP} and t_{FRP}). Additionally, impact of all abovementioned patch parameters was also studied on the stress intensity factor SIF for the crack opening mode (K_I), at the crack tip of the crack in the repaired steel plate being patched with the FRP layers. The results of this study specifically highlighted difference in stress distribution within the interface adhesive layer as well as in the SIF at the crack tip, between identical ETR patches, which can help in explaining the huge variation found in the fatigue life of tested cracked metal/steel plates bonded with identical ETR patches. Some parameters have been highlighted that greatly affect and control the interface stress distribution and SIF at the crack tip, other than the basic patch parameters of the study alone.

After developing good understanding of the factors and parameters affecting the magnitude and distribution of interface stresses, as well as the SIF at the crack tip in the patched plate, the next phase of current research was intended towards studying the impact of failure of the

interface adhesive layer, on the SIF at the crack tip in steel plate. It was because the previous research phase had already highlighted the presence of high shear stresses around the crack, indicating existence of some localized adhesive failure zone near the crack. The localized failure of adhesive or bond layer at the interface of FRP and steel plate physically causes a localized delaminated zone beneath the FRP patch, and therefore, in the current study, the impact of localized patch delamination has been studied numerically by introducing the strength failure of adhesive layer under high shear stresses. The study of impact of patch delamination was carried out numerically, through finite element analysis of cracked steel plates, with bonded CFRP patches with varying CFRP and adhesive properties. The results of study highlighted the impact of patch delamination on the SIF within the CFRP patches, having identical patch ETR but with different CFRP and adhesive properties.

An experimental phase was also planned and carried out to study the fatigue behavior of edge cracked steel plates, with varying patch parameters, including: ETR, E_{FRP}, E_A, t_{FRP}, t_A and the adhesive shear strength τ. Two different forms of CFRP with different E_{FRP} were used along with three different adhesives. Additionally, adhesive thickness was also varied in one type of the adhesive. Fatigue tests were carried out under constant amplitude tension-tension loading with stress range ($\Delta\sigma$) of 180 MPa and stress ratio (R) of 0.1. Test results showed two different delamination failure modes; near-crack delamination and the patch-end delamination. The patch-end delamination mode was found to be devastating and resulting in much reduced fatigue life. It mostly occurred in the specimens with more than one layer of higher modulus CFRP patches, which required a thicker adhesive layer. Test results also showed difference in the fatigue life up to 51% within identical ETR repair patches with different adhesive and CFRP types, excluding those specimens which failed in the patch-end delamination failure mode.

Validation of fatigue life of the experimentally tested specimens, was also carried out by numerically developing the geometric factors $f_{(a/b)}$ of the tested specimens through FEA and then using these in the Paris equation to predict the fatigue life of the tested specimens. Additionally, the impact of localized patch delamination was also introduced in the FEA through modelling the failure of interface adhesive layer, around the crack, under high shear stresses. Therefore, the developed geometric factors $f_{(a/b)}$ for the tested specimens were also

incorporating the impact of patch delamination. It was found that the geometric factors incorporating the impact of patch delamination provided close prediction of the fatigue life of tested specimens.

After successfully validating fatigue life of the tested specimens, using the developed methodology for predicting the fatigue life of cracked steel plates with bonded CFRP patches, an extensive parametric study was then carried out in the last part of the current research work. The main task of the parametric study was to develop the geometric factor $f_{(a/b)}$ corresponding to the variation of other patch parameters, including patch ETR, modulus of elasticity and thickness of CFRP and adhesive (E_{FRP}, E_A, t_{FRP}, t_A), adhesive shear stiffness (G_A/t_A) and adhesive shear strength (τ). Adhesive shear strength was selected as a parameter in order to have a source of introduction of localized patch delamination around the crack, which has shown to be providing more realistic geometric factors $f_{(a/b)}$. The geometric factors were developed for a range of the selected parameters but for the two more general crack locations; edge crack and the central crack.

8.2 Conclusions

The following conclusions are drawn on the basis of combination of numerical analysis of edge crack and central crack steel plates with double-sided bonded CFRP patch, under uniform tensile stress, as well as on the basis of experimental investigation of edge crack steel plates with double-sided bonded CFRP patch:

1. Results of FEA of edge cracked steel plates, with double-sided bonded CFRP patch, showed that the adhesive properties greatly affect the magnitude and distribution of interface adhesive stresses around the crack, as well as the stress intensity factor (K_I) at crack tip of the crack in the steel plate, while keeping the applied far-field tensile stress and the CFRP properties constant.

2. K_I always found to be varied inversely with the peak adhesive shear stress at the crack location.

3. Peak adhesive shear stress developed near the crack increases with either decrease in the adhesive thickness (t_A) or increase in its modulus of elasticity (E_A), while the SIF at the crack tip in steel plate increases with either increase in the adhesive thickness (t_A) or decrease in the adhesive modulus (E_A).

4. Adhesive G_A/t_A is found to be a better adhesive parameter than its thickness t_A or elastic modulus E_A in studying the variation of SIF at the crack tip or the variation of interface adhesive shear stress near the crack. For identical ETR CFRP patches, the interface peak adhesive shear stress near the crack increases by increasing the adhesive G_A/t_A, with a simultaneous decrease in the K_I at the crack tip of the crack in plate and vice versa.

5. Peak value of peel stress at patch-end is not affected by varying adhesive thickness t_A, rather it increases with increase in the adhesive elastic modulus E_A or the CFRP thickness t_{FRP}.

6. Without considering patch delamination in the numerical analysis, ETR is found to be the K_I controlling parameter, while keeping the interface adhesive properties constant. Same conclusion is also valid if patch delamination is considered in the numerical analysis, but at the same time the adhesive shear strength is quite high so that a negligible patch delamination is caused.

7. FEA is found to be a good tool for evaluating the K_I at the crack tip of crack in plates with bonded CFRP patches, and further to study the impact of localized patch delamination around the crack on the evaluated K_I.

8. Keeping the patch ETR and the applied far-field stress constant, the SIF (K_I) at the crack tip is found to be increased by the introduction of localized patch delamination around the crack in steel plate. The increase in K_I increases with the size or magnitude of the delaminated region.

9. For a given CFRP patched specimen the size of patch delaminated region depends upon the adhesive G_A/t_A and the adhesive shear strength τ, because G_A/t_A controls the distribution and magnitude of the peak adhesive shear stress around the crack, and the adhesive shear strength τ determines the boundary of failed adhesive region.

10. The K_I values at the crack tip of crack in steel plate, bonded with CFRP patch, with a higher ETR value, can increase above the K_I values of a steel plate with lower ETR patch, if the adhesive properties in the two patches are such that larger patch delamination occurs in higher ETR patch and negligible or very less patch delamination occurs in the lower ETR patch.

11. Experimental results of fatigue tests of edge cracked steel plate with double sided bonded CFRP patches showed that the specimens with higher ETR and higher elastic modulus CFRP patch mostly failed in the patch-end delamination mode, while none of the specimen with lower elastic modulus CFRP patch failed under the patch-end delamination failure mode.

12. Patch-end failure mode reduces the patch efficiency, as well as the expected fatigue life of thicker CFRP patches, fabricated using higher elastic modulus CFRP by more than 10 times compared to the specimens of lower elastic modulus CFRP.

13. Hybrid CFRP patched specimens also failed in the patch-end delamination failure mode because the first CFRP layer and the interface adhesive layer used in these were same as that of higher modulus CFRP specimens, which have already failed in the governing patch-end delamination failure mode. But the rate of delamination growth was slower in these, compared to the pure high modulus CFRP patches. Therefore the hybridization could not be successful until the interface adhesive properties not improve.

14. Fatigue life of specimens, not failed in the governing patch-end failure mode, can be well predicted using the currently developed methodology, which works on the numerically evaluated geometric factors $f_{(a/b)}$ for any patched specimen, with given adhesive and CFRP properties.

15. Fatigue life of the specimens, failed in the governing patch-end failure mode, could not be predicted using the currently developed methodology because of very less sensitivity of the K_I on the patch end delamination.

16. Fatigue life of the tested specimens, if predicted using the $f_{(a/b)}$ developed without consideration of patch delamination in the finite element analysis, is shown to be at least two to three times higher than that predicted considering the patch delamination in the finite element analysis.

17. From the parametric study, it can be concluded that adhesive shear strength is a significant parameter which can increase the SIF in a stiffer patch (with higher ETR), if it is provided with a weaker adhesive, due to more patch delamination caused by the adhesive shear failure.

8.3 Recommendations

From the experimental results of current research work it is obvious that the patch-end delamination under fatigue loading greatly reduces the predicted and expected fatigue life of bonded CFRP repaired steel plates provided with higher elastic modulus E_{FRP} CFRP. It might be because of weaker adhesive shear and bond strengths or it might also be because of the porous finish of the interface adhesive resulted in initiation of patch-end delamination from any weak point which then grew rapidly under the fatigue loading. It is therefore recommended to repeat those tests with inclusion of the following different options to avoid the patch end failure mode:

a. Using smaller applied stress range $\Delta\sigma$ with σ_{max} lesser than used here.
b. Using a different compatible adhesive with higher shear and bond strengths along with a smooth finish like the one used in the lower E_{FRP} CFRP specimens in current tests.
c. Using longer taper at the ends of high E_{FRP} CFRP plates than used in the current tests.

It has already been shown numerically in the current research that the K_I is sensitive to the patch delamination around the crack and K_I variation depends upon the magnitude of delaminated area but the delamination itself depends upon the adhesive (G_A/t_A) and shear strength (τ). It is therefore recommended to validate the patch delamination experimentally by performing fatigue tests with different adhesive shear strengths and shear stiffness and by monitoring the patch delamination during the test using either an optical telescope or any ultrasonic device. This validation will also increase the level of confidence in working of the methodology developed in this research. Care should be taken to avoid the patch end delamination by selecting strong adhesives and providing larger patch-end tapering.

The methodology developed in the chapter 6 to predict the fatigue life of the double sided bonded repaired cracked steel specimens could not predict the fatigue life of the specimens failed in the governing patch-end delamination failure mode. It is therefore recommended to develop similar methodology which could incorporate the patch-end delamination growth rate

with number of fatigue cycles until it reached the near-crack region. It may require some specific data of the delamination growth at the plate interface with different adhesive strengths and incorporating any interaction with the patch ETR.

Based on the SIF variation (or their corresponding geometric factors $f_{(a/b)}$ variations) provided in sections 7.5.1, 7.5.3, 7.5.5, 7.5.8, 7.5.10 and 7.512 it can be seen that the SIF or the $f_{(a/b)}$ variations are lying closely for the adhesive G_A/t_A of 0.25 and 1 as well as for the adhesive G_A/t_A of 10 and 20 but there is a noticeable gap between the SIF or the $f_{(a/b)}$ variations of adhesive G_A/t_A of 1 and 10. It is therefore recommended to generate the $f_{(a/b)}$ functions for more adhesive G_A/t_A cases ranging between 1 and 10.

The polynomial functions of the geometric factors $f_{(a/b)}$ are developed in the current research work using the results from four finite element models of each CFRP patched steel plate, corresponding to the four crack lengths (a/b) of 0.1, 0.2 0.3 and 0.4. It is therefore recommended to use more intermediate crack lengths models for each specimen in order to generate more refine polynomial functions of the geometric factors $f_{(a/b)}$.

The geometric factors $f_{(a/b)}$ are developed in the current research work for the two general cases of the edge crack and central crack locations with uniform far field applied stress. It is recommended to develop the geometric factors $f_{(a/b)}$ for the other crack geometries and loading conditions especially for the case of partial width CFRP patch which is more realistic for the repair of smaller cracks in large plate area.

List of References

Ahmad, A. S. 2011. Modelling wet lay-up CFRP–steel bond failures at extreme temperatures using stress-based approach. *International Journal of Adhesion & Adhesives*. 31: 416 – 428.

Alam, M.S. 2005. *Structural integrity and fatigue crack propagation life assessment of welded and weld-repaired structures*. Thesis, Department of Mechanical Engineering, Louisiana State University.USA.

Alawi, H. and Saleh, I. 1992. Fatigue crack growth Retardation by Bonding Patches. *Journal Engineering Fracture Mechanics*. 42, No. 5: 861-868.

Baker, A. A. 1987. Fiber composite repair of cracked metallic aircraft components – practical and basic aspects. *Composites*, September, 293 – 308.

Baker, A. A. 1993. Repair efficiency in fatigue-cracked aluminum components reinforced with boron/epoxy patches. *Fatigue & Fracture of Engineering Materials & Structures Ltd.* 16 (7): 753 – 765.

Barsoum, R.S. 1976. On the use of isoparametric finite elements in linear fracture mechanics. *International Journal for Numerical Methods in Engineering*. 10: 25-37.

Barsome, J. F and Rolfe, S.T. 1999. *Fracture and Fatigue Control in Structures: Application of Fracture mechanics*. Conshohokin: ASTM, Pennsylvania, USA.

Bassetti, A., Nussbaumer, A. and Colombi, P. 2000. Repair of riveted bridge members damaged by fatigue using CFRP materials, *Advanced FRP Materials for Civil Structures*, Bologna, Italy, 19th October 2000, pp. 33 – 42.

Bayraktar, E., and Kaplan, D. 2004. Mechanical and metallurgical investigation of martensite–austenite constituents in simulated welding conditions. *Material processing technology*. 153-154: 87-92.

Benrahou, K.H., Ameur, A., Tounsi, A., Benyoucef, S. and Bedia, A. 2010. Influence of adhesive characteristics on the interfacial stress concentrations in externally FRP plated steel beams. *Composite Interfaces*. 17: 283–300.

Bocciarelli, M., Colombi, P., Fava, G. and Poggi, C. 2009. Fatigue performance of tensile steel members strengthened with CFRP plates. *Composite Structures.* 87: 334-343.

Broek, D. 1986. *Elementary Engineering Fracture Mechanics*. Martinus Nijhoff, The Hague, Boston, USA.

Callinan, R., Sanderson, S. and Keeley, D. 1996. 3D FE Analysis of a bonded repair to an F-111 wing. *Proceeding of Australian Conference on Applied Mechanics* (ACAM 96), Institute of Engineers, Melbourne, Australia.

Chester, R. J, Walker, K. F. and Chalkley, P. D. 1999. Adhesively bonded repairs to primary aircraft structure. *International Journal of Adhesion and Adhesives*, 19: 1-8.

Colombi, P., Bassetti, A., and Nussbaumer, A. 2002. crack growth induced delamination on steel members reinforced by prestressed composite patch. *Fatigue and Fracture Engineering of Materials and Structures*, 26: 429 –437.

Colombi, P., Bassetti, A. and Nussbaumer, A. 2003a. Delamination effects on cracked steel members reinforced by prestressed composite patch, *Theoretical and Applied Fracture Mechanics*, 39: 61 – 71.

Colombi, P., Bassetti, A. and Nussbaumer, A. 2003b. Crack growth induced delamination on steel members reinforced by prestressed composite patch. *Fatigue and fracture Engineering Materials and Structures*. 26: 429-437.

Colombi, P., Bassetti, A., and Nussbaumer, A. 2003c. Analysis of cracked steel members reinforced by pre-stress composite patch, *Fatigue and Fracture Engineering of Materials and Structures*, 26: 59 – 66.

Dassault Systèmes Simulia Corporation (2010). *ABAQUS CAE 6.10*, Rhode Island, USA.

Dawood, M., Rizkalla, S, and Sumner, E. 2007. Fatigue and overloading behavior of steel–concrete composite flexural members strengthened with high modulus CFRP materials, *Journal of Composites for Construction, ASCE*, 11: 6(69).

Denney, J.J and Mall, S. 1997. Characterization of Disbond Effects on Fatigue Crack Growth behavior in Aluminum Plate with Bonded Composite Patch. *Engineering Fracture Mechanics*, 57, No. 5: 507-525

Duong, C. N. and Wang, C.H. 2007. *Composite repair-Theory and design*. Elsevier, Amsterdam, London.

Elber, W. 1971. The significance of fatigue crack closure, *ASTM STP 486*, *American Society for Testing and Materials*. 230-242.

Haris, J.A. and Fay, P.A. 1991. Fatigue life evaluation of structural adhesives for automotive applications. *International Journal of adhesion and adhesives*. 12(1): 9-18.

Hart-Smith, L. J. 1973. *Adhesive-bonded double-lap joints*. National Aeronautics and Space Administration, CR-112235, Langley Research Centre.

Holden, T. A. 2012. *Fatigue repair of coped steel beams using carbon fibre reinforced polymers*. Thesis, Department of Civil and Environmental Engineering, University of Alberta, Edmonton. Canada.

Irwin, G.R. 1957. Analysis of stresses and strains near the end of a crack transversing a plate. *Journal of Applied Mechanics*. 24:361.

Jones, R. and Callinan, R. J. 1976. Finite element analysis of patched cracks. *Journal of Structural Mechanics*, 7 (2): 107 – 130.

Jones, S. C. and Civjan, S. A. 2003. Application of fiber reinforced polymer overlays to extend steel fatigue life, *Journal of Composites for Construction*, 7, No. 4: 331 – 338.

Karbhari, V. M., and Shulley, S. B. 1995. Use of Composites for Rehabilitation of Steel Structures – Determination of Bond Durability. *Journal of Materials in Civil Engineering*, ASCE 7, No. 4: 239 – 245.

Kennedy, G.D. and Cheng, J.J.R.1988. *Repair of cracked steel elements using composite fiber patching.* Structural Engineering Report 221, Department of Civil and Environmental Engineering, University of Alberta, Edmonton, Canada.

Lam, A.C.C. and Cheng, J.J.R. 2008. *Repair of cracked steel structures by FRP patching.* Structural Engineering Report 285, Department of Civil and Environmental. Engineering. University of Alberta, Edmonton. Canada.

Leitner, M., Stoschka, M., Schanner, R. and Eichlseder. 2012. *Influence of high frequency peening on fatigue of high-strength steels*. Faculty of Mechanical Engineering Transaction, Belgrade, 40: 99 – 104.

Lin, C.T., Kao, P.W. 1995. Effect of fiber bridging on the fatigue crack propagation in carbon fiber reinforced aluminum laminates. *Materials Science and Engineering*. A190: 65-73.

Link, L.R. 1990. Fatigue crack growth of weldments. *Fatigue and Fracture Testing of Weldments, ASTM STP 1058*: 16 – 33.

Linwari, A., Thepchatri, T. and Albercht, P. 2006. Debonding strength of steel beams strengthened with CFRP plates. *Journal of Composites for Construction, ASCE*, 10: 1(69).

Liu, H., Al-Mahaidi, R. and Zhao, X. 2009. Experimental study of fatigue crack growth behaviour in adhesively reinforced steel structures. *Composite Structures*. 90: 12-20.

Madani, K., Touzan, S., Feaugas, X., Benguediab, M., and Ratwani, M. 2008. Numerical analysis for determination of stress intensity factors and crack opening displacements in plates repaired with single and double composite patches. *Computational materials Science*, 42: 385 - 393.

Meguid, S.A. 1989. *Engineering Fracture Mechanics*. Elsevier, Amsterdam, London.

Mertz, D.R., Gillespie, J.W., Chajes, M.J., Sabol, S.A., 2002. *Rehabilitation of steel bridge girders using advanced composite materials*. Transportation research board, NCHRP-IDEA Project-51.

Mobeen, S.S. and Cheng, J.J.R. 2015. Fatigue behaviour of cracked steel plates repaired with high and low modulus carbon fiber reinforced polymers. *3rd Speciality Conference on Material Engineering and Applied Mechanics, CSCE*, Regina, Canada.

Mokhtari, M., Madani, K., Belhouari, M., Touzain, S., Feaugas, X. and Ratwani, M. 2012. Effects of composite adherend properties on stresses in double lap bonded joints. *Materials and Design*. (Accepted manuscript).

Naboulsi, S. and Mall, S. 1996. Modeling of a cracked metallic structure with bonded composite patch using the three-layer technique. Composite structures, 35: 295-308.

Naboulsi, S. and Mall, S. 1997. Characterization of fatigue crack growth in aluminium panels with a bonded composite patch. *Composite structures*, 37 No. 34: 321-334.

Papanikos, P., Tserpes, K.I. and Pantelakis, S. 2007. Initiation and progression of composite patch debonding in adhesively repaired cracked metallic sheets. *Composite Structures.* 81:301-311.

Paris, P.C. and Erdogan, F. 1960. A critical analysis of crack propagation laws. *Journal of Basic Engineering*, 85: 528-534.

Parker, E.R., 1957. *Brittle Behavior of Engineering Structures*. National Academy of Sciences, National Research Council, John Wiley & Sons, New York.

Ratwani, M. 1979. Analysis of cracked, adhesively bonded metallic structures. *American Institute of Aeronautics and Astronautics,* 17: 988 - 994.

Rice, J. R. 1968. A path independent integral and approximate analysis of strain concentration by notches and cracks. *Journal of Applied Mechanics*. 35: 379-386.

San, J., C., S. 2005. Experiments on epoxie, polyurethane and ADP adhesives. Appendix A, Technical Report, C.C. Lab-2000.1b/1. *Composite Construction laboratory*, Ecole Polytechnique.

Schubbe, J. J. and Mall, S. 1999. Investigation of a cracked thick aluminum panel repaired with a bonded composite patch, *Engineering Fracture Mechanics*. 63: 305 – 323.

Schield, C., Hajjar, J., Nozaka, K, 2004. *Repair of fatigued steel bridge girders with carbon fiber strips*. Minnesota department of transportation. Report No. MN/RC – 2004-02.

Sika Canada Inc. *Product Data Sheet.* July 20013.

Tada, H., Paris, P.C., and Irwin, G.R. 1985. *The Stress Analysis of Cracks Handbook. 2nd ed*. Paris Productions, Inc. St. Louis.

Taljsten, B, Hansen, C. S., and Schmidt, J. W. 2009. Strengthening of old metallic structures in fatigue with prestressed and non-prestressed CFRP laminates. *Construction and Building materials*. 23: 1665 – 1677.

Tavakkolizdeh, M., and Saadatmanesh. H. 2003. Fatigue strength of steel girders strengthened with carbon fibre reinforced polymers. *Journal of Structural Engineering.* 129(2): 186-196.

Wu, C., Zhao, X., Duan, W., Al-Mahaidi, R. 2012. Bond charactersticks between ultra high modulus CFRP laminates and steel. *Thin-Walled Structures*. 51: 147 – 157.

Xia, S.H., Teng, J.G. 2005. Behaviour of FRP-Steel bonded joints. *Proceedings of the International Symposium on Bond Behaviour of FRP in Structures*. International Institute for FRP in Construction. 411-418.

Zhao, X. L., and Zhang, L. 2007. State-of-the-art review on FRP strengthened steel structures. *Engineering Structures*. 29:1808-1823.